THE JOURNAL
OF
CHEMICAL PHYSICS

VOLUME 33, NUMBER 2 AUGUST, 1960

On Inversion of the Linear Laws of Irreversible Thermodynamics

EUGENE HELFAND
Bell Telephone Laboratories, Inc., Murray Hill, New Jersey

(Received December 14, 1959)

A procedure is developed for inverting the linear laws of irreversible thermodynamics in spite of the singular nature of the admittance matrix when barycentric diffusion currents are employed. The procedure is symmetric in that it is unnecessary to identify one species as a reference solvent. Explicit relations are given for the new coefficients (resistance matrix, heats of transport, Soret thermal conductivity) in terms of the old. Constraints on the new coefficients are also obtained.

1. INTRODUCTION

IN handling the heat-matter linear laws of irreversible thermodynamics one is often confronted with a conflict between the retention of physically simple variables and mathematical convenience. On the one hand, it is desirable to define forces and fluxes for individual components. On the other hand, when this is done the matrix of phenomenological coefficients is singular so that certain required inversions cannot be directly performed with the usual techniques.

In the past, several authors have attempted to circumvent this difficulty by lowering the order of the matrix of phenomenological coefficients. DeGroot's[1] procedure is to define diffusion forces relative to a reference component. Bearman and Kirkwood[2] and Bearman[3] use related approaches. These efforts are well grounded in that the reduced matrices are the only uniquely defined measurables of the system. Nevertheless, such reduction schemes often result in a loss of physical clarity, especially in the development of microscopic theories. Furthermore, they have led to the custom of reporting heats of transport and resistance constants relative to one component designated, often arbitrarily, as solvent. Thus, if one begins by considering dilute solutions of A in B it is unphysical to still regard B as solvent when its mole fraction becomes small. The alternative of switching reference components is equally undesirable.

The point we wish to make is that the singularity of the phenomenological matrix does not preclude inversion of the linear phenomenological laws. The problem is similar to that encountered in the construction of a Hamiltonian formulation in relativity theory,[4] and to the situation which gives rise to coordinate conditions in the theory of gravitation or gauge conditions in electrodynamics. In this case the relation among the barycentric diffusion currents and the Gibbs-Duhem condition completely fix, so to speak, the gauge.

The new technique is mathematically no more difficult to comprehend, nor operationally difficult to perform, than an ordinary inversion. In the following section, the nature of the dilemma in the theory of isothermal diffusion is considered. In its barest mathematical terms the problem is solved in Sec. 3 and then the physical correspondence is drawn. Finally, the extension to nonisothermal situations is presented.

2. NATURE OF THE PROBLEM

One of the simplest problems upon which we may focus our attention arises with an n-component, isothermal, diffusing system wherein the linear laws are applicable

$$j_i=\sum_{k=1}^{n}L_{ik}X_k, \qquad i=1,\cdots,n; \tag{2.1}$$

or in matrix notation[5]

$$\mathbf{j}=\mathbf{L}\cdot\mathbf{X}. \tag{2.2}$$

[1] S. R. DeGroot, *Thermodynamics of Irreversible Processes* (North-Holland Publishing Company, Amsterdam, 1952), p. 103.
[2] R. J. Bearman and J. G. Kirkwood, J. Chem. Phys. **28**, 136 (1958).
[3] R. J. Bearman, J. Chem. Phys. **28**, 662 (1958).
[4] R. H. Penfield, Phys. Rev. **84**, 737 (1951).
[5] The vector nature of the fluxes j_i and forces X_k in a continuous system is evident so that they need not be denoted by boldface. In any event, they are usually all parallel so that a signed magnitude suffices as a specification. We avail ourselves of the boldface type for row and column matrices.

Copyright © 1960 by the American Institute of Physics

The Onsager reciprocal relations state that the phenomenological matrix, L, is symmetric. The diffusion forces X_k are negative gradients of the total chemical potential and are related by the Gibbs-Duhem equation

$$\sum_{k=1}^{n}\rho_k X_k=-\nabla p+\sum_{k=1}^{n}\rho_k F_k=W, \tag{2.3}$$

where ρ_k is the mass density of k, p is the pressure, F_k is the external force on unit mass of k, and W is defined by Eq. (2.3). In the usual state of mechanical equilibrium W is zero,[6] but for our mathematical development there is no need to specialize to this situation.

The barycentric mass diffusion currents are defined relative to the center of mass motion and are thus related by

$$\sum_{i=1}^{n}j_i=0. \tag{2.4}$$

When Eq. (2.1) is summed over i and use is made of Eq. (2.4) and the independence of the forces one finds

$$\sum_{i=1}^{n}L_{ik}=0, \qquad k=1,\cdots,n. \tag{2.5}$$

The L matrix is therefore singular and its inverse does not exist. Nevertheless, Eq. (2.1) may be written with the flows as independent variables and the forces as dependent variables, as we shall see in the following sections.

3. INVERSION OF LINEAR LAWS WITH A SINGULAR MATRIX

Let us consider a mathematical problem, the solution of which will provide us with the way out of the dilemma so far posed. We are given a set of variables y_i which are linearly related to variables z_k by the equations (in matrix form)

$$\mathbf{y}=\mathsf{A}\cdot\mathbf{z}, \tag{3.1}$$

where the matrix A is symmetric. The vector $\mathbf{y}$ is constrained to be orthogonal to a given direction,

$$\mathbf{y}\cdot\mathbf{e}_1=0. \tag{3.2}$$

On dotting Eq. (3.1) into $\mathbf{e}_1$ we find, if $\mathbf{z}$ may take on all values,

$$\mathsf{A}\cdot\mathbf{e}_1=0; \tag{3.3}$$

i.e., $\mathbf{e}_1$ is an eigenvector of A with eigenvalue zero. Finally, the value of the projection of $\mathbf{z}$ in the direction $\mathbf{e}_1$ is given by

$$\mathbf{z}\cdot\mathbf{e}_1=m. \tag{3.4}$$

The problem is to write Eq. (3.1) with $\mathbf{y}$ as the independent variable and $\mathbf{z}$ as the dependent variable.

[6] See DeGroot (footnote 1), p. 106.

A symmetric matrix may be written in terms of its eigenvalues α_s and its eigenvectors $\mathbf{e}_s$, which form an orthonormal basis for the space, as

$$\mathsf{A}=\sum_{s=1}^{n}\alpha_s\mathbf{e}_s\mathbf{e}_s. \tag{3.5}$$

In the case under consideration, the eigenvalue α_1 goes to zero. The inverse of A is

$$\mathsf{A}^{-1}=\sum_{s=1}^{n}\alpha_s^{-1}\mathbf{e}_s\mathbf{e}_s, \tag{3.6}$$

which indicates how A^{-1} blows up as $\alpha_1\to 0$. When, however, both sides of (3.1) are multiplied by A^{-1} we find

$$\mathbf{z}=\mathbf{e}_1\left(\frac{\mathbf{e}_1\cdot\mathbf{y}}{\alpha_1}\right)+\sum_{s=2}^{n}\alpha_s^{-1}\mathbf{e}_s\mathbf{e}_s\cdot\mathbf{y}, \tag{3.7}$$

so that, by Eq. (3.2), the singularity is removed. The value of the indeterminant form $\mathbf{e}_1\cdot\mathbf{y}/\alpha_1$ may be found by multiplying Eq. (3.7) by $\mathbf{e}_1$ and apply Eq. (3.4) to obtain

$$\mathbf{e}_1\cdot\mathbf{y}/\alpha_1=m. \tag{3.8}$$

The result of this inversion is

$$\mathbf{z}=m\mathbf{e}_1+\mathsf{B}\cdot\mathbf{y}, \tag{3.9}$$

where B is a symmetric matrix defined by

$$\mathsf{B}=\sum_{s=2}^{n}(1/\alpha_s)\mathbf{e}_s\mathbf{e}_s. \tag{3.10}$$

By dotting B into $\mathbf{e}_1$ we find

$$\mathsf{B}\cdot\mathbf{e}_1=0, \tag{3.11}$$

so that $\mathbf{e}_1$ is also an eigenvector of B with zero eigenvalue.

4. APPLICATION TO THE LINEAR LAWS FOR DIFFUSION

The correspondence between the diffusion problem of Sec. 2 and the mathematical problem of Sec. 3 involves the identifications

$$y_i=j_i/\rho_i^{\frac{1}{2}}, \tag{4.1}$$

$$z_k=\rho_k^{\frac{1}{2}}X_k, \tag{4.2}$$

$$A_{ik}=L_{ik}/\rho_i^{\frac{1}{2}}\rho_k^{\frac{1}{2}}. \tag{4.3}$$

Equation (2.4) indicates that the vector $\mathbf{e}_1$ is

$$e_{1,i}=\rho_i^{\frac{1}{2}}/\rho^{\frac{1}{2}}, \tag{4.4}$$

where $\rho=\sum\rho_i$ is the total mass density. The Gibbs-Duhem equation may be used so show that

$$m=W. \tag{4.5}$$

After dividing through by $\rho_k^{\frac{1}{2}}$, Eq. (3.9) becomes

$$X_k=\rho^{-1}W+\sum_{i=1}^{n}R_{ki}j_i, \qquad k=1,\cdots,n, \tag{4.6}$$

where the resistance matrix is given in terms of B by

$$R_{ki}=B_{ki}/\rho_k^{\frac{1}{2}}\rho_i^{\frac{1}{2}}, \tag{4.7}$$

and is symmetric. Since $\mathbf{e}_1$ is an eigenvector of B with eigenvalue zero, the R_{ki}'s are related by

$$\sum_{i=1}^{n}R_{ki}\rho_i=0. \tag{4.8}$$

For numerical evaluation of $\mathbf{R}$ one may proceed by determining the eigenvalues and vectors of $\mathbf{A}$ and applying Eqs. (3.10) and (4.7). Alternatively, one may use the representation of $\mathbf{R}$ in terms of $\mathbf{L}$ derived in Appendix I.

5. NONISOTHERMAL SYSTEMS

Transport phenomena in nonisothermal systems are described by the linear laws

$$q=L_{00}X_0+\sum_{k=1}^{n}L_{0k}X_k, \tag{5.1}$$

$$j_i=L_{i0}X_0+\sum_{k=1}^{n}L_{ik}X_k, \tag{5.2}$$

where the heat flow q is the energy flow less the diffusive flow of enthalpy; the heat force is $X_0=-\nabla \ln T$; and the diffusion forces are now negative isothermal gradients of chemical potential, $X_k=-\nabla_T\tilde{\mu}_k=-\nabla\tilde{\mu}_k-\bar{S}_k\nabla T$.[7] The reciprocal relations now state that

$$L_{ik}=L_{ki}, \qquad i,k=0,1,\cdots,n. \tag{5.3}$$

The extended form of Eq. (2.5) is

$$\sum_{i=1}^{n}L_{ik}=0, \qquad k=0,1,\cdots,n. \tag{5.4}$$

In certain cases, such as in studying the Soret effect or in developing a statistical mechanical formalism,[2] it is convenient to have the force X_0 and the flows j_i as independent variables. Such a partial inversion may be achieved with the technique of the previous sections. One finds that

$$q=(\lambda T)X_0+\sum_{k=1}^{n}Q_k^*j_k, \tag{5.5}$$

$$X_i=-Q_i^*X_0+\sum_{k=1}^{n}R_{ik}j_k+\rho^{-1}W. \tag{5.6}$$

The thermal conductivity in Soret stationary state, λ, is defined by

$$\lambda T=L_{00}-\sum_{i,k=1}^{n}L_{0i}R_{ik}L_{k0}. \tag{5.7}$$

The heats of transport are given by

$$Q_i^*=\sum_{k=1}^{n}L_{0k}R_{ki}, \tag{5.8}$$

which when multiplied by ρ_1 and summed over i, yields, according to Eq. (4.8), the constraint

$$\sum_{i=1}^{n}\rho_iQ_i^*=0. \tag{5.9}$$

There exist $(n-1)$ independent measurements which can be performed to yield relations among the Q^*'s. These, together with Eq. (5.9), determine the individual heats of transport.

Equation (5.9) has an interesting consequence for electrolytic solutions, as has been pointed out elsewhere.[8] The heat of transport of a strong electrolyte is equal to a constant plus a term of order $c^{\frac{1}{2}}$ (where c is ionic concentration). The relation among the Q^*'s tells us that the heat of transport of the solvent must begin with $0(c)$. Therefore the difference between absolute and relative heats of transport first effects the electrolytes Q^* in the c term.

6. CONCLUSION

In conclusion we would like to point out other possible applications of this work in the field of irreversible thermodynamics. Obviously the procedure may be reversed to determine the admittance matrix $\mathbf{L}$ from the resistance matrix $\mathbf{R}$.

Further restraints, such as the existence of instantaneous chemical equilibria among some of the constituents, introduce more zero eigenvalues, which may be handled in a similar manner.

7. ACKNOWLEDGMENT

The author wishes to express his appreciation to Dr. Melvin Lax of the Bell Telephone Laboratories for pointing out the advantages of representing the solution to this problem in terms of eigenvectors and eigenvalues, and for valuable comments on the manuscript.

APPENDIX

In this appendix we shall derive a rather simple expression for the $\mathbf{R}$ matrix in terms of the $\mathbf{L}$ matrix.

To calculate $\mathbf{B}$ we increase the first eigenvalue of $\mathbf{A}$ by γ; i.e., we write

$$\mathbf{G}=\mathbf{A}+\gamma\mathbf{e}_1\mathbf{e}_1. \tag{A.1}$$

The definition of $\mathbf{B}$ is equivalent to

$$\mathbf{B}=\lim_{\gamma\to\infty}\mathbf{G}^{-1}. \tag{A.2}$$

[7] This choice of forces and fluxes, corresponding to the double prime units in Sec. 52. II of DeGroot,[1] is convenient for the description of heat-matter cross effects, but, of course, is in no way essential to the argument.

[8] E. Helfand and J. G. Kirkwood, J. Chem. Phys. 32, 857 (1960).

Using the correspondence of Eqs. (4.3) and (4.4) one has

$$G_{ik}=\rho_i^{-\frac{1}{2}}\rho_k^{-\frac{1}{2}}L_{ik}+\gamma\rho^{-1}\rho_i^{\frac{1}{2}}\rho_k^{\frac{1}{2}}. \tag{A.3}$$

The initial step in determining $\mathbf{G}^{-1}$ is to calculate the determinant, $|\mathbf{G}|$, given by

$$|\mathbf{G}|=(\prod_{i=1}^{n}\rho_i)\,|\mathbf{C}+\rho^{-1}\gamma\mathbf{S}^{(n)}|, \tag{A.4}$$

where the matrices $\mathbf{C}$ and $\mathbf{S}^{(n)}$ are given by

$$C_{ik}=L_{ik}/\rho_i\rho_k, \tag{A.5}$$

$$S_{ik}^{(n)}=1, \qquad i,k=1,\cdots,n. \tag{A.6}$$

By application of the usual rules for determinants[9] and the fact that $|\mathbf{C}|=0$ it can be shown that

$$|\mathbf{C}+\rho^{-1}\gamma\mathbf{S}^{(n)}|=\rho^{-1}\gamma\sum_{i,k=1}^{n}(-1)^{i+k}|\mathbf{C}^{ik}| \tag{A.7}$$

where $|\mathbf{C}^{ik}|$ is the ik minor of $\mathbf{C}$; i.e., $\mathbf{C}^{ik}$, which we shall call a minor matrix, is formed by striking out the ith row and kth column of $\mathbf{C}$. The matrix $\mathbf{C}^a$, whose ik element is $(-1)^{i+k}|\mathbf{C}^{ki}|$ is called the adjoint of $\mathbf{C}$. Since $\mathbf{C}$ is a matrix of order n and rank $(n-1)$, its adjoint is a dyad of the form $\beta\mathbf{v}\mathbf{v}$ where $\mathbf{v}$ obeys the condition[10]

$$\mathbf{C}\cdot\mathbf{v}=0. \tag{A.8}$$

[9] H. Margenau and G. M. Murphy, *Mathematics of Physics and Chemistry* (D. Van Nostrand Company, Inc., Princeton, New Jersey, 1956), p. 303, rules 1b, 4, and Eq. (10-2).

[10] R. A. Frazer, W. J. Duncan, and A. R. Collar, *Elementary Matrices* (Cambridge University Press, New York, 1946), Secs. 1.10, 1.12, and 4.12.

Relation (2.5) expressed in terms of the C_{ik} is

$$\sum_{i=1}^{n}C_{ki}\rho_i=0, \qquad k=1,\cdots,n. \tag{A.9}$$

so that $\mathbf{v}$ is identified as the vector whose ith element is ρ_i. In order to determine the constant β we may look at any element of $\mathbf{C}^a$. For example, the ik element, $(-1)^{i+k}|\mathbf{C}^{ki}|$, must equal $\beta\rho_i\rho_k$, so that $\beta=(-1)^{i+k}|\mathbf{C}^{ki}|/\rho_i\rho_k$ is a constant. Inserting this result into Eq. (A.7) we obtain

$$|\mathbf{G}|=\gamma(-1)^{i+k}|\mathbf{C}^{ki}|\,\rho\rho_i^{-1}\rho_k^{-1}\prod_{j=1}^{n}\rho_j.$$

By a straightforward application of the same determinant rules we find that the adjoint of $\mathbf{G}$ is given by

$$\begin{aligned}G_{ik}{}^a&=(-1)^{i+k}|\mathbf{G}^{ki}|\\&=(-1)^{i+k}|\mathbf{C}^{ki}+\rho^{-1}\gamma\mathbf{S}^{(n-1)}|\\&=(-1)^{i+k}[\rho_i^{-\frac{1}{2}}\rho_k^{-\frac{1}{2}}\prod_{j=1}^{n}\rho_j]\\&\cdot[|\mathbf{C}^{ki}|+\rho^{-1}\gamma\sum_{l=1\neq k}^{n}\sum_{m=1\neq i}^{n}(-1)^{l+m}|(\mathbf{C}^{ki})^{lm}|].\end{aligned} \tag{A.10}$$

The inverse is defined as the adjoint divided by the determinant so that (using the symmetry of the matrices)

$$\begin{aligned}R_{ik}&=\rho_i^{-\frac{1}{2}}\rho_k^{-\frac{1}{2}}\lim_{\gamma\to\infty}G_{ik}{}^{-1}\\&=\rho^{-2}\sum_{l=1\neq k}^{n}\sum_{m=1\neq i}^{n}(\mathbf{C}^{ki})_{lm}{}^{-1};\end{aligned} \tag{A.11}$$

i.e., R_{ik} is equal to the sum of the elements of the inverse ki minor matrix of $\mathbf{C}$, divided by ρ^2.

Perturbation of Molecular Rotation-Vibration Energy Levels by Rare Gases*

D. H. RANK, D. P. EASTMAN, W. B. BIRTLEY,† AND T. A. WIGGINS

Physics Department, The Pennsylvania State University, University Park, Pennsylvania

(Received February 26, 1960)

The shift in frequency of lines of the 2–0 band of HCl and of the $\nu_1+\nu_3$ band of C_2H_2 due to the presence of krypton and xenon as foreign gases has been measured. A marked J dependence was observed. The relative shifts in the upper and lower states of the transitions were calculated from the shifts in the $\Delta_2F''(J)$ and $\Delta_2F'(J)$ values obtained from the measured line shifts. In the case of HCl the shifts in the rotational levels were markedly different in the upper and lower states, the upper state shift being proportional to J, while the lower-state energy-level shifts approach an asymptotic value for high J. For C_2H_2 the shifts in both levels resembled the shift in the lower state of HCl.

I. INTRODUCTION

RECENTLY in communications to this Journal announcements have been made by Kimel, Hirshfeld, and Jaffe[1,2] and Rank, Birtley, Eastman, and Wiggins[3] of measurements made on the shifts of molecular band lines whose wavelengths are perturbed by foreign gases. The salient features of these perturbations are that they are relatively small and definitely J dependent. Furthermore, the perturbations increase for high J's approximately proportionally to the optical polarizability of the foreign gas. In spite of the smallness of the perturbations it has been demonstrated that the infrared spectrometers available at Rehovoth, Israel, and University Park, Pennsylvania, are both capable of measuring these shifts with considerable precision.

We have now made measurements on the shifts produced on the lines of the 2–0 band of HCl produced both by krypton and xenon. We were able to make measurements in the P and R branches of this band to $J=10$. We have also measured the shifts produced by krypton and xenon of the P- and R-branch lines of the $\nu_1+\nu_3$ band of C_2H_2 In the case of C_2H_2 the measurements were made on selected band lines whose J values were as large as $J=29$.

II. EXPERIMENTAL

The absorption spectra were obtained using an absorption tube of 1-m length. The pressure of HCl or C_2H_2 required to produce sufficient absorption for accurate measurements ranged from a small fraction of a millimeter for the strongest lines up to 1 or 2 cm for the very weakest line (highest J value). The krypton or xenon pressures used approached atmospheric pressure in magnitude.

The spectrograph used to measure the line shifts has been described previously.[4] We have further modified this instrument thus improving its performance considerably. A complete description of the modified instrument is now in press.[5] In our recent communication[3] on this subject we have illustrated the method used to measure the wavelength shifts of the band lines.

It is of course only possible to measure the shifts of the spectrum lines which are transitions between two rotational levels. The interesting feature of this phenomenon is to extract as much information as possible concerning the upper and lower states from the experimental data. In order to examine the upper and lower states in the most quantitative manner it is necessary to have as precise experimental data as possible. In the case of HCl, Hirshfeld, Jaffe, and Kimel[2] have published their experimental data for perturbation produced by krypton. Dr. Jaffe has communicated his results for xenon in advance of publication.

In Fig. 1 we have plotted the experimental results obtained by us and also the results of Jaffe and his coworkers on the shifts of the HCl lines vs m for the P and R branches of the 2–0 band. For the R branch $m=J+1$, for the P branch $-m=J$. The experimental measurements have been normalized to 1 atm of gas under standard conditions assuming linearity of shift with gas density. The points indicated by circles in Fig. 1 represent data obtained by Jaffe and his co-workers. Our experimental points are represented by triangular points. It can be seen from Fig. 1 that the agreement between the two sets of measurements is excellent.

We are indebted to Dr. Jaffe for communicating his results on the xenon shifts in advance of publication. The availability of two independent sets of data gives us increased confidence in the analysis which follows.

In Fig. 2 we have displayed our experimental measurements made on the shifts produced by krypton and xenon of the C_2H_2 band lines in a manner identical to that used to prepare Fig. 1. In both Fig. 1 and Fig. 2

* This research was assisted by support from the Office of Naval Research.

† The participation of W. B. B. in this work was supported by HRB-Singer, Inc., State College, Pennsylvania.

[1] S. Kimel, M. A. Hirshfeld, and J. H. Jaffe, J. Chem. Phys. **31**, 81 (1959).

[2] M. A. Hirshfeld, J. H. Jaffe, and S. Kimel, J. Chem. Phys. **32**, 297 (1960).

[3] D. H. Rank, W. B. Birtley, D. P. Eastman, and T. A. Wiggins, J. Chem. Phys. **32**, 296 (1960).

[4] D. H. Rank, G. D. Saksena, G. Skorinko, D. P. Eastman, T. A. Wiggins, and T. K. McCubbin, Jr., J. Opt. Soc. A. **49**, 1217 (1959).

[5] D. H. Rank, D. P. Eastman, W. B. Birtley, G. Skorinko, and T. A. Wiggins, J. Opt. Soc. Am. (to be published).

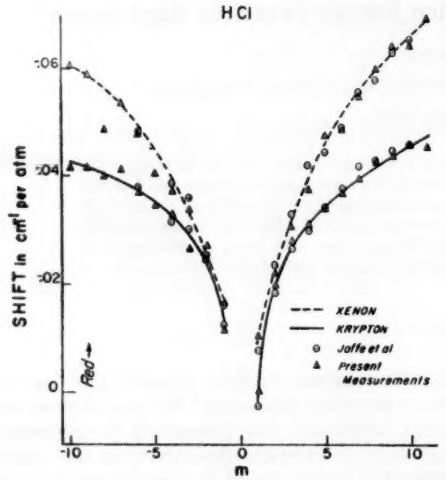

FIG. 1. Frequency shift in cm^{-1} of lines of the 2–0 band of HCl due to standard atmospheres of krypton and xenon as foreign gases.

we have drawn smooth curves to give what we consider to be the best representation of the fit of the data points.

III. ANALYSIS OF THE DATA

From the curves shown in Figs. 1 and 2 we have obtained smoothed values for the shifts of the various spectral lines which have been measured. These smoothed values obtained from the curves are given in Tables I and II.

It can be seen by inspection of Figs. 1 and 2 that the shifts of the spectral lines are not symmetric about the origin of coordinates thus suggesting that the perturbations produced by the foreign gas are different for upper and lower states. It is of course immediately obvious that one can apply the combination principle to the shifts in the same way as it is normally applied to the line frequencies themselves. For the lower and upper state we can write the combination relations

$$\delta_2 F'' = \delta R(J-1) - \delta P(J+1)$$

$$\delta_2 F' = \delta R(J) - \delta P(J),$$

where $\delta R(J)$, etc., refer to pressure-induced shifts and the $\delta_2 F$ values express the perturbation of the interval between the two levels in question.

From Table I we have calculated the $\delta_2 F''$ and $\delta_2 F'$ values for HCl gas perturbed by a standard atmosphere of krypton and xenon. We have plotted these values

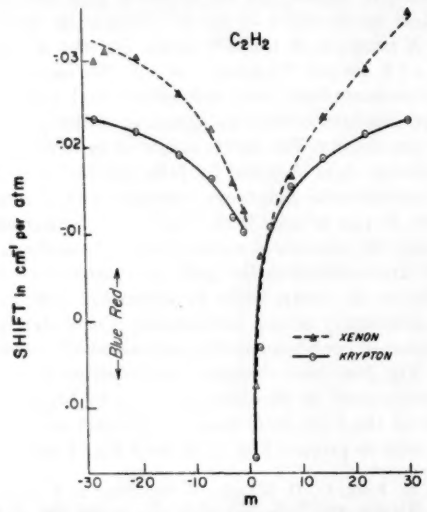

FIG. 2. Frequency shift in cm^{-1} of lines of the $\nu_1+\nu_3$ band of C_2H_2 due to standard atmospheres of krypton and xenon as foreign gases.

TABLE I. Smoothed values of the shift in cm^{-1} of lines of the 2–0 band of HCl for a standard atmosphere of krypton or xenon as the foreign gas.

	R branch		*P* branch	
J	Kr	Xe	Kr	Xe
0	+0.0015	−0.0087		
1	−0.0190	−0.0236	−0.0118	−0.0163
2	−0.0270	−0.0323	−0.0243	−0.0262
3	−0.0315	−0.0395	−0.0289	−0.0334
4	−0.0331	−0.0456	−0.0323	−0.0388
5	−0.0380	−0.0502	−0.0350	−0.0441
6	−0.0403	−0.0547	−0.0369	−0.0483
7	−0.0422	−0.0589	−0.0388	−0.0524
8	−0.0441	−0.0627	−0.0403	−0.0555
9	−0.0452	−0.0657	−0.0414	−0.0589
10	−0.0460	−0.0688	−0.0422	−0.0616

TABLE II. Measured and smoothed values for the shifts in cm^{-1} of lines in the $\nu_1+\nu_3$ band of C_2H_2 for standard atmosphere of krypton and xenon as foreign gases.

	Kr		Xe	
J	Meas	Smooth	Meas	Smooth
R(0)	+0.0157	+0.0176	+0.0073	+0.0075
1	+0.0030	+0.0024	−0.0075	−0.0065
3	−0.0108	−0.0092		
7	−0.0155	−0.0154	−0.0167	−0.0169
13	−0.0188	−0.0191	−0.0235	−0.0234
21	−0.0217	−0.0217	−0.0290	−0.0298
29	−0.0232	−0.0233	−0.0355	−0.0347
P(1)	−0.0103	−0.0096	−0.0127	−0.0127
3	−0.0120	−0.0128	−0.0158	−0.0168
7	−0.0164	−0.0165	−0.0220	−0.0220
13	−0.0192	−0.0194	−0.0262	−0.0262
21	−0.0218	−0.0218	−0.0303	−0.0302
27			−0.0321	−0.0324
29	−0.0233	−0.0233	−0.0300	−0.0330

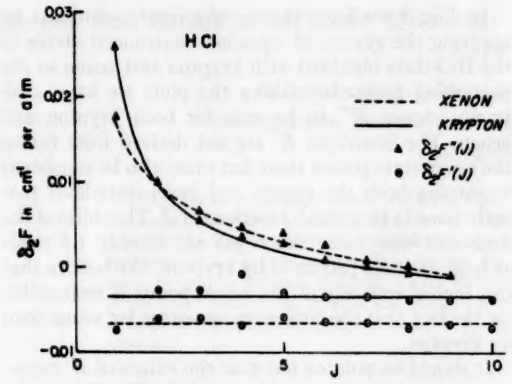

FIG. 3. Change in the values $\Delta_2F'(J)$ and $\Delta_2F''(J)$ for HCl in cm^{-1} due to a standard atmosphere of krypton and xenon plotted vs J. (*Note.* Ordinate scale is incorrect. The decimal point should be moved to read 0.01, etc.)

obtained from Table I vs J in Fig. 3. The points indicated in Fig. 3 merely reflect the smoothness or lack of smoothness of the original curves displayed in Fig. 1 (the plots of the original experimental data on the line shifts). Inspection of Fig. 3 shows that the δ_2F' values are perturbed by a constant amount independent of J. We believe that the experimental results show that the perturbation of the upper-state Δ_2F' values is different from zero and larger for xenon than for krypton. The curves shown in Fig. 3 which represent the δ_2F'' values for the ground state show a very marked J dependence.

The results shown in Fig. 3 demonstrate that for HCl the B' value for the perturbed gas approaches its unperturbed value for high J, i.e., perturbation of B' value will be $\delta_2F'/4J+2$, $\delta_2F'=$constant. This same conclusion can also be drawn in an approximate manner for the B' of C_2H_2 from the plots shown in Fig. 4.

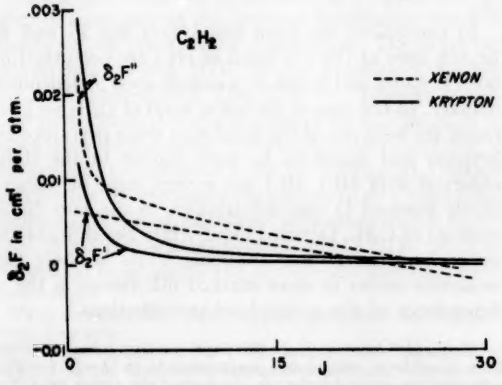

FIG. 4. Change in the values of $\Delta_2F'(J)$ and $\Delta_2F''(J)$ for C_2H_2 in cm^{-1} due to a standard atmosphere of krypton and xenon plotted vs J. (*Note.* Ordinate scale is incorrect. The decimal point should be moved to read 0.01, etc.)

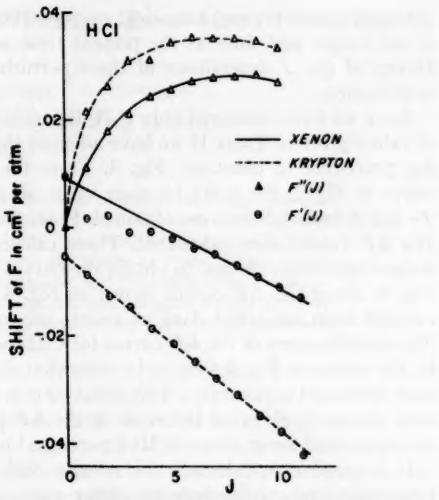

FIG. 5. Relative shift in cm^{-1} in the rotational energy levels in HCl for the upper and lower states due to a standard atmosphere of krypton and xenon. The shift of the lower-state level for $J=0$ is assumed to be zero for each foregin gas. (*Note.* The $F''(J)$ curves are incorrectly labeled. The krypton curve is the one indicated by the dashed line. The $F'(J)$ curves are labeled correctly.)

However, in the case of C_2H_2 the experimental data seems to show that because of the apparent slight J dependence of the δ_2F' values the approach of the perturbed B' value to its unperturbed value is more rapid than in HCl.

It would, of course, be possible to fit the curves in Figs. 3 and 4 that involve the lower state to some mathematical expression. We have not attempted this

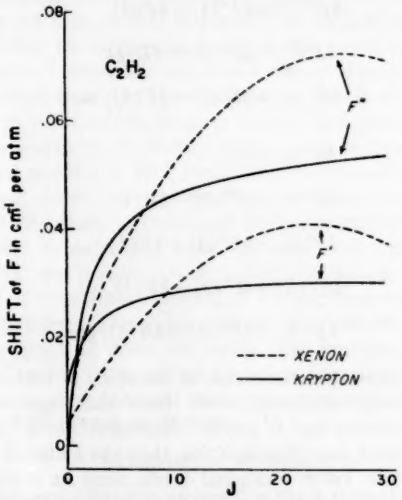

FIG. 6. Relative shift in cm^{-1} in the rotational energy levels in C_2H_2 for the upper and lower states due to a standard atmosphere of krypton and xenon. The shift of the lower-state level for $J=0$ is assumed to be zero for each foreign gas.

seriously, since the mathematical expression obviously is not simple and since at the present time no known theory of the J dependence of these perturbations is in existence.

Since we have measured only C_2H_2 line shifts for the J values given in Table II we have adopted the following procedure to construct Fig. 4. From the smooth curve in Fig. 2 the shifts for each value of J for the P- and R-branch lines were obtained. From these shifts the δ_2F values were calculated. These calculated δ_2F values have been plotted to obtain the curves given in Fig. 4. Since the δ_2F curves shown in Fig. 4 are calculated from smoothed data no points are indicated. The perturbations of the δ_2F curves for C_2H_2 portrayed by the curves in Fig. 4 seem to be somewhat similar for both lower and upper states. This behavior is in contrast with the quite different behavior of the δ_2F plots for the upper and lower states of HCl portrayed in Fig. 3.

It is possible to calculate the relative shifts of the rotational levels themselves for either state, since by definition

$$\Delta_2F(J)=F(J+1)-F(J-1).$$

However, it is not possible to obtain information from the spectrum with regard to the absolute shift of any rotational level. We shall assume that the shifts of the $J=0$ levels for the upper and lower states are K' and K'', respectively.

If we indicate shifts (perturbations) by the symbol δ we can write the following equations:

$$\delta F''(0)=K''$$

$$\delta F'(1)=\delta F''(0)+\delta R(0)$$

$$\delta F''(2)=\delta F'(1)-\delta P(2)$$

$$\delta F'(3)=\delta F''(2)+\delta R(2)$$

$$\delta F''(4)=\delta F'(3)-\delta P(4), \text{ etc},$$

and

$$\delta F'(0)=K'$$

$$\delta F''(1)=\delta F'(0)-\delta P(1)$$

$$\delta F'(2)=\delta F''(1)+\delta R(1)$$

$$\delta F''(3)=\delta F'(2)-\delta P(3)$$

$$\delta F'(4)=\delta F''(3)+\delta R(3), \text{ etc.},$$

which allow the calculation of the shifts of both upper and lower rotational levels from the experimental measurements and K' and K''. Neither K' nor K'' can be determined but the condition that the shifts of both upper and lower rotational levels must fit a smooth function of J allows the difference between K' and K'' to be determined.

In Fig. 5 we have plotted the results obtained by applying the system of equations mentioned above to the HCl data obtained with krypton and xenon as the perturbing gases. In making the plots we have arbitrarily chosen K'' to be zero for both krypton and xenon. The intercepts K' are not derived from fitting the lower-state points alone but must also be consistent in causing both the upper- and lower-state-level perturbations to be smooth functions of J. The shifts of the measured lines using xenon gas are roughly 1.5 times as large as those produced by krypton. We believe that this higher accuracy of the xenon points is responsible for the fact that the curves are smoother for xenon than for krypton.

It should be pointed out that the values of K' necessary to produce the smooth curves in Fig. 5 are very sensitive to small errors in the determination of the shifts of lines arising from low J's. The shifts of these low-J lines are the most difficult to measure with accuracy both because of their breadth and the smallness of their shifts. In view of these facts it seems idle to speculate concerning the values obtained for $K'-K''$ for krypton- and xenon-perturbed HCl levels. It can, however, be pointed out unequivocally from reference to Fig. 5 that the upper- and lower-state levels are perturbed by both krypton and xenon in completely different manners. The upper-state perturbation seems to be increasing linearly with J while the lower-state perturbations probably approach an asymptotic value at high J's.

Figure 6 portrays a plot of the perturbations of the upper- and lower-state levels of C_2H_2 as a function of J. We have used the same fundamental procedure in constructing these curves as was used in constructing Fig. 5 for HCl. The shifts of the C_2H_2 levels, as was also the case for the shifts of the C_2H_2 δ_2F values, do not behave in the same manner as was observed for HCl. The perturbations of the upper and lower states for C_2H_2 appear to be similar when plotted as a function of J.

In conclusion, we have found that the P- and R-branch lines of the 2/0 band of HCl are perturbed by both krypton and xenon in a complicated J-dependent manner. In the case of the $\nu_1+\nu_3$ band of C_2H_2 we have found the behavior of the band lines when perturbed by krypton and xenon to be very similar to the shifts observed with HCl. HCl has a very large permanent dipole moment in contradistinction to the zero dipole moment of C_2H_2. Detailed inquiry into the shifts of the upper- and lower-state rotational levels of these two molecules seems to show marked differences in the J dependence of the energy-level perturbations.[6]

[6] *Note added in proof.* Since this paper was first submitted it has been possible to extend our measurements to $J=17$ for HCl perturbed by xenon for the use of a heated absorption tube. The results of these further experiments will be reported at some future time.

Shapes and Breadths of Some Molecular Rotation-Vibration Band Lines Perturbed by Rare Gases*

D. H. RANK, D. P. EASTMAN, W. B. BIRTLEY,† AND T. A. WIGGINS

Physics Department, The Pennsylvania State University, University Park, Pennsylvania

(Received February 26, 1960)

The shape of absorption lines of HCl and C_2H_2 broadened with krypton and xenon as foreign gases is shown to be that due to collision broadening. Corrections for instrumental width are made in the manner described by Pigott and Rank to determine the half-intensity width. These widths show a small J dependence with low-J lines being the broadest. No difference between the widths of P and R lines of the same J could be detected. For high J's the quotient of the shift of the line and the width of the line is approximately constant for krypton and xenon. The breadth of HCl and C_2H_2 lines are not markedly different in spite of the difference in dipole moment. No asymmetry of lines perturbed by these foreign gases was observed.

I. INTRODUCTION

IN order to determine strictly the line profile of a spectrum line it is necessary either to employ infinite resolving power or to be able to make accurate corrections for the finite instrument width. Rank, Shearer, and Bennett[1] have shown that high-quality modern diffraction gratings produce the instrumental line shapes to be expected from theoretical consideration. Furthermore it was shown that the line shape produced using slits of finite width is in accord with Schuster's[2] calculations. The above authors have shown that for Doppler-broadened lines the line contours obtained are probably the contours to be expected when suitable correction for the Doppler distribution is made to the instrumental line shape. (The above conclusion is inferred from resolving-power measurements in which it was shown that neon lines and mercury lines gave the same resolving power if correction for Doppler broadening and the effect of the finite slit were taken into account.)

II. INSTRUMENT CORRECTION

Pigott and Rank[3] by calculation have analyzed the effect of a line having the Doppler distribution which is broadened by the Lorentz distribution. The observed half-intensity width HIW of the pressure-broadened line is designated by θ. The HIW of a Doppler-broadened monochromatic line is denoted by θ_0. The HIW θ_0 arises from the following factors: (a) resolving power of the grating; (b) effect of finite slit width; (c) Doppler distribution. If we assume the grating to give theoretical resolution, θ_0 can be calculated with considerable exactness. If one makes measurements of the HIW using an absorption or emission line at very low pressure, $\theta=\theta_0$ for a perfect instrument. Measurements made here using very high-quality diffraction gratings in the near infrared have shown that under the above-mentioned conditions the condition $\theta=\theta_0$ is very closely approached by our instruments.

In order to obtain the line broadening due to pressure from the observed HIW Pigott and Rank[3] have made the following computations. The pressure broadening was assumed to give a Lorentz distribution for a monochromatic line with a Lorentz HIW designated by Δ. Calculations were made applying the appropriate Lorentz distribution to the Doppler-broadened instrumental line shape. The results of these calculations have been portrayed in Fig. 4 of the paper by Pigott and Rank,[3] where Δ/θ is plotted against θ/θ_0. The vital result shown by this curve from an experimental standpoint is that for a θ/θ_0 ratio of 2.5:1, 90% of the observed HIW$\sim\theta$ is the result of the Lorentz broadening. For larger values of θ/θ_0, θ approaches Δ even more exactly. It has not been proved in Pigott and Rank's[3] calculations that for large values of θ/θ_0 the observed line contour is Lorentzian, but since θ closely approaches Δ the assumption that the Lorentz contour is obtained for large values of θ/θ_0 does not seem to be unreasonable.

The spectrograph which we have used to determine the line profiles of HCl and C_2H_2 lines broadened by krypton and xenon had a resolving power well in excess of 150 000. Doppler-broadened HCl lines at 5800 cm^{-1} recorded at extremely small pressure (less than 0.1 mm Hg) had a half-intensity width of 0.035 cm^{-1}. The shape of these lines observed at low pressure was that expected for a Doppler-broadened line recorded by a spectrograph of finite slit width. The line shapes observed at low pressure are shown in Fig. 1, curve A, where the data obtained both from $R(9)$ and $P(9)$ of the 2–0 HCl band are plotted.

III. EXPERIMENTAL RESULTS

Contours of lines up to $J=10$ in the 2–0 band of HCl have been observed using approximately an atmosphere pressure of xenon as the perturbing gas. The absorption

* This research was assisted by support from the Office of Naval Research.

† The participation of W. B. B. in this work was supported by HRB-Singer, Inc., State College, Pennsylvania.

[1] D. H. Rank, J. N. Shearer, and J. M. Bennett, J. Opt. Soc. Am. **45**, 762 (1955).

[2] A. Schuster, Astrophys. J. **21**, 197 (1905).

[3] M. T. Pigott and D. H. Rank, J. Chem. Phys. **26**, 384 (1957).

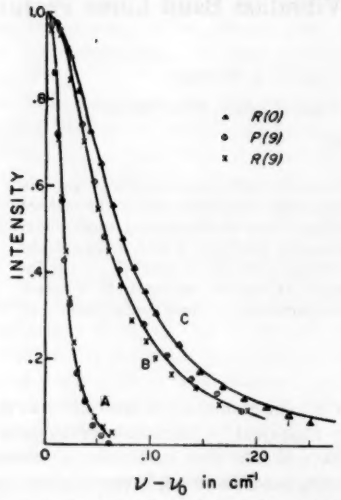

FIG. 1. Intensity of several lines of the 2–0 band of HCl plotted vs frequency difference from the line center in cm^{-1}. Curve *A* gives the intensity distribution of a line recorded with minimum HCl pressure. Curves *B* and *C* show the resulting distribution for several lines when broadened with a standard atmosphere of xenon. The solid lines drawn in curves *B* and *C* represent the Lorentz distribution for the estimated half-intensity width.

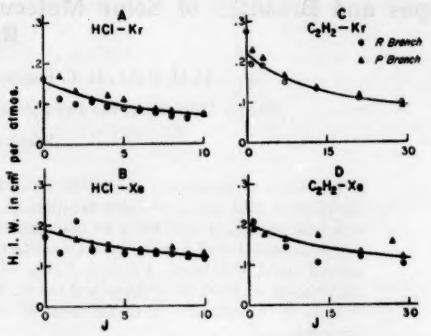

FIG. 2. Half-intensity widths in cm^{-1} of lines in HCl and C_2H_2 broadened by a standard atmosphere of krypton and xenon plotted vs *J*. The widths plotted have been corrected for the effect of instrument and Doppler widths.

was measured as a function of the frequency distance from the line centers. The absorptions measured were converted to intensities and were normalized so that they could be plotted on Fig. 1. In curve *B* of Fig. 1, we have plotted data obtained from both $R(9)$ and $P(9)$, and in curve *C*, we have plotted the data obtained for $R(0)$. The Lorentz-intensity distribution can be expressed by

$$I(\nu)=I(\nu_0)\{(\Delta/2)^2/[(\nu-\nu_0)^2+(\Delta/2)^2]\}, \qquad (1)$$

where ν_0 is the frequency at the center of the line and the other symbols have the meaning already defined. Curves *B* and *C* in Fig. 1 were not drawn to give a best fit of the experimental data points but were constructed using Eq. (1) and the Δ value estimated from the experimental points. Inspection of these curves, shows that the experimentally observed line contour is indistinguishable from the Lorentz contour defined by Eq. (1). Shapes of numerous other HCl lines were determined in the same manner and all profiles were in agreement with the Lorentz contour, the only difference being their half-intensity width.

Since the line shapes have been shown to have the Lorentz contour we can make use of Fig. 4 in the paper of Pigott and Rank[3] to correct the measured θ values to obtain Δ, the Lorentz HIW. We have made the assumption that Δ is a linear function of gas density in order to normalize our measurements to a standard atmosphere. The pressures of krypton or xenon used varied slightly from line to line but in general were about 70 cm Hg at 24°C. Thus the density correction is not large and is nearly the same for all of the lines measured.

In Fig. 2 we have plotted the measured HIW values obtained normalized to standard atmospheric density of the perturbing gas, as a function of *J*. *A* and *B* represent the results obtained for the lines of the 2–0 band of HCl using krypton and xenon, respectively, as the perturbing gas. The points representing the *R*-branch lines are indicated by circles, the *P*-branch-line data are plotted as triangular points. We have plotted similar data obtained for the $\nu_1+\nu_3$ band of C_2H_2 in *C* and *D*.

In conclusion we can state that perturbation of the 2–0 band lines of HCl by xenon produces a broadened line profile which we have not been able to distinguish from a strictly Lorentz shape. The measured half-intensity widths of the 2–0 band lines of HCl and the $\nu_1+\nu_3$ band lines of C_2H_2 when perturbed by krypton or xenon seem to decrease slowly with increasing *J*. For high-*J* lines the ratio of the shift of the center of the line to the half-intensity width seems to be constant for the two gases, krypton and xenon, which have been used to produce perturbation. We have not been able to observe any asymmetry in the profiles of the band lines broadened by krypton and xenon.

Nuclear Magnetic Resonance Spectrum of B^{11} in Inderite*

K. S. PENNINGTON† AND H. E. PETCH

Departments of Physics and Metallurgy, Hamilton College, McMaster University, Hamilton, Ontario, Canada

(Received March 28, 1960)

The quadrupolar splitting of the B^{11} nuclear magnetic resonance signal in a single crystal of inderite $Mg_2B_6O_{11}\cdot 15H_2O$ at room temperature has been investigated in a magnetic field of 7187 gauss. The spectra obtained as the crystal was rotated in turn about three mutually perpendicular axes held normal to the magnetic field were interpreted on the basis that the six B^{11} sites per unit cell belong to three distinct types with the two sites of each type related by a center of symmetry. The electric quadrupole coupling constants C_s and asymmetry parameters η at the three unique B^{11} sites were determined to be

$C_s=eQ\phi_{zz}/h$	355±5 kc/sec	517±7 kc/sec	2546±10 kc/sec
$\eta=(\phi_{xx}-\phi_{yy})/\phi_{zz}$	0.51±0.03	0.76±0.01	0.066±0.003

It has been inferred from the foregoing values that two of the boron atoms in the asymmetric unit of inderite have tetrahedral coordinations whereas the third has triangular coordination. The orientations of the principal axes of the electric field gradient tensors at the B^{11} sites have also been determined.

INTRODUCTION

THIS work was undertaken as part of a systematic experimental investigation of the B^{11} nuclear magnetic resonance (nmr) spectra in a number of borate minerals. Its object was to obtain quantitative data on the quadrupole coupling tensors at the B^{11} sites in inderite.

Inderite, from the Inder borate deposits in West Kazakstan, Inder mountains, U.S.S.R., was first named and described by Boldyreva.[1] The material is triclinic with one formula unit of $Mg_2B_6O_{11}\cdot 15H_2O$ per unit cell. Although the exact locality is unknown, a new occurrence of what probably is the same mineral has been reported by Heinrich[2] who described a number of its properties. Recently, Frondel and Morgan[3] have reported the discovery of a mineral, tentatively identified as inderite, at two mines in the Kramer district, California. The mineral from the Kramer district is identical with the mineral described by Heinrich although it is not clear that this mineral is identical with the original, rather ill-defined Russian inderite. As used in this paper, inderite refers to the mineral conditionally described as inderite by Frondel and Morgan.

THEORY

An isolated nucleus of spin I and magnetic moment μ placed in a magnetic field $\mathbf{H}_0$ has available to it $2I+1$ equally spaced Zeeman levels. The $2I$ transitions between adjacent levels give rise to a single absorption line at the Larmor frequency $\nu_0=\mu H_0/hI$. If the nucleus also possesses an electric quadrupole moment eQ and is situated in an electric field with a nonvanishing gradient $\nabla\mathbf{E}$, then, as Pound[4] has shown, each of the Zeeman levels is perturbed, and the single line is split into $2I$ components.

We have studied experimentally this so-called quadrupolar splitting of the B^{11} ($I=\frac{3}{2}$) resonance in inderite and have analyzed our data following the method developed by Volkoff[5] for the case where the electric quadrupole interaction is weak compared to the interaction between the nuclear magnetic dipoles and $\mathbf{H}_0$. For convenience of reference and to establish notation, a summary of the relevant theory, specialized to the case $I=\frac{3}{2}$, is reproduced below. Each unique nuclear site gives rise to three lines: a central line ν_c from the transition $m=+\frac{1}{2}\rightleftharpoons-\frac{1}{2}$, and two "satellites" ν_s' and ν_s'' from the transitions $m=\pm\frac{3}{2}\rightleftharpoons\pm\frac{1}{2}$. According to standard perturbation theory, the frequencies of the central line and of the centroid of the satellites, $\frac{1}{2}(\nu_s'+\nu_s'')$, show no displacement from ν_0 provided the quadrupole interaction is so weak that it is permissible to neglect all perturbation terms higher than the first. The frequency difference between the two satellites is given, for a rotation of the crystal about any axis maintained perpendicular to $\mathbf{H}_0$, by

$$\nu_s''-\nu_s'=a+b\cos 2\theta+c\sin 2\theta, \qquad (1)$$

where θ is the angle of rotation. In the case of somewhat stronger quadrupole coupling, the first-order perturbation term may be inadequate and the second-order perturbation term must also be used. The second-order term contributes nothing new to the equation describing the frequency difference between the satellites, but predicts a shift from ν_0 of the centroid of the satellites and of the central line. Thus, for a rotation about any

* This work was supported by the Defence Research Board of Canada.

† Holder of a Studentship awarded by the National Research Council of Canada.

[1] A. M. Boldyreva, Mem. Soc. Russe Min. Ser. 2, **66**, 651 (1937).

[2] E. W. Heinrich, Am. Mineral **31**, 71 (1946).

[3] C. Frondel and V. Morgan, Am. Mineral **41**, 839 (1956).

[4] R. V. Pound, Phys. Rev. **79**, 685 (1950).

[5] G. M. Volkoff, Can. J. Phys. **31**, 820 (1953).

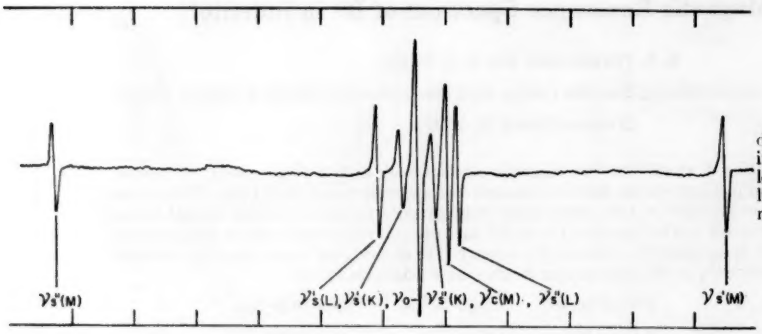

FIG. 1. A tracing of the recorded derivatives of the B^{11} absorption lines in inderite at a crystal orientation selected to show the eight resolved lines. The frequency scale is approximately 120 kc/sec per chart division.

axis perpendicular to $\mathbf{H}_0$

$$\bar{\nu}_s-\nu_0=\bar{n}+\bar{p}\cos 2\theta+\bar{r}\sin 2\theta+\bar{u}\cos 4\theta+\bar{v}\sin 4\theta \quad (2)$$

$$\nu_c-\nu_0=n+p\cos 2\theta+r\sin 2\theta+u\cos 4\theta+v\sin 4\theta, \quad (3)$$

where $\bar{\nu}_s$ stands for $\frac{1}{2}(\nu_s'+\nu_s'')$, the centroid of the pair of satellites. Note that Eq. (1) neglects perturbation terms of third and higher odd order while Eqs. (2) and (3) neglect perturbation terms of fourth and higher even order.

If the crystal is rotated in turn about each of three mutually perpendicular axes X, Y, and Z which are fixed with respect to the crystal, then three independent sets of the coefficients a, b, c, n, p, r, u, v may be obtained from the experimentally observed curves of the dependence of $\nu_s''-\nu_s'$, $\bar{\nu}_s-\nu_0$, and $\nu_c-\nu_0$ on θ_X, θ_Y, and θ_Z (the subscripts denote the rotation axes). These coefficients are related to the components of the quadrupole coupling tensor $\Psi_{ij}=eQ\phi_{ij}/h$ (where ϕ is the electrostatic potential at the nuclear site and $\phi_{ij}\equiv\partial^2\phi/\partial q_i\partial q_j$) expressed in terms of the X, Y, Z axes. For the X rotation, the coefficients in Eq. (1) are given by

$$a_X=\tfrac{1}{2}(\Psi_{YY}+\Psi_{ZZ}),$$
$$b_X=\tfrac{1}{2}(\Psi_{YY}-\Psi_{ZZ}),$$
$$c_X=-\Psi_{YZ}. \quad (4)$$

Corresponding relations for the rotations about the Y and Z axes may be obtained by a cyclic permutation of the subscripts. As a consequence of Laplace's equation

$$a_X=\tfrac{1}{2}(b_Y-a_Y)=-\tfrac{1}{2}(b_Z+a_Z)$$
$$b_X=-\tfrac{1}{2}(3a_Y+b_Y)=\tfrac{1}{2}(3a_Z-b_Z). \quad (5)$$

These identities are useful as a check on the experimental accuracy.

Volkoff[5] has shown that the coefficients in Eqs. (2) and (3) for the shifts of the centroid of the satellite signals and the central signal, respectively, are related to the coefficients in Eq. (1). However, we shall not state them explicitly since, in this work, they were used only for a check on the values of a, b, and c.

The values of a, b, and c, obtained from the $\nu_s''-\nu_s'$ curves lead, through Eqs. (4), to values for the components of the quadrupole coupling tensor Ψ_{ij} in the X, Y, Z coordinate system. The relative, but not the absolute, signs of these components are determined because in this experiment it was not possible to find out which of the two observed satellites ν_s', ν_s'' corresponded to which of the two transitions $m=\pm\frac{3}{2}\rightleftarrows\pm\frac{1}{2}$. This tensor can then be diagonalized by standard procedures to yield the quadrupole coupling constant $C_s\equiv eQ\phi_{zz}/h$ and the asymmetry parameter $\eta\equiv(\phi_{xx}-\phi_{yy})/\phi_{zz}$. The process of diagonalization will also give, with respect to the X, Y, Z axes, the direction cosines of the principal axes x, y, z of the electric field gradient tensor. For a second-rank tensor the orientation but not the sense of the principal axes is significant so only the relative signs of the direction cosines are determined.

APPARATUS AND EXPERIMENTAL PROCEDURE

The nuclear magnetic resonance spectrometer, of conventional design, consisted of an oscillating detector of the type described by Volkoff, Petch, and Smellie,[6] a narrow-band audio amplifier tuned to the magnetic field modulation frequency (210 cps), a Schuster-type phase sensitive detector[7] and a recording milliammeter. The externally applied magnetic field of 7187 gauss, produced by a 12 in. Varian electro-magnet, was stabilized by means of a proton resonance control circuit. A General Radio heterodyne frequency meter Type 620-A, with the aid of a Hallicrafter Model SX-62A communications receiver, was used to make frequency measurements with an accuracy of about one kc/sec.

A transparent crystal of inderite from the Kramer district was used for all the work reported here. The crystal was cleaved to produce a specimen roughly rectangular in shape and approximately 2.1 cm × 1.8 cm × 1.5 cm in size. The intersections between two perfect cleavage faces, the (010) and the (100) and a very good crystal face, the (001), defined the triclinic crystallographic axes. This orientation was confirmed by x-ray diffraction. The orthogonal axes, **X**, **Y**, and

[6] G. M. Volkoff, H. E. Petch, and D. W. Smellie, Can. J. Phys. **30**, 270 (1952).
[7] N. A. Schuster, Rev. Sci. Instr. **22**, 254 (1951).

Z, were chosen to make **X** parallel to the **a** and **Y** parallel to the **c**×**a** directions because the external features of the crystal made it easy to recognize these directions.

The crystal was mounted on an arc system from an x-ray goniometer which was, in turn, held within the magnetic field by a rotator and dial assembly which permitted the crystal to be rotated about an axis maintained perpendicular to $\mathbf{H}_0$. A circular vernier made it possible to read the rotation angle on the dial assembly to within 0.1°. A Griffin and George coordinate cathetometer was used to orient the crystal, on the basis of its external features, as accurately as possible with the desired axis, *X*, *Y*, or *Z*, parallel to the rotation axis. It is believed that the desired orientation was obtained to within one degree.

EXPERIMENTAL RESULTS AND DISCUSSION

The spin of B^{11} is known to be $\frac{3}{2}$ so that a "simple" spectrum of only three lines, a central component and two satellites, would be expected if all the boron sites were equivalent. However, the B^{11} spectrum in inderite at room temperature is considerably more complex, consisting of a maximum of 8 resolved lines as shown in Fig. 1. The frequency of the central line, which is more intense than the others, remains fixed at the calculated unperturbed value whereas the frequencies of the remaining lines are strongly dependent upon the angular orientation of the crystal. Four of the lines occur in pairs with two members of each pair symmetrically situated at frequencies slightly (never more than 125 kc/sec) above and below the unperturbed value. They are obviously satellite lines arising from two nonidentical sets of sites at which the quadrupole interaction is weak. The central components arising from these two sets of sites will not be shifted from the unperturbed frequency for any crystal orientation and therefore coincide to give rise to the very intense line which we observed at that frequency. Two other lines which for many crystal orientations are separated by large frequency differences from the unperturbed value make up a third pair. The members of this pair are not symmetrically situated with respect to the unperturbed frequency and we have observed that the centroid of this pair is separated from the unperturbed frequency by an amount which depends upon the crystal orientation as is shown for the *X* rotation in Fig. 2. These must be satellite lines which arise in a set of boron sites at which the quadrupole interaction is strong. The remaining line to be identified must be the central line arising at these sites. Its observed behavior, shown for the *X* rotation in Fig. 2, is qualitatively just what one would expect for a central line shifted from the unperturbed value. Thus, after classification, the complex pattern of lines reveals itself as a superposition of three simple spectra. The three sites in the asymmetric unit will hence forth be denoted as the *K*, *L*, and *M* sites where the *K* and *L* sites are those at which the quad-

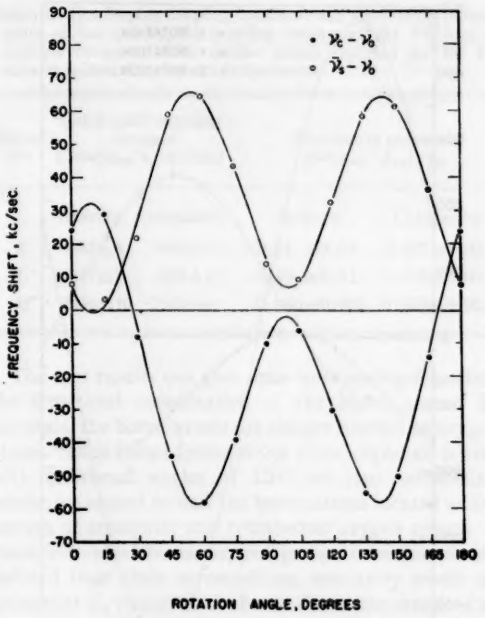

FIG. 2. Frequency shift from the unperturbed frequency ν_0 of the centroid of the satellite lines $\bar{\nu}_s$ and of the central line ν_c of the B^{11} spectrum arising at the *M* site in inderite for a rotation about the *X* axis. The curves were obtained from Eqs. (2) and (3) using coefficients calculated from the values given in Table I.

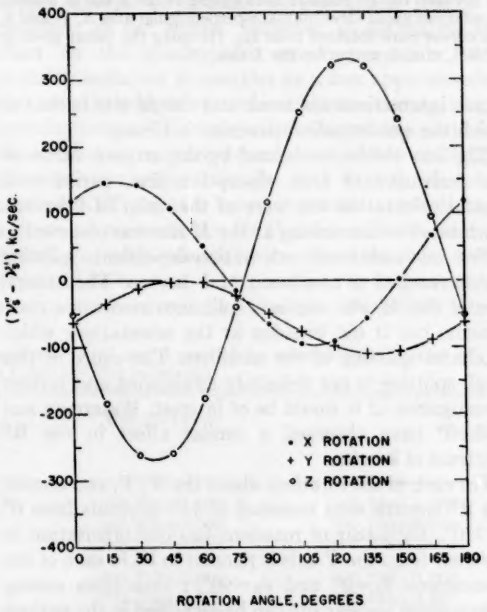

FIG. 3. Angular dependence of the frequency difference ($\nu_s''-\nu_s'$) between the B^{11} satellite lines arising at the *K* site in inderite for rotations about three mutually perpendicular axes *X*, *Y*, and *Z*. The curves were obtained from Eq. (1) using the values given in Table I, of *a*, *b*, and *c*, for the *K* site.

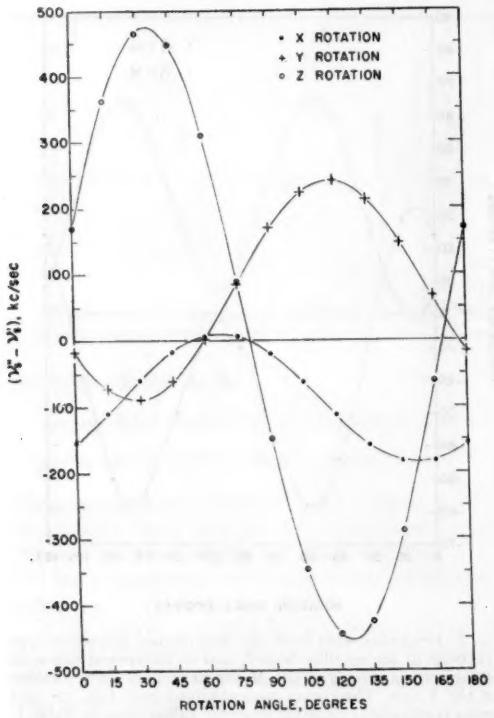

FIG. 4. Angular dependence of the frequency difference ($\nu_s''-\nu_s'$) between the B^{11} satellite lines arising at the *L* site in inderite for rotations about three mutually perpendicular axes *X*, *Y*, and *Z*. The curves were obtained from Eq. (1) using the values given in Table I, of *a*, *b*, and *c*, for the *L* site.

rupole interactions are weak and the *M* site is that at which the quadrupole interaction is strong.

The line widths, as defined by the extreme values in the derivative of each absorption line, varied with crystal orientation but were of the order of 9 kc/sec. Each satellite line arising at the *M* site was observed to suffer an additional orientation-dependent splitting which reached a maximum of 6 kc/sec. The central line of the *M* site was not split into resolvable components but it did broaden at the orientations which produced splitting of the satellites. The cause of this small splitting is not definitely established and further investigation of it would be of interest. Waterman and Volkoff[8] have observed a similar effect in the B^{11} spectrum of kernite.

For each of the rotations about the *X*, *Y*, and *Z* axes, the B^{11} spectra were recorded at 15° intervals from 0° to 360°. Each pair of rotations has one orientation in common (e.g., the *Y* axis is parallel to $\mathbf{H}_0$ in each of the orientations $\theta_X=0°$ and $\theta_Z=90°$); thus lines arising from a given nuclear site can be identified in the various rotations. For a complete rotation of the crystal, the frequencies of the lines are predicted by theory to be periodic with a period of 180°. In fact, the experimental values at $\theta°$ and $\theta°+180°$ were found in each case to differ by very little and were averaged. Also, whenever a satellite line arising at the *M* site showed splitting the mean of the two frequencies was used. The experimental values of $\nu_s''-\nu_s'$ are shown in Figs. 3–5. These experimental points were then fitted by the 12-point analysis method of Whittaker and Robinson[9] with equations of the type

$$f_i(\theta)=a_i+\sum_{n=1}^{5}b_i(n)\cos n\theta+\sum_{n=1}^{6}c_i(n)\sin n\theta,$$

where $i=X$, Y or Z. As expected, the coefficients of all terms involving angles other than 2θ turned out to be negligible within experimental error. The coefficients a_i, $b_i(2)$, and $c_i(2)$ are listed in Table I (without ambiguity these will be written *a*, *b*, and *c* with the subscripts given where needed to denote the rotations); each value of *a* and *b* is an average of the three values that can be obtained from the three rotations by using Eq. (5). The curves in Figs. 3, 4, and 5 were obtained from Eq. (1) using the values for *a*, *b*, and *c* given in Table I for the *K*, *L* and *M* sites respectively. The *a*,

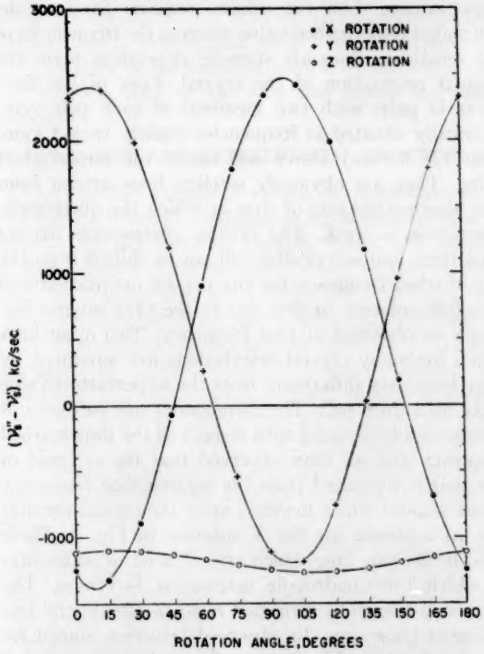

FIG. 5. Angular dependence of the frequency difference ($\nu_s''-\nu_s'$) between the B^{11} satellite lines arising at the *M* site in inderite for rotations about three mutually perpendicular axes *X*, *Y*, and *Z*. The curves were obtained from Eq. (1) using the values given in Table I, of *a*, *b*, and *c*, for the *M* site.

[8] H. H. Watermann and G. M. Volkoff, **Can. J. Phys. 33,** 156 (1955).

[9] E. Whittaker and G. Robinson, *The Calculus of Observations* (Blackie and Son Ltd., London, 1944).

TABLE I. Experimental values of the Fourier coefficients (in kc/sec) of the frequency separations, $\nu_s''-\nu_s'$, of the B^{11} satellite lines arising in the three nonequivalent sites in inderite at room temperature.

Boron Site	Rotation	Fourier Coefficients		
		a	*b*	*c*
K	*X*	+25.8±0.8	+92.1±2.0	+81.5±2.0
	Y	−58.0±1.2	−6.7±2.5	+54.3±1.2
	Z	+32.2±0.6	−84.3±2.5	−288.4±3.0
L	*X*	−85.7±0.8	−67.0±2.7	+70.2±3.0
	Y	+76.2±0.9	−94.2±2.4	−137.3±2.0
	Z	+9.5±1.0	+161.3±2.5	+435.1±4.0
M	*X*	+554.9±0.9	−1792±10	−625.5±1.5
	Y	+617.7±3.6	+1721.8±5.4	+587.8±3.5
	Z	−1172.6±5.6	+64.1±7.0	+50.7±6.0

b, and *c* values for the *M* site in Table I were checked by using them to calculate the coefficients for Eqs. (2) and (3) which were then used to predict the shift of $\bar{\nu}_s$ and $\bar{\nu}_c$, respectively, from ν_0. The agreement with experiment was very good as is illustrated for the *X* rotation in Fig. 2.

The *a*, *b*, and *c* coefficients of Table I determine the tensors Ψ_{ij} in the *X*, *Y*, *Z* coordinate system. These were diagonalized to yield the values for the quadrupole coupling constants and the asymmetry parameters listed in Table II. The direction cosines, with respect to the *X*, *Y*, and *Z* axes, of the principal axes of the quadrupole coupling tensors are given in Table III. Probable errors are given with the values listed in Tables I, II, and III.

On the basis of chemical data and the unit cell dimensions, inderite contains 6 boron atoms per unit cell. Remembering that two sites in a unit cell are identical from the point of view of the nmr experiment only if they are related by a center of symmetry, it is apparent that inderite must have a centrosymmetrical structure since we have found that the 6 boron sites occupy only 3 nonidentical sites. Since inderite is triclinic, its spacegroup must be $P\bar{1}$.

TABLE II. Quadrupole coupling constants and asymmetry parameters of the quadrupole coupling tensors at the B^{11} sites in inderite compared with similar values reported for the B^{11} sites in colemanite at room temperature.

Boron site	Quadrupole coupling constant $C_s \equiv eQ\phi_{zz}/h$, (kc/sec)		Asymmetry parameter $\eta \equiv (\phi_{xx}-\phi_{yy})/\phi_{zz}$	
	Inderite	Colemanite	Inderite	Colemanite
K	355±5	436±1	0.51 ±0.03	0.487±0.002
L	517±7	309±1	0.76 ±0.01	0.825±0.003
M	2546±10	2541±4	0.066±0.003	0.059±0.003

The nmr results can give some information regarding the structural coordination of the boron atoms. In minerals, the boron atoms are always bonded to oxygen atoms. Since boron forms either three coplanar bonds, with interbond angles of 120°, or four tetrahedral bonds, we expect to find the boron atoms located at the centers of triangular and tetrahedral oxygen groups. If these individual boron-oxygen groups were completely isolated from their surroundings, symmetry would require that C_s vanish at the boron site at the center of an oxygen tetrahedron but for the boron site at the center of an oxygen triangle symmetry would place no limitation on C_s but would require η to vanish. In complicated structures such as inderite, the effects of other atoms in the structure and of the linking together of boron-oxygen groups by sharing oxygen atoms results in distortion of the groups. However, in estimating the effect on the quadrupolar coupling constant it is probably sufficient to consider as a first approximation that only the oxygen nearest-neighbors make significant contributions to $\nabla\mathbf{E}$ at each of the boron sites and that the boron-oxygen groups can be considered as slightly distorted equilateral triangles and slightly distorted tetrahedra. Thus, at a boron site with tetrahedral coordination, one would expect C_s to be small whereas at a boron site with triangular coordination, one would expect C_s to be much larger and η to be very small. In the case of colemanite ($CaB_3O_4(OH)_3 \cdot H_2O$) these

TABLE III. Direction cosines, with respect to the mutually perpendicular *X*, *Y*, and *Z* axes, of the principal axes (*x*, *y*, *z*) of the quadrupole coupling tensors at the B^{11} sites in inderite.

Boron sites	Reference axes	Principal axes		
		x	*y*	*z*
K	*X*(a)	∓0.160±0.001	∓0.796±0.008	∓0.583±0.005
	Y(c×a)	∓0.164±0.005	±0.604±0.006	∓0.780±0.008
	Z	∓0.973±0.002	±0.032±0.001	±0.228±0.006
L	*X*	±0.196±0.005	∓0.577±0.005	±0.793±0.008
	Y	∓0.198±0.005	∓0.815±0.005	∓0.544±0.001
	Z	∓0.960±0.005	±0.051±0.005	±0.274±0.003
M	*X*	∓0.943±0.02	±0.297±0.005	∓0.159±0.002
	Y	∓0.317±0.005	∓0.933±0.02	±0.163±0.002
	Z	∓0.100±0.002	±0.205±0.004	±0.974±0.01

expectations have been confirmed.[10] A comparison, Table II, of the values of C_z and η obtained for inderite with those reported for colemanite strongly suggests that in inderite two of the boron sites in the asymmetric unit have tetrahedral coordinations, whereas the third has triangular coordination.

[10] F. Holuj and H. E. Petch, Can. J. Phys. **38**, 515 (1960).

THE JOURNAL OF CHEMICAL PHYSICS VOLUME 33, NUMBER 2 AUGUST, 1960

Induction Studies in Several Groups of Halogen-Containing Organic Compounds by Their Cl^{35}, Br^{79}, or Br^{81} Pure Quadrupole Resonance Spectra*

H. O. Hooper and P. J. Bray

Department of Physics, Brown University, Providence, Rhode Island

(Received February 29, 1960)

Induction studies have been carried out in several groups of halogen-containing organic compounds by means of the halogen pure quadrupole spectra. In several straight-chain compounds inductive effects have been examined as a function of the length of the chain in some monohalogenated-paraffin hydrocarbons and as a function of the number of carbon atoms separating halogen atoms attached to either end of dihalogenated-paraffin hydrocarbons. The effects of the hybridization of the carbon atom have also been examined in some aliphatic hydrocarbons. Chlorine pure quadrupole resonance frequencies from chlorine atoms bonded to atoms other than carbon, such as silicon, nitrogen, and sulfur, have been measured, and the effects of these different atoms upon the Cl^{35} resonance frequencies are qualitatively discussed.

Inductive effects have also been examined in different groups of aromatic compounds. The inductive effect in several chlorobenzyl compounds is found to be about $\frac{3}{4}$ of what it is in the corresponding chlorobenzene compounds as determined from a comparison of the Cl^{35} resonance frequencies. Definite discrepancies have been observed between the Cl^{35} spectra obtained from several aromatic compounds which have molecular structures similar to anthraquinone and the Cl^{35} frequencies that can be predicted from data obtained from chlorobenzene compounds and Hammett σ values.

Employing the linear relationship between Cl^{35} resonance frequency and Hammett σ values, several Cl^{35} frequencies were predicted and compared to the measured frequencies in some chlorobenzene compounds. Some unknown σ values have also been predicted. A linear relationship between Br^{81} resonance frequencies and Hammett σ values has been developed from measured bromine quadrupole frequencies. Several halogen frequencies from some unrelated compounds have been measured and are tabulated in this paper.

INTRODUCTION

PURE quadrupole[1] resonance studies are useful in the determination of the distributions of molecular electrons. The effect of various substituents on the electron distributions in chloro- and bromobenzenes has been studied,[2,3] and from this study a linear correlation between the halogen pure quadrupole resonance frequency and the Hammett[4] sigma value of the substituent has been established. This pure quadrupole study has been extended to several nitrogen-containing heterocyclic compounds.[5,6]

In the present paper the inductive effects in some straight-chain compounds are examined by means of the pure quadrupole resonance frequencies of the substituted halogens. Changes in resonant frequency for halogens at the 1 position in several straight-chain hydrocarbons are examined as a function of the chain length. The inductive effect of one halogen upon another is examined in several dihalogenated-paraffin hydrocarbons as a function of the number of CH_2 groups which separate the two halogens. An examination is made of the electron distribution at chlorine atoms bonded to carbon atoms of various hybridizations. Similarly, the chlorine resonances from chlorine atoms bonded to atoms other than carbon (such as nitrogen, silicon, and sulfur) are discussed. The effects of oxygen atoms upon the charge distributions in some aliphatic as well as some aromatic hydrocarbons are examined. A study of induction by a comparison of the resonance frequencies in some substituted chlorobenzenes with the resonance frequencies in similar substituted benzyl compounds is made.

From the resonance data for a few substituted halobenzene compounds, Hammett σ values are evaluated by means of Eq. (1) and Eq. (2) which express the linear relationship between the halogen pure quadrupole resonance frequency and Hammett σ value:

$$f(Cl^{35}) = 34.826 \text{ Mc} + 1.024 \sum_i \sigma_i \qquad (1)$$

$$f(Br^{81}) = 226.932 \text{ Mc} + 7.639 \sum_i \sigma_i. \qquad (2)$$

* This work supported by a grant from the National Science Foundation.

[1] H. G. Dehmelt, Am. J. Phys. **22**, 110 (1954).
[2] P. J. Bray and R. G. Barnes, J. Chem. Phys. **27**, 551 (1957).
[3] P. J. Bray and R. G. Barnes, J. Chem. Phys. **22**, 2023 (1954).
[4] L. P. Hammett, *Physical Organic Chemistry* (McGraw-Hill Book Company, Inc., New York, 1940).
[5] P. J. Bray, S. Moskowitz, H. O. Hooper, R. G. Barnes, and S. L. Segel, J. Chem. Phys. **28**, 99 (1958).
[6] H. O. Hooper, P. J. Bray, J. Chem. Phys. **30**, 957 (1959).

In Eq. (1) and Eq. (2) f is the frequency in Mc, and the sum over σ values is a sum of the σ values of all the substituents on the ring.

EQUIPMENT AND PROCEDURE

The Cl^{35} resonances were detected using a self-quenched superregenerative spectrometer[2] with a narrow band lock-in amplifier[7] and phase-sensitive detector[7] coupled to a recorder. However, some of the Cl^{35} resonances were detected and measured using the self-quenched superregenerative spectrometer with only oscilloscope display. All the Br^{79} or Br^{81} resonances reported here were observed using a self-quenched superregenerative oscillator of the push-pull Lecher-wire tuned type. Measurements were made at liquid-nitrogen temperature using either a Gertsch Model FM–3 V.H.F. frequency meter or a U.S. Army surplus BC–221–T frequency meter.

Unless otherwise noted in the following tables, the limits of error for the resonant frequencies measured in this laboratory are ± 0.002 Mc for Cl^{35} resonances measured with oscilloscope display, ± 0.025 Mc for Cl^{35} resonances measured with recorder techniques, and ± 0.050 for the Br^{79} or Br^{81} resonances measured with oscilloscope display. The limits of error for the Cl^{35} resonances measured with oscilloscope display arise entirely from the difficulty in locating the center of the resonance line. The larger limits of error for the Cl^{35} resonances measured with recorder display arise from the difficulty in matching the center side band of the signal from the frequency meter with the center side band of the resonance from the sample. Limits of error for the bromine resonances are again due to the difficulty in determining the center of the resonance line; however, any measurement could have an additional error equal to the quench frequency of approximately 150 kc.

The signal-to-noise ratios listed in the several tables have little correlation between compounds. However, the signal-to-noise ratios listed for more than one resonance in a single compound sometimes help to establish which resonance frequency corresponds to each of the halogens at different positions in the molecule. In the column for signal-to-noise ratios in the tables to follow, an S signifies oscilloscope display while an R refers to measurement using recorder techniques.

In examining the data one finds that often there are more resonances in a particular compound than there are inequivalent halogen atoms in a molecule. This may be attributed to crystal-structure effects. It has been found that the average crystal-structure effect in chlorobenzenes[2] is about 200 kc, but crystal effects as large as 600 kc have been observed. These different crystal structure effects may split or displace single resonance lines. This fact must be kept in mind while examining the data which follow.

In preparing the samples for the experiments, the compounds which are solid at room temperature were packed into 2-dram vials. In a few cases the samples were melted into the vials if there was no decomposition of the compound upon melting. The compounds which are liquid at room temperature were cooled over liquid nitrogen and then immersed into the liquid nitrogen as slowly as possible. In many cases these liquid compounds formed glassy solids in which no resonances were found. All the compounds listed in the following tables which we have examined were purchased from Eastman Kodak Company unless otherwise noted in the tables.

INDUCTION IN A CHAIN OF CH_2 GROUPS

In the present section the effect of paraffin-hydrocarbon chain length upon a chlorine atom bonded to a carbon atom at one end of the chain is examined. An examination is also made of the inductive effect for two halogens separated by increasing numbers of carbon atoms. A similar study is made for identical molecules which have had the chlorine atom replaced by a bromine atom.

In Table I the Cl^{35} pure electrical quadrupole resonance frequencies have been listed for some 1-chloroparaffins. There is a sharp drop in resonant frequency from chloromethane to chloroethane and then a gradual increase in resonant frequency with increase in molecule size. This sharp drop in frequency from 1-chloromethane to 1-chloroethane can be explained in the following manner. 1-chloroethane may be considered to be 1-chloromethane with one hydrogen replaced by a methyl group. The methyl group is more electropositive[8] than the single hydrogen, and an increase in ionic character of the chlorine bond is to be expected. This would cause a lowering of the transition frequency as is indeed the case. In the longer molecules there is increasingly greater shielding of the methyl group from the single chlorine which tends to eliminate some of the effect of the methyl group on the chlorine atom. This reasoning is supported by the observed gradual increase in frequency with increase in molecule size. With 1-chloropropane and the larger molecules the Cl^{35} frequency can be considered constant (approximately 33.00 Mc) since the small variations in frequency listed in Table I can be attributed to crystal effects. These data (Table I) therefore indicate that when the chlorine is separated from the CH_3 group by two carbons the CH_3 group has no effect upon the charge distribution at the chlorine nucleus as measured by the pure quadrupole resonance.

In Table II are listed Cl^{35} resonance frequencies for some dichloroparaffin hydrocarbons where the chlorines are bonded at opposite ends of the chain. From a comparison of data in Table I with the data in Table II one can see that the inductive effect is strong for two chlorines separated by one carbon atom and almost as

[7] G. D. Watkins, Ph.D. thesis, Harvard University, 1952.

[8] R. Livingston, J. Phys. Chem. **57**, 496 (1953).

TABLE I. Measured frequencies for Cl^{35} in some monochloroparaffin hydrocarbons at 77°K.

Compound		Frequency in Mc at 77°K	Signal-to-noise ratio
1-Chloromethane	CH_3Cl	34.029[a]	
1-Chloroethane	CH_3CH_2Cl	32.649	$5S$
		32.759	$8S$
		33.080[a] / 32.891 } 20°K	
1-Chloropropane	$CH_3CH_2CH_3Cl$	32.968[a]	
1-Chlorobutane	$CH_3[CH_2]_2CH_2Cl$	33.255	$2.5S$
1-Chloropentane	$CH_3[CH_2]_3CH_2Cl$	33.103	$7R$
1-Chlorohexane	$CH_3[CH_2]_4CH_2Cl$	32.968	$6R$
1-Chloroheptane	$CH_3[CH_2]_5CH_2Cl$	33.106	$1.2S$
1-Chlorooctane	$CH_3[CH_2]_6CH_2Cl$	33.009	$5R$
1-Chlorodecane	$CH_3[CH_2]_8CH_2Cl$	33.024	$3R$

[a] R. Livingston, J. Phys. Chem. **57**, 496 (1953).

TABLE II. Measured frequencies for Cl^{35} in some dichloroparaffin hydrocarbons at 77°K.

Compound		Frequency in Mc	Signal-to-noise ratio	$\Delta\nu$
Dichloromethane	CH_2Cl_2	35.991[a]		+1.962
1,2-Dichloroethane	CH_2ClCH_2Cl	34.361[b]		+1.657
1,3-Dichloropropane	$CH_2ClCH_2CH_2Cl$	32.952 / 33.130 } 33.041 Av	$30R$	+0.073
1,4-Dichlorobutane	$CH_2Cl[CH_2]_2CH_2Cl$	32.850	S	−0.405
1,5-Dichloropentane	$CH_2Cl[CH_2]_3CH_2Cl$	33.222	$10R$	+0.119
1,6-Dichlorohexane[c]	$CH_2Cl[CH_2]_4CH_2Cl$	33.008	$17R$	+0.040

[a] R. Livingston, J. Phys. Chem. **57**, 496 (1953).
[b] R. Livingston, J. Chem. Phys. **20**, 1170 (1952).
[c] Sample purchased from Aldrich Chemical Company, Milwaukee, Wisconsin.

TABLE III. Measured frequencies for Br^{81} in some monobromoparaffin hydrocarbons at 77°K.

Compound		Frequency in Mc at 77°K	Signal-to-noise ratio
1-Bromomethane	CH_3Br	220.981[a]	
1-Bromoethane	CH_3CH_2Br	207.790[a]	
1-Bromopropane	$CH_3CH_2CH_2Br$	210.277[a]	
1-Bromobutane	$CH_3[CH_2]_2CH_2Br$	208.86[b] 208.579	S
1-Bromohexane	$CH_3[CH_2]_4CH_2Br$	249.255 (Br^{79}) 208.38 (Calc Br^{81})	$7S$
1-Bromoheptane	$CH_3[CH_2]_5CH_2Br$	208.343	S
1-Bromooctane	$CH_3[CH_2]_6CH_2Br$	249.285 (Br^{79}) 208.42 (Calc Br^{81})	$6S$

[a] H. Zeldes and R. Livingston, J. Chem. Phys. **21**, 1418 (1953).
[b] S. Kojuna, K. Tsukada, S. Ogawa, and A. Shimouchi, J. Chem. Phys. **21**, 1415 (1953).

TABLE IV. Measured frequencies for Br^{81} in some dibromoparaffin hydrocarbons at 77°K.

Compound		Frequency in Mc	Signal-to-noise ratio	$\Delta\nu$
Dibromomethane	CH_2Br_2	234.805, 235.601 •235.203 Av		+14.222
1,2-Dibromoethane	CH_2BrCH_2Br	216.827, 218.977 •217.902		+10.112
1,3-Dibromobutane	$CH_2Br[CH_2]_2CH_2Br$	209.771	S	+0.192
1,5-Dibromopentane	$CH_2Br[CH_2]_3CH_2Br$	212.512	S	...

• H. Zeldes and R. Livingston, J. Chem. Phys. 21, 1418 (1953).

strong when the two chlorines are separated by two atoms. However, when the two chlorines are separated by three carbon atoms (1,3-dichloropropane), there seems to be no inductive effect. Within the limits of crystal effects, there is also no inductive effect present when the two chlorines are separated by more than three carbons. In Table II $\Delta\nu$ is obtained by subtracting the frequency obtained for the monochloroparaffin hydrocarbon (Table I) from the frequency obtained for the corresponding dichloroparaffin hydrocarbon. The $\Delta\nu$ are an indication of the strength of the inductive effect between the two chlorines.

The data for the bromo hydrocarbon compounds in Tables III and IV illustrate essentially the same phenomena which are present in the chloro hydrocarbons. The resonant frequencies listed are for the Br^{81} resonance unless otherwise noted. In cases where the Br^{79} resonance frequencies were measured, the frequencies were converted to Br^{81} resonance frequencies using the well-established ratio of $Br^{79}/Br^{81}=1.1970$[1] for the quadrupole moments. The lists in Tables III and IV are not as complete as one might desire; nevertheless, the inductive effects are again illustrated. The resonance frequencies for the bromine nuclei are much higher than the resonance frequencies in chlorine because of the larger quadrupole moment of the bromine nuclei and $\langle 1/r^3 \rangle$ is larger for the $4p$ state of a bromine atom than for the $3p$ state of a chlorine atom (92×10^{24} cm^{-3} and 48×10^{24} cm^{-3}, respectively[9]).

EFFECT OF THE CH_3 GROUP

The data listed in Table V show how the electropositive-acting methyl group causes a lowering of the chlorine resonant frequency. The resonant frequency in 2-chloropropane has been lowered by about 1 Mc below the resonant frequency found in 1-chloropropane (Table I). This can be attributed to the two methyl groups which are bonded to the 2-position carbon. In 2-chlorooctane the resonant frequency is again lower than the resonant frequency found in the corresponding 1-chloro compound (1-chlorooctane). Since there is only one methyl group attached to the 2-position carbon and not two methyl groups as in 2-chloropropane, the resonance in 2-chlorooctane is slightly higher in frequency than that in 2-chloropropane.

The higher of the two resonant frequencies found in 1,3-dichlorobutane can be assigned to the 1-position chlorine. This frequency is only slightly higher than the frequency found for 1-chlorobutane (Table I). The increased frequency can be attributed to the inductive effect of the additional chlorine in 1,3-dichlorobutane. The lower frequency in 1,3-dichlorobutane can be assigned to the 3-position chlorine. This lower frequency is essentially the same as the resonant frequency found for 2-chloropropane where there are two methyl groups present. This implies that the 1-chloroethyl group in 1,3-dichlorobutane acts with electropositive action equal to that of a methyl group. From this one can deduce that the ethyl group (without the chlorine) is more electropositive than a single methyl group.

In 2,4-dichloropenthane two resonances were found. The splitting was probably caused by crystal-structure differences between the chlorine atoms, which appear equivalent in the molecular structure. In this compound each chlorine is acted upon by a methyl group and the inductive effect from the other chlorine. One can assume that the methyl group which is three carbon atoms distant from the chlorine will not affect this chlorine. This assumption is based upon the data in Tables I and II. The action of one methyl group and the other chlorine would cause the frequency to rise above that of 2-chloropropane, as is the case. In 2,5-dichlorohexane the inductive effect of the chlorines upon one another has been reduced, consequently lowering the resonant frequency below the resonant frequency of 2,4-dichloropentane.

The effect of three electropositive methyl groups is illustrated in 2-chloro-2-methylpropane by the dropping of the resonance frequency below the resonance frequency in 2-chloropropane. An even lower frequency is observed in 2-chloro-2-methylbutane. The compound 2-chloro-2-methylbutane can be thought of as 2-chloro-2-methylpropane with one methyl group replaced by an ethyl group. Since the frequency is lowered by this replacement, the ethyl group can be said to have a greater electropositive action on the chlorine; that is, an ethyl group must have a lower electronegativity than a methyl group.

[9] R. G. Barnes and W. V. Smith, Phys. Rev. 93, 95 (1954).

TABLE V. Cl^{35} resonance frequencies in some paraffin hydrocarbons which illustrate the effect of the CH_3 group upon the chlorine atom.

Compound		Frequency in Mc at 77°K	Signal-to-noise ratio
2-Chloropropane	$CH_3CHClCH_3$	31.939[a]	5*S*
2-Chlorooctane	$CH_3CHCl[CH_2]_5CH_3$	32.302	1.5*R*
1,3-Dichlorobutane[b]	$CH_2ClCH_2CHClCH_3$	31.949 33.485	11*R* 13*R*
2,4-Dichloropentane[b]	$CH_3CHClCH_2CHClCH_3$	32.686 32.333	7*R* 8*R*
2,5-Dichlorohexane[b]	$CH_3CHCl[CH_2]_2CHClCH_3$	31.819±0.005	1.2*S*
2-Chloro-2-methylpropane	$CH_3CCl[CH_3]_2$	31.067	4*S*
2-Chloro-2-methylbutane	$CH_3CCl[CH_3]CH_2CH_3$	30.878±0.005	1.5*S*
1-Chloro-3-methylbutane	$CH_3CH[CH_3]CH_2CH_2Cl$	32.720±0.005	1.2*S*

[a] Measured at 20°C by R. Livingston, J. Phys. Chem. **57**, 496 (1953).
[b] Sample purchased from Columbia Organic Chemicals, Inc., Columbia, South Carolina.

TABLE VI. Cl^{35} resonance frequencies in some multichlorosubstituted-paraffin hydrocarbons.

Compound		Frequency in Mc at 77°K	Signal-to-noise ratio
Carbon tetrachloride	CCl_4	15 lines 40.817–40.465[a] 40.640 (Av)	
Trichloromethane	$CHCl_3$	38.309[a] 38.254	
Hexachloroethane	C_2Cl_6	40.761[a] 40.714 40.685 40.551	
1,1,1,2,3,3,3-Heptachloropropane	C_3Cl_7H	40.200 (Av)[b]	
1,1,1,2,2,3,3-Heptachloropropane[c]	C_3Cl_7H	38.267 39.140 39.754 39.900 40.440 41.186 41.276	30*R* 20*R* 20*R* 20*R* 20*R* 20*R* 20*R*
1,1,1,5-Tetrachloropentane[d]	$CCl_3[CH_2]_3CH_2Cl$	38.535 38.038 37.879 33.363	1.5*S* 1.5*S* 1.5*S* 1.5*S*
1,1,2,3,3-Pentachloropropane[d]	$CHCl_2CHClCHCl_2$	38.109 37.629 37.196 37.186	2*S* 3*S* 3*S* 3*S*
1,1,2,2-Tetrachloroethane	$CHCl_2CHCl_2$	37.481 37.667 37.989	3*S* 3*S* 3*S*
1,1-Dichlorobutane	$CHCl_2[CH_2]_2CH_3$	35.117 35.210	5*S* 5*S*
2,2-Dichlorobutane[d]	$CH_3CCl_2CH_2CH_3$	34.793 34.722	5*S* 5*S*
2,2-Dichloropropane	$CH_3CCl_2CH_3$	34.883[a]	

[a] R. Livingston, J. Phys. Chem. **57**, 496 (1953).
[b] S. L. Segel (private communication).
[c] Sample purchased from Aldrich Chemical Company, Milwaukee, Wisconsin.
[d] Sample purchased from Columbia Organic Chemicals, Inc., Columbia, South Carolina.

TABLE VII. Cl^{35} resonance frequencies in some hydrocarbons containing carbon atoms in different valence states.

Compound		Frequency in Mc at 77°K	Signal-to-noise ratio
1-Chloropropane	$CH_3CH_2CH_2Cl$	32.968[a]	
α-Chlorotoluene		33.627[a]	
(3-Chloropropenyl) benzene	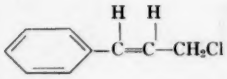	33.612	1.2*S*
Allyl chloride[b]	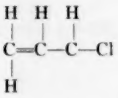	33.455	5*S*
3-Chloropropyne	$H-C\equiv C-CH_2Cl$	35.812[c]	
1,4-Dichloro-2-butene[d]	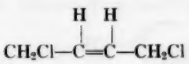	34.109	3*R*
Perchloroethylene[e]		38.342 38.526 38.648 38.799	1.7*S* 1.5*S* 1.7*S* 1.8*S*

[a] R. Livingston, J. Phys. Chem. **57**, 496 (1953).
[b] Sample obtained from Monomer-Polymer, Leominster, Massachusetts.
[c] E. Hirota, T. Oka, and Y. Morino, J. Chem. Phys. **29**, 444 (1958).
[d] Sample obtained from Peninsular Chemical Research, Inc., Gainesville, Florida.
[e] Sample obtained from Diamond Alkali Company, Cleveland 14, Ohio.

The resonant frequency in 1-chloro-3-methylbutane is only slightly lower than that of 1-chlorobutane (Table I). This indicates again that the effects of various changes in the molecule only slightly change the charge distribution near a chlorine nucleus if these changes occur at the carbon which is three carbon atoms distant from the chlorine (see 1,3-dichloropropane data in Table II).

EFFECT OF MULTICHLOROSUBSTITUTION

In Table VI the Cl^{35} pure electrical quadrupole resonance frequencies are listed for several paraffin hydrocarbons to which more than one chlorine atom has been bonded. Livingston[8] found that the replacement of hydrogen atoms with chlorine atoms produced increases in transition frequencies, reaching the limit of 41 Mc for CCl_4. These increases are attributed to a reduction in the ionic character of the carbon-chlorine bonds, the reduction arising from increased competition among the chlorines for the carbon electrons. It can be seen from Table VI that all of the multichlorosubstituted-paraffin hydrocarbons listed have transition frequencies appreciably greater than the 33.0 Mc frequency which occurs for a single chlorine attached to a paraffin hydrocarbon as seen in Tables I and II. The first seven compounds in Table VI all have resonances which approach a limit of about 41.0 Mc. It should be noted that the chlorine in the 5 position in 1,1,1,5-tetrachloropentane has a resonance frequency of 33.363 Mc which is only slightly higher (200 kc) than the resonance frequency in 1-chloropentane (Table I). This again indicates that there is very little inductive effect between chlorine atoms separated by five carbon atoms.

The resonance frequencies are seen to drop as the number of chlorines bonded to the same carbon decreases. For three chlorines attached to the same carbon the resonance frequency lies in the 37–38-Mc region, while for dichlorosubstitution on the same carbon atom the resonance frequency drops to the 35-Mc region (1,1-dichlorobutane).

TABLE VIII. Variation of the C—Cl bond length with hybridization.

Hybridization	Compound	Bond length A
sp^3	$ClCH_2CH_3$	1.76
sp^2	$ClCHCH_2$	1.69
sp	ClCCH	1.63

TABLE IX. Cl^{35} resonance frequencies in some chlorohydrocarbons containing C=O or C—O—C groups.

Compound		Frequency in Mc at 77°K	Signal-to-noise ratio
1. Chloro-2-propanone	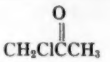	35.071 } 35.280 Av. 35.485 } 35.075 } [a] 35.484 }	3*S* 1.5*S*
2. 1,3-Dichloro-2-propanone		35.943[a]	[$\Delta\nu$=0.665]
3. Chloromethyl methyl ether	$CH_2Cl—O—CH_3$	29.817 30.206	40*R* 16*R*
4. *bis*(Chloromethyl) ether	$CH_2Cl—O—CH_2Cl$	32.484[b]	[$\Delta\nu$=2.473]
5. *bis*(2-Chloroethyl) ether	$C_2H_4Cl—O—C_2H_4Cl$	33.997±0.005 33.391	1.2*S* 3*S*
6. α-Chloro-2,4-dimethyl acetophenone	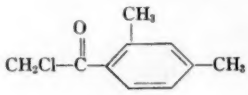	35.602	3*S*
7. β-Chlorophenetole	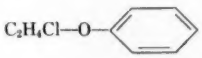	34.316	5*S*
8. 1,2-*bis*(2-Chloroethoxy) ethane	$C_2H_4Cl—O—C_2H_4—O—C_2H_4Cl$	33.932 33.724 33.249	*S* *S* *S*
9. 2-Chloroethyl acetate	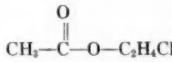	34.104	6*S*
10. *bis*(2-Chloroethyl) carbonate	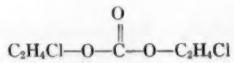	34.311 33.775	*S* *S*
11. *n*-Butyl chloroacetate	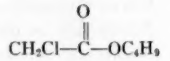	36.363 36.136	4*S* 10*S*
12. Phenyl chloroacetate	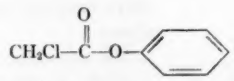	36.897 } 36.430 } 36.471 Av. 36.386 } 36.172 }	2*S* 3*S* 2*S* 2*S*
13. Chloroacetic acid	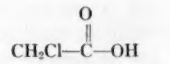	36.131[a] 36.429	
14. β-Chloropropionic acid	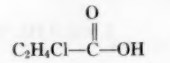	33.953	2.5*S*
15. Dimethyl chloroacetal	$CH_2ClCH[OCH_3]_2$	34.608±0.005	1*S*
16. 2,2,2-Trichloro-1-ethoxy ethanol	$CCl_3CHOH—O—C_2H_5$	39.137 38.703 38.516	2*S* 3*S* 2*S*

TABLE IX.—(*Continued*)

Compound		Frequency in Mc at 77°K	Signal-to-noise ratio
17. Methyl dichloroacetate	$CHCl_2—\overset{\overset{O}{\|\|}}{C}—O—CH_3$	38.724	3*S*
		38.334	3*S*
		37.828	2*S*
		37.621	2*S*
		37.385	3*S*
		38.351	3*S*
		37.306	3*S*
18. Methyl trichloroacetate[c]	$CCl_3—\overset{\overset{O}{\|\|}}{C}—O—CH_3$	40.152	3*S*
		39.867	2.5*S*
		39.763	1.5*S*
		39.681	4*S*

[a] H. C. Allen, Jr., J. Am. Chem. Soc. **74**, 6074 (1952).
[b] R. Livingston, J. Phys. Chem. **57**, 496 (1953).
[c] Sample purchased from Columbia Organic Chemicals, Inc., Columbia, South Carolina.

In 2,2-dichlorobutane the resonant frequency has dropped below that in 1,1-dichlorobutane. This can be accounted for by the presence of both a methyl group and an ethyl group bonded to the 2-position carbon. Both the methyl and ethyl groups are more electropositive than a hydrogen atom so that they cause the chlorine frequency to be lowered. In 2,2-dichloropropane there are two methyl groups bonded to the 2-position carbon causing the resonant frequency to drop below that in 1,1-dichlorobutane. However, the resonant frequency in 2,2-dichlorobutane is lower than that in 2,2-dichloropropane indicating that the ethyl group is more electropositive than the methyl group. This fact is demonstrated in several places thoughout this paper.

IONIC CHARACTER OF CARBON ATOMS OF DIFFERENT VALENCE

The sequence of compounds in Table VII demonstrates how the Cl^{35} resonance frequency rises as the electronegativity of the carbon atom (attached to the carbon atom of the carbon-chlorine bond) rises. That is, the effect of the hybridization[10] of the second-nearest carbon atom on the Cl^{35} frequency is shown in Table VII. The difference between an sp^3-hybridized carbon atom and an sp^2-hybridized carbon atom is small (about 500 or 600 kc), as can be seen by frequencies listed for the first four compounds. There is a definite jump in frequency with the sp-hybridized carbon atom (3-chloropropyne). The rise in resonant frequency in 1,4-dichloro-2-butene above that of allyl chloride can possibly be accounted for by the additional chlorine atom present. The resonant frequency in 1,4-dichloro-2-butene can also be compared with the resonant frequency found for 1,4-dichlorobutane (32.850 Mc, Table II). The increase in frequency can be attributed to the increased electronegativity of the carbon atoms due to the change from sp^3 hybridization in 1,4-dichlorobutane to sp^2 hybridization in 1,4-dichlorobutene. Likewise the 1-Mc increase in resonant frequencies in perchloroethylene over 1,1,2,2-tetrachloroethane (Table VI) can be attributed to this change in hybridization from sp^3 in 1,1,2,2-tetrachloroethane to sp^2 in perchloroethylene.

These increases in frequency with change in type of hybridization are what might be expected from an examination of the bond lengths of the chlorine-carbon bond of the various hybridized structures. R. Bersohn[11] has pointed out that there is an increase in the electronegativity of a carbon orbital with increase in *s* character resulting in (1) "a smaller effective atomic radius and therefore decreased bond length with respect to any attached atom" and (2) "a decreased ionic character of the C—Cl bond and therefore an increase in quadrupole coupling constant."[11] This is illustrated by a comparison of the bond lengths listed in Table VIII and the frequencies listed in Table VII.

EFFECT OF C=O OR C—O—C GROUPS

In Tables I–VI the data exhibit induction in a chain of tetrahedral (sp^3) carbon atoms. The question arises as to what happens if one or more of the carbon atoms is replaced by another atom or by sp^2 carbon atoms. Table IX contains data for several compounds in which oxygen atoms have replaced a carbon in the chain, or an sp^2 carbon atom has replaced an sp^3 carbon atom. The difference between the resonance frequencies in 1,3-dichloro-2-propanone and 1-chloro-2-propanone is 0.665 Mc, which indicates that the inductive effect of the two chlorine atoms upon each other is larger than that in 1,3-dichloropropane. The effect of introducing

[10] C. A. Coulson, *Valence* (Oxford University Press, New York, 1953).

[11] R. Bersohn, J. Chem. Phys. **22**, 2078 (1954).

TABLE X. Cl^{35} resonance frequencies in some nitrogen mustards.

Compound		Frequency in Mc at 77°K	Signal-to-noise ratio
1. β-Dimethylaminoethyl chloride hydrochloride[a]	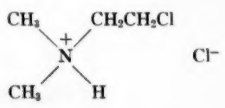	35.065	12*R*
2. γ-Dimethylaminopropyl chloride hydrochloride[a]	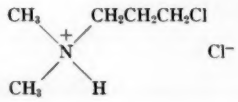	33.239±0.005	20*R*
3. β-Diethylaminoethyl chloride hydrochloride[a]	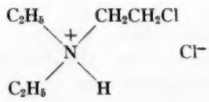	34.660±0.002	20*R*
4. Methyl *bis*(β-chloroethyl)amine hydrochloride[b]	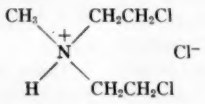	35.075±0.002	20*R*
5. β,β′-Dichlorodiethylamine hydrochloride[c]	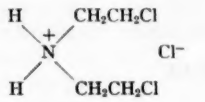	35.412±0.002 (34.244±0.002)	20*R* 25*R*
6. Tri(β-chloroethyl)amine hydrochloride[d]	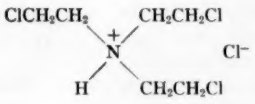	35.558 35.124	1.3*S* 2.5*S*
7. 2-Chloroethyldimethylamine	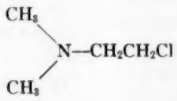	33.266	10*R*

[a] Sample obtained from Michigan Chemical Company, St. Louis, Michigan.
[b] Sample obtained from H.W. Bond, Consultant in Chemistry, Cancer Chemotherapy National Service Center, National Cancer Institute, Bethesda 14, Maryland.
[c] Sample purchased from Beacon Chemical Company, Cambridge, Massachusetts.
[d] Sample obtained from Army Chemical Corps.

an oxygen into a chain of carbon atoms is even larger than the effect caused by the introduction of the sp^2 carbon atom. This is illustrated by the large frequency difference (2.473 Mc) between the resonance frequencies of *bis*(chloromethyl) ether and chloromethyl methyl ether. Even in *bis*(2-chloroethyl) ether the effect of the oxygen is still noticeable when the resonance frequencies are compared with the resonance frequency in 1,5-dichloropentane. Both α-chloro-2,4-dimethyl acetophenone and β-chlorophenetole show that the phenyl group has a higher electronegativity than either the methyl (chloro-2-propanone) or chloroethyl (*bis* [2-chloroethyl] ether) groups. The resonant frequency in 1,2-*bis*(2-chloroethoxy) ethane is essentially unchanged from the resonant frequency in *bis*(2-chloroethyl) ether, which is not very surprising since the only difference between the two molecules occurs five atoms away from the chlorine atoms. The resonant frequencies found for 2-chloroethyl acetate and *bis*(2-chloroethyl) carbonate are slightly higher than the resonant frequencies found in *bis*(2-chloroethyl) ether which again indicates that the sp^2 carbon bonded to the oxygen acts with a greater electronegativity than an sp^3 carbon. The frequencies in 2-chloroethyl acetate and *bis*(2-chloroethyl) carbonate are very close to the frequency found in β-chlorophenetole, which is to be expected since in both cases an sp^2 carbon is present in the chain. The resonant frequencies in *n*-butyl chloroacetate, phenyl chloroacetate, and chloroacetic acid show how the various groups or atoms bonded to the oxygen in the chain vary the chlorine resonant frequency. Both the hydrogen atom in chloroacetic acid and the *n*-tetragonal butyl group in *n*-butyl chloroacetate seem to exhibit about the same effect on the chlorine resonant frequency while the sp^2 carbon atom of the phenyl group in phenyl chloroacetate raises the chlorine resonant frequency as has been indicated above. The large difference in frequency of over 2 Mc between the resonance frequencies found in chloroacetic acid and β-chloropropionic acid indicate again how rapidly the inductive effect decreases as the chlorine atom is separated from the perturbing group by an additional CH_2 group.

Dimethyl chloroacetal can best be compared with *bis* (2 - chloroethyl) ether and 1 , 2 - *bis* (2 - chloroethoxy) ethane, in which compounds the chlorine atom is separated from the oxygen atom by two carbon atoms, resulting in Cl^{35} resonance frequencies between 33.3 and 34.0 Mc. The Cl^{35} resonance frequency in dimethyl chloroacetal is higher by at least 600 kc which can be attributed to the additional oxygen atom. The last three compounds in Table IX contain two or more chlorine atoms bonded to one carbon atom which would increase the resonance frequency above any monochlorosubstituted compound. 2,2,2-trichloro-1-ethoxy ethanol can be compared with 1,1,1,5-tetrachloropentane (Table VI) to see that the effect of the hydroxyl group and the oxygen atom in the chain is to raise the resonant frequencies slightly above the frequencies found for the three chlorines at the 1 position in 1,1,1,5-tetrachloropentane. The sp^2 carbon bonded to two oxygens in methyl di- and trichloroacetate increases the resonant frequencies above those found in similar multichloro straight-chain hydrocarbons (see Table VI).

EFFECT OF NITROGEN ON Cl^{35} RESONANT FREQUENCIES IN SOME NITROGEN MUSTARDS

An excellent example of how potent the charged nitrogen atom is in its inductive effect on the Cl atom in a straight-chain-type compound can be found in the data listed in Table X. One can consider compound 1 as the basic compound to which all the other compounds in Table X can be referred. The insertion of an extra CH_2 group between the positive N and Cl atom lowers the resonant frequency by about 2 Mc to a frequency only slightly (0.27 Mc) higher than the frequency observed in 1-chloropropane (Table I). This indicates that the charged N atom has a very strong inductive effect upon a Cl atom which is separated from it by only two carbon atoms.

Compound 3 differs from compound 1 in that both CH_3 groups have been replaced by C_2H_5 groups. One would expect only a small change in resonant frequency since the ethyl groups are separated from the chlorine atom by two carbon atoms and the nitrogen. The lower frequency for compound 3, below that of compound 1, illustrates the fact that the ethyl group is less electronegative than the methyl group. In compound 4 one of the CH_3 groups of compound 1 has been replaced by a C_2H_4Cl group and the resonance frequency is unchanged. This means that any lowering effect of the C_2H_5 group is compensated by the tendency of the additional chlorine to increase the frequency of the other chlorine via their inductive effect.

In compound 5 both CH_3 groups were replaced, one by a hydrogen atom and the other by a C_2H_5Cl group. One would expect that the substitution of the CH_3 by a C_2H_4Cl would cause little or no change in frequency as was the situation in compound 4. However, the replacement of a CH_3 group by a hydrogen atom should cause an increase in resonant frequency. This effect is exhibited experimentally when one compares the frequencies of chloroethane and chloromethane. The frequency change in the nitrogen-mustard compound would not be so pronounced since the CH_3 group (or hydrogen atom) is separated from the chlorine atom by two carbons and the nitrogen. In the present discussion we have assumed that the resonant frequency which is applicable here is the 35.412-Mc line. There is something very strange occurring here because a difference of 1.2 Mc between two frequencies for compound 5 is not expected from previous pure quadrupole data. A shift of about 0.600 Mc due to crystalline effects is the maximum observed. A possible explanation for this large frequency difference is that the sample of compound 4 used for the resonance experiment may

TABLE XI. Comparison of Cl^{35} resonance frequencies in some chlrosilanes with the Cl^{35} resonance frequencies in corresponding chlorohydrocarbons.

Chlorosilanes				Chlorohydrocarbons			
Compound		Frequency in Mc at 77°K	Signal-to-noise ratio	Compound		Frequency in Mc at 77°K	ν_{C-Cl}/ν_{Si-Cl}[a]
1. Silicon tetrachloride	$SiCl_4$	20.467[b] 20.415 20.408 20.273		1. Carbon tetrachloride	CCl_4	40.64 (Av)[b]	1.99
2. Hexachlorodisilane[c]	Si_2Cl_6	19.319 19.287 19.271	3*S* 3*S* 3*S*	2. Hexachloroethane	C_2Cl_6	40.679 (Av)[b]	2.11
3. Trichlorosilane	$SiHCl_3$	19.163[d] 19.030 18.917	5*S* 1.5*S* 5*S*	3. Methyltrichloride	$CHCl_3$	38.309[b] 38.254	2.01
4. Methyltrichlorosilane[c]	CH_3SiCl_3	19.155 19.020 18.955	10*R* 6*R* 10R	4. 1,1,1-Trichloroethane	CH_3CCl_3	37.829[f] 38.052	1.99
5. Ethyltrichlorosilane[c]	$C_2H_5SiCl_3$	18.928 18.861 18.765 18.865[e] 18.842 18.756	1.5*S* 2*S* 2.5*S*	5. 1,1,1-Trichloropropane	$C_2H_5CCl_3$	Resonance not known	
6. Phenyltrichlorosilane[c]	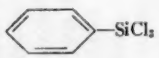	19.148	2*S*	6. α,α,α-Trichlorotoluene	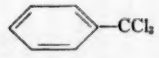	38.702 (Av)[b]	2.02
7. Vinyltrichlorosilane[c]	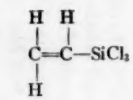	19.316 19.119 18.962	2*S* 2*S* 2.5*S*	7. 3,3,3-Trichloro-1-propene	$CH_2{=}CHCCl_3$	Resonance not known	

TABLE XI.—*Continued*

Chlorosilanes				Chlorohydrocarbons			
Compound		Frequency in Mc at 77°K	Signal-to-noise ratio	Compound		Frequency in Mc at 77°K	ν_{C-Cl}/ν_{Si-Cl}[a]
8. α-Chlorovinyltrichlorosilane[e]		20.361 19.401	3*S* 3*S*	8. 2,3,3,3-Tetrachloro-1-propene	$CH_2{=}CClCCl_3$	Resonance not known	
9. α,β-Dibromoethyltrichlorosilane[e]	$CH_2BrCHBrSiCl_3$	19.839 19.150	10*R* 5*R*	9. 1,1,1-Trichloro-2,3-dibromopropane	$CH_2BrCHBrCCl_3$	Resonance not known	
10. Ethyldichlorosilane[e]	$SiHCl_2C_2H_5$	18.179 17.954	20*R* 20*R*	10. 1,1-Dichloropropane	$CHCl_2C_2H_5$	Resonance not known	
11. Dimethyldichlorosilane[e]	$SiCl_2[CH_3]_2$	17.756±0.005	1.3*S*	11. 2,2-Dichloropropane	$CH_3CCl_2CH_3$	34.883[b]	1.96
12. Diethyldichlorosilane[e]	$C_2H_5SiCl_2C_2H_5$	17.740 17.515	10*R* 5*R*	12. 3,3-Dichloropentane	$C_2H_5CCl_2C_2H_5$	Resonance not known	
13. Trimethylchlorosilane[e]	$SiCl[CH_3]_3$	16.506	20*R*	13. 2-Chloro-2-methyl propane	$CH_3CHCl[CH_3]_2$	31.067	1.89
						Av $\nu_{C-Cl}/\nu_{Si-Cl}=2.00\pm0.11$[i]	

[a] The ratio of the resonance frequency for chlorine atoms in a carbon-chlorine bond to the resonance frequency for a chlorine atom in a silicon-chlorine bond in similar molecules.
[b] R. Livingston, J. Phys. Chem., **57**, 496 (1953).
[c] Sample purchased from Anderson Laboratories, Inc., Weston, Michigan.
[d] One line found at 20°K by R. Livingston (see footnote b).
[e] Sample purchased from Peninsular Chemical Research, Inc., Gainesville, Florida.
[f] R. Livingston, J. Chem. Phys. **20**, 1170 (1952).
[g] Q. Williams and T. L. Weatherly, J. Chem. Phys. **22**, 572 (1954).
[h] D. W. McCall and H. S. Gutowsky, J. Chem. Phys. **21**, 1300 (1953).
[i] A value of $\nu_{C-Cl}/\nu_{Si-Cl}=1.89$ is obtained from a comparison of microwave data for SiH_3Cl and CH_3Cl. These data are found in the Appendix of Townes and Schawlow, *Microwave Spectroscopy* (McGraw-Hill Book Company, Inc., New York, 1955).

have contained some impurity (containing a carbon-chlorine bond), in rather large amounts. However, the melting point of this sample was measured and found to be within the temperature region specified by the manufacturer (210° to 218°C).

Compound 6 differs from compound 4 in that the CH_3 group has been replaced by a CH_2CH_2Cl group. One of the resonant frequencies, which is probably due to two of the chlorine atoms (the signal-to-noise ratio of this frequency is twice the signal-to-noise ratio of the other frequency), is essentially the same as that found in compound 4. This indicates that the added CH_2CH_2Cl group has a negligible effect on the other chlorine atoms as was found in comparing compounds 4 and 5 with compound 1. The higher frequency measured for compound 6 may be due to a crystal-structure effect. The knowledge of the crystal structure of compound 6 would be helpful in the assignment of frequency to each of the three chlorine atoms.

Compound 7 is placed in Table X to allow a direct comparison of the resonant frequencies found in this group of compounds with the frequencies found in the straight-chain hydrocarbons (Table I). The frequency of 33.266 is only moderately higher than that exhibited by 1-chloroethane. The increase above the frequencies found in 1-chloroethane can be attributed to the nitrogen atom. The frequency of compound 7 is below that of compound 1 which can be explained by the fact that compound 1 is the hydrochloride of compound 7. The raising of resonant frequency when one examines the hydrochloride of a parent compound has been observed previously[12] and found to be of the order of 10%. In the present case the shift in frequency is in agreement with the previous data.

In concluding the discussion of the data in this table it can be stated that the large inductive effect of the charged nitrogen on the chlorine as shown in compounds 1 and 2 is the most pronounced effect which appears.

CHLOROSILANES

The Cl^{35} pure quadrupole resonance frequencies in several chlorosilane compounds have been detected, and the resonant frequencies are listed in Table XI. The chlorine resonant frequencies in the chlorosilanes are lower than the chlorine resonances in corresponding hydrocarbon compounds by a factor of about 2. This lowering is due to the difference in electronegativities[13] of the silicon atom (1.8) and the carbon atom (2.5). If the various groups and atoms bonded to a silicon atom, other than the chlorine atom being studied, have no influence on the formation of a silicon-chlorine double bond through use of silicon *d* orbitals, one should expect the ratio of the transition frequencies for a carbon-chlorine compound to its equivalent silicon-chlorine compound to be the same for all compounds. However, if these groups and atoms do have considerable influence, then one should find wide variations in the above-mentioned ratio from one set of similar compounds to another. The ratios are listed in Table XI and the average of seven such values is 2.00 ± 0.11. The variation of this ratio is such that no strong conclusion can be drawn from the ratio as to whether the groups and atoms bonded to the silicon atoms have an influence on the formation of a silicon-chlorine double bond.

Reasoning similar to that used in describing the effects of various atoms and groups upon the carbon-chlorine bonds in the previous data can be applied to the data in Table XI concerning the silicon-chlorine bonds. The resonant frequencies in silicon tetrachloride seem to form an upper bound upon the chlorine frequencies for atoms in the chlorine-silicon bond, just as was the case in carbon tetrachloride. The frequencies in hexachlorodisilane are about 1 Mc below the frequencies in silicon tetrachloride, while the frequencies for trichlorosilane fall below those of silicon tetrachloride by about 1.3 Mc. The frequencies found for methyl-, phenyl-, and vinyltrichlorosilanes are all about the same as the frequencies found in trichlorosilane with the exception that both the phenyl- and vinyltrichlorosilanes show a slight rise in frequency above trichlorosilane, indicating that both the vinyl and phenyl groups are slightly more electronegative than a single hydrogen. This is due to the change in hybridization of the carbon bonded to the silicon.

The methyl group in methyltrichlorosilane does not show its usual lowering effect upon the chlorine resonance frequency. However, the ethyl group which is slightly more electropositive than the methyl group has caused a definite decrease in frequency from that of trichlorosilane as is exhibited by the data for ethyltrichlorosilane. For α-chlorovinyltrichlorosilane two frequencies are listed and should be assigned to the chlorine atoms bonded to the silicon atom and not to the one chlorine in the chlorine-carbon bond. These two lines were of about equal intensity which seems to indicate that two resonant frequencies were not found. One of these frequencies would be for the chlorine bonded to the carbon and be at much higher frequency (in the 30-Mc region). The additional chlorine in α-chlorovinyltrichlorosilane has caused an increase in the transition frequencies above those found in vinyltrichlorosilane. In α,β-dibromoethyltrichlorosilane the resonance frequencies have been raised by the inductive effect of the two bromine atoms so that the resonance frequencies are above those found in ethyltrichlorosilane. Bromine with an electronegativity[13] of 2.8 is very similar in its action to chlorine with an electronegativity of 3.0. Therefore, additional bromine atoms would raise the resonant frequency just as additional chlorine atoms raise the resonant frequency.

The two resonant frequencies found for ethyldichlorosilane are 1 Mc below the resonant frequencies in tri-

[12] S. L. Segel, R. G. Barnes, and P. J. Bray, J. Chem. Phys. **25**, 1286 (1956).

[13] L. Pauling, *The Nature of the Chemical Bond* (Cornell University Press, Ithaca, New York, 1948).

TABLE XII. Cl^{35} resonances in some compounds which contain chlorine atoms bonded to nitrogen atoms.

Compound	Frequency in Mc at 77°K	Signal-to-noise ratio
Chloramine T[a]	45.724	1.5*S*
Dichloramine T[b]	51.600	1*S*
N-chloro-*p*-quinoneimide	44.992[c]	
N-chlorosuccinimide	54.100[c]	
1,3 Dichloro 5,5-dimethylhydantoin[d]	55.950 53.627	2*S* 2*S*

[a] Sample obtained from Fluka A.G., Chemische Fabrik, Buchs SG Switzerland.
[b] Sample purchased from British Drug Houses Ltd., Poole, England.
[c] S. L. Segel, R. G. Barnes, and P. J. Bray, J. Chem. Phys. **25**, 1286 (1956).
[d] Sample purchased from Matheson Coleman and Bell, East Rutherford, New Jersey.

chlorosilane. This change is due to the fact that there is one less chlorine atom bonded to the silicon atom in ethyldichlorosilane, and also the electropositive ethyl group is bonded to the silicon atom. In dimethyldichlorosilane the two methyl groups act in a more electropositive manner than the single hydrogen atom and ethyl group which are attached to the silicon atom in ethyldichlorosilane. Therefore, the frequency in dimethyldichlorosilane is lower than the frequency found in ethyldichlorosilane. In diethyldichlorosilane two ethyl groups are bonded to the silicon atom and act in a manner similar to that of the two methyl groups in dimethyldichlorosilane. The fact that the resonance frequencies in diethyldichlorosilane are slightly lower than the resonant frequency in dimethyldichlorosilane illustrates again that the ethyl group is less electronegative than the methyl group.

Trimethylchlorosilane is the only monochlorosilane in which a resonance has been detected. The resonance is about 3 Mc below the resonance in trichlorosilane, owing to the removal of two of the chlorine atoms. The three methyl groups also act in their usual electropositive manner to lower the resonance frequency. Because of the three methyl groups in trimethylchlorosilane one might expect that 16.506 Mc is an approximate lower bound on chlorine resonant frequencies from chlorine nuclei in chlorine atoms bonded to silicon atoms.

COMPOUNDS CONTAINING A NITROGEN-CHLORINE BOND

Several compounds in which a chlorine atom is bonded to a nitrogen atom have been investigated. Data for five such compounds are found in Table XII. All the resonant frequencies listed are near the resonant frequency of chlorine in Cl_2 (54.248 Mc at 77°K)[14]. This is very reasonable since both nitrogen and chlorine atoms are assigned the same electronegativity.[13] This means that both the N—Cl bond and the Cl—Cl bond would have the same amount of ionic character. These five compounds fall into two groups as suggested by Segel, Barnes, and Bray.[12] For compounds 1, 2, and 3

[14] R. Livingston, J. Chem. Phys. **19**, 1434, 803 (1951).

TABLE XIII. Cl^{35} resonances in some sulfur containing compounds.

Compound		Frequency in Mc at 77°K	Signal-to-noise ratio
Sulfur monochloride[a]	S_2Cl_2	35.605 35.994	10*R* 10*R*
Perchloromethylmercaptan[b]	CCl_3SCl	39.166 39.827 40.117	3*S* 2.5*S* 5*S*
2,5-Dichlorothiophene[b]	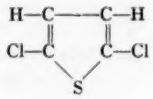	37.018 37.071	2*S* 5*S*
2-Chlorobenzothiazole	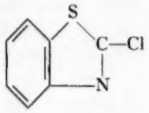	36.210	1.5*S*
2-Chloroethyl-*p*-toluenesulfonate	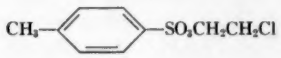	34.590	3*S*
2-Chloroethyl chlorosulfinate[c]	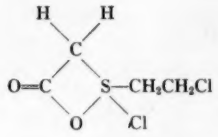	34.320	2*S*
m-(Chlorosulfonyl) benzoic acid	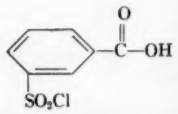	33.672	*S*

[a] Sample obtained from Stauffer Chemical Company, New York 17, New York.
[b] Sample purchased from Aldrich Chemical Company, Milwaukee, Wisconsin.
[c] Sample purchased from Naugatuck Chemical Company, Naugatuck, Connecticut.

in Table XII the most probable resonance structure contains a negatively charged nitrogen regardless of whether sp^2-trigonal or sp-digonal orbitals are used. The chlorine in these three compounds may acquire some of this charge increasing the ionic character of the N—Cl bond and lowering the resonant frequency. Dichloromine *T* is not an exception because the added chlorine would cause an increase in frequency as has previously been shown.

In compounds 4 and 5 the electron distribution at the nitrogen atom probably resembles that in pyrrole. The sp^2-trigonal orbitals are all used for bonding and the nonbonding pair occupies the π orbital. Therefore, the probable resonance structures in this case contain only a positively charged nitrogen. The chlorines in these two compounds would have a higher resonant frequency as the positive nitrogen acts in a manner similar to the positive nitrogen in the compounds listed in Table X. The two different resonant frequencies found in compound 5 can be attributed to the two chlorines which each have a different environment in the molecule. The higher frequency is probably due to the chlorine atom bonded to the nitrogen atom which has two adjacent carbons that are both bonded to oxygen atoms as in compound 4. The lower frequency can be assigned to the chlorine bonded to the nitrogen which has one adjacent carbon bonded to an oxygen and one adjacent carbon bonded to two methyl groups. The two methyl groups act to reduce the chlorine frequency as shown by the data in Table V.

SULFUR-CONTAINING COMPOUNDS

The electronegativity of the sulfur atom is commonly given as identical with that of the carbon atom (2.5),[13] so that one might expect that Cl^{35} resonances from chlorine atoms bonded to sulfur atoms would be very close to the frequencies for Cl^{35} resonances from chlorine atoms bonded to carbon atoms. However, upon exam-

ining the resonance frequencies of Cl^{35} nuclei bonded to sulfur atoms, or to carbon atoms which are bonded to sulfur atoms, one is confronted with the fact that sulfur can exhibit several valence states and, therefore, will have different electronegativity values.[15] It is found that an increased valence state increases the electronegativity.[15,16] For the compounds in Table XIII this generally would cause an increase in the Cl^{35} resonance frequency.

In sulfur monochloride (Table XIII) and perchloromethylmercaptan the sulfur atom seems to act in a manner equivalent to that of a carbon atom in a similar situation in the molecule. One of the resonances from S_2Cl_2 is seen to be almost identical with the resonance in CH_2Cl_2 (Table II), and the other resonance line from S_2Cl_2 is within possible crystal-structure shifts. This seems strange since the sulfur atom is in a different valence state from the carbon atom in this situation. The data for perchloromethylmercaptan can be compared with the resonances found for Cl^{35} nuclei in similar situations as in heptachloropropane (Table VI). On comparison it is seen that the sulfur compound and both heptachloropropane compounds have similar Cl^{35} resonant frequencies. The signal-to-noise ratios for perchloromethylmercaptan indicate that two of the four chlorine atoms are in equivalent positions. The lowest of the three frequencies is probably due to the chlorine atom bonded to the sulfur atom since the inductive effect from the other chlorine atoms is smaller.

Resonances in 2,5-dichlorothiophene have been reported elsewhere by Dewar and Lucken.[17] They have reported six lines, two of which correspond to the values listed here, and the other four lines are lower in frequency. Thiophene is found to resemble benzene very closely in its properties and in its electronic structure.[18] However, the Cl^{35} resonances in 2,5-dichlorothiophene are seen to be about 2–3 Mc above similar chlorobenzene compounds. This can be attributed to the increased valence of sulfur (*d* orbitals are required for bonding[18]) which causes an increase in electronegativity. This argument was previously used by Dewar and Lucken[17] and seems to account for the increase in resonance frequency of the Cl^{35} nuclei in 2,5-dichlorothiophene.

In 2-chlorobenzothiazole the sulfur atom is probably in a bonding state similar to that in 2,5-dichlorothiophene. However, the frequency has decreased by almost 0.9 Mc. This decrease can be attributed to the presence of the nitrogen atom in 2-chlorobenzothiazole. The nitrogen acts in a manner similar to that in 2-chloropyridine.[5] In 2-chloropyridine the Cl^{35} resonance frequency was found to decrease (below the Cl^{35} frequency in chlorobenzene). This decrease was attributed to an increased double-bond character of the carbon-chlorine bond. Therefore, a similar increase in double-bond character of the carbon-chlorine bond in 2-chlorobenzothiazole would account for the 0.9-Mc decrease in frequency below 2,5-dichlorothiophene.

TABLE XIV. Comparison of Cl^{35} resonance frequencies in some groups with structures related to $-SO_2Cl$.

Sulfur compound (group)	Frequency in Mc	Carbon compound (group)	Frequency in Mc
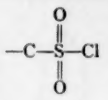	32.5–33.5[a]	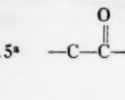	29–31[b]
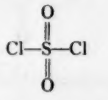	37.7[b]	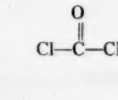	35.7[a]

[a] P. J. Bray and D. Estara, J. Chem. Phys. **22**, 570 (1954).
[b] P. J. Bray, J. Chem. Phys. **23**, 703 (1955).

The resonant frequency in 2-chloroethyl-*p*-toluenesulfonate is very close to that in 1,2-dichloroethane (Table II), which indicates that the *p*-toluenesulfonate group is approximately equivalent to a chlorine in that the *p*-toluenesulfonate group raises the resonant frequency to a value higher than the resonant frequency in 1-chloroethane or 1-chloropropane. Some of this increase in frequency might well be due to the increased electronegativity of sulfur as a consequence of the increased valence state of sulfur. It is difficult to make comparisons between this type of sulfur compound and similar carbon compounds because the sulfur atoms exhibit a higher valence state than carbon atoms.

In 2-chloroethyl chlorosulfinate only one resonance was detected indicating that one resonance was overlooked or that both resonances occurred at the same frequency. The resonance in 2-chloroethyl chlorosulfinate is very close to that in 2-chloroethyl-*p*-toluenesulfonate, so that this one frequency might well be assigned to the chlorine atom in the 2-chloroethyl group. However, one cannot exclude the possibility that the observed resonance arises from the chlorine atom in the sulfur-chlorine bond.

The Cl^{35} resonant frequency in *m*(chlorosulfonyl)benzoic acid agrees with previous data[19] given for Cl^{35} atoms in the $-SO_2Cl$ groups. For a further comparison of the effect of sulfur and carbon atoms upon the Cl^{35} resonance frequencies, the data in Table XIV are of interest. The frequency ranges stated in Table XIV for Cl^{35} in the $-CSO_2Cl$ group and the $-CCOCl$ group are the upper and lower limits of the Cl^{35} resonance frequencies in several compounds containing these respective groups. From Table XIV it can be seen that the oxygen atom in the $-CCOCl$ group lowers the Cl^{35} frequency below that of 1-chloroethane. Also there is a large

[15] H. O. Pritchard and H. A. Skinner, Chem. Revs. **55**, 745 (1955).
[16] M. Haissinsky, J. phys. radium **7**, 7 (1946).
[17] J. S. Dewar and E. A. C. Lucken, J. Chem. Soc. **1959**, 426.
[18] Longuet-Higgins, Trans. Faraday Soc. **45**, 173 (1949).
[19] P. J. Bray and D. Esteva, J. Chem. Phys. **22**, 570 (1954).

TABLE XV. Cl^{35} resonances in some chloroquinones and related compounds.

Compound		Frequency in Mc at 77°K	Signal-to-noise ratio
1-Chloroanthraquinone[a,b]	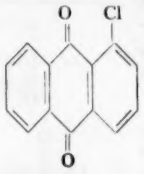	37.529±0.030	5*R*
2-Chloroanthraquinone	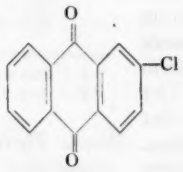	35.390	7*R*
1,5-Dichloroanthraquinone[a,b]	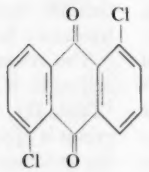	36.885	6*R*
1,8-Dichloroanthraquinone[a]	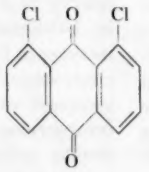	36.777	3*R*
2,3-Dichloronaphthaquinone[c]	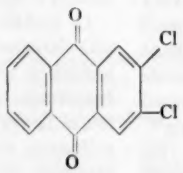	37.111 36.667	2*S* 2*S*
Tetrachlorophthalic acid[b]	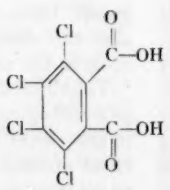	38.424 38.140	1.2*S* 1.3*S*
Tetrachlorophthalic anhydride[b]	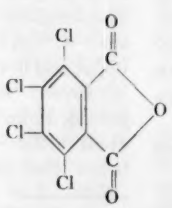	38.413 38.249	1*S* 1.1*S*

TABLE XV.—*Continued*

Compound		Frequency in Mc at 77°K	Signal-to-noise ratio
Chloromaleic anhydride	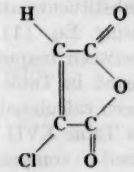	37.187	7*S*

[a] Sample purchased from Aldrich Chemical Company, Milwaukee, Wisconsin.
[b] Sample purchased from British Drug House Ltd., Poole, England.
[c] Sample purchased from Naugatuck Chemical Company, Naugatuck, Connecticut.

inductive effect between the two chlorine atoms in ClCOCl as is indicated by the increase in frequency of about 5.5 Mc above the Cl^{35} frequency from —CCOCl groups. There is a similar increase in frequency for the sulfur compounds due again to the large inductive effect of the chlorine atoms upon one another. However, the Cl^{35} frequencies in both of the sulfur compounds are above the frequency in the corresponding carbon compound. This indicates that the SO_2 group raises the Cl frequency above that of a Cl bonded to a CO group. Since the oxygen atom seems to decrease the frequency (compare the Cl^{35} frequencies in 1-chloroethane with those in the —CCOCl group), these data indicate again that the sulfur atom in its higher valence state effects the chlorine atom in a different manner than does the carbon atom.

CHLOROQUINONES AND RELATED COMPOUNDS

The Cl^{35} resonant frequencies in Table XV show how the doubly bonded oxygen effects the charge distributions at various positions in several aromatic compounds. The resonant frequency of a chlorine attached to the 2 position in anthraquinone is about 1.3 Mc above the resonant frequency found in chlorobenzene.[20–22] This rise in frequency can be predicted from an analysis employing Hammett[4] σ values and the linear relation between Hammett σ values and Cl^{35} resonance frequencies.[2] In such an analysis the quinone ring can be considered equivalent to two CHO groups. The 2-position chlorine has a *meta*-CHO and a *para*-CHO group while the 1-position chlorine has an *ortho*-CHO and a *meta*-CHO group. σ values for *meta*-CHO and *para*-CHO can be taken as 0.382 and 0.216, respectively.[23] The σ value for *ortho*-CHO can be calculated from the resonant frequency in 2,4-dichlorobenzaldehyde (Table XVII) if one assumes the linear relation between Cl^{35} resonant frequencies and Hammett σ values as expressed by Eq. (1). If one now uses the σ values for the CHO group to predict the frequencies, good agreement is obtained with the resonant frequency for the chlorine at the 2 position, but the predicted frequency for the 1-position chlorine is about 1.5 Mc lower than the measured frequency. It is quite possible that the *ortho*-CHO σ value used here is a poor approximation to the real σ value in this situation so that this 1.5-Mc discrepancy means very little. However, the σ-value analysis does show that the frequency for 1-chloroanthraquinone should be higher than the frequency for 2-chloroanthraquinone owing to the increased inductive effect of the oxygen atom. The frequencies for 1,5- and 1,8-dichloroanthraquinone should also be above the frequency in 2-chloroanthraquinone because of this increased inductive effect of the oxygen atom.

If one now compares the resonance frequencies from the two dichloroanthraquinones with the frequency in 1-chloroanthraquinone, it is surprising to find that the frequencies are lower for the dichloroanthraquinones than for 1-chloroanthraquinone. Previous data indicate that dichloro compounds usually have higher resonance frequencies than similar monochloro compounds owing to the inductive effect between the two chlorine atoms. A possible explanation for the relative frequencies in the two dichloroanthraquinones and 1-chloroanthraquinone may lie in the value of the asymmetry parameter for the chlorine atoms in these molecules. Anthraquinone is a planar molecule as determined from x-ray data.[24] However, it is quite possible that the oxygen chlorine repulsion for chlorine atoms in the 1, 5, or 8 positions in anthraquinone may distort the molecule from a planar structure. This would cause a change in the asymmetry parameter of these chlorine atoms which would alter the resonance frequency. This distortion from planar structure could well be larger for the dichloroanthraquinones than for 1-chloroanthraquinone. The larger asymmetry parameter would account for the frequencies in the dichloroanthraquinones being lower than the frequency in 1-chloroanthraquinone.[6,11]

The resonance frequencies in 2,3-dichloronaphthoquinone and chloromaleic anhydride are essentially the same which indicates that the oxygen in the ring of

[20] H. C. Meal, J. Am. Chem. Soc. **74**, 6121 (1952).
[21] R. Livingston, Phys. Rev. **82**, 289 (1951).
[22] C. Dean and R. V. Pound, J. Chem. Phys. **22**, 195 (1952).
[23] H. H. Jaffe, Chem. Revs. **53**, 191 (1953).
[24] S. N. Sen, Indian J. Phys. **22**, 347 (1948).

chloromaleic anhydride must act to raise the frequency in a strong manner, just as the additional chlorine in 2,3-dichloronapthoquinone has a strong inductive effect upon the other chlorine. The frequencies found in tetrachlorophthalic acid and tetrachlorophthalic anhydride are essentially the same which indicates that the change from an acid to the anhydride occurs at a position too far removed from the chlorines to cause appreciable change in the charge distributions at the chlorine nuclei.

A STUDY OF INDUCTION BY MEANS OF BENZYL COMPOUNDS

In Table XVI a comparison has been made between the Cl^{35} resonance frequencies in some chlorobenzene derivatives and the corresponding chlorobenzyl compounds. The resonance frequencies from the chlorine atoms in the benzyl groups are lower than the resonance frequencies from the chlorine atoms attached to the benzene ring in similar compounds. This is to be expected from the change in hybridization of the carbon to which the chlorine is bonded (see Table VII). The data in Table XVI also indicate that the effect of a ring substituent on the chlorine atom, separated by a CH_2 group from the benzene ring, is substantially less than if the chlorine atom is directly attached to the benzene ring. This fact is indicated by the $\Delta\nu$ values listed in Table XVI, where the $\Delta\nu$ for each of the chlorobenzyl compounds is less than the $\Delta\nu$ for the corresponding chlorobenzene. For the chlorobenzene derivatives, $\Delta\nu$ is the difference in frequency between the particular benzene derivative and the frequency in chlorobenzene. Similarly, for the chlorobenzyl compounds, $\Delta\nu$ is the difference in frequency between the particular chlorobenzyl compound and benzyl chloride.

From the ratios of $\Delta\nu$ for the benzene compound to $\Delta\nu$ for the corresponding benzyl compound, it can be seen that the effect of the ring substituent on the chlorine atom in the benzyl group is about three-quarters of what it is in the chlorobenzene derivative. The one discrepancy seems to arise from the low frequency in *p*-chlorobenzyl chloride for the chlorine bonded directly to the benzene ring. From the known σ value (+0.184) for *p*-CH_2Cl and Eq. (1), one can predict a resonance frequency of about 35.01 Mc for the chlorine attached to the benzene ring in *p*-chlorobenzyl chloride. This rather large difference between the measured frequency and the frequency predicted from Hammett σ values is unusual in the case of only a para substituent attached to chlorobenzene. This frequency shift could possibly be due to crystal effects.

In the calculation of $\Delta\nu$ for *o*-dichlorobenzene, an average frequency of the four frequencies was used. In the case of α, *o*-dichlorotoluene, the two lower frequencies were averaged and assigned to the chlorine in the benzyl group.

CHLOROBENZENE COMPOUNDS

In discussing Cl^{35} resonances in chlorobenzene derivatives, it is possible in many cases to predict accurately the resonant frequencies if the Hammett[4] substituent parameters, σ, are known. This can be done using Eq. (1), which expresses the linear relation between frequency and σ values. For the compounds listed in Table XVII, Cl^{35} resonant frequencies have been calculated using Eq. (1). For several compounds in Table XVII the observed resonant frequencies were used to compute unknown σ values. In all of this work two main assumptions have been used. First of all, in computing a resonant frequency for a multisubstituted chlorobenzene, the σ values of each substituent were added algebraically except in the cases where σ values for disubstitution have been given by Jaffe.[23] Secondly, it must be remembered that possible crystal effects can be present which may shift the Cl^{35} resonance frequency.

In 4-amino-2,6-dichlorophenol agreement between experimental and predicted frequencies is good, even though the σ_oOH value has only been estimated approximately from other quadrupole resonance data.[2]

Only one resonance has been found in α,2,4-trichlorotoluene, where one would expect three resonances, since the three chlorine atoms are in nonequivalent positions in the molecule. Using known σ values, the frequency for the 4-position chlorine was predicted and found to be within a possible crystal-structure shift of the measured frequency. If one uses the same observed frequency for the 2-position chlorine to calculate $\sigma_o CH_2Cl$, the value of $\sigma_o CH_2Cl = 0.289$ is obtained. This is slightly higher than the $\sigma_p CH_2Cl = 0.184$ value given by Jaffe.[23] Since the inductive effect depends on the distance between two chlorine atoms, one expects that the three σ values for the CH_2Cl group would obey the condition $\sigma_o CH_2Cl > \sigma_m CH_2Cl > \sigma_p CH_2Cl$.

Four resonances were found for α,3,4-trichlorotoluene, where one would expect three different resonances. There is an indication from the observed signal-to-noise ratios that there may have been only two resonance lines located, each of these lines being split by about 200 kc. Therefore, the problem of assignment of experimental resonance frequencies to the various chemically inequivalent chlorine atoms arises. The calculation of the frequency for the 4-position chlorine atom gives a value of 36.306 Mc which is very close to the average of the two higher of the four measured frequencies. Since the *m*-CH_2Cl σ value is not known, one cannot predict the frequency for the 3-position chlorine. If one uses the average of the two lower of the four frequencies to predict $\sigma_m CH_2Cl$, then a negative σ value of $\sigma_m CH_2Cl \sim -0.39$ is obtained. This does not seem realistic when compared to other σ values given by Jaffe.[23] Another possible assignment of frequencies to the chlorine atoms attached to the different ring positions is to assign the 36.232-Mc frequency to the 4-position chlorine (which agrees within a small crystal effect with the predicted

TABLE XVI. Comparison of Cl^{35} resonance frequencies in some chlorobenzene compounds and corresponding chlorobenzyl compounds.

Compound	Frequency in Mc	$\Delta\nu$	Signal-to-noise ratio	Footnote reference
Chlorobenzene compounds				
1. Chlorobenzene 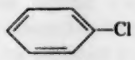	34.622	0		20–22
2. *p*-Dichlorobenzene	34.779	+0.157		20, 22[a]
3. *m*-Chloronitrobenzene 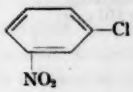	35.457	+0.835		20
4. *p*-Chlorobenzyl chloride 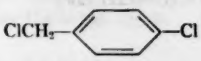	34.567	−0.055		20
5. *o*-Dichlorobenzene 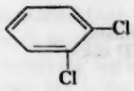	35.824 35.755 35.580	+1.107		20
Chlorobenzyl compounds				
1. Benzyl chloride 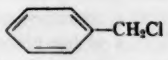	33.627	0		20
2. *p*-Chlorobenzyl chloride 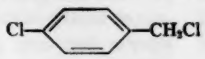	33.754	+0.127		20
3 *m*-Nitrobenzyl chloride 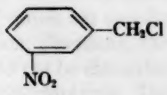	34.216	+0.589	3*S*	
4. α,α'-Dichloro-*p*-xylene	33.863	+0.206	3*S*	
5. α,o-Dichlorotoluene 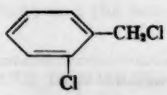	35.225 34.560 34.795	+0.765	4.5*R* 9*R* 10*R*	

[a] See also T. C. Wang, C. H. Townes, A. L. Schawlow, and A. N. Holden, Phys. Rev. 86, 809 (1952).

TABLE XVII. Cl^{35} resonance frequencies in some previously unreported chlorobenzene compounds at 77°K.

Compound	σ Values[a]	Frequency in Mc calc	Frequency in Mc obs	Signal-to noise ratio
4-Amino-2,6-dichlorophenol[b] 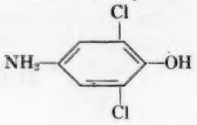	$\sigma_m Cl+\sigma_m NH_2+\sigma_o OH$[c]	35.956±0.38	35.950	2*R*
α,2,4-Trichlorotoluene 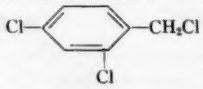	$\sigma_p CH_2Cl+\sigma_m Cl$ (4 position) $\sigma_m Cl+(\sigma_o CH_2Cl=+0.289$ calc) [2 position]	35.397	35.505	1*S*
α,3,4,-Trichlorotoluene 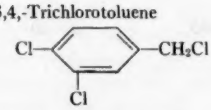	$\sigma_p CH_2Cl+\sigma_o Cl$[c] (4 position) $\sigma_o Cl+(\sigma_m CH_2Cl=0.310$ calc) [3 position]	36.306	36.232 36.436 35.854 35.673	13*R* 6*R* 12*R* 6*R*
2,5-Dichloroacetophenone 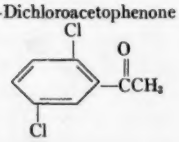	$\sigma_p Cl+\sigma_m COCH_3$ (5 position) $\sigma_p Cl+(\sigma_o COCH_3=0.221$ calc) [2 position]	35.372	35.335 35.285	1*S* 1*S*
2,4-Dichlorobenzaldehyde 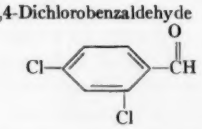	$\sigma_m Cl+\sigma_p CHO$ [4 position] $\sigma_m Cl+(\sigma_o CHO=0.757$ calc) [2 position]	35.340	35.461 35.986	10*R* 10*R*
3-Chloro-*p*-toluene sulfonic acid sodium salt 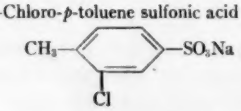	$\sigma_o CH_3$[c]$+\sigma_m SO_3Na$[c]	35.280	34.911	1*S*
o-Chlorophenyl isocyanate 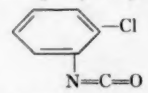	$\sigma_o NCO=-0.186$ (calc)		34.635	2*S*
3,4-Dichlorobenzaldehyde 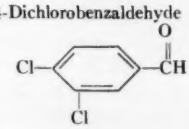	$\sigma_o Cl$[c]$+\sigma_p CHO$ $\sigma_o Cl+\sigma_m CHO$	36.336 36.506	35.685[d] 36.762	3*R* 3*R*
2,6-Dichlorotoluene[e] 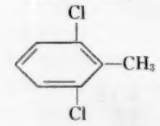	$\sigma_m Cl+\sigma_o CH_3$[c]	35.508	34.788 34.755	1.5*S* 2*S*

[a] σ-Values are taken from H. H. Jaffe, Chem. Revs. **53**, 191 (1953) unless otherwise noted.
[b] Sample purchased from British Drug House Ltd., Poole, England.
[c] σ-Values are taken from P. J. Bray and R. G. Barnes, J. Chem. Phys. **27**, 551 (1957).
[d] This resonance is a spread-out resonance 25.65–36.0 Mc.
[e] Sample obtained from R. Bersohn, Columbia University.

36.306 Mc), to assign the 36.436 frequency to the 3-position chlorine, and to assign the two lower frequencies to the chlorine in the methyl group. In this case the calculated value of $\sigma_m CH_2Cl$ is +0.310, which seems reasonable compared to $\sigma_p CH_2Cl$, but indicates that the $\sigma_o CH_2Cl$ value calculated from α,2,4-trichlorotoluene may be too low.

The calculated resonance frequency for the 5-position chlorine in 2,5-dichloroacetophenone agrees closely with the higher of the observed frequencies for this compound. The lower frequency can be assigned to the 2-position chlorine, from which, using Eq. (1), a $\sigma_o COCH_3$ value of 0.221 is predicted.

A process similar to that carried out for 2,5-dichloroacetophenone has been carried out for 2,4-dichlorobenzaldehyde leading to the result that $\sigma_o CHO = 0.757$.

In 3-chloro-*p*-toluene sulfonic acid sodium salt the σ values derived from previous quadrupole resonance data[2] were used to predict the resonant frequency. Agreement is not good but well within reasonable shifts caused by crystal structure.

The single resonant frequency observed in *o*-chlorophenyl isocyanate was used to calculate the ortho sigma value for the isocyanate group.

One of the predicted resonances in 3,4-dichlorobenzaldehyde does not agree well with the observed resonance (35.685 Mc). It should be mentioned that this resonance is a spread-out resonance with several peaks (signal-to-noise ratio of about $2R$) occurring between 35.6 and 36.0 Mc. The value of 35.685 Mc is for the largest peak.

The predicted resonant frequency in 2,6-dichlorotoluene is in very poor agreement with the observed resonant frequencies. A possible explanation, other than a very large crystal effect, for this disagreement is that the individual σ values in this case should not be added to get the total effective σ value. This is in agreement with the conclusions of Jaffe[23] who points out that the sum of the individual sigma values obtained from monosubstituted chlorobenzene reactions does not always agree with the total σ value found in the di- or trisubstituted benzene reactions. In cases of two substituents on chlorobenzene, the additivity of σ values has usually been found to be a good approximation. Therefore, the concept of additivity of σ values should not be discarded on the basis of the data from 2,6-dichlorotoluene. The compound 2,6-dichlorotoluene is a particularly bad case because the CH_3 group is ortho to the chlorine.

The data in Table XVII indicate that Eq. (1) can be used to good advantage in predicting resonance frequencies in most cases. However, discrepancies do arise due primarily to the crystal-structure effects and the nonadditivity of individual σ values.

BROMOBENZENE COMPOUNDS AND HAMMETT σ VALUES

It has previously been indicated[3] that a linear relation exists between the Br^{81} (or Br^{79}) pure quadrupole resonance frequency and the Hammett σ value. Such a relationship has been experimentally obtained for Cl^{35} pure quadrupole resonances. From the data listed in Table XVIII a linear relationship,

$$f(Br^{81}) = 226.932 \text{ Mc} + 7.639 \sum_i \sigma_i, \qquad (2)$$

has been calculated. The root-mean-square deviation in megacycles per second (Mc) of the experimentally determined f values from those predicted by the straight line is $S = 2.98$. Table XVIII contains all available bromine pure quadrupole data at 77°K. The frequencies quoted in this table are either the experimentally measured Br^{81} resonance frequencies or the converted experimentally measured Br^{79} resonance frequencies. The Br^{79} frequencies were converted to equivalent Br^{81} resonant frequencies using the ratio 1.1970.[3] In some cases average values of the frequencies are used. These cases are indicated by Av following the resonance frequency in Table XVIII. The σ values used are taken from Jaffe's[23] article or from the results of Cl^{35} resonance measurements.[2] Linear additivity of σ values is assumed unless di- and trisubstitution[23] σ values are known.

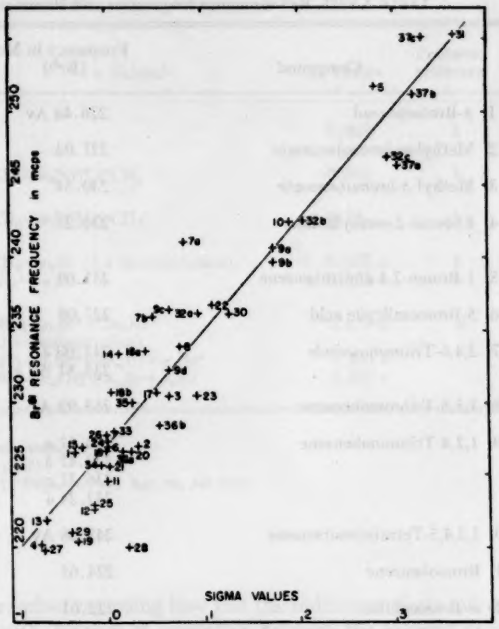

FIG. 1. A plot of Br^{81} pure quadrupole resonance frequencies vs Hammett sigma values.

In Fig. 1 a plot is made of the Br^{81} frequencies against the sum of the σ values (the data being taken from Table XVIII). The straight line in this plot is the calculated linear relation derived from the data in Table XVIII employing the method of least squares.

In Table XIX several previously unreported Br^{79} and Br^{81} resonances are listed. The first five of these

TABLE XVIII. Br^{81} resonance frequencies and Hammett sigma values for some bromobenzene compounds at 77°K.[a]

Compound	Frequency in Mc (Br^{81})	σ Values[b]	$\Sigma\sigma$ Values	Footnote reference
1. *p*-Bromophenol	226.44 Av	$\sigma_p OH$	−0.357	3
2. Methyl-*m*-bromobenzoate	227.04	$\sigma_m COOCH_3$	0.315	3
3. Methyl-*p*-bromobenzoate	230.54	$\sigma_p COOCH_3$	0.636	3
4. 4-bromo-2-methylaniline	220.23	$\sigma_m CH_3+\sigma_p NH_2$ (3,4 disubstitution)	−0.716	3
5. 1-Bromo-2,4-dinitrobenzene	251.69	$\sigma_o NO_2{}^c+\sigma_p NO_2$	2.807	3
6. 5-Bromosalicylic acid	227.08	$\sigma_m COOH+\sigma_p OH$	0.000	3
7. 2,4,6-Tribromoanisole	241.60 *a* 235.81 Av *b*	$\sigma_o OCH_3{}^c+2\sigma_m Br$ (3,5 disubstitution) $\sigma_m Br+\sigma_p OCH_3+\sigma_m Br$ (3,5 disubstitution)	0.829 *a* 0.479 *b*	3
8. 1,3,5-Tribromobenzene	233.92 Av	$2\sigma_m Br$ (3,5 disubstitution)	0.720	3
9. 1,2,4-Tribromobenzene	240.67 *a* 239.47 *b* 236.37 *c* 232.24 *d*	$\sigma_o Br^c+\sigma_m Br$ $\sigma_o Br^c+\sigma_m Br$ $\sigma_m Br+\sigma_p Br$ $\sigma_m Br+\sigma_p Br$	1.739 *a* 1.739 *b* 0.623 *c* 0.623 *d*	3
10. 1,2,4,5-Tetrabromobenzene	242.38 Av	$\sigma_o Br^c+\sigma_m Br+\sigma_p Br$	1.971	3
11. Bromobenzene	224.61		0.000	3
12. *m*-Bromoaniline	222.61	$\sigma_m NH_2$	−0.161	3
13. *p*-Bromoaniline	221.86	$\sigma_p NH_2$	−0.660	3
14. *o*-Bromoanisole	233.25	$\sigma_o OCH_3{}^c$	0.109	3
15. *p*-Bromoanisole	226.69	$\sigma_p OCH_3$	−0.268	3
16. *p*-Bromoacetanilide	226.80	$\sigma_p NHCOCH_3$	−0.015	3
17. *p*-Bromoacetophenone	230.67	$\sigma_p COCH_3$	0.516	3
18. 2,4,6-Tribromoaniline	233.56 *a* 230.43 Av *b*	$2\sigma_m Br+\sigma_o NH_2{}^c$ (3,5 disubstitution) $2\sigma_m Br+\sigma_p NH_2$	0.390 *a* 0.060 *b*	3
19. *o*-Bromoaniline	220.26	$\sigma_o NH_2{}^c$	−0.33±0.32	3
20. *p*-Dibromobenzene	226.49	$\sigma_p Br$	0.223	3[d]
21. 4,4′-Dibromobiphenyl	225.53 Av	$\sigma_p C_6H_4Br$ (approximate with $\sigma_p C_6H_5$)	+0.009	3
22. *p*-Bromobenzenesulfonyl chloride	236.64	$\sigma_p SO_2Cl^c$	1.11	e
23. *o*-Bromophenol	230.48	$\sigma_o OH^c$	0.89±0.38	f
24. *m*-Bromophenol	227.31 Av	$\sigma_m OH$	−0.002	f
25. *p*-Bromophenetole	222.91	$\sigma_p OC_2H_5$	−0.151	f
26. *p*-Bromophenylphenyl ether	227.65	$\sigma_p OC_6H_5$	−0.028	f
27. *p*-Bromo-*n*,*n*-diethylaniline	219.87 Av	$\sigma_p N(C_2H_5)_2{}^c$	−0.70	f
28. 2-Bromo-1,4-dimethylbenzene	219.99	$\sigma_o CH_3{}^c+\sigma_m CH_3$	+0.223	f
29. 2-Bromo-4-methylaniline	221.05	$\sigma_o NH_2{}^c+\sigma_m CH_3$	−0.40±0.32	f
30. *o*-Dibromobenzene	236.02 Av	$\sigma_o Br^c$	1.348	g
31. Hexabromobenzene	255.20 Av	$2\sigma_m Br+\sigma_p Br+2\sigma_o Br^c$ (3,5 disubstitution)	3.648	g
32. 1,2,3,5-Tetrabromobenzene	236.04 *a* 242.47 Av *b* 246.80 Av *c*	$2\sigma_m Br+\sigma_p Br$ (3,5 disubstitution) $2\sigma_m Br+\sigma_o Br^c$ (3,5 disubstitution) $2\sigma_o Br^c+\sigma_p Br$	0.952 *a* 2.068 *b* 2.928 *c*	g

TABLE XVIII.—*Continued*

Compound	Frequency in Mc (Br^{81})	σ Values[b]	$\Sigma\sigma$ Values	Footnote reference
33. 1-Bromo-4-fluorobenzene	228.14 Av	$\sigma_p F$	0.062	h
34. 4-Bromo-2-methyl acetanilide	225.47	$\sigma_m CH_3+\sigma_p NHCOCH_3$	−0.084	h
35. 2-Bromo-4-methyl acetanilide	229.93	$\sigma_m CH_3+\sigma_o NHCOCH_3$[e]	0.25	h
36. 2,5-Dibromotoluene	226.51 *a* 228.29 *b*	$\sigma_m CH_3+\sigma_p Br$ (3,4 disubstitution) $\sigma_o CH_3$[e]$+\sigma_p Br$	0.150 *a* 0.524 *b*	h h
37. Pentabromophenol	246.370 *a*	$\sigma_p OH+2\sigma_o Br$[e]$+2\sigma_m Br$ (3,5 disubstitution)	3.059 *a*	h
	251.05 *b*	$\sigma_o OH$[e]$+\sigma_o Br$[e]$+2\sigma_m Br+\sigma_o Br$[e]	3.190 *b*	
	255.01 Av *c*	$2\sigma_o Br$[e]$+\sigma_m OH+\sigma_m Br+\sigma_p Br$	3.317 *c*	

[a] The italic letters *a–d* are used to label the frequencies.
[b] σ-Values are taken from H. H. Jaffe, Chem. Revs. **53**, 191 (1953) unless otherwise stated.
[c] σ-Values are taken from P. J. Bray and R. G. Barnes, J. Chem. Phys. **27**, 551 (1957).
[d] Measurement made at room temperature only by E. Manring, C. Brown, and D. Williams, Phys. Rev. **90**, 348 (1953).
[e] J. Hatton and B. V. Rollin, Trans. Faraday Soc. **50**, 358 (1954).
[f] P. J. Bray, J. Chem. Phys. **22**, 1787 (1954).
[g] P. J. Bray, J. Chem. Phys. **22**, 950 (1954).
[h] See Table XIX.

compounds were used in the computation of Eq. (2). The other three compounds in Table XIX were not used in the computation since the σ values were not known.

The frequency groupings for pentabromophenol indicated by the brackets in Table XIX were used to compute three average frequencies corresponding to the three unequivalent bromine positions. These average frequency values were used in the frequency vs Hammett σ-value analysis (see Table XVIII).

MISCELLANEOUS COMPOUNDS

Cl^{35} resonances and Br^{79} resonances in several unrelated compounds have been located and measured in this laboratory. These resonant frequencies are listed in Table XX. Two of the compounds listed, 9,10-dichloroanthracene and 1-chloronaphthalene, are the only resonances detected in a series of compounds involving various combinations of benzene rings. The resonances in these two compounds give some insight into the effect of the various ring structures when they are compared with the resonances in compounds such as chlorobenzene and *p*-dichlorobenzene. Several unsuccessful attempts were made to locate a resonance in 2-chloronaphthalene. Most of the other compounds in Table XX can not be readily compared because of their somewhat complicated structure.

CONCLUSIONS

It has been shown here that the pure quadrupole resonance measurements give a great deal of insight into the charge distributions in both aliphatic and aromatic hydrocarbons. From the present examination of halogen resonance frequencies, conclusions can be reached regarding how fast the inductive effects fall off with distance of separation between the chlorine atom and the perturbing group and how various atoms other than carbon atoms alter the inductive effect when these atoms are inserted in a hydrocarbon chain. The inductive effect between two chlorine atoms on opposite ends of a hydrocarbon chain is negligible in chains of greater length than propane as indicated by the halogen resonance frequency. Both methyl and ethyl groups have been found to cause a lowering of the resonance frequency when they are bonded to atoms near the chlorine atom in the molecule. The resonance frequencies in multichlorosubstituted compounds are found to be higher than the frequencies in the similar monochlorosubstituted compounds which can be attributed to the competition between the chlorine atoms for the available electrons.

The effect of the hybridization of the carbon atom has been examined, and it has been found that the resonance frequency increases as the hybridization of the carbon atom goes from sp^3 to sp^2 to sp. It has been shown that an oxygen atom bonded directly in a hydrocarbon chain or in a C=O group causes a definite change in the inductive effect between two chlorine atoms which are bonded one at each end of the hydrocarbon chain. The data also show that these oxygen structures raise the resonant frequencies above those found in simple straight-chain hydrocarbons.

From an examination of Cl^{35} resonant frequencies in some nitrogen mustards it has been noted that the positively charged nitrogen atom has a very potent inductive effect upon the chlorine atom. The resonant frequencies from chlorine atoms bonded directly to nitrogen atoms have been examined and are found to be

TABLE XIX. Bromine nuclear quadrupole resonance frequencies at 77°K in some previously unreported bromobenzene derivatives.

Compound	Br^{79} Frequency in Mc at 77°K	Signal-to-noise ratio
1-Bromo-4-fluorobenzene 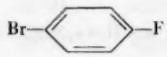	271.104 275.072	6*S* 6*S*
4-Bromo-2-methyl acetanilide 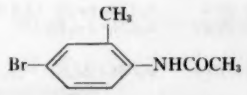	269.892	12*S*
2-Bromo-4-methyl acetanilide 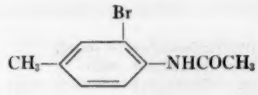	275.230	6*S*
2,5-Dibromotoluene 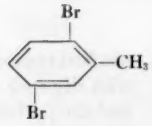	271.173 273.261	5*S* 6*S*
Pentabromophenol 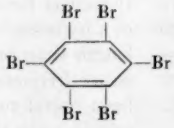	246.370 (Br^{81}) 249.397 (Br^{81}) 250.327 (Br^{81}) 253.418 (Br^{81}) 253.973 (Br^{81}) 255.254 (Br^{81}) 255.807 (Br^{81})	10*S* 2*S* 4*S* 15*S* 10*S* 3*S* 2*S*
2,4,6-Tribromophenyl-*p*-toluenesulfonate 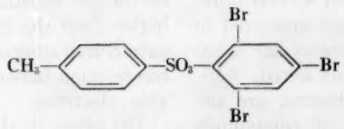	239.438 (Br^{81}) 244.424 (Br^{81}) 250.744 (Br^{81})	7*S* 7*S* 7*S*
p-Bromophenylhydrazine·HCl 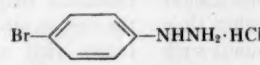	280.131	2*S*
bis(*p*-Bromophenyl) ether 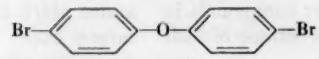	278.461	20*S*

TABLE XX. Cl^{35} and Br^{79} resonances in some miscellaneous compounds.

Compound		Frequency in Mc at 77°K	Signal-to-noise ratio
Chloropicrin	CCl_3NO_2	41.546	10*S*
		41.235	10*S*
		41.003	10*S*
Butyl chloral hydrate[a]	$CH_3CHClCCl_2CH(OH)_2$	37.425	5*R*
		36.954	4*R*
		35.017	3*R*
Muchochloric acid	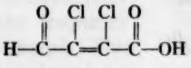	37.344	3*S*
		36.576	1.5*S*
1,4-*bis*(Trichloromethyl) benzene[b]		39.627	2*S*
		39.406	2*S*
		39.200	2*S*
		38.901	1*S*
		38.722	1.5*S*
		38.302	1*S*
Lindane (γ isomer of benzene hexachloride)[c]		37.341	3*S*
		36.892	4*S*
		36.819	4*S*
		36.365	2.5*S*
		36.133	2.5*S*
Hexachlorocyclopentadiene	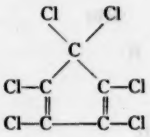	39.082	4*S*
		38.812	5*S*
		37.453	6*S*
		37.280	7*S*
		36.953	4*S*
Tetrachlorotetrahydronaphthalene	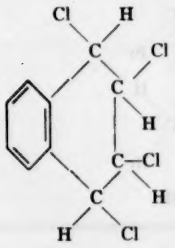	36.775[d]	4.5*S*, 10*R*
		35.254	2.5*S*, 6*R*
9,10-Dichloroanthracene	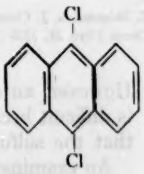	34.899	3.5*S*
1-Chloronaphthalene	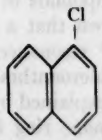	34.606	10*R*

TABLE XX.—*Continued*

Compound		Frequency in Mc at 77°K	Signal-to-noise ratio
β-Bromophenetole	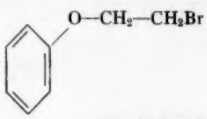	262.548	20*S*
β-Bromostyrene	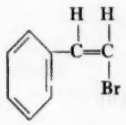	268.043 267.364	5*S* 5*S*
2-Bromoethyl acetate	$CH_3COOCH_2CH_2Br$	261.785	3*S*
d-3-Bromocamphor	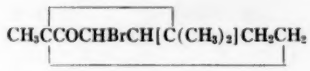	270.564	1*S*
β-Bromopropionic acid	$CH_2BrCH_2—COOH$	259.997	15*S*
2-Bromoethylamine·HBr	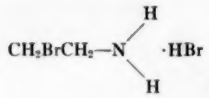	263.874	10*S*
1,2,3,4,5,6-Hexabromocyclohexane	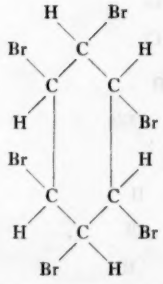	237.645 239.477 (Br^{81}) 241.396	9*S* 5*S* 5*S*

[a] Sample purchased from British Drug House Ltd., Poole, England.
[b] Sample obtained from Hooker Chemical Company, Niagara Falls, New York.
[c] Measured at room temperature by Y. Morino, I. Niyagawa, T. Chiba, and T. Shimozawa, J. Chem. Phys. 25, 185 (1956).
[d] Four very weak lines previously reported by P. J. Bray and P. J. Ring, J. Chem. Phys. 21, 2226 (1953).

close to the Cl^{35} resonant frequency in Cl_2 which might be expected since chlorine and nitrogen have the same atomic electronegativity.

It has been found from the measurement of some Cl^{35} resonances from chlorine atoms bonded to silicon atoms that $\nu_{C-Cl}/\nu_{Si-Cl}=2.00\pm0.11$ is the ratio between Cl^{35} resonant frequencies for chlorohydrocarbon compounds and the Cl^{35} resonant frequencies for corresponding chlorosilicon compounds.

The effects of the sulfur atom upon the Cl^{35} resonant frequencies have been examined indicating that in some cases sulfur acts in a manner similar to that of carbon. However, an analysis of sulfur-containing compounds is difficult because of the many possible valence states that the sulfur atom can exhibit.

An examination of Cl^{35} resonances in some aromatic compounds of structure similar to anthraquinone has shown that a definite discrepancy arises between the Cl^{35} resonances in 1-chloroanthraquinone and in the dichloroanthraquinones. This discrepancy may possibly be explained by a large distortion of the planar anthraquinone ring in the chloroanthraquinone compounds.

Inductive effects examined by comparing frequencies in chlorobenzyl compounds and chlorobenzene com-

pounds have shown that the inductive effect in the chlorobenzyl compounds is about $\frac{3}{4}$ of what it is in the corresponding chlorobenzene compound.

Employing the linear relationship between Cl^{35} resonance frequency and Hammett σ values, resonant frequencies were predicted and compared to the measured frequency values for several chlorobenzene compounds. Some unknown σ values were also predicted. Agreement is good in most cases; however, there are indications that strict additivity of σ values does not give the proper total σ value in multisubstituted chlorobenzene compounds. From the known bromine resonant frequencies in several bromobenzene compounds a linear relation between the frequency and Hammett σ values has been calculated. This relationship is similar to the relationship found for chlorine resonant frequencies.

The halogen pure quadrupole resonance frequency analysis gives a great deal of insight into the charge distributions in molecules and the changes in these charge distributions caused by various perturbing groups. A limiting factor in the analysis is the possible presence of crystal-structure effects which may shift or split the resonance frequencies.

ACKNOWLEDGMENTS

We are deeply indebted to Dr. Richard Bersohn of Columbia University for his many ideas and suggestions as to the analysis and presentation of these resonance data.

We wish to thank Dr. Philip A. Casabella, J. George O'Keefe, and Saul Moskowitz of Brown University for locating and measuring several resonances reported here.

Comparison of the Effects of High Pressure and Low Temperature on the Absorption Spectra of Some Condensed-Ring Aromatics*

W. W. ROBERTSON

Department of Physics, The University of Texas, Austin 12, Texas

(Received March 7, 1960)

A comparison of the spectral shifts obtained by lowering the temperature of a solution to those obtained by increasing its hydrostatic pressure shows that the temperature shift is composed of two oppositely directed components. The larger one is the red shift due to solvent density increase with temperature decrease and the accompanying increase in dispersion forces. The second and usually smaller effect is a blue shift that results from a change in the shape of the band as a result of a decrease in the population of the higher vibrational levels with a decrease in temperature.

INTRODUCTION

THE sharpening of electronic absorption bands and the accompanying frequency shifts that result from lowering the temperature of an absorber are effects that are well-known. As early as 1926 Kronenberger and Pringsheim[1] observed the absorption spectrum of solid benzene at low temperatures. Kronenberger[2] attributed the shift of the group maximum to a relative change in the intensities of the components of the group, rather than to any actual frequency shift of the individual components. Sponer *et al.*[3] concluded that each member of the group at low temperature was shifted relative to its vapor spectrum by intermolecular forces.

Sambursky, Halperin, and Henig[4] recorded the spectrum of benzene vapor from room temperature to above the critical temperature and at the corresponding pressures of the saturated vapor (from a few mm of mercury pressure to above 50 atm). No change was observed in the positions of the individual members of a group, but the change in intensity distribution among the various members was such as to produce a red shift of the maximum of the group with increasing temperature. The results of Sambursky *et al.* were said to support the interpretation of Kronenberger.[2]

Robertson, Babb, and Matsen[5] subjected dilute solutions of benzene and monosubstituted benzenes in *n*-pentane to hydrostatic pressures of the order of 5000 atm and observed red shifts that were attributed to increases in London—van der Waals type forces. Their results were taken to substantiate the interpretation of the low-temperature shift given by Sponer *et al.*[3]

Mayneord and Roe[6] observed the solution absorption spectrum of benzene, naphthalene, anthracene, and phenanthrene at temperatures to −120° C. They observed no shift for benzene or for the long-wavelength naphthacene bands, blue shifts for the long-wavelength phenanthrene bands, and red shifts for the others. No interpretation was given. Similar results were reported by Deal[7] and by Coggeshall and Pozefsky[8] for the low-temperature spectra of a number of condensed-ring aromatics. It was noted further that the magnitude of the red shift was correlated directly with the intensity of the transition.[7,8]

Brodersen and Langseth[9] assumed that the only effect of a temperature change on the solution absorption spectra of aromatic compounds was that of an intensity redistribution among the components of the bands. Neglecting to consider the possibility of a frequency shift due to changes in intermolecular forces with temperature, they attempted to locate the 0–0 transitions by statistical analysis of spectra obtained in alcohol solution at 20° and 70°C.

Oksengorn[10] separated the effects of density change from those of temperature by observing the frequency shifts of the band maxima of liquid benzene with increase in hydrostatic pressure at temperatures of 50°, 75°, 95°, and 110°C. From the four resulting curves of wavelength shift with density he obtained the wavelength shift with temperature at a given density. The resulting red shift was interpreted in terms of the effect of increasing temperature on the assumed π-molecular complex of Shuler.[11]

In the work reported here, the condensed-ring aromatics were used, on the one hand, because they provide a wide range of transition oscillator strengths and so should allow the effects of dispersion forces, which are proportional to oscillator strength, to be singled out. On the other hand, the effects of increasing

* This work was supported by the Air Force Office of Scientific Research, Air Research and Development Command.

[1] A. Kronenberger and P. Pringsheim, Z. Physik **40**, 75 (1926).

[2] A. Kronenberger, Z. Physik **63**, 494 (1930).

[3] H. Sponer, G. Nordheim, A. L. Sklar, and E. Teller, J. Chem. Phys. **7**, 207 (1939).

[4] S. Sambursky, A. Halperin, and H. Henig, J. Chem. Phys. **21**, 2041 (1953).

[5] W. W. Robertson, S. E. Babb, Jr., and F. A. Matsen, J. Chem. Phys. **26**, 367 (1957).

[6] W. V. Mayneord and E. M. F. Roe, Proc. Roy. Soc. (London) **A158**, 634 (1937).

[7] W. E. Deal, Jr., Doctoral dissertation, University of Texas, 1951.

[8] N. D. Coggeshall and A. Pozefsky, J. Chem. Phys. **19**, 980 (1951).

[9] S. Brodersen and A. Langseth, Dan. Mat. Fys. Medd. **26**, No. 3 (1951).

[10] Boris Oksengorn, Compt. rend. **242**, 2324 (1956).

[11] Kurt E. Shuler, J. Chem. Phys. **20**, 1865 (1952).

solvent density for these compounds were already known from high-pressure work[12] and so could be used to separate the effects due to increased density from other low-temperature effects. Also a single solvent was used to keep from introducing solvent shifts into the results and the temperature range of this solvent was limited to prevent phase change shifts.

EXPERIMENTAL

As stated before, most of the high-pressure data used in this work as well as a description of the apparatus by which it was obtained have been published.[5,12,13] The density values for the *n*-pentane solvent at the various pressures and temperatures used were interpolated graphically from data given by Bridgman.[14]

The low-temperature cell consisted of either a 1-cm or a 5-cm absorption cell in a suitable Dewar with quartz windows. The four equilibrium temperatures, room, ice, mercury, and dry-ice, were considered sufficient to cover the useable temperature range of the liquid *n*-pentane solvent. Most of the spectra were recorded photographically on a 3-m spectrograph with the band maxima being chosen from microphotometer traces. The density of the solvent at the various low temperatures was calculated from the formula given in the *American Physical Society Handbook*.

The absorption spectrum of naphthalene at constant vapor density was obtained by sealing the proper quantity of the vapor in a 60-cm heated quartz cell.

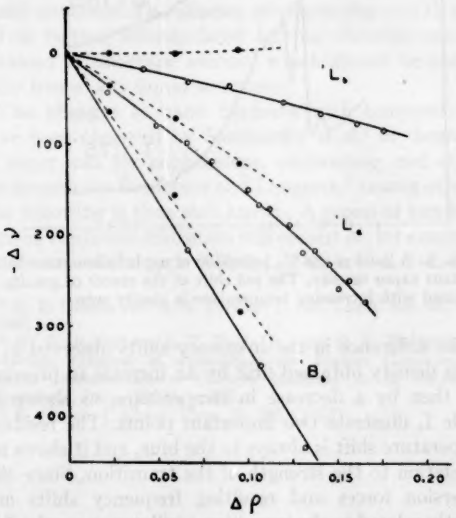

FIG. 1. Frequency shifts in cm^{-1} of the ^1L_b naphthalene transition and the ^1L_a and ^1B_b anthracene transitions with density change (g/cm^3) of *n*-pentane solvent. High pressure (——), low temperature (------).

TABLE I. The difference in frequency of absorption at −80°C, atmospheric pressure, and at the same solvent density, room temperature, high pressure.

Transition	^1L_b	^1L_a	^1B_b
Benzene	8		
Naphthalene	46		
Anthracene		26	30
Phenanthrene	49	34	35
Naphthacene			55
Pyrene	49	64	64
Chrysene	64	22	39

DATA AND RESULTS

The frequency shifts with solvent density are shown in Fig. 1 for three typical transitions, the weak ^1L_b of naphthalene, the much stronger ^1L_a, and the very strong ^1B_b of anthracene. The density increase in the one case is obtained by an increase of hydrostatic pressure (solid curves) and in the other case by a decrease in temperature (dashed curves). The frequency shifts appear linear with density within the limit of experimental error and increase with increasing transition oscillator strength.

The method chosen for presenting the results in Table I reflects the judgment that the frequency shifts resulting from temperature changes are the result of the superposition of at least two effects, that of the density change and that of the thermal energy change. If the temperature shifts were due to density changes alone, the solid and dashed curves in Fig. 1 would coincide. The measure of the thermal effect is then the difference between the dashed and solid curves of Fig. 1 at a given density. This difference is listed in Table I for the various transitions observed at the density of the *n*-pentane at −80°C.

The frequency shifts of a ^1L_a band of anthracene with density of the pentane solvent are presented in Fig. 2 for several different temperatures. The dashed curves are only likely extrapolations of a single data point at temperatures of 0°, −40°, and −80°C, for which pressure data were not attainable. The shift in the maximum of absorption at one density, again that of *n*-pentane at −80°C, is read from the curves of Fig. 2 and plotted in Fig. 3. The curve indicates a decreasing rate of shift to the blue with decreasing temperature.

Figure 4 shows how the maximum of a group of vapor bands shifts to the red with increasing temperature. The spectrum reproduced is from the ^1L_b transition of naphthalene and the density of the vapor is maintained constant. There is no evident shift of the individual components of the group, but the intensities of the 1–1

[12] W. W. Robertson, O. E. Weigang, Jr., and F. A. Matsen, J. Mol. Spectroscopy **1**, 1 (1957).
[13] D. S. Hughes and W. W. Robertson, J. Opt. Soc. Am. **46**, 557 (1956).
[14] P. W. Bridgman, *The Physics of High Pressure* (G. Bell and Sons, London, 1944).

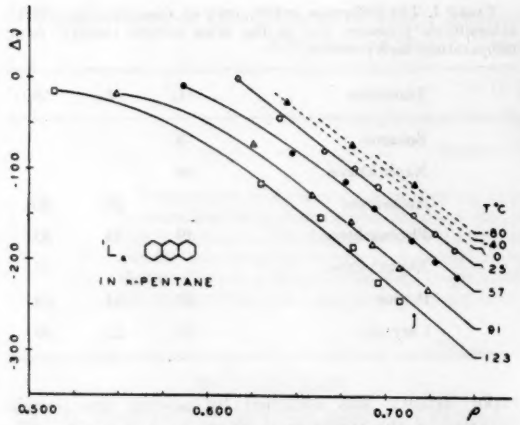

FIG. 2. Frequency shifts of the ^1L_a transition of anthracene with density of *n*-pentane solvent at several temperatures. Increased density obtained by increase in hydrostatic pressure on sample. The arrow indicates the density at which the data for Fig. 3 was taken.

type transitions increase with increasing temperature and so contribute to a red shift of the center of gravity of the band.

DISCUSSION

On the basis of previous experience it was decided that the most meaningful way of looking at frequency shifts due to temperature changes in solution absorption spectra was to separate the effects of the density change of the solvent from other thermal effects that might be present. These other effects could be such things as a change in the average effective intermolecular separation of molecules with change in translational energy, a change in the relative orientation of absorber and solvent molecules, solvent structure changes, changes in the solvent radial distribution function, and changes in adsorption band contours.

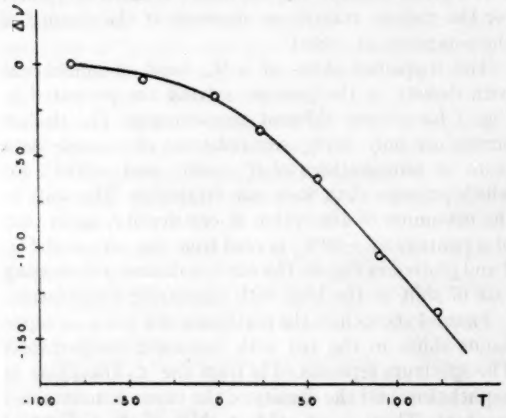

FIG. 3. Frequency shift with temperature at constant density. Data from Fig. 2.

The data presented in Fig. 1 show, first of all, that the larger part of the temperature shift for the stronger ^1L_a and ^1B_b transitions is a red shift due to density changes, and thus to the corresponding changes in dispersion forces, and that the residual thermal effect is a relative shift to the blue with decreasing temperatures. For the ^1L_b band with its low oscillator strength and correspondingly small red shift with increasing density, the residual thermal effect with its apparent blue shift predominates and the band maximum shifts slightly to the blue with decreasing temperature.

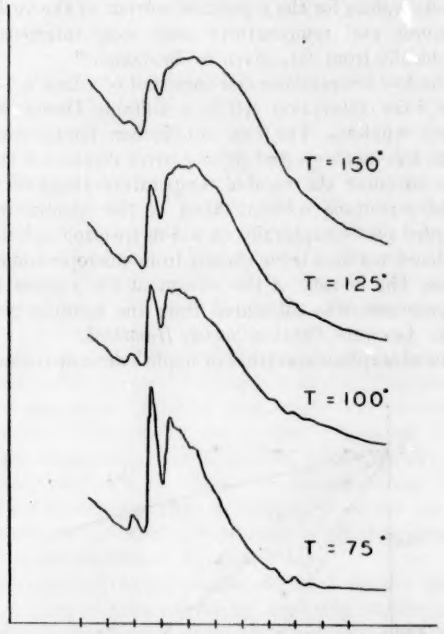

FIG. 4. A band of the ^1L_b transition of naphthalene recorded at constant vapor density. The red shift of the center of gravity of the band with increasing temperature is clearly seen.

The difference in the frequency shifts observed at a given density obtained first by an increase in pressure and then by a decrease in temperature, as shown in Table I, illustrate two important points. The residual temperature shift is always to the blue, and it shows no correlation to the strength of the transition. Since the dispersion forces and resulting frequency shifts are directly related to the transition oscillator strengths,[12,15] the results of Table I show that the residual temperature effect is in no way due to dispersion forces. The importance of this conclusion is that it immediately allows the rejection of several mechanisms that were considered as possibilities in the interpretation of the effect.

[15] H. Margenau and W. W. Watson, Revs. Modern Phys. 8, 22 (1936).

Gibson and Loeffler[16] observed a red shift in the complex spectra of aromatic amines and aromatic nitro and nitroso compounds with increasing temperature at constant volume. Shuler[11] interpreted the shift in terms of a decrease in the average separation of the molecules forming the collision complex due to the higher translational energy and the resulting closer distance of approach of the interacting molecules. Oksengorn[10] seems to have adopted this interpretation for the benzene red shift with increasing temperature at constant density. Although it seems evident that the pressure shift observed in benzene is due to dispersion forces and not to a molecular complex[12,17] as suggested by Shuler,[18] the relatively short-range nature of the dispersion forces might result in a decrease in the average effective molecular separation with increasing temperature. However, if the red shifts observed here for the condensed-ring aromatics were due to a decrease in the average effective molecular separation, the shift would be larger in the order $^1B_b > {}^1L_a > {}^1L_b$. Since this typical dispersion effect is not obtained, this cannot be the explanation for the red shift with increasing temperature at constant density.

The fact that the residual thermal shifts listed in Table I are not the results of changes in dispersion forces means that the shifts are not due to such things as (1) orientation-dependent interactions, (2) changes in radial distribution function, or (3) change in solvent liquid structure. The absence of effects due to (1) and (3) is further substantiated by the identical results obtained in isooctane solvent, which should be essentially free of any liquid structure.

The changes in band contours with temperatures have been observed by Sambursky *et al.*[4] for benzene in vapor and for naphthalene, anthracene, and other compounds by Brodersen and Langseth,[9] among others. The following is thus well known. A group of bands in a given electronic transition will consist of, for example, transitions of the type 0–0, 1–1, 2–2, or 0–1, 1–2, 2–3. Transitions arising from the higher vibrational frequencies, such as 1–1 or 2–2, will generally lie to the red of the transitions arising from the vibrational ground state due to the lower vibrational frequencies in the electronic excited state. The appearance of the group will depend on the number of low-lying vibrational levels in the molecule, the breadth of the components of the group, and the temperature. The individual components might be resolved, as in the case of benzene, in the low-density vapor spectrum, but in solution they broaden and overlap to form the characteristically broad and asymmetrical solution absorption band. An increase in the solution temperature should result in an increase in population of the higher vibrational states, with a resulting increase in the intensity of 1–1 type transitions relative to the 0–0 transition. The maximum of absorption, owing to the change in Boltzmann distribution over the vibrational levels, thus shifts to the red with increasing temperature. The rate of the shift depends upon the number of low-lying vibrational levels coupled to the electronic transition.

This thermal effect is superimposed, as was stated previously, on the oppositely directed frequency shift resulting from density changes in the solvent with temperature. For strong transitions the density change leads to the greater shift. For the ^1B_b band of anthracene in ethanol, for example, a temperature change from 20° to 70° leads, as a result of a decrease in density, to a dispersion-force shift of some 120 cm^{-1} to the blue, overlooked by Brodersen and Langseth,[9] compared to a shift of only $\sim$20 cm^{-1} due to the change in band shape.

The data reported in Fig. 2, similar to that of Oksengorn's[10] for benzene, can be used to get the temperature shift at constant solvent density for a range of temperatures. The plot of Fig. 3 is the result and qualitatively, at least, it seems to be in accord with the above explanation. The results presented in Fig. 4 further substantiate this interpretation. Since the naphthalene vapor density is constant, the resolved component of the band is seen to show zero shift. The position of the maximum of absorption of the band, which is what would be measured in a solution spectrum, is seen to shift to the red with increasing temperature.

[16] R. E. Gibson and O. H. Loeffler, J. Am. Chem. Soc. **62**, 1324 (1940).

[17] W. W. Robertson, S. E. Babb, Jr., and O. E. Weigang, Jr., *Proprietes Optiques et Acoustiques des Fluides Comprimes et Actions Intermoleculaires* (Centre National de la Recherche Scientifique, Paris, 1959), p. 293.

[18] K. Shuler, J. Chem. Phys. **21**, 965 (1953).

Structure of Glass-Forming Halides. II. Liquid Zinc Chloride

J. D. MACKENZIE AND W. K. MURPHY

General Electric Research Laboratory, Schenectady, New York

(Received March 31, 1960)

Measurements of viscosity and electric conductivity in liquid zinc chloride indicate that at temperatures near the melting point, the melt is associated. The degree of association diminishes rapidly with increasing temperature as shown by the decreasing energies of activation for both viscous flow and conduction. Liquid $ZnCl_2$ is thus not a normal fused salt such as $CdCl_2$ or $MgCl_2$. From the crystal structure and Raman absorption spectra, a mechanism of fusion and the structure of the melt are postulated. The ease of glass formation is discussed in terms of the liquid structure.

INTRODUCTION

THE majority of commonly encountered glass-forming systems are based on mixtures of two *types* of oxides, a "glass former" and a "glass modifier." In general, the kinetic barrier to crystallization, when the melt is cooled below its liquidus or melting temperature, is primarily the result of the network or polymeric nature of the glass former present, such as silica or germania. Vitreous-halide systems, on the other hand, are uncommon, some exceptions being those based on beryllium fluoride or zinc chloride. In a previous publication,[1] it was shown that the ease of glass formation in the case of BeF_2 can be attributed to the highly associated nature of the melt which is structurally similar to liquid SiO_2 and GeO_2.[2] In the present study, the mechanism of fusion of $ZnCl_2$ and the structure of the liquid at temperatures in the vicinity of the melting point are examined in the light of the results of viscous flow and electric conductance measurements. Limited measurements were also carried out for liquid $ZnBr_2$.

EXPERIMENTAL

Mallinckrodt A.R.-grade $ZnCl_2$ (mp 318°C) and Matheson Coleman and Bell reagent-grade $ZnBr_2$ (mp 394°C) were partially dehydrated in a vacuum oven (~1 mm Hg) overnight at 150°C. The charge was contained in a 50-cc Pt-20% Rh crucible and placed inside the apparatus in an atmosphere of dry N_2 (2 ppm H_2O). At temperatures about 50° above the melting point, final dehydration was made by the passage of dry N_2 *via* a ¼-in. i.d. Pt tubing through the melt for 1 hr with constant stirring.

The apparatus was essentially the same as that used in a previous study of liquid BeF_2.[1] Viscosity was measured by the counter-balance technique employing two Pt-20% Rh bobs of different dimensions. For electric conductance, the central suspension was adopted as one electrode and the crucible the other. Density measurements were also made by the simple Archimedean method. The calibrations and other details of the apparatus are described elsewhere.[3] Temperature measurements were made with a Pt-10% Rh thermocouple, the hot junction being placed adjacent to the crucible at the same level as the immersed bob. The temperature gradient along the crucible was 1° and measurements were accurate to ±1°.

RESULTS

For $ZnCl_2$, measurements were made at alternate descending and ascending temperatures between 320° and 400°C, the upper limit being set by the fluidity of the melt. Two sets of results were obtained by the use of two bobs. The viscosity (η), electric conductivity (κ), and density (ρ) data, taken at 20° intervals from the corresponding smooth plots against temperature are presented in Table I. Over this temperature interval, density is given by

$$\rho = 2.6607 - [4.48 \times 10^{-4}\, t^{\circ}\mathrm{C}]. \quad (1)$$

The expansivity is similar in magnitude to that for most fused salts.[4] The present data are in agreement with those of Klemm[5] to within 0.3%.

The relationship between log viscosity and the reciprocal of the absolute temperature is shown in Fig. 1. The empirical equation,

$$\eta = A_\eta \exp(E_\eta/RT), \quad (2)$$

is not obeyed. The energy of activation for viscous flow, E_η, decreases from about 38 kcal/mole at 320°C to 18 kcal/mole at 380°C. Over the range 2000–10 000 cps, conductance is independent of the frequency. On the average, the present specific conductivity data are 10% lower than those of Bockris and Crook[6] but 10% greater than those of Biltz and Klemm.[7] Because of the high energy of activation for conduction, this difference can arise from only a 2° variation in the temperature. The

[1] J. D. Mackenzie, J. Chem. Phys. **32**, 1150 (1960).
[2] J. D. Mackenzie, J. Chem. Phys. **29**, 605 (1958).
[3] J. D. Mackenzie, Rev. Sci. Instr. **27**, 297 (1956).
[4] For collected data, see C. J. Smithells, *Metals Reference Book* (Interscience Publishers, Inc., New York, 1955), Vol. II.
[5] W. Klemm, Z. anorg. u. allgem. Chem. **152**, 235 (1926).
[6] J. O'M. Bockris and E. H. Crook (private communication).
[7] W. Biltz and W. Klemm, Z. anorg. u. allgem. Chem. **152**, 266 (1926).

TABLE I. Viscosity, electric conductivity, and density of liquid zinc chloride.

Temp (°C)	Viscosity (poise)	Specific conductivity ($ohm^{-1}cm^{-1}$) $\times 10^3$	Density g cm^{-3}
320	44.7	1.99	2.517
340	15.0	4.19	2.508
360	7.48	6.81	2.499
380	4.79	9.44	2.490
400	3.55	11.9	2.481

simple Arrhenius equation

$$\kappa = A_\kappa \exp(-E_\kappa/RT) \qquad (3)$$

is not satisfactory, as illustrated in Fig. 2. Similar to E_η, the activation energy for conduction, E_κ, decreases from about 32 kcal/mole at 320°C to 12 kcal/mole at 380°C.

Because of its higher melting point and the comparatively higher fluidity at this temperature, measurements on liquid $ZnBr_2$ were only made at 400°. At this temperature, the viscosity is 4.0 poise and the specific conductivity 0.014 ohm^{-1} cm^{-1}.

DISCUSSION

The crystal structure of $ZnCl_2$ is similar to those of $CdCl_2$ and $MgCl_2$ in which the cations are situated in octahedral holes between two infinite layers of chlorines.[8] The double chlorine layers are held together

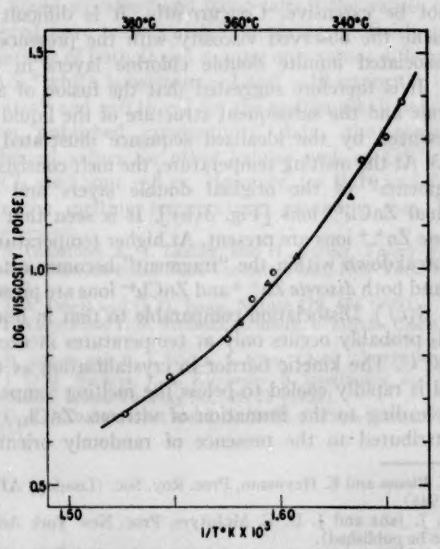

FIG. 1. Relation between log viscosity and $1/T$ for liquid $ZnCl_2$: ○ = large bob; △ = small bob.

[8] A. F. Wells, *Structural Inorganic Chemistry* (Clarendon Press, Oxford, 1950), Chap. VIII.

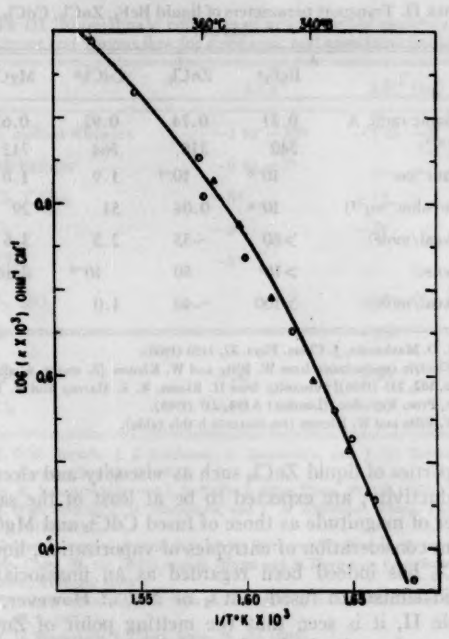

FIG. 2. Relation between log specific conductivity and $1/T$ for liquid $ZnCl_2$: ○ = large bob; △ = small bob.

in the crystal by van der Waals forces. There are thus three anions above, and three below each cation to give $M\,Cl_6$ groups which may be regarded as the basic unit in such structures [Fig. 3(a)]. As the ionic radius of Zn^{++} is between that of Cd^{++} and Mg^{++}, certain

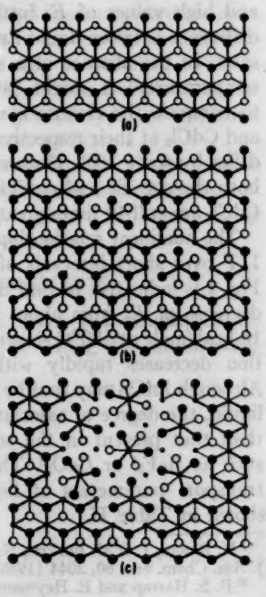

FIG. 3. Schematic representation of the fusion of crystalline $ZnCl_2$ (a), to give liquid near the melting point (b), and then liquid at higher temperatures (c): • = Zn; ○ and ● = Cl at planes above and below Zn.

TABLE II. Transport parameters of liquid BeF_2, $ZnCl_2$, $CdCl_2$, and $MgCl_2$.

	BeF_2[a]	$ZnCl_2$	$CdCl_2$[b]	$MgCl_2$[c]
Cationic radii, A	0.31	0.74	0.97	0.65
T_m(°C)	540	318	564	712
κ($ohm^{-1}cm^{-1}$)	10^{-6}	10^{-3}	1.9	1.0
Λ($cm^2ohm^{-1}eq^{-1}$)	10^{-4}	0.04	51	29
E_κ(kcal/mole)	>80	~35	2.3	3.6
η (poise)	$>10^6$	50	10^{-2}	fluid
E_η(kcal/mole)	>100	~40	4.0	

[a] J. D. Mackenzie, J. Chem. Phys. 32, 1150 (1960).
[b] Electric conductance from W. Biltz and W. Klemm [Z. anorg. u. allgem. Chem. 152, 235 (1926)]; viscosity from H. Bloom, B. S. Harrap and E. Heymann, Proc. Roy. Soc. (London) A194, 237 (1948).
[c] W. Biltz and W. Klemm (see footnote b this table).

properties of liquid $ZnCl_2$ such as viscosity and electric conductivity, are expected to be at least of the same order of magnitude as those of fused $CdCl_2$ and $MgCl_2$. From consideration of entropies of vaporization, liquid $ZnCl_2$ has indeed been regarded as an unassociated liquid similar to fused $CdCl_2$ or NaCl.[9] However, in Table II, it is seen that the melting point of $ZnCl_2$ is anomalous. Both electric conductivity and viscosity at the melting temperature, and the respective energies of activation, E_κ and E_η, are grossly different from those of $CdCl_2$ and $MgCl_2$. For most other metallic halide melts at temperatures in the vicinity of the melting point, viscosity is in the order of 10^{-2} poise[4] and E_η seldom exceeds 10 kcal/mole.[10] The respective values for $ZnCl_2$ are 50 poise and 40 kcal/mole. The abnormally low values of specific or equivalent conductance and high values of E_κ further indicate the structural difference between liquid $ZnCl_2$ and other typical fused salts. In the absence of a satisfactory "corresponding temperature," it might be considered inappropriate to compare the electric conductances of liquid $ZnCl_2$ and $CdCl_2$ at their respective melting points since these differ by some 250°. However, at 564°, (mp of $CdCl_2$), both the specific and equivalent conductivity of liquid $CdCl_2$ are still 10 times greater than that of $ZnCl_2$.[7]

The nonlinear relationship between log viscosity and $1/T$ over short intervals of temperature as shown in Fig. 1 is indicative of that of an associated liquid. The decrease of E_η from about 38 kcal/mole at 320°C to 18 kcal/mole at 380°C shows that the degree of association decreases rapidly with increasing temperature. Although $ZnCl_2$ may thus be considered as an associated liquid, the degree of association is much less extensive than that present in the so-called "network" liquids such as BeF_2[1] or GeO_2[2]. The differences between the transport parameters of liquid $ZnCl_2$ and BeF_2 are shown in Table II.

[9] H. Bloom, J. O'M. Bockris, N. E. Richards and R. G. Taylor, J. Am. Chem. Soc. 80, 2044 (1958).
[10] B. S. Harrap and E. Heymann, Chem. Revs. 48, 5 (1951).

In general, electric conduction in fused salts is primarily attributed to the movement of the smaller ionic species present. In viscous flow, however, both ions are involved and hence E_η is usually greater than E_κ.[11] Similarity between E_η and E_κ is indicative of association or complex formation in the melt as exemplified by $HgBr_2$,[12] KSCN, and NaSCN,[13] and BeF_2.[1] In the case of $ZnCl_2$, between 320–400°C, the ratio of E_η/E_κ is about 1–1.5 and thus suggests that comparable energy barriers are involved in the two processes. For most fused salts in which dissociation is extensive, the specific conductivity (κ) near the melting temperature varies between 1–5 ohm^{-1} cm^{-1}, equivalent conductivity (Λ) between 30–150 cm^2 ohm^{-1} eq^{-1}, and E_κ between 1–5 kcal/mole.[7,11] In the case of $HgBr_2$, where the degree of dissociation is considerably smaller and the ionic species present are probably the larger $HgBr^+$ and $HgBr_3^-$, E_κ is still less than 7 kcal/mole.[12] A low κ of about 10^{-3} ohm^{-1} cm^{-1} and a high E_κ of about 35 kcal/mole for $ZnCl_2$ suggest that at these temperatures, dissociation is slight and that the dominant conducting ion is probably not Zn^{++}.

The Raman absorption spectra of crystalline and liquid $ZnCl_2$[14,15] are similar, there being only one observed band at 233 cm^{-1}. This has been ascribed to the $ZnCl_4$ group.[16] If this assignment is correct, the dissociation in liquid $ZnCl_2$ may be represented by

$$3ZnCl_2 \rightleftharpoons 2Zn^{++} + ZnCl_4^{--},$$

as the 233-cm^{-1} band is observed up to 600°C. However, the magnitude of κ would indicate that this dissociation cannot be extensive. Concurrently, it is difficult to reconcile the observed viscosity with the presence of undissociated infinite double chlorine layers in the melt. It is therefore suggested that the fusion of zinc chloride and the subsequent structure of the liquid be represented by the idealized sequence illustrated in Fig. 3. At the melting temperature, the melt consists of "fragments" of the original double layers and individual $ZnCl_4^{--}$ ions [Fig. 3(b)]. It is seen that no *discrete* Zn^{++} ions are present. At higher temperatures, the breakdown within the "fragment" becomes extensive and both *discrete* Zn^{++} and $ZnCl_4^{--}$ ions are present [Fig. 3(c)]. Dissociation comparable to that in liquid $CdCl_2$ probably occurs only at temperatures in excess of 600°C. The kinetic barrier to crystallization as the liquid is rapidly cooled to below the melting temperature, leading to the formation of vitreous $ZnCl_2$, can be attributed to the presence of randomly oriented

[11] H. Bloom and E. Heymann, Proc. Roy. Soc. (London) A194, 392 (1948).
[12] G. J. Janz and J. D. E. McIntyre, Proc. New York Acad. Sci. (to be published).
[13] D. W. Plester, S. E. Rogers, and A. R. Ubbelohde, Proc. Roy. Soc. (London) A235, 469 (1956).
[14] W. Bues, Z. anorg. u. allgem. Chem. 279, 104 (1955).
[15] E. J. Salstrom and L. Harris, J. Chem. Phys. 3, 241 (1935).
[16] B. McCarroll and T. F. Young, ONR Report No. 5, Contract No. N6ori-02045, University of Chicago (June 1, 1959).

"fragments" and the dislocated $ZnCl_6$ groups. It should be noted that the formation of a glassy network involving six-coordinated cations is uncommon. The present hypothesis concerning vitreous $ZnCl_2$ must therefore await confirmation from direct structural studies such as x-ray diffraction.

That liquid $ZnCl_2$ is of a structural *type* different from other fused salts is further illustrated by (a) the ratio $\Delta E_{vap}/E_\eta$, ΔE_{vap} being the energy of vaporization, and (b) the entropies of activation for electric conductance and viscous flow. For most fused salts,[10] $\Delta E_{vap}/E_\eta$ varies between 4–5, for liquid metals,[17] it is 8–25 and for molecular liquids,[17] 3–4. However, for some hydroxylic liquids such as iso-butanol at temperatures near the freezing point, it is of the order of unity.[18] For the network liquids BeF_2[1] and As_2O_3[19] it is 0.8 and 0.5. The heat of vaporization of $ZnCl_2$ is 32 kcal/mole, the vapor species being monomeric.[20] The ratio $\Delta E_{vap}/E_\eta$ is thus only about 0.8 at 320°C, and 1.7 at 380°C. This would indicate that viscous flow represents a complex cooperative mechanism involving "entities" somewhat larger than the vaporizing unit.

From the theory of rate processes,[17] the entropy of activation for electric conduction, ΔS_A^*, may be evaluated from

$$\Lambda = 5.18\times10^{18} \times (D+2)zd^2 \exp(\Delta S_A^*/R) \exp(-\Delta H_A^*/RT), \quad (4)$$

in which D is the dielectric constant, z the charge, and d the half-migration distance of the conducting species. For liquid silicates[21] and fused salts,[22] the values of D adopted have been 5 and 3, respectively. Fairly large variations of both D and d cause only minor differences in ΔS_A^* which is between -1 and -10 eu for the ionic silicates[21] and -6 to -7 for the molten alkali halides.[22] From published conductivity data, the presently evaluated values for other halides such as $CdCl_2$ and $MgCl_2$ are about -8 eu. However, for BeF_2 and $ZnCl_2$ near the melting temperature, assuming that BeF_4 and $ZnCl_6$ to be the respective mobile entities, ΔS_A^* is highly positive as shown in Table III. Similarly, the entropy of activation for viscous flow may be obtained from

$$\eta = [(Nh/v) \exp(-\Delta S_\eta^*/R)] \exp(\Delta H_\eta^*/RT). \quad (5)$$

Values of ΔS_η^* for the ionic liquids are negative whereas those for the associated melts are positive. Although no quantitative significance may be attached to these values presented in Table III, it does demonstrate the difference between the two general *types* of structure present in these high-temperature liquids.

It is pertinent to remark that the crystal structure of $ZnCl_2$ is based on powder-diffraction data. The anomalies mentioned above suggest that a redetermination based on single crystals is desirable.

TABLE III. Approximate entropies of activation for electric conductance and viscous flow for some ionic and associated liquids.

	ΔS_A^*	ΔS_η^* (eu)
Ionic molten silicates	-1 to -10[a]	-1 to -8[e]
Alkali halides	-6 to -7[b]	
$CdCl_2$, $CdBr_2$	-8[d]	-7[d]
$PbCl_2$	-8[d]	-5[e]
$MgCl_2$	-8[d]	
GeO_2, SiO_2		$+50$[f]
B_2O_3		$+10$[g]
BeF_2[h]	$+30$	$+30$
$ZnCl_2$	$+30$	$+30$

[a] J. O'M. Bockris, J. A. Kitchener, S. Ignatowicz, and J. W. Tomlinson, Trans. Faraday Soc. 48, 75 (1952).
[b] E. R. Van Artsdalen and I. S. Yaffe, J. Phys. Chem. 59, 118 (1955).
[c] J. O'M. Bockris, J. D. Mackenzie, and J. A. Kitchener, Trans. Faraday Soc. 51, 1734 (1955).
[d] Presently evaluated from data of W. Biltz and W. Klemm, Z. anorg. u. allgem. Chem. 59, 118 (1955), and H. Bloom and E. Heymann, Proc. Roy. Soc. (London) A194, 392 (1948).
[e] Presently evaluated from data of B. S. Harray and E. Heymann, Chem. Revs. 48, 5 (1951).
[f] J. D. Mackenzie, J. Chem. Phys. 29, 605 (1958).
[g] J. D. Mackenzie, Trans. Faraday Soc. 52, 1564 (1956).
[h] J. D. Mackenzie, J. Chem. Phys. 32, 1150 (1960).

ACKNOWLEDGMENTS

The authors are grateful to Dr. J. E. Burke for his interest and to Dr. W. B. Hillig for stimulating discussions.

[17] S. Glasstone, K. J. Laidler, and H. Eyring, *Theory of Rate Processes* (McGraw-Hill Book Company, Inc., New York, 1941), Chap. 9.
[18] J. A. Pryde and G. O. Jones, Nature 170, 685 (1952).
[19] I. Karutz and I. N. Stranski, Z. anorg. u. allgem. Chem. 292, 330 (1957).
[20] H. Bloom and B. J. Welch, J. Phys. Chem. 62, 1594 (1958).
[21] J. O'M. Bockris, J. A. Kitchener, S. Ignatowicz, and J. W. Tomlinson, Trans. Faraday Soc. 48, 75 (1952).
[22] E. R. Van Artsdalen and I. S. Yaffe, J. Phys. Chem. 59, 118 (1955).

Osmotic Pressure of Moderately Concentrated Polymer Solutions

MARSHALL FIXMAN

Mellon Institute, Pittsburgh, Pennsylvania

(Received March 17, 1960)

By two methods, a linearization and a variational principle, the Born-Green-Kirkwood equation for the radial distribution function is solved approximately and the osmotic pressure of chain polymer solutions computed at arbitrary concentration. The gaussian intermolecular potential energy of Flory and Krigbaum is used, and this restricts the range of validity of the theory to volume fractions less than one-tenth. It is shown how the distribution of polymer molecules in the solvent becomes random as the concentration is increased. For good solvents, the quantity $[(P/c^2)-RT/\mathrm{Mc}]$, where P is the osmotic pressure and M the molecular weight, is predicted to increase rapidly with concentration c, and then to level off rapidly, the whole effect being accomplished at quite low concentrations as the molecules are forced to overlap. Some experimental corroboration is displayed. Severe doubt is cast on the practicality of the virial expansion of P, and possibly on the validity, beyond quite low concentrations.

I. INTRODUCTION

As the first stage in a calculation of the changes in polymer dimensions with concentration, and for its own interest, we present here a discussion of the osmotic pressure of chain polymer solutions of moderate concentration.

As the concentration of polymer molecules increases through the range of interest here, a particular polymer molecule begins to overlap the domain occupied by other molecules until at sufficiently high concentrations the solution satisfies one of the assumptions of the Flory-Huggins theory, and the centers of the polymer molecules become almost randomly distributed in the solvent. The behavior of thermodynamic or dimensional properties in the transition range of concentration is exceedingly interesting both from the experimental and theoretical side.[1] The bearing on polymer science needs no comment, but the model of polymer interactions in dilute solution, devised by Flory[2] and to be applied here, also furnishes a very interesting application of the general statistical mechanics of fluids and solutions. The intermolecular potential is very soft and weak as measured by the usual standards of this field. The centers of two or more molecules may occupy the same volume element with appreciable probability, and moreover, an increase in concentration, instead of leading to a more ordered structure, as is common, may produce a more random distribution of molecules!

In the model we use, the polymer molecule is pictured as a continuous, spherically symmetric distribution of segments, the average number of segments in a unit volume being peaked at the center of mass and spherical symmetry of the molecule. The interaction energy of one polymer molecule with another is assumed to be an integral over an energy density, which is in turn assumed to be proportional to the product of segment densities (number of segments per unit volume), at each point. The assumption by Flory and Krigbaum that the segment density is a gaussian function of the distance from the point of observation to the center of mass, has as its consequence that the intermolecular potential is a gaussian function of the distance between molecular centers. It is this potential that we shall use in subsequent calculations.

When we speak of intermolecular potentials here, it is no doubt clear that we refer to potentials of average force, the average being with respect to the configuration of all solvent molecules. Many molecular formulas for thermodynamic functions of single species systems may be used in the theory of mixtures if the potential of "instantaneous" force is replaced by the potential of average force. This was demonstrated by McMillan and Mayer[3]; see also Hill.[4] It is true of the cluster expansion of the pressure, in particular, which becomes the osmotic pressure under the transformation from intermolecular potentials to potentials of average force evaluated at infinite dilution.

Unfortunately, it is not true that the potential of average force between solute molecules is in general independent of solute concentration. The nature and distribution of the solvent molecules implicitly affects the potential of average force, and the distribution will change with solute concentration. We shall, however, assume as a first approximation[5] that this potential *is* independent of concentration and pairwise additive,

[1] L. Kotin, Doctoral Dissertation, Harvard University, 1959. Kotin has given an extensive discussion of the observed effects, and several approaches to the theory. Occasional observations of apparent discontinuities in the rate of change of thermodynamic or dimensional properties with concentration have been made. In this work we shall attempt neither a critique of nor extensive comparison with experiment.

[2] P. J. Flory and W. R. Krigbaum, J. Chem. Phys. **18**, 1086 (1950).

[3] W. G. McMillan and J. E. Mayer, J. Chem. Phys. **13**, 276 (1945).

[4] T. L. Hill, *Statistical Mechanics* (McGraw-Hill Book Company, Inc., New York, 1956), Chap. 6.

[5] The second approximation, which we only anticipate and do not use here, will take into account the change in potential caused by the change with concentration of polymer dimensions. The latter change is in fact our ultimate object, and presumably may be evaluated by minimization of the free energy of the solution.

and we may expect the assumption to be fairly good up to some finite concentration. Both experimental and theoretical arguments may be adduced *a priori* for the belief that the limit of validity is a solute volume fraction of about 0.1, and the quantitative comparison with experiment seems to confirm this expectation. An experimental observation in favor of this limit comes from the behavior of osmotic pressure as a function of concentration under conditions such that the second virial coefficient vanishes. For an intermolecular potential which is a monotonic function of intermolecular separation (the kind we consider), the second virial coefficient may be made to vanish only by making the potential vanish, and in this situation all higher virial coefficients vanish. But in practice[6,7] the osmotic pressure in these solvents begins to deviate noticeably from ideal solution behavior at volume fractions of about 0.1. On the theoretical side, we refer to Flory's derivation of the intermolecular potential.[3] The energy density was calculated from the Flory-Huggins free energy of mixing, with the suppression of terms arising from the entropy of mixing solute molecules (these being at specified positions). In the course of the derivation an expansion of the entropy term $\ln(1-v_2)$, where v_2 is the local solute volume fraction, was made $\ln(1-v_2)=-v_2-(v_2^2/2)-(v_2^3/3)-\cdots$. Terms of order v_2^3 and higher were suppressed.[8] It may be supposed as a very rough consideration that this assumption is adequate at a bulk volume fraction $\bar{v}_2$ such that $(2\bar{v}_2/3)\ll 1$, and that it breaks down when the inequality becomes feebler, at say $\bar{v}_2>0.1$.

In sum, we here take the intermolecular potential $V(R)$ to be independent of concentration, pairwise additive, and

$$V(R)=kTX\exp(-BR^2), \tag{1}$$

where a relating of the parameters X and B to the dimensions of the polymer chain and to the segment-segment excluded volume will be deferred to part V.

With the choice of potential established, there now remains the choice of a statistical mechanical method of calculation. Two broad categories are lattice model calculations, and integral-differential equations for the radial distribution function $g(R)$ that are based on the superposition approximation. We have excluded lattice calculations for three reasons: first, we are interested in concentrations sufficiently high that a restriction to nearest neighbor interactions only would not suffice, and so the major simplification of lattice calculations is lost; secondly, because the possibility of rapid changes in thermodynamic properties in the transition concentration range would seem so innate in a lattice model that their finding could easily be regarded as an artifact of the calculation, and third, because of the well-known inadequacy of lattice models at very low concentrations.[9]

From the radial distribution function approaches we select the Born-Green-Yvon-Kirkwood[4] method, which begins with

$$kT\nabla_1 g(12)+g(12)\nabla_1 V(12)+\rho\int g(1,2,3)\nabla_1 V(13)\,d\mathbf{R}_3=0, \tag{2}$$

an equation rigorous under the assumption of a pairwise additive potential. Equation (2) relates the radial distribution function $g(12)$ to the triplet correlation function $g(1, 2, 3)$ for assigned number density ρ (polymer molecules per unit volume), and intermolecular potential $V(R)$. In Eq. (2) the integers 1, 12 stand for $\mathbf{R}_1$, $\mathbf{R}_{12}=\mathbf{R}_2-\mathbf{R}_1$, and so on. The equation is purely formal until the superposition approximation

$$g(1,2,3)=g(12)g(23)g(13) \tag{3}$$

is employed.[10] Its use in Eq. (2) yields

$$kT\nabla_1 \ln g(12)+\nabla_1 V(12)+\rho\int g(13)g(23)\nabla_1 V(13)\,d\mathbf{R}_3=0, \tag{4}$$

which is sufficient to determine $g(R)$ and through it the thermodynamic properties. The exact solutions of Eq. (4) seem to be quite good, though not perfect determinations[4] of $g(R)$; but to obtain these exact solutions is a numerical problem of the first magnitude and does not seem warranted here. We will look into two other possibilities. First, Eq. (4) may be linearized,[11,12] and when so modified, its solution becomes tractable (after a few other approximations). We will follow the linearization procedure in part II, but we originally regard the method with distrust in the context of this work. For the basic assumption of the linearization method is that $g(R)\sim\exp[-V(R)/kT]$, the latter being the exact solution at low concentrations, whereas we wish to be able to follow $g(R)$ through the concentration range in which the molecules become randomly distributed, that is $g(R)\sim 1$ for all R. We desire, at least, that this be a possible outcome of the calculation, and the linearization would seem to exclude it. However, the actual outcome of part II is qualita-

[6] W. R. Krigbaum and D. O. Geymer, J. Am. Chem. Soc. **81**, 1859 (1959).

[7] P. J. Flory and H. Daoust, J. Polymer Sci. **25**, 429 (1957).

[8] See T. A. Orofino and P. J. Flory, J. Chem. Phys. **26**, 1067 (1957), where the second virial coefficient is discussed without this assumption.

[9] See work cited in footnote reference 4, Chap. 8.

[10] It should be understood that the additivity of average forces has been assumed in two different connections: first for V, where the average is with respect to the positions of all solvent molecules, and second in Eq. (3), where the additional average is over the positions of all but two solute molecules.

[11] M. Born and H. S. Green, *A General Kinetic Theory of Liquids* (Cambridge University Press, New York, 1949), Chap. II.

[12] A. E. Rodriguez, Proc. Roy. Soc. (London) **A196**, 73 (1949).

tively quite similar to the result of the more extended calculation of part IV, probably because of the linearization of $\exp(-V/kT)$ in part II.

Our second approach to Eq. (4) entails the construction of a variational principle equivalent to Eq. (4), and use of a suitably simple trial function for its solution. The trial function that we use is unrealistic for large X, and the number of variational parameters in $g(R)$ is restricted to two for small X, and one for large X. Nevertheless, the trial $g(R)$ is most strained, and the thermodynamic properties most sensitive to the choice of parameters in the very low concentration range, where the calculation of the second virial coefficient[2] is available as an encouraging check.

The calculations are carried to the numerical stage only for positive deviation of the osmotic pressure from ideal behavior, that is $X \geq 0$.

II. LINEAR THEORY

A. General Derivation

The original derivation[11,12] of the linear approximation to Eq. (4) proceeds through an equation derived from Eq. (4) by a very complicated integration by parts. As far as the requirements of the linear theory go, this was a pointless detour. By an application of the desired approximations directly to Eq. (4), the linear theory can be derived almost as quickly as the approximations can be stated. To demonstrate this, and to make this section self-contained, we here proceed with such a derivation.

Put

$$g(R) \equiv \exp[f(R) - V(R)/kT] \tag{5}$$

$$\alpha(R) \equiv [\exp - V(R)/kT] - 1, \tag{6}$$

as the definitions of $f(R)$ and $\alpha(R)$, respectively. The motivation of Eq. (5) is the hope that $f(R)$ is small, so that when the definitions are entered into Eq. (4) the expansion

$$g(R) \cong [1+\alpha(R)][1+f(R)] \tag{7}$$

may be used on the rhs. The substitutions of (5), (6), and (7) being made, Eq. (4) becomes

$$\nabla_1 f(12) - \rho \int [1+f(13)][\alpha(23)+1] \times [1+f(23)] \nabla_1 \alpha(13) d\mathbf{R}_3 = 0. \tag{8}$$

A further approximation is now introduced, motivated by the desire that Eq. (8) be simply soluble by Fourier transformation, which is possible only when the integral has the form of a convolution; that is, the integrand is a product of a known or easily evaluated function of R_{13} and $f(23)$. This form is obtained by the assumption that where $f(R)$ is multiplied by $\alpha(R)$ or its derivative, these being very short range functions, $f(R)$ may be replaced by the constant $\epsilon - 1$, an average value in the neighborhood of the origin

$$f(R) \to \epsilon - 1 = \int f(R)\alpha(R) d\mathbf{R} \Big/ \int \alpha(R) d\mathbf{R}. \tag{9}$$

This step and the observation that

$$\int \nabla_1 \alpha(13) d\mathbf{R}_3 = 0,$$

because $\alpha(R)$ is spherically symmetric, short range and bounded, bring Eq. (8) to the form

$$\nabla_1 f(12) - \rho\epsilon \int [f(23) + \epsilon\alpha(23)] \nabla_1 \alpha(13) d\mathbf{R}_3 = 0. \tag{10}$$

Fourier resolutions of $f(R)$ and $\alpha(R)$ are now introduced into Eq. (10)

$$f_k \equiv (2\pi)^{-3} \int f(R) \exp -i\mathbf{k}\cdot\mathbf{R} d\mathbf{R};$$

$$f(R) = \int f_k \exp i\mathbf{k}\cdot\mathbf{R} d\mathbf{k} \tag{11}$$

$$\alpha_k = (2\pi)^{-3} \int \alpha(R) \exp -i\mathbf{k}\cdot\mathbf{R} d\mathbf{R};$$

$$\alpha(R) = \int \alpha_k \exp i\mathbf{k}\cdot\mathbf{R} d\mathbf{k} \tag{12}$$

are the definitions, while

$$\int f(23)\alpha(13) d\mathbf{R}_3 = (2\pi)^3 \int f_k \alpha_k \exp i\mathbf{k}\cdot\mathbf{R}_{12} d\mathbf{k}. \tag{13}$$

Substitution of Eqs. (11), (12), and (13) into Eq. (10) gives

$$\int \{ f_k - (2\pi)^3 \rho\epsilon\alpha_k [f_k + \epsilon\alpha_k] \} \mathbf{k} \exp i\mathbf{k}\cdot\mathbf{R}_{12} d\mathbf{k} = 0. \tag{14}$$

The factor in curly brackets must be zero to within an arbitrary additive multiple of a δ function of $\mathbf{k}$, since

$$\int \delta(\mathbf{k}) \mathbf{k} \exp i\mathbf{k}\cdot\mathbf{R}_{12} d\mathbf{k} = 0. \tag{15}$$

But a δ function in f_k contributes a constant term to $f(R)$, as may be seen in Eq. (11), and this constant term must be zero, since $g(R) \to 1$ as $R \to \infty$. Therefore, the arbitrary multiple of $\delta(\mathbf{k})$ is a zero multiple and Eq. (14) gives

$$f_k = 8\pi^3 \rho (\epsilon\alpha_k)^2 / (1 - 8\pi^3 \rho\epsilon\alpha_k). \tag{16}$$

Equations (7) and (16) constitute the Green[11]-Rodriguez[12] linear approximation to $g(R)$.

B. Application to Chain Polymers

We will first evaluate f_k explicitly, and then use it to obtain the osmotic pressure. Even with all the approxi-

mations made to obtain Eq. (16), a computation of the transform α_k with $V(R)$ given by Eq. (1) cannot be effected in finite terms. Consequently we employ the device used by Stockmayer and Casassa[13] in their calculation of the third virial coefficient. They make the approximation

$$\alpha(R)\cong\alpha_0(R)\equiv -X_0\exp(-B_0R^2), \tag{17}$$

and for given X and B choose X_0 and B_0 so as to give the correct second virial coefficient, and by a graphical comparison, an adequate similarity of $\alpha(R)$ to $\alpha_0(R)$. The graphical agreement is thought to be adequate for $X<4$. From Eqs. (12) and (17),

$$\alpha_k=-X_0(2\pi)^{-3}\int\exp(-B_0R^2-i\mathbf{k}\cdot\mathbf{R})d\mathbf{R}. \tag{18}$$

The integration is effected by completion of the square in the exponential, and gives

$$\alpha_k=-X_0[\exp(-k^2/4B_0)]/8(\pi B_0)^{\frac{3}{2}}. \tag{19}$$

Next in Eq. (16) we must get ϵ as a function of ρ, X_0, and B_0. We substitute in Eq. (9)

$$\int\alpha(R)d\mathbf{R}=-X_0(\pi/B_0)^{\frac{3}{2}}, \tag{20}$$

and from (11) and (12), we get

$$\int f(R)\alpha(R)d\mathbf{R}=\int f_k\alpha(R)\exp i\mathbf{k}\cdot\mathbf{R}d\mathbf{R}d\mathbf{k}$$

$$=(2\pi)^3\int\alpha_k f_k d\mathbf{k}, \tag{21}$$

which gives

$$\epsilon-1=-8(\pi B_0)^{\frac{3}{2}}X_0^{-1}\int\alpha_k f_k d\mathbf{k}. \tag{22}$$

Substitution of Eqs. (18) and (16) into (22) gives

$$\epsilon-1=(\rho\epsilon^2X_0^2/8B_0^3)\int_0^\infty\frac{4\pi k^2\exp(-k^2/4B_0)dk}{1+\epsilon\rho X_0(\pi/B_0)^{\frac{3}{2}}\exp(-k^2/4B_0)}, \tag{23}$$

which has to be solved for ϵ as a function of ρ, X_0, and B. The following scheme accomplishes this, though only numerically. This, however, is sufficient since the calculation is now at a late stage. Put

$$\gamma\equiv(\pi/B_0)^{\frac{3}{2}}\epsilon\rho X_0, \tag{24}$$

and also in Eq. (23) change variables to

$$k=2B_0^{\frac{1}{2}}x.$$

Equation (23) becomes

$$\epsilon-1=(4\epsilon X_0/\pi^{\frac{3}{2}})\gamma I(\gamma),$$

or

$$\epsilon=1/1-(4X_0/\pi^{\frac{3}{2}})\gamma I(\gamma), \tag{25}$$

where

$$I(\gamma)=\int_0^\infty\frac{x^2\exp-3x^2dx}{1+\gamma\exp-x^2}. \tag{26}$$

The procedure now is to obtain $I(\gamma)$ in terms of tabulated functions, tabulate ϵ as a function of γ for a specified X_0 using Eq. (25), and then divide the values of γ by ϵX_0 to get from (24)

$$\nu_0=(\gamma/\epsilon X_0)=(\pi/B_0)^{\frac{3}{2}}\rho. \tag{27}$$

The result amounts to a tabulation of ϵ against the dimensionless measure of concentration ν_0 for the desired X_0.

First, then, expand the integrand of $I(\gamma)$, Eq. (26), in partial fractions,

$$I(\gamma)=\gamma^{-3}\int_0^\infty\Big[\gamma^2\exp(-2x^2)-\gamma\exp(-x^2)$$

$$+\frac{\gamma\exp(-x^2)}{1+\gamma\exp(-x^2)}\Big]x^2dx. \tag{28}$$

The first two terms integrate readily, and in the last term, the substitution $x^2=y$ permits the integral to be written as a tabulated function

$$I(\gamma)=(\pi^{\frac{3}{2}}/4\gamma^3)(2^{-\frac{3}{2}}\gamma-1)+(1/2\gamma^3)F_{\frac{3}{2}}(\zeta), \tag{29}$$

where

$$\zeta=\ln\gamma$$

$$F_p(\zeta)=\int_0^\infty\frac{y^pdy}{1+\exp(y-\zeta)}. \tag{30}$$

The functions $F_p(\zeta)$ occur in the Fermi-Dirac statistics,[14] and have been tabulated by McDougall and Stoner[15] and Beer *et al.*[16]

The numerical completion of the procedure described in the foregoing furnishes f_k, Eq. (16). We now compute the osmotic pressure P from[4]

$$P\equiv\rho kT-(2\pi\rho^2/3)\int_0^\infty R^3g(R)\partial V(R)/\partial RdR \tag{31}$$

$$=\rho kT\Big\{1+(2\pi\rho/3)\int_0^\infty R^3[1+f(R)]\partial\alpha(R)/\partial RdR\Big\}, \tag{32}$$

the second form deriving from Eqs. (6) and (7). We may note that the status of Eq. (31) for the osmotic

[13] W. H. Stockmayer and E. F. Casassa, J. Chem. Phys. **20**, 1560 (1952).

[14] A. H. Wilson, *The Theory of Metals* (Cambridge University Press, New York, 1953), p. 332.

[15] J. McDougall and E. C. Stoner, Phil. Trans. Roy. Soc. (London) **A237**, 67 (1938).

[16] A. C. Beer, M. N. Chase, and P. F. Choquard, Helv. Phys. Acta **28**, 529 (1955).

pressure is somewhat lower than the equivalent form for the hydrostatic pressure, as Eq. (31) requires[4] pairwise additivity of the potentials of average force $V(R_{ij})$.

The problematical integral in Eq. (32) is the one involving $f(R)$. It may, however, be reduced by a procedure analogous to that used for ϵ

$$L\equiv\int R^2 f(R)\partial\alpha(R)/\partial R dR$$

$$=(4\pi)^{-1}\int f(R)\mathbf{R}\cdot\nabla_R\alpha(R)d\mathbf{R}$$

$$=(4\pi)^{-1}\int f(R)\alpha_k\mathbf{k}\cdot\nabla_k \exp i\mathbf{k}\cdot\mathbf{R}d\mathbf{k}d\mathbf{R}, \quad (33)$$

after introducing the Fourier representation of $\alpha(R)$. The divergence theorems may be used in k space to rewrite the k integral, giving

$$L=-(4\pi)^{-1}\int[3\alpha_k+\partial\alpha_k/\partial k]f(R)\exp i\mathbf{k}\cdot\mathbf{R}d\mathbf{k}d\mathbf{R},$$

or with Eq. (11)

$$L=-2\pi^2\int[3\alpha_k f_k+k f_k\partial\alpha_k/\partial k]dk. \quad (34)$$

Equation (22) provides the first term on the rhs, in terms of $\epsilon-1$. In the second term, with Eqs. (16) and (19) for f_k and α_k, respectively, the identical changes of variables used subsequent to Eq. (22) here give

$$-2\pi^2\int k f_k\partial\alpha_k/\partial k d\mathbf{k}=-2\epsilon X_0^2 B_0^{-\frac{1}{2}}J(\gamma), \quad (35)$$

where

$$J(\gamma)=\gamma\int\frac{x^4\exp-3x^2dx}{1+\gamma\exp-x^2}, \quad (36)$$

or

$$J(\gamma)=(3\pi^{\frac{1}{2}}/8\gamma)(2^{-5/2}\gamma-1)+(1/2\gamma^2)F_{\frac{1}{2}}(\zeta), \quad (37)$$

where $F_{\frac{1}{2}}(\zeta)$ is defined in Eq. (30). We now put all the pieces, namely Eqs. (33), (34), (22) [to be used in (34)], and (35), back into Eq. (32) for P

$$\rho^{-1}[(P/\rho kT)-1]$$

$$=\epsilon X_0(\pi/B_0)^{\frac{1}{2}}(1/2)[1-8X_0J(\gamma)/3\pi^{\frac{1}{2}}]. \quad (38)$$

For comparison of Eq. (38) with experiment or with the results of the variational calculation, it will be convenient to introduce the concentration c in g/ml

$$c=M\rho/N_0, \quad (39)$$

where M is the polymer molecular weight and N_0 is Avogadro's number. Furthermore, we define an "apparent second virial coefficient" S as

$$S\equiv[(P/c)-(RT/M)](RTc)^{-1}; \quad (40)$$

the verbal description of S arises from the fact that

$$\lim_{c\to 0}S=A_2, \quad (41)$$

the second virial coefficient. Equations (38) and (40) give

$$S=N\epsilon X_0(\pi/B_0)^{\frac{1}{2}}(1/2M^2)[1-8X_0J(\gamma)/3^{\frac{1}{2}}]. \quad (42)$$

We will not compare Eq. (42) directly with experiment, but we will compare it with the variational calculation for a value of X which has accidentally turned out to be close to an X used in the experimental comparison in part V. We take $X_0=\sqrt{2}$, which corresponds, according to Stockmayer and Casassa,[13] to $X=4$ in Eq. (1). From their paper the requirement that the exact and approximate α's give the same A_2 results in

$$(B_0/B)^{\frac{1}{2}}=0.579 \quad (43)$$

for $X_0=1.4$, so that the dimensionless variable

$$\nu=\rho(\pi/B)^{\frac{1}{2}} \quad (44)$$

used in part V, is

$$\nu=0.579\nu_0. \quad (45)$$

We now compare S/A_2 for the two methods. Equations (41) and (42) give

$$S/A_2=\epsilon[1-8X_0J(\gamma)/3\pi^{\frac{1}{2}}]. \quad (46)$$

From Eqs. (25), (29), and (37) we have tabulated in Table I, ϵ and (S/A_2) for a range of γ, and from Eqs. (27) and (45), the corresponding values of ν. As an incidental result, the differences between ϵ and S/A_2 give a rough measure of the validity of replacing $f(R)$ by an average value where it multiplies $\alpha(R)$ or $\alpha'(R)$ in Eq. (8); if the same substitution were made for the f occurring in Eq. (32) for P, it would turn out that $S/A_2=\epsilon$.

In Fig. 1 is a graph of S/A_2 vs ν from Eq. (46), curve (3), and from the results of part V, curve (2). The latter was obtained from Table III[17] in part V at $A=X\pi^{\frac{1}{2}}/4=1.8$. We also present in Fig. 1 the osmotic pressure expansion

$$S/A_2=1+(A_3/A_2)c+\cdots \quad (47)$$

broken off at the term containing the third virial coefficient. The Stockmayer-Casassa equations for A_3 give, in general,

$$S/A_2=1+(2X_0^2/3^{5/2})\nu_0+\cdots, \quad (48)$$

or, with Eq. (45) and $X_0=\sqrt{2}$, we have for curve (1)

$$S/A_2=1+0.443\nu+\cdots. \quad (49)$$

Several conclusions can be drawn from Fig. 1. (1) The linear theory gives the correct third virial coefficient.

[17] To fill out the curve, the table was extended to a few smaller values of ν by the procedure described at the end of part IV.

This is not surprising; it is known[18] that the linear theory does in general give the correct A_3, but the numerical verification is a good check on lengthy calculations. (2) The variational calculation is in quite good agreement with the linear theory in the region of small ν. This is surprising, and we should understand clearly what it means. The variational calculation gives an A_2 about 2% too large for $A=1.8$, as is shown by comparison with the Flory-Krigbaum theory[2,8] (see Table IV). The consequence of Fig. 1 is that according to Eq. (47), the variational calculation also gives A_3 about 2% too large, and, in sum, A_3/A_2 correctly, if we accept the A_3 of Stockmayer and Casassa. (3) At a quite low concentration, the virial series broken off at A_3 becomes a grossly inadequate description of the osmotic pressure ($\nu=1$ corresponds to a concentration of about 2g/100 ml for the experiment considered in part V). (4) At large ν, the linear theory makes S/A_2 much too small, the variational calculation makes S/A_2 slightly too small. We assert this because the variational calculation must give $S(\infty)$ correctly if the calculation has any merit at all; the value of $S(\infty)$ involves the results of the calculation only to the qualitative extent that $g(R)\to 1$, all R, as $\nu\to\infty$. On the other hand, A_2 is made about 2% too large; hence $S(\infty)/A_2=1.65$, according to part V, is 2% too small, and $S(\infty)/A_2=1.5$ according to the linear theory, is 10% too small.

The quantitative defects of the virial series through A_3 suggests to us that the virial series itself has a finite radius of convergence that may be exceeded experimentally. Of course we cannot prove this assertion, because we don't know the true virial coefficients, but it is easily shown that the linear theory assigns a finite radius of convergence to a virial expansion. We examine,

TABLE I. Linear theory. Average $\epsilon-1$ of $f(R)$ near the origin, and "apparent second virial coefficient" S tabulated against dimensionless measures of concentration γ and ν. Potential energy parameter $X=2^{\frac{1}{2}}$.

γ	ϵ	ν	S/A_2
0.1353	1.035	0.053	1.023
0.6065	1.136	0.219	1.087
1.105	1.217	0.371	1.136
2.014	1.328	0.621	1.199
3.669	1.459	1.029	1.270
6.686	1.596	1.714	1.338
12.18	1.719	2.899	1.394
40.45	1.887	8.764	1.463
∞	2	∞	1.5

[18] G. S. Rushbrooke and H. I. Scoins, Phil. Mag. 42, 582 (1951).

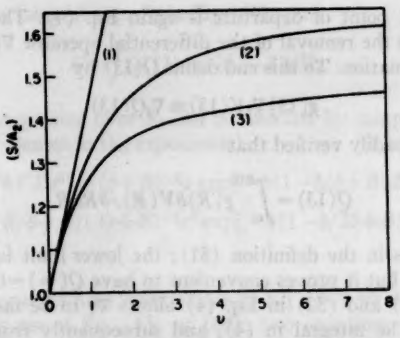

FIG. 1. Apparent second virial coefficient S divided by $S(0)=A_2$, vs dimensionless measure of concentration ν. $X=2^{\frac{1}{2}}$. Curve (1) third virial coefficient. Curve (2) variational theory. Curve (3) linear theory.

in Eq. (42), a series expansion of $J(\gamma)$. From Eq. (36),

$$J(\gamma)=\gamma\sum_{n=0}^{\infty}\int x^4(-\gamma)^n\exp-(3+n)x^2dx$$

$$=(3\gamma\pi^{\frac{1}{2}}/8)\sum_{0}^{\infty}{}'(-\gamma)^n/(3+n)^{5/2}. \quad (50)$$

Consequently the series diverges at $\gamma=1$. The same radius applies to ϵ, in Eqs. (25) and (26). A value of $\gamma=1$ corresponds, for the example considered here ($X=4$), to $\nu\sim 0.34$, as Table I shows. Nothing very remarkable occurs at $\nu=0.34$ in Fig. I, and for just this reason an attempt to fit the lower part of curve (2) by a virial series would yield virial coefficients in severe disagreement with the values actually predicted by the linear theory.

Two remarks are pertinent in conclusion. First, the comments on the divergence of the virial series have relevance only for fairly good solvents. For sufficiently poor solvents the divergence will occur at a concentration greater than the anticipated limit of validity of the original potential, Eq. (1). Secondly, the divergence might well be an artifact of the linearization procedure; we indicate a question rather than claim an answer.

III. VARIATIONAL PRINCIPLE

Our reasons for discontent with the linear theory have been mentioned at the end of part I and in various places in II. In brief, the linear theory is *a priori* unreliable except at very low concentrations (though the suspicion is relieved by the qualitative agreement with part IV), numerically tedious, and most importantly, because of the approximate potential we were forced to use, subjective in the relation between (X_0, B_0) and (X, B). Stockmayer and Casassa thought the approximate potential so poor for $X>4$, that they abandoned its use. Here we lay the basis for our variational calculation, but as such an approach may have other applications, we discuss it more fully than our particular application might warrant.

The point of departure is again Eq. (4). The first step is the removal of the differential operator ∇_1 from the equation. To this end define $Q(13)$ by

$$g(13)\nabla_1 V(13) \equiv \nabla_1 Q(13). \tag{51}$$

It is readily verified that

$$Q(13) = \int_{\infty}^{R_{13}} g(R)\partial V(R)/\partial R dR \tag{52}$$

suffices in the definition (51); the lower limit is arbitrary, but it proves convenient to have $Q(\infty)=0$. Use of (51) and (52) in Eq. (4) allows ∇_1 to be factored from the integral in (4), and subsequently from the whole equation. These operations yield

$$kT\ln(12)+V(12)+\rho\int Q(13)g(23)d\mathbf{R}_3=K, \tag{53}$$

where K is a constant of integration which is found from Eq. (53) and the boundary conditions: $1-g(R)$ and $V(R)$ approach zero as $R\to\infty$,

$$K=\rho\int Q(13)d\mathbf{R}_3. \tag{54}$$

During the variational procedure $Q(13)$, and therefore K, will be kept constant, so it is interesting to note that K is linear in the pressure (here, osmotic pressure); from Eqs. (52) and (54), an integration by parts gives

$$\begin{aligned} K &= -(4\pi\rho/3)\int R_{13}^3\partial Q(R_{13})/\partial R_{13}dR_{13} \\ &= -(4\pi\rho/3)\int R^3 g(R)\partial V(R)/\partial R dR, \end{aligned} \tag{55}$$

or

$$K=2(P-\rho kT)/\rho, \tag{56}$$

by comparison of Eq. (55) with (31).

There is no unique variational function for a given equation, and although variational functions can be constructed by formal procedures,[19] we will simply present such a functional W and demonstrate its suitability. Let

$$\begin{aligned} W = kT\int g(12)\ln(12)d\mathbf{R}_1 + \int V(12)g(12)d\mathbf{R}_1 \\ +(\rho/2)\int Q(13)(g(23)-1)g(12)d\mathbf{R}_3 d\mathbf{R}_1. \end{aligned} \tag{57}$$

Possible variations δg of g are subject to the constraint

$$\int \delta g(12)d\mathbf{R}_1 = 0, \tag{58}$$

which we impose to maintain $g(\infty)=1$. We assert that $\delta W=0$, together with Eq. (58), yields Eq. (53) if $Q(13)$ is treated as known and not subject to variation. Variation of W gives

$$\begin{aligned} \delta W = \int\Big[kT\ln(12)+V(12)+\rho\int Q(13)g(23)d\mathbf{R}_3 \\ +kT+M-K/2\Big]\delta g(12)d\mathbf{R}_1 \end{aligned} \tag{59}$$

with the aid of an interchange of the dummy variables in the double integral of (57); M is a Lagrange multiplier for Eq. (58). Now if the variations in $g(12)$ are subject to completely arbitrary variation, it follows from $\delta W=0$ that the coefficient of $\delta g(12)$ in (59) is identically zero. Thus, Eq. (53) is recovered, after imposition of $g(\infty)=1$ gives $M=-(kT+K/2)$ for the Lagrange multiplier. Therefore, W is an adequate variation function.

If $g(R)$ is not subject to arbitrary variation, but has an assigned functional form with several parameters a_n, it is no longer true that $\delta W=0$ implies (53). Rather, by the usual application of a variation procedure, and

$$\delta g = \sum_n (\partial g/\partial a_n)\delta a_n,$$

$\delta W=0$ and Eq. (59) give the "best" values of the parameters from

$$\int\left[kT\ln(12)+V(12)+\rho\int Q(13)g(23)d\mathbf{R}_3-K\right] \times(\partial g(12)/\partial a_n)d\mathbf{R}_1=0, \tag{60}$$

with one such equation for each n. Evaluation of $Q(13)$ with the trial $g(R)$ in Eq. (52) completes the set of equations for the determination of all a_n.

The resemblance of Eq. (57) to cell model calculations of the free energy is strong, and suggests that W might be simply related to a free energy expression under the terms of the Kirkwood superposition approximation. We have not been able to confirm this suspicion. Rather the treatment of $Q(13)$, and therefore K, as constants in the variational process, seems to have the physical interpretation of a mechanical equilibrium condition. Since (1), K is the contribution of intermolecular forces to the pressure, Eq. (56), and (2), the lhs of Eq. (53) gives an estimate of K for every value of the intermolecular separation R_{12}, Eq. (60) determines $g(12)$ by attempting to make the pressure the same at all points $\mathbf{R}_2$ when it is known that a molecule is at $\mathbf{R}_1$.

An attempt to force a free energy out of Eq. (53) by comparison of it with Kirkwood's expressions[20] for the chemical potential μ and $g(R)$, which are based on a coupling parameter,[20] yielded only

$$\mu = kT\ln\rho\Lambda^3+K, \tag{61}$$

[19] P. M. Morse and H. Feshbach, *Methods of Theoretical Physics* (McGraw-Hill Book Company, Inc., New York, 1953), Chap. 9.

[20] See work cited in footnote reference 4, pp. 192 and 203.

where $\Lambda=h(2\pi mkT)^{-\frac{1}{2}}$. Equation (61) is incorrect beyond the second virial coefficient, the meager result stemming from the fact that the comparison involves the superposition approximation in the first term of a virial expansion of the excess chemical potential; consequently, the coefficient of the second power of ρ will be incorrect.

IV. APPLICATION OF VARIATIONAL PRINCIPLE

In an application of Eq. (60), the choice of a trial function $g(R)$ is governed by three considerations: the ease of the numerical work, the desired flexibility of the trial function, and our intuition regarding the expected form of the correct $g(R)$. If $X>0$, the intermolecular potential Eq. (1) decreases monotonically to zero from a finite maximum XkT, as R increases. It seems unlikely, then, that a calculation of the osmotic pressure would be greatly affected by the suppression of maxima and minima in $g(R)$. To be sure, the latter behavior results even for a hard sphere potential,[4] which $V(R)$ may somewhat resemble when $X\gg1$, but the "surface" of a polymer molecule remains soft, and any maxima and minima in $g(R)$ must be more diffuse than for the hard sphere. We could reasonably begin by restricting $g(R)$ to monotonic functions. Two further conditions on $g(R)$ would seem advantageous: that $g(R)$ can have the form $\exp(-V(R)/kT)$ at small concentrations, and that $g(R)$ has the possibility of becoming identically unity for all R at high concentrations. A $g(R)$ having these properties would be

$$\ln g=-K_1\exp(-K_2R^2),$$

where K_1 and K_2 are variation parameters. However, this form appeared to be too troublesome for hand calculation of the double integral in Eq. (60), and we consequently chose the qualitatively similar

$$g(R)=1-a\exp(-bR^2). \tag{62}$$

This form is not very good for large X and small concentrations, because of the difficulty of making $g(R)$ stay small for sufficiently large R; but the analytical convenience of Eq. (62) outweighs this disadvantage, at least for a preliminary look at a concentration region that has not yet received much study, either experimental or theoretical.

In what follows we use the exact potential of Eq. (1), and calculate the functions entering into Eq. (60). From Eq. (62)

$$\partial g/\partial a=-\exp(-bR^2) \tag{63}$$

$$\partial g/\partial b=aR^2\exp(-bR^2). \tag{64}$$

From Eqs. (1) and (52)

$$Q(13)=kTX[(\exp-BR_{13}^2)-(aB/b+B)\times\exp-(b+B)R_{13}^2]. \tag{65}$$

For the integral over R_3 in Eq. (60), put

$$N\equiv\int Q(13)(g(23)-1)d\mathbf{R}_3. \tag{66}$$

The integration over R_3 can be effected by completion of the squares in the exponential

$$(-N/kTX\pi^{\frac{3}{2}})=(b+B)^{-\frac{1}{2}}a\exp[-b(1-b/b+B)R_{12}^2]-(B/b+B)(2b+B)^{-\frac{1}{2}}a^2\exp[-b(1-b/2b+B)R_{12}^2]. \tag{67}$$

For the remaining integrations in Eq. (60) we need to specify use of Eq. (63) or (64); two equations result. These are most concisely given by replacing $(\partial g/\partial a_n)$ in (60) by

$$\partial g/\partial a_n\rightarrow R^{2n}\exp(-bR^2), \tag{68}$$

where $n=0$, 1 furnishes the two equations to be solved; see (63) and (64). Substitution of Eqs. (1), (62), (67), and (68) into Eq. (60), and integration over R_{12} yields

$$\int_0^\infty\ln[1-a\exp(-bR^2)]R^{2n+2}\exp(-bR^2)dR+\frac{X1\cdot3\cdots(2n+1)\pi^{\frac{3}{2}}}{2^{n+2}(b+B)^{n+\frac{3}{2}}}-X\pi^2\rho\left\{\frac{a1\cdot3\cdots(2n+1)}{(b+B)^{\frac{1}{2}}2^{n+2}(2b-b^2/b+B)^{n+\frac{3}{2}}}-\frac{Ba^2\cdot1\cdot3\cdots(2n+1)}{(b+B)(2b+B)^{\frac{1}{2}}2^{n+2}(2b-b^2/B+2b)^{n+\frac{3}{2}}}\right\}=0. \tag{69}$$

Introduce now the reduced variables

$$\delta\equiv b/B \tag{70}$$

$$\nu\equiv\rho(\pi/B)^{\frac{3}{2}},$$

as in Eq. (44), and for convenience let

$$A=X\pi^{\frac{3}{2}}/4. \tag{71}$$

Substitution of these new variables into Eq. (69) gives, upon putting $n=0$, 1, the final form of the variational equations for δ and a in terms of A and ν

$$I_2(a)+A(\delta/1+\delta)^{\frac{3}{2}}-A\nu a[(2+\delta)^{-\frac{3}{2}}-a(1+\delta)^{-1}(2+3\delta)^{-\frac{3}{2}}]=0, \tag{72}$$

$$I_4(a)+(3A/2)(\delta/1+\delta)^{5/2}-(3A\nu a/2)[(1+\delta)(2+\delta)^{-5/2}-a(1+2\delta)(1+\delta)^{-1}(2+3\delta)^{-5/2}]=0, \tag{73}$$

where

$$I_m(a)=\int_0^\infty\ln[1-a\exp(-x^2)]x^m\exp(-x^2)dx. \tag{74}$$

Equations (72) and (73) were solved for $A>0$ by an inverted procedure. Selected values of a and δ were

TABLE II. Variational theory. Parameters a and δ in trial radial distribution function $g(R)=1-a\exp-\delta BR^2$, for potential $V(R)=kT(4A/\pi^{\frac{1}{2}})\exp-BR^2$, and $\nu=\rho(\pi/B)^{\frac{1}{2}}$, with ρ the number density.

a	A	ν	A	ν
	$\delta=1$		$\delta=1.5$	
0.1	0.0467	0.3797	0.0659	14.590
0.4	0.2257	0.5372	0.3065	0.0549
0.7	0.5042	0.6365	0.6578	2.6170
1.0	1.1599	0.9206	1.4290	2.2414
	$\delta=2$		$\delta=3$	
0.1	0.0894	29.409	0.1481	60.866
0.4	0.4053	7.7307	0.6486	15.558
0.7	0.8473	4.6918	1.3102	9.1320
1.0	1.7776	3.6491	2.6298	6.7028

	A	δ	
0.1	0.0462	0.9862	$\nu=0$
0.4	0.2149	0.9209	
0.7	0.4641	0.8322	
1.0	1.0637	0.6212	

entered, and the corresponding values of A and ν computed. This procedure was dictated by the much simpler way in which A and ν appear than do a and δ. The values of a and δ were $a=0.1, 0.4, 0.7, 1.0$; $\delta=1$, 1.5, 2, 3; a few miscellaneous values of a and δ were used before the ranges useful and appropriate to $A>0$ became apparent. The integrals $Im(a)$, Eq. (74), were computed by a four point Gauss numerical integration[21] after first bringing the range of integration to $0<Z<1$ by the substitution $x=(\ln Z^{-1})^{\frac{1}{2}}$. This procedure resulted in Table II. We obtained the entries under $\nu=0$ in Table II by setting $\nu=0$ in Eqs. (72) and (73), and solving for A and δ as functions of a.

An inspection of the entries under $\nu=0$ in Table II will immediately indicate a major problem. Because $g(R)$ has the physical meaning of a probability, $g(R)$ can have immediate physical significance only if $g(R)\geq 0$, and necessarily then $a\leq 1$. Equation (74) requires this inequality from a purely mathematical standpoint if a is real. But the apparent result of this restriction on a is that $A\leq 1.064$. It is not, of course, a real result even mathematically; A is an independent variable and can be assigned an arbitrarily large value. The objective, and at least formally undisputable way out of this dilemma, is to recognize that for $A>1.064$ and a restricted to the real axis, our inability to find solutions of Eqs. (72) and (73) *together* (for $\nu=0$) implies merely that a is no longer subject to arbitrary variation in Eq. (60). Rather $a=1$ for $A>1.064$, Eq. (72) is rejected, as it arises from variation of a, and δ is obtained as a function of A from Eq. (73) only, with $a=1$ and $\nu=0$. If $\nu=0$, then a can be a good variational parameter even for $A>1.064$, but for *any* $A>1.064$, as ν is decreased, ν will eventually become too small for real solutions of Eqs. (72) and (73) to exist, and then we set $a=1$, and solve only Eq. (73) for δ.

If $A>1.8$, the required use of Eq. (73) only, extends to a concentration so high that a great deal of overlapping of molecules occurs, and S is very close to its asymptotic value. Because Eq. (73), with $a=1$, is relatively easy to solve (most conveniently by obtaining ν as a function of A and δ; we record that $I_4(1)=-0.14502$), we will not take up space with a full tabulation of its solution.

We give in Table III a tabulation of corresponding (horizontal entries) values of δ, a and ν for values of $0<A<1.8$, where the entries for $a<1$ were obtained by graphical interpolation of curves constructed from Table II (A vs a, ν vs a, for $\delta=1$, 1.5, 2, 3). The entries for $a=1$ were obtained from Eq. (73), as heretofore described, when the graphs indicated that no simultaneous solution of Eqs. (72) and (73) for a and ν existed for the given A and δ.

V. COMPUTATION OF THE OSMOTIC PRESSURE

A. General

For a calculation of the osmotic pressure on the basis of the variational theory, we again use Eq. (31), but it is pertinent to note, now that Table III shows $g(R)\to 1$,

TABLE III. Symbols as in Table II.

δ	a	ν	δ	a	ν
	$A=0.2$			$A=0.4$	
3	0.137	46.8	3	0.261	25.5
2	0.216	15.0	2	0.395	7.83
1.5	0.277	5.84	1.5	0.498	3.32
1.0	0.362	0.42	1.0	0.607	0.60
0.928	0.377	0	0.854	0.640	0
	$A=0.6$			$A=0.8$	
3	0.374	16.9	3	0.478	13.1
2	0.548	5.78	2	0.678	4.80
1.5	0.663	2.69	1.5	0.782	2.42
1.0	0.765	0.68	1.0	0.870	0.78
0.791	0.796	0	0.722	0.902	0
	$A=1.0$			$A=1.2$	
3	0.574	10.9	3	0.658	9.6
2	0.776	4.43	2	0.858	4.17
1.5	0.871	2.30	1.5	0.939	2.26
1.0	0.950	0.86	1.0	1	0.95
0.648	0.979	0	0.575	1	0
	$A=1.4$			$A=1.8$	
3	0.731	8.8	3	0.845	8.0
2	0.922	3.92	2	1	3.66
1.5	0.993	2.22	1.5	1	2.39
1.0	1	1.06	1.0	1	1.21
0.522	1	0	0.450	1	0

[21] H. Margenau and G. M. Murphy, *The Mathematics of Physics and Chemistry* (Van Nostrand Company, Inc., New York, 1943), p. 462.

all R, as $\nu \to \infty$, why we did not use the alternative[4]

$$kT(\partial\rho/\partial P)_T = 1+\rho\int_0^\infty (g(R)-1)4\pi R^2 dR, \quad (75)$$

which gives more accurate virial coefficients for at least one approximate theory[22] of $g(R)$ and does not require pairwise additivity of $V(R_{ij})$. (There is, of course, no reason to expect an approximate molecular theory to give completely self-consistent thermodynamic functions.)[23,24] Aside from the numerical disadvantage of Eq. (75), a numerical integration being required to obtain P, it depends most sensitively on the small difference between $g(R)$ and unity, and thus discards the major information to come out of the variational calculation, that $g \to 1$.

Substitution of Eqs. (1) and (62) into Eq. (31) gives

$$(P/\rho kT)-1 = (\pi^{\frac{1}{2}}\rho X B^{-1}/2)(1-\eta), \quad (76)$$

where

$$\eta \equiv a(1+\delta)^{-5/2}, \quad (77)$$

and is a function of $A = X\pi^{\frac{1}{2}}/4$, and ν. Transformation of ρ to the observed concentration variable c, Eq. (39), and introduction of the "apparent second virial coefficient" S, Eq. (40), gives

$$S = [(P/c)-(RT/M)](RTc)^{-1}$$
$$= (\pi^{\frac{1}{2}} X B^{-1} N_0/2M^2)(1-\eta). \quad (78)$$

As we previously noted, S reduces to A_2 at zero concentration. It is interesting to compare the A_2 of Eq. (78) with that of Flory and Krigbaum.[2] The factor multiplying $(1-\eta_0)$ (where η_0 is η at $c=0$), is the same for both results, but the Flory-Krigbaum result has instead of $(1-\eta_0)$ a numerically computed function $F(X)$, the correct multiplier for the potential of Eq. (1). In Table IV $(1-\eta_0)$ is compared with $F(X)$ for a range of X, and also with a closed approximation to $F(X)$, $F^{OF}(X)$, devised by Orofino and Flory,[8] and utilized by Stockmayer[25b]

$$F^{OF}(X) = (4/X\pi^{\frac{1}{2}})\ln(1+X\pi^{\frac{1}{2}}/4)$$
$$= A^{-1}\ln(1+A). \quad (79)$$

The range of A in Table IV is approximately that covered by polymer systems hitherto studied, and within that range the variational calculation gives fairly good values of A_2, almost as good as the data, or the agreement of A_2 theories with the data. At the larger values of A, the predicted A_2 are too large because the trial $g(R)$ is unnaturally forced to rise too quickly from its minimum value at the origin. A slightly more flexible $g(R)$ at large A, say $g(R) = 1-(1+dR^2)\exp(-bR^2)$, should be completely adequate, and even $d=b$, though yielding a more tedius variational calculation than what we have used, $d=0$, should better represent the physical situation.

TABLE IV. Proportionality factors in the second virial coefficient against potential energy parameter $A = X\pi^{\frac{1}{2}}/4$; $(1-\eta_0)$ from variational calculation, $F(X)$ from Flory and Krigbaum,[2] and $F^{OF}(X)$ from Orofino and Flory.

A	$1-\eta_0$	$F(X)$	$F^{OF}(X)$
0	1	1	1
0.2	0.927	0.93	0.911
0.6	0.815	0.80	0.784
1.0	0.719	0.72	0.693
1.4	0.650	0.65	0.625
1.8	0.605	0.59	0.572
2.6	0.542	0.51	0.492
3.8	0.480	0.42	0.412
5.0	0.439	0.37	0.358

With this encouragement we now anticipate a comparison of theory and experiment. Such a comparison requires first a consistent relationship between X, B and precisely defined molecular parameters. We shall not follow the identification made by Flory and Krigbaum,[2] which to our mind rests on too literal an identification of the radius of the segment density distribution used to evaluate intermolecular potentials with the radius of gyration. Rather we follow Stockmayer[25b] and make an identification which agrees with the perturbation theory of A_2 and the excluded volume effect. Without going into any but the most necessary details, we observe that the perturbation theory of A_2[26,27] gives

$$A_2 = (N_0 n^2\beta/2M^2)[1-32(7-4\cdot 2^{\frac{1}{2}})Z/15\alpha^3+\cdots], \quad (80)$$

where β is a segment-segment excluded volume, n is the number of segments

$$Z = (3/2\pi R_0^2)^{\frac{3}{2}}\beta n^2, \quad (81)$$

R_0^2 is the mean square end-to-end distance of the random flight polymer chain, and α is a factor which accounts for molecular expansion due to intra-chain repulsion. On the other hand, Eq. (1) gives exactly[2]

$$A_2 = (\pi/B)^{\frac{1}{2}}(N_0 X/2M^2)(1-X2^{\frac{1}{2}}/8+\cdots). \quad (82)$$

Comparison of Eqs. (80) and (32) permits the identification

$$A = 7.18Z/\alpha^3 \quad (83)$$

$$B = 9.61/\alpha^3 R_0^2. \quad (84)$$

[22] J. K. Percus and G. J. Yevick, Phys. Rev. **110**, 1 (1958).
[23] G. S. Rushbrooke and H. I. Scoins, Proc. Roy. Soc. (London) **A216**, 203 (1953).
[24] J. E. Mayer and G. Careri, J. Chem. Phys. **20**, 1001 (1952).
[25] (a) W. H. Stockmayer, J. Polymer Sci. **15**, 595 (1955). (b) Also see a paper presented at the International Symposium on Macromolecules, Wiesbaden, October, 1959. (Private communication; to be published.) Stockmayer used Eq. (79) in his comparison with perturbation theory.
[26] B. Zimm, J. Chem. Phys. **14**, 164 (1946).
[27] A. C. Albrecht, J. Chem. Phys. **27**, 1002 (1957).

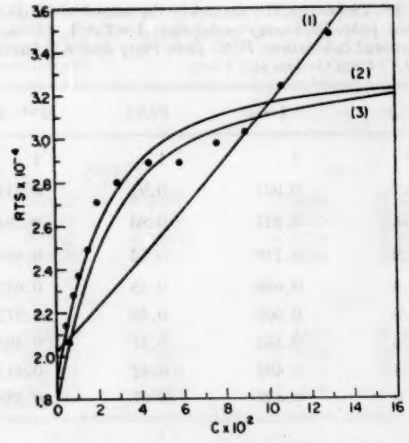

FIG. 2. Apparent second virial coefficient $S=[(P/c)-(RT/M)](RT)^{-1}$, with P in g(wt)/cm³, c in g/cm³, for polyisobutylene in cyclohexane[7]; $M=9\times10^4$, $T=303°$K. Points are experimental.[7] Curve (1) Flory-Huggins theory. Curve (2) variational theory, $\alpha=1.18$, $R_0=284\times10^{-8}$ cm. Curve (3) variational theory, $\alpha=1.21$, $R_0=257\times10^{-8}$ cm.

If α is taken to be the expansion factor appropriate to the radius of gyration of an isolated chain[25,28], then

$$\alpha^5-\alpha^3=134Z/105. \tag{85}$$

Equation (85) permits elimination of Z from (83)

$$A=5.63(\alpha^2-1), \tag{86}$$

and so allows A and B to be expressed as functions of polymer dimensions.

B. Comparison with Experiment

There do not seem to be many careful determinations of the osmotic pressure in the full range of volume fractions less than about 0.15. Furthermore, only very good solvents are predicted to cause the flattening out of $S(c)$ in this concentration range, and since this is the most unusual effect of the theory, we particularly require data on very good solvents. Because of the lack of data and also because some small quantitative, though not qualitative changes in the theory are expected when the variation of polymer dimensions with concentration is taken into account, we will confine our comparison to one experiment, that of Flory and Daoust[7] on the osmotic pressure of polyisobutylene in cyclohexane, with $M=9\times10^4$, $T=303°$K.

The comparison is most simply made if we write Eq. (78) in the form

$$S(c)=S(\infty)(1-\eta) \tag{87}$$

$$S(\infty)=(\pi/B)^{\frac{1}{2}}XN_0/2M^2. \tag{88}$$

A rough estimate of $S(0)=A_2$, and $S(\infty)$ is obtained from the data, Fig. 2. From Eq. (87) then follows $(1-\eta_0)$ and entry into Table IV furnishes A. Equation (88) then yields B. With B, Eqs. (39) and (44), one obtains the proportionality constant relating c to ν, and hence the complete curve of $S(c)$, by use of Table III or its extension (see end of part IV).

In Fig. 2 are displayed the data and two variational curves

$$\text{Curve (2):}\quad A=2.2;\qquad B^{\frac{1}{2}}=7.91\times10^{17}\ \text{cm}^{-3}$$
$$\alpha=1.18;\qquad R_0=284\times10^{-8}\ \text{cm} \tag{89}$$

$$\text{Curve (3):}\quad A=2.6;\qquad B^{\frac{1}{2}}=9.37\times10^{17}\ \text{cm}^{-3}$$
$$\alpha=1.21;\qquad R_0=257\times10^{-8}\ \text{cm}. \tag{90}$$

Also in Fig. 2 is a Flory-Huggins curve,[7] which describes the system very well at the higher concentrations displayed and beyond. The general form of this curve is

$$PV_1/RT=(v_2/x)+(\tfrac{1}{2}-\chi_1)v_2^2+\tfrac{1}{3}v_2^3+\tfrac{1}{4}v_2^4+\cdots \tag{91}$$

with V_1 the molar volume of solvent, x the ratio of the molar volume of polymer to V_1, and χ_1 a constant with respect to v_2. With $V_1=108$ cm³/mole, and $\chi_1=0.429$,[7] we obtain curve (1)

$$10^{-4}RTS=2.02+10.4c+8.6c^2+\cdots. \tag{92}$$

The values of the dimensional parameters α and R_0 in curves (2) and (3) may be compared with the values determined by Fox and Flory[18,29] from intrinsic viscosity measurements

$$\alpha=1.30;\qquad R_0=238\times10^{-8}\ \text{cm}. \tag{93}$$

The agreement of the experimental data and theoretical curves (2) and (3) in Fig. 2, and the agreement of the parameters in the theoretical curves with those obtained from the fairly well-established viscosity method is good, though not perfect. Such systematic deviations as seem to occur may be rationalized or over-rationalized, as follows: (1) The molecular weight is probably closer[7,8] to 8×10^4 than the considerably extrapolated $M=9\times10^4$ given by Flory and Daoust. A smaller M would of course depress the experimental points primarily at small c and favor a larger A; (2) The expectation that $\alpha\to1$ as $c\to\infty$ makes it reasonable

[25] E. F. Casassa, J. Chem. Phys. **31**, 800 (1959) has suggested a different choice of the numerical constant in Eq. (85) on the basis of his calculation of intramolecular repulsion in the A_2 theory. That is, α would not be the expansion of the radius of gyration. His suggestion is well taken, but the effect of his change would be minor here.

[29] T. G. Fox and P. J. Flory, J. Am. Chem. Soc. **73**, 1909 (1951).

that an α taken independent of c, $\alpha \sim 1.2$ in (89) or (90), should lie between unity and $\alpha = 1.3$ obtained at infinite dilution.[29]

These rationalizations should not be taken too seriously, but the agreement between experiment and theory and between the different computations of A_2 and A_3 seems good enough to warrant acceptance of three statements as working hypotheses: (1) The effect observed by Flory and Daoust is not an experimental artifact and is worth seeking elsewhere. (2) The calculations presented herein give a semiquantitatively accurate description of the thermodynamic properties of chain polymer solutions up to a volume fraction of ca 0.1. (3) An adequate basis has been laid for a calculation of the change of α with c by free energy minimization.

THE JOURNAL OF CHEMICAL PHYSICS VOLUME 33, NUMBER 2 AUGUST, 1960

Solvent Effects on $n \rightarrow \pi^*$ Transitions in Pyrazine*

V. G. KRISHNA AND LIONEL GOODMAN

Whitmore Chemical Laboratory, The Pennsylvania State University, University Park, Pennsylvania

(Received February 5, 1960)

The $T \rightarrow S$ and $S \rightarrow S'$ spectra of pyrazine and 2,5-dimethylpyrazine in hydrocarbon and EPA glasses has been measured. The $S \rightarrow S'$ and $S \rightarrow T$ spectra of the same compounds in ethanol and isopentane are also reported. When due correction is made for the effect of the rigid media, solvent shifts (from hydrocarbon to EPA) of 60 cm^{-1} to the red in emission and the same amount to the blue in absorption are obtained for the 0-0 band. The absorption maximum is shifted by approximately 1200 cm^{-1} to the blue and the emission maximum by about 600 cm^{-1} to the *red*. The data is explained in terms of the weak hydrogen bonding and the Franck-Condon strain resulting therefrom. It is suggested that due to the change in the extension of the π orbitals in nitrogen atoms of N heterocyclics, a Franck-Condon destabilization energy results in protonic solvents. The role of the Franck-Condon principle in the $n \rightarrow \pi^*$ blue shift phenomenon is found to be of considerable importance in accordance with Pimentel's views. The previously reported discrepancy of 500 cm^{-1} in the 0-0 bands of the $T \rightarrow S$ emission and $S \rightarrow T$ absorption of these compounds is entirely explained by media effects.

INTRODUCTION

IN a previous communication[1] it was noted that a discrepancy in $S \rightarrow T$ and $T \rightarrow S$ 0-0 bands for pyrazine multiplicity-forbidden transitions exist. In the absence of media effects the 0-0 bands for emission and absorption should be superimposed unless the transition is orbitally forbidden. The purpose of the present investigation is to ascertain whether this discrepancy is due to the media effects or due to the inherent nature of the transition itself.

The results of this investigation throw some light on the importance of the Frank-Condon principle in solvent effects on $n \rightarrow \pi^*$ transitions. The restriction placed by the Frank-Condon principle on solvent effects has been recognized before [2,3] and extended more rigorously by Pimentel[4] to cases where hydrogen bonding effects the $n \rightarrow \pi^*$ spectra. However, no data on $n \rightarrow \pi^*$ transitions has been available up to now for the purpose of testing such a restriction, though its need has been recognized by Pimentel.[4] The major work on solvent effects on emission, though undertaken with a different aim for $\pi \rightarrow \pi^*$ transitions has been due to Mataga.[5]

In the following, the singlet-singlet and triplet-singlet spectra of two nitrogen heterocyclic compounds—pyrazine and its 2,5-dimethyl derivative—are compared in a hydrocarbon and hydroxylic solvent and an interpretation suggested. The multiplicity-forbidden transitions studied here were unambiguously assigned to be $n \rightarrow \pi^*$ transitions by both solvent effects and substituent perturbation.[6,7]

As far as the Franck-Condon restriction is concerned, emission and absorption differ in that in the former the excited state and in the latter the ground state are in equilibrium with solvent environment; thus a comparison of the solvent shifts in emission and absorption is of importance in understanding the role of the Franck-Condon principle in solvent effects. Such a study of $n \rightarrow \pi^*$ transitions is necessary as there is a question as to whether the $n \rightarrow \pi^*$ blue-shift phenomenon can be attributed to hydrogen bonding from the solvent to the solute in the ground state involving the lone pair of

* This investigation was supported by the Office of Naval Research.

[1] L. Goodman and M. Kasha, J. Mol. Spectroscopy **2**, 58 (1958).
[2] H. McConnell, J. Chem. Phys. **20**, 700 (1952).
[3] N. S. Bayliss and E. G. McRae, J. Phys. Chem. **58**, 1002 (1954).
[4] G. C. Pimentel, J. Am. Chem. Soc. **79**, 3323 (1957).
[5] N. Mataga, Bull. Chem. Soc. Japan **29**, 465 (1956).
[6] F. Halverson and R. C. Hirt, J. Chem. Phys. **19**, 711 (1951).
[7] L. Goodman and R. W. Harrell, J. Chem. Phys. **30**, 1131 (1959).

TABLE I. Position of bands in singlet-singlet and singlet-triplet spectra of pyrazine (P) and 2,5-dimethylpyrazine (DMP).

	Band positions (cm^{-1})					
	EPA		Hydrocarbon[b]		Shift[a]	
	ν_{0-0}	ν_{max}	ν_{0-0}	ν_{max}	$\Delta\nu_{0-0}$	$\Delta\nu_{max}$
In solution at 298°K						
$S\rightarrow S'$ spectra						
P	30 670	31 800	30 610		+60	+1190
DMP	30 840	31 940	30 770		+70	+1170
$S\rightarrow T$ spectra						
P	26 630	27 770	26 560		+70	+1210
DMP	26 700	27 800	26 640		+60	+1160
In rigid media at 77°K						
$S\rightarrow S'$ spectra						
P	30 380	31 550	30 550		−170	+1000
DMP	30 520	31 770	30 680		−160	+1090
$T\rightarrow S$ spectra						
P	26 170	25 920		26 420	−300	−500
DMP	26 260	26 010		26 470	−290	−460
$T\rightarrow S$ spectra[a]						
P	26 490	26 240		26 530	−70	−270
DMP	26 580	26 330		26 560	−60	−230

[a] Corrected for the effect of the rigid media. $S\rightarrow S'$ bands undergo a red shift of 320 cm^{-1} in EPA and 90 cm^{-1} in hydrocarbon glasses with respect to solution spectra. These quantities are added to $T\rightarrow S$ 0-0 band positions and the resulting values can be compared to $S\rightarrow S'$ and $S\rightarrow T$ solution spectra.
[b] $\nu_{0-0}=\nu_{max}$ in hydrocarbon solvent. For emission ν_{max} is a corrected Franck-Condon maximum. See footnote reference 11a.
[c] $\nu_{EPA}-\nu_{hydrocarbon}$.

electrons.[8,9] In spite of its success in pyridazine and other compounds, the explanation cannot be extended to all $n\rightarrow\pi^*$ blue shifts. Indeed in heterocyclic bases of small pK_a values the hydrogen bonding might play a negligible part. A comparison of solvent effects in emission and absorption is expected to clarify the nature of the blue shifts. In cases where hydrogen bonding is known to effect the spectra such data will indicate the amount of hydrogen bonding in the excited state.

EXPERIMENTAL AND RESULTS

Pyrazine (Aldrich Chemical Company) and 2,5-dimethylpyrazine (Wyandotte Chemical Corporation) were purified by repeated vacuum sublimation and vacuum distillation, respectively. EPA (5,5,2 parts by volume of ether, isopentane, and ethanol) and methylcyclohexane-isopentane (1:4) glasses were used as solvents. For the emission spectra, solutions of pure compounds were excited in a glassy state at 77°K. A band-pass combination mainly transmitting at 3341 A isolated from a G.E. mercury AH-6 lamp by a No. 5970 Corning glass filter and nickel-sulfate solution,[10] was used as an excitation source. The emission spectra were photographed with a Steinheil Model GH spectrograph in Raman setting using Type 103-a Kodak spectroscopic plates. The plates were calibrated by a G.E. mercury AH-4 lamp.

Absorption measurements of $S\rightarrow S'$ and $S\rightarrow T$ bands were carried out on a Beckman Model DU spectrophotometer with an automatic recording accessory of Warren Electronics, Inc. For low-temperature measurements of $S\rightarrow S'$ absorption bands a cell of 1-cm optical path, which could be kept at liquid-nitrogen temperature by a surrounding metal Dewar, was used. $S\rightarrow S'$ and $S\rightarrow T$ absorption bands were measured at room temperature in isopentane and ethanol. The spectral changes of $S\rightarrow S'$ bands of pyrazine in isopentane on progressive addition of ethanol and ethanol-hydrochloric acid mixtures were also studied. In all measurements the 0-0 band and the band maximum were located as precisely as possible. In pure ethanol, where the 0-0 band could not be identified definitely, it was found by extrapolation of 0-0 band positions in solvent mixtures containing varying quantities of ethanol and isopentane. The results on pyrazine are reproduced in Figs. 2-6 and summarized in Table I.

DISCUSSION

The relation of solvent shifts in emission and absorption is brought out in Fig. 1. The levels drawn in broad lines correspond to states in equilibrium with the hydrocarbon solvent, where the frequencies of transition approach those in gas phase. The thin lines correspond to energy levels in EPA. The energy levels in EPA can

[8] M. Kasha, Discussions Faraday Soc. **9**, 14 (1950).
[9] G. J. Brealey and M. Kasha, J. Am. Chem. Soc. **77**, 4462 (1955).
[10] M. Kasha, J. Opt. Soc. Am. **38**, 929 (1948).

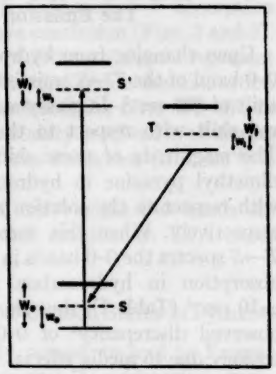

FIG. 1. Scheme of energy levels in hydrocarbon and EPA glasses.

be expected to be lower than those in the hydrocarbon system because of the stabilization energy resulting from the interaction of the nonbonding electrons with the polar solvent. The dotted lines represent energies of the metastable Franck-Condon states.

As a consequence of the Franck-Condon principle the solvent environment around the solute molecules can not change during the electronic transition, but will change after the transition through a process of relaxation into the equilibrium state.[2-4] The electronic transitions in solution either in emission or in absorption occur from an initial state having the solvent environment at equilibrium to a final state having the solvent environment in metastable configuration.

Pimentel[4] has discussed the role of the Franck-Condon principle on $n \rightarrow \pi^*$ transitions in general. His equations for the present case are given below.

From Figs. 1 and 7 it can be seen that $\Delta\nu_a$, the shift of frequency in changing from hydrocarbon to polar solvent for $S \rightarrow S'$ absorption, is given by

$$\Delta\nu_a = W_0 - W_1 + w_1,$$

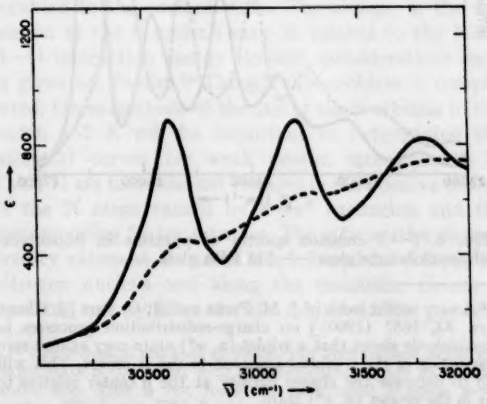

FIG. 2. Absorption spectra of pyrazine at room temperature in isopentane —— in 50% ethanol -----.

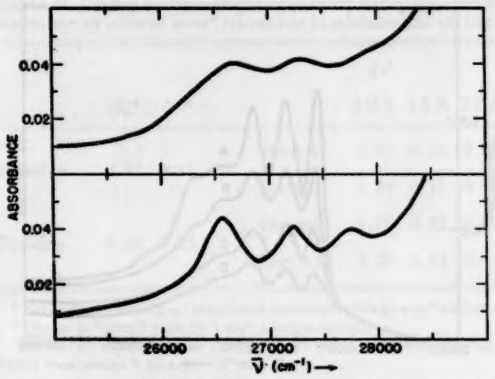

FIG. 3. $S \rightarrow T$ absorption spectra of pyrazine; upper: 50% ethanol; lower: isopentane; concentration 0.1155 M. Optical path 10 cm.

for the $T \rightarrow S$ emission the shift $\Delta\nu_e$ is given by

$$\Delta\nu_e = W_0 - W_1 - w_0,$$

and the over-all change in the process $S \rightarrow S' - T \rightarrow S$ is given by

$$\Delta\nu_a - \Delta\nu_e = w_1 + w_0.$$

It is convenient to define the quantities w_0 and w_1 as the Franck-Condon destabilization energies for absorption and emission, respectively.

The Absorption Blue Shift

In absorption (Figs. 2 and 3) the 0-0 band is blue shifted by 60 cm^{-1} and the maximum by about 1200 cm^{-1}. The low-temperature spectra (Fig. 4) do not show any further resolution of the bands, indicating the observed spectra are not a superposition of two different spectra corresponding to the hydrogen-bonded and the nonhydrogen-bonded species. The hydrogen-bonding tendency in pyrazine is very low compared to pyridazine as indicated by the pK_a values (pyridazine 2.33;

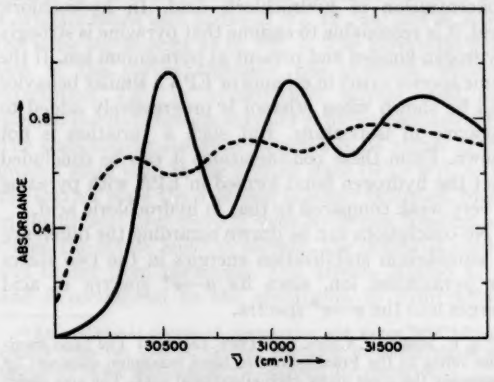

FIG. 4. Absorption spectra at 77°K in isopentane-methylcyclohexane glass ——; in EPA glass -----. Concentration uncertain due to the contraction of the solvent at 77°K.

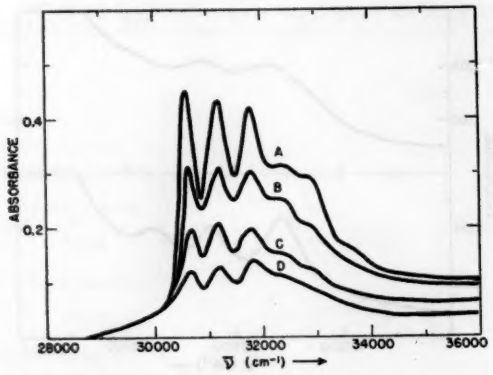

FIG. 5. Variation of $S \rightarrow S'$ spectra of pyrazine in isopentane with the addition of 15% hydrochloric acid in ethanol. (*A*) 0.0, (*B*) 0.5, (*C*) 2.0, and (*D*) 10.0% of the mixtures. Concentration of pyrazine: 2.5×10^{-4} *M*.

pyrazine 0.6).[11] The 0–0 band shift of 60 cm^{-1} corresponds to the difference of equilibrium stabilization energies $W_0 - W_1$, and the 1200-cm^{-1} shift of absorption maximum to the ground-state equilibrium stabilization energy and the excited-state Franck-Condon destabilization energy w_1. The results indicate that the excited-state stabilization (W_1) is considerable in pyrazine and that the major part of the blue shift results from the Franck-Condon destabilization term (w_1).

In Fig. 5 the effect of continuous addition of ethanol-hydrochloric acid mixture to the solution of pyrazine in isopentane can be seen. The intensity of the bands is reduced progressively while their position is relatively unchanged and the transition disappears completely in acid. This behavior is similar to that of pyridazine in ethanol studied by Brealey and Kasha[9] and indicates that the amount of the hydrogen-bonded compound, the transition of which lies further in the blue, is increasing, while the concentration of the nonhydrogen-bonded compound is decreasing, with the increasing concentration of hydrochloric acid. In hydrochloric acid, it is reasonable to assume that pyrazine is strongly hydrogen bonded and present as pyrazinium ion. If the same species exists in ethanol or EPA a similar behavior will be shown when ethanol is progressively added to pyrazine in isopentane. But such a variation is not shown. From these considerations it can be concluded that the hydrogen bond formed in EPA with pyrazine is very weak compared to that in hydrochloric acid.

No conclusions can be drawn regarding the difference of equilibrium stabilization energies in the two states for pyrazinium ion, since its $n \rightarrow \pi^*$ spectra in acid merges into the $\pi \rightarrow \pi^*$ spectra.

[11] S. F. Mason, J. Chem. Soc. **1959**, 1240; (a) The band maximum refers to the Franck-Condon band maximum obtained by comparing the areas under each vibrational peak. The area under the 0–0 peak is smaller in EPA than in hydrocarbon glass and the area under peaks 0–1 ··· 0–6 is greater in EPA glass than in hydrocarbon glass.

The Emission Red Shift

Upon changing from hydrocarbon to EPA glass the 0–0 band of the $T \rightarrow S$ emission (Fig. 6) undergoes a *red* shift of 300 cm^{-1}. In glassy state the spectra undergo a red shift with respect to the solution data (Fig. 5). The magnitude of these shifts for pyrazine and 2,5-dimethyl pyrazine in hydrocarbon and EPA glasses with respect to the solution are 90 and 320 cm^{-1}, re-respectively. When this correction is applied to the $T \rightarrow S$ spectra the 0–0 bands in $T \rightarrow S$ emission and $S \rightarrow T$ absorption in hydrocarbon solvent coincide within ± 10 cm^{-1} (Table I), thus showing that the previously observed discrepancy[1] of 0–0 bands for pyrazine is entirely due to media effects.

When the glassy-state correction is made, the 0–0 band shift in $T \rightarrow S$ emission corresponds to 60 cm^{-1} and the band maximum[11a] to about 270 cm^{-1}, both to the *red*. These shifts are opposite in direction to those in absorption.

In pyrazine the lowest triplet and the lowest singlet states correspond to identical orbital occupancies and therefore may be assumed to have nearly the same charge distributions.[12] This assumption is supported by the absence of low-lying configurations with proper symmetry for interaction with either singlet or triplet states. Therefore identical solvation energies are assumed for S' and T states and it can be predicted that the phosphorescence emission shifts observed here will be close to the shifts for the unobserved fluorescence emission.[13] Experimentally, the same amount of blue

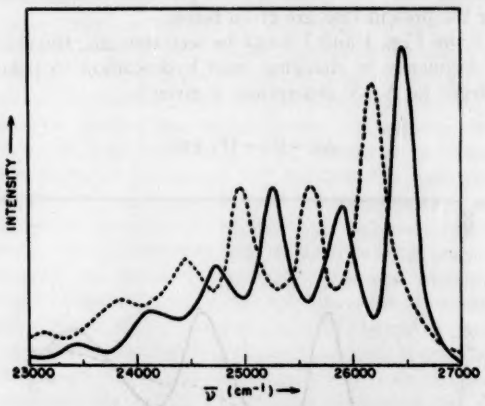

FIG. 6. $T \rightarrow S$ emission spectra of pyrazine in isopentane-methylcyclohexane glass ——; in EPA glass ------.

[12] A very recent work of J. M. Parks and R. G. Parr [J. Chem. Phys. **32**, 1657 (1960)] on charge-redistribution processes in formaldehyde shows that a triplet (n, π^*) state may exhibit spin polarization of the π orbital adjacent to the n center. This will tend to decrease the charge density at the n center relative to that in the singlet (n, π^*) state.

[13] The lack of spin polarization effect in the S' state predicts that the fluorescence should undergo a slightly smaller red shift (*vide infra*).

shift is observed for both S–S' and S–T absorption spectra, justifying the above conclusion (Figs. 2 and 3).

The corrected red shift of 270 cm^{-1} should represent the lowest value for the Franck-Condon destabilization energy (w_0), since w_0 counteracts the term W_1-W_0 in Eq. (2). Owing to the uncertainty involved in obtaining the Franck-Condon frequency this value (270 cm^{-1}) is only approximate.

The discrepancy of 120 cm^{-1} in the 0–0 bands obtained from absorption and emission in EPA needs further investigation.

The Nature of the Franck-Condon States in Pyrazine

Two effects are usually argued to lead to Franck-Condon destabilization energy: (1) orientation strain, when the suitable orientations of the solvent for the ground and excited states of solute are different; and (2) packing strain, when the solute has different sizes in the two states. Orientation strain is not expected to play a role in pyrazine, where symmetry eliminates any permanent dipole moment. The concept of packing strain cannot be justified in terms of bond distances or angles whatever the changes in the charge distribution engendered by the excitation because of the vertical nature of the transition. However, in cases where there is either specific hydrogen bonding or an electrostatic interaction between the solute and the solvent, the change in the *electronic size* of the molecule upon excitation may lead to Franck-Condon strain.

The existence of such a strain can be demonstrated for $n \rightarrow \pi^*$ transitions. The excitation of a nonbonding electron to an antibonding level will leave the atom containing the n orbital with a sizable positive charge. The effect of this charge on the electronic extension of the N heterocyclic molecule can be viewed, in a first approximation, as taking place through an increase in the effective nuclear charge acting on the nitrogen-atom valence orbitals. The main result will be a decrease in the size of the n orbital[14] which is singly occupied in the excited state. The change in the extension of the n orbitals may be related to the N···H—O interaction energy through considerations such as given by Paolini.[15] Though this problem is complicated, the magnitude of the tail of the n orbitals in the region 1–2 A will be important in determining the potential curves for weak proton interaction.[16] In Table II are listed the net changes in the positive charge at the N atom caused by $n \rightarrow \pi^*$ excitation and the corresponding Slater Z values. The estimated n charge-density values at distances 1.0, 1.5, and 2.0 A from the nitrogen nucleus and along the molecular C_2 axis in pyrazine and pyridine are also included. The pyrazine nitrogens are left with approximately $+\frac{3}{2}e$ charge and the pyridine nitrogen nearly $+\frac{3}{2}e$. It is to be noted that the magnitude of the change in Z values as estimated by this procedure (Slater rules) is likely to be too small since the increase in the screening of an n electron by the charge contribution from the nitrogen $p_z(\pi)$ orbital should not have the same weight as the decrease in screening caused by the removal of an n electron.[16] Mataga and Mataga[17,18] have shown that in the field of a proton the N-atom electronegativity is raised compared to that in the isolated heterocyclic. This causes the nitrogen atom in a protonated excitation to be left with even higher formal charge than in the gas-phase excitation because of a decrease of the excited π-orbital coefficients.

TABLE II. Change in the nonbonding electron distribution for the lowest-energy allowed $n \rightarrow \pi^*$ transitions in pyrazine and pyridine.

	ΔQ[a]	ΔZ[b]		q_n[c] 1.0 A	1.5 A	2.0 A
Pyrazine	0.42	0.15	Ground	1.65	0.24	0.02
			Excited	1.39	0.17	0.01
Pyridine	0.69	0.25	Ground	1.78	0.25	0.02
			Excited	1.30	0.14	0.01

[a] Net positive charge (a.u.) engendered on nitrogen atom by $n \rightarrow \pi^*$ excitation.
[b] Change in Slater Z value for 2-shell nitrogen orbitals.
[c] $4\pi r^2\psi\psi^*(r)$ along molecular C_2 axis for sp^2-hybrid Slater orbitals using Z values from column 3 (in a.u.).

It can be seen from Table II that the n orbitals contract markedly in the excited state in the region $r \geq 1$ A. Since the N···H—O distance depends upon the extension of the n orbitals, its equilibrium distance will be smaller in the excited state than in the ground state. As this distance cannot change during the transition, Franck-Condon destabilization results in protonic solvents.

Figure 7 shows the schematic potential curves for the ground and excited states, with the contraction of the n orbitals taken into account. W_0, W, w_0, and w_1 have the same significance as in Fig. 1. The horizontal portion of the curves represent the situation without interaction, e.g., in hydrocarbon solvent, and the minima the stabilization energies in hydroxylic solvents. The stabilization energy is expected to be higher in the ground state than in the excited state ($W_0 > W_1$), as in the excited state the n orbital is singly occupied. Since in the present case there is weak hydrogen bonding between the solute and the solvent, the potential curves will be far from parabolic. The arrows labeled 1, 2, and 3 correspond to the absorption in hydrocarbon

[14] The 0–0 band red shift of 90 cm^{-1} in hydrocarbon liquid to a glassy state is consistent with the postulated change in the electronic size. This is not found in substituted benzene $\pi \rightarrow \pi^*$ spectra. The larger EPA liquid to glassy-state shift is also consistent with the above viewpoint.
[15] L. Paoloni, J. Chem. Phys. **30**, 1045 (1959).
[16] An additional source of contraction not taken into account results from the loss of electron repulsion in configuration $n)^1$ compared to $n)^2$ with concurrent decrease in s character.
[17] S. Mataga and N. Mataga, Bull. Chem. Soc. Japan **32**, 511, 529 (1959).
[18] S. Mataga and N. Mataga, Z. physik. Chim. **19**, 231 (1959).

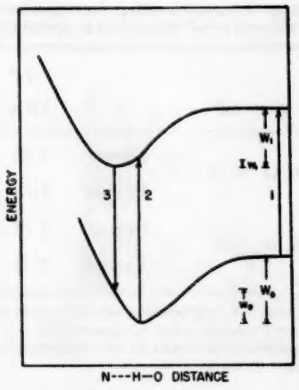

FIG. 7. Schematic potential energy curves depicting the relation of solvent effects in emission and absorption. Arrows 1, 2, and 3 correspond to absorption in hydrocarbon, absorption in EPA, and emission in EPA, respectively.

solvent, the absorption in EPA, and emission in EPA, respectively.

The $n\rightarrow\pi^*$ Blue Shift

It can be seen that there are compelling reasons for believing that Franck-Condon destabilization plays a major role in the observed spectral shifts. Compounds containing n electrons can interact with the hydroxylic solvents to different degrees, the two extreme cases being represented by strong hydrogen bonding and very weak electrostatic interaction. The result of any such interaction is the production of a potential minimum as shown in Fig. 7 as a function of the N···H—O distance, where the depth of the minimum is equal to the stabilization energy. Since the minima in these curves for the ground and excited states may not coincide, Franck-Condon destabilization for any type of interaction can occur.

This leads to the suggestion that a considerable portion of the observed blue shifts in $n\rightarrow\pi^*$ transitions are caused by the Frank-Condon destabilization resulting from the change in the N···H—O distance in addition to the difference in the equilibrium stabilization energies. In cases where hydrogen bonding is strong in the ground state, e.g., pyridazine, the potential functions should be steep and a high Franck-Condon strain should result even for a slight distortion of the N···H—O distance. Thus the Franck-Condon destabilization effect, the magnitude of which can be expected to depend upon the degree of n-orbital contraction, as well as the equilibrium stabilization energies, is predicted to be especially large for such strong bases as pyridine and pyridazine ($pK_a=5.23$ and 2.33, respectively)[11] where unusually large decreases in the N-atom charge densities are exhibited on $n\rightarrow\pi^*$ excitation. The Franck-Condon strain effect should play a major role in all $n\rightarrow\pi^*$ spectra, especially in the large N heterocyclics, since in these cases the n-orbital shrinking on excitation naturally provide a cause for the solvent cage contraction.[19]

ACKNOWLEDGMENTS

The authors thank Dr. N. Mataga and Dr. E. G. McRae for their helpful criticism.

[19] *Note added in proof.* Further results [V. G. Krishna and L. Goodman (to be published)] on emission spectra of pyrazine hydrochloride and pyrimidine hydrochloride show that the emission is from a nonhydrogen-bonded excited state. As a consequence of the hydrogen bond breaking in the (n, π^*) excited state $W_1\sim0$ and w_0, $w_1>0$ consistent with the corrected red shift of 270 cm^{-1} observed for the pyrazine emission arising from emission to a nonhydrogen-bonded ground state ($W_0=0$).

Heat Capacity of Uranium Tetrafluoride from 1.3° to 20°K and the Thermodynamic Functions to 300°K. Calorimeter for the Range 0.8° to 20°K*

JOHN H. BURNS, DARRELL W. OSBORNE, AND EDGAR F. WESTRUM, JR.†

Argonne National Laboratory, Lemont, Illinois

(Received February 26, 1960)

The heat capacity of uranium tetrafluoride has been determined from 1.3° to 20°K in an isothermal calorimeter with an integral gas thermometer and vapor-pressure bulb for calibration of a carbon resistance thermometer. The enthalpy, entropy, and free-energy functions were evaluated from these data and previous measurements at higher temperatures. At 298.15°K, the values of $S°$, $(H°-H_0°)/T$, and $-(F°-H_0°)/T$ are 36.25±0.04, 18.08±0.02, and 18.17±0.02 cal mole^{-1} deg^{-1} for uranium tetrafluoride. A Schottky-type anomaly occurs in the heat capacity at 6.4°K, presumably as a consequence of ligand-field splitting of the electronic energy levels.

INTRODUCTION

THE heat capacity of uranium tetrafluoride between 20° and 350°K has previously been reported by Brickwedde, Hoge, and Scott[1] and that between 5° and 300°K by Osborne, Westrum, and Lohr.[2] It seemed desirable to extend the measurements to still lower temperatures in order to obtain reliable entropies for thermodynamic calculations and to evaluate the nonlattice contributions to the heat capacity and the entropy. The heat capacity of uranium tetrafluoride changes comparatively little between 5° and 10°K in contrast to the approximately T^3 variation found for that of thorium tetrafluoride.[3] This behavior made extrapolation to 0°K difficult and led to the inference that an anomaly might exist in the heat capacity of uranium tetrafluoride below 5°K. Moreover, preliminary measurements by Bailey[4] on an impure sample indicated the presence of an anomaly at approximately 7°K.

The heat capacities[2] reported previously from this Laboratory were not considered to be highly accurate below 14°K, because the thermometer which was employed (a platinum resistance thermometer) was calibrated at 4.2° and 14°K but at no other temperature in this interval and also because the thermometer is rather insensitive in this region. To improve the accuracy in the range 5° to 14°K and to extend the measurements to lower temperatures a new cryostat and calorimeter, which have the important feature that a carbon thermometer can be calibrated *in situ*, have been constructed. As described in this paper, these have been used to measure the heat capacity of UF_4 from 1.3° to 20°K.

* Based on work performed under the auspices of the U. S. Atomic Energy Commission.

† Chemistry Department, University of Michigan, Ann Arbor, Michigan.

[1] F. G. Brickwedde, H. J. Hoge, and R. B. Scott, J. Chem. Phys. **16**, 429 (1948).

[2] D. W. Osborne, E. F. Westrum, Jr., and H. R. Lohr, J. Am. Chem. Soc. **77**, 2737 (1955).

[3] H. R. Lohr, D. W. Osborne, and E. F. Westrum, Jr., J. Am. Chem. Soc. **76**, 3837 (1954).

[4] C. A. Bailey, Clarendon Laboratory, Oxford, England (private communication).

EXPERIMENTAL

Uranium Tetrafluoride Samples

Heat capacities were determined for two samples of UF_4, which are designated "powdered" and "granular." The powdered one was the purified sample on which measurements were made by Osborne, Westrum, and Lohr.[2] The granular sample was prepared in essentially the same manner as the powdered sample, with an additional step in which the twice-sublimed UF_4 was melted by induction heating at about 1000°C in a platinum crucible under a helium atmosphere. The solidified melt was cracked into smaller pieces in a helium-filled dry box, and those pieces which were retained on a screen with a 1-mm mesh were used in the heat capacity determinations. The mass of the powdered sample used for the calorimetric measurements was 124.092 g and that of the granular sample was 110.637 g.

The analyses of the powdered sample have been given before.[2] Those of the granular sample were as follows. Bromine trifluoride dissolution[5] showed the presence of 0.009% oxygen. Uranium was determined by ignition to U_3O_8 to be 75.81% (theoretical, 75.80%), and fluorine was determined by pyrohydrolysis and titration of the HF formed to be 24.18% (theoretical 24.20%). Spectrochemical analyses showed the presence of the following elements (in parts per million): 5 Al, 0.2 Ba, 0.8 Cr, 10 Cu, 0.1 Li, 6 Mg, 0.1 Mn, 40 Mo, 3 Ni, 15 Si, and 2 Zr. The following elements were not detected (the numbers indicate the limits of sensitivity in parts per million): 1 Ag, 10 As, 0.1 B, 0.01 Be, 1 Bi, 20 Ca, 2 Ce, 2 Co, 1 Dy, 0.4 Er, 0.1 Eu, 2 Fe, 1 Gd, 1 Ho, 20 K, 0.4 La, 0.1 Lu, 10 Na, 2 Nd, 50 P, 1 Pb, 2 Pr, 50 Pt, 1 Sb, 0.1 Sc, 5 Sn, 1 Sr, 50 Ta, 2 Tb, 2 Th, 0.5 Ti, 2 Tm, 0.05 Y, 0.05 Yb, and 50 Zn.

X-ray powder photographs of portions of the powdered UF_4 and of the granular UF_4 after grinding for a few minutes in a mortar were identical, except that the diffraction lines of the first sample were broader and more diffuse, presumably due to its smaller particle size.

[5] H. R. Hoekstra and J. J. Katz, Anal. Chem. **25**, 1608 (1953).

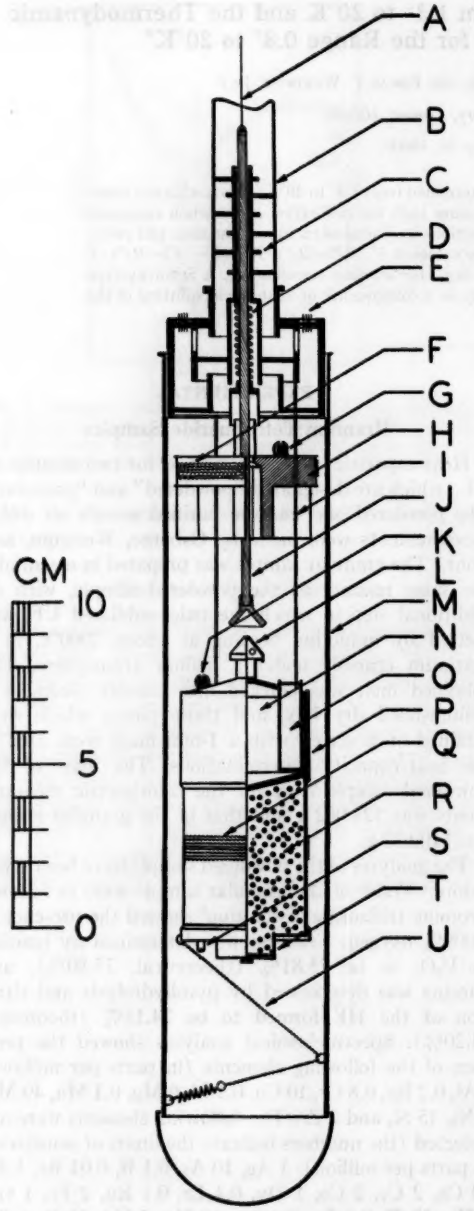

FIG. 1. Partially sectioned view of calorimeter (P) and submarine (M) showing the guard block (H), the gas thermometer (N), the vapor-pressure bulb (O), and the contacting mechanism (J). Other parts are identified in the text.

Cryostat and Calorimeter

The crystat, which was similar in general to one depicted previously,[6] consisted of coaxial, cylindrical glass Dewars for liquid helium and nitrogen. A submarine (M, Fig. 1) containing the calorimeter (P) was suspended by a pumping tube (B) from a removable, neoprene-gasketed cover, which also served as a mounting plate for the electrical terminals, vacuum couplers, connections to the manometers, etc. The submarine was normally evacuated and immersed in liquid helium near the bottom of the helium Dewar. It contained, in addition to the calorimeter, a guard block (H), and a mechanism (J) for establishing contact between the calorimeter and the refrigerant bath surrounding the submarine.

The calorimeter (P), which was machined from OFHC copper and assembled with 50-50 lead-tin solder, contained a 23.2-cm³ gas thermometer (N), a 1.8-cm³ vapor-pressure bulb (O), and a 41.38-cm³ sample space (R) provided with six radial vanes in spring contact with the walls. A removable cover was soldered in place with Cerroseal-35 (50-50 indium-tin solder) and was separated from the copper shell by a short tube of thin stainless steel (T). A small hole in a stainless steel spur (S) permitted sealing the calorimeter with Cerroseal solder after evacuation of the sample space and addition of helium gas for thermal contact with the sample. The calorimeter thermometer (K) was a carbon resistor (Speer Carbon Company, 1 w, nominal 120 ohms) with the outer plastic shell ground off, covered with a layer of cigarette paper and cemented with Formvar varnish in a closely fitting copper receptacle.

The guard block (H), which acted as a thermal barrier and as an isothermal heat reservoir, was a relatively massive copper cylinder provided with a carbon resistance thermomenter (G) and a heater (F). Several blackened baffles (C) in thermal contact with the bath prevented room-temperature radiation from impinging on the calorimeter.

A contacting mechanism obviated the use of exchange gas in cooling the apparatus to low temperature. An OFHC copper rod (J) which was in thermal contact with the bath through braided copper wire, terminated in a conical receptacle that mated with a cone (L) on the calorimeter top. The contacting force was applied by a spring (D). The rod was withdrawn by a windlass (situated above the mounting plate) and a braided silk cord (A).

Leading from the room-temperature portion of the apparatus through the pumping tube (B) were two identical tubes for the gas thermometer and a tube for the vapor-pressure bulb, which were soldered together at 15-cm intervals and to the baffles and the guard block. (The purpose of the extra tube to the gas thermometer is described below.) The gas thermometer tubes were of No. 347 stainless steel, 0.5-mm i.d., and the vapor-pressure tube was of cupronickel, 1.0-mm i.d., down to the baffles and then of No. 347 stainless steel, 0.5-mm i.d. These tubes terminated about 1 cm below the lower surface of the guard block. There they were soft-

[6] B. M. Abraham, D. W. Osborne, and B. Weinstock, Phys. Rev. 80, 366 (1950).

soldered to three No. 347 stainless steel tubes (I), 0.50-mm i.d.×0.62-mm o.d., which were attached to the calorimeter. The upper tubes were counterbored to fit the tubes attached to the calorimeter, so that the joints could be unsoldered when it was desired to remove the calorimeter and then resoldered during the reassembly without appreciable volume change. Three spring-loaded silk cords (U) between the bottom of the calorimeter and hooks in the wall of the submarine minimized vibration of the calorimeter.

A 1000-ohm heater (Q) of No. 40 B and S-gauge Advance wire was wound bifilarly around the calorimeter. The current leads (No. 38 Advance) and potential leads (No. 40 Advance) to the calorimeter heater and the four leads to the calorimeter resistance thermometer (No. 40 Advance) were successively wound around the calorimeter shell, the guard block, and the baffles, and were brought into thermal contact with Formvar enamel. In order to allow for the heat developed in the two current leads to the heater, half of which goes to the calorimeter and half to the guard block, one of the branch points was located where the leads left the guard block and the other was located where the leads reached the calorimeter. The leads left the submarine through tubes in diminutive Stupakoff seals (E), at the top of which they were soldered to No. 36 copper leads.

Temperature Scale

The temperature scale was based on a combination of gas thermometry and vapor-pressure measurements. The resistance thermometer was calibrated against the vapor pressure of He^3 up to 3°K, against the vapor pressure of He^4 from 2° to 4.2°K, against a helium-filled gas thermometer in the range from 4.2° to 20°K, and against the vapor pressure of n-hydrogen near 20°K, at intervals of approximately 0.1T.

Pressures were measured with constant-volume mercury manometers (18-mm i.d.) and a Wild cathetometer that could be read to 0.01-mm. Corrections were applied to the manometer readings for capillary depression,[7] and for the thermomolecular pressure difference, [8,9] as well as for the temperature of the mercury and for the ratio between the local acceleration due to gravity and the standard value, 980.665 cm sec^{-2}.

For the calibrations below 4.2°K He^3 or He^4 was condensed into the vapor-pressure bulb. The temperatures of the liquid helium bath around the submarine and of the guard block were held constant at slightly higher values than the temperature of the calorimeter, while simultaneous observations were made of the resistance thermometer and vapor pressure. He^3 vapor pressures were converted into temperatures on the T_{LSS} scale by means of an equation given by Sydoriak and Roberts,[10] and He^4 vapor pressures were converted into temperatures on the same scale by means of the tables of van Dijk and Durieux.[11]

For the gas thermometry the cryostat was filled with liquid helium, and sufficient He^4 was admitted to the gas thermometer to produce about one atmosphere pressure at the hydrogen boiling point. With this amount of gas the sensitivity was 38 mm Hg deg^{-1}. Then a series of measurements was made from 4.2° to about 20°K. At each calibration point the guard block was held at a constant temperature near that of the calorimeter, so that the temperature of the calorimeter changed fairly slowly, while the resistance of the thermometer and the positions of the mercury menisci were observed.

In order to determine the amount of He^4 in the gas thermometer the liquid helium in the cryostat was replaced with liquid hydrogen, and n-hydrogen was condensed directly from a cylinder at room temperature into the vapor-pressure bulb. Then a comparison of the resistance thermometer, gas thermometer, and vapor pressure was made before the ortho-para conversion could proceed appreciably. Care was taken to have all parts of the apparatus warmer than the calorimeter during these measurements. The temperature was obtained from the vapor-pressure equation of Woolley, Scott, and Brickwedde,[12] but a correction of 0.01° was subtracted because this equation gives 20.39°K as the normal boiling point of n-hydrogen rather than the presently accepted value of 20.38°K.[11] In one calibration series the hydrogen vapor pressure was used to calibrate the resistance thermometer down to 14°K, but it was usually more convenient to use the gas thermometer over the range from 4.2° to 20°K.

The gas thermometer readings were reduced to temperatures by means of the following equations:

$$pV(1+B/\tilde{V})/T+p\sum_i V_i/T_i=nR, \qquad (1)$$

$$p\tilde{V}(1+B/\tilde{V})=RT. \qquad (2)$$

Here p is the pressure, V and T are the volume and temperature of the gas thermometer, B is the second virial coefficient of He^4 at T,[13] $\tilde{V}$ is the molal volume of He^4 at p and T, V_i and T_i are the volumes and temperatures of the various sections of the connecting tubes and of the manometer, and R is the gas constant. The number of moles, n, was evaluated from the comparison of the gas thermometer with the vapor pressure of n-hydrogen near 20°K. The volume of the gas thermometer was obtained by filling it with water and weighting at 300°K and then correcting to 20°K

[7] W. Cawood and H. S. Patterson, Trans. Faraday Soc. **29**, 514 (1933).
[8] S. Weber and G. Schmidt, Leiden Comm. No. 246c (1936).
[9] T. R. Roberts and S. G. Sydoriak, Phys. Rev. **102**, 304 (1956).
[10] S. G. Sydoriak and T. R. Roberts, Phys. Rev. **106**, 175 (1957), Eq. (9).
[11] H. van Dijk and M. Durieux, Physica **22**, 760 (1956); **24**, 1 (1958).
[12] H. W. Wooley, R. B. Scott, and F. G. Brickwedde, J. Research Natl. Bur. Standards **41**, 379 (1948), Eq. (7.2).
[13] J. E. Kilpatrick, W. E. Keller, and E. F. Hammel, Phys. Rev. **97**, 9 (1955).

by use of the known expansion coefficients of copper.[14] The contraction below 20°K is insignificant, and the gas thermometer was sufficiently rigid for the change in volume with pressure to be neglected. The volumes of the connecting tubes were determined by gas expansion experiments before the assembly of the apparatus. The volume in the short arm of the manometer was calibrated in terms of the distance of the crown of the meniscus below a fiducial point, and a correction was made for the covolume of the meniscus.[15] Special care was taken to evaluate the average T_i^{-1} for the tubing between the gas thermometer and the top of the cryostat, one of the two identical tubes to the gas thermometer being used for this purpose. The average value of T_i^{-1} in this tube, which was plugged at the point where it was soldered to the calorimeter, was determined by measuring the pressure of a known quantity of He^4 gas with a mercury manometer having a small, calibrated bore.

In order to obtain a smooth relation between the temperature, T, and the resistance, R, of the carbon thermometer we used the "resistance temperature" T_R, calculated from Eq. (3),[16]

$$1/T_R=(a^2/\log R)+b^2\log R+2ab, \qquad (3)$$

and a deviation plot of T_R-T vs T_R. In the first calibration the constants a and b were adjusted to make $T_R=T$ at the boiling points of hydrogen and helium, the experimental values of T_R-T were plotted against T_R, and a smooth curve was drawn.

The same values of a and b were used for subsequent calibrations, which were made each time the calorimeter was warmed above 30°K. All the resistances in each such calibration were multiplied by a factor (differing from unity by 1% or less) such that the corrected $\log R$ gave $T_R=T$ at the boiling point of hydrogen, and a new deviation plot was made.

Operation of the Calorimeter

The calorimeter was usually cooled from 77° to 2°K by the thermal contacting mechanism without the use of an exchange gas. Whenever helium had been present in the submarine the gas was evacuated with the oil diffusion pump at temperatures higher than the maximum temperature at which heat capacity measurements were to be made. A helium leak detector was used to monitor the vacuum pump exhaust from the submarine and thus to provide a sensitive indication of the presence of gaseous helium in the insulating vacuum at low temperatures. A convenient technique for rapidly cooling to the lowest temperature was vaporization of liquid He^3 from the vapor-pressure bulb by means of a Toepler pump. A temperature of 0.8°K was easily reached by this method.

Heat capacities were determined by measuring the temperature increment obtained upon the addition of electrical energy. The currents and the potentials across the heater and the carbon resistance thermometer were measured with a calibrated White double potentiometer, calibrated resistors, and a calibrated standard cell. Time intervals were measured with an automatic timer operated by a calibrated tuning fork and an amplifier. Thermometer currents of 2.8 μa were used below 2°K and of 10 μa at higher temperatures. The guard block was manually controlled at a constant temperature for several consecutive runs by means of its electrical heater and its carbon thermometer, the resistance of which was observed with a Wheatstone bridge. Fore and after drifts of the calorimeter were measured for each heating period and were extrapolated to the middle of the heating period in the usual manner.

RESULTS AND DISCUSSION

Heat Capacities

The heat capacity of the calorimeter with a small amount of gaseous helium was first determined over the range 1.3° to 20°K. The heat capacity of the copper calorimeter varied from 0.00047 cal deg^{-1} at 1.36°K to 0.0168 cal deg^{-1} at 19.6°K. Next, the calorimeter was loaded with the powdered uranium tetrafluoride sample and gaseous helium at 21 mm Hg (at 300°K). Adsorption of the helium made measurements at temperatures lower than 11°K impossible because of loss of thermal contact of the calorimeter with the sample. Increase of the helium pressure to 143 mm Hg permitted measurements down to 4.4°K.

In order to decrease the absorption of helium it was necessary to use a sample with a smaller specific surface. The sample of granular UF_4 was then prepared and measured over the range 1.3° to 20°K. Large drifts at the lowest temperatures were caused by the natural alpha radioactive disintegration of the U^{238} in the sample which liberates approximately 2.9×10^{-5} cal $(\text{min g at})^{-1}$. This energy release produced a heating effect of 7×10^{-5} deg min^{-1} at 10°K and 5×10^{-3} deg min^{-1} at 1.3°K for the calorimeter loaded with granular UF_4. The large drift rates precluded accurate measurements at lower temperatures.

The results of heat capacity measurements on the two samples of UF_4 are presented in chronological sequence in Table I and in Fig. 2. These data have an estimated probable error of 2% at 1.3°K, 0.6% at 2°K. 0.2% from 2.4 to 16°K, and 0.4% at 20°K. The approximate temperature increments used may be inferred from the differences in the mean temperatures of the successive determinations. The increments were usually less than 10% of the mean absolute temperature. A small "curvature" correction, $-(d^2C_p/dT^2)$

[14] T. Rubin, H. W. Altman, and H. L. Johnston, J. Am. Chem. Soc. 76, 5289 (1954).
[15] J. Kistemaker, Physica 11, 270 (1944).
[16] J. R. Clement, J. K. Logan, and J. Gaffney, Naval Research Laboratory Rept. 4542 (1955).

TABLE I. Molal heat capacity of uranium tetrafluoride.
Molecular weight = 314.07. The footnotes refer to the temperature-scale calibrations for the different series.

T (°K)	C_p (cal deg^{-1} mole^{-1})	T (°K)	C_p (cal deg^{-1} mole^{-1})	T (°K)	C_p (cal deg^{-1} mole^{-1})
		Series I[a], powdered UF_4 sample			
4.442	0.1961	7.350	0.2817	12.888	0.455
4.726	0.2141	8.050	0.2918	14.072	0.533
4.972	0.2248	8.814	0.3039	15.456	0.646
5.293	0.2373	8.820	0.3034	16.976	0.792
5.713	0.2502	9.737	0.3237	18.497	0.959
6.142	0.2612	10.680	0.3517		
6.712	0.2720	11.748	0.3947		
		Granular UF_4 sample			
	Series II[b]		Series IV[b]		Series VI[c]
4.177	0.2096	10.304	0.3334	1.303	0.0041
		11.231	0.3630	1.486	0.0079
	Series III[b]	12.248	0.4068	1.645	0.0111
		13.354	0.467	1.810	0.0148
2.486	0.0583	14.603	0.554	2.036	0.0253
2.652	0.0738	15.998	0.671	2.231	0.0379
2.808	0.0879	17.481	0.821	2.418	0.0524
3.014	0.1080	19.158	1.017		
3.253	0.1314				Series VII[d]
3.524	0.1567		Series V[c]		
3.830	0.1833			13.753	0.492
4.197	0.2109	1.630	0.0108	15.063	0.590
4.606	0.2360	1.826	0.0154	16.350	0.710
5.062	0.2561	1.993	0.0230	17.870	0.871
5.595	0.2717	2.188	0.0349		
6.226	0.2826	2.370	0.0485		Series VIII[d]
6.875	0.2893	2.554	0.0642		
7.544	0.2944	2.753	0.0828	14.951	0.581
8.280	0.3000	2.957	0.1025	16.247	0.698
9.094	0.3089	3.191	0.1255	17.626	0.841
9.982	0.3253	3.476	0.1525	19.200	1.029

[a] He^4 gas thermometer 4°–20°K.
[b] He^4 vapor pressure 2°–4°K, He^4 gas thermometer 4°–20°K.
[c] He^3 vapor pressure 0.8–3°K, He^4 vapor pressure 2°–4°K.
[d] H_2 vapor pressure 14°–20°K.

$(\Delta T)^2/24$, has been applied to each experimental $\Delta H/\Delta T$ value to convert it to the true C_p. This correction amounted to 0.15% of the heat capacity or less. The data are expressed in terms of the defined thermochemical calorie of 4.1840 absolute joules, and the molecular weight of UF_4 was taken to be 314.07. The heat capacity of the empty calorimeter was 21% of the total at 1.3°K, 4% at 4°K, and 30% at 19.2°K. Appropriate corrections were applied for the residual amount of He^3 gas in the vapor-pressure bulb and for the amount of He^4 gas in the sample space.

In addition to the data from this investigation the previously reported determinations[2] on uranium tetrafluoride have also been shown in Fig. 2. It will be noted that the previous measurements are in excellent agreement with the present ones on the same powdered sample over the range 13° to 20°K, and they are in fair agreement at lower temperatures when allowance is made for the estimated probable error in the previous measurements (5% at 5°K, 1% at 14°K, 0.1% above 25°K).

A greater divergence over the common range of these investigations is noted between the powdered and granular samples. Since entirely independent confirmatory determinations over a considerable part of the range have been made on both samples with different calibrations of the temperature scale, it is considered that the difference between samples is real and not the result of experimental error. Because the granular sample certainly approximates more nearly the macroscopic thermodynamic reference state, we regard it as giving the properties of bulk uranium tetrafluoride. These samples are presumably identical in all respects, except of particle size. We assume that the large surface development of the powdered material and the adsorption of helium gas are the chief causes of the differences between the two samples.

Values of the heat capacity of the granular UF_4 sample read from a smooth curve through the experimental points are given in Table II.

Heat Capacity Anomaly

The lattice contribution to the heat capacity of UF_4 was separated from the total by assuming that it could be represented by the heat capacity[3] of diamagnetic,

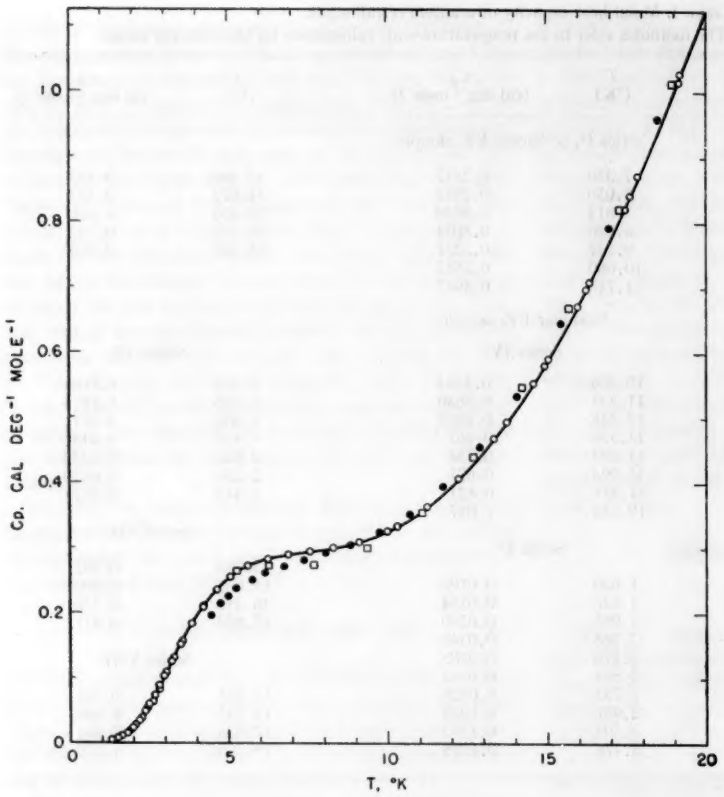

FIG. 2. Heat capacity of UF_4. ○: Granular sample; ●: present measurements on the powdered sample; □: previous measurements on the powdered sample (see footnote reference 3).

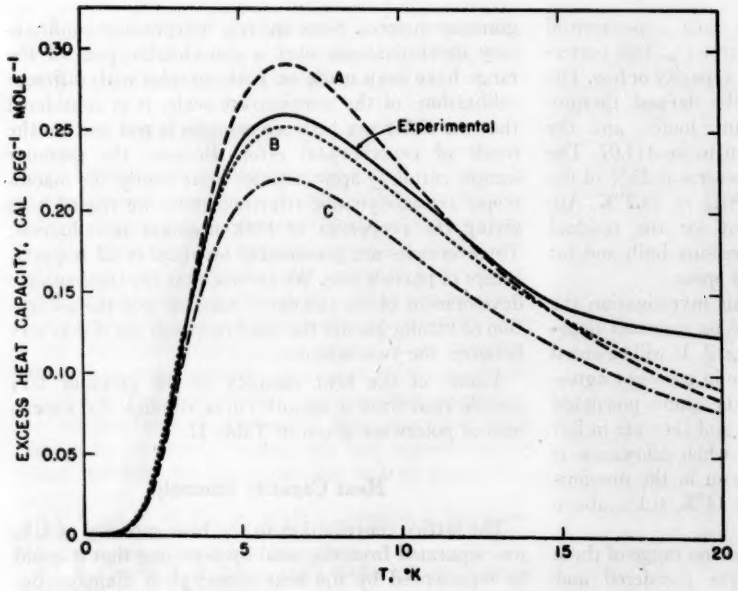

FIG. 3. Excess heat capacity of UF_4. The solid curve gives the experimental heat capacity of UF_4 less the heat capacity of ThF_4. Curves *A*, *B*, and *C* are Schottky functions discussed in the text.

isostructural[17] ThF_4. The heat capacity remaining after subtraction of this lattice contribution is given in Table II and is shown by the solid line in Fig. 3. This excess (i.e., nonlattice) heat capacity reaches a maximum of 0.26 cal deg^{-1} $mole^{-1}$ at 6.4°K and has the shape of a Schottky anomaly. The entropy corresponding to the excess heat capacity between 0° and 20°K is 0.401 cal deg^{-1} $mole^{-1}$.

C. A. Bailey has also observed an anomaly with this general shape,[4] but sufficient information is not available for a detailed comparison.

The thermodynamic properties for a Schottky anomaly can be readily derived from the partition function

$$Z=\sum_i g_i \exp(-\epsilon_i/kT),$$

where g_i represents the degeneracy and ϵ_i the energy of the ith level. The heat capacity is obtained from the relation

$$C=RT\partial^2(T\ln Z)/\partial T^2$$

and for the case of a single level close to the ground level, all other levels being at much higher energies, the heat capacity is

$$C=R(\epsilon/kT)^2 g_0 g_1 \exp(\epsilon/kT)/[g_0\exp(\epsilon/kT)+g_1]^2$$

with $\epsilon=\epsilon_1-\epsilon_0$.

If $g_0=g_1$, the Schottky heat capacity has a maximum value of 0.87 cal deg^{-1} $mole^{-1}$, approximately three times the observed maximum. In order to fit the observed curve, it is necessary to assume either that g_0 is greater than g_1 or that only part of the U^{4+} ions have a low-lying excited energy level. The best fit, shown as curve B in Fig. 3, is provided by assuming $g_0/g_1=4$ and $\epsilon/k=13.6$°K for all the uranium ions. It is known, however, that the uranium ions in UF_4 do not all occupy equivalent sites; two-thirds of them occupy general fourfold positions of the $C2/c$ space group while one-third are situated on twofold rotation axes.[17] It therefore seems possible that the uranium ions in one set of positions may have a low-lying excited level and that those in the other set may have no excited levels sufficiently low to contribute to the Schottky anomaly.[18] An approximate fit (curve C in Fig. 3) is obtained by assuming that the only contribution comes from two-thirds of the uranium ions that have $g_0/g_1=3$ and $\epsilon/k=13.8$°K. Another possibility providing a reasonable fit (curve A in Fig. 3) is that one-third of the uranium ions have a nondegenerate ground level and a nondegenerate level at $\epsilon/k=15.4$°K and that the other two-thirds have a nondegenerate ground level and no other low-lying levels.

We believe that the existence of a degenerate ground level in UF_4 is rendered unlikely both by the absence of paramagnetic resonance at low temperatures[19] and by the magnetic susceptibility measurements between 2° and 20°K.[20] The lowest degenerate energy level which can arise (as discussed below) from the effect of a cubic field in the crystal on the electronic configuration of the free U^{4+} ion yields a magnetic susceptibility much

TABLE II. Total heat capacity and excess heat capacity of granular UF_4 at rounded temperatures.

T (°K)	C_p (cal deg^{-1} $mole^{-1}$)	ΔC_p[a] (cal deg^{-1} $mole^{-1}$)	T (°K)	C_p (cal deg^{-1} $mole^{-1}$)	ΔC_p[a] (cal deg^{-1} $mole^{-1}$)
1	(0.0018)	(0.0017)	9	0.3076	0.2327
2	0.0232	0.0225	10	0.3258	0.2170
3	0.1067	0.1042	12	0.3947	0.1859
4	0.1969	0.1909	14	0.509	0.154
5	0.2537	0.2421	16	0.674	0.138
6	0.2794	0.2593	18	0.883	0.129
7	0.2904	0.2580	20	1.129	0.124
8	0.2976	0.2476			

[a] $\Delta C_p=C_p(UF_4)-C_p(ThF_4)$.

TABLE III. Thermodynamic functions of uranium tetrafluoride.

T (°K)	C_p (cal $mole^{-1}$ deg^{-1})	S° (cal $mole^{-1}$ deg^{-1})	$H^\circ-H_0^\circ$ (cal $mole^{-1}$)	$-(F^\circ-H_0^\circ)/T$ (cal $mole^{-1}$ deg^{-1})
5	0.2537	0.124	0.45	0.034
10	0.3258	0.325	1.92	0.133
15	0.585	0.496	4.07	0.225
20	1.128	0.734	8.26	0.321
25	1.898	1.064	15.74	0.435
30	2.811	1.490	27.48	0.574
40	4.863	2.576	65.74	0.932
50	6.955	3.885	124.81	1.389
60	8.980	5.334	204.57	1.924
70	10.90	6.865	304.13	2.520
80	12.67	8.436	421.99	3.161
90	14.30	10.024	556.98	3.835
100	15.76	11.608	707.40	4.534
110	17.09	13.173	871.73	5.248
120	18.30	14.712	1048.7	5.973
130	19.41	16.221	1237.3	6.704
140	20.42	17.698	1436.5	7.437
150	21.31	19.137	1645.2	8.169
160	22.12	20.539	1862.4	8.899
170	22.84	21.902	2087.3	9.624
180	23.48	23.225	2318.9	10.343
190	24.05	24.510	2556.5	11.055
200	24.58	25.757	2799.7	11.759
210	25.05	26.968	3047.9	12.455
220	25.47	28.143	3300.5	13.141
230	25.85	29.284	3557.1	13.818
240	26.21	30.392	3817.4	14.486
250	26.53	31.468	4081.1	15.144
260	26.83	32.514	4347.9	15.792
270	27.09	33.532	4617.5	16.430
280	27.33	34.522	4889.7	17.059
290	27.55	35.485	5164.1	17.678
300	27.76	36.422	5440.7	18.287
273.15	27.17	33.84	4703	16.63
298.15	27.73	36.25	5390	18.17
	±0.03	±0.04	±6	±0.02

[17] W. H. Zacharaisen, Acta Cryst. 2, 388 (1949).

[18] This suggestion is due to Dr. W. P. Wolf.

[19] S. N. Ghosh, W. Gordy, and D. G. Hill, Phys. Rev. 96, 36 (1954).

[20] M. Leask, D. W. Osborne, and W. P. Wolf, Clarendon Laboratory, Oxford, England (unpublished results).

larger in magnitude and more strongly temperature dependent than that observed experimentally. On the other hand, the system of energy levels proposed for curve *A* seems to be consistent with the magnetic susceptibility measurements.

The configuration of the two unpaired electrons in UF_4 is $5f^2$, and if Russell-Saunders coupling is assumed, the lowest energy level of the free uranium ion is $^3H_4$. The actual ground level of the free ion is probably a mixture of $^3H_4$, $^3F_4$, and $^1G_4$.[21] In the crystal, however, this level is split by the ligand field due to the surrounding fluoride ions. The positions of the fluoride ions in UF_4 are not known, although Burbank[22] has proposed an eightfold coordination scheme based on chemical and packing considerations and in approximate agreement with the available x-ray diffraction data. If the ligand field is cubic, the $^3H_4$ level (or the mixture of $^3H_4$, $^3F_4$, and $^1G_4$) splits into a nondegenerate, a doubly degenerate, and two triply degenerate levels which are designated in Bethe's terminology as Γ_1, Γ_3, Γ_4, and Γ_5, respectively.[23] According to Hutchison and Candela's calculations,[24] either the triply degenerate Γ_5 or the nondegenerate Γ_1 is lowest, depending on the relative sizes of the fourth- and sixth-degree terms in the potential energy. A possible explanation[25] of the scheme of electronic energy levels presented here for UF_4 depends on the influence of two rather small distortions from cubic symmetry acting on the Γ_5 levels, which are assumed to lie lowest in the cubic approximation. For one-third of the uranium ions it is assumed that the distorting potential splits the Γ_5 multiplet into a nondegenerate ground state, a second nondegenerate state at $\epsilon/k=15.4$°K, and a third state at much higher energy. For the other two-thirds of the uranium ions it is assumed that Γ_5 is split into a nondegenerate ground level and two excited states at energies too high for them to be appreciably populated at 20°K.

[21] J. G. Conway, J. Chem. Phys. **31**, 1002 (1959).
[22] R. D. Burbank, U. S. Atomic Energy Commission Rept. AECD-3126 (1951).
[23] H. A. Bethe, Ann. Physik **3**, 133 (1929).
[24] C. A. Hutchison, Jr., and G. A. Candela, J. Chem. Phys. **27**, 707 (1957).
[25] This suggestion was made by B. Bleaney and W. P. Wolf to explain the magnetic-susceptibility data.

Thermodynamic Functions

The heat capacity at selected temperatures and the thermodynamic functions calculated from it are presented in Table III. In order to evaluate the heat capacity at rounded temperatures, a smooth curve was drawn through a large scale plot of the experimental points. In drawing this curve the present measurements on the granular sample were used up to 19.2°K and the previous measurements on the powdered sample were used at higher temperatures. Since there is a small discrepancy (0.20 cal $mole^{-1}$ deg^{-1}) at 19.2°K between the data on the granular sample and those on the powder, the curve was drawn to join the data on the powdered sample smoothly at a higher temperature (28°K). The curve was extrapolated below 1.3°K by means of the equation $C_p=0.0019\ T^3$, which joins the experimental data smoothly. The entropy $S°$ and the enthalpy increment $H°-H_0°$, were obtained by numerical quadrature of the smooth curve, and the free-energy function, $-(F°-H_0°)/T$, was obtained from the relation $F=H-TS$. We have assumed that the lowest energy level for each ion in the crystal is nondegenerate, as discussed above. The values for the entropy and free-energy function do not include contributions from nuclear spin or isotope mixing and therefore are the correct ones for use in chemical calculations.

ACKNOWLEDGMENTS

The authors thank Dr. Werner P. Wolf and Dr. Gordon L. Goodman for many helpful discussions; Ralph W. Bane, Joseph A. Goleb, and John P. Faris for the analytical and spectrochemical results; Dr. Harold M. Feder and Dr. Charles Rosen for use of their vacuum induction furnace; Mrs. Elizabeth Sherry for taking the x-ray powder photographs of the samples; and Joseph Tague for assistance with the measurements.

Paramagnetic-Resonance Studies of Irradiated High-Density Polyethylene. I. Radical Species and the Effect of Environment on Their Behavior

ELLIOTT J. LAWTON, J. S. BALWIT, AND R. S. POWELL

Research Laboratory, General Electric Company, Schenectady, New York

(Received March 10, 1960)

Linear polyethylene (Marlex-50) was irradiated at different temperatures with 800-kv (peak) electrons. It was examined for paramagnetic resonance at +25° and −196°C to determine the radical species and their postirradiation behavior as well as that of the crystalline trapping medium. At low doses the spectrum is composed of two radical species which decay at different rates at room temperature. The predominant radical decays to zero in about five days; its six-line hyperfine structure is attributed to $-CH_2-CH-CH_2-$. The fast decay supports a previous suggestion that the polymer radicals are formed in pairs on adjacent chains. The other radical has a basic five-line spectrum with additional "very fine" structure. It lasts for months at room temperature. The behavior of the "very fine" structure on cooling to liquid-nitrogen (*LN*) temperature and the initial low concentration of the radical suggest its probable structure to be $-CH_2-H_2C\cdot|\cdot CH_2-CH_2-$. The relative numbers of each radical trapped at room temperature depend on the rigidity of the crystal and, therefore, on temperature during irradiation. The six-line radical pairs exist as several groups decaying at different rates at room temperature. The half-life of the fastest decaying group was 10 sec, that of the slowest, 25 hr. The fastest group comprises pairs in which the two radicals are formed nearly opposite each other on adjacent chains. They cause spin-spin line broadening in the time-zero *LN* spectrum. The decay rate of the radical pair is determined by the rigidity of the crystal. An apparent transition point for the crystal exists at −70°C, below which there is only a slight decay of the closest-spaced radicals. The total number of radicals produced and trapped by 40 megaroentgens at *LN* temperature was 6.2×10^{18}/g which corresponded to a G(total radicals) = 3.0.

INTRODUCTION

FREE radicals are formed as intermediates in polymers exposed to ionizing radiation. Depending on the physical state of the polymer during and following the irradiation, some of these radicals can react to form secondary products immediately during the irradiation, while others become entrapped as long-lived radicals that can enter only into delayed reaction. It is important to identify the primary radicals formed and the concentrations of each formed during the irradiation as aids in formulating the mechanisms involved in the irradiation process. It is equally important to understand the postirradiation behavior of the trapped radicals as well as that of the trapping medium in order to account for all the secondary products formed. It has been pointed out that there are three basic conditions for trapping radicals in hydrocarbon polymers[1]; namely, that the polymer must exist in a crystalline, glassy or highly crosslinked state during and following the irradiation. In each of these three states the rigidity of the system is the factor which determines the life of the radicals; the detailed rigidity on an atomic scale is especially important when the *polymer* radicals are formed close together in pairs.

The technique of electron paramagnetic resonance (EPR) has been used in detecting and studying the primary radicals trapped in polymers and low-temperature glasses. Most of the work reported has been concerned mainly with identifying the radical species.[2–10] The present study emphasizes the use of the paramagnetic-resonance technique in studying the detailed behavior of the primary radicals as related to their environment.

In certain polymer systems a great deal has already been determined about the primary radicals through radiation-chemistry studies of the secondary products formed. Polyethylene is an example of such a polymer[1,11,12]; and because of its crystalline structure, it was chosen as a suitable polymer to use in our paramagnetic study.

The predominant radicals formed in polyethylene lead to crosslinking by a mechanism[13,14] in which a radical is formed in the polymer chain by loss of a hydrogen atom, that then produces a similar polymer radical by hydrogen abstraction on a nearby polymer chain. Thus, these two polymer radicals are formed as

[1] E. J. Lawton, J. S. Balwit, and R. S. Powell, J. Polymer Sci. **32**, 257–289 (1958), parts I and II.

[2] E. E. Schneider, M. Day, and G. Stein, Nature **168**, 645 (1951).

[3] J. Combrisson and J. Uebersfeld, Compt. rend. **238**, 1397 (1954).

[4] D. J. E. Ingram, W. G. Hodgson, C. A. Parker, and W. T. Rees, Nature **176**, 1227 (1955).

[5] D. Bijl and A. C. Rose-Innes, Nature **175**, 82 (1955).

[6] W. B. Ard, H. Shields, and W. Gordy, J. Chem. Phys. **23**, 1727 (1955).

[7] Yu. D. Tsvetkov, N. N. Boubnov, M. A. Makoulsky, Yu. S. Lazurkin, and V. V. Voevodsky, Doklady Akad. Nauk. S.S.S.R. **122**, 1053 (1958).

[8] B. Smaller and M. S. Matheson, J. Chem. Phys. **28**, 1169 (1958).

[9] R. S. Alger, T. H. Anderson, and L. A. Webb, J. Chem. Phys. **30**, 695 (1959).

[10] R. S. Powell, E. J. Lawton, and J. S. Balwit, Bull. Am. Phys. Soc. Ser. II, **4**, (May 1, 1959).

[11] F. A. Bovey, *The Effect of Ionizing Radiation on Natural and Synthetic High Polymers* (Interscience Publishers, Inc., New York, 1958), Chap. V, pp. 97–114.

[12] A. Charlesby and A. J. Swallow, Ann. Revs. Phys. Chem. **10**, 305–310 (1959).

[13] A. A. Miller, E. J. Lawton, and J. S. Balwit, J. Polymer Sci. **14**, 503 (1954).

[14] A. A. Miller, E. J. Lawton, and J. S. Balwit, J. Phys. Chem. **60**, 599 (1956).

a pair with only one radiation event required, leaving the two radicals in a favorable position to crosslink with a minimum of movement of the chain segment required. The other dominant reaction is the formation of a transvinylene group, but this is by a molecular[14,15] rather than a radical process. Another radical process which has been reported by others[16,17] is carbon-carbon scission of the main chain, but this occurs in very low concentration compared to the crosslinking reaction, the reported scission-to- crosslinking ratio ranging from 0.18 to 0.3. The tighter crystalline structure of high-density linear polyethylene, of which Marlex-50 is a good example, makes it a more suitable material to use in studying the radical behavior at room temperature than the low-density, low-melting polyethylene.

The study is presented in two parts. Part I describes the radicals produced at low dose levels and at various irradiation temperatures as well as the post irradiation behavior of the radicals and of the trapping medium as determined by paramagnetic-resonance measurements at room temperature and liquid-nitrogen temperature. Part II[18]covers the extension of these studies to high dose levels (up to 4000 megaroentgens).

EXPERIMENTAL

Sample Preparation and Irradiation Procedures

The high-density highly crystalline polyethylene used was Marlex-50 manufactured by the Phillips Petroleum Company.[19] The crystal melting temperature is about 136°C. The samples used were in sheet form 0.002 in. thick and 1 in. wide by 2 in. long. They were selected to fall within a weight range of 58 to 61 mg. A number of samples were degassed on a high-vacuum system by heating for several days at 90°C, followed by prolonged pumping at room temperature. Dry nitrogen was admitted to the vacuum system when a sample was needed and the transfer to the temperature-controlled irradiation chamber (which was being continuously flushed with nitrogen) was made in a carefully controlled nitrogen atmosphere. The sample was irradiated in the nitrogen atmosphere with electrons of 800-kv (peak) energy from a GE resonant-transformer type of electron generator.[20,21]

Irradiation-dose and absorption measurements were made with a specially constructed air ionization chamber. For convenience, irradiation dose is expressed in roentgen units, where 1 r = 83.8 ergs/g of air. The radiation yields or G values (radicals/100 ev) calculated are based on the assumption that the roentgen equivalent to 5.24×10^{13} ev/g of air is also the same in this ethylene polymer.

Following the irradiation the sample was rolled into a 1-in. long cylinder and shoved into the thin-walled glass spectrometer sample tube. The tube was being flushed with nitrogen during this procedure and in the subsequent resonance measurement. The transfer and loading was done in such a way that the sample was always in a dry nitrogen atmosphere. It is emphasized that in order to obtain reliable and reproducible results, it was necessary to exercise extreme care during the transfer and handling procedure, to ensure that the sample was at *all* times in a dry nitrogen atmosphere. This was especially important after the sample had been irradiated, for then it was very sensitive to slight traces of oxygen. A momentary exposure to air caused an appreciable change in intensity of the resonance signal, especially at the higher levels of irradiation. The thin-walled glass sample tubes used were specially selected to have nearly equal outside diameter (0.187 in.) and wall thickness (0.012 in.), so that the combined weight of glass and polyethylene in the resonance cavity would be constant for each run.

Resonance Detection Equipment

The electron-paramagnetic-resonance (EPR) measurements were made using a standard Varian Model V4500 spectrometer operated at 9400 Mc. The measurements were made at low rf-power levels to avoid saturation effects.

Low-Temperature Cavity and Sample Handling Procedure

The resonance measurements at room temperature were made using the standard cavity furnished with the spectrometer. The measurements at liquid-nitrogen temperature were more complicated. It was necessary to alter both the cavity design and the handling procedure so that all transfers and loading operations could be made under liquid nitrogen, as well as in a nitrogen atmosphere. Special jigs had to be made in order that the thin irradiated sample could be rolled into its cylindrical form and shoved into the glass sample tube and cavity while under liquid nitrogen.

The experimental arrangement used in making the resonance measurements at liquid-nitrogen temperature is shown in Fig. 1. The cold cavity C is a reflection type made from a piece of standard waveguide and has about the same dimensions as the room-temperature cavity. Radio-frequency power transmitted along waveguide G is fed to the cavity through iris I. This section of guide is made of thin stainless steel about 9 in. long and serves as a heatbreak to isolate the cold cavity C. The upper end of guide section G is isolated from the rest of the guide system by the demountable rf glass window W and the neoprene gasket B so as to prevent moisture from condensing inside the cold cavity. The cavity is

[15] L. M. Dorfman, J. Phys. Chem. **60**, 826 (1956).
[16] A. Charlesby, Proc. Roy. Soc. (London) **222A**, 60 (1954).
[17] A. C. Baskett and C. W. Miller, Nature **174**, 364 (1954).
[18] E. J. Lawton, J. S. Balwit, and R. S. Powell, J. Chem. Phys. **33**, 405 (1960), following paper, this issue.
[19] D. C. Smith, Ind. Engr. Chem. **48**, 1161 (1956).
[20] E. J. Lawton, Science **112**, 419 (1950).
[21] E. E. Charlton and W. F. Westendorp, Gen. Elec. Rev. **44**, 652 (1941).

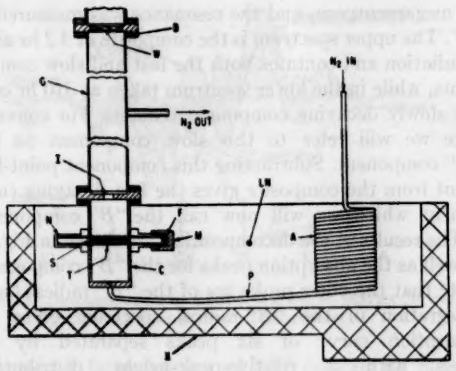

FIG. 1. Experimental arrangement used in making EPR measurements at liquid-nitrogen temperature.

supported in a narrow Styrofoam box *X* filled with liquid nitrogen *LN*, the box being just wide enough to wedge between the pole pieces of the magnet. The cavity and companion guide section *G* are continuously flushed with nitrogen, which enters the cavity at liquid nitrogen temperature after passing through copper coil *A* and pipe *P*.

During the loading procedure the combined cavity and guide section, as well as the copper coil, were all immersed in a large liquid-nitrogen bath inside a sealed work box provided with a window, the box being flushed with nitrogen. At this stage, cap *M* was removed and the cavity system was being flushed with helium. After loading the irradiated sample *S* into the glass tube *T*, which operation was also done in the same liquid-nitrogen bath, the cavity was sealed by replacing cap *M*. The purpose of the small Styrofoam plug *F* was to wedge the glass tube in place. The cavity was then turned upside down rapidly to dump out the liquid nitrogen, and the unit quickly transferred to the liquid-nitrogen-filled Styrofoam box *X*. After connecting the cavity and guide section to the spectrometer, the flushing gas was changed from helium to a slow regulated flow of nitrogen. The reason for using helium at the start was that there was no danger of its liquefying as was the case with nitrogen, which had to have a more critically controlled flow in order to prevent formation of liquid nitrogen in the cavity. A temperature measurement of the sample was made with a fine-wire (0.005-in.) thermocouple and was found to be that of liquid nitrogen.

Instead of using sweep coils (to modulate the static magnetic field) fastened directly to the cavity walls, as in the case of the standard room-temperature cavity, special coils were mounted on the tips of the magnet pole pieces.

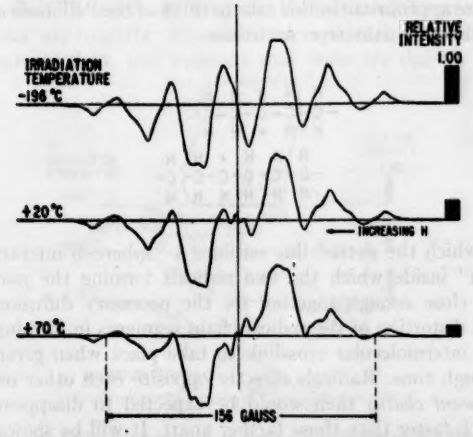

FIG. 2. Typical EPR spectra, taken at room temperature, of Marlex-50 irradiated to 40 megaroentgens at different temperatures.

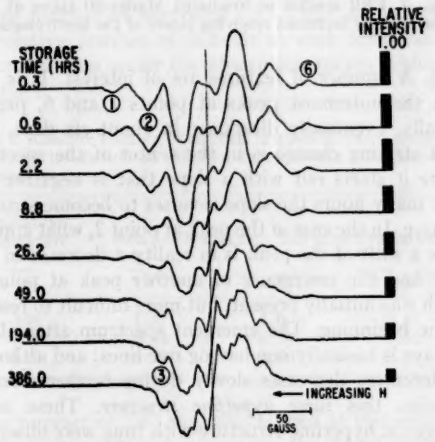

FIG. 3. Change and decay of EPR spectrum of Marlex-50, irradiated to 40 megaroentgens, on storage at room temperature in a nitrogen atmosphere.

RESULTS AND DISCUSSION

Typical EPR Spectrum at Room Temperature

Typical spectra for Marlex-50 taken at room temperature soon after irradiation are shown in Fig. 2, for three different irradiation temperatures: liquid nitrogen (*LN*), room temperature (*RT*), and +70°C. All samples were irradiated to a dose of 40 megaroentgens. The spectrum in each case is predominantly one having six lines with an over-all spread of 156 gauss modified by additional structure.

Change in Hyperfine Structure of the Spectrum with Decay at Room Temperature

If the samples are observed repeatedly for many hours at room temperature, an array of spectra, shown in Fig. 3, can be accumulated that shows the change in hyperfine structure as the resonance signal decays with

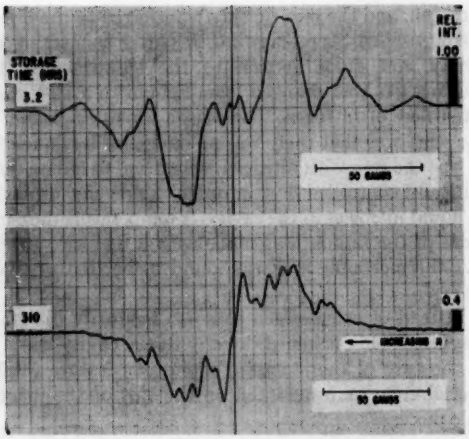

FIG. 4. EPR spectra of irradiated Marlex-50 taken at room temperature at increased resolving power of the spectrometer.

time. A number of features are of interest. It is seen that the outermost peaks at points 1 and 6, present initially, eventually disappear in about six days. The most striking change is in the center of the spectrum where it starts out with a slope that is negative and after many hours the slope reverses to become strongly positive. In the case of the peak at point 2, what appears to be a shift of the peak is in reality a decrease in this peak and the emergence of another peak at point 3, which was initially present, but more difficult to resolve at the beginning. The emergent spectrum after about six days is basically one having five lines; and although the intensity decreases slowly during further storage, it retins this *same hyperfine structure*. These same changes in hyperfine structure with time were observed in the case of samples irradiated at +70°C and at *LN* temperature; however, an examination of Fig. 2 shows that in the *LN* irradiation case the component responsible for the initial predominant six-line spectrum is much stronger than when the irradiation was at room temperature, whereas in the +70°C case this component is much weaker. The emergent spectra for all three irradiation temperatures not only have the same hyperfine structure but are of nearly equal intensity (see Fig. 6). It appears then that the initial spectrum at this irradiation dose is really a composite one made up of two different radical components, one of which decays to zero in a relatively short time, and the other of which decays very slowly indeed and which has been observed to last for thousands of hours at room temperature.

Decomposition of Spectrum

For the spectra shown in Fig. 4, the resolving power of the spectrometer was increased (slower scan rate of 13 gauss/min, finer small modulation of 1.8 gauss, and on a large recorder) so as to bring out the structure. The irradiation in this case was at room temperature and at 40 megaroentgens, and the resonance was measured at *RT*. The upper spectrum is the composite at 3.2 hr after irradiation and contains both the fast and slow components, while in the lower spectrum taken at 310 hr only the slowly decaying component remains. For convenience we will refer to this slow component as the "*R*" component. Subtracting this component point-by-point from the composite gives the fast-decaying component which we will now call the "*B*" component.

The results of the decomposition are shown in Fig. 5, as well as the absorption peaks for the "*B*" component. Note that the outer peaks are of the "*B*" radical only. Integration of the "*B*"-radical spectrum gives an absorption curve of six peaks separated by 31 gauss with a relative-peak-height distribution 1:4.6:10:9.9:4.5:1. This is quite close to the theoretical distribution expected for equal interaction of the unpaired electron with the nuclear magnetic moments of five equivalent protons. This is the component reported by Tsvetkov, Boubnov, Makoulsky, Lazurkin, and Voevodsky[7] in an electron-irradiated polyethylene and is also the radical observed by Smaller and Matheson[8] in gamma-irradiated Marlex-50 at liquid-nitrogen temperatures.

It is believed that this spectrum is given by the radical $-CH_2-\dot{C}H-CH_2-$ resulting from a C—H scission during the irradiation. The interaction of the unpaired electron with only the five nearest H atoms supports the idea of the α-β hypothesis.[22] This is the radical which combines with a like radical on a nearby chain to form an intermolecular crosslink. Because of its crystalline structure, diffusion of large chain segments in Marlex-50 would necessarily be limited to intermolecular distances. The relatively fast decay of the "*B*" radical supports the idea that these radicals are formed in pairs on adjacent chains as previously suggested[1,13] through the process of H abstraction following the initial C-H scission. It therefore might be more appropriate in this case to think of the "*B*" radical in terms of pairs represented as

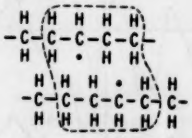

in which the dotted line outlines a "sphere-of-interaction" inside which the two radicals forming the pair are close enough together for the necessary diffusion and distortion of the radical chain segments in forming the intermolecular crosslink to take place when given enough time. Radicals directly opposite each other on *adjacent chains* then would be expected to disappear much faster than those farther apart. It will be shown

[22] J. F. Gibson, D. J. E. Ingram, M. C. R. Symons, and M. Townsend, Trans. Faraday Soc. **53**, 914 (1957).

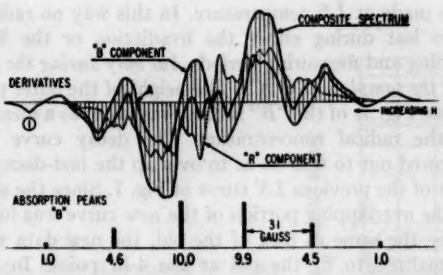

FIG. 5. Decomposition of EPR spectrum of Marlex-50 irradiated to 40 megaroentgens at room temperature.

later that a large fraction of "*B*" radicals do indeed decay at a very much faster rate than others.

The identity of the slowly decaying "*R*" radical is not yet as well established as that of the "*B*" radical. The fact that the detailed structure is preserved over hundreds of hours of additional decay time and also that the same detailed structure is present in samples irradiated at widely different temperatures (*LN*, *RT*, and +70°C) makes it look like a single radical type. The derivative curves of the "*R*" component at 510 hr for the three irradiation temperatures as well as the basic absorption curve are shown in Fig. 6. Even with all of the extra "very fine" structure the absorption curve suggests a basic five-line spectrum with approximately 20-gauss splittings; however, since the peaks are so poorly resolved, the relative-peak-height distribution shown in the figure can only be taken on a qualitative basis. A five-line spectrum, however, might belong to several types of proton configuration in the molecule such as a C-C scission within the main chain, or possibly radicals in the neighborhood of double bonds. The "very fine" structure, that is, the small peaks with spacings from 4.2 to 6.9 gauss throughout the "*R*" spectrum, may be due to additional weak splittings of the five-line spectrum. Since the intensities of the small peaks are slightly dependent on orientation in the magnetic field, this suggests that they are due to a

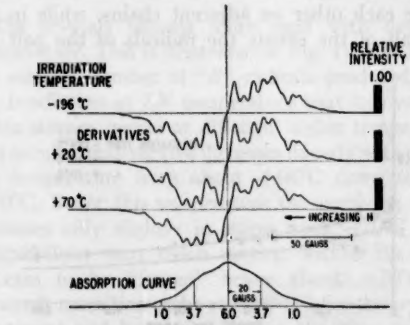

FIG. 6. EPR spectra taken at room temperature of irradiated Marlex-50 after 510 hr storage at room temperature in a nitrogen atmosphere. Irradiation dose 40 megaroentgens at three irradiation temperatures.

restricted motion imposed on the radical group by the crystalline order. The resonance signals for the film samples used in this study differ very little from that for *unoriented* samples. Likewise there was very little difference in the shape of the resonance signal when the sample was in powdered form. The possible identity of the "*R*" radical and the origin of the "very fine" structure will be discussed later after more data are presented.

Relative Number of "*B*" and "*R*" Radicals Trapped at Room Temperature as a Function of Irradiation Temperature

A point-by-point decomposition of the composite spectra *taken at room temperature* for Marlex-50 that had been irradiated at different temperatures (−196°C, +20°C, and +70°C) was made to determine the relative number of surviving "*B*" and "*R*" radicals. The relative number of radicals at each temperature in terms of area under the absorption curves is shown in Table I.

TABLE I. Relative number of radicals trapped at room temperature after irradiation at different temperatures (irradiated to 40 megaroentgens).

Irradiation temperature	Relative No. at zero time after irradiation		
(°C)	Total	"*B*" radical	"*R*" radical
−196	1.37	1.0	0.37
+20	0.71	0.34	0.38
+70	0.39	0.087	0.30

The number of "*R*" radicals trapped at this irradiation level was about the same for the liquid-nitrogen and room-temperature irradiations, but was slightly lower following the 70°C irradiation. The number of "*B*", or fast-decaying, radicals trapped after irradiation at liquid-nitrogen temperature, on the other hand, was much larger than the number found after irradiation at either the room or the 70°C temperatures. This is not because more are made at *LN* than at *RT*; but rather, because of the reduced chain mobility at *LN* temperature, fewer are lost during the irradiation.[23] Thus more are present at the time of the first EPR measurement at *RT*.

Radical Decay at Room Temperature: "*B*" Radical Pairs

Decay of the relative intensity of the resonance signal with time for the "*B*" and "*R*" radicals at *room temperature* is shown in Figs. 7 and 8, respectively, for the

[23] In an earlier paper[1] we indicated that the crosslinking produced during the irradiation was mainly in the amorphous areas of the polymer. The present more detailed study of the crosslinking "*B*" radical indicates that crosslinking can take place even in the crystalline region during the irradiation.

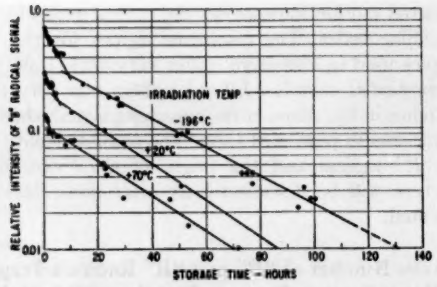

FIG. 7. Decay of the six-line "*B*" radical at room temperature in Marlex-50 irradiated to 40 megaroentgens at three irradiation temperatures. Storage in a nitrogen atmosphere.

above three irradiation temperatures. The change in height of the outer peak at point 1 of the composite derivative curve (see Fig. 5) has been plotted for the "*B*"-radical decay, while the deflection at the "*B*"-radical crossover point *A*, where the contribution of the "*B*" component to the total is zero, has been take to measure the "*R*"-radical decay.

Both "*B*" and "*R*" radical types decay at an exponential rate. The similarity of the curves in Fig. 7, for the three different irradiation temperatures, indicates that the "*B*"-radical decay is by the same mechanism in each case and that the effectiveness of the trapping medium at *room temperature* is not appreciably altered by irradiating the material to 40 megaroentgens at any one of the three irradiation temperatures. The "*B*"-radical pairs that survive the above irradiation and sample loading time at *RT* appear to be made up of two main groups, one of which decays at a faster rate than the other and presumably comprises radical pairs in which the average spacing between the radicals of each pair is less than that in the other group. The numbers in each group diminish with time by a first-order relationship. There are fewer of the fast-decaying group that survive the irradiation at 70°C than at either *RT* or *LN* temperature, which fact can be attributed mainly to a decreased rigidity of the crystal trapping medium during the irradiation at 70°C compared with that at *RT* or *LN* temperatures.

Certain activity considerations (to be discussed at another time) suggested that initially there were more "*B*"-radical pairs formed during the irradiation at *LN* temperature than are indicated by the simple extrapolation of the faster-decaying group of the *LN* curve of Fig. 7 to zero time. These decayed in a matter of seconds and minutes to crosslinks and were, therefore, lost during the warmup and *RT* sample loading periods. In order to check this, the thin sample was irradiated at *LN* temperature and then warmed quickly to *RT* in a dry nitrogen atmosphere, where it was then held for a predetermined time, following which it was plunged into *LN* to stop any further decay. The sample was then loaded into the glass sample tube while still under *LN* and prior to the EPR measurements which were also made at *LN* temperature. In this way no radicals were lost during either the irradiation or the EPR loading and measuring periods, *but only during the time that the sample was at RT*. The height of the outer peak 1 (see Fig. 5) of the "*B*" radical was taken as a measure of the radical concentration. The decay curve was followed out to 6 hr so as to overlap the fast-decaying part of the previous *LN* curve of Fig. 7. Since the slope of the overlapping portion of the new curve was found to be the same as that of the old, the new data were normalized to fit the old at the 4-hr point. In this manner it was possible to extend effectively the *LN* curve of Fig. 7 to time zero and also to determine a relative value for the total number of "*B*" radicals formed during the irradiation at *LN* temperature. The results are shown in Fig. 9. The data for the entire decay of "*B*" radicals at *RT* are shown in curve A, while the early points on this curve are replotted in the insert on two different expanded time scales to show more clearly the decay rate immediately after irradiation. The *LN* curve of Fig. 7 has been replotted to form part of this curve and the new data, which extend the curve to time zero, is shown by the circle points. The results indicate that initially there were actually 3.3 times more "*B*" radicals formed during the *irradiation at LN* than are indicated by the extrapolation of the *LN* curve of Fig. 7 to time zero. About $\frac{2}{3}$ of the total number of "*B*" radicals formed during irradiation were lost during the 20-min loading and handling time at *RT* prior to the EPR measurements. The insert shows that a large fraction of these decay at a very rapid rate, having an apparent half-life of about 10 sec. These must be the pairs in which the two radicals are formed nearly opposite each other on adjacent chains. These are also the pairs responsible for the spin-spin broadening that is observed in the time-zero *LN* spectrum, since broadening was nearly absent in the 5-sec spectrum and completely absent in those runs in which the decay time was longer than 15 sec. This is shown in Fig. 10 for the 8.8 sec case. Thus it appears that during the pair forming process, about half of the irradiation events result in pairs in which the radicals are nearly opposite each other on adjacent chains, while in the other half of the events the radicals of the pair are

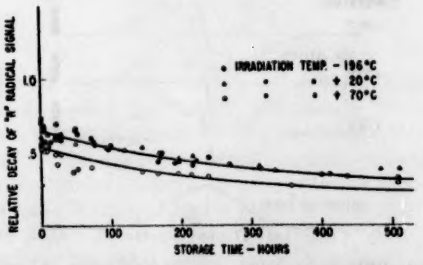

FIG. 8. Decay of the five-line "*R*" radical at room temperature in Marlex-50 irradiated to 40 megaroentgens at three irradiation temperatures. Storage in a nitrogen atmosphere.

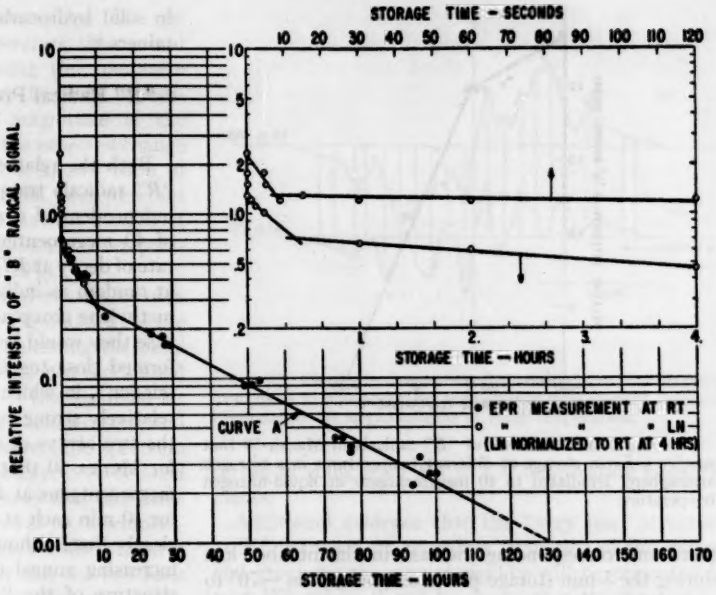

FIG. 9. Decay of the six-line "*B*" radical at room temperature in Marlex-50 irradiated to 40 megaroentgens at liquid-nitrogen temperature. Storage in a nitrogen atmosphere.

further apart. The relatively large fraction of closely spaced radicals (those nearly opposite each other) suggests that, in this case, the radical pair might be formed by a molecular process in which the initial irradiation act removes a molecule of hydrogen by simultaneously cleaving two C-H bonds directly opposite each other on adjacent chains, or else one involving immediate abstraction by a "hot" H atom, while in the other case where the radicals are further apart the pairs are formed by a radical abstraction process as previously suggested.[1,13] The factor that determines the rate of decay of the two radicals forming a pair is the rigidity of the crystal, which in the case of the closest-spaced radicals apparently is not enough at *RT* to hold them apart for any appreciable time.

Crystal Rigidity and Freezing Point

The crystals become more rigid with decreasing temperature. This is illustrated in Fig. 11, which shows the relative number of "*B*" radicals produced during the irradiation at *LN* temperature that can survive a 5-min storage period at different higher temperatures. The number that survive increases linearly with decreasing temperature from about +96°C down to about −70°C. Below this temperature the surviving number increases only slightly in going from −70°C to *LN* temperature; thus chain motion within the crystal appears to be "frozen" below about −70°C. The apparent transition point at −70°C is for the *crystalline component* and has as an analog the glass transition point in amorphous polyethylene. Specifically, in this case, it refers to the temperature below which motion within the crystal is "frozen" to the point that the minute lateral migration (interchain distance) of the two radical chain segments (required to convert the initial transient hole defect in the crystal lattice to a permanent crosslink defect) cannot take place during the 5-min storage period. Both x-ray diffraction[24] and dilatometric studies[25] have been reported which show that the degree of crystallinity in Marlex-50 does not change appreciably with increasing temperature up to about 100°C, but decreases rapidly above this temperature becoming zero at 136°C, the crystal melting point. Similar results have been reported for linear polymethylene.[26] The decrease in the number of surviving radical

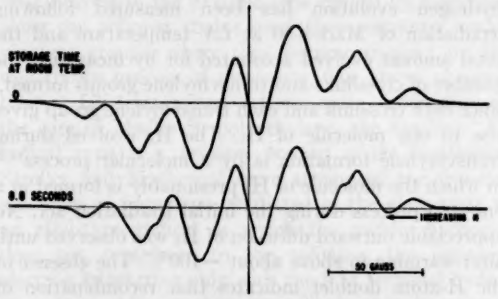

FIG. 10. Change in spin-spin broadening as a result of warming to room temperature. Spectra, taken at liquid-nitrogen temperature, of Marlex-50 irradiated to 40 megaroentgens at liquid-nitrogen temperature.

[24] D. W. McCall and W. P. Slichter, J. Polymer Sci. **26**, 171 (1957).
[25] A. Charlesby and L. Callaghan, Phys. Chem. Solids **4**, 227, 306 (1958).
[26] L. Mandelkern, M. Hellmann, D. W. Brown, D. E. Roberts, and F. A. Quinn, Jr., J. Am. Chem. Soc. **75**, 4093 (1953).

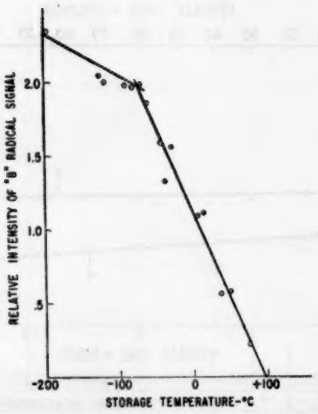

FIG. 11. Relative number of "*B*" radicals in Marlex-50 that survive a 5-min storage at different temperatures in a nitrogen atmosphere. Irradiated to 40 megaroentgens at liquid-nitrogen temperature.

pairs and corresponding increase in the number lost during the 5-min storage period in going from −70° to +96°C, therefore, is not due to a decrease in the total number of crystals, but rather to a decrease in the rigidity of the crystal lattice. The "*B*" radical pairs that *decay* during the 5-min storage period in the temperature range between −70° and +15°C are mainly those of the very-fast-decaying group (see Fig. 9 insert) in which the radicals forming the pairs are closest together (those nearly opposite each other); whereas above this temperature the radicals that decay are entirely those of the slowly decaying group in which the two radicals of the pair are further apart.

The H-atom doublet (splitting of 508.7 gauss)[27] was not observed in the samples irradiated at *LN* temperature and measured at *LN* temperature. Molecular-hydrogen evolution has been measured following irradiation of Marlex-50 at *LN* temperature and the total amount evolved accounted for by measuring the number of crosslinks and transvinylene groups formed,[1] since each crosslink and each transvinylene group gives rise to one molecule of H_2. The H_2 evolved during transvinylene formation is by a molecular process[14,15] in which the molecule of H_2 presumably is formed in a one-step process during the initial irradiation act. No appreciable outward diffusion of H_2 was observed until after warming to above about −100°C. The absence of the H-atom doublet indicates that recombination of H atoms—specifically those involved in the "*B*"-radical forming process—can take place readily in Marlex-50 at *LN* temperature. The absence of H atoms trapped in solid hydrocarbons at *LN* temperature has been reported by Alger, Anderson, and Webb[9]; however, Smaller and Matheson found a weak hydrogen doublet in solid hydrocarbons when irradiated in quartz containers.[8]

[27] C. K. Jen, S. N. Foner, E. L. Cochran, and V. A. Bowers, J. Am. Chem. Soc. **104**, 846 (1956).

"*R*" Radical Production at *LN* Temperature and Possible Identity

Both the relative number and the rate of decay of "*R*" radicals trapped at *RT* was shown to be nearly independent of irradiation temperature at a dose level of 40 megaroentgens (see Table I). Their very slow rate of decay at *RT* suggests that they are either formed at random as individual radicals (e.g., at an activated methylene group adjacent to a double bond), in which case they would be widely spaced, or else that they are formed close together in pairs (e.g., by a main chain scission), in which the two radicals are held apart by relatively strong restraining forces. An examination of the two arrays of spectra (measured at *RT*), Fig. 12, for Marlex-50 that had been irradiated at 40 and 160 megaroentgens at *RT* and then subsequently annealed for 10 min each at different temperatures, shows quite clearly that, although the total number decreases with increasing anneal temperature, the detailed hyperfine structure of the "*R*" radical (see the spectra above 75°C) is retained to within a few degrees of the crystal melting point where it disappears. This is an indication that the spectrum is that of a single species, that the radical is trapped in the crystalline portion, and that its disappearance depends on the mobility of the radical chain segment.

The EPR measurements at *LN* temperature indicate that the "*R*" radical is produced as readily by the *irradiation at LN temperature* as it is at room temperature. It is present, however, as a smaller fraction of the total and can only be detected in the composite spectrum as a small shoulder on the side of the peak at point 2 (see Fig. 3), which, as explained earlier, is the position for the outermost peak of the five-line "*R*" spectrum. Similar small shoulders can also be seen on close examination of the spectrum of polyethylene at

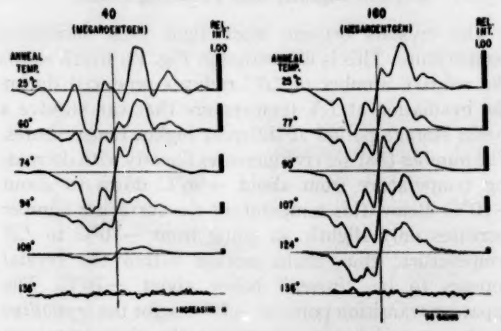

FIG. 12. Effect of anneal temperature on the shape of the EPR spectra taken at room temperature of Marlex-50 irradiated to 40 and 160 megaroentgens at room temperature. Samples heated for 10 min at each temperature in a nitrogen atmosphere.

77°K shown by Voevodsky.[7,28] Since neither "*B*" nor "*R*" components decay at *LN temperature*, the method previously described for decomposing the composite *RT* spectrum could not be applied. It could be estimated, however, from both the magnitude of the shoulder on the peak at point 2 and the expected change in shape of the center peak—had a known ratio of numbers of "*R*"-to-"*B*" radicals been present—that the concentration was very low and that the number of "*R*" radicals produced by the irradiation at *LN* temperature could not have been more than 20%.

A change in shape of the "*R*" radical was observed in going from *RT* to *LN* temperature. Figure 13(a) is the "*R*" radical spectrum taken at *RT*, showing the basic five lines with the previously mentioned additional "very fine" structure. Figure 13(b) is the spectrum for the same sample but measured at *LN* temperature, and a marked change to an apparent seven-line spectrum with additional fine structure is observed. A detailed examination of the two spectra shows that the same peaks are recognizable in both spectra at room temperature and liquid-nitrogen temperature, but their relative amplitudes are different. The center and the two *basic* outer peaks 1 and 5, change but little, the main change appearing in the intermediate peaks of the *"very fine" structure* at points *x* and *y* of spectrum (a). Ingram, Fujimoto, and Saxena[29] have pointed out that there are two basic types of molecular motion that can produce changes in the electron-resonance spectrum. The first is due to an actual movement, or diffusion, of the *radical molecule* through the medium to react with a new molecule to form a new radical species; while the second is due to a change in the internal motion of groups within the molecule brought about by a physical change in the medium—e.g., the quenching of the rotation of a methyl end group about its C—C bond axis on cooling to 77°K—to cause nonequivalence of interacting protons and resultant change in hyperfine structure but not a change in radical species. The first type is most unlikely in crystalline Marlex-50; and since the change in shape is a *reversible* process in going from *RT* to *LN* and back again to *RT*, it can definitely be ruled out. The change in shape then of the "very fine" structure in going from *RT* to *LN* temperature suggests that the "*R*" radical is one having significantly greater motional freedom at *RT*, such as, for example, the end group of a broken chain, but whose rotational motion suffers only a slight restraint due to rigidity of the crystal at *RT*, while it is quenched at *LN* temperature. It is significant to note that, in the case of the "*B*"-radical spectrum, no unusual change in the spectrum shape other than the dipolar line broadening due to the very closely spaced group of radicals was observed in going from *RT* to *LN* temperature measurements.

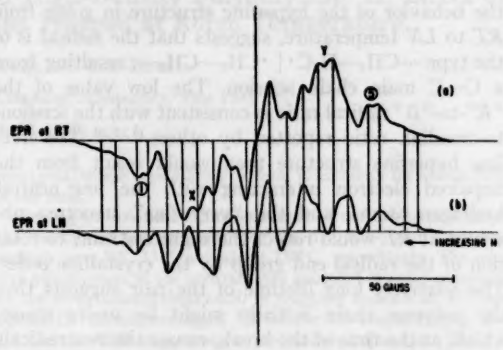

FIG. 13. Change in shape of the "*R*"-radical spectrum in going from room to liquid-nitrogen temperature measurement. Samples irradiated to 40 megaroentgens at room temperature.

Additional evidence that the "very fine" structure at *RT* is caused by restraints to motion of the radical end group by the crystal rigidity will be presented in part II[18], where it will be shown that the "very fine" structure disappears as the crystal is weakened by increasing irradiation.

The absence of any induction period as the radiation dose is increased suggests that the appearance of the "*R*" radical does not depend on the presence of irradiation-produced functional groups, e.g., transvinylene unsaturation or crosslinks. Voevodsky[28] has attributed the five-line spectrum in irradiated polyethylene to an allyl radical of the type —CH_2—CH=CH—CH—CH_2—. He suggests that the radical is not produced initially by the irradiation at 77°K but rather is the result of a secondary reaction in which, on warming to 300°K, some of the six-line radicals (the "*B*" radicals) convert to the five-line-type radical by migrating along the polymer chains until they encounter transvinylene groups, where they become trapped by the well-known process of resonance. Our above observations at *LN* temperature indicate quite clearly that, in the case of Marlex-50 polyethylene, the five-line "*R*" radical type is a *primary product of the irradiation*. Samller and Matheson[8] have attributed the five-line spectrum of propylene irradiated in the glass state to an allyl-type radical in which the middle hydrogen does not contribute to the splitting, the unpaired electron interacting only with the four terminal hydrogens. It would seem more than likely that, because of the potentially greater number of H atoms with which the unpaired electron could interact in the case of an allyl radical of the *transvinylene type*, it would be identified by a hyperfine structure having more than five lines.

The relatively low concentration of "*R*" radicals compared to the large number of "*B*" radicals produced during the irradiation at *LN* temperature, along with

[28] V. V. Voevodsky, Paper B-V-1 presented at the Fourth International Symposium on Free Radical Stabilization at National Bureau of Standards, Washington, D. C., August 31–September 2, 1959.

[29] D. J. E. Ingram, M. Fujimoto, and M. C. Saxena, Arch. Des. Sci. **12**, 185 (1959).

the behavior of the hyperfine structure in going from *RT* to *LN* temperature, suggests that the radical is of the type $—CH_2—H_2C\cdot \mid \cdot CH_2—CH_2—$, resulting from a C—C main chain scission. The low value of the "*R*"-to-"*B*" radical ratio is consistent with the scission-to-crosslink ratio reported by others.[16,17,30] The five-line hyperfine structure then would result from the unpaired electron interacting with the four nearest hydrogen atoms, and the "very fine" structure observed at *RT* would reflect the slight restraint to rotation of the radical end group by the crystalline order. The relatively long lifetime of the pair suggests that the polymer chain initially might be under strain, which, at the time of the break, causes the two radicals to become separated (or else the radiation scission imparts some kinetic energy to separate the ends). This same force would subsequently hold them apart, thus preventing their ready recombination.

Radiation Efficiency at *LN* Temperatures

Estimates of the radiation efficiency for radical production, G(total radicals) were made by comparing the time-zero measurements at *LN* temperature of Fig. 9 with a known concentration of 1,1-diphenyl-2-picryl hydrazyl radicals (DPPH) in benzene as a standard. It did not seem advisable to make a direct comparison of absorption-curve areas between the polymer spectrum and the spectrum of solid DPPH because of the strong exchange narrowing of the resonance signal encountered in the case of solid DPPH. An indirect method was used in which a ratio of the areas under the absorption curves for a sample irradiated to 40 megaroentgens at *LN* temperature to that for a like sample irradiated to the same level at *RT* was determined, *both measurements* being made at *LN temperature*. The spin concentration in the sample irradiated at *RT* was then determined by comparing its absorption curve area with that for the DPPH standard, the comparison in this case, however, being between spectra *measured at RT*. The total radical concentration produced by the 40-megaroentgen irradiation at *LN* temperature was determined simply by multiplying the spin concentration for the sample irradiated at *RT*, as determined from the DPPH comparison, by the above *LN/RT* area ratio. The concentration determined in this manner was found to be 6.2×10^{19} spins/g and corresponds to an irradiation efficiency G(total radicals) $=3.0$. The spread in the time-zero *LN* data indicates that this value could be as high as 3.6. Several solutions of DPPH were prepared at different times, as well as solutions from batches of DPPH prepared from two different hydrazine sources to test the reproducibility of the DPPH standard. The reproducibility between the EPR spectra taken at *RT* at equal concentrations was found to be better than 10% when precautions were taken to exclude oxygen, which had a pronounced effect on the spectrum, due to a strong spin-spin interaction between the DPPH and oxygen radicals.[31]

The radiation efficiency for delayed crosslink formation has been previously determined from the yield for net H_2 production,[1] G(net H_2), obtained by subtracting the yield for transvinylene formation from the radiation yield for total hydrogen production, G(total H_2). The value of G(net H_2) obtained in this way at *LN* temperature was found to be 2.0, from which the radiation yield for "*B*" radical production must be equal to $2\times2=4.0$. The G value for total radical production obtained, using DPPH as a standard, agrees fairly closely with the value obtained from the net hydrogen evolution.

ACKNOWLEDGMENTS

We wish to acknowledge the many helpful discussions with Dr. A. A. Miller concerning this work.

[30] A scission-to-crosslink ratio of 0.3 was reported by Charlesby[16] and 0.18 by Baskett and Miller[17]; however, it is to be pointed out that these values are for low-density polyethylene and that the values for the high-density material could be different.

[31] Unpublished.

Paramagnetic-Resonance Studies of Irradiated High-Density Polyethylene. II. Effect of Irradiation Dose on the Radical Species Trapped at Room Temperature

ELLIOTT J. LAWTON, J. S. BALWIT, AND R. S. POWELL

Research Laboratory, General Electric Company, Schenectady, New York

(Received March 10, 1960)

The previous paper presented a study of the radical species in irradiated Marlex-50 at low dose levels. This paper extends that study to a level of 4000 megaroentgens. The kind and relative number of each radical trapped at room temperature (*RT*) depends on the degree and tightness of the crystalline and crosslinked fractions during irradiation. At least two of three distinct species, having different hyperfine structures (six-, five-, and a single-line) are present in varying concentrations at all doses. The six- and five-line radicals are trapped in the crystal, whereas the single-line radical is trapped in the highly crosslinked medium. *During irradiation at RT and liquid-nitrogen (LN) temperature*, the crystal is not as effective in trapping the six-line radical as in the absence of irradiation. At 640 megaroentgens the six-line radical does not survive *during irradiation at RT*, leaving the five- and single-line radicals above this level. The single-line radical appears at 320 megaroentgens and increases until at 3000 megaroentgens, where crystallinity is zero, it accounts for about 70% of the total.

Heating the irradiated samples causes all radicals to disappear; the "extinction temperatures" for the six-, five-, and single-line radicals were 90°, 135°, and about 250°C, respectively. The relative effectiveness of the preirradiated annealed samples compared to the nonirradiated Marlex-50 in trapping radicals at *RT* was 0.5 for the 20-megaroentgen, 1.0 for the 320-megaroentgen, and 1.4 for the 4000-megaroentgen preirradiated material. There is evidence in the uv spectrum for conjugated double bonds in the highly irradiated samples. It is proposed that the single-line radical is initially formed adjacent to the conjugated sequence and then becomes trapped *within* the sequence by resonance. The radical could be represented as

$$\overset{\longleftarrow\cdot\longrightarrow}{-CH{=}CH-CH{=}CH-CH-CH{=}CH-CH{=}CH-}.$$

INTRODUCTION

IN part I[1] of this study it was shown that during the irradiation of Marlex-50 at low dose levels two radical species are formed. The predominant species, the crosslinking radical, is formed in pairs, each radical having the structure $-CH_2-\dot{C}H-CH_2-$. The lesser radical is thought to be a C—C scission having the structure $-CH_2-H_2C\cdot\,|\,\cdot CH_2-CH_2-$. The relative number of each species trapped depends on the temperature of the sample during irradiation. Likewise, it was found that the postirradiation decay depends on the rigidity of the crystal and, therefore, is markedly dependent on the storage temperature above an apparent transition temperature *for the crystal* at −70°C. In the present paper the studies are extended to very high dose levels to show the changes in radical species that take place as the structure of the polymer is changed from a highly crystalline to a highly crosslinked one with increasing irradiation up to 4000 megaroentgens.

In part I the crosslinking radical was referred to as the "*B*" radical, and the scission one as the "*R*" radical. This nomenclature will be adopted in this paper. The reader is also referred to part I for the experimental procedure, which was the same for both parts of this study.

RESULTS AND DISCUSSION

Change in Hyperfine Structure with Increasing Irradiation

The effect of increasing irradiation at *RT* and *LN* temperature on the shape of the EPR spectrum taken at *RT* is shown in Fig. 1. The *RT* series covers the dose range from 10 megaroentgens, where Marlex-50 is still a highly crystalline polymer, to 4000 megaroentgens, where crystallinity is completely destroyed and where structurally the material bears no resemblance to Marlex-50. The height of the relative intensity bars is proportional to the total number of radicals at each irradiation dose. The strong six-line spectrum at low dose levels indicates that at both irradiation temperatures the "*B*" radical is the major component of the composite spectrum. An examination of the *RT* series shows that this component first increases and then decreases steadily with increasing irradiation dose. This is accompanied by a steady increase in the "*R*" radical component as evidenced by the decrease in the outer "*B*" radical peaks of the spectra and the change from a negative to a strongly positive slope of the center peak. At 640 megaroentgens, few if any of the "*B*" radical pairs survive the irradiation at *RT*, and the five-line "*R*" radical becomes the predominant one present at the time of the first EPR measurement. This component appears to increase in intensity up to about 1500 megaroentgens. As dose is increased still further there appears to be a decrease in the "*R*" radical and the growth of a new radical component of uncertain identity having a single-line absorption spectrum. The five lines characterizing the "*R*" radical can be detected in the spectra up to about 2000 megaroentgens, but they become lost between 3000 and 4000 megaroentgens, where the single-line component appears to be the predominant one in the spectrum. This new component, which is believed to be a discreet radical species, will be referred to as the "*G*" radical. It has a line width between points of maximum slope of 26 gauss.

[1] E. J. Lawton, J. S. Balwit, and R. S. Powell, J. Chem. Phys. 33, 395 (1960), preceding paper, this issue.

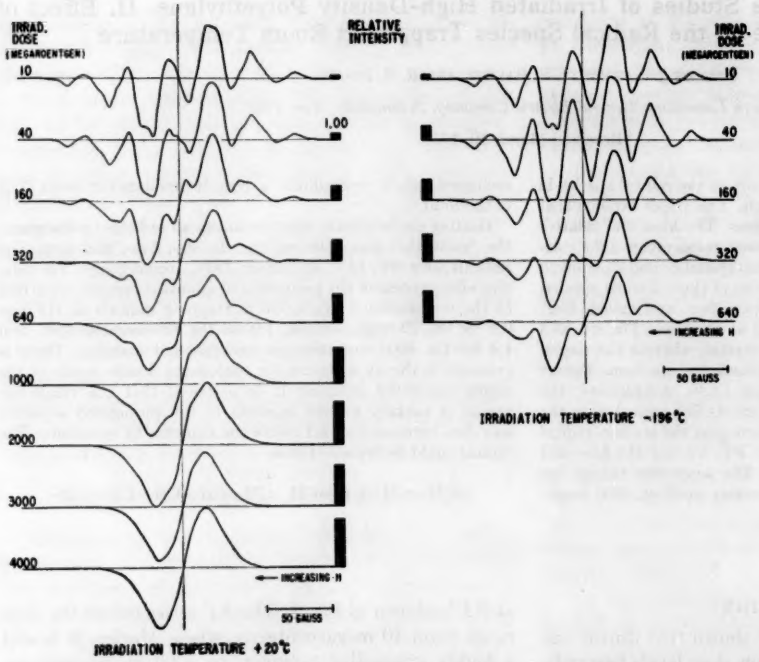

FIG. 1. Change in shape of EPR spectra, taken at room temperature, of Marlex-50 irradiated to increasing dose levels at room and liquid-nitrogen temperatures.

An examination of the *LN* irradiation series, which covers only the dose range up to 640 megaroentgens, shows that the "*B*" and "*R*" radicals are the main ones trapped. Although the shapes of the spectra are similar to those in the *RT* array, it is evident that there is a larger number of "*B*" radicals present than there is following the irradiation at *RT*. Even at 640 megaroentgens the "*B*" radical is still a strong component in the composite spectrum.

Relative Number of "*B*" and "*R*" Radicals; Effect of Increasing Irradiation

Following the procedure outlined in part I[1] it was possible to make a point-by-point decomposition of the composite spectrum for each irradiation dose up to 640 megaroentgens and thereby determine the relative number of "*B*" and "*R*" radicals *trapped at RT*, following irradiation at *RT* and *LN* temperature. In this dose range crystallinity is still the factor responsible for the trapping. The results are shown in Fig. 2 and indicate that the relative numbers of radicals (measured by the area under the absorption curve) do not increase linearly with irradiation dose. In the low dose range up to approximately 80 megaroentgens, about the same number of "*R*" radicals are formed during irradiation at *RT* as at *LN* temperature. At 640 megaroentgens there appear to be fewer "*R*" radicals produced during the irradiation at *LN* than at *RT*, the *LN*-to-*RT* number ratio having a value of 0.76. This may be due to an effectively tighter "cage" surrounding the two radical chain ends at *LN* than at *RT*. That is, at *LN* temperature the two ends would not be pulled apart as far as at *RT*, with the result that not all of the pairs that are made at *LN* temperature are able to escape the "cage" during the warming to *RT*.

The number of "*B*"-radical pairs present at the time of the first EPR measurement is larger following the irradiation at *LN* temperature than at *RT*. As pointed out before in part I,[1] this is not because more are made at *LN* than at *RT* but rather, because of decreased radical chain mobility at *LN* temperature, fewer are lost during the irradiation; thus more are present at the start of the EPR measurements. The number of "*B*" radicals present following an irradiation dose of 320 megaroentgens at *RT* is only about 0.16 of the number present following the same amount of irradiation at *LN* temperature. The decrease is not as pronounced in the lower dose range, the ratios amounting to about 0.4 and 0.66 at 40 and 20 megaroentgens, respectively. The large decrease cannot be accounted for by the normal decay process (in the absence of irradiation) at *RT*, as several hours elapsed time would have been required for the radical concentration to decay to 0.16 of its initial value. This is much longer than the 18-min irradiation time for the 320-megaroentgen dose. Thus, it is concluded that *during the irradiation at RT* Marlex is not as effective in trapping "*B*" radicals as it is in the absence of irradiation. The "catalytic" action of the radiation is probably due to increased thermal vibration of the crystal lattice, bringing the two radicals of the pair closer together, causing recombination.

The apparent saturation of the "*B*" radical component at *RT* with increasing dose at both irradiation temperatures can be attributed to a decrease in both degree and rigidity of the crystalline fraction and, therefore, in the effectiveness of Marlex as a "*B*"-radical trapping medium. Evidence supporting a decreased rigidity of the crystal with increasing irradiation is the change in half-life of the fastest decaying groups of "*B*"-radical pairs at *RT* (as explained in part I) which decreased from about 25 hr at 40 megaroentgens to 7 hr at 640 megaroentgens. A saturation effect was also observed in samples irradiated at *LN* temperature and measured at *LN* temperature; the nonlinearity with increasing irradiation up to 320 megaroentgens being about the same (although the total number was larger) as that when the samples were measured at *RT*. The total (relative) number of radicals increased only 3.4 times when the irradiatoin dose was increased from 40 to 320 megaroentgens. The corresponding increase in the "*B*" radical (as determined by the change in height of the outermost peak of the "*B*" spectrum) was 2.3 times. The larger increase in the total number of radicals indicates that the "*R*" radical is increasing at a faster rate with increasing dose than the "*B*" radical. The slower buildup of the "*B*" radical suggests that the effectiveness of the crystal trapping medium is also reduced *during the irradiation at LN temperature*. In the absence of irradiation there was no decay in the intensity of the EPR signal during the several hours measurement at *LN* temperature.

Changes in "Very-Fine" Structure with Increasing Irradiation

The "very fine" structure present in the "*R*"-radical spectrum (described in part I) changes with increasing dose, as shown by the series of spectra in Fig. 3. Position and regularity of spacing appear to be changed only slightly with increasing dose. The main effect is one of decreasing peak amplitude of the "very fine" structure as dose is increased, until at 640 megaroentgens the structure has nearly all disappeared, leaving the well-defined five-line spectrum. Since the "*R*" radical is trapped in the crystalline regions which are being progressively weakened with increasing irradiation, the disappearance of the "very fine" structure can be considered as additional evidence that this structure is caused by restraints to the motion of the hydrogen atoms of the "*R*"-radical group by the crystal forces. Slichter and Mandell,[2] in their studies of molecular structure and motion in irradiated Marlex-50 polyethylene, report that increasing irradiation causes a spreading apart of the chains, as evidenced by an increase in the principal spacings describing the lateral separation between chains in the crystalline lattice, as well as an increase in the spacing of the amorphous halo. At 900×10^6 rep the 110 spacing is reported to increase from 4.12 to 4.15 A, while the 200 spacing increases from 3.70 to 3.77 A. Thus it could be interpreted that a spreading apart of the chains by as little as 0.03 A is enough to materially reduce the restraints to rotation of the radical end group which are thought to be responsible for the "very fine" structure superimposed on the five-line "*R*"-radical spectrum.

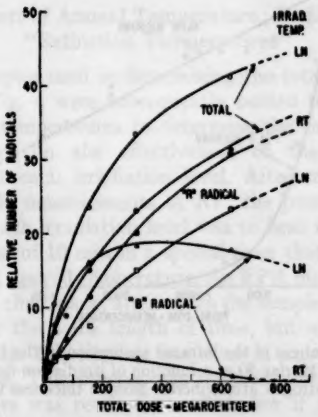

FIG. 2. Relative number of six-line "*B*" and five-line "*R*" radicals in Marlex-50 irradiated at room and liquid-nitrogen temperature as a function of irradiation dose. EPR measured at room temperature.

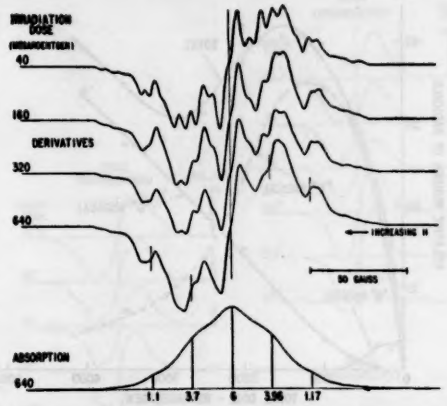

FIG. 3. Change in the "very fine" structure of the "*R*"-radical spectrum with increasing irradiation. EPR measured at room temperature.

Influence of Physical Structure of the Medium on Radicals Trapped at *RT*

The results thus far indicate that the kinds of radicals and the relative numbers of each kind making up the total number *trapped at RT* will depend on (1) the irradiation temperature, which determines the extent of the "catalytic" action of the radiation on the effectiveness of the crystal trapping medium *during the irradiation*; and (2) on the physical state of the trapping

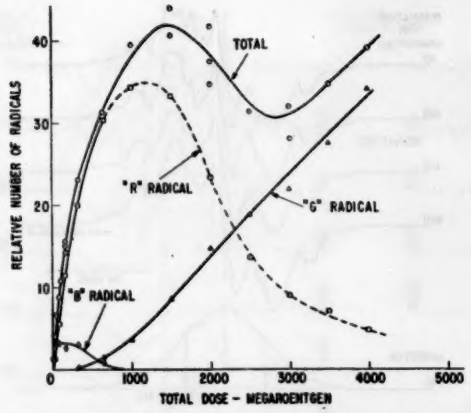

FIG. 4. Relative number of radicals in Marlex-50 irradiated at room temperature as a function of irradiation dose. EPR measured at room temperature.

medium—that is, on the degree and tightness of the crystalline and highly crosslinked fractions, which change with increasing irradiation. Thus in the dose range up to about 640 megaroentgens the total number of radicals trapped at *RT* was shown to be made up predominantly of the "*B*" and "*R*" radicals and the relative numbers of each present depended on the irradiation temperature; whereas above this level the "*B*" radical could no longer survive the irradiation at *RT*, and the "*R*" and "*G*" radicals became the predominant ones.

The effect of increasing irradiation at *RT* on the *total* number of radicals trapped at *RT* is shown by the curve of Fig. 4 for the complete dose range up to 4000 megaroentgens. The complete decomposition of this curve into its components will be discussed later. Increasing irradiation causes a continuous decrease in degree and order of the crystalline fraction up to about 3000 megaroentgens where crystallinity is completely destroyed.[2,3] Accompanying this is the steady increase in the crosslinked fraction, resulting in the buildup of a glasslike highly crosslinked trapping medium. At the point of maximum trapping, which occurs at 1500 megaroentgens, radicals are still predominantly trapped in the crystalline region, the highly crosslinked region contributing but little to the over-all effectiveness of the polymer as a trapping matrix. At 3000 megaroentgens, where the curve goes through a minimum, radicals are trapped entirely in the highly crosslinked medium. Increase in irradiation above this level increases both degree and "tightness" of the crosslinked fraction, thereby increasing its effectiveness, causing the curve to rise again. It is of interest to note that the dip in the radical trapping curve at 3000 megaroentgens occurs at about the same dose as that reported by Slichter and Mandell[2] for the disappearance of crystallinity and the maximum in the characteristic Bragg spacing for the amorphous region of Marlex-50. Their findings indicate that decrease in density with increasing dose parallels an increase in the Bragg spacing of the principal amorphous halo up to about 3500×10^6 rep. Above this level the network continues to tighten, causing an increase in density and contraction of the principal spacing between chains in the noncrystalline polymer.

Frequency of Network Defects

Some idea of the average spacing between defects (crosslinks, transvinylene, scissions, etc.) at the maximum irradiation dose can be estmated from the behavior of the infrared absorption band at 13.8 μ. This absorption band is due to a rocking vibration of hydrogen atoms in chain segments containing three or more consecutive $-CH_2-$ groups.[4] In straight-chain crystalline hydrocarbons, splitting of the band occurs because of vibrational coupling (perpendicular to chain axis)[5] between adjacent chains in the crystal, resulting in a doublet with absorption maxima at 13.7 and 13.88 μ. A plot of absorbance at these two wavelengths vs irradiation dose is shown in Fig. 5. As irradiation is increased the intensity of both bands decreases, the net deflection at 13.7 μ (the band associated with but not necessarily proportional to degree of crystallinity) becoming zero at approximately 3000×10^6 where the material becomes noncrystalline as determined by x-ray diffraction measurements. The net intensity of the peak at 13.88 μ decreases linearly with increasing

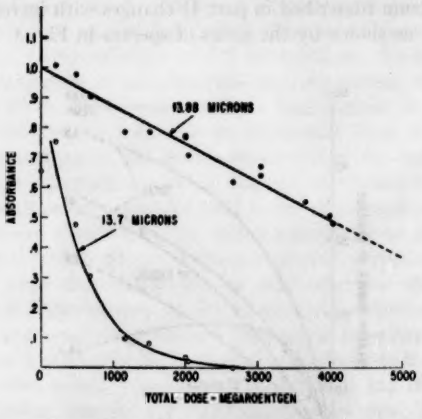

FIG. 5. Changes in the infrared absorption in the 13.8-μ region in irradiated Marlex-50 as a function of irradiation dose. Samples handled in nitrogen atmospheres. Sample thickness 0.002 in.

[2] W. P. Slichter and Elaine R. Mandell, J. Phys. Chem. **62**, 334 (1958).

[3] E. J. Lawton, J. S. Balwit, and R. S. Powell, J. Polymer Sci. **32**, 257-289 (1958).

[4] N. Sheppard and G. B. B. M. Sutherland, Nature **159**, 729 (1947).

[5] F. M. Rugg, J. J. Smith, and J. V. Atkinson, J. Polymer Sci. **9**, 579 (1952).

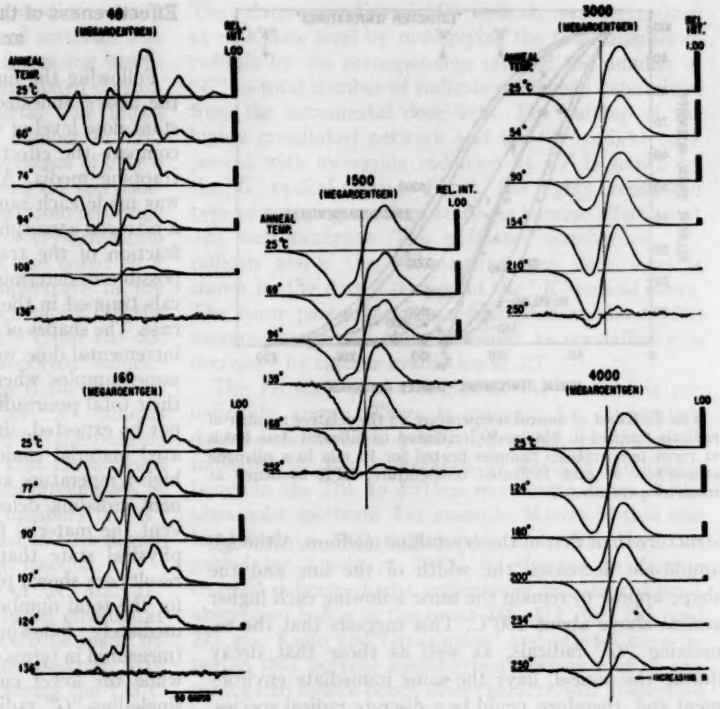

FIG. 6. Effect of anneal temperature on the shape of the EPR spectra of Marlex-50 irradiated to different dose levels at room temperature. Samples heated for 10 min at each temperature in a nitrogen atmosphere. Spectra measured at room temperature.

dose out to 4000 megaroentgens. The curve extrapolates to zero at about 8000 megaroentgens at which level the average length of $-CH_2-$ sequences must be equal to three, which corresponds to a network defect every $3+1=4$ carbon atoms. Thus at 4000 megaroentgens there is a defect every seven carbon atoms. This corresponds to an over-all *average G* value for all types of defects of ~ 2.5.

Effect of Anneal Temperature; Radical "Extinction Temperatures"

The samples used in determining the total trapping curve of Fig. 4 were subsequently heated to different annealing temperatures to determine the influence of temperature on the effectiveness of the trapping medium at each irradiation level. After making the initial EPR measurements at *RT*, the procedure followed at each irradiation level was to heat the sample for a period of 10 min in a special oven that had been preset to a desired temperature. An EPR measurement at *RT* was then made, after which the sample was again heated for the same length of time, but at a higher temperature. The heating was done in a dry nitrogen atmosphere. This process was repeated until finally a temperature was reached at which few if any of the radicals could survive.

The effect of temperature on the shape of the EPR spectra taken at *RT* following anneal is shown by the series of spectra in Fig. 6 for samples that had been irradiated at *RT* to dose levels of 40, 160, 1500, 3000, and 4000 megaroentgens. The 40- and 160-megaroentgen arrays typify the behavior of radicals trapped in the highly crystalline fraction. Both "*B*" and "*R*" radicals, present initially at 25°C, are completely annealed out on heating to 136°C (the crystal melting point of the unirradiated polymer), indicating that these two types are trapped in the crystalline fraction and that the manner in which they disappear depends on the mobility of the polymer chains. The lifetime of the "*B*"-radical pair was previously shown in part I[1] to be much shorter than that of the "*R*" radical; likewise it was found that the "*B*" radical annealed out at a lower temperature than the "*R*" radical.

The "extincton temperature" for the "*B*" radical appears to be about 90°C. The five-line "*R*" radical is seen to retain its detailed hyperfine structure upon heating to within a few degrees of the crystal melting point which, as pointed out in part I, indicates that the spectrum is characteristic of a single-radical species. The 3000- and 4000-megaroentgen series illustrate the behavior of the highly crosslinked trapping medium. At this dose level the predominant radical is the single-line "*G*" radical. The "extinction temperature" for this radical is in excess of 250°C (see Fig. 6), which is much higher than that for either the "*B*" or "*R*" radicals, and indicates that it resides in a much tighter

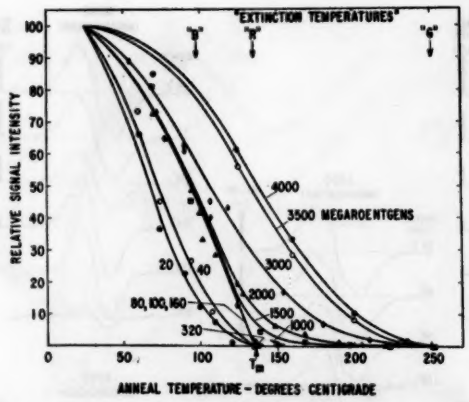

FIG. 7. Effect of anneal temperature on the relative number of radicals trapped in Marlex-50 irradiated to different dose levels at room temperature. Samples heated for 10 min in a nitrogen atmosphere at each indicated temperature. EPR measured at room temperature.

structure than that of the crystalline medium. Although amplitude decreases, the width of the line and the shape appear to remain the same following each higher anneal above about 150°C. This suggests that the remaining "*G*" radicals, as well as those that decay during the anneal, have the same immediate environment and, therefore, could be a discrete radical species. At 3000 megaroentgens the slight evidence for the presence of the "*R*" radical disappears on heating to 154°C, leaving only the "*G*" radical, which has a line width (at maximum slope) of 26 gauss. It is evident from the 1500-megaroentgen array that both "*R*" and "*G*" radicals are present initially, the "*R*" radical disappearing first when the sample is heated at 139°C, to be followed by the "*G*" radical which persists to 250°C.

The relative number of radicals surviving the high-temperature anneal is shown plotted in Fig. 7 as a function of anneal temperature for the entire dose range. Relative amplitude of the major peak of the EPR signal following each incremental heating has been plotted. Since the spectrum in most cases is a composite one, the shapes of the curves must be taken as approximate. The irradiation level at which the glasslike highly crosslinked medium starts to become effective, that is, where radicals can survive an anneal temperature T_m that melts the crystalline medium, appears to be at about 320 megaroentgens. At the 4000-megaroentgen level about one-half of the total number of radicals can survive an anneal at 136°C. The approximate "extinction temperatures" for the "*B*," "*R*," and "*G*" types as indicated by the arrows at the top of the graph are 90°, 135°, and about 250°C, respectively.

Effectiveness of the Preirradiated Trapping Medium and the "*G*" Radical

Following the final high-temperature anneal each of the above annealed samples was irradiated to a constant dose level of 40 megaroentgens at *RT* in order to compare the effectiveness of the irradiation-produced trapping media. After the initial EPR measurement was made each sample was then heated for 10 min in a nitrogen atmosphere at 136°C to melt the crystalline fraction of the trapping medium, thereby making it possible to determine the relative number of "*G*" radicals trapped in the highly crosslinked network in each case. The shapes of the spectra in all cases following the incremental dose were nearly the same as those for the same samples when they were initially irradiated to their total preirradiation doses. Identical shapes would not be expected, since the physical state of the irradiated material could never be the same following the high-temperature anneal as before because the permanent crosslink defects would act as restraints to prevent the material from returning to exactly the same physical state that it had prior to the anneal. The results are shown plotted in Fig. 8. The upper curve is for the total number of all radicals trapped at *RT* immediately following the incremental dose at *RT* (measured in terms of area under the absorption curve), while the lower curve shows the relative number of single-line "*G*" radicals that survive the 135°C anneal. Both are plotted against irradiation-produced trapping media in terms of the ***initial total dose level*** to which each had been irradiated prior to the initial high-temperature anneal. The first few structural defects markedly reduce the effectiveness of the irradiation-produced trapping medium over that of the initial highly crystalline material for the reason just men-

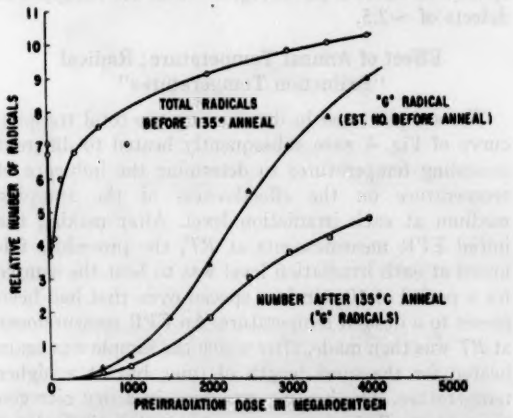

FIG. 8. Effectiveness of preirradiated annealed Marlex-50 as a radical trapping medium and the relative number of "*G*" radicals trapped in the highly crosslinked fraction following a 10-min 135°C anneal in a nitrogen atmosphere, both as a function of *preirradiation* dose. Test dose 40 megaroentgens, EPR measured at room temperature.

tioned. The 20-megaroentgen trapping medium is only one-half as effective as the nonirradiated material. The trapping effectiveness increases with increasing irradiation, becoming greater than the nonirradiated crystalline material above 320 megaroentgens. The initial reduction is almost entirely in the number of "*B*" radicals trapped, indicating that the presence of only a few restraints to molecular motion during the recrystallization period will prevent the material from returning to the same high degree and order of crystallization that it had in the beginning. This is also noted by a lowering of the crystal melting temperature in the irradiated medium, which was as much as 4°C for the 10-megaroentgen material and about 8°C for the 40-megaroentgen, in agreement with reported values.[6] The increase up to 320 megaroentgens is the result of an increase in the relative number of "*R*" radicals trapped. An examination of the curve for the radicals surviving the 135°C anneal indicates that the increase in the relative number above 320 megaroentgens is due to an increase in the relative numbers of "*G*" radicals, which accompanies the increase in both degree and tightness of the highly crosslinked fraction.

An estimate of the relative number of "*R*" and "*G*" radicals trapped in the 3000-megaroentgen medium at *RT* following the incremental dose could be made by comparing the shape of the composite spectrum with that of the "*B*"-radical spectrum following the 135°C anneal after it was referred to time zero and *RT*. The results indicate that the "*G*" radical accounted for approximately 70% of the total, the remainder being the "*R*" radical. The middle curve of Fig. 8 shows the estimated relative number of "*G*" radicals *present at RT* for other preirradiated trapping media. It was obtained by normalizing the 135°C anneal curve so as to pass through the above estimated point at *RT* for the 3000-megaroentgen preirradiated trapping medium. The fraction of the "*G*" radicals present initially at *RT* in each of the other preirradiated materials can be determined by dividing the relative number of "*G*" radicals given by the middle curve by the total number of radicals represented in the upper curve.

Decomposition of the Total Trapping Curve

The decomposition of the total trapping curve of Fig. 4 into "*B*"- and "*R*"-radical components has already been made up to 640 megaroentgens (see Fig. 2) by the method described in part I.[1] These results are indicated by the solid-line portion of the "*R*"- and "*B*"-radical curves. The decomposition into "*R*"- and "*G*"-radical components above the 640-megaroentgen level was made by first determining the relative number of "*G*" radicals present at each dose level and then subtracting this number from the total number to determine the relative number of "*R*" radicals present. The relative number of "*G*" radicals was determined at each dose level by multiplying the total number of radicals by the corresponding ratio of the number of "*G*"-to-total number of radicals previously determined from the incremental dose data. The buildup of the highly crosslinked network and the "*G*"-radical component with increasing radiation at *RT* is shown by the "*G*"-radical curve in Fig. 4. The highly crosslinked type of trapping medium starts to become effective at 320 megaroentgens. The estimated number of "*R*" radicals above the 640-megaroentgen dose level is shown by the dotted portion of the "*R*"-radical curve. The curve passes through a maximum at about 1500 megaroentgens and then decreases as crystallinity is decreased by further irradiation at *RT*.

The identity of the single-line "*G*" radical is not definitely known. There is evidence for conjugated-double-bond formation with increasing irradiation as indicated by the appearance of multiple absorption bands in the 270- to 350-mμ wavelength range of the ultraviolet spectrum. For example, Marlex-50 that was irradiated to 2000 megaroentgens at *RT*—then annealed for 5 min at 250°C in nitrogen to destroy trapped radicals—had a yellow color and showed weak absorption bands in the uv at 356, 322, 307, 285, and 275 mμ. Kuhn and Grundmann[7] and others[8] have reported that polyene hydrocarbons having four to five conjugated double bonds show characteristic absorption bands in this range of the uv spectrum; thus 2,4,6,8 decatetraene, which is faint yellow in color, has absorption bands at 320, 297, 283, and 272 mμ.[7] It is proposed that the "*G*" radical is trapped by resonance within the conjugated sequence. Thus the lack of hyperfine structure would be an indication that the odd electron is oscillating rapidly back and forth along the sequence and spending too little time adjacent to any hydrogen or group of hydrogens, whether within or at either end of the conjugated system, to produce any resolvable splitting. The radical might be represented as

$$\overset{\longleftarrow\cdot\longrightarrow}{\text{—CH=CH—CH=CH—CH—CH=CH—CH=CH—.}}$$

Hanna and McConnell[9] working with x-irradiated conjugated polyene acids observed similar single-line spectra of comparable widths.

The buildup of the conjugated sequence (within the highly crosslinked network) could be by a preferential radical formation at activated sites adjacent to double bonds. The first radical formed would remain at the double bond until a second one was formed, at which time the two would combine to form another double bond of the conjugated sequence. Thus the double

[6] L. Mandelkern and F. P. Price, J. Am. Chem. Soc. (to be published).

[7] R. Kuhn and C. Grundmann, Ber. deut. chem. Ges. **71**, 442 (1938).

[8] A. D. Mebane, J. Am. Chem. Soc. **74**, 5227 (1952).

[9] M. W. Hanna and Harden M. McConnell, Bull. Am. Phys. Soc. Ser. II, **4**, (November 27, 1959).

bond can also act as a "sink" in which the radicals can disappear.

Shape of the Total Trapping Curve; Analog for Other Polymers

It is of interest to speculate about the expected shape of the total trapping curve for other polymers.

Marlex-50 is an example of a highly crystalline polymer in which crosslinking is predominant over degradation. The shape of the total trapping curve was shown to depend on the disappearance of crystallinity and the buildup of a highly crosslinked trapping medium. The total number of radicals trapped was seen to rise at first, pass through a maximum, then decrease with decreasing crystallinity, only to rise again as the degree and tightness of the crosslinked medium increased with further increase in irradiation.

The shape of the total trapping curve for other polymers might be expected to have as analogs the shapes of the curves for the individual radical components making up the total trapping curve for Marlex-50.

Analog 1. The amorphous polymer in which crosslinking is the predominant reaction, e.g., silicone. No trapping would be expected until the degree and tightness of the crosslinked trapping medium began to develop; then the total number would rise and continue to do so as both degree and tightness were increased with increasing irradiation. This behavior is analogous to buildup of the "*G*" radical in the highly crosslinked fraction of Marlex.

Analog 2. The crystalline or glassy polymer in which degradation is the predominant reaction, e.g., polymethyl methacrylate. The total number of radicals would be expected to increase at first, pass through a maximum, and then decrease as the rigidity of the crystal or glass decreases with increasing irradiation, finally becoming zero when the crystalline or glassy regions are destroyed. The behavior here corresponds to that of the "*R*" component in Marlex-50.

Analog 3. The highly crystalline crosslinking type of polymer in which a high degree of scission also occurs, e.g., possibly crystalline polypropylene.[10] The depth of the dip in the trapping curve for Marlex-50 at the higher dose levels should depend on the rate of buildup of the crosslinked fraction. Thus, in this case in which the crosslinking efficiency only slightly exceeds that of degradation, a much deeper dip would be expected than in the case of Marlex-50 where crosslinking is the predominant reaction.

ACKNOWLEDGMENT

We wish to acknowledge the many helpful discussions with Dr. A. A. Miller concerning this work.

[10] R. M. Black and B. J. Lyons, Nature **180**, 1346 (1957).

Sparking Potential and Molecular Structure of Unsaturated Hydrocarbon Gases

R. W. CROWE* AND J. C. DEVINS

General Electric Research Laboratory, Schenectady, New York

(Received November 9, 1959)

In earlier experiments, we have shown that it is possible to relate sparking potentials of saturated hydrocarbon gases to certain molecular properties. From measurements of electric breakdown in a series of these gases, it has been found that the effective molecular cross section for electron scattering is proportional only to the number of carbon-hydrogen bonds in the molecule and is independent of their disposition. The lack of a contribution by the carbon-carbon bonds has been attributed to a shielding effect.

In the present paper, we describe and discuss the results of a similar investigation of breakdown in unsaturated hydrocarbon gases. It was found that, for a series of olefin gases, the cross section associated with the carbon-carbon double bond is greater than three times that of the carbon-hydrogen bond, while that of the carbon-carbon single bond is essentially zero as it was in the alkane series. An attempt is made to interpret this observation in terms of (1) a decrease in the shielding effect, and (2) the larger spatial configuration of the π-electron orbitals associated with the ethylenic linkage. Variations in the position of the double bond within the molecule has little or no effect upon its contribution to the total cross section.

Breakdown measurements in butadiene-1,3 and benzene indicate that conjugation results in an increase in the effective cross section of each double bond, as might be expected. Evidence of a small but measurable amount of double-bond character was also found in cyclopropane from sparking potential measurements. This is in agreement with the predictions of other investigators.

I. INTRODUCTION

ONE of the first attempts to correlate sparking potentials of complex gases with molecular structure was that by Wilson, Simons, and Brice.[1] They showed that, to a first approximation, the sparking potentials of simple saturated fluorocarbon gases could be expressed as a linear function of gas density, the latter being varied by changes in both pressure and molecular weight. Correlations of a similar nature have also been observed by other investigators[2,3,4] from measurements of breakdown in various series of electronegative gases.

In an effort to obtain as much general information of a fundamental nature as possible regarding the influence of molecular properties upon the electric breakdown in gases, it has seemed advisable initially to limits our investigations to molecular gases in which attachment processes are unimporant. Accordingly, we have measured the sparking potentials of a large number of saturated and unsaturated hydrocarbon gases. The results obtained for the saturated hydrocarbons have already been published in detail.[5,6] On the other hand, only a brief description of our preliminary results for the olefins is available in the literature.[7] Because of the fact that these latter measurements and their interpretation differ in certain respects from those reported recently by Heylen and his co-workers,[8-11] it has appeared worth while to present them in greater detail at this time.

II. MECHANISM OF BREAKDOWN

A. Theoretical Considerations

Perhaps the most widely accepted criterion for the breakdown of a gas in a uniform electric field is that postulated by Townsend, which may be written

$$\gamma[\exp(\alpha\delta)-1]=1. \tag{1}$$

In this expression δ is the electrode separation and α and γ are the primary and secondary ionization coefficients, respectively.[12] Because the coefficient α is determined by the fraction of electrons having energy in excess of the molecular ionization energy of the gas, it should be dependent upon the electric field E, the gas pressure P, and the scattering cross sections of the molecule which determine the amount of energy lost by an electron on collision. If one assumes that the inelastic cross section of the molecule is of the form

$$\sigma(\epsilon)=\sigma_o(\epsilon-\epsilon_e), \tag{2}$$

* Present Address: Thomas A. Edison Research Laboratory, McGraw-Edison Company, West Orange, New Jersey.

[1] W. A. Wilson, J. H. Simons, and T. J. Brice, J. Appl. Phys. **21**, 203 (1950).

[2] N. R. McCormick and J. D. Craggs, Brit. J. Appl. Phys. **5**, 171 (1954).

[3] R. W. Crowe and J. C. Devins, Ann. Rept., Conf. on Elect. Insul. (1955).

[4] C. N. Works and E. W. Lindsay, Ann. Rept., Conf. on Elect. Insul. (1955).

[5] J. C. Devins and R. W. Crowe, Ann. Rept., Conf. on Elect. Insul. (1953).

[6] J. C. Devins and R. W. Crowe, J. Chem. Phys. **25**, 1053 (1956).

[7] R. W. Crowe and J. C. Devins, Nature, **179**, 976 (1957).

[8] A. E. D. Heylen and T. J. Lewis, Brit. J. Appl. Phys. **7**, 411 (1956).

[9] A. E. D. Heylen, Nature **180**, 703 (1957).

[10] A. E. D. Heylen and T. J. Lewis, Can. J. Phys. **36**, 721 (1958).

[11] A. E. D. Heylen, J. Chem. Phys. **29**, 813 (1958).

[12] See, for example, L. B. Loeb, *Fundamental Processes of Electrical Discharge in Gases* (John Wiley & Sons, Inc., New York, 1939) Chap. IX.

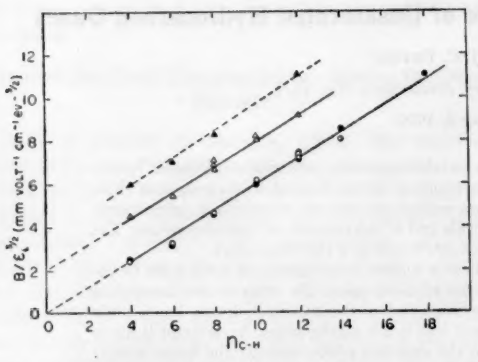

FIG. 1. Dependence of $B/\epsilon_i^{\frac{1}{2}}$ upon the number of carbon-hydrogen bonds per molecule for hydrocarbon gases. ○ alkanes; ● alkanes (Heylen and Lewis); △ olefins; ▲ olefins (Heylen and Lewis).

and that the elastic cross section θ is essentially independent of electron energy ϵ, then it is possible to show from theoretical calculations of the distribution in energy of electrons[13] that α is of the form,

$$\alpha/P=A(E/P)\exp(-BP/E),$$
$$B=K(\sigma_o\theta)^{\frac{1}{2}}(\epsilon_i-\epsilon_e)^{\frac{1}{2}},$$
$$K=1.154/ekT. \tag{3}$$

In this expression, A is a constant, ϵ_e and ϵ_i are the excitation and ionization energies of the molecule, e is the electronic charge, k is the Boltzmann constant, and T is the absolute temperature.

By introducing Eq. (3) into the Townsend criterion for breakdown we have

$$V_s=BP\delta/[\ln V_s+\ln(A/r)],$$
$$r=\ln(1+1/\gamma), \tag{4}$$

which is a relationship between the sparking potential V_s and the product $P\delta$ (Paschen's law). In most cases, r can be assumed constant because γ does not usually vary strongly with E. Thus, we are provided with a means of determining the constant B in Eq. (3) from breakdown measurements alone.

In order to determine the manner in which the composite cross section $(\sigma_o\theta)^{\frac{1}{2}}$ varies with molecular size and shape for a series of structurally similar gases, information about the energy difference $(\epsilon_i-\epsilon_e)$ is desirable. However, since values of ϵ_e for most gases are not available, it is necessary to introduce an assumption regarding them. It does not seem unreasonable to assume that they are approximately proportional to the first ionization potentials, particularly for a series of simply related molecules. Granting the validity of this approximation, we have

$$B=K\nu^{\frac{1}{2}}(\sigma_o\theta)^{\frac{1}{2}}\epsilon_i^{\frac{1}{2}}$$
$$\nu=(\epsilon_i-\epsilon_e)/\epsilon_i, \tag{5}$$

where ν is constant for a given series.

B. Application to Saturated Hydrocarbons

It has already been mentioned that the results of the investigation of electric breakdown in the aliphatic hydrocarbons have been published elsewhere.[5,6] Consequently, they will be presented here in summary form only as an introduction to the present work on the unsaturated hydrocarbons.

To facilitate the interpretation of our results for the alkane series, we assumed that, when a free electron approaches a gas molecule, it is scattered by an electron distribution which shows, on the average, a higher density in the regions of the chemical bonds. Consequently, separate and additive elastic cross sections were assigned to each kind of bond in the molecule; that is,

$$\theta=N_{C-H}\theta_{C-H}+N_{C-C}\theta_{C-C}, \tag{6}$$

where N_{C-H} and N_{C-C} represent the number per molecule of carbon-hydrogen and carbon-carbon bonds, respectively. For the alkane series, then, we could write that

$$B/\epsilon_i^{\frac{1}{2}}=K\nu^{\frac{1}{2}}\rho^{\frac{1}{2}}[N_{C-H}(\theta_{C-H}+\tfrac{1}{2}\theta_{C-C})-2\theta_{C-C}].$$
$$\rho=\sigma_o/\theta, \tag{7}$$

where ρ may or may not be a constant for the series.

Equation (7) implies that a plot of $B/\epsilon_i^{\frac{1}{2}}$ vs N_{C-H} should give a linear relationship provided that ρ remains independent of molecular size and shape. The results for the alkanes are summarized in Fig. 1, which also includes values obtained independently by Heylen and Lewis[10] for some of the gases. Note that the points fall on a straight line which extrapolates to the origin. This observation led us to conclude that the electrons associated with the carbon-carbon bonds do not contribute significantly to the effective molecular cross section. Such behavior might well be the result of shielding by electrons associated with neighboring carbon-hydrogen bonds.

It was also found that Eq. (7) with $\theta_{C-C}=0$ is applicable to both straight chain, cyclic and branched chain alkanes, since the values of B depend only upon N_{C-H} and not upon their disposition.[6] It is of interest to note that Brüche[14,15] has also observed no dependence of the Ramsauer cross sections upon chain branching for butane and pentane isomers.

[13] R. W. Crowe, J. K. Bragg, and J. C. Devins, J. Appl. Phys. **26**, 1121 (1955).

[14] E. Brüche, Ann. Physik **4**, 387 (1930).

[15] E. Brüche, Ann. Physik **5**, 281 (1930).

III. EXPERIMENTAL METHOD

A description of the breakdown cell, the high-voltage source, and the general procedure followed for making the breakdown measurements has been given previously.[6] Consequently, only that part of the technique which has been questioned by recent investigators will be described in detail at this time.

Heylen and Lewis[8,10,11] have pointed out recently that the sparking potentials we have reported thus far are considerably lower than their results for the same gases. Furthermore, they suggest that the higher results can be obtained only if the initial photocurrent, produced by ultraviolet illumination of the cathode, is restricted to a value sufficiently low that pre-breakdown pulse activity cannot lead to premature breakdown due to distortion of the electric field by space charges in the gap. This, of course, implies that the intensity of illumination used in our experiments was sufficiently high to yield a breakdown characteristic considerably below that predicted by Eq. (4).

Although the reason for the observed influence of illumination upon the sparking potential is not clear at this time, its importance cannot be overemphasized. In fact, a more thorough investigation of the phenomenon may provide valuable information about the mechanism of breakdown in these relatively complex molecular gases. Such an investigation is now in progress. Until the problem has been resolved, however, we can only describe as accurately as possible the experimental conditions and present the results obtained under those conditions.

In the present investigation, the intensity of ultraviolet illumination was increased in a stepwise manner until (1) the sparking potential became independent of the intensity, (2) the results became independent of the rate of voltage rise, and (3) the results obtained for a wide range of pressures and gap spacings fell on the same V_s vs $P\delta$ curve for each gas. In all cases, these conditions could be satisfied by placing two 4-watt G.E. germicidal lamps about one inch from the quartz breakdown cell. Possible decomposition of the gas by the ultraviolet was prevented by switching the lights on for a very short time as the sparking threshold was approached.

With the exception of benzene, those hydrocarbons which are normally liquid at room temperature were Phillips "pure grade" (>99%). The benzene sample was of *reagent* grade. The gaseous materials were obtained from the Matheson Company and were also labeled greater than 99% pure. Further purification of all of the gases was accomplished by distillation and repeated freezing and pumping cycles.

IV. EXPERIMENTAL RESULTS AND DISCUSSION

A. Straight Chain Olefins

The sparking potentials of a series of straight-chain olefin gases, in which the carbon-carbon double bond is located between the first and second carbon atoms, are plotted in Fig. 2 as functions of the product $P\delta$. Where possible, the measurements were made over a pressure range from 100 mm Hg to near atomospheric pressure. The electrode separation, in all cases, varied from 0.04 to 0.50 cm. Note that, within experimental error, Paschen's law is obeyed.

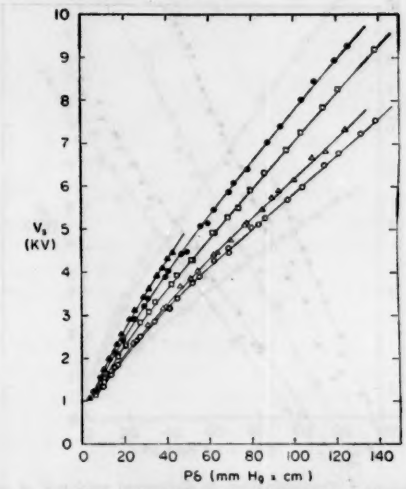

FIG. 2. Sparking potentials as functions of $P\delta$ for a series of *n*-alkene-1 gases. ○ ethylene; △ propylene; □ *n*-butene-1; ● *n*-pentene-1; ▲ *n*-hexene-1.

It is of interest to note at this time that Heylen and Lewis[8,11] appear to have made their measurements by using a standard gap of 0.3175 cm although they state parenthetically[8] that Paschen's law was obeyed in the range of $P\delta > 30$. The evidence upon which this statement is based is not given. *It is mandatory in testing the validity of Paschen's law that both the gap and pressure be varied over a considerable range.* Furthermore, the law must be verified before Eq. (4) can be used with confidence to interpret breakdown data in terms of molecular structure.

The results in Fig. 2 show that, for a given value of $P\delta$, the sparking potential increases with increasing chain length of the hydrocarbon molecule. In fact, the trend is similar to that observed for the straight-chain alkanes, the essential difference being that the actual values of sparking potential are greater for the olefins.

As is predicted by Eq. (4), the relationship between $\ln V_s$ and $P\delta/V_s$ for the straight-chain olefins is, within experimental error, a linear one (see Fig. 3). Values for the constants B and A/r, determined from the data by the method of least squares, are tabulated in Table I. Included also are corresponding values of $B/\epsilon_i^{\frac{1}{2}}$ for these gases. The values of ϵ_i listed in Table I are those reported by Honig.[16] Note that, as in the case of the alkanes, a definite relationship exists between $B/\epsilon_i^{\frac{1}{2}}$ and the length of the hydrocarbon chain.

[16] R. E. Honig, J. Chem. Phys. **16**, 105 (1948).

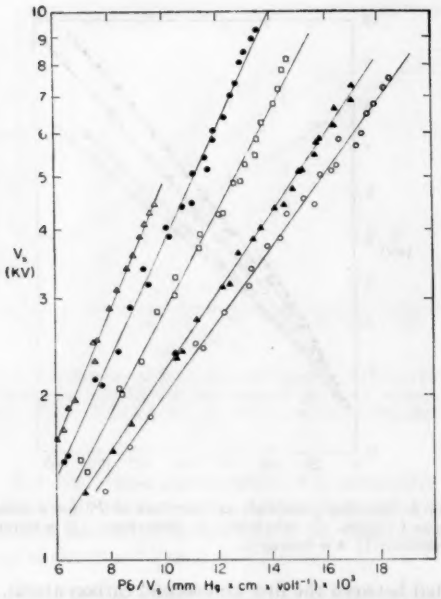

FIG. 3. Log V_s vs $P\delta/V_s$ for series of *n*-alkene-1 gases. ○ ethylene; ▲ propylene; □ *n*-butene-1; ● *n*-pentene-1; △ *n*-hexene-1.

If we modify Eq. (7) to include a cross section for the double bond $\theta_{C=C}$, then we get

$$B/\epsilon_i^{\frac{1}{2}} = K\nu^{\frac{1}{2}}\rho^{\frac{1}{2}}[N_{C-H}(\theta_{C-H}+\tfrac{1}{2}\theta_{C-C})-2\theta_{C=C}+\theta_{C=C}] \quad (8)$$

for the olefin series. Provided again that ρ remains constant for the series, we should expect to find a linear relationship between $B/\epsilon_i^{\frac{1}{2}}$ and N_{C-H}. That this is approximately true is shown in Fig. 1. Included also are the corresponding results reported by Heylen and Lewis,[10] which are noticeably higher than those obtained in the present investigation. This consistent difference is not surprising in view of the fact that Heylen and Lewis also report higher values of sparking potential for these gases. It has already been pointed out that an accurate interpretation of this discrepancy must await a more thorough investigation of the influence of ultraviolet illumination upon sparking potential.

It is of interest to note that the best straight line through the data for the straight-chain olefins in Fig. 1 is of the same slope as that for the alkanes. This implies that $\theta_{C-H}+\frac{1}{2}\theta_{C-C}$ is the same for both series provided, of course, that ρ is also the same. Furthermore, if it can be assumed that θ_{C-H} has the same value in both series, then it must be concluded that shielding of the electrons associated with the C—C bonds is as effective in the olefin molecule as it was in the alkanes; that is $\theta_{C-C}\simeq 0$. If this is true, then the intercept of the olefin curve in Fig. 1 is a measure of the contribution of the C=C bond to the molecular cross section. Note that this contribution is substantial. In fact, the results indicate that $\theta_{C=C}\simeq 3.3\theta_{C-H}$.

At first glance, it may seem unreasonable that the contribution of the C=C bond should be greater than three times that of the C—H bond, especially when the C—C bond contributes nothing. However, it should be emphasized that the elimination of two C—H bonds to form the ethylenic linkage may result in a substantial decrease in the shielding effect. Furthermore, the C=C bond may offer a better electron target due to the larger spatial configuration of the π-electron orbitals associated with it.

B. Effect of Chain Branching and Double Bond Position

Because of the fact that extensive variations in the shape of a saturated hydrocarbon molecule had little or no effect upon its effective cross section, it seemed of interest to extend our investigations to include available butene and pentene isomers. Accordingly, the sparking potentials of *n*-butene-2, isobutylene, and 2-methyl-butene-2 were measured over a wide range of $P\delta$. The results are compared with those obtained for *n*-butene-1 and *n*-pentene-1 in Figs. 4 and 5. Note that in both cases branching of the hydrocarbon chain resulted in a slight reduction in the magnitude of the sparking potential over the entire range of $P\delta$. A similar effect was produced by moving the C=C bond of the *n*-butene molecule to the number two position. This reduction is considerably more pronounced and consistent than that found in the alkane series.

From the plots of $\ln V_s$ vs $P\delta/V_s$ (not shown here) for the above isomers, the values of B and A/r listed in Table I were calculated. Note that, for all three gases, B is somewhat smaller than that observed for the corresponding *n*-alkene-1 isomer. However, because branching and changing of double-bond position also results in a corresponding reduction in ϵ_i, the apparent influence of such changes upon $B/\epsilon_i^{\frac{1}{2}}$ is slight (see Table I and Fig. 1). Thus, Eq. (8) provides an adequate description of the behavior of field-accelerated electrons

TABLE I. Sparking potential constants for the unsaturated hydrocarbons.

Hydrocarbon	B Vmm^{-1} cm^{-1}	Std. dev. in B	A/r $V^{-1}\times 10^3$	ϵ_i ev	$B/\epsilon_i^{\frac{1}{2}}$ Vmm^{-1} cm^{-1} ev$^{-\frac{1}{2}}$
Ethylene	155.0	3.1	2.38	10.62	4.48
Propylene	166.2	2.7	2.41	9.84	5.39
n-Butene-1	214.3	4.8	3.04	9.76	7.04
n-Pentene-1	244.5	4.3	3.09	9.66	8.19
n-Hexene-1	273.1	4.7	3.15	9.59	9.19
n-Butene-2	198.0	4.7	3.39	9.29	6.98
Isobutene	188.3	4.1	2.84	9.35	6.64
2-Methylbutene-2	211.1	4.2	3.37	8.85	8.01
Butadiene-1,3	257.2	4.7	2.56	9.20	9.20
Benzene	306.3	10.8	2.55	9.43	10.59
Cyclopropane	129.7	1.9	4.17	10.15	4.01

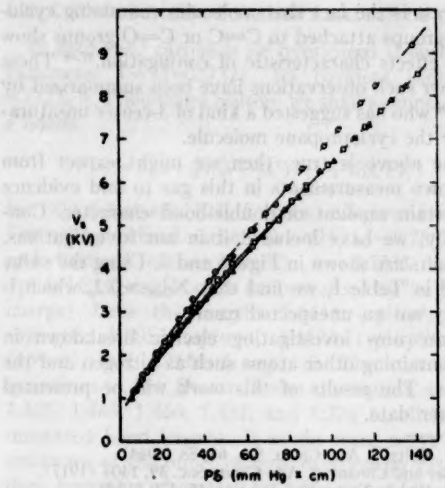

FIG. 4. Sparking potentials of butene isomers. ○ *n*-butene-1; □ isobutene; △ *n*-butene-2.

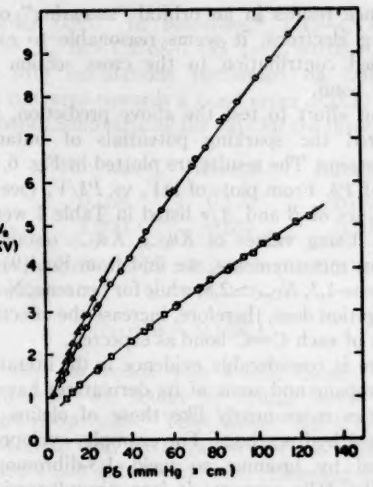

FIG. 6. Sparking potentials of cyclopropane □, butadiene-1,3 ○, and benzene △ as functions of $P\delta$.

in all of the hydrocarbon gases thus far considered. In fact, its use as a tool for predicting certain aspects of breakdown in more complex hydrocarbon gases does not seem unwarranted at this time.

In contrast to the results tabulated in Table I, the recent measurements of Heylen[11] indicate that stepwise methyl substitution on the basic ethylenic structure has little or no effect upon the constant B. As a result, he finds it more natural to assign a single cross section to all ethylenic derivatives independent of methyl substitution or location. Although the validity of such an interpretation cannot be discounted at this time, it is based upon results which are not in agreement with those of the present investigation. Further comment must await a more extensive investigation of the breakdown mechanism in these complex molecular gases.

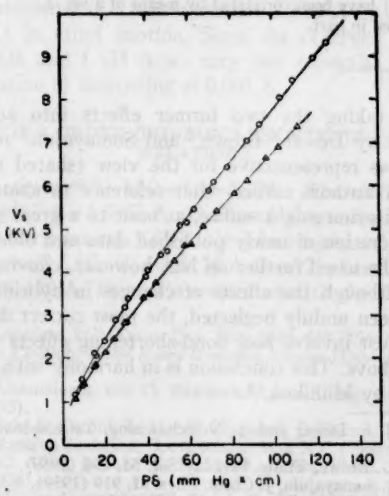

FIG. 5. Sparking potentials of pentene isomers. ○ *n*-pentene-1; △ 2-methylbutene-2.

C. Butadiene, Benzene, and Cyclopropane

As a result of the foregoing, it should be possible to simplify and generalize Eq. (8) to read

$$B/\epsilon_i^{\frac{1}{2}} = K'\theta = K'(N_{C-H}\theta_{C-H} + N_{C-C}\theta_{C-C}),$$

$$K' = K\nu^{\frac{1}{2}}\rho^{\frac{1}{2}} \quad (9)$$

which should apply to any hydrocarbon gas containing C—H, C—C, and C═C bonds. In this form, it can be extended to include molecules containing more than one C═C bond. In most such gases, the most stable configuration is one in which the C═C bonds alternate, giving rise to conjugation and resonance effects. Since

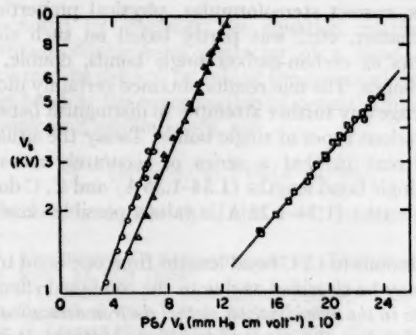

FIG. 7. Log V_s vs $P\delta/V_s$ for cyclopropane □, butadiene-1,3 △, and benzene ○.

resonance results in an orbital "smearing" of the π-bonding electrons, it seems reasonable to expect na increased contribution to the cross section of each double bond.

In an effort to test the above prediction, we have measured the sparking potentials of butadiene-1,3 and benzene. The results are plotted in Fig. 6, as functions of $P\delta$. From plots of $\ln V_s$ vs $P\delta/V_s$ (see Fig. 7), the values of B and A/r listed in Table I were determined. Using values of $K\theta_{C-H}$ $K\theta_{C=C}$ obtained from previous measurements, we find from Eq. (9) that for butadiene-1,3, $N_{C=C}\simeq 2.8$, while for benzene, $N_{C=C}\simeq 3.5$. Conjugation does, therefore, increase the effective cross section of each C=C bond as expected.

There is considerable evidence in the literature that cyclopropane and some of its derivatives have certain properties more nearly like those of olefins than of saturated hydrocarbons. For example, cyclopropane is attacked by bromine to yield 1,3-dibromopropane. Similarly, HBr converts it into propylbromide. Also of interest is the fact that molecules containing cyclopropyl groups attached to C=C or C=O groups show certain effects characteristic of conjugation.[17,18] These and other such observations have been summarized by Walsh,[19] who has suggested a kind of 3-center unsaturation for the cyclopropane molecule.

If the above is true, then we might expect from breakdown measurements in this gas to find evidence of a certain amount of double-bond character. Consequently, we have included it in our investigations. The results are shown in Figs. 6 and 7. Using the value of B/ϵ_i[4] in Table I, we find that $N_{C=C}\simeq 0.2$, which is certainly not an unexpected result.

We are now investigating electric breakdown in gases containing other atoms such as nitrogen and the halogens. The results of this work will be presented at a later date.

[17] I. M. Koltz, J. Am. Chem. Soc. **66**, 88 (1944).
[18] Kohler and Conant, J. Am. Chem. Soc. **39**, 1404 (1917).
[19] A. D. Walsh, Trans. Faraday Soc. **45**, 179 (1949).

THE JOURNAL OF CHEMICAL PHYSICS VOLUME 33, NUMBER 2 AUGUST, 1960

Molecular Structure Correlations

BØRGE BAK AND LISE HANSEN-NYGAARD

Chemical Laboratory of the University of Copenhagen, Copenhagen, Denmark

(Received December 21, 1959)

The molecular structure of methane, ethane, ethylene, acetylene, ethyl fluoride, benzene, butadiene, allene, butatriene, propylene, cyclooctatetraene, methyl acetylene, diacetylene, methyl cyanide, methyl *iso*cyanide, vinyl cyanide, carbon dioxide, formaldehyde, acetaldehyde, propynal, acrolein, formic acid, methyl formate, formamide, and acetyl cyanide (25 molecules) have been correlated by means of a set of empirical parameters, the physical meaning of which is discussed in part.

UNTIL recently the great success of organic chemists in predicting chemical reaction possibilities, correct stereoformulas, physical properties of bulk matter, etc., was partly based on such simple concepts as carbon-carbon single bonds, double, and triple bonds. The fine results obtained certainly did not encourage any further attempts to distinguish between, say, various types of single bonds. Today the situation is different in that a series of accurately measured C, C single bond lengths (1.54–1.36 A) and C, C double bond lengths (1.34–1.28 A) awaits a possible classification.

Variations in C, C bond lengths from one bond to the next may be classified as due to the combined effects of *changes in the hybridization status, electron delocalization,* and influences of a not yet identified character. It is the aim of the present paper to show how far one can get by solely taking the two former effects into account. Papers by Dewar,[1] Brown,[2] and Somayajulu[3] may be taken as representative for the view (shared by the present authors earlier) that reference to changes in hybridization might suffice, at least to a great extent. Consideration of newly published data and older data to be discussed further on has, however, convinced us that although the effects of changes in hybridization have been unduly neglected, the most correct description must involve *both* bond-shortening effects underlined above. This conclusion is in harmony with recent papers by Mulliken.[4,5]

[1] M. J. S. Dewar and A. N. Schmeising, Tetrahedron **5**, 166 (1959).
[2] M. G. Brown, Trans. Faraday Soc. **55**, 694 (1959).
[3] G. R. Somayajulu, J. Chem. Phys. **31**, 919 (1959).
[4] R. S. Mulliken, Tetrahedron **5**, 253 (1959).
[5] R. S. Mulliken, Tetrahedron **6**, 68 (1959).

I. C, C SINGLE BOND. COVALENT RADIUS OF CARBON

In diamond,[6] carbon is sp^3 hybridized (hybridization parameter $\lambda=\sqrt{3}=1.732$). Its covalent radius $r_C=0.7722_8$ A. Following Coulson[7] we shall assume, that for σ bonds

$$r_C=k(1+\tfrac{4}{3}\sqrt{3}\lambda+\tfrac{3}{2}\lambda^2)/(1+\sqrt{3}\lambda+\lambda^2) \qquad (1)$$

for $1\leqslant\lambda\leqslant 2$. $r_C=0.7722_8$ A and $\lambda=\sqrt{3}$ gives $k=0.5690_3$. For sp^2-hybridized carbon ($\lambda=\sqrt{2}$), $r_C=0.7587$ A, for sp-hybridized carbon ($\lambda=1$), $r_C=0.7333$ A. Thus, "pure" C, C single bonds (unperturbed by "migrating" charge) have the lengths 1.5445 (sp^3-sp^3), 1.5309 (sp^3-sp^2), 1.5055 (sp^3-sp), 1.5174 (sp^2-sp^2), 1.4920 (sp^2-sp), and 1.4666 (sp-sp) A. The corresponding quantities in the Dewar-Brown description are 1.544, 1.510, 1.465, 1.466, 1.432, and 1.374 A, all based on measured bond lengths. It might seem naive to base estimates of the effect of hybridization on Eq. (1) as done here. One advantage by doing so can immediately be pointed out (Coulson[7]). Taking $d_{CH}=1.093$ A in methane, one calculates d_{CH} (ethylenic) $=1.093-(0.7722-0.7587)=1.0795$ A and d_{CH} (acetylenic) $=1.093-(0.7722-0.7333)=1.0541$ A in good agreement with experiment. In the Dewar-Brown description it is rather troublesome, although not meaningless *a priori*, that carbon has one covalent radius in a C,C bond, and a quite different in a C, H bond.

λ is, of course, not limited to the values $\sqrt{3}$, $\sqrt{2}$, and 1. Data for *ethane*[8] and *ethyl fluoride*[9] used with the formula

$$\lambda_i\lambda_j\cos\theta=-1 \text{ (orthogonality condition)} \qquad (2)$$

for bonds i, j forming the angle θ gives $\lambda(C, C)=1.678$ for ethane. For ethyl fluoride the C, C linkage ha $\lambda=1.649$ in the CH_3 end, and $\lambda=1.654$ in the CH_2F end. Both are converted to covalent radii and added. The calculated C, C distances are 1.540 A in ethane, 1.538 A in ethyl fluoride. Since the observed values are 1.536 and 1.533 A we may just recognize a (delocalization ?) shortening of 0.005 A.

II. BOND ORDER (BO)-BOND SHORTENING (BS) RELATIONS

In *ethylene*[10,11] $\lambda(C{=}C)=1.301$. Therefore, the "σ-length," $l_\sigma=1.5057$ A. The bond shortening due to the 2 π-electrons is 1.5057–1.338 (obs length) $=0.168$ A. In *benzene*,[12] $l_\sigma(C, C)=1.5174$ A ($\lambda=\sqrt{2}$); bs $=1.5174-1.397=0.120$ A. This bs is associated with the Coulson bond order 0.667. In *butadiene*,[13] $\lambda(C{-}C)=1.408$, $l_\sigma=1.5168$ A, bs $=1.5168-1.483$ (obs) $=0.034$ A. Numerous MO calculations performed on butadiene[4] seem to converge towards a bond order of 0.20 for the central bond. Summarizing the data for the three bonds:

	Ethylene	Benzene	Butadiene
bs A	0.168	0.120	0.034
bo	1.000	0.667	0.202

it is seen that the bo–bs relation is practically linear. The formula

$$\text{bo}=\text{bs A}/0.168\text{ A} \qquad (3)$$

can be used for bonds with $\lambda\sim\sqrt{2}$. Closely related "π shortenings" are found for double bonds with a sp^2-sp and sp-sp "core." Thus, *allene*[14] has $\lambda(C{=}C)=1.290$ (at CH_2) and 1.000 (at $=C=$). $l_\sigma=1.4855$ A. bs $=1.4855-1.309$ (obs) $=0.177$ A. Assuming linearity as in Eq. (3)

$$\text{bo}=\text{bs A}/0.177\text{ A} \qquad (4)$$

for bonds with $\lambda\sim1.15$. The central bond in *butatriene*[15] has $\lambda=1$, $l_\sigma=1.4666$ A, bs $=1.4666-1.284$ (obs) $=0.183$ A. Hence

$$\text{bo}=\text{bs A}/0.183\text{ A} \qquad (5)$$

for bonds with $\lambda\sim1$. By extrapolation from these equations, sp^3-sp^2 bonds obey Eq. (6) ($\lambda\sim1.60$):

$$\text{bo}=\text{bs A}/0.162\text{ A} \qquad (6)$$

Figure 1[16] gives a graph of Eqs. (3)–(6) and it shows also how the corresponding curves would seem to be according to Dewar-Brown (dotted curves).

In view of the close physical relationship which presumably exists between double bonds only differing in σ character, the neat bunching of the fully drawn curves is appealing, while the large scatter in the dotted Dewar-Brown curves (sketched) is harder to understand.

III. ESTIMATION OF "π" CHARGE OF BONDS

As noted by Pauling[17] the equation relating the percentage double-bond character of a bond to its length may be derived by taking the potential function of the bond as the superposition of potential functions for single and double bonds, viz.,

$$V=\tfrac{1}{2}k_1(s-x)^2w_1+\tfrac{1}{2}k_2(x-d)^2w_2$$

in which k_1 is the C—C, k_2 the C=C force-constant,

[6] K. Lonsdale, Phil. Trans. Roy. Soc. **A240**, 219 (1946).
[7] C. A. Coulson, *Victor Henri Memorial Volume* (Desoer, Liege, 1948), p. 15.
[8] A. Almenningen and O. Bastiansen, Acta Chem. Scand. **9**, 815 (1955).
[9] B. Bak, S. Detoni, L. Hansen-Nygaard, J. Tormod Nielsen, and J. Rastrup-Andersen, Spectrochim. Acta XX (1960).
[10] H. C. Allen, Jr., and E. K. Plyler, J. Am. Chem. Soc. **80**, 2673 (1958).
[11] J. M. Dowling and B. P. Stoicheff, Can. J. Phys. **37**, 703 (1959).
[12] A. Langseth and B. P. Stoicheff, Can. J. Phys. **34**, 350 (1956).
[13] A. Almenningen, O. Bastiansen, and M. Traetteberg, Acta Chem. Scand. **12**, 1221 (1958).
[14] B. P. Stoicheff, Can. J. Phys. **33**, 811 (1955).
[15] B. P. Stoicheff, Can. J. Phys. **35**, 837 (1957).
[16] H. C. Longuet-Higgins and F. H. Burkitt, Trans. Faraday Soc. **48**, 1077 (1952).
[17] L. Pauling, *The Nature of the Chemical Bond* (Cornell University Press, Ithaca, New York, 1945).

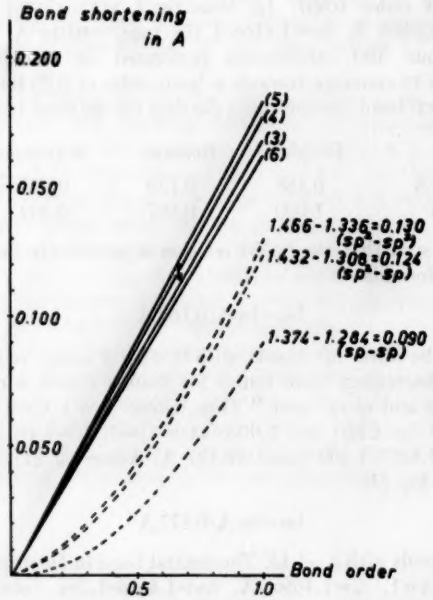

FIG. 1. Bond order-bond distance curves (the straight lines) according to the authors' description. Dotted curves according to a Dewar-Brown description. For the central bond in butatriene, Longuet-Higgins gives the bond order 1.447.[16]

s and d are the lengths of pure single and double bonds, and w_1 and w_2 are weight functions, $w_1+w_2=1$. The equilibrium position is fixed by putting $\partial V/\partial x=0$, resulting in

$$k_1w_1/k_2w_2=(x-d)/(s-x). \tag{7}$$

If there are n_π electrons in the bond, $n_\pi=2\,w_2$. Consequently

$$n_\pi=2/\{[(x-d)/(s-x)]K_{12}+1\} \tag{8}$$

where the magnitude of $K_{12}=k_2/k_1=\mu_2\nu_2^2/\mu_1\nu_1^2$ may be estimated from spectroscopic data. ν_i is the vibration frequency associated with the vibrating, reduced mass μ_i. $\mu_i\nu_i^2$ depends upon the type of hybridization of the σ bonds involved. In methyl acetylene,[18] the C—C (sp^3-sp) bond has $\mu_2\nu_2^2\sim526$. In propylene,[18] the C—C (sp^3-sp^2) bond has $\mu_2\nu_2^2\sim814$. In ethane,[18] the C—C (sp^3-sp^3) bond has $\mu_2\nu_2^2\sim740$. The C=C bond in ethylene has $\mu_2\nu_2^2\sim1844$, and about the same is found for, e.g., allene.[18] According to these data, $2.26<K_{12}=k_2/k_1<3.50$.

Now, force constants are reliable numbers only close to the position of equilibrium. Are we close enough throughout the whole bond-length interval in question, i.e., for sp^2-sp^2 bonds in the 1.35–1.52 A region? In an *intermediate* point, e.g., the benzene point ($x=1.397$ A, $s-x=0.120$ A, $x-d=0.049$ A, $w_1=w_2=\frac{1}{2}$)

$$V=\tfrac{1}{2}\cdot k_1\cdot0.120^2\cdot10^{-16}\cdot\tfrac{1}{2}+\tfrac{1}{2}\cdot k_2\cdot0.048^2\cdot10^{-16}\cdot\tfrac{1}{2}$$

With $k_1=4.5\cdot10^5$ d/cm and $k_2=0.5\cdot10^5$ d/cm, we get

$$V=\tfrac{1}{2}\cdot1630\text{ cm}^{-1}+\tfrac{1}{2}\cdot550\text{ cm}^{-1}$$

Since the vibrational frequencies refer to points on the single- and double-bond potential curves in the 500–1500 cm^{-1} region for the single bond, and 800–2400 cm^{-1} for the double bond we are well within the domain where k_1 and k_2 may be taken as constants.

At *the end points*, e.g., near $x=d$, $\frac{1}{2}\cdot k_1\cdot(s-x)^2\sim\frac{1}{2}\cdot4.5\cdot10^5\ 0.168^2\cdot10^{-16}$ which amounts to 3200 cm^{-1}, i.e., between the second and third excited level. Taking the frequencies as being 1–2% "anharmonic" per excitation, the "effective" k_1 will be about 6% *higher* than at equilibrium, because we are at the *compression* side of the single bond potential curve. Similarly, close to $x=s$, $\frac{1}{2}\cdot k_2\cdot0.168^2\cdot10^{-16}$ ergs/mole$=6750$ cm^{-1} in the region of the fourth excited level. An anharmonicity in the frequencies of 1–2% per excitation means that the "effective" k_2 will be about 12% *lower* than at equilibrium, because we are at the "dissociative" side of the C=C potential curve. Therefore, at $x-d$, the effective $K_{12}^{eff}=k_2^{eff}/k_1^{eff}$ is about 6% *lower* than at the benzene point. At $x=s$, K_{12}^{eff} is about 12% *lower* than in intermediate points. K_{12}^{eff} is, therefore, limited to the interval $2<K_{12}^{eff}<3$ for all points.

The actual value of K_{12}^{eff} is now traditionally fixed by inserting $n_\pi=1$ and $x=1.397$ A (C, C in benzene) in Eq. (8). For double bonds with a sp^2-sp^2 "core," $d=1.350$ A [the length of the C=C bond in (hypothetical) sp^2-sp^2 hybridized ethylene$=1.338$ (measured)$+1.5174-1.5057=1.3497$ A], and $s=1.517$ A. $K_{12}=(s-x)/(x-d)=2.55$. Experimental inaccuracy taken into regard, $K_{12}=2.55\pm0.20$. The K to use at the end points may be 6–12% smaller, but even with this included we are well within the $2<K_{12}<3$ interval.

Now let us take a corresponding Dewar-Brown description. Unless the legitimacy of the whole procedure is highly questioned, they would have to put $K_{12}=(1.466-1.397)/(1.397-1.338)=1.17\pm0.20$, if we include experimental inaccuracy. Confronted with the condition $2<K_{12}<3$, there is no doubt which description is the better.

A quite similar consideration for *three bonds with a sp-sp "core"* (the central bond in diacetylene, the central bond in butatriene, and acetylene) shows that if the single and triple bond potential curves were parabolas in the whole 1.201–1.465 A interval, K_{13} in the equation

$$n_\pi=4/\{[(x-1.201)/(1.465-x)]K_{13}+1\} \tag{9}$$

would be the ratio of the triple-bond force constant, k_3, to the single-bond force constant, k_1. This ratio is about three, but the "effective" k_3 deviates considerably

[18] G. Herzberg, *Molecular Spectra and Molecular Structure. II.* (D. Van Nostrand Company, Princeton, New Jersey, 1954).

from the "equilibrium," k_3, near $x=1.465$ A as much as 30–40%. Also, $k_1^{eff} \sim 1.30\ k_1$ near $x=1.201$ A. At $x=1.201$ A, $k_3^{eff}/k_1^{eff} \sim 3/1.30=2.30$, at $x=1.465$ A, $k_3^{eff}/k_1^{eff} \sim 3 \cdot 0.65=1.95$.

Setting $n_\pi=2$ for $x=1.284$ A (butatriene) we calculate $K_{12}=2.18$ in good agreement with our estimates.

Again, in a Dewar-Brown description $K_{12}=(1.374-1.284)/(1.284-1.201)=1.08$, far below what to be expected.

IV. ADJACENT BONDS

The natural basis for the view that hybridization is the dominant factor to produce bond shortening is that such short bonds are usually adjacent to multiple bonds of apparently unchanged length. To take *methyl acetylene*,[19] its C—C distance is 1.458 A, whereas its C≡C distance is 1.207 A. An unperturbed C≡C distance is presumably present in acetylene, where it is measured to 1.201 A. The difference 1.207–1.201 A may be taken as 0.006±0.004 A, taking experimental inaccuracy into account. The easy conclusion to draw from data like these is, that the multiple-bond stretching is negligible, so that the C—C bond shortening would be due solely to hybridization. This is, in fact, the Dewar-Brown description. It is only justified if the multiple-bond stretchings to be expected are large enough to be measured with certainty. Up-to-date π-electron theory shows that these stretchings should, indeed, be small.[5] We shall try to estimate their order of magnitude by means of Eq. (8).

(1) One double bond donates charge to one adjacent single bond, (e.g., propylene). If x_2, the donor length, is greater than d, the bond has donated the charge

$$\frac{2K_{12}(x_2-d)e}{K_{12}(x_2-d)+(s-x_2)}=\frac{2K_{12}\beta e}{\beta(K_{12}-1)+(s-d)}, \tag{10}$$

defining $\beta=x_2-d$. e is the electronic charge. Simultaneously, the acceptor bond of length x_1 accepts

$$\frac{2(s-x_1)e}{K_{12}(x_1-d)+(s-x_1)}=\frac{2\alpha e}{\alpha(1-K_{12})+K_{12}(s-d)}. \tag{11}$$

Equating (10) and (11) gives

$$\beta=\frac{\alpha(s-d)}{(s-d)K_{12}^2-\alpha K_{12}(K_{12}-1)-\alpha(K_{12}-1)}$$

$$=\frac{\alpha(s-d)}{(s-d-\alpha)K_{12}^2+\alpha}. \tag{12}$$

Setting $\alpha=0.050$ A, $s-d=0.168$ A, $K_{12}=2.55$ gives

$$\beta=0.010 \text{ A}.$$

We shall investigate whether published data for propylene,[20] and cyclooctatetraene[21] are in accordance with this. For *propylene*, l_σ(C—C) = 1.5148 A, bs = 1.5148 − 1.479 (obs) = 0.036 A. The calculated double bond stretching = 0.007 A. Actually, l_σ(C=C) = 1.5101 A, so that the unstretched bond would be 1.342 A. The bond stretching is, therefore, 1.357 (obs) − 1.342 = 0.015 A. The discrepancy is well within the experimental error.

In a Dewar-Brown description, propylene is impossible to fit because the predicted sp^3-sp^2 distance is 1.510 A, leaving 0.031 A unexplained.

For *cyclooctatetraene*, l_σ(C—C) = 1.5114 A, bs = 1.5114 − 1.462 (obs) = 0.049 A. The predicted double-bond stretching = 0.010 A. Since l_σ(C=C) = 1.4968 A, the unstretched bond would be 1.329 A. The observed bond length is 1.334 A, leaving 0.005 A unexplained, well within the experimental error. In a Dewar-Brown description a sp^2-sp^2 bond, nonshortened by migrating charge, is simply *defined* to be 1.462 A long. See, however, a later remark on cyclooctatetraene.

(2) One triple bond donates charge to one adjacent single bond.

When the triple bond loses a small amount of charge, it approximately tends to change towards the double bond which we find in the central bond of butatriene. We shall put

$$n_\pi=2+2/\{K_{23}[(x-t)/d-x)]+1\}$$

for this situation, K_{23} being the ratio between a triple-bond and a double-bond force constant, $t=1.201$ A and $d=1.284$ A. Abbreviating $x-t=\gamma$, we find that a triple bond, stretched γ A, has donated

$$2K_{23}\gamma/[\gamma(K_{23}-1)+(d-t)].$$

Therefore

$$\gamma=\frac{\alpha(d-t)}{(s-d)K_{12}K_{23}-\alpha K_{23}(K_{12}-1)-\alpha(K_{23}-1)}$$

$$=\frac{\alpha(d-t)}{(s-d-\alpha)K_{12}K_{23}+\alpha}. \tag{13}$$

Setting $d-t=0.083$ A, $s-d=0.168$ A, $K_{12}=2.55$, K_{23} (estimated) = 1.5, and $\alpha=0.050$ A gives

$$\gamma=0.008 \text{ A}.$$

In methyl acetylene, l_σ (C—C) = 1.5006 A, bs = 1.5006 − 1.458 (obs) = 0.043 A, corresponding to an expected C≡C lengthening of 0.007 A. The observed lengthening is 0.006±0.004 A, in fine agreement with the calculated.

(3) Two double bonds donate charge to one connecting single bond, (e.g., butadiene),

$$\beta=\tfrac{1}{2}\alpha(s-d)/[(s-d-\alpha)K_{12}^2+\alpha]. \tag{14}$$

[19] L. F. Thomas, E. I. Sharrard, and J. Sheridan, Trans. Faraday Soc. 51, 619 (1955).

[20] D. H. Christensen and D. R. Lide, Jr., National Bureau of Standards, Washington, D. C. (private communication).

[21] O. Bastiansen, L. Hedberg, and K. Hedberg, J. Chem. Phys. 27, 1311 (1957).

TABLE I.

	l_σ(C—C)	(C—C exptl)	bs	Triple-bond lengthening predicted	found
CH_3CN	1.5046	1.458	0.047	0.008	0.012 A
CH_3NC	1.4511	1.427	0.024	0.004	0.022 A
	l_σ(C—N)	(C—N exptl)			

From the single-bond shortening 0.050 A, a double-bond stretching of 0.005 A is calculated. Data from butadiene[13] give l_σ (C—C) = 1.5168 A, bs = 1.5168 − 1.483 (obs) = 0.034 A. The calculated bond stretching of each of the double bonds is 0.0034 A. l_σ (C═C) = 1.5070 A, so that the length of the unstretched bond would be 1.339 A. The observed length is 1.337± 0.005 A, i.e., we observe a slight *contraction*.

(4) Two triple bonds donate charge to one connecting single bond,

$$\gamma = \tfrac{1}{2}\alpha(d-t)/[(s-d-\alpha)K_{12}K_{23}+\alpha]. \qquad (15)$$

For a single-bond shortening of 0.050 A, a triple-bond stretching of 0.004 A is foreseen. In diacetylene,[22] l_σ (C—C) = 1.4666 A, bs = 1.4666 − 1.376 (obs) = 0.091 A. The calculated triple-bond lengthening is 0.007 A. Callomon and Stoicheff assumed that the C≡C distance was 1.205 A, i.e., that the lengthening is 0.004 A. Under these conditions the agreement is not bad.

To summarize, no data exist in today's literature that seriously disagree with a "Mulliken" description. The argument, that multiple-bond lengthenings are *not* observed, is probably not valid since lengthenings are found, roughly agreeing with expectance.

As mentioned by Mulliken,[5] the fact that multiple bonds are conjugated, *eo ipso* means a multiple-bond *shortening*, compensated or overcompensated by the delocalization lengthening. This effect would not seem to exist in the case of one double bond adjacent to one single bond, but in this respect, cyclooctatetraene should rather have been placed under (3) than under (1).

One cannot, however, leave the subject without feeling the need to emphasize the usefulness of fresh experiments, performed to get structure determinations of higher accuracy. Special efforts must be directed towards reliable extrapolation of the data to the hypothetical, vibrationless state, since the error of omittance of this is comparable in magnitude to some of the effects discussed here.

V. COVALENT RADII

Improvements in structural determinations have made it possible to renew the discussion on the existence of fixed differences in covalent radii, e.g., $r_C - r_N = D(C, N)$, $r_C - r_O = D(C, O)$. Although the physical basis for such constants seems rather reasonable, disagreement arose, partly because of neglect of hybridization status and migrating charge existence.

Data for *methyl amine*[23] indicate that a C, C bond with the same hybridization constants as the C, N bond ($\lambda = 1.732$ at CH_3 and $\lambda = 1.393$ at NH_2) would have $l_\sigma = 1.530$ A. Since the measured length is 1.474 A, $D(C, N) = 0.056$ A. We can quickly verify that the number is reasonable. Subtracting it from the C, C distance of 1.397 A in benzene, we practically "land" on the C, N distance in pyridine (1.340 A). Subtracting it from the (pure sp^2-sp^2) C═C distance in ethylene of 1.350 A, we get 1.294 A, close to measured C═N lengths. Also, subtracted from the acetylenic C, C distance of 1.201 A we get 1.145 A, just below the length of most C≡N bonds.

We shall assume that if $D(C, N)$ is first added to the measured C, N distance, it is legitimate to use Eqs. (8)–(15) for estimation of charge transfer. The viewpoint seems confirmed by data (see Table I) from CH_3CN[19] and CH_3NC.[24]

Vinyl cyanide,[25] has l_σ (C—C) = 1.4966 A, bs = 1.4966 − 1.425$_6$ (obs) = 0.071 A, l_σ (C═C) = 1.5001 A, so that the bond lengthening = 1.339 (obs) − (1.500 − 0.168) = 0.007 A. This can be done at the expense of 0.035-A shortening of a single-bond which is available. The triple bond, C≡N, is stretched by 1.164 (obs) − 1.145 = 0.019 A. This, in itself, would more than compensate the whole C—C shortening of 0.071 A. Roughly, the observed C—C shortening accounts for about half the multiple-bond lengthenings. Under the present circumstances this is not too dissatisfactory.

Although fairly complete data exist for CH_3OH,[26] they do not suffice for fixing the hybridization status of the C, O bond at the oxygen end, since all that we know is $\lambda_{O-C} \cdot \lambda_{O-H} \cos\theta = -1$, where $\theta = 108°52'$. If we turn to double-bonded oxygen in aldehydes, ketones, etc., the hybridization status is also uncertain. However, in O═C═O, where the C═O distance is 1.6000 A,[27]

[22] J. H. Callomon and B. P. Stoicheff, Can. J. Phys. **35**, 373 (1957).

[23] D. R. Lide, Jr., J. Chem. Phys. **27**, 343 (1957).

[24] M. Kessler, H. Ring, R. Trambarulo, and W. Gordy, Phys. Rev. **79**, 54 (1950).

[25] C. C. Costain and B. P. Stoicheff, J. Chem. Phys. **30**, 777 (1959).

[26] P. Venkateswarlu and W. Gordy, J. Chem. Phys. **23**, 1200 (1955).

[27] G. Herzberg and L. Herzberg, J. Opt. Soc. Am. **43**, 1037 (1953).

we may guess, that O is sp hybridized, i.e. has the same hybridization as the central carbon in butatriene. Here, the appropriate C=C distance is 1.284 A, so that accordingly $D(C, O) = 0.124$ A.

Formaldehyde,[28] has l_σ (C=O) = 1.5290 − 0.124 = 1.405 A (assuming sp^2 oxygen). The shortening effect of 2π electrons being taken as 0.168 A, we calculate a C=O length of 1.237 A. The experimental value is 1.230±0.017 A.

In *acetaldehyde*,[29] l_σ (C—C) = 1.5227 A, the observed length is 1.501 A, so that bs = 0.0217 A. This would account for a 0.004–0.005-A lengthening of the C=O bond. The measured C=O bond length = 1.216 A. *Assuming* that O is sp^2 hybridized ($\lambda = \sqrt{2}$), l_σ (C=O) = 1.5123 − 0.124 = 1.388 A. The 2π bond shortening is 0.168 A, so that the predicted bond length for sp^2-hybridized oxygen is 1.220 A. The fit is satisfactory.

For *propynal*,[30] (assuming again sp^2 oxygen), l_σ (C=O) = 1.5037 − 0.124 = 1.380 A. Setting the 2 π shortening to 0.168, we get a calculated length of 1.212 A, excellently agreeing with the observed value, 1.215 A. The C—C bond has l_σ = 1.4979 A, bs = 1.4979 − 1.4446 = 0.053 A. This would account for a lengthening of the adjoining C≡C bond amounting to 0.008 A. The experimental value is also 0.008 A.

Acrolein[31] has l_σ (C=O) = 1.5177 − 0.124 = 1.394 A. The unperturbed C=O bond would be 1.394 − 0.168 = 1.226 A long. One finds 1.22 A. The C—C length in acrolein is 1.45 A. l_σ (C—C) = 1.5124 A, so that bs = 0.062 A. This would account for a 0.012-A lengthening of the C=C bond. l_σ (C=C) = 1.512 A. The unperturbed C=C bond length = 1.512 − 0.168 = 1.344 A, the observed bond length 1.36 A. The observed stretching = 0.016 A, agreeing with the predicted.

Apparently, aldehyde oxygen may be sp^2 hybridized. Let us investigate, an ester and an acid.

In *methyl formate*,[32] l_σ (O—CH_3) = 1.550 − 0.124 = 1.426 A. The observed length is 1.437 A. l_σ (C—OCHO) = 1.529 − 0.124 = 1.405 A. The observed length is 1.334 A, so that bs = 0.071 A. This would account for a double bond lengthening of 0.014 A. l_σ (C=O) = 1.492 − 0.124 = 1.368 A. Subtracting 0.168 A for 2 π shortening, the unperturbed length 1.200 A is calculated. This is exactly the experimental value.

In *formic acid* proper,[33] l_σ (C—OH) = 1.5268 − 0.124 = 1.403 A. Thus, 1.403 − 1.312 (obs) = 0.091 A, which would explain a bond stretching in the adjoining C=O bond of 0.018 A l_σ (C=O) = 1.513 − 0.124 = 1.389 A. Subtracting 0.168 A for the double bond, the calculated unperturbed length = 1.221 A. The experimental bond length is 1.245 A, i.e., the bond lengthening = 0.024 A (calc 0.018 A).

Therefore, in both acid and methyl ester the double bonded oxygen could fit in as sp^2 hybridized.

We will finally treat a few examples of molecules containing both C, H, N, and O.

In *formamide*,[34] the l_σ (C—N) = 1.525 − 0.056 = 1.469 A. Therefore, bs = 1.469 − 1.376 (obs) = 0.093 A. accounting for a 0.019-A lengthening in an adjoining double bond. If we assume oxygen to be sp^2 hybridized, l_σ (C=O) = 1.502 − 0.124 = 1.378 A. Subtracting 0.168 A for the π-electron effect, we get 1.210 A as compared to 1.193 A experimentally. Taking instead O as sp hybridized gives l_σ (C=O) = 1.477 − 0.124 = 1.353 A. Subtracting for sp^2-sp π-bond shortening 0.177 A gives an unperturbed length of 1.176 A. 1.193 (obs) − 1.176 (calc) = 0.017 A, in fine agreement with the calculated lengthening of 0.019 A.

In *acetyl cyanide*,[35] the C=O bond is close to normal for sp^2-hybridized oxygen. l_σ (C—CN) = 1.501 − 1.466 (obs) = 0.035 A, being capable of explaining a stretching of the adjoining C≡N bond by 0.006 A. The measured stretching is 0.019 A.

In a Dewar-Brown description the predicted C—CN length is 1.432 A, i.e., the measured length would be 0.034 A too *long*.

As a whole, the existence of electron delocalization in compounds like formic acid, its methyl ester, and its amide is very hard to deny in view of their geometry.

Hence, the concepts, "σ length," "π shortening," and "covalent radius" as defined here seem to be useful in correlating structures of rather great diversity.

ACKNOWLEDGMENT

The research reported in this paper has been sponsored in part by the Air Force Office of Scientific Research of the Air Research and Development Command U.S. Air Force, through its European Office.

[28] D. W. Davidson, B. P. Stoicheff, and H. J. Bernstein, J. Chem. Phys. **22**, 289 (1954).
[29] R. W. Kilb, Chun Chia Lin, and E. B. Wilson, Jr., J. Chem. Phys. **26**, 1695 (1957).
[30] C. C. Costain and J. R. Morton, J. Chem. Phys. **31**, 389 (1959).
[31] R. Wagner, J. Fine, J. W. Simmons, and J. H. Goldstein, J. Chem. Phys. **26**, 634 (1957).
[32] R. F. Curl, Jr., J. Chem. Phys. **30**, 1529 (1959).
[33] R. G. Lerner, B. P. Dailey, and J. P. Friend, J. Chem. Phys. **26**, 680 (1957).
[34] C. C. Costain and J. M. Dowling, J. Chem. Phys. **20**, 158 (1960).
[35] L. C. Krisher and E. B. Wilson, Jr., J. Chem. Phys. **31**, 882 (1959).

Utilization of Order-Disorder Theory in Physical Adsorption. I. Fundamental Equations*

S. BUMBLE† AND J. M. HONIG‡

Department of Chemistry, Purdue University, Lafayette, Indiana

(Received February 2, 1959)

The order-disorder theory of Hijmans and de Boer is adapted to a description of equilibrium between a gas and a phase forming a localized submonolayer on an energetically uniform surface. Isotherm equations are derived for adsorption in the absence of lateral interactions, and in the presence of nearest- and next-nearest-neighbor interactions. The Langmuir and Fowler-Guggenheim equations result as special cases of the present treatment. The general theory is then applied to adsorption processes on sites in hexagonal configurations. A discussion of the resulting isotherm equations is presented.

1. FUNDAMENTALS AND DEFINITIONS

IN a series of remarkable papers Hijmans and de Boer[1] have developed a general treatment of order-disorder theory by which the exact solution can be approached to any desired degree of approximation using their systematic and well-delineated procedure. In the present paper this method has been applied to a study of localized physical adsorption processes; it will first be shown that the Langmuir[2] and Fowler-Guggenheim[3] isotherms result as zero- and first-order cases of this more generalized approach. The theory will then be generalized in stages so that the effect of next-nearest-neighbor interactions can be explicitly taken into consideration.

Before going into procedural details the fundamental concepts will be briefly reviewed; for verification of all results quoted below the reader is referred to the original publications[1] and to other sources.[4] Except for a number of minor changes, the original notation[1] is utilized throughout.

The following approximations are necessary in the treatment given below: (a) The surface is considered as consisting of a regular array of repetitive units, termed *sites*, which are the smallest localities that act as centers for gas adsorption. The aggregate of sites forms a *lattice*, which is presumed to be sufficiently large (or closed on itself) so that edge effects may be neglected. (b) Any particle held on the surface is assumed to be localized at a site; no translation can occur in the plane of the surface. (c) All sites are equivalent; in particular, the difference between the lowest energy levels of a particle in the gas phase and on a site is the same for all adsorption centers. (d) Each site can accommodate only one molecule of the adsorbate; sites containing adsorbed molecules are said to be *occupied*. (e) It is assumed that molecules at surface sites remain in the ground state characteristic of the adsorbed species. In actual fact, the large majority of such molecules possess internal degrees of freedom; these effects are ignored to avoid needless complications of the subsequent mathematical analysis. It will be shown later that upon elimination of restriction (e) an extra scaling factor is introduced in the final isotherm equation.

The next approximation (f) is one of methodology and consists in replacing the lattice by a suitable representation amenable to a reasonably simple analysis in terms of statistical mechanics. In the method used by Hijmans and de Boer, the lattice is decomposed into *subfigures*, which represent a limited number of sites in close proximity, abstracted from the lattice. The largest subfigure taken into consideration is termed the *basic figure*, and a collection of identical subfigures is known as a *figure assembly*. The proper procedure for effecting this decomposition has been treated in detail.[1]

The specification of the set of lattice sites which are occupied under prescribed conditions is known as a *configuration* or *occupation state*. Each occupation state of the lattice is reflected in an appropriate configuration of the various figure assemblies; examples of such configurations are furnished in Table I.

Having represented possible distributions of adsorbate among lattice sites by proper occupation states of the figure assemblies, one assigns to each configuration of a given subfigure an energy and a probability of occurrence. From these quantities, the energy and entropy of the system of these assemblies may then be computed. This yields an expression for the free energy; after minimization, the chemical potential of the adsorbed phase is equated with the chemical potential for the gas phase. The resulting expression is equivalent to an isotherm equation. There exist always just enough

* This work was supported by a grant from the Purdue Research Foundation.

† Present address: Eastern Laboratory, E. I. du Pont de Nemours and Company, Gibbstown, New Jersey.

‡ Present address: Lincoln Laboratory, Massachusetts Institute of Technology, Lexington 73, Massachusetts.

[1] J. Hijmans and J. de Boer, Physica **21**, 471, 485, 499 (1955).

[2] I. Langmuir, J. Am. Chem. Soc. **38**, 2267 (1916); **40**, 1361 (1918).

[3] R. H. Fowler and E. A. Guggenheim, *Statistical Thermodynamics* (Cambridge University Press, New York, 1939), Chap. XII.

[4] A fairly complete exposition of the subject material is presented by S. Bumble, Ph.D. thesis, Purdue University, August, 1958. A set of mimeographed notes is also available on request.

TABLE I. Configurations for the triangular lattice.

Figure	Letter designation	$k\eta s$	Distribution number	Multiplicity	Energy
●	a	0	$p_0^{(a)}$ or α_0	1	0
●	a	1	$p_1^{(a)}$ or α_1	1	$-\varepsilon$
●—●	b	0	$p_0^{(b)}$ or β_0	1	0
●—●	b	1	$p_1^{(b)}$ or β_1	2	$-\varepsilon$
●—●	b	2	$p_2^{(b)}$ or β_2	1	$-2\varepsilon+w$
△	c	0	$p_0^{(c)}$ or γ_0	1	0
△	c	1	$p_1^{(c)}$ or γ_1	3	$-\varepsilon$
△	c	2	$p_2^{(c)}$ or γ_2	3	$-2\varepsilon+w$
△	c	3	$p_3^{(c)}$ or γ_3	1	$-3\varepsilon+3w$
◇	d	0	$p_0^{(d)}$ or δ_0	1	0
◇	d	1,1	$p_{1,1}^{(d)}$ or $\delta_{1,1}$	2	$-\varepsilon$
◇	d	1,2	$p_{1,2}^{(d)}$ or $\delta_{1,2}$	2	$-\varepsilon$
◇	d	211	$p_{211}^{(d)}$ or δ_{211}	1	$-2\varepsilon+w$
◇	d	212	$p_{212}^{(d)}$ or δ_{212}	4	$-2\varepsilon+w$
◇	d	22	$p_{22}^{(d)}$ or δ_{22}	1	$-2\varepsilon+w'$
◇	d	31	$p_{31}^{(d)}$ or δ_{31}	2	$-3\varepsilon+3w$
◇	d	32	$p_{32}^{(d)}$ or δ_{32}	2	$-3\varepsilon+2w+w'$
◇	d	4	$p_4^{(d)}$ or δ_4	1	$-4\varepsilon+5w+w'$

constraining conditions to permit the determination of the gas pressure that corresponds to a given degree of coverage of the surface.

The approximation introduced in this procedure is to regard the results pertaining to the figure assemblies as also applicable to the lattice proper. Clearly, this is a serious oversimplification; however, as successively larger basic figures are adopted, the results become increasingly exact. Naturally, the requisite algebraic manipulations also become very much more difficult.

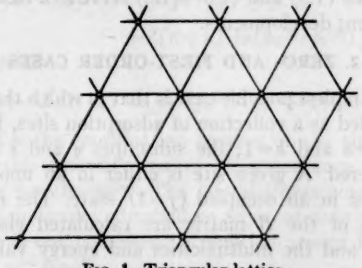

FIG. 1. Triangular lattice.

In what follows, we shall restrict our considerations to the case of the triangular lattice depicted in Fig. 1. The treatment of other types of geometric arrays involves no new fundamental principles.

The first task is to decompose the lattice into groups of representative figure assemblies; the appropriate subfigures are listed in Table I in order of increasing complexity. Each species is assigned a representative symbol, $a, b, c, d, \cdots, m, n$; the letter m also represents the running index for the various arrays, n being reserved for the basic figure.

The various possible modes of occupation for the subfigures are shown in Table I. Each distinguishable configuration is designated by a *distribution number* $p_{j\xi r}^{(m)}$. The first index gives the total number of sites in the m figure that are occupied. In the present notation, the second integer ξ is introduced only if needed, to distinguish between various possible arrangements of the j occupied sites among available positions in the subfigure. Finally, the integer r is introduced, if needed, to distinguish between configurations in which j and ξ are the same, but where different sets of nonequivalent

sites are involved. The purpose of these integers should be clear by reference to Table I. A comma between two subscripts indicates that the integer ξ is missing. Frequently, another triplet of numbers will be needed, and this will be designated as $k\eta s$.

With each configuration, one can associate an energy $\epsilon_{j\xi r}{}^{(m)}$ and a multiplicity $\lambda_{j\xi r}{}^{(m)}$. The total energy of the figure assemblies in their various configurations is then given by

$$E^{(S)}=L\sum_{m=a}^{n}y_n{}^{(m)}\sum_{j\xi r}\lambda_{j\xi r}{}^{(m)}p_{j\xi r}{}^{(m)}\epsilon_{j\xi r}{}^{(m)}, \quad (1.1)$$

where L is the number of lattice sites. The $y_n{}^{(m)}$ represent the number of subfigures of type m in the representative figure assembly; numerical values are obtained by following the procedure of Hijmans and de Boer. The entropy is found by writing out the general combinatorial formula $\Omega(p_{j\xi r}{}^{(m)})$ for the number of complexions corresponding to a given distribution.

After application of Stirling's approximation, the equation reads

$$S^{(S)}=k\ln\Omega=k\sum_{m=a}^{n}y_n{}^{(m)}\ln\Omega(p_{j\xi r}{}^{(m)})$$

$$=-kL\sum_{m=a}^{n}y_n{}^{(m)}\sum_{j\xi r}\lambda_{j\xi r}{}^{(m)}p_{j\xi r}{}^{(m)}\ln p_{j\xi r}{}^{(m)}. \quad (1.2)$$

The total number of particles in the adsorbed phase is given by $N^{(S)}=p_1{}^{(a)}L$.

To characterize the equilibrium state, it will ultimately be necessary to make Eq. (1.2) an extremum, subject to certain constraints. The difficulty here is that the various $p_{j\xi r}{}^{(m)}$ are not mutually independent. To obtain a set of independent variables, Hijmans and de Boer introduce the concept of the *occupied subfigure* g associated with the subfigure m. This refers to the geometric pattern of the k occupied sites, abstracted from all those comprising the m figure. Occupation numbers for the g figures will be designated by the symbol $q_{k\eta}$; it can be shown that the indices s and (m) are superfluous, in the sense that

$$q_{k\eta 1}{}^{(m)}=q_{k\eta 2}{}^{(m)}=\cdots\equiv q_{k\eta}{}^{(m)};$$
$$\cdots=q_{k\eta}{}^{(I)}=q_{k\eta}{}^{(m)}=q_{k\eta}. \quad (1.3)$$

Furthermore, the $q_{k\eta}$ are linearly independent. Equations (1.3) is an analytic representation of the fact that certain occupied subfigures appear to be different when mapped onto the figure assemblies—and hence are assigned different $p_{j\xi r}{}^{(m)}$ symbols—whereas they are really indistinguishable when mapped onto the lattice itself. The requirements (1.3) are known as *consistency conditions*.

One can now write out the number of complexions associated with a given distribution of particles among energy levels pertaining to the adsorbed state and to the gas phase. The logarithm of this quantity is then to be maximized, subject to the restriction that the energy of the total system and the number of particles in this system remain constant. After introducing the method of Lagrangian multipliers one obtains two separate equations,[5] associated with the gas and the adsorbed species, respectively. The Lagrangian multipliers may be identified from the first equation; the second then reads as follows:

$$-(kT)^{-1}(\partial E^{(S)}/\partial q_{k\eta})+(\partial\ln\Omega^{(S)}/\partial q_{k\eta})$$
$$+\mu^{(G)}(\partial N^{(S)}/\partial q_{k\eta})=0 \quad (1.4)$$

$(k=1, 2\cdots;$ all η consistent with a given $k)$.

Upon substituting for $N^{(S)}$ and introducing (1.1) and (1.2) and on taking account of the independent variables, one finds

$$\sum_{m=a}^{n}y_n{}^{(m)}\sum_{j\xi r}\lambda_{j\xi r}{}^{(m)}\left[\epsilon_{j\xi r}{}^{(m)}\frac{\partial p_{j\xi r}{}^{(m)}}{\partial q_{k\eta}}+kT\frac{\partial(p_{j\xi r}{}^{(m)}\ln p_{j\xi r}{}^{(m)})}{\partial q_{k\eta}}\right]$$
$$=\mu^{G}(\partial p_1{}^{(a)}/\partial q_{k\eta}) \quad (1.5)$$

$(k=1, 2\cdots;$ all η consistent with a given $k)$.

After proper evaluation of the differentials in (1.5), one obtains

$$\sum_{m=a}^{n}y_n{}^{(m)}\sum_{j\xi r}\lambda_{k\eta s}{}^{(m)}B_{j\xi r}{}^{(m)}{}_{;k\eta s}[\epsilon_{j\xi r}{}^{(m)}+kT\ln p_{j\xi r}{}^{(m)}]$$
$$=\mu^{(G)}B_{1;1}{}^{(a)}\delta_{1k} \quad (1.6)$$

$(k=1, 2, 3\cdots;$ all η consistent with a given $k)$,

where the elements of the B matrix represent numbers that may be readily determined.[1,4] Equations of the type (1.5) are known as *equilibrium conditions*; it is to be noted that the integer $k=0$ is excluded.

The $p_{j\xi r}{}^{(m)}$ must also satisfy certain other requirements. One set arises from the condition (1.3), coupled with the following functional dependence[1]:

$$\lambda_{k\eta s}{}^{(m)}q_{k\eta s}{}^{(m)}=\sum_{j\xi r}(-1)^{(j-k)}B_{k\eta s;j\xi r}{}^{(m)}\lambda_{j\xi r}{}^{(m)}p_{j\xi r}{}^{(m)}. \quad (1.7)$$

A second set is represented by the *normalization conditions*

$$\sum_{j\xi r}\lambda_{j\xi r}{}^{(m)}p_{j\xi r}{}^{(m)}=1. \quad (1.8)$$

Equations (1.3) and (1.6)–(1.8) serve as a basis for all subsequent developments.

2. ZERO- AND FIRST-ORDER CASES

The simplest possible case is that in which the lattice is regarded as a collection of adsorption sites. For this case, $n=a$ and $k=1$; the subscripts η and s are not encountered. A given site is either in an unoccupied $(j=0)$ or in an occupied $(j=1)$ state. The required elements of the B matrix are calculated elsewhere; $y_a{}^{(a)}=1$, and the multiplicities and energy values ap-

[5] G. S. Rushbrooke, *Statistical Mechanics* (Clarendon Press, Oxford, 1949), Chap. XIII.

propriate to this case are listed in Table I. Equation (1.6) then simplifies to

$$\mu^{(G)} = -kT \ln p_0^{(a)} - \varepsilon + kT \ln p_1^{(a)}. \quad (2.1)$$

There are no consistency requirements, and the normalization condition reads

$$p_0^{(a)} + p_1^{(a)} = 1. \quad (2.2)$$

Now let P represent the gas pressure, $j^{(G)}$ be the internal partition function of a molecule in the gas phase, and define

$$P^* = (2\pi mkT)^{\frac{1}{2}} kT j^{(G)} [\exp(-\varepsilon/kT)]/h^3. \quad (2.3)$$

Then one can write

$$(\mu^{(G)} + \varepsilon)/kT = \ln P/P^* \quad (2.4)$$

and upon introducing (2.4) and (2.2) in (2.1) and solving for $p_1^{(a)} \equiv \theta$ one obtains

$$\theta = 1/[1 + P^*/P] \quad (2.5)$$

In the proper Langmuir equation the quantity P^* is replaced by $P^*/Q^{(s)} \equiv P^0$, where $Q^{(s)}$ is the partition function of an adsorbed molecule on a surface site.[3] To introduce the quantity $Q^{(s)}$ into (2.5) it becomes necessary to take account of the internal degrees of freedom of the adsorbed molecules while deriving the equilibrium relations. This matter is not demonstrated here since no new principles are involved. Equation (2.5) shows that the Langmuir equation represents the zero order approximation in the present theory. This is entirely reasonable; for, in regarding the lattice simply as a collection of sites, each point is treated as an independent entity. Under conditions where the adsorbed molecule is regarded as isolated from all others on the surface, the theoretical analysis must necessarily lead to the Langmuir equation.

In the next higher approximation, the lattice is decomposed into bonds and points; the various configurations encountered in the representative figure assembly and other pertinent information is shown in the first five rows of Table I. In the present case, $n = b$; the $y_n^{(m)}$ numbers and elements of the B matrix may be read off published tables. One can then write out two equilibrium conditions: for $k = 1$

$$-\mu^{(G)} = (1-Z)[\varepsilon + kT \ln(p_0^{(a)}/p_1^{(a)})] + Z[\varepsilon + kT \ln(p_0^{(b)}/p_1^{(b)})] \quad (2.6)$$

and for $k = 2$

$$0 = (Z/2)\{kT \ln[p_0^{(b)} p_2^{(b)}/(p_1^{(b)})^2] + w\}, \quad (2.7)$$

where Z is the coordination number of any site in the lattice; this quantity makes its appearance on substituting for the $y_b^{(m)}$. The lateral interaction energy between molecules adsorbed on adjacent sites is w.

There is one consistency condition arising from the relation $q_1^{(a)} = q_1^{(b)}$,

$$p_1^{(a)} = p_1^{(b)} + p_2^{(b)}, \quad (2.8)$$

and there are two normalization conditions:

$$p_0^{(a)} + p_1^{(a)} = 1 \quad (2.9)$$

$$p_0^{(b)} + 2p_1^{(b)} + p_2^{(b)} = 1. \quad (2.10)$$

To solve this set of equations, rewrite (2.6) as

$$p_1^{(b)}/p_0^{(b)} = Ka_1, \quad (2.11)$$

where

$$K = (K'/a_1)^{1/z} \quad (2.12)$$

and

$$K' = \exp[(\mu^{(G)} + \varepsilon)/kT] Q^{(S)} = P/P^0;$$

$$a_1 = p_1^{(a)}/p_0^{(a)}, \quad (2.13)$$

where K' has been equated with P/P^0 rather than P/P^* by introducing the factor $Q^{(S)}$ in the manner described earlier. By using (2.11) and (2.7), we find

$$p_2^{(b)}/p_0^{(b)} = C(p_1^{(b)}/p_0^{(b)})^2 = C(Ka_1)^2 \quad (2.14)$$

with

$$C = \exp(-w/kT). \quad (2.15)$$

From (2.8) and (2.10) it is easily established that $p_0^{(a)} = p_0^{(b)} + p_2^{(b)}$. Hence it follows that

$$a_1 = \frac{p_1^{(b)} + p_2^{(b)}}{p_0^{(b)} + p_1^{(b)}} = \frac{Ka_1(1 + CKa_1)}{1 + Ka_1}, \quad (2.16)$$

which yields a quadratic polynomial in K with the solution

$$K = (1/2Cp_1^{(a)})\{2p_1^{(a)} - 1 + [1 + 4p_1^{(a)}(1 - p_1^{(a)})(C-1)]^{\frac{1}{2}}\}. \quad (2.17)$$

After setting $\beta = [1 + 4p_1^{(a)} p_0^{(a)}(C-1)]^{\frac{1}{2}}$ and returning to (2.12) one obtains ($\theta \equiv p_1^{(a)}$)

$$P/P^0 = [\theta/(1-\theta)][(\beta - 1 + 2\theta)/2\theta]^z \exp(Zw/kT). \quad (2.18)$$

This is the well-known Fowler-Guggenheim isotherm equation, which follows in the present case as the first order result of a more general approach. In comparing (2.18) to the relation cited in the literature,[3] one should bear in mind the differences in the definitions of w.

The foregoing findings are quite reasonable; for, in regarding the lattice as a superposition of bonds and sites, only the effect of nearest neighbors can be taken into consideration. Under these conditions, one can expect to recover Eq. (2.18), which has previously been demonstrated[3] to apply to this particular physical situation. It is believed that the present approach is somewhat simpler than the one provided in the original treatment.

The properties and applicability of Eq. (2.18) are too well known to require further comment at this point.

3. TRIANGLE APPROXIMATION

We consider now the first extension of our above results, in which the basic figure is a triangular array of

points; $n=c$ and $1\leq k\leq 3$. Again, as shown in Table I, the indices η and s can be disregarded. The required $y_n^{(m)}$ values, multiplicities, energy parameters, and matrix elements are found in Table I and the literature. The following equilibrium relations, based on (1.6) are obtained:

For $k=1$

$$(p_1^{(a)}/p_0^{(a)})[p_0^{(b)}p_1^{(c)}/p_1^{(b)}p_0^{(c)}]^Z=K', \tag{3.1}$$

where K' is defined as in (2.12).

For $k=2$, we have

$$\frac{[p_1^{(b)}p_0^{(c)}p_2^{(c)}]^2}{[p_0^{(b)}p_2^{(b)}][p_1^{(c)}]^4}=C, \tag{3.2}$$

where C is defined as in (2.15).

For $k=3$ we obtain

$$[p_1^{(c)}/p_2^{(c)}]^3/[p_3^{(c)}/p_0^{(c)}]=1. \tag{3.3}$$

In addition, there are the normalization conditions (2.9) and (2.10) and

$$p_0^{(c)}+3p_1^{(c)}+3p_2^{(c)}+p_3^{(c)}=1. \tag{3.4}$$

There exist three consistency relations: $q_1^{(a)}=q_1^{(b)}=q_1^{(c)}$ and $q_2^{(b)}=q_2^{(c)}$. These lead to

$$p_1^{(a)}=p_1^{(b)}+p_2^{(b)} \tag{3.5}$$

$$p_1^{(a)}=p_1^{(c)}+2p_2^{(c)}+p_3^{(c)} \tag{3.6}$$

$$p_2^{(b)}=p_2^{(c)}+p_3^{(c)}. \tag{3.7}$$

Equations (3.1) through (3.7), (2.9), and (2.10) will now be solved so as to furnish an interrelation between $p_1^{(a)}$ and K' involving only the parameter C. For this purpose we rewrite (3.1), (3.2), and (3.3), respectively, as

$$p_1^{(c)}/p_0^{(c)}=K\tau \tag{3.8}$$

$$p_2^{(c)}/p_1^{(c)}=K\sigma \tag{3.9}$$

and

$$p_3^{(c)}/p_0^{(c)}=K^3\sigma^3, \tag{3.10}$$

where

$$K=[K'p_0^{(a)}/p_1^{(a)}]^{1/Z}, \qquad \tau=p_1^{(b)}/p_0^{(b)}$$

$$\sigma=[Cp_2^{(b)}/p_0^{(b)}]^{\frac{1}{3}}. \tag{3.11}$$

By multiplication of (3.8) with (3.9), we obtain

$$p_2^{(c)}/p_0^{(c)}=K^2\tau\sigma. \tag{3.12}$$

Next rewrite the consistency conditions as

$$p_2^{(b)}/p_0^{(c)}=p_2^{(c)}/p_0^{(c)}+p_3^{(c)}/p_0^{(c)}=K^2\sigma[\tau+K\sigma^2] \tag{3.13}$$

$$p_1^{(a)}/p_0^{(c)}=p_1^{(c)}/p_0^{(c)}+2p_2^{(c)}/p_0^{(c)}+p_3^{(c)}/p_0^{(c)}$$

$$=K\tau+2K^2\tau\sigma+K^3\sigma^3 \tag{3.14}$$

$$p_1^{(b)}/p_0^{(c)}=p_1^{(a)}/p_0^{(c)}-p_2^{(b)}/p_0^{(c)}=K\tau[1+K\sigma]. \tag{3.15}$$

A relation between τ and σ may now be found as follows: One can prove from the normalization conditions that $p_0^{(b)}=p_0^{(c)}+p_1^{(c)}$; hence, using (3.8),

$$p_0^{(b)}/p_0^{(c)}=1+p_1^{(c)}/p_0^{(c)}=1+K\tau. \tag{3.16}$$

Keeping in mind the definition for τ and dividing (3.15) by (3.16), one can solve for

$$\tau=[K(1+K\sigma)-1]/K. \tag{3.17}$$

In similar fashion, division of (3.15) by (3.13) yields

$$p_1^{(b)}/p_2^{(b)}=C\tau/\sigma^2=K\tau(1+K\sigma)/K^2\sigma(\tau+K\sigma^2). \tag{3.18}$$

On rewriting this equation as a quadratic in σ and eliminating τ *via* (3.17), one obtains

$$\sigma=C(K-1)/(1-CK), \tag{3.19}$$

where the negative root has been rejected as physically meaningless. Use of (3.19) in (3.17) yields

$$\tau=(K-1)[1+CK(K-1)]/K(1-CK). \tag{3.20}$$

Finally, a polynomial in K will be set up as follows: Divide both sides of (3.5) by $p_0^{(b)}$ and introduce τ and σ on the right-hand side of the resulting equation. This leads to

$$1/p_0^{(b)}=[\tau+\sigma^2C^{-1}]/p_1^{(a)}. \tag{3.21}$$

Likewise, divide (2.10) by $p_0^{(b)}$ on both sides to find

$$1/p_0^{(b)}=1+2\tau+\sigma^2/C. \tag{3.22}$$

On equating (3.21) with (3.22) and eliminating σ and τ by use of (3.19) and (3.20), one obtains a quartic polynomial in K

$$K^4-a_1K^3+a_2K^2-a_3K+a_4=0 \tag{3.23}$$

with

$$a_1=[(2-5\theta)C+(2-3\theta)]/C(1-2\theta)$$

$$a_2=[(C+5)/C] \quad p_1^{(a)}\equiv\theta$$

$$a_3=[(3-5\theta)C+(1-3\theta)]/C^2(1-2\theta)$$

$$a_4=1/C^2. \tag{3.24}$$

That this is the desired isotherm equation follows from the definition of K in (3.11) and the definition of K' as given in (2.13), and the remarks immediately following. Thus, $K'=P/P^0=K^Z\theta/(1-\theta)$, and (3.23) is indeed a relation between θ and P, which involves only w, T, $Q^{(S)}$, and other constants as parameters. It is readily verified that if $C=1$, i.e., if $w=0$, then (3.23) reduces to $(K-1)^4=0$, which is equivalent to the Langmuir equation.

The solution of Eq. (3.23) for $Z=6$ by numerical methods will be discussed in a later section.

4. RHOMBUS AS THE BASIC FIGURE

We now consider the case where the rhombus occurs as the basic figure. This allows for the introduction of next-nearest neighbor interactions w' along the long body diagonal of the rhombus. In physical adsorption

processes attractive lateral interactions arise from van der Waals-London dispersion forces, where the energy of attraction falls off roughly as the sixth power of the distance between adsorbed molecules. Hence one might anticipate that inclusion of the next-nearest neighbor interaction terms will lead to some improvement in the isotherms. This is of even greater importance if repulsive energies due to parallel alignment of molecules with permanent dipoles must be taken into account; these energies vary inversely with the cube of the distance between dipoles.

The calculations, though more tedious than before, follow those of earlier sections in all essentials. One must now take into account the triplet of integers $k\eta s$ as outlined in Table I. The equilibrium relations shown below are derived from (1.6), using $Z=6$, and the energy parameters listed in Table I. The equations are as follows:

For $k=1$ and $s=1$ or 2

$$(p_1^{(a)}/p_0^{(a)})(p_0^{(c)}/p_1^{(c)})^{12}(p_{1,1}^{(d)}/p_0^{(d)})^6(p_{1,2}^{(d)}/p_0^{(d)})^6=K', \tag{4.1}$$

where K' is defined as in (2.13).

For $k=2$, $\eta=1$ and $s=1$ or 2,

$$\left(\frac{p_{212}^{(d)}}{p_0^{(c)}p_2^{(c)}p_{1,2}^{(d)}}\right)^4\frac{p_{211}^{(d)}(p_0^{(d)})^5(p_1^{(c)})^8}{(p_{1,1}^{(d)})^6}=C. \tag{4.2}$$

For $k=2$, $\eta=2$,

$$p_0^{(d)}p_{22}^{(d)}/(p_{1,2}^{(d)})^2=C'\equiv\exp(-w'/kT), \tag{4.3}$$

where w' is the lateral interaction energy between atoms on next-nearest neighbor sites.

For $k=3$, $\eta=1$

$$\left[\frac{p_0^{(c)}(p_2^{(c)})^3}{(p_1^{(c)})^3p_2^{(c)}}\right]^2\left[\frac{(p_{1,1}^{(d)})^2p_{1,2}^{(d)}p_{21}^{(d)}}{p_{211}^{(d)}(p_{212}^{(d)})^2p_0^{(d)}}\right]^3=1. \tag{4.4}$$

For $k=3$, $\eta=2$

$$(p_{1,1}^{(d)}/p_0^{(d)})(p_{1,2}^{(d)}/p_{212}^{(d)})^2(p_{22}^{(d)}/p_{22}^{(d)})=1. \tag{4.5}$$

For $k=4$

$$\frac{p_0^{(d)}p_{211}^{(d)}p_{22}^{(d)}p_4^{(d)}(p_{212}^{(d)})^4}{[p_{1,1}^{(d)}p_{1,2}^{(d)}p_{21}^{(d)}p_{22}^{(d)}]^2}=1. \tag{4.6}$$

Consistency relations may be found from (1.3) and (1.7),

$$p_{211}^{(d)}+p_{21}^{(d)}=p_{212}^{(d)}+p_{22}^{(d)} \tag{4.7}$$

$$p_{1,1}^{(d)}+p_{211}^{(d)}+p_{21}^{(d)}=p_{1,2}^{(d)}+p_{22}^{(d)}+p_{32}^{(d)} \tag{4.8}$$

$$p_1^{(a)}=p_1^{(b)}+p_2^{(b)}=p_1^{(c)}+2p_2^{(c)}+p_3^{(c)}$$
$$=p_{1,2}^{(d)}+2p_{212}^{(d)}+p_{22}^{(d)}+p_{21}^{(d)}+2p_{32}^{(d)}+p_4^{(d)} \tag{4.9}$$

$$p_2^{(b)}=p_2^{(c)}+p_3^{(c)}=p_{211}^{(d)}+2p_{21}^{(d)}+p_4^{(d)} \tag{4.10}$$

$$p_3^{(c)}=p_{21}^{(d)}+p_4^{(d)}. \tag{4.11}$$

Finally, there exist the normalizing relations (2.9), (2.10), (3.4), and

$$p_0^{(d)}+2p_{1,1}^{(d)}+2p_{1,2}^{(d)}+p_{211}^{(d)}+4p_{212}^{(d)}+p_{22}^{(d)}$$
$$+2p_{21}^{(d)}+2p_{32}^{(d)}+p_4^{(d)}=1. \tag{4.12}$$

Equations (4.1)–(4.12), (2.9), (2.10), and (3.4) represent 18 equations in the 18 distribution numbers $p_{jk\tau}^{(m)}$. Two methods have been devised to obtain a solution to these equations. The first calls for a systematic method of introducing simplifications; because the systematics introduce new theoretical concepts which require a separate study, this procedure will not be detailed here. The second method calls for an iterative procedure, for which the requisite equations will now be developed.

To simplify the notation the Greek symbols of Table I are now introduced to replace the $p_{jk\tau}^{(m)}$; also we set $a_i=\alpha_i/\alpha_0$, $b_i=\beta_i/\beta_0$, $c_i=\gamma_i/\gamma_0$, and $d_{ijk}=\delta_{ijk}/\delta_0$. Then the equilibrium conditions may be simplified as follows:

Combine (4.3) and (4.5) to obtain

$$d_{1,1}d_{22}/d_{212}^2=C'. \tag{4.13}$$

Use (4.13) and (4.3) in (4.6); this yields

$$d_{211}d_4/d_{21}^2=C'. \tag{4.14}$$

Rewrite Eq. (4.1), taking account of (2.12)

$$d_{1,1}d_{1,2}=Kc_1^2. \tag{4.15}$$

Introduce (4.15) into (4.2) and rearrange terms

$$d_{212}^4d_{211}/d_{1,1}^2=Cc_2^4K^4. \tag{4.16}$$

Utilize the last two equations in (4.4) to find

$$d_{21}^2/d_{211}=Cc_3^{4/3}K^3. \tag{4.17}$$

Finally, rewrite (4.3) as

$$d_{22}/d_{1,2}^2=C'. \tag{4.18}$$

The various consistency and normalization conditions may be readily transformed into the following simple set:

$$\delta_{21}+\delta_4=\gamma_3 \tag{4.19}$$

$$\delta_{212}+\delta_{22}=\delta_{211}+\delta_{21}=\gamma_2 \tag{4.20a, b}$$

$$\delta_{1,1}+\delta_{212}=\delta_{1,2}+\delta_{22}=\gamma_1 \tag{4.21a, b}$$

$$\delta_0+\delta_{1,2}=\gamma_0 \tag{4.22}$$

$$\gamma_2+\gamma_3=\beta_2 \tag{4.23}$$

$$\gamma_1+\gamma_2=\beta_1 \tag{4.24}$$

$$\gamma_0+\gamma_1=\beta_0 \tag{4.25}$$

$$\beta_1+\beta_2=\alpha_1 \tag{4.26}$$

$$\beta_0+\beta_1=\alpha_0 \tag{4.27}$$

$$\alpha_0+\alpha_1=1. \tag{4.28}$$

In order to explain the method of solution of the foregoing equations, additional relations are required in

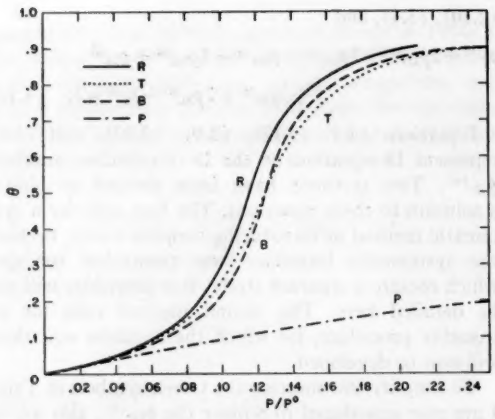

FIG. 2. Adsorption isotherms corresponding to the point (P), bond (B), triangle (T), and rhombus (R) approximations. $C=2$.

which the various $\delta_{j\xi\tau}$ are expressed solely in terms of the γ_k; these expressions are also of intrinsic interest. Combine (4.19), (4.20b), and (4.14); this yields a quadratic in δ_{31} with the solution

$$\delta_{31}=\frac{-(\gamma_2+\gamma_3)+[(\gamma^2+\gamma_3)^2+4(C'-1)\gamma_2\gamma_3]^{\frac{1}{2}}}{2(C'-1)} \tag{4.29}$$

$$\approx[\gamma_2\gamma_3/(\gamma_2+\gamma_3)]\{1-(C'-1)[\gamma_2\gamma_3/(\gamma_2+\gamma_3)^2]\}$$

$$\text{for } (C'-1)\to 0. \tag{4.29}$$

Another interrelation is found upon combining (4.21b), (4.18), and (4.22). This leads to

$$\delta_{1,2}=\frac{-(\gamma_0+\gamma_1)+[(\gamma_0+\gamma_1)^2+4(C'-1)\gamma_0\gamma_1]^{\frac{1}{2}}}{2(C'-1)}$$

$$\approx[\gamma_0\gamma_1/(\gamma_0+\gamma_1)]\{1-(C'-1)[\gamma_0\gamma_1/(\gamma_0+\gamma_1)^2]\}$$

$$\text{for } (C'-1)\to 0. \tag{4.30}$$

A final equation is found by combining (4.20a) and (4.21a),

$$\delta_{32}-\delta_{1,1}=\gamma_2-\gamma_1. \tag{4.31}$$

When this relation is substituted, together with (4.21a) into (4.13) and the resulting quadratic is solved, one obtains

$$\delta_{1,1}=\frac{(\gamma_2+\gamma_1)+2(C'-1)\gamma_1-[(\gamma_1+\gamma_2)^2+4(C'-1)\gamma_1\gamma_2]^{\frac{1}{2}}}{2(C'-1)}$$

$$\approx[\gamma_1^2/(\gamma_1+\gamma_2)]\{1+(C'-1)[\gamma_2^2/(\gamma_1+\gamma_2)^2]\}$$

$$\text{for } (C'-1)\to 0. \tag{4.32}$$

It is unlikely that an analytic solution of the set of equations (4.13)–(4.28) can be found; some type of approximation method is therefore required. The one finally adopted is to "linearize" Eqs. (4.13)–(4.18) by using a new set of variables

$$D_{j\xi\tau}=\delta_{j\xi\tau}-\delta_{j\xi\tau}^{(0)}; \qquad C_j=\gamma_j-\gamma_j^{(0)};$$

$$B_j=\beta_j-\beta_0^{(0)} \qquad \Delta K=K-K^{(0)}, \tag{4.33}$$

where the symbols with the zero superscripts represent the zero order approximations to the corresponding independent variables; the $D_{j\xi\tau}$, C_j, B_j, and ΔK are thus small corrections which approach zero in successive approximations. Thus when (4.33) is used in (4.13), for example, this equation becomes to first powers in the $D_{j\xi\tau}$,

$$1+D_{1,1}/\delta_{1,1}^{(0)}+D_{32}/\delta_{32}^{(0)}-2D_{212}/\delta_{212}^{(0)}$$

$$=C'(\delta_{212}^{(0)})^2/\delta_{1,1}^{(0)}\delta_{32}^{(0)}. \tag{4.34}$$

Similarly, Eq. (4.24) now reads

$$C_1+C_2-B_1=\beta_1^{(0)}-\gamma_1^{(0)}-\gamma_2^{(0)}. \tag{4.35}$$

In this manner, the set of equations (4.13)–(4.28) is replaced by a set which is linear in the unknowns $D_{j\xi\tau}$, C_j, B_j, and ΔK.

The method of successive approximations is then as follows: Numerical values are assigned to C and C' and a value of α_1 is selected for study; the corresponding $K^{(0)}$ is found by numerical solution of the quartic equation (3.23) in the triangle approximation. The quantities σ and τ are next calculated from (3.19) and (3.20) and a set of $\gamma_j^{(0)}$ ($j=0, 1, 2, 3$) is computed from (3.4), (3.8), (3.10), and (3.12). These can be used to determine the $\beta_j^{(0)}$ ($j=0, 1, 2$) from (4.23)–(4.25) as well as the $\delta_{j\xi\tau}^{(0)}$ via (4.29), (4.30), (4.32), and (4.19)–(4.22). These zero order values are now substituted in the linearized set which is solved numerically for the increments $D_{j\xi\tau}$, C_j, B_j, and ΔK. The resulting corrections are added as increments to the corresponding initial zero order quantities to yield a set of first-order results $\delta_{j\xi\tau}^{(1)}$, $\gamma_j^{(1)}$, $\beta_j^{(1)}$, and $K^{(1)}$. The process of solving the linearized set is then repeated until the resulting increments differ from zero by less than 1 part in 10^5. Corresponding calculations are then carried out for other prescribed values of α_1.

5. NUMERICAL RESULTS AND DISCUSSION

To illustrate the theory, several calculations were carried through with the various approximations described earlier, using $Z=6$ for the hexagonal arrangement of surface sites. Machine calculations were carried out for various C which correspond to negative w values; the results are shown in Figs. 2–4. Assuming that the lateral interaction force is of the van der Waals-London type, with the primary contribution to the attractive interaction falling off as the sixth power of distance between particles, it is easy to show that $w'=w/27$ and $C'=C^{1/27}$.

Inspection of the isotherms shows the following: For a given C value and a fixed P/P^0, the isotherm associated with the rhombus approximation (case R) indicates a

greater degree of surface coverage than the corresponding isotherms based on the bond (case B) or triangle (case T) approximations. This effect is attributable to the additional lateral interactions which are taken into account in the rhombus approximation. The next-nearest-neighbor interaction is clearly of much less importance than the nearest neighbor interaction (compare the passage from the Langmuir to the Fowler-Guggenheim isotherm) but by no means negligible.

Careful examination of Figs. 2–4 shows that the cooperative phenomena assume increasing importance as one proceeds through the triangle-rhombus-bond approximation sequence. Thus, the size of the loops in Fig. 4 increases in the order mentioned; in Fig. 3, the B isotherm displays a loop, while of the remaining two that do not, curve R increases more rapidly with P/P^0 than curve T.

Intuitively, one might expect that as the representative figures are increased in size, entropy effects become more prominent at intermediate coverage. For, as the choice of empty sites on which a particle may locate is increased, the entropy effects tend to counteract energy gains which would result if clustering occurred. This is reflected in the increase of the critical C value C_{Cr} from 2.248 to 2.777 in passing from case B to case T.[1] If one takes $w'=0$, then case R becomes identical

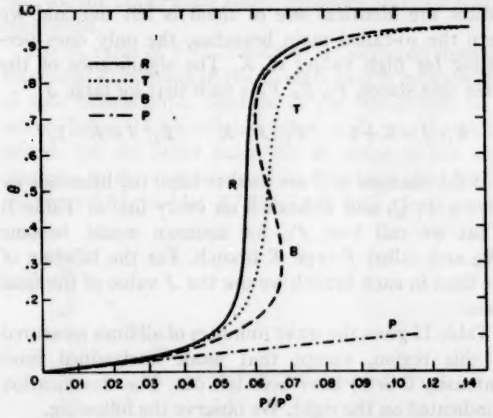

FIG. 3. Adsorption isotherms corresponding to the point (P), bond (B), triangle (T), and rhombus (R) approximations. $C=2.5$.

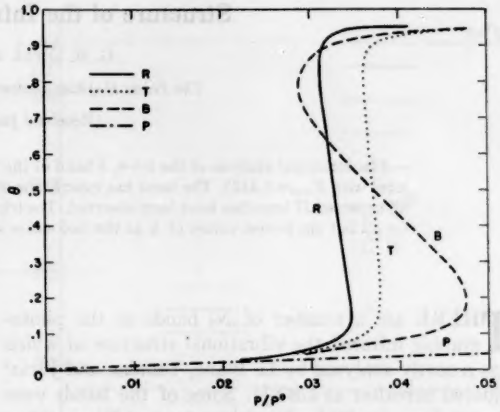

FIG. 4. Adsorption isotherms corresponding to the point (P), bond (B), triangle (T), and rhombus (R) approximations. $C=3$.

with case T; this fact was already pointed out by Hijmans and de Boer, and may be verified by comparing the results of Secs. 3 and 4. Consequently, C_{Cr} is not increased until the hexagon is selected as the next higher basic figure. However, if one sets $w'=w/27$, then C_{Cr} for case R is diminished to approximately 2.62. The decrease in C_{Cr} of 0.16 relative to case R with $w'=0$ reflects the effect of the increased lateral interactions due to next-nearest neighbor effects. The exact value[1] is given as $C_{Cr}=3.001$ for an infinite two-dimensional lattice.

In conclusion, it is seen that the method of Hijmans and de Boer offers a very powerful tool for the theoretical study of gas adsorption phenomena. One can also specialize the above results so that they become applicable to order-disorder problems involving only one phase, such as the behavior of binary alloys or of ferromagnetic materials.

ACKNOWLEDGMENTS

The authors are indebted to R. R. Kenyon and to the staff of the Purdue Statistical Laboratory, as well as to Ann Sherman and staff members of the Group 81 Computer Section of the M.I.T. Lincoln Laboratory for performing the actual calculations.

Structure of the Infrared Y Bands of N_2†

G. H. DIEKE AND D. F. HEATH

The Johns Hopkins University, Baltimore 18, Maryland

(Received January 14, 1960)

The rotational analysis of the $n+4$, 3 band of the "Y" system of N_2 shows that the initial state is a $^3\Sigma_u^-$ level with $B_{n+4}=1.3325$. The band has exactly the structure to be expected from a $^3\Sigma_u^- \rightarrow {}^3\Pi_g$ transition and all expected 27 branches have been observed. The triplet separation of the $^3\Sigma$ state degenerates into a doublet for all but the lowest values of K as the two states with $J=K\pm1$ nearly coincide.

THERE are a number of N_2 bands in the photographic infrared the vibrational structure of which was recently analyzed by Le Blanc, Tanaka, and Jursa[1] (quoted hereafter as LBTJ). Some of the bands were observed previously by Kistiakowsky and Warneck[2] to differ in excitation conditions from the bands of the first positive group among which they are difficult to find in an ordinary discharge. They also showed isotope shifts proving them to belong to a different system which was called the Y system.

LBTJ attribute the system to a $^3\Delta_u \rightarrow B\,^3\Pi_g$ transition without being too positive about the initial state.

We have photographed the system in a discharge similar to that used by LBTJ, the afterglow, cooled by liquid nitrogen, of a high-frequency electrodeless discharge in a mixture of nitrogen and argon (pressure about 20 mm, 4% N_2 in Ar). Under these conditions the intensity of the otherwise overpowering first positive group is sufficiently reduced to bring out the new system without too much interference so that we could obtain it with a large grating with a dispersion of 1.2 A/mm. Under these conditions the rotational structure is fully resolved. We give here the rotational analysis of the $n+4 \rightarrow 3$ band at 7780 A.

The analysis confirms that the $v=3$ level of $B\,^3\Pi$ is without question the final state of the band. We find however the initial state to be a $^3\Sigma_u^-$ state and definitely not $^3\Delta_u$ as tentatively proposed by LBTJ. This $^3\Sigma$ stage is clearly the state predicted by Mulliken[3] at about 70 700 cm^{-1} above the ground state.

TABLE I. The 27 branches of a $^3\Sigma \rightarrow {}^3\Pi$ transition.

N_{13}	O_{13}	P_{13}				
		P_{23}	Q_{23}	R_{23}		
	O_{23}	P_{23}	Q_{23}			
	O_{12}	P_{12}	Q_{12}			
			Q_{22}	R_{22}	S_{22}	
		P_2	Q_2	R_2		
		P_1	Q_1	R_{11}	S_{11}	T_{11}
			Q_{21}	R_{21}	S_{21}	

The structure of the band is very similar to that of the bands of the first positive group ($B\,^3\Pi_g \rightarrow A\,^3\Sigma_u^+$) when allowances are made for the fact that the $^3\Sigma$ state is the upper state and is a Σ_u^- instead of a Σ_u^+ level; Table I lists the 27 branches.

Here the symbols N, O, P, Q, R, S, T signify that the rotational quantum number K, appropriate for Hund's case b, changes by -3 to $+3$, respectively. This has the advantage of having main branches and close satellites indicated by the same letter. The two indices refer to the spin state of the upper ($Y\,^3\Sigma$) and lower ($B\,^3\Pi$) state, respectively. When the two indices are identical one of them is left out and we have the so-called main branches, the only ones persisting for high values of K. The significance of the three spin states, F_1, F_2, F_3 is such that for large J

$$F_1: J=K+1 \qquad F_2: J=K \qquad F_3: J=K-1.$$

If the changes in J are used to label the branches we have a P, Q, and R branch on every line of Table I. What we call here P_{13} for instance would become $^PR_{13}$ and called P-type R branch. For the labeling of the lines in each branch we use the J value of the final state.

Table II gives the wave numbers of all lines measured in this region, except that weak unclassified lines (intensity 0 or 1) have been left out. The classification is indicated on the right. We observe the following.

All 27 branches are well developed. There are very few unclassified lines of any strength. The correctness of the classification can be tested by numerous combination relations which are satisfied to a few times 0.01 cm^{-1} unless evidently poor lines (blends, very weak, or diffuse lines) are involved. One way of doing this is to take the known levels of the $v=3$ $B\,^3\Pi$ state and calculate the rotational levels of the $^3\Sigma$ state. Each such rotational level is obtained from nine different lines and thus gives ample evidence for the correctness of the classification.

† Supported in part by the U. S. Atomic Energy Commission under the auspices of the Los Alamos Scientific Laboratory, and the Geophysics Research Directorate, Air Force Cambridge Research Center, Air Research and Development Command.

[1] F. LeBlanc, Y. Tanaka, and A. Jursa, J. Chem. Phys. **28**, 979 (1958).

[2] G. B. Kistiakowsky and P. Warneck, J. Chem. Phys. **27**, 1417 (1957).

[3] R. S. Mulliken, *The Threshold of Space* (Pergamon Press, New York, 1957), p. 169.

The triplet separation of the $^3\Sigma$ state which can be directly determined from the empirical data is indicated in Fig. 1. It shows that except for the lowest values of K the F_1 and F_3 components practically coincide. This has as a consequence that the branches linked by a bracket in Table I coincide except for the first few lines which is what is observed. The lines of these coinciding branches are marked by an asterisk (*) in Table II.

The intensity distribution is very similar to that of the first positive group.[4] In the liquid-nitrogen-cooled discharge usually no lines above $J=15$ appear. The Q_1 branch is the strongest branch and the low lines of the P_2, Q_2, R_2 branches are extremely weak as in the first positive group. On the other hand the rotational levels of $^3\Sigma$ with even K give rise to the strong lines whereas this was the case for the odd K for $A\,^3\Sigma_u^+$ indicating that the new level is a $^3\Sigma_u^-$ level.

LBTJ give three heads for each band and state that their separation is that of the spin states of $B\,^3\Pi$. This, however, is accidental as the heads are those of the S_{21}, R_{21}, and R_2 branches.

For a $^3\Delta\rightarrow{}^3\Pi$ transition there should be twice as many branches. If because of unresolved lambda doubling some of these should coincide there should be no intensity alternations which clearly are present. $^3\Sigma_u^-$ for the upper state seems therefore an unescapable conclusion.

The B_v value of $Y\,^3\Sigma$ ($v=n+4$) is calculated from the rotational differences of the F_2 state as it is independent of spin interactions. Because of the limitations to J values below 14 no reliable value of D_v can be determined. On the other hand the B_v value is not very sensitive to the magnitude of D_v. We have used for D_v the value $5.84\cdot10^{-6}$ for $A\,^3\Sigma$ and find with a least-square calculation from the first 11 rotational differences

$$B_v=1.3325 \qquad (v=n+4)$$

which is very close[4] to $B_0=1.3338$ of $A\,^3\Sigma$.

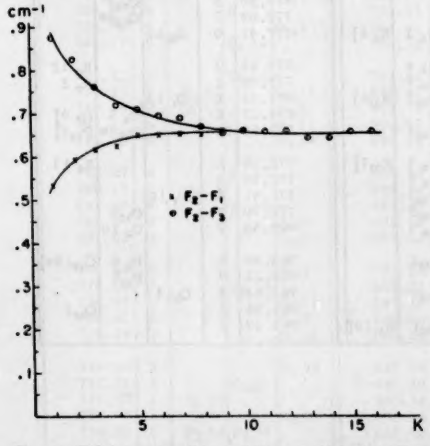

FIG. 1. Triplet separations of the $n+4$ level of $Y\,^3\Sigma_u^-$.

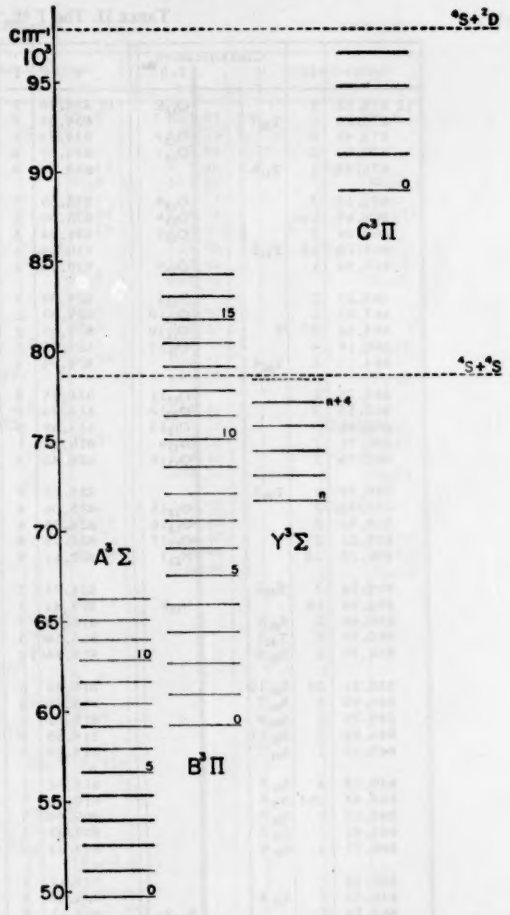

FIG. 2. Vibrational levels of the known triplet states of N_2.

In an ordinary discharge in N_2 the 7, 6 band of the first positive group is considerably stronger and hides the $n+4$, 3 band of the Y system. Nevertheless on high-resolution plates of such a discharge all the stronger lines of the Y-system band can be picked out without difficulty from among the lines of the first positive 7, 6 band.[4]

The lowest rotational level of $Y\,^2\Sigma_u^-$ ($K=0$ of F_1 $v=n+4$) is 77 133.20 cm^{-1} above the ground level ($X\,^1\Sigma$ $K=0, v=0$) of the N_2 molecule which places the n, $n+1$, $n+2$, $n+3$ levels approximately at 71 685, 73 082, 74 456, 75 805 above the ground state.

The analysis of the one band does not allow us to make any further contribution to the analysis of the vibrational structure. If we assume the vibrational analysis of LBTJ as correct we obtain the vibrational

[4] We take the data for the first positive group from a recent report: G. H. Dieke and D. F. Heath, "The first and second positive bands of N_2," Johns Hopkins Spectroscopic Rept. No. 17 (1959).

TABLE II. The $F\,^3\Sigma_u^-(n+4)$ to $B\,^3\Pi_g(3)$ band.

ν	I	Classification	2-0[a]	ν	I	Classification		ν	I	Classification		
12 875.88	4		$O_{12}6$	12 835.58	9	$R_{21}4$[b]		12 797.73	3		$R_{32}10$	
875.25	0	$T_{31}7$		834.95	7	$R_1\,4$		796.86	1	$R_{21}16$		
873.49	6		$O_{12}7$	834.23	6	$R_{21}5$		796.19	2	$R_1 16$*		
872.00	2		$O_{13}7$	833.59	4	$R_1\,5$*		795.89	3		$R_2\,11$	
871.85	1	$T_{31}6$		833.04	0	$Q_{21}1$		795.37	5	$P_1\,7$		
871.19	3		$O_{12}8$	832.59	9	$R_{21}6$		795.22	3		$R_{32}11$	
869.69	1bd		$O_{13}8$	832.50	5	$Q_1\,1$		794.36	2	$Q_{21}10$		
869.04	5		$O_{12}9$	831.94	8	$R_1\,6$*		793.69	7	$Q_1\,10$		
868.20	1d	$T_{31}5$		830.64	6	$R_{21}7$		793.27	2		$Q_{12}1$	
867.58	1		$O_{13}9$	830.14	2		$S_{32}10$	792.88	2		$Q_{32}1$	
867.23	2		$N_{13}5$	829.98	5	$R_1\,7$*		792.52	5			
867.03	2		$O_{12}10$	829.82	1	$Q_{21}2$		792.37	4		$Q_{12}2$	
865.54	0		$O_{13}10$	829.45	2		$S_{32}9$	792.16	7		$Q_{32}2$	
865.19	4		$O_{12}11$	829.27	5	$Q_1\,2$		791.67	1		$Q_2\,3$	
864.17	2	$T_{31}4$		828.94	3	$P_1\,2$		791.09	3		$Q_{12}3$	
863.75	1		$O_{13}11$	828.35	8	$R_{21}8$		790.92	4		$Q_{23}3$	
863.53	2		$O_{12}12$	828.25	2		$S_{32}8$	790.66	5		$P_{12}1$	
862.05	3		$O_{12}13$	827.69	8	$R_1\,8$*		790.46	1	$R_1 17$*		
861.71	1		$N_{13}6$	826.56	1		$S_{32}7$	789.94	4		$Q_2\,4$	
860.78	1		$O_{12}14$	826.42	4	$Q_{21}3$		789.70	4			
859.91	1	$T_{31}3$		825.82	9	$Q_1\,3$		789.33	7		$Q_{12}4$	
859.70	2		$O_{12}15$	825.06	4	$R_1\,9$*		789.22	7		$Q_{32}4$	
858.82	0		$O_{12}16$	824.36	4		$S_{32}6$	788.72	2		$R_{32}13$	
858.21	1		$O_{12}17$	822.75	8	$Q_{21}4$	$P_1\,3]$ $R_{21}10]$	788.42	3	$Q_{21}11$		
856.28	2d		$N_{13}7$	822.11	9	$R_1 10$*	$Q_1\,4]$	787.75	10	$P_1\,8$	$Q_2\,5$	
855.34	3	$T_{31}2$		821.71	3		$S_{32}5$	787.06	7		$Q_{12}5$*	$P_{12}2]$
850.94	1d		$N_{13}8$	819.41	3	$R_{21}11$		785.08	6		$Q_2\,6$	
850.66	1	$S_{21}9$		818.78	7	$Q_{21}5$	$R_1 1^{1}$*]	784.44	8b		$Q_{12}6$*	$O_{12}2]$
850.50	4	$T_{31}1$		818.56	5		$S_{32}4$	783.63	2		$P_2\,3$	
850.39	2	$S_{21}8$		818.16	10	$Q_1\,5$		783.42	3			$R_3\,7$
850.21	2d	$S_{21}10$		816.32	6	$P_1\,4$		783.13	5			$R_3\,6$
849.95	5	$S_{21}7$		815.71	4	$R_{21}12$		783.03	9b		$P_{12}3$	
849.79	1	$S_{31}8$		815.01	5	$R_1 12$*	$S_{32}3$	782.14	4	$Q_{21}12$		$R_3\,5$
849.64	2	$S_{21}11$		814.55	3	$Q_{21}6$		781.95	4		$Q_2\,7$	
849.30	1	$S_{31}7$		813.90	8	$Q_1\,6$		781.44	5	$Q_1\,12$		
849.18	4	$S_{21}6$		811.62	1	$R_{21}13$		781.27	4		$Q_{12}7$*	
848.48	1bd	$S_{21}6$		810.91	5	$R_1 13$*	$S_{32}2$	780.53	5			$R_3\,4$
848.10	6	$S_{21}5$		809.99	5	$Q_{21}7$		779.80	5	$P_1\,9$		
847.41	3	$S_{31}5$		809.63	5	$P_1\,5$		779.16	2		$P_2\,4$	
846.73	4	$S_{21}4$		809.34	10	$Q_1\,7$		778.55	7		$P_{12}4$	
846.30	1			807.12	2	$R_{21}14$		778.32	7		$Q_2\,8$	$R_3\,11$
846.03	2	$S_{31}4$		806.42	4	$R_1 14$*	$S_{32}1$	778.08	1			$R_3\,3$
845.74	2		$N_{13}9$	805.11	3	$Q_{21}8$		777.80	5		$Q_{12}3$	
845.37	2	$T_{31}0$		804.47	7	$Q_1\,8$		777.63	7		$Q_{12}8$*	
845.08	7	$S_{21}3$		803.53	3		$R_2\,5$ $R_2\,6]$	777.41	0	$Q_{21}13$		
844.36	3	$S_{31}3$		803.17	1		$R_2\,4$	775.65	3			$R_3\,12$
843.16	4	$S_{21}2$		802.94	4		$R_2\,7$	775.08	2			$R_3\,2$
842.39	2	$S_{31}2$		802.84	8		$R_{32}5$ $R_{32}6]$	774.75	8	$Q_1\,13$		
840.99	6	$S_{21}1$		802.65	7	$P_1\,6$		774.22	6		$P_2\,5$	$Q_2\,9]$
840.65	1d		$N_{13}10$	802.44	5		$R_{32}4$	773.61	10		$Q_{12}9$*	$P_{12}5]$
840.17	3	$S_{31}1$		802.27	7		$R_2\,3$ $R_{32}7]$	772.36	2			$R_3\,13$
838.57	3	$S_{21}0$		801.90	2		$R_2\,8$	772.08	5			
837.94	4	$R_{21}1$		801.55	8	$R_1 15$*	$R_{32}3$	771.51	8	$P_1\,10$		
837.70	3	$S_{31}0$ $R_1\,0]$		801.25	3		$R_{32}8$	770.70	8		$Q_{12}4$	
837.42	8	$R_{21}2$ $R_1\,1]$		800.39	4		$R_2\,9$	769.58	7		$Q_2\,10$	
837.06	1	$R_{31}1$		800.18	5		$R_{32}2$	768.89	6		$P_2\,6$	$Q_{12}10$*]
836.83	5	$R_1\,2$		12 799.91	4	$Q_{21}9$		768.22	7		$P_{12}6$	
836.63	5	$R_{21}3$ $R_{31}2]$		799.73	5		$R_{32}8$	767.64	4	$Q_1 14$		
836.02	4	$R_1\,3$		799.25	10	$Q_1\,9$		765.56	3			$Q_{23}3$
835.80	1	$R_{31}3$		798.34	7		$R_{32}1$ $R_2\,10]$	765.39	2			

TABLE II.—*Continued.*

ν	I	Classification			ν	I	Classification			ν	I	Classification		
12 764.84	7			Q_3 3	12 734.26	4			$O_{13}5$	12 680.97	1			$N_{13}9$
764.51	7		Q_2 11	Q_3 4	734.00	5		$P_{12}11$		679.33	2	P_1 19		
764.42	4			Q_3 2	733.15	7			$P_{23}8$	677.85	2			
764.20	3			$Q_{23}5$	732.99	1			$Q_{23}13$	677.45	2		P_2 17	
764.02	1			R_3 15	732.66	5			$N_{13}4$	677.00	2			$P_{23}15$
763.80	2		$Q_{12}11$*		732.47	7			P_3 8*	676.34	2			P_3 15*
763.51	9			Q_3 5	732.35	5			Q_3 13	675.90	2	c		
763.16	5		$O_{12}5$		731.51	3		Q_2 16		673.66	3		$O_{12}14$	
763.00	5		P_2 7		728.26	5		$O_{12}9$		672.44	2			$O_{23}12$
762.85	5	P_1 11			727.86	5			$O_{23}6$	668.72	1			$N_{13}10$
762.50	2			$Q_{23}6$	727.21	3			$O_{13}6$	667.40	2			
762.35	9		$P_{12}7$		726.86	4			$P_{23}9$	667.03	1	P_1 20		
761.80	6			Q_3 6	726.35	2		P_2 12		666.73	2			$P_{23}16$
760.82	1	$Q_{23}15$			726.20	4			P_3 9*	666.42	2			
760.13	7	Q_1 15		$Q_{23}7$	725.87	3	Q_1 19			666.07	2			P_3 16*
759.43	9			Q_3 7	725.67	2		$P_{12}12$		664.01	2			
758.87	6		Q_2 12		724.40	2	P_1 15			661.18	3		$O_{12}15$	$O_{23}13$
758.20	3		$Q_{12}12$*		723.64	2			$N_{13}5$	665.32	1			P_3 17
757.17	6		$[Q_{23}8$	$P_{23}2$	723.40	1		Q_2 17		654.45	1		P_2 19	
756.64	3		P_2 8	$P_{13}2$	721.59	2				649.30	0			$O_{23}14$
756.42	6			Q_3 8	720.16	7			$O_{23}7$	648.35	2		$O_{12}16$	
756.34	6			P_3 2	719.97	5			$P_{23}10$	645.62	1			
755.99	5		$P_{12}8$		719.51	3			$O_{13}7$	644.67	0			$P_{23}18$
755.15	8		$O_{12}6$		719.31	6			P_3 10*	643.99	1			P_3 18*
754.91	5			$P_{23}3$	718.77	3	c			636.95	2			$O_{23}15$
754.31	1			$P_{13}3$	718.54	1			Q_3 15					
754.15	5			P_3 3	718.33	6		$O_{12}10$						
753.82	6	P_1 12			717.55	5		P_2 13						
753.46	2			$Q_{23}9$	716.87	4		$P_{12}13$						
752.78	9		Q_2 13	Q_3 9	716.26	1	Q_1 20							
752.20	3	Q_1 16			714.85	2		Q_2 18						
752.07	1		$Q_{12}13$*		713.93	4			$N_{13}6$					
751.91	9			$P_{23}4$	713.75	4	P_1 16							
751.82	6			$O_{23}2$	712.50	3			$P_{23}11$					
751.20	8			P_3 4*	711.83	7		$[O_{23}8$	P_3 11*					
749.80	6		P_2 9		711.16	2			$O_{13}8$					
749.15	8		$P_{12}9$	$Q_{23}10$	708.25	2		P_2 14						
748.69	6			$N_{13}2$	707.89	3		$O_{12}11$						
748.55	4			Q_3 10	706.37	1	Q_1 21							
748.23	6			$P_{23}5$	704.44	4			$P_{23}12$					
747.52	6			P_3 5*	703.80	5			P_3 12*					
746.91	9			$O_{23}3$	703.55	2			$N_{13}7$					
746.67	6		$O_{12}7$		703.03	2								
746.32	5			$O_{13}3$	702.86	6			$O_{23}9$					
746.17	5		Q_2 14		702.70	1	P_1 17							
745.51	1		$Q_{12}14$*		702.22	1			$O_{13}9$					
744.40	5	P_1 13		$Q_{23}11$	698.47	3		P_2 15						
743.86	10	Q_1 17		$P_{23}6$	697.79	2		$P_{12}15$						
743.72	6			Q_3 11	696.97	4		$O_{12}12$						
743.16	8			P_3 6*	696.28	1		Q_2 20						
742.47	4		P_2 10		695.84	1			$P_{23}13$					
742.19	2				695.19	3			P_3 13*					
741.82	4		$P_{12}10$		693.30	3			$O_{23}10$					
741.27	6			$O_{23}4$	692.56	3			$N_{13}8$					
741.02	3			$N_{13}3$	691.63	2	c							
740.64	3			$O_{13}4$	691.24	3	P_1 18							
739.08	2		Q_2 15		688.21	1		P_2 16						
738.97	1			$Q_{23}12$	687.48	1bd		$P_{12}16$						
738.82	5			$P_{23}7$	686.68	2d			$P_{23}14$					
738.33	3			Q_3 12	686.03	4			P_3 14*					
738.14	5			P_3 7*	685.56	2		$O_{12}13$						
737.72	7		$O_{12}8$		685.22	2								
735.07	2	Q_1 18			683.38	2	c							
734.90	8			$O_{23}5$	683.16	4			$O_{23}11$					
734.63	6	P_1 14	P_2 11		682.50				$O_{13}11$					

[a] The first positive system.

[b] Also R_{11}, Q_{33}, or P_{13}, respectively (hereafter this is denoted by *).

[c] The strongest lines of the first positive 7, 6 band.

levels as given above and as indicated in Fig. 2 in relation to the other known triplet levels. Possibly there may be some additional levels of $Y\ ^3\Sigma_u^-$ below the lowest one indicated. The N_2^{14}, N_2^{15} isotope shifts should allow us to settle this point. Bayes and Kistiakowsky[5] conclude that $n=4$. Their reported isotope shifts[2,5] however are not entirely free from contradictions with any choice of the vibrational quantum numbers.

R. Herman[6] and Carroll and Sayers[7] have reported on a new infrared system of N_2 lying in the same region as the Y system. Some of their strong bands lie very close to the strong bands of the Y system. While this of course does not preclude the possibility that both systems are genuine and distinct it suggests that the two systems may be at least partly identical and this possibility should be further investigated.

In the $n+4$, 3 band for instance the wavelengths of the S_{21}, R_{21}, and R_2 heads, respectively, are at 7780, 7787, and 7807 A and this agrees closely with the values given by LBTJ. Kistiakowsky and Warneck[2] give 7823 A for the same band while Carrol and Sayers give 7828 to 7868 A for the five heads they measured. All these wavelengths are well within the limits of the band which extends from 7764 to 7911 A at the low-temperature conditions, and these limits would be extended at higher temperatures. The possibility that the different development of the rotational structure at high temperatures coupled with observations at low dispersion might suggest a different structure or even a shading in the opposite direction cannot be completely discarded. Undoubtedly further work will clear up these points.

A number of other bands of the Y system appear on our high dispersion plates and we hope to report on them in the future.

[5] K. D. Bayes and G. B. Kistiakowsky, J. Chem. Phys. **29**, 949 (1958).
[6] R. Herman, J. Phys. Radium **6**, 183 (1945); Ann. phys. **20**, 241 (1945).
[7] P. K. Carroll and N. D. Sayers, Proc. Phys. Soc. (London) **A66**, 1138 (1953).

THE JOURNAL OF CHEMICAL PHYSICS VOLUME 33, NUMBER 2 AUGUST, 1960

Search for a Jahn-Teller Effect in IrF_6†

HOWARD H. CLAASSEN* AND BERNARD WEINSTOCK
Argonne National Laboratory, Lemont, Illinois

(Received February 1, 1960)

An investigation of the vibrational spectra of IrF_6 has failed to reveal the anomalies found for OsF_6 that were attributed to a Jahn-Teller coupling. This is taken to indicate that the Γ_8 ground electronic state of IrF_6 has a strong spin character. For the vapor in the NaCl range the observed absorption frequencies (cm^{-1}) and their assignments were: 720 (σ_3), 852 ($\sigma_2+\sigma_6$), 921 ($\sigma_2+\sigma_4$), 979 ($\sigma_1+\sigma_4$), 1364 ($\sigma_1+\sigma_3$), and 1425 ($\sigma_1+\sigma_3$). A Raman shift of 651 cm^{-1} ascribed to σ_2 was obtained for a solution of IrF_6 in n-C_7F_{16}.

THE vibrational spectra of IrF_6 have been examined for evidence of the Jahn-Teller effect.[1] Since the electronic ground state of this molecule is a Γ_8 quartet,[2] it would be expected to show anomalies in its spectra similar to those we have pointed out for ReF_6 and OsF_6 as due to a Jahn-Teller vibronic coupling.[3,4] Previous workers have listed infrared absorption bands for IrF_6 and made assignments of the six fundamental frequencies without giving information about the band shapes.[5] We have reexamined part of the infrared spectrum and made measurements of the Raman spectrum of this molecule in order to make pertinent comparisons with ReF_6 and OsF_6 for the Jahn-Teller effect.

The techniques used for obtaining the spectra were similar to those described earlier.[4] For the purpose of this investigation we have examined only the NaCl range in the infrared. The observed absorption frequencies in cm^{-1} and their assignments are as follows: 720(σ_3), 852($\sigma_2+\sigma_6$), 921($\sigma_2+\sigma_4$), 979($\sigma_1+\sigma_4$), 1364-($\sigma_2+\sigma_3$), and 1425($\sigma_1+\sigma_3$). From these the derived values for the fundamental frequencies are: 705(σ_1), 644(σ_2), 720(σ_3), 276(σ_4), and 208(σ_6). The fundamental σ_5 is not listed because for this molecule it would be derived from $\sigma_5+\sigma_6$ which lies beyond the NaCl range. Our measurements are in essential agreement with those reported by the previous workers[5] who covered a more extended frequency range; their values for the fundamental frequencies are: 696(σ_1),

† Based on work performed under the auspices of the U. S. Atomic Energy Commission.
* Permanent address, Wheaton College, Wheaton, Illinois.
[1] H. A. Jahn and E. Teller, Proc. Roy. Soc. (London) **A161**, 220 (1937).
[2] W. Moffitt, G. L. Goodman, M. Fred, and B. Weinstock, Mol. Phys. **2**, 109 (1959).
[3] B. Weinstock and H. H. Claassen, J. Chem. Phys. **31**, 262 (1959).
[4] B. Weinstock, H. H. Claassen, and J. G. Malm, J. Chem. Phys. **32**, 181 (1960).
[5] H. C. Mattraw, W. J. Hawkins, D. R. Carpenter, and W. W. Sabol, J. Chem. Phys. **23**, 985 (1955).

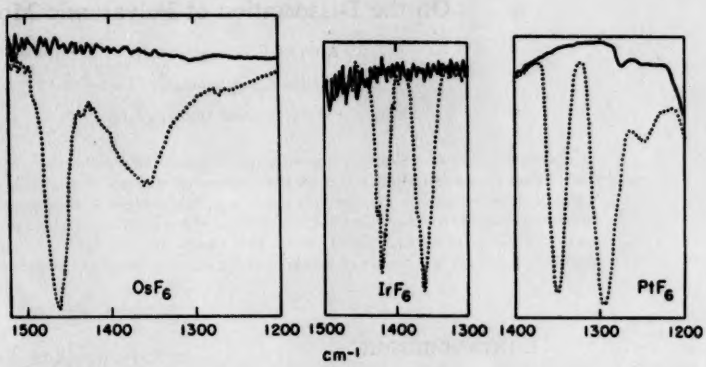

FIG. 1. The infrared combination bands $\sigma_1+\sigma_3$ (on the left) and $\sigma_2+\sigma_3$ (on the right) for the transition series hexafluorides, OsF_6, IrF_6, and PtF_6. The ordinate indicates the energy absorption which increases in the downward direction and the abscissa gives the reciprocal wavelength in cm^{-1}.

643(σ_2), 718(σ_3), 276(σ_4), 260(σ_5), and 205(σ_6). In Fig. 1 are shown the combination bands $\sigma_1+\sigma_3$ and $\sigma_2+\sigma_3$ for OsF_6 and PtF_6 as previously reported[4] and for IrF_6 as now observed. For each of the nine hexafluorides for which the Jahn-Teller effect is not possible these two bands appear adjacent to each other with almost equal sharpness and intensity as exemplified in the figure for PtF_6. By contrast, in the spectrum shown for OsF_6 and also reported for ReF_6,[6] $\sigma_2+\sigma_3$ appears squat relative to the sharp $\sigma_1+\sigma_3$, which change we have attributed to the Jahn-Teller coupling.[3] Surprisingly, IrF_6 appears to be like PtF_6 and the nine other hexafluorides rather than like OsF_6 and ReF_6.

Another anomaly that we ascribed to the Jahn-Teller effect was the fact that σ_2 did not appear in the Raman spectrum of OsF_6 under conditions where both σ_1 and σ_5 were observed. An attempt to measure the Raman spectrum of liquid IrF_6, made in order to compare directly with our previous measurements with liquid OsF_6, failed because of absorption by the brown liquid in the 5461-A spectral region. We did succeed in obtaining a Raman spectrum for IrF_6 using a 20 mole % solution in n-C_7F_{16} and 5461-A excitation and remeasured the Raman spectrum of OsF_6 under similar conditions for comparison. For IrF_6, σ_2 was clearly observed at 651 cm^{-1}; the difference between this value and our infrared derived value of 644 can be accounted for as a combination of experimental error and vapor-liquid shift. Neither σ_1 nor σ_5 were observed; σ_1 coincides with the 5677-A Hg line and σ_5 is obscured because of absorption and greater scattering background. Direct comparison with OsF_6 of equal exposure times would be meaningless because of greater absorption of the IrF_6 sample. As a criterion for comparable exposures, the intensity of a Raman band of the solvent, n-C_7F_{16}, at about 740-cm^{-1} shift was used. In a pair of equivalent exposures of OsF_6 and IrF_6, σ_2 was clearly seen for IrF_6 but missing for OsF_6 although conditions were favorable for its possible observation. In fact in our previously reported study of the Raman effect of OsF_6 conditions were much more favorable for observation of σ_2 than here for IrF_6. The position of ReF_6 in this respect is intermediate between OsF_6 and IrF_6 in that σ_2 is observed in the Raman spectrum but is weak and diffuse.[6] The ease with which σ_2 is observed in the Raman spectrum of IrF_6 is consistent with the failure to observe an anomaly in the σ_2 sum bands of IrF_6. It is clear that the anomalous behavior for σ_2 and its sum bands that we found for OsF_6 and have attributed to a Jahn-Teller vibronic coupling do not occur in IrF_6. This is perhaps an unexpected result because Γ_8 states are not excluded by symmetry arguments from participation in a Jahn-Teller effect.[7] The failure of IrF_6 to show an anomaly in its vibrational spectra seems to indicate that its ground quartet approaches the spin character that it would have under Russell-Saunders coupling. Such behavior is in agreement with Jahn's conclusions concerning the effect of spin degeneracy; his paper includes a demonstration that distortion forces arising from spin effects are negligible.[7] In any case the subtlety of the effect for OsF_6 and ReF_6 and its absence for IrF_6 emphasize the weakness of the Jahn-Teller coupling for the ground states of these transition-metal hexafluorides.

[6] J. Gaunt, Trans. Faraday Soc. **50**, 209 (1954).

[7] H. A. Jahn, Proc. Roy. Soc. (London) **A164**, 117 (1938).

On the Dissociation of Polyatomic Molecules

ROBERT J. RUBIN* AND KURT E. SHULER

National Bureau of Standards, Washington 25, D. C.

(Received December 28, 1959)

The dissociation of a simple model of a linear four-atomic molecule is treated classically by considering the motion of configuration points in the configuration space of the molecule. The usual configurational criterion for dissociation, i.e., the crossing of a critical surface in configuration space, is used. The specific problem studied here is the effect of the recrossing of a critical surface by a configuration point corresponding to the "healing" of a "dissociated" bond. It is shown that, for the model considered here, the above effect results in a greater probability of breaking of the exterior bonds as compared to the interior one.

I. INTRODUCTION

IT was pointed out many years ago in discussions on the use of potential energy surfaces in problems of chemical reaction rates that configuration points which have crossed a critical surface in configuration space may recross this surface and return to their initial state.[1] Wigner was concerned with the passage of configuration points across a potential energy barrier which separates the reactant and product states. We wish to discuss here the problem of the passage of configuration points out of a region which corresponds to an activated state and their possible subsequent return. This problem arises in a treatment of the unimolecular dissociation of polyatomic molecules when the dissociation process is represented by the passage of a configuration point across a critical surface in configuration space.

Slater[2] has given a treatment of the rates of unimolecular dissociations in which he uses a configurational criterion for determining the state of the molecule, i.e., whether it is dissociated or not. According to this criterion, there is a critical bond length and every extension of the bond in excess of this critical length is counted as a dissociation of the molecule. In this paper, we wish to examine a limitation of this criterion by investigating the frequency of "healing" of bonds which have been extended beyond their critical length. In terms of the configuration space of the molecule, we wish to determine the frequency with which configuration points will return across a critical surface defined by a critical bond extension. In order to make our problem tractable, we limit ourselves to the dissociation of a linear four-atomic molecule with nearest-neighbor interactions only.

Pelzer[3] has considered the dissociation of a linear harmonic chain molecule consisting of atoms of equal mass and equal nearest-neighbor force constants without taking into account the possibility of "bond healing." For such a molecule Pelzer has shown that the frequency of dissociation of a bond as determined by its extension beyond a critical length, equal for all bonds, is independent of its location in the molecule. As Pelzer has remarked, this result is in contradiction with ones' intuitive notion that the end bonds should dissociate with greater probability than the interior bonds. For our model of a linear molecule we will show in the following sections that if proper account is taken of the possible "healing" of a bond extended beyond its critical length, one finds indeed that the end bonds dissociate with greater probability than the interior ones.

II. MOLECULAR MODEL

Our model of a linear polyatomic molecule is that of a chain of four atoms which interact with their nearest neighbors according to truncated square-well potentials with hard-sphere cores. The atoms are taken to be of equal mass, and the range and depth of the interaction potential are the same for each pair of atoms. In this one-dimensional model the atoms are constrained to move along the molecular axis. It can readily be seen from the properties of a hard-sphere square-well potential that this model leads to the same result of equal probability of bond breaking for all bonds as Pelzer's harmonic model if the healing of bonds is ignored. The molecule and the interatomic potential $V(r_{i,i+1})$ are shown schematically in Fig. 1. The distances a and b are, respectively, the hard-sphere

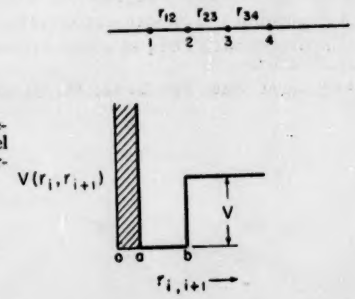

FIG. 1. Square-well potential model for a linear four-atomic molecule.

* Supported by the U. S. Atomic Energy Commission.

[1] See, for example, E. P. Wigner, Trans. Faraday Soc. **34**, 29 (1938).

[2] See, for example, N. B. Slater, Proc. Roy. Soc. (London) **A194**, 112 (1948), and subsequent papers.

[3] H. Pelzer, Z. Elektrochem. **39**, 608 (1933); Nature **160**, 576 (1947); and N. B. Slater, Nature **160**, 576 (1947).

diameter and the critical bond length. For a molecule with all three of its bonds intact, all interatomic distances, $r_{i,i+1}$, satisfy the inequality, $a \leq r_{i,i+1} \leq b$, where a and b have the same values for each pair of atoms. We have chosen the foregoing model because the rectilinear motion of the atoms should facilitate following the paths of the configuration points in configuration space.

If one separates out and ignores the motion of the center of mass, then the kinetic energy E of the internal motion of the four-atomic chain is given by

$$E=\tfrac{1}{2}m[\tfrac{3}{4}\dot{r}_{12}^2+\dot{r}_{23}^2+\tfrac{3}{4}\dot{r}_{34}^2+\dot{r}_{12}\dot{r}_{23}+\tfrac{1}{2}\dot{r}_{12}\dot{r}_{34}+\dot{r}_{23}\dot{r}_{34}], \quad (1)$$

where the dots in Eq. (1) denote differentiation of the coordinates $r_{i,i+1}$ with respect to the time and m is the mass of one of the atoms. Equation (1) can be rewritten in matrix form as

$$E=\tfrac{1}{2}m\dot{\mathbf{r}}^T\mathbf{A}\dot{\mathbf{r}}, \quad (2)$$

where $\dot{\mathbf{r}}$ denotes the column vector $(\dot{r}_{12}, \dot{r}_{23}, \dot{r}_{34})$, $\mathbf{A}$ denotes the matrix

$$\begin{pmatrix} \frac{3}{4} & \frac{1}{2} & \frac{1}{4} \\ \frac{1}{2} & 1 & \frac{1}{2} \\ \frac{1}{4} & \frac{1}{2} & \frac{3}{4} \end{pmatrix}$$

and $\dot{\mathbf{r}}^T$ is the transpose of $\dot{r}$. We now wish to introduce a new set of coordinates $\boldsymbol{\varrho}$ which is linearly related to $\mathbf{r}$ such that the kinetic energy E can be written as

$$E=\tfrac{1}{2}m\dot{\boldsymbol{\varrho}}^T\mathbf{I}\dot{\boldsymbol{\varrho}}, \quad (3)$$

where $\mathbf{I}$ is the 3×3 unit matrix. In the new coordinate system, the internal motion of the four atoms is represented by the rectilinear motion of a single particle of mass m.[4] The transformation matrix $\mathbf{B}$, which transforms $\dot{\mathbf{r}}$ to $\dot{\boldsymbol{\varrho}}$ as well as $\mathbf{r}$ to $\boldsymbol{\varrho}$, is (see Appendix I)

$$\mathbf{B}=\begin{pmatrix} \frac{1}{2} & 0 & -\frac{1}{2} \\ (\frac{1}{2})(1+1/\sqrt{2})^{\frac{1}{2}} & (\frac{1}{2})^{\frac{1}{2}}(1+1/\sqrt{2})^{\frac{1}{2}} & (\frac{1}{2})(1+1/\sqrt{2})^{\frac{1}{2}} \\ (\frac{1}{2})(1-1/\sqrt{2})^{\frac{1}{2}} & -(\frac{1}{2})^{\frac{1}{2}}(1-1/\sqrt{2})^{\frac{1}{2}} & (\frac{1}{2})(1-1/\sqrt{2})^{\frac{1}{2}} \end{pmatrix}, \quad (4)$$

where $\boldsymbol{\varrho}=\mathbf{Br}$. If the components of $\mathbf{r}$ are taken to be orthogonal, then the $\mathbf{r}$-configuration space of the molecule is a cube. The corresponding $\boldsymbol{\varrho}$-configuration space which is a parallelipiped is shown in Fig. 2.

As mentioned above, the vibration of a molecule in $\mathbf{r}$ space is represented by the rectilinear motion of a configuration point mass m in $\boldsymbol{\varrho}$ space. It follows from the treatment in Appendix I that motion in the direction a to c' corresponds to an extension of the interior bond coordinate r_{23}, and that motion in the directions a to b' and a to h' corresponds, respectively, to extension of the exterior bond coordinates r_{12} and r_{34}. The boundary surfaces *bdfe*, *cdfg*, and *ghef* in Fig. 2 represent configurations in which one of the bonds is at its critical extension for dissociation. We shall call these surfaces $\mathcal{E}$ surfaces. The surfaces *bdfe* and *ghef* correspond to the critical extension of the exterior bonds r_{12} and r_{34}. As shown in Appendix I, these two surfaces are completely equivalent as should be expected for our model. The surface *cdfg* corresponds to the critical extension of the interior bond r_{23}. The boundary surfaces *ac'd'b'*, *ah'g'c'*, and *ah'e'b'* represent configurations in which two of the hard-sphere atoms are in contact. We shall call these surfaces C surfaces. When a configuration point encounters a C surface, the normal component of its velocity is reversed while the tangential component is unchanged. When a configuration point encounters an $\mathcal{E}$ surface, there are two possible results. If the component of velocity $v_\perp$ normal to the surface is such that the kinetic energy $E_\perp=(\frac{1}{2})mv_\perp^2$ is greater than the depth of the potential well V, then the configuration point will cross the $\mathcal{E}$ surface with a reduced normal velocity component corresponding to

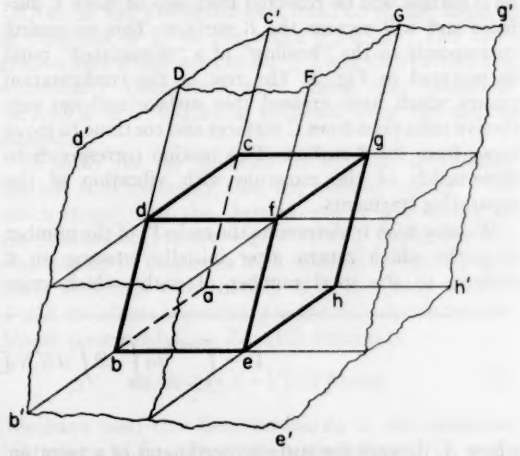

FIG. 2. $\boldsymbol{\varrho}$-configuration space for linear four-atomic model. $\mathcal{E}$ surfaces: *bdfe*, *dcgf*, and *efgh*. Angle between planes *bdca* and *acgh*=90°; angles between planes *bdca* and *bahe* and between *acgh* and *bahe*=60°. Relative lengths of edges *ba*:*ac*:*ah*=1:2/$\sqrt{3}$:1.

[4] This diagonalization of the kinetic energy has been employed previously in similar problems, see, e.g., H. Eyring and M. Polanyi, Z. physik. Chem. **B12**, 279 (1931). For a general discussion of these types of transformations see J. O. Hirschfelder and J. S. Dahler, Proc. Natl. Acad. Sci. U. S. **42**, 363 (1956); and J. O. Hirschfelder and D. W. Jepsen, *ibid.* **45**, 249 (1959).

FIG. 3. Successive configurations during the "dissociation" and "healing" of an interior bond in the time sequence

$$t_0<t_1<t_2<t_3.$$

the energy $E_\perp - V$ and an unchanged tangential component. If $E_\perp < V$, the normal velocity component of the configuration point will be reversed, and the tangential (i.e., parallel) component will remain unchanged.

We now wish to consider the motion of the configuration points after they have crossed an $\mathcal{E}$ surface. As may be seen from Fig. 2 and the analysis presented below, some of the configuration points which have crossed an $\mathcal{E}$ surface will be reflected from one or more C surfaces and will recross the $\mathcal{E}$ surface. This recrossing corresponds to the "healing" of a "dissociated" bond as pictured in Fig. 3. The rest of the configuration points which have crossed this surface undergo successive reflections from C surfaces and continue to move away from the $\mathcal{E}$ surface. This motion corresponds to dissociation of the molecule with vibration of the separating fragments.

We now wish to determine the ratio Γ, of the number of paths which return after initially crossing an $\mathcal{E}$ surface, to the total number of paths which cross this surface. As was noted earlier, there are really only two $\mathcal{E}$ surfaces involved in this analysis, namely the surface $\mathcal{E}_i$ [surface *cdfg*] corresponding to the critical extension of the interior bond and the surface $\mathcal{E}_e$ [surfaces *bdfe* and *ghef*], corresponding to the critical extension of an exterior bond. The two quantities to be determined are Γ_i and Γ_e, which refer, respectively, to $\mathcal{E}_i$ and $\mathcal{E}_e$ surfaces. The aim of this study is to compare the magnitudes of Γ_i and Γ_e in order to determine for our model the relative probability of the dissociation (or healing) of the interior to the exterior bonds.

III. DETERMINATION OF Γ_i AND Γ_e

We now wish to calculate the phase-average values of Γ_i and Γ_e for a molecule with internal kinetic energy E. The initial configurations of the molecule correspond to all bonds being intact. Since all these initial configurations of the molecule have the same *a priori* probability, the configuration points are uniformly distributed in ϱ space. Furthermore the velocity distribution of the configuration points in ϱ space is uniform and isotropic throughout the volume *abehcdfg*, consistent with the internal energy E.[5]

In order to carry out the calculation we now present a more detailed description of the crossing of an $\mathcal{E}$ surface at the point P by a configuration point, Fig. 4. The quantities $\dot{\varrho}$, $v_{||}$, and $v_\perp$ are, respectively, the velocity of the configuration point incident on the $\mathcal{E}$ surface and the parallel and perpendicular components of $\dot{\varrho}$. The primed quantities $\dot{\varrho}'$, $v_{||}'$, and $v_\perp'$ refer to the velocity of the configuration point and its components after the crossing of the $\mathcal{E}$ surface. The angles α and ϕ are, respectively, the angles between the trajectory of the configuration point and the normal to the $\mathcal{E}$ surface before and after the crossing of the $\mathcal{E}$ surface. The azimuthal angle θ refers to the rotation of the plane containing the trajectory around AB, the normal to the $\mathcal{E}$ surface at the point P.

In terms of the coordinates α and θ, the quantity Γ_i, which is the ratio of the phase average of the number of paths which cross the $\mathcal{E}_i$ surface and return, to the total number of paths which cross can be written as

$$\Gamma_i = \int_0^{\alpha_{crit}} d\alpha \int_0^{2\pi} d\theta \int_{\mathcal{E}_i} dS_i K_i[\alpha, \theta, S_i] \Big/ \int_0^{\alpha_{crit}} d\alpha \int_0^{2\pi} d\theta \int_{\mathcal{E}_i} dS_i, \tag{5}$$

where S_i denotes the surface coordinates of a point on the $\mathcal{E}_i$ surface and where

$$K_i[\alpha, \theta, S_i] = \begin{cases} 1, & \text{if path recrosses} \\ 0, & \text{if path does not recross.} \end{cases} \tag{6}$$

The quantity α_{crit} is defined such that for $\alpha > \alpha_{crit}$ the configuration point has insufficient energy to cross the $\mathcal{E}$ surface. An expression analogous to Eq. (5) holds for Γ_e. To obtain a more convenient form for Γ_i for purposes of calculation we replace the independent variable α by ϕ and obtain

$$\Gamma_i = \int_0^{\pi/2} d\phi \frac{d\alpha}{d\phi} \langle K_i(\phi) \rangle_{Av} \Big/ \int_0^{\pi/2} d\phi \frac{d\alpha}{d\phi}, \tag{7}$$

[5] Both of these assumed properties correspond to the physical situation in which the collision frequency is large compared to the dissociation frequency, i.e., for sufficiently high density.

where

$$\langle K_i(\phi)\rangle_N = \int_0^{2\pi} d\theta \int_{\mathcal{E}_i} dS_i K_i[\alpha(\phi), \theta, S_i] \Big/ \int_0^{2\pi} d\theta \int_{\mathcal{E}_i} dS_i. \quad (8)$$

As will be shown in Appendix II, the function $\alpha(\phi)$ is

$$\alpha(\phi) = \sin^{-1}\{[(E-V)/E]^{\frac{1}{2}} \sin\phi\} \quad (9)$$

so that

$$d\alpha/d\phi = \{[E/(E-V)] - \sin^2\phi\}^{-\frac{1}{2}} \cos\phi. \quad (10)$$

We have evaluated the expressions (7) and (8) by means of an analog computer because the analytical evaluation would have involved some tedious and complicated solid geometery. Since the motion of the configuration points is rectilinear and since they are specularly reflected from C surfaces, the most convenient analog computer for calculating $\langle K_i(\phi)\rangle_N$ and $\langle K_e(\phi)\rangle_N$ involves the application of geometrical optics. We therefore constructed two "computers," one for the $\mathcal{E}_i$ surface and one for an $\mathcal{E}_e$ surface, which consisted of a set of plane mirrors representing the portion of ρ space corresponding to a dissociated molecule, i.e., the regions outside the planes *cdfg* and *bdfe* (or *efgh*) of Fig. 2. The portion of ρ space above the $\mathcal{E}_i$ surface represents the configuration space for the two diatomic fragments 1-2 and 3-4 and the portions of ρ space outside the $\mathcal{E}_e$ surfaces represent the configuration space for the atom 1 (or 4) and the triatomic molecule 2-3-4 (or 1-2-3). As an example, the arrangement of mirrors above the $\mathcal{E}_i$ surface *cdfg* is shown in Fig. 2 where *cc'Gg*, *GgfF*, *FfdD*, and *Ddcc'* are the mirrors which rest on the base plane *cdfg*. The introduction of a light beam through a point in an $\mathcal{E}$ surface and its subsequent reflection(s) in the mirror system corresponds exactly to the motion of a representative point in ρ-configuration space. For the $\mathcal{E}_i$ surface, for instance, reflection of the light beam from the planes (mirrors) *Ddcc'* and *cc'Gg* corresponds to hard-sphere collisions between atoms 1 and 2 and atoms 3 and 4 in the two diatomic fragments (see Fig. 3). Reflection of the light beam from the planes (mirrors) *GgfF* and *FfdD* corresponds to the other phase of the vibration of the diatomic fragments 1–2 and 3–4.

The analog computers were used to calculate the $\langle K_i(\phi)\rangle_N$ and $\langle K_e(\phi)\rangle_N$ of Eq. (8) where these quantities are the fraction of paths which return after crossing an $\mathcal{E}$ surface at the angle ϕ to the normal. The base plane was divided into 64 equal areas by an 8×8 grid. Provisions were made to admit a narrow pencil of light through the center of each grid square over the range of angles $0 \leq \theta \leq 2\pi$ and $0 \leq \phi \leq \frac{1}{2}\pi$. For each grid square and for a fixed angle ϕ, the quantity

$$\langle K_i(\phi, S_i)\rangle_N = \int_0^{2\pi} d\theta K_i[\alpha(\phi), \theta, S_i] \Big/ \int_0^{2\pi} d\theta \quad (11)$$

was determined by rotating the light beam 360° around the normal and noting the fraction of the range of θ for which the light beam was reflected back onto the base surface. The surface integration

$$\int_{\mathcal{E}_i} dS_i$$

which gives $\langle K_i(\phi)\rangle_N$ of Eq. (8) was carried out by averaging $\langle K_i(\phi, S_i)\rangle_N$ over the 64 grid squares. $\langle K_i(\phi)\rangle_N$ was evaluated as a function of the angle ϕ at intervals of 5° in the range $0 \leq \phi \leq \frac{1}{2}\pi$. The integration over ϕ indicated in Eq. (7) was then carried out numerically (Simpson's rule) using the values of $\langle K_i(\phi)\rangle_N$ and $\langle K_e(\phi)\rangle_N$ obtained from the analog computer.

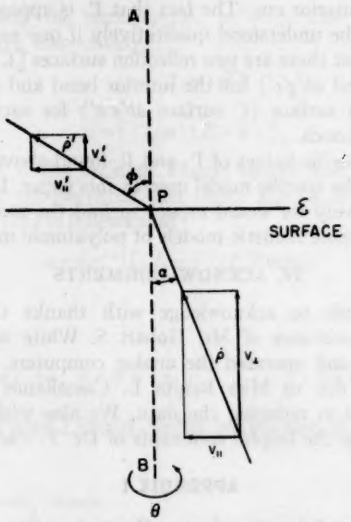

FIG. 4. Path of a configuration point across an $\mathcal{E}$ surface.

In order for the molecule to have an appreciable lifetime it is necessary that the binding energy V be much larger than the thermal energy kT. Owing to the Boltzmann factor $\exp[-E/kT]$ governing the distribution of molecules with internal energy E, only those molecules with energies E in the range $0 < E - V \ll E$ contribute appreciably to the dissociation process. Under these conditions, Eq. (10) reduces to

$$d\alpha/d\phi \cong [(E-V)/E]^{\frac{1}{2}} \cos\phi. \quad (12)$$

We have used this form for $d\alpha/d\phi$ in the numerical integration of Eq. (7) to obtain the values

$$\Gamma_i = 0.187$$

and

$$\Gamma_e = 0.105,$$

which are in this approximation [Eq. (12)] independent of E and V. This result shows that when the healing of bonds is taken into account, the probability of dissociation, $1-\Gamma$, is greater for the end bonds than

for the interior one. The fact that Γ_i is approximately $2\Gamma_e$ can be understood qualitatively if one notes from Fig. 2 that there are two reflection surfaces [C surfaces $ac'd'b'$ and $ah'g'c'$) for the interior bond and only one reflection surface (C surface $ab'e'h'$) for each of the exterior bonds.

The specific values of Γ_i and Γ_e found above pertain only to the specific model used in this paper. However, qualitatively we would expect to find the same effect also for more realistic models of polyatomic molecules.

IV. ACKNOWLEDGMENTS

We wish to acknowledge with thanks the very skillful assistance of Mr. Hobart S. White who constructed and operated the analog computers. Thanks are also due to Miss Benita L. Castellanos for her assistance in reducing the data. We also wish to acknowledge the helpful comments of Dr. T. Carrington.

APPENDIX I

Transformation from r Space to ρ Space

In Eq. (2) the kinetic energy is expressed as a quadratic form

$$E=\tfrac{1}{2}m\dot{\mathbf{r}}^T\mathbf{A}\dot{\mathbf{r}}, \tag{A.1}$$

where $\dot{\mathbf{r}}$ denotes the column vector $(\dot{r}_{12}, \dot{r}_{23}, \dot{r}_{34})$ and $\dot{\mathbf{r}}^T$ denotes the transposed vector. We wish to express the kinetic energy in the form

$$E=\tfrac{1}{2}m\dot{\boldsymbol{\rho}}^T\mathbf{I}\dot{\boldsymbol{\rho}}, \tag{A.2}$$

where $\mathbf{I}$ is the unit matrix and $\boldsymbol{\rho}=(\rho_1, \rho_2, \rho_3)$ is a new set of coordinates. We first note that a real symmetric matrix such as $\mathbf{A}$ can be reduced to diagonal form by an orthogonal matrix $\mathbf{C}$

$$\mathbf{C}^T\mathbf{A}\mathbf{C}=\mathbf{\Lambda}, \tag{A.3}$$

where $\mathbf{\Lambda}$ is a diagonal matrix whose elements are the eigenvalues λ_i, of $\mathbf{A}$. If $\mathbf{C}_i$ is the eigenvector of $\mathbf{A}$ associated with λ_i, the matrix $\mathbf{C}$ is of the form $(\mathbf{C}_1, \mathbf{C}_2, \mathbf{C}_3)$. Then we have, since $\mathbf{C}\mathbf{C}^T=\mathbf{1}$

$$\begin{aligned}E&=\tfrac{1}{2}m\dot{\mathbf{r}}^T\mathbf{C}\mathbf{C}^T\mathbf{A}\mathbf{C}\mathbf{C}^T\dot{\mathbf{r}}\\&=\tfrac{1}{2}m\dot{\mathbf{r}}^T\mathbf{C}\mathbf{\Lambda}\mathbf{C}^T\dot{\mathbf{r}}\\&=\tfrac{1}{2}m(\mathbf{C}^T\dot{\mathbf{r}})^T\mathbf{\Lambda}(\mathbf{C}^T\dot{\mathbf{r}}).\end{aligned} \tag{A.4}$$

If the matrix $\mathbf{A}$ is written as $\mathbf{D}\mathbf{I}\mathbf{D}^T$, where

$$\mathbf{D}=\begin{pmatrix}\lambda_1^{\frac{1}{2}} & 0 & 0\\ 0 & \lambda_2^{\frac{1}{2}} & 0\\ 0 & 0 & \lambda_3^{\frac{1}{2}}\end{pmatrix},$$

then E can be expressed as

$$E=\tfrac{1}{2}m(\mathbf{D}^T\mathbf{C}^T\dot{\mathbf{r}})^T\mathbf{I}(\mathbf{D}^T\mathbf{C}^T\dot{\mathbf{r}}),$$

or

$$E=\tfrac{1}{2}m\dot{\boldsymbol{\rho}}^T\mathbf{I}\dot{\boldsymbol{\rho}}, \tag{A.5}$$

where

$$\dot{\boldsymbol{\rho}}=\mathbf{D}^T\mathbf{C}^T\dot{\mathbf{r}}\equiv\mathbf{B}\dot{\mathbf{r}}.$$

The eigenvalues λ_i and eigenvectors $\mathbf{C}_i$ can be shown to be, respectively,

$$\lambda_1=\tfrac{1}{2}, \qquad \lambda_2=1+1/\sqrt{2}, \qquad \lambda_3=1-1/\sqrt{2}$$

and

$$\mathbf{C}_1=\begin{pmatrix}(\frac{1}{2})^{\frac{1}{2}}\\ 0\\ -(\frac{1}{2})^{\frac{1}{2}}\end{pmatrix}, \qquad \mathbf{C}_2=\begin{pmatrix}\frac{1}{2}\\ (\frac{1}{2})^{\frac{1}{2}}\\ \frac{1}{2}\end{pmatrix}, \qquad \mathbf{C}_3=\begin{pmatrix}\frac{1}{2}\\ -(\frac{1}{2})^{\frac{1}{2}}\\ \frac{1}{2}\end{pmatrix}.$$

The transformation matrix $\mathbf{B}$ in Eq. (A.5) then becomes

$$\mathbf{B}=\begin{pmatrix}\frac{1}{2} & 0 & -\frac{1}{2}\\ (\frac{1}{2})(1+1/\sqrt{2})^{\frac{1}{2}} & (\frac{1}{2})^{\frac{1}{2}}(1+1/\sqrt{2})^{\frac{1}{2}} & (\frac{1}{2})(1+1/\sqrt{2})^{\frac{1}{2}}\\ (\frac{1}{2})(1-1/\sqrt{2})^{\frac{1}{2}} & -(\frac{1}{2})^{\frac{1}{2}}(1-1/\sqrt{2})^{\frac{1}{2}} & (\frac{1}{2})(1-1/\sqrt{2})^{\frac{1}{2}}\end{pmatrix}. \tag{A.6}$$

Having obtained the matrix $\mathbf{B}$, the next items to be discussed are the dimensions and angles between faces of the ρ-configuration space of the molecule (volume *abehcdfg* in Fig. 2). The r-configuration space is a cube. The ρ-configuration space is obtained according to the transformation matrix $\mathbf{B}$ which rotates and stretches the original cube. The set of unit column vectors in r space $\mathbf{u}_1=(1, 0, 0)$, $\mathbf{u}_2=(0, 1, 0)$, $\mathbf{u}_3=(0, 0, 1)$ is transformed, respectively, into vectors $\mathbf{Bu}_1$, $\mathbf{Bu}_2$, $\mathbf{Bu}_3$ whose magnitudes are in the ratio $1:2/\sqrt{3}:1$. The angles between the planes containing the vector pairs: ($\mathbf{Bu}_1$, $\mathbf{Bu}_2$) and ($\mathbf{Bu}_1$, $\mathbf{Bu}_3$); ($\mathbf{Bu}_1$, $\mathbf{Bu}_2$) and ($\mathbf{Bu}_2$, $\mathbf{Bu}_3$); ($\mathbf{Bu}_2$, $\mathbf{Bu}_3$) and ($\mathbf{Bu}_1$, $\mathbf{Bu}_3$) are, respectively, 60°, 90°, and 60°. The correspondence of these dimensions to the ρ-configuration space (Fig. 2) is as follows: the ratios of the lengths *ab*:*ac*:*ah* are $1:2/\sqrt{3}:1$ and the angles between the faces (*abdc* and *abeh*), (*abdc* and *acgh*), (*acgh* and *abeh*) are, respectively, 60°, 90°, and 60°. It is clear that the δ surfaces, *bdfe* and *efgh*, are equivalent and are thus to be associated with extension of the exterior bonds r_{12} and r_{34} in Fig. 1.

APPENDIX II

The Function $\alpha(\phi)$

We will now derive the relation (9) between the angles α and ϕ shown in Fig. 4. The following expressions are

evident from Fig. 4

$$\sin\phi = v_{||}'/\dot{\rho}' \tag{B.1}$$

and

$$\sin\alpha = v_{||}/\dot{\rho}. \tag{B.2}$$

From Eqs. (B.1) and (B.2), it follows that

$$\sin\phi/\sin\alpha = \dot{\rho}/\dot{\rho}', \tag{B.3}$$

where we have made use of the fact that the component of velocity parallel to an $\mathcal{E}$ surface is unchanged in crossing the surface, i.e., $v_{||}' = v_{||}$. The speeds $\dot{\rho}$ and $\dot{\rho}'$, are, respectively,

$$\dot{\rho} = [(2/m)E]^{\frac{1}{2}} \tag{B.4}$$

and

$$\dot{\rho}' = [(2/m)(E-V)]^{\frac{1}{2}}, \tag{B.5}$$

where E is the incident kinetic energy and V is the depth of the potential well (with $E > V$). From Eqs. (B.3)–(B.5) it follows that

$$\alpha = \sin^{-1}\{[(E-V)/E]^{\frac{1}{2}} \sin\phi\}. \tag{B.6}$$

THE JOURNAL OF CHEMICAL PHYSICS VOLUME 33, NUMBER 2 AUGUST, 1960

Application of Ehrenfest Equations to Liquid-Vapor and Liquid-Solid Mixtures of He^4†

O. V. Lounasmaa*

Argonne National Laboratory, Argonne, Illinois

(Received March 4, 1960)

Ehrenfest equations for the constant-volume phase transitions from the mixed liquid-vapor or liquid-solid system to pure liquid or vapor have been derived and applied in the case of He^4. Such processes serve as a model of second-order phase transitions. The reasonably good agreement found indicates that these equations may be used to check experimental data at the boundaries of two-phase regions and to determine unknown quantities entering into them.

INTRODUCTION

An example of second-order phase transitions is obtained by considering a vessel of constant volume filled with liquid and its saturated vapor. If the volume V of the sample is larger than its critical volume V_c the amount of vapor gradually increases at the expense of liquid when temperature is raised. The thermal capacity of this system (excluding the heat capacity of the vessel) is the sum of the heat capacities of liquid and vapor and of the latent heat of evaporation. When the last drop of liquid has evaporated, the system no longer follows the liquid-vapor equilibrium curve in the p–T plane but departs to the vapor phase. At this point a discontinuous drop occurs in the thermal capacity, the specific heat of the vapor at constant volume being smaller than the apparent specific heat of the mixed phase. The entropy S of this system is a continuous function of temperature, but $(\partial S/\partial T)_V$ has a discontinuity at the point where the sample departs from the liquid-vapor equilibrium curve. It was first pointed out by Gorter[1] that the constant volume process from the two-phase liquid-vapor system to pure vapor has the characteristics of a second-order phase transition. The previous considerations apply equally well when $V < V_c$. In this case, however, the amount of vapor is gradually decreasing when temperature is raised until the sample departs to pure liquid phase.

EHRENFEST EQUATIONS

The Ehrenfest[2] equations for this type of second-order phase transition can be derived easily. In the T–V plane (Fig. 1) the sample follows a horizontal V = con-

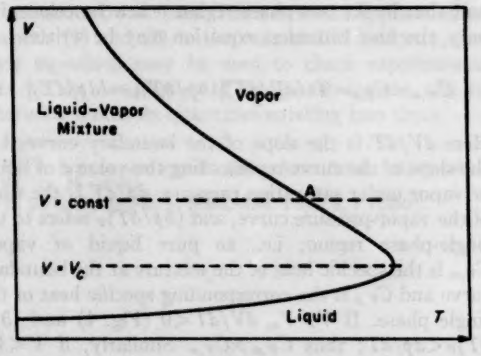

FIG. 1. Schematic drawing of the T–V plane. The sample follows a horizontal V = constant line as its temperature is raised at constant volume and undergoes a second order phase transition when crossing the boundary curve of the two-phase region at A.

* On leave from the Wihuri Physical Laboratory, University of Turku, Turku, Finland.

† Based on work performed under the auspices of the U. S. Atomic Energy Commission.

[1] W. H. Keesom, *Helium* (Elsevier Publishing Company, Amsterdam, 1942), p. 259.

[2] P. Ehrenfest, Proc. Acad. Sci. (Amsterdam) **36**, 153 (1933).

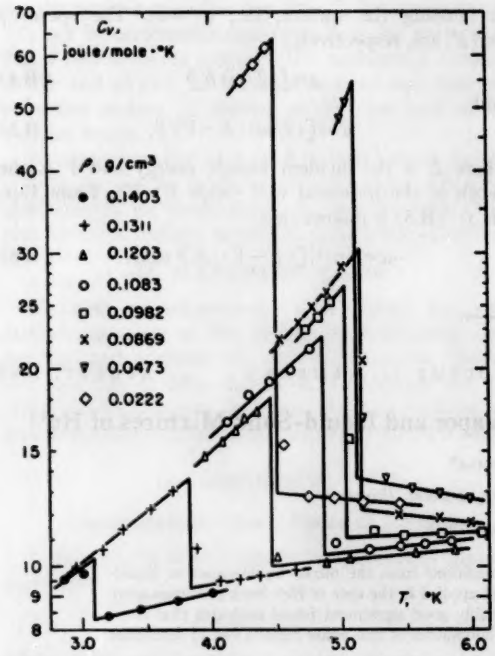

FIG. 2. C_V curves for He^4 showing phase transitions from the liquid-vapor mixture to pure vapor (for densities $\rho=0.0473$ and 0.0222 g/cm³) or to pure liquid (for all other densities) according to Hill and Lounasmaa.[4]

stant line when its temperature is raised. As the entropy is continuous at crossing the boundary curve surrounding the two-phase region, we may write $dS_m=dS_s$. Here dS_m and dS_s are the corresponding entropy increases of the mixed and single phases along the boundary curve, respectively. We thus get $(\partial S_m/\partial T)_V dT+(\partial S_m/\partial V)_T dV=(\partial S_s/\partial T)_V dT+(\partial S_s/\partial V)_T dV$. By observing that $(\partial S/\partial V)_T=(\partial p/\partial T)_V$, $(\partial S/\partial T)_V=C_V/T$, and that in the two-phase region p is a function of T only, the first Ehrenfest equation may be written

$$C_{V,m}-C_{V,s}=T\cdot(dV/dT)[(\partial p/\partial T)_V-(dp/dT)]. \quad (1)$$

Here dV/dT is the slope of the boundary curve; i.e., the slope of the curve representing the volume of liquid or vapor under saturation pressure, dp/dT is the slope of the vapor-pressure curve, and $(\partial p/\partial T)_V$ refers to the single-phase region; i.e., to pure liquid or vapor. $C_{V,m}$ is the specific heat of the mixture at the boundary curve and $C_{V,s}$ is the corresponding specific heat of the single phase. If $V>V_c$, $dV/dT<0$ (Fig. 1) and $(\partial p/\partial T)_V<dp/dT$; thus $C_{V,m}>C_{V,s}$. Similarly, if $V<V_c$, $dV/dT>0$ and $(\partial p/\partial T)_V>dp/dT$; thus also in this case $C_{V,m}>C_{V,s}$. Consequently, there is always a drop in the specific heat when the boundary curve is crossed.

By using the fact that pressure is also continuous across the boundary curve the second Ehrenfest equation is obtained:

$$(\partial p/\partial T)_V-(dp/dT)=-(dV/dT)(\partial p/\partial V)_T. \quad (2)$$

Here $(\partial p/\partial V)_T$ refers to the single phase and the other quantities have the same meaning as in Eq. (1). Relations (1) and (2) have been given by Goldstein[3]; his derivation of (1) is more complicated than the one presented in this paper.

APPLICATIONS TO He^4

Hill and Lounasmaa[4] made a study of the thermal and state properties of He^4 in the temperature region 3–20°K and up to pressures of 100 atm. The directly measured quantities were C_V, $(\partial p/\partial T)_V$, and p, all as a function of T and V. Their results of C_V measurements showing transitions from the two-phase to the single-phase region are plotted in Fig. 2. The discontinuous drop in the values of C_V at the boundary curve is quite sharp, although some anticipation of it, probably due to fluctuations, was observed on the single-phase side near critical conditions. For this reason curves corresponding to molar volumes very close to V_c are not plotted in Fig. 2.

All quantities entering into relations (1) and (2) are known for He^4 and the applicability of Ehrenfest equations may thus be tested. The values of $C_{V,m}-C_{V,s}$ and $(\partial p/\partial T)_V$ are given by Hill and Lounasmaa,[4]

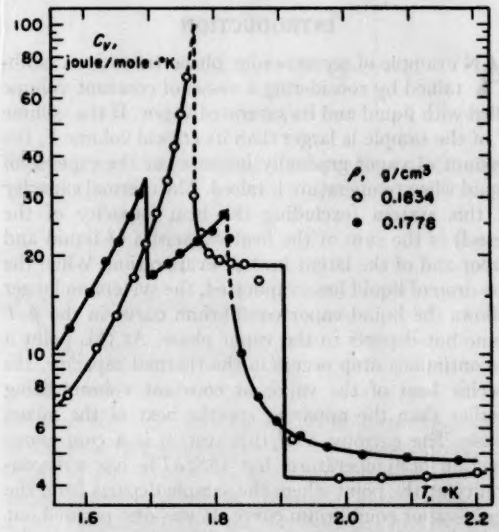

FIG. 3. C_V for two liquid-solid mixtures of He^4 by Lounasmaa and Kojo.[5] For $\rho=0.1834$ g/cm³ the λ transition in liquid helium occurs at 1.771°K (upper λ point) and the liquid-solid to pure-liquid transition at 1.905°K. For $\rho=0.1778$ g/cm³ the liquid-solid to liquid transition occurs at 1.697°K and the λ transition at 1.819°K. Observe the different shapes of the specific-heat curves on the high-temperature sides of the two types of transitions.

[3] L. Goldstein, J. Washington Acad. Sci. **40**, 97 (1950).
[4] R. W. Hill and O. V. Lounasmaa, Phil. Trans. Roy. Soc. (London) **252**, 357 (1960).

TABLE I. Test of Ehrenfest equations (1) and (2) for liquid-vapor and liquid-solid mixtures of He⁴.

ρ g/cm³	T °K	Eq. (1)[d] joule/mole·°K		Eq. (2)[d] atm/°K		dV/dT[e] cm³/mole·°K	
0.1403[a]	3.091	2.05	2.02	3.24	2.65	1.99	2.02
0.1311[a]	3.833	4.40	4.48	3.32	2.95	3.47	3.41
0.1203[a]	4.460	8.05	7.89	2.72	2.94	6.41	6.63
0.1083[a]	4.857	12.0	12.7	1.87	2.62	13.8	13.1
0.0982[a]	5.035	15.8	18.7	1.27	1.93	28.8	24.6
0.0869[a]	5.148	18.3	31.8	0.74	...	82.7	47.6
0.0473[b]	5.114	41.4	43.4	−0.47	...	−179	−173
0.0222[b]	4.500	51.0	52.7	−0.63	...	−184	−178
0.1834[c]	1.905	14.5	13.9	...	...	...	...
0.1778[c]	1.697	17.5	13.9	...	...	...	...

[a] Liquid-vapor to liquid transitions.
[b] Liquid-vapor to vapor transitions.
[c] Liquid-solid to liquid transitions.
[d] First column=left side of equation; second column=right side of equation.
[e] Values in the first column from footnote reference 6; values in the second column computed by using Eq. (1).

$(\partial p/\partial V)_T$ may be calculated from the equation of state for He⁴ by Lounasmaa,[5] dV/dT is obtained from a compilation of experimental data by Berman and Mate,[6] and dp/dT may be computed from the helium-vapor-pressure temperature scale T_{58}.[7] (As most of the original measurements considered here have been made by using T_{58}, this temperature scale was retained in the present paper for reasons of convenience.) The results of this comparison are presented in Table I and, if transitions close to the critical temperature 5.20°K are excluded, good agreement is observed in the case of Eq. (1). For relation (2) the discrepancies are somewhat bigger, mainly because the values of $(\partial p/\partial V)_T$ are known less accurately than the other quantities. Near the critical point, dV/dT is changing rapidly and the experimental values available for this derivative are very inaccurate. This explains the larger discrepancies found near 5.20°K. In fact, relatively accurate values of dV/dT should be obtained by using Eq. (1); such computations are presented in the last column of Table I.

Relations (1) and (2) obviously can be applied to the constant-volume phase transition from the mixed liquid-solid system to pure liquid. Some experimental data are available for He⁴. The measurements of C_V by Lounasmaa and Kojo[8] along the liquid-solid equilibrium curve are shown in Fig. 3. The discontinuities in C_V at the transition point are clearly seen together with the λ-transition peaks of the specific heat of the liquid. Other quantities entering into Eq. (1) have been determined from the measurements of Grilly and Mills.[9] Here dp/dT is the slope of the melting curve and the other derivatives refer to the solidifying liquid. Comparisons are presented for Eq. (1) in Table I and the agreement is reasonably good.

CONCLUSIONS

Accurate tests of the applicability of Ehrenfest equations are often impossible either owing to lack of reliable experimental data or too rapid variation of the quantities involved. The constant-volume changes from a mixed to a single-phase system serve as a model of second-order transitions. The successful application of relations (1) and (2) in the case of He⁴ indicates that these equations may be used to check experimental data at the boundaries of two-phase regions and to determine unknown quantities entering into them.

[5] O. V. Lounasmaa, Ann. Acad. Sci. Fennicae A VI, No. 38 (1959).
[6] R. Berman and C. F. Mate, Phil. Mag. 3, 461 (1958).
[7] J. R. Clement, J. K. Logan, and J. Gaffney, Phys. Rev. 100, 743 (1955), note added in proof.
[8] O. V. Lounasmaa and E. Kojo, Ann. Acad. Sci. Fennicae A VI, No. 36 (1959).
[9] E. R. Grilly and R. L. Mills, Ann. Phys. 8, 1 (1959).

Transferability of Urey-Bradley Force Constants. IV. Methyl Halides

JOHN OVEREND AND JAMES R. SCHERER

Chemical Physics Research Laboratory, The Dow Chemical Company, Midland, Michigan*

(Received April 4, 1960)

Urey-Bradley force constants have been fitted by least squares to the vibrational frequencies of CH_3F, CH_3Cl, CH_3Br, CH_3I, and their fully deuterated isotopes. Both observed and zeroth-order frequency data have been used and the corresponding sets of force constants have been compared.

INTRODUCTION

THE vibrational analysis of many molecules, particularly those of moderate size and low symmetry, is severely limited by the fact that there are seldom sufficient data to fix all the parameters in a realistic potential function, even when the frequencies of isotopically-substituted molecules are available. As we have already discussed in the previous papers in this series,[1-3] hereafter referred to as I, II, and III, the most promising approach to this problem appears to be that of transferring force constants from related molecules, and for this purpose tables of typical values of common force constants are needed. An excellent compilation of Urey-Bradley force constants (UBFC) has already been prepared by Mizushima and Shimanouchi,[4] but there still remain many gaps to be filled. Further, there are cases where the force constant associated with a particular coordinate (e.g., the stretching of a carbon-hydrogen bond) shows significant variation over a series of molecules containing that coordinate. If this variation can be correlated with some other parameter (e.g., the bond length, or the hybridization of the terminal atoms) a value of the force constant may be estimated from the correlation function even though it is not possible to transfer the force constant directly from another molecule.[5]

The methyl halides have been subject to previous normal-coordinate calculations[6-8] with a general quadratic valence force field but no work has been done with a UBFF save an approximate treatment of CH_3F and CH_3Cl by Tanaka[9] in which he factored the CH-stretching modes from the secular equation.

The present analysis was carried out with the primary purpose of obtaining typical sets of UBFC for the methyl group and establishing the broad underlying principles governing their transferability. As harmonic frequencies and exact geometrical parameters are available for this series of molecules, we have taken this opportunity to test the effect of the neglect of anharmonicity and the small deviations of the true geometry from the tetrahedral angle on the UBFC.

The potential energy was taken in the Urey-Bradley form

$$2V=\sum_i[2K_i'r_i\Delta r_i+K_i(\Delta r_i)^2]+\sum_i[2H_i'\Delta\alpha_i+H_i(\Delta\alpha_i)^2]+\sum_{i<j}[2F_{ij}'q_{ij}\Delta q_{ij}+F_{ij}(\Delta q_{ij})^2], \quad (1)$$

and the redundant coordinates q_{ij} were removed by the usual substitution,[1] leading to the expression of the potential energy in the form

$$\mathbf{F}=\mathbf{Z}\Phi. \quad (2)$$

However, in order to retain the molecular symmetry in the potential energy, it is necessary to take all six angle changes as coordinates in the potential function. These are not independent but are related by an equation

$$R(\alpha_i)=0, \quad (3)$$

which may be expanded as a Taylor series in the α_i; for present purposes we require terms through quadratic. The coefficients are easily obtained by Crawford's determinantal method[10] and for this particular case with C_{3v} symmetry, R simplifies to

$$R(\alpha)=s_\beta D_1\sum_i\Delta\beta_i+s_\alpha D_2\sum_i\Delta\alpha_i+\tfrac{1}{2}[(c_\beta D_1+s_\beta^2 s_\alpha^2)\sum_i(\Delta\beta_i)^2+(c_\alpha D_2+s_\alpha^2 s_\beta^2)\sum_i(\Delta\alpha_i)^2]-[s_\beta^2 D_2'\sum_i\sum_{j<i}(\Delta\beta_i)(\Delta\beta_j)+s_\beta s_\alpha D_{12}'\sum_i\sum_{j\neq i}(\Delta\beta_i)(\Delta\alpha_j)+s_\alpha^2 D_1'\sum_i\sum_{j<i}(\Delta\alpha_i)(\Delta\alpha_j)]=0, \quad (4)$$

where the angles α_i and β_i are defined as in footnote reference 7, Fig. 1, and where $s_\alpha=\sin(\mathrm{HCH})$, $c_\alpha=\cos(\mathrm{HCH})$, $s_\beta=\sin(\mathrm{HC}X)$ and $c_\beta=\cos(\mathrm{HC}X)$. The

* Formerly Spectroscopy Laboratory.

[1] J. Overend and J. R. Scherer, J. Chem. Phys. **32**, 1289 (1960).

[2] J. Overend and J. R. Scherer, J. Chem. Phys. **32**, 1296 (1960).

[3] J. R. Scherer and J. Overend, J. Chem. Phys. **32**, 1720 (1960).

[4] S. Mizushima and T. Shimanouchi, *Sekigaisen Kyushu to Raman Koka* (Kyoritsu Shuppan, Tokyo, 1958).

[5] See, for example, the work of S. Califano and B. L. Crawford (paper presented at the meeting of the European Spectroscopy Group, Bologna, 1959) on the UBFF of benzene, in which they estimated K_{CC} from a correlation of carbon-carbon stretching force constant vs r_{CC}.

[6] Tsu-Shen Chang, dissertation, University of Michigan, 1954.

[7] W. T. King, I. M. Mills, and B. L. Crawford, J. Chem. Phys. **27**, 455 (1957).

[8] G. D. Barnett, dissertation, University of Washington, 1957.

[9] C. Tanaka, J. Chem. Soc. Japan **79**, 686 (1958).

[10] B. L. Crawford (unpublished).

coefficients D, obtained by expansion of the determinants of the cosines, are given by

$$D_1 = c_\beta D_2' - D_{12}'$$

$$D_2 = c_\beta D_{12}' - D_2'$$

$$D_1' = c_\alpha - c_\beta^2$$

$$D_2' = c_\alpha - c_\alpha^2$$

$$D_{12}' = c_\beta - c_\alpha c_\beta.$$

We follow the usual custom and take care of this angular redundancy by Lagrange's method of undetermined multipliers; thus, at equilibrium,

$$\bar{V} = V + \kappa R(\alpha)$$

has an unrestricted minimum and the linear terms vanish, leaving the quadratic terms in (4) as coefficients of an extra force constant κ, the intramolecular tension.[11] The coefficients of the quadratic terms in (4) with an additional factor of $\frac{1}{2}$ then appear as an extra column of the **Z** matrix.

In the limiting case of a tetrahedral configuration, $\alpha=\beta$ and (4) reduces to the form given by Shimanouchi [footnote reference 11 Eq. (6)] after dividing through by a factor of $32\sqrt{2}/81$. Consequently, it is important to note that the values of κ for tetrahedral configurations derived from the Shimanouchi equation are not directly comparable with those determined for nontetrahedral configurations through (4), and for comparison, the tetrahedral κ must be multiplied by $81/32\sqrt{2}$.[12]

The Urey-Bradley force constants were fitted to the frequency data with a program (POCO II) written for the Burroughs 220 computer and described in detail in I and III. We used the symmetry coordinates given by King, Mills, and Crawford[7,13] with the exception that the bending coordinate was taken as $\Delta\alpha_i$ rather than as $r_{CH}\Delta\alpha_i$. **G** and **Z** matrices were set up on the computer in the usual way, although it was necessary to enter manually the column of **Z** corresponding to the nontetrahedral κ as described in III. The weight matrices **P** were taken as unit matrices, corresponding to a relative weight of $1/\lambda_i$ for each frequency, except in the case of the uncertain perpendicular CD stretching frequency of methyl iodide which was arbitrarily given a weight of $0.2/\lambda$.

The observed frequency data for methyl chloride, bromide, and iodide were taken from King's paper[7] and references to the original spectroscopic measurements are given there. The anharmonicity corrections were calculated by Chang[6] using the Dennison-Hansen[14,15] method. The frequencies of CH_3F are due to Pace[16] and those of CD_3F to Edgell and Parts.[17] Anharmonic frequencies were derived by Barnett,[8] again using the Dennison-Hansen method. These data are summarized in Tables I–IV with the best estimates of the frequencies calculated from the different sets of UBFC's, viz., (i) observed frequencies, exact geometry; (ii) observed frequencies, tetrahedral angles; (iii) harmonic frequencies, exact geometry; and (iv) harmonic frequencies, tetrahedral angles. The geometrical parameters used in the exact calculations are given in Table V with the original references; in the tetrahedral approximation, we used the bond lengths from the true configurations. The final sets of refined UBFC's are collected in Table VI with the dispersions obtained from the error matrices. The tetrahedral κ's have been scaled as described in the preceeding and are directly comparable with the nontetrahedral ones but not, in general, with the values given by Mizushima and Shimanouchi.[4]

DISCUSSION OF RESULTS

The assumption of the UBFF implies certain relationships between the vibrational frequencies, and if isotopic data are included in the vibrational analysis, the frequencies are further related by isotope rules.[18] In general, neither set of relationships obtains exactly for the observed frequencies ν_i, although the harmonic frequencies ω_i are usually adjusted to fit the isotope rules. Thus, the in the least-squares process we calculate a set of best estimates $\bar{\nu}_i$ and $\bar{\omega}_i$ (for which these relationships do obtain), and the corresponding values of the parameters in the force-field equations, $\bar{\phi}_j$.[19] The force constants $\bar{\phi}_j$ are not unique but are mean values with a dispersion $\sigma\{\bar{\phi}_j\}$. This uncertainty in the force constant is propagated into the best estimates of the frequencies which have a dispersion $\sigma\{\bar{\nu}_i\}$, not to be confused with σ which is the mean error of an observation of unit weight. In Tables I–IV we have included the experimental data ν_{obs}, the best estimates $\bar{\nu}_i$, the dispersions σ and $\sigma\{\bar{\nu}_i\}$, and the errors, $e_i=[(\nu_{obs})_i-\bar{\nu}_i]$: The same quantities are also given for the harmonic frequencies ω_i. In each molecule the over-all quality of the fit, as revealed by the values of σ, is somewhat better for the harmonic frequencies than for the observed ones. It is instructive to examine the fit of the potential function in greater detail, and for this purpose we turn to the errors e_i and the dispersions

[11] T. Shimanouchi, J. Chem. Phys. **17**, 245 (1949).

[12] It is not possible to make this comparison by redefining the nontetrahedral κ as the scaling factor is only defined when $\alpha=\beta$.

[13] The expression for S_2 given in footnote reference 7 has been corrected for an obvious normalization error.

[14] D. M. Dennison, Revs. Modern Phys. **12**, 175 (1940).

[15] G. E. Hansen and D. M. Dennison, J. Chem. Phys. **20**, 313 (1952).

[16] E. L. Pace, J. Chem. Phys. **18**, 881 (1950).

[17] W. F. Edgell and L. Parts, J. Am. Chem. Soc. **78**, 2358 (1956).

[18] S. Brodersen and A. Langseth, Mat. Fys. Skr. Dan. Vid. Selsk., Bind **1**, No. 5 (1958).

[19] An excellent description of the least-squares adjustment process is given by Arley and Busch [*Introduction to the Theory of Probability and Statistics* (John Wiley & Sons, Inc., New York 1950), Chap. 12], and we have adopted their statistical nomenclature in this paper.

TABLE I. CH_3F and CD_3F. Experimental frequencies, best estimates, dispersions, and errors in cm^{-1}.

			(i) True geometry			(ii) Tetrahedral				(iii) True geometry			(iv) Tetrahedral		
	Mode	ν_{obs}	$\bar{\nu}_i$	e_i	$\sigma\{\bar{\nu}_i\}$	$\bar{\nu}_i$	e_i	$\sigma\{\bar{\nu}_i\}$	ω_i	$\bar{\omega}_i$	e_i	$\sigma\{\bar{\omega}_i\}$	$\bar{\omega}_i$	e_i	$\sigma\{\bar{\omega}_i\}$
	ν_1	2862.9	2874.9	−12.0	17	2873.4	−10.5	18	3026.7	3027.5	−0.8	15	3026.6	0.1	16
A_1	ν_2	1467.9	1476.3	−8.4	23	1477.9	−10.0	19	1509.7	1515.0	−5.3	15	1516.5	−6.8	18
	ν_3	1049.5	1049.8	−0.3	17	1049.8	−0.3	18	1070.9	1068.3	2.6	15	1068.1	2.8	17
	ν_4	3009	3027.8	−18.8	16	3028.2	−19.2	17	3090.4	3109.7	−19.3	14	3110.1	−19.7	16
E	ν_5	1469.7	1476.2	−6.5	17	1479.9	−10.2	19	1497.0	1502.0	−5.0	15	1505.8	−8.8	17
	ν_6	1200	1186.0	14.0	14	1180.5	19.5	15	1212.5	1197.7	14.8	12	1193.1	19.4	13
	ν_1	2089.7	2064.7	25.0	11	2065.8	23.9	12	2175.6	2169.3	6.3	10	2170.7	4.9	11
A_1	ν_2	1136.9	1135.0	1.9	17	1134.4	2.5	19	1161.8	1163.8	−2.0	15	1163.5	−1.7	17
	ν_3	991.8	992.7	−0.9	16	993.1	−1.3	18	1010.7	1013.3	−2.6	14	1013.4	−2.7	16
	ν_4	2258.0	2239.0	19.0	12	2239.2	18.8	13	2319.5	2297.1	22.4	11	2297.3	22.2	12
E	ν_5	1073.3	1061.6	11.7	13	1057.0	16.3	14	1087.0	1077.9	9.1	11	1073.4	13.6	12
	ν_6	911.0	920.9	−9.9	15	923.2	−12.2	16	920.9	933.7	−12.8	13	936.0	−15.1	15
				$\sigma=0.0311$			$\sigma=0.0336$				$\sigma=0.0269$			$\sigma=0.0303$	

TABLE II. CH_3Cl and CD_3Cl: experimental frequencies, best estimates, dispersions, and errors, in cm^{-1}.

			(i) True geometry			(ii) Tetrahedral				(iii) True geometry			(iv) Tetrahedral		
	Mode	ν_{obs}	$\bar{\nu}_i$	e_i	$\sigma\{\bar{\nu}_i\}$	$\bar{\nu}_i$	e_i	$\sigma\{\bar{\nu}_i\}$	ω_i	$\bar{\omega}_i$	e_i	$\sigma\{\bar{\omega}_i\}$	$\bar{\omega}_i$	e_i	$\sigma\{\bar{\omega}_i\}$
	ν_1	2937	2954.5	−17.5	15	2951.4	−14.4	15	3062	3069.6	−7.6	6	3065.8	−3.8	4
A_1	ν_2	1354.9	1352.5	2.4	17	1357.2	−2.3	16	1398.2	1395.8	2.4	7	1399.3	−1.1	5
	ν_3	732.1	733.4	−1.3	15	733.1	−1.0	15	732.7	731.5	1.2	2	731.4	1.3	4
	ν_4	3041.8	3055.4	−13.6	15	3057.4	−15.6	14	3208.6	3206.1	2.5	6	3207.6	1.0	4
E	ν_5	1454.6	1457.8	−3.2	15	1464.3	−9.7	15	1520.0	1517.0	3.0	6	1523.3	−3.3	4
	ν_6	1015.0	1020.4	−5.4	14	1012.3	2.7	13	1049.4	1052.7	−3.3	6	1045.1	7.6	4
	ν_1	2141	2112.2	28.8	10	2117.5	23.5	10	2207	2195.2	11.8	4	2200.5	6.5	3
A_1	ν_2	1029	1031.6	−2.6	17	1029.9	−0.9	16	1053.8	1055.8	−2.0	7	1053.9	−0.1	5
	ν_3	695	693.0	2.0	14	693.8	1.2	14	695.6	696.8	−1.2	6	697.1	−1.5	4
	ν_4	2286	2269.6	16.4	11	2268.1	17.9	11	2379.0	2382.3	−3.3	5	2380.5	−1.5	3
E	ν_5	1058	1053.1	4.9	11	1043.9	14.1	11	1092.2	1096.2	−4.0	4	1087.0	5.2	3
	ν_6	775	767.4	7.6	12	774.2	0.8	12	794.9	791.2	3.7	5	798.2	−3.3	4
				$\sigma=0.0284$			$\sigma=0.0274$				$\sigma=0.0113$			$\sigma=0.0079$	

TABLE III. CH_3Br and CD_3Br: experimental frequencies, best estimates, dispersions, and errors in cm^{-1}.

			(i) True geometry			(ii) Tetrahedral				(iii) True geometry			(iv) Tetrahedral		
	Mode	ν_{obs}	$\bar{\nu}_i$	ϵ_i	$\sigma\{\bar{\nu}_i\}$	$\bar{\nu}_i$	ϵ_i	$\sigma\{\bar{\nu}_i\}$	ω_i	$\tilde{\omega}_i$	ϵ_i	$\sigma\{\tilde{\omega}_i\}$	$\tilde{\omega}_i$	ϵ_i	$\sigma\{\tilde{\omega}_i\}$
	ν_1	2935	2948.9	−13.9	12	2945.2	−10.2	13	3060.5	3064.3	−3.8	4	3060.2	0.3	4
A_1	ν_2	1305	1305.2	−0.2	14	1309.4	−4.4	14	1331.7	1331.0	0.7	5	1333.9	−2.2	4
	ν_3	611	614.4	−3.4	12	614.1	−3.1	12	614.1	614.2	−0.1	4	614.1	0	3
	ν_4	3056.8	3067.1	−10.3	11	3069.0	−12.2	12	3213.4	3209.2	4.2	4	3210.7	2.7	3
E	ν_5	1444	1449.1	−5.1	12	1454.8	−10.8	13	1505.5	1503.0	2.5	4	1508.8	−3.3	4
	ν_6	954	954.6	−0.6	11	947.3	6.7	12	975.4	977.6	−2.2	4	971.0	4.4	3
	ν_1	2130	2107.9	22.1	8	2113.6	16.4	9	2196	2190.2	5.8	3	2196.0	0	2
A_1	ν_2	993	993.5	−0.5	13	991.1	1.9	14	1002.2	1002.5	−0.3	4	1000.6	1.6	4
	ν_3	578	573.9	4.1	11	574.7	3.3	12	579.9	579.8	0.1	4	579.9	0	3
	ν_4	2293	2280.7	12.3	9	2278.9	14.1	10	2381.1	2386.2	−5.1	3	2384.1	−3.0	3
E	ν_5	1056.4	1049.0	7.4	( )	1040.5	15.9	9	1084.4	1087.9	−3.5	3	1079.2	5.2	3
	ν_6	712	710.3	1.7	( )	716.2	−4.2	10	730.1	727.6	2.5	3	734.0	−3.9	3
				σ=0.0222			σ=0.0237				σ=0.0075			σ=0.0067	

TABLE IV. CH_3I and CD_3I: experimental frequencies, best estimates, dispersions, and errors in cm^{-1}.

			(i) True geometry			(ii) Tetrahedral				(iii) True geometry			(iv) Tetrahedral		
	Mode	ν_{obs}	$\bar{\nu}_i$	ϵ_i	$\sigma\{\bar{\nu}_i\}$	$\bar{\nu}_i$	ϵ_i	$\sigma\{\bar{\nu}_i\}$	ω_i	$\tilde{\omega}_i$	ϵ_i	$\sigma\{\tilde{\omega}_i\}$	$\tilde{\omega}_i$	ϵ_i	$\sigma\{\tilde{\omega}_i\}$
	ν_1	2933	2948.3	−15.3	12	2944.1	−11.1	10	3060	3070.0	−10.0	8	3065.4	−5.4	5
A_1	ν_2	1251.5	1250.7	0.8	14	1253.5	−2.0	12	1288.3	1287.1	1.2	9	1289.5	−1.2	5
	ν_3	532.8	535.4	−2.6	11	535.6	−2.8	10	533.1	535.2	−2.1	7	535.3	−2.2	4
	ν_4	3060.3	3064.2	−3.9	13	3064.6	−4.3	12	3229.2	3229.0	0.2	5	3229.2	0	3
E	ν_5	1440.3	1442.3	−2.0	12	1447.9	−7.6	10	1504.4	1500.7	3.7	8	1506.4	−2.0	2
	ν_6	880.1	885.4	−5.3	11	879.3	0.8	9	905.8	909.3	3.5	7	903.3	2.5	4
	ν_1	2130	2106.1	23.9	8	2112.5	17.5	7	2210	2194.4	15.6	5	2201.2	8.8	3
A_1	ν_2	950.7	951.7	−1.0	13	949.8	0.9	11	975.0	975.9	−0.9	9	974.0	1.0	5
	ν_3	501.4	498.1	3.3	11	498.1	3.3	9	501.7	499.3	2.4	7	499.1	2.6	4
	ν_4	(2300)	2280.0	20.0	11	2276.8	23.2	9	(2400)	2404.1	−4.1	7	2400.5	−0.5	4
E	ν_5	1048.7	1045.9	2.8	8	1037.5	11.2	7	1082.6	1087.7	−5.1	5	1079.4	3.2	3
	ν_6	661.5	654.1	7.4	9	660.2	1.3	8	675.8	671.6	4.2	6	677.8	−2.0	3
				σ=0.0218			σ=0.0189				σ=0.0142			σ=0.0068	

TABLE V. Geometry of the methyl halides.

Molecule	r_{CH}, A	r_{CX}, A	α	β
CH_3F[a]	1.109	1.398	110°	108°56′
CH_3Cl[b]	1.097	1.780	111°30′	107°21′
CH_3Br[b]	1.090	1.936	111°44′	107°4′
CH_3I[b]	1.092	2.139	112°7′	106°40′

[a] O. R. Gilliam, H. D. Edwards, and W. Gordy, Phys. Rev. 75, 1014 (1949).
[b] T. S. Chang (footnote reference 6) quoted by W. T. King, I. M. Mills, and B. L. Crawford (footnote reference 7).

$\sigma\{\bar{\nu}_i\}$ and $\sigma\{\bar{\omega}_i\}$ in Tables I–IV. When observed-frequency data are used, the errors for the CH stretching frequencies are systematically negative in sign, whereas those for the CD stretching frequencies are systematically positive. Moreover, in the heavy molecules, the errors e_1 and e_4 are approximately double the estimates of the dispersions $\sigma\{\bar{\nu}_1\}$ and $\sigma\{\bar{\nu}_4\}$. If harmonic frequencies are used, we note that, although in a few instances the errors in these frequencies exceed the dispersion, there is no systematic anomoly apparent. This result suggests that if observed frequency data from the light molecules only were used to determine force constants, the best quadratic approximation to the true potential function would have a slightly shallower cross section in the CH stretching coordinate and if data from the heavy molecule only were used, the cross section would be deeper. The use of harmonic frequencies circumvents this difficulty.

As one would expect, the values of the force constants determined from the harmonic frequencies differ significantly from those determined from the observed ones. The problem of anharmonicity is extremely important to the chemical spectroscopist as the molecules he habitually deals with are far too complex to allow rigorous calculation of harmonic frequencies, and it is general practice to ignore anharmonicity. This procedure may be rationalized by the following argument: Although the force constants determined from the harmonic frequencies are exactly defined, by the coefficients of the quadratic cross terms in the Taylor expansion of the potential energy, as $(\partial^2 V/\partial q^2)$ evaluated at

TABLE VI. Urey-Bradley force constants. The bond-stretching force constants K_{ij} and the nonbonded interaction constants F_{ij} are expressed in units of md/A. The bending force constants F_{ij} and the intramolecular tension κ, after multiplying by a factor of 10^{11}, are in ergs/(radian)^2.

	(i)		(ii)		(iii)		(iv)		(v)	(vi)	(vii)
CH_3F	$\bar{\phi}_i$	$\sigma\{\bar{\phi}_i\}$	$\bar{\phi}_i$	$\sigma\{\bar{\phi}_i\}$	$\bar{\phi}_i$	$\sigma\{\bar{\phi}_i\}$	$\bar{\phi}_i$	$\sigma\{\bar{\phi}_i\}$	(iii)−(i)	(iii)−(iv)	Tanaka[a]
K_{CH}	4.372	0.091	4.399	0.097	4.600	0.077	4.627	0.086	0.228	−0.027	...
K_{CF}	3.459	0.234	3.488	0.256	3.643	0.204	3.672	0.233	0.184	−0.029	3.135
H_{HF}	0.270	0.084	0.281	0.128	0.303	0.072	0.330	0.124	0.033	0.027	0.105
H_{HH}	0.643	0.038	0.609	0.032	0.584	0.032	0.551	0.029	−0.059	0.033	0.4
F_{HF}	1.118	0.146	1.080	0.154	1.103	0.117	1.065	0.129	−0.015	0.038	1.674
F_{HH}	−0.108	0.043	−0.117	0.047	0.027	0.036	0.020	0.041	0.135	0.007	0.427
κ	0.091	0.077	0.034	0.051	0.074	0.064	0.009	0.048	−0.013	0.063	−0.0455
CH_3Cl											
K_{CH}	4.731	0.081	4.763	0.082	5.221	0.037	5.256	0.026	0.490	−0.035	...
K_{CCl}	2.098	0.340	2.148	0.317	1.936	0.145	2.005	0.097	−0.162	−0.069	1.960
H_{HCl}	0.295	0.120	0.405	0.180	0.278	0.056	0.392	0.055	−0.017	−0.114	0.168
H_{HH}	0.520	0.025	0.531	0.027	0.591	0.011	0.606	0.008	0.071	−0.015	0.4
F_{HCl}	0.567	0.164	0.536	0.153	0.651	0.078	0.611	0.052	0.084	0.040	0.633
F_{HH}	0.039	0.034	0.009	0.034	−0.010	0.014	−0.044	0.010	−0.049	0.034	0.46
κ	0.043	0.057	−0.118	0.057	0.053	0.024	−0.116	0.017	0.010	0.169	−0.056
CH_3Br											
K_{CH}	4.822	0.065	4.856	0.071	5.274	0.024	5.311	0.022	0.452	−0.037	
K_{CBr}	1.722	0.301	1.768	0.304	1.532	0.102	1.611	0.087	−0.190	0.079	
H_{HBr}	0.251	0.108	0.341	0.154	0.197	0.042	0.308	0.048	−0.054	−0.111	
H_{HH}	0.518	0.018	0.537	0.019	0.574	0.007	0.598	0.005	0.056	−0.024	
F_{HBr}	0.483	0.143	0.455	0.145	0.592	0.056	0.547	0.047	0.109	0.045	
F_{HH}	0.018	0.026	−0.015	0.029	−0.016	0.009	−0.054	0.009	−0.034	0.038	
κ	0.046	0.046	−0.107	0.046	0.047	0.017	−0.120	0.013	0.001	0.167	
CH_3I											
K_{CH}	4.851	0.068	4.886	0.061	5.416	0.047	5.455	0.028	0.565	−0.039	
K_{CI}	1.349	0.304	1.432	0.249	1.276	0.209	1.375	0.114	−0.073	−0.099	
H_{HI}	0.219	0.114	0.323	0.123	0.219	0.018	0.335	0.058	0	−0.116	
H_{HH}	0.508	0.018	0.535	0.015	0.578	0.013	0.612	0.007	0.070	−0.034	
F_{HI}	0.393	0.140	0.353	0.127	0.428	0.100	0.379	0.054	0.035	0.049	
F_{HH}	0.028	0.028	−0.006	0.025	−0.030	0.019	−0.070	0.012	−0.058	0.040	
	0.043	0.044	0.127	0.035	0.043	0.031	−0.138	0.016	0	0.181	

[a] C. Tanaka, footnote reference 9.

equilibrium, in so far as we have neglected higher terms in V, the potential energy is not particularly well described by this quadratic function at large deviations from equilibrium, viz., at the extremes of the vibrational displacements. On the other hand, it is comforting to think of the use of observed vibrational frequencies as the fitting of a parabolic hypersurface to that part of the potential function swept out by the molecule in its first excited state, and whilst this surface might not exactly fit the true potential at any point, it does approximate the general shape of the lower part. But the real chemical sanction for neglect of anharmonicity in force-constant calculations comes from past demonstrations that the force constants so obtained are useful molecular parameters and correlate with other parameters of chemical importance. It is in the light of this criterion that we shall discuss the different sets of force constants given in Table VI. For convenience we have listed the differences between observed and harmonic UBFC [i.e., column (iii)−column (i)] under column (v), and the differences resulting from neglect of the slight deviations from tetrahedral angles [i.e., column (iii)−column (iv)] under column (vi).

The values of K_{CX} vary quite markedly throughout the series of the methyl halides, but unfortunately have a high dispersion which makes any correlation rather insensitive. Despite this high uncertainty, the present values correlate quite well with the Pauling electronegativity of the halogen atom (see Fig. 1). The harmonic and observed values of K_{CX} appear to fall on about the same line and the differences between these values can hardly be regarded as significant; certainly the differences between geometrically-correct and tetrahedral UBFC are negligible.

The nonbonded repulsive constants F_{HX} also show a systematic trend, and have been correlated with the Pauling electronegativity in Fig. 2. It is notable that the correlation with the harmonic force constants is more

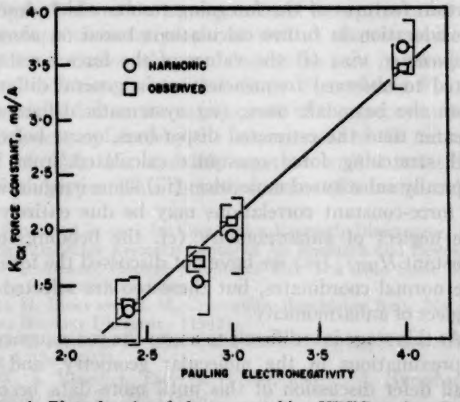

FIG. 1. Plot of carbon-halogen stretching UBFC against Pauling electronegativity of the halogen atom. The brackets about each point indicate the dispersion of the force constant.

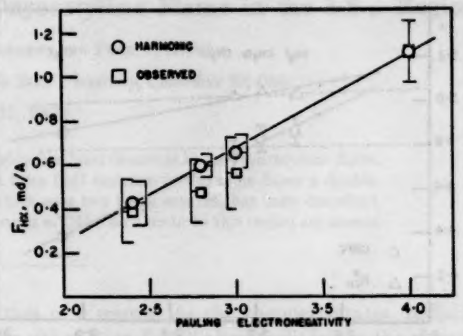

FIG. 2. Plot of nonbonded interaction F_{CX} against Pauling electronegativity of the halogen atom. The brackets about each point indicate the dispersion.

pleasingly linear than that with the observed force constants; the value found for F_{HF} (observed) appears to be too high, but again, the rather large uncertainty in this force constant discourages us from proposing a more detailed interpretation.

The carbon-hydrogen stretching force constants are by far the most sensitive to anharmonicity. They are determined with considerable precision as the C–H stretching modes are such excellent group frequencies. Therefore although some of the variations in K_{CH} with halogen substituent are quite small, we believe that they are real and reflect the slight variations in the electronic structure of the CH bonds. Coulson[20] has previously discussed variations in K_{CH} in terms of the sp hybridization of the carbon orbitals; we follow his approach and express the carbon orbitals as linear functions of $2s$ and $2p$ atomic orbitals:

$$\psi(\lambda)=(1+\lambda^2)^{-\frac{1}{2}}\{\psi(2s)+\lambda\psi(2p)\}. \qquad (11)$$

Assuming that the orbitals are orthonormal, we find in the particular case of molecules CXY_3 which have C_{3v} symmetry, that the value of λ for the carbon orbitals directed towards the Y atoms is

$$\lambda=[-\cos(YCY)]^{-\frac{1}{2}}. \qquad (12)$$

In Fig. 3 we show the values of K_{CH} calculated from observed frequencies plotted against λ^2; again, there is a good linear correlation. The harmonic force constants shown in Fig. 4 also fall on a straight line displaced to higher values.

The coordinates used in the UBFF are not independent, and in particular, the stretching of a single CH bond involves not only K_{CH} but also F_{XH} and F_{HH}. It is convenient to consider another force constant K^*, defined by

$$2V(r,\alpha)=\sum_i K_i^*(\Delta r_i)^2+\sum_i H_i^*(\Delta\alpha_i)^2,$$

where the valence coordinates r_i are now independent.

[20] C. A. Coulson, *Victor Henri Memorial Volume* (Desoer, Liege, 1948), p. 15.

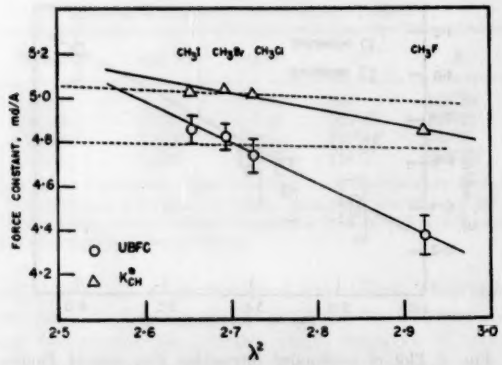

FIG. 3. Correlation of carbon-hydrogen stretching force constants based on observed frequencies with the sp hybridization of the carbon atom.

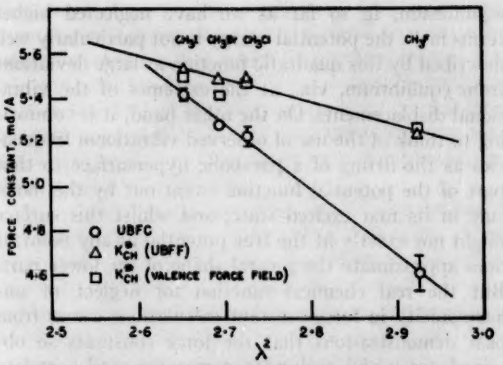

FIG. 4. Correlation of carbon-hydrogen stretching force constants, based on harmonic frequencies, with the sp hybridization of the carbon atom.

The values found for K_{CH}* reflect the work involved in stretching a single CH bond and are comparable with the valence force constants K_{CH} determined by fitting to a general quadratic valence force field. In Fig. 4 we have included general-quadratic-VFF points taken from footnote references 7 and 8 in addition to our UBFF values of K_{CH}* and the agreement is satisfactory.

It does not seem unreasonable to take the difference between the methane and ethylene values as a measure of the dependence of K_{CH} and K_{CH}* on the degree of sp hybridization. Taking the values[21] $K_{CH}=4.76$, $K_{CH}^*=4.96$, $\lambda^2=3$, and $K_{CH}=4.80$, $K_{CH}^*=5.14$, $\lambda^2=2.18$, for methane and ethylene, respectively, quasi-theoretical correlations between K_{CH}, K_{CH}*, and λ are obtained; these are shown by broken lines in Fig. 3. The points corresponding to K_{CH}* for CH_3Cl, CH_3Br and CH_3I fall very close to the line, but that for CH_3F falls off the line by a bit more than the calculated dispersion of K_{CH}, and the discrepancy may be significant. Similarly, the K_{CH} values of CH_3Cl, CH_3Br, and CH_3I fall on the second line, but in this case the point for CH_3F deviates widely. The over-all effect of these deviations is to make a linear correlation of K_{CH} or K_{CH}* vs λ^2 for the methyl halides have a much steeper slope than the quasi-theoretical one. Alternately, we may regard the fluoride results as anomolous.

In the least-squares adjustment process there is a strong correlation[22] between K_{CH} and F_{HX} and there is a possibility that the low value of $K_{CH}(CH_3F)$ may be spurious, arising through this correlation and the fact that the value of F_{HX} is determined largely by the bending frequencies.

The bending force constants H_{HH} are determined with considerable precision and show an interesting phenomenon; the harmonic force constant is, to all intents and purposes, independent of the halogen and has a constant value of ca. 0.580×10^{-11} ergs/radian).[2]

However, this invariance is not found in the force constants calculated from the observed frequencies, but the value of H_{HH} for CH_3F is asequential; see Table VI. Here is a case where the regularity in a series of force constants is obscured if observed frequencies are used.

We have not attempted correlations with the remaining force constants as H_{HX} has a rather high uncertainty and the calculated values fall in random order, and the values of F_{HH} and κ are both very small. The values of κ do not depend much on whether we use observed or harmonic frequencies, but the dependence on assumed geometry appears to be quite critical. Unfortunately the absolute values are small, and we cannot estimate the importance of this effect in cases where κ is an important force constant, (e.g., CCl_4 etc.).

This analysis of the methyl halides indicates that we may still expect to find correlations which facilitate transfer of force constants and which in some cases throw light on molecular structure, even though we use observed frequencies in the place of the theoretically desirable harmonic frequencies. There are, however, certain features of the foregoing results which deserve consideration in future calculations based on *observed frequencies*, viz., (i) the values of the force constants fitted to observed frequencies are in general different from the harmonic ones; (ii) systematic differences, greater than the estimated dispersions, occur between CH stretching force constants calculated from isotopically substituted molecules; (iii) some irregularities in force-constant correlations may be due entirely to the neglect of anharmonicity (cf. the bending force constant H_{HH}); (iv) we have not discussed the form of the normal coordinates, but these too are affected by neglect of anharmonicity.

At this stage is is difficult to assess the consequence of approximations in the molecular geometry, and we shall defer discussion of this until more data become available, particularly for molecules where the intramolecular tension is important.

[21] J. Overend and J. R. Scherer (unpublished data).

[22] UBFC correlation matrices were calculated for each set of force constants in Table VI. These have been filed and are available on request to the authors.

Emission Spectrum of the OH Radical in an Oxyacetylene Flame in the 1.5-μ Region*

WILLIAM H. ROGGE, FREDERICK L. YARGER, AND FRED P. DICKEY

Department of Physics and Astronomy, The Ohio State University, Columbus 10, Ohio

(Received March 17, 1960)

The emission spectrum of the OH radical in the 1.5-μ region has been observed in an oxyacetylene flame. In order to eliminate the strong background which results from H_2O emission in the same flame a double-beam method has been used. The double-beam method, which uses two flame sources, has been described. The spectrum of the 2–0, 3–1, and 4–2 vibration-rotation bands of OH which occur in this region are shown.

INTRODUCTION

THE emission spectrum of the OH radical has been studied by several investigators. Dieke and Crosswhite[1] have made extensive studies of various bands in the ultraviolet region. They have determined energy levels which may be used to predict the line frequencies in the infrared region. More recently Allen, Blaine, and Plyler[2] have observed the fundamental vibration-rotation band in the infrared region using an oxyacetylene flame as a source. Benedict, Plyler, and Humphreys[3] have observed the first-overtone vibration-rotation band in a like manner. Some of the pure-rotation lines have been observed by Dickey and Hoffman[4] using a phase-discrimination method of detection so as to eliminate the H_2O background.

The present work is concerned with the OH spectrum in the region of the first-overtone vibration-rotation band. In order to eliminate the effects of the H_2O spectrum in this region a double-beam method has been used.

EXPERIMENTAL

A prism-grating high-resolution spectrometer was used to obtain the spectrum. The grating was a 7500-lines-per-in. replica and the detector was an uncooled lead-sulfide cell. A Perkin-Elmer model-81 amplifier was used in conjunction with a Brown Electronik recorder.

Figure 1 shows the arrangement of the optics external to the spectrometer proper as well as the two sources and the radiation chopper. As can be seen in the diagram, radiation from either flame F_1 or flame F_2 can be made to fall on the entrance slit of the spectrometer. This is accomplished by the arrangement of the mirrors M_1, M_2, M_3, M_4, and M_5 together with a rotating-mirror chopper. This chopper consists of a semicircular section of a mirror. As the chopper rotates, radiation from either F_1 or F_2 will alternately fall on the entrance slit of the spectrometer. The rather extensive shielding required in the external optics system is not shown as it would obscure the detail in Fig. 1. The effective radiation from flame F_1 is almost doubled by the use of mirror M_6.

The chopper is driven by a shaft connected to the mechanical rectifier of the Perkin-Elmer amplifier and the spectrometer is thus essentially a double-beam system. The observation of the OH spectrum without the overlapping H_2O spectrum is made possible by the characteristics of the two sources. Ideally, if the two

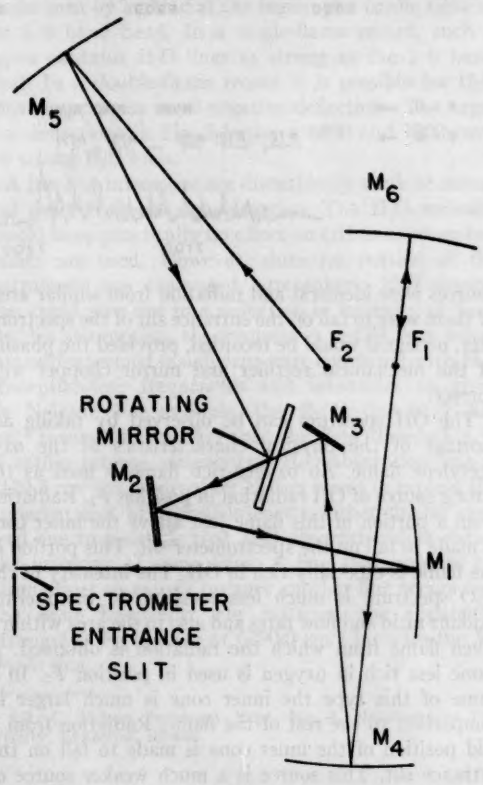

FIG. 1. Source optics external to the spectrometer.

* Supported in part by Geophysics Research Directorate, Air Force Cambridge Research Center of Air Research and Development Command, through a contract with The Ohio State University Research Foundation.

[1] G. H. Dieke and H. M. Crosswhite, Bumblebee Rept. No. 87, Johns Hopkins University (1948).

[2] H. C. Allen, L. R. Blaine, and Earle K. Plyler, Spectrochim. Acta 9, 126 (1957).

[3] W. S. Benedict, Earle K. Plyler, and C. J. Humphreys, J. Chem. Phys. 21, 398 (1953).

[4] F. P. Dickey and J. M. Hoffman, J. Chem. Phys. 28, 1253 (1958).

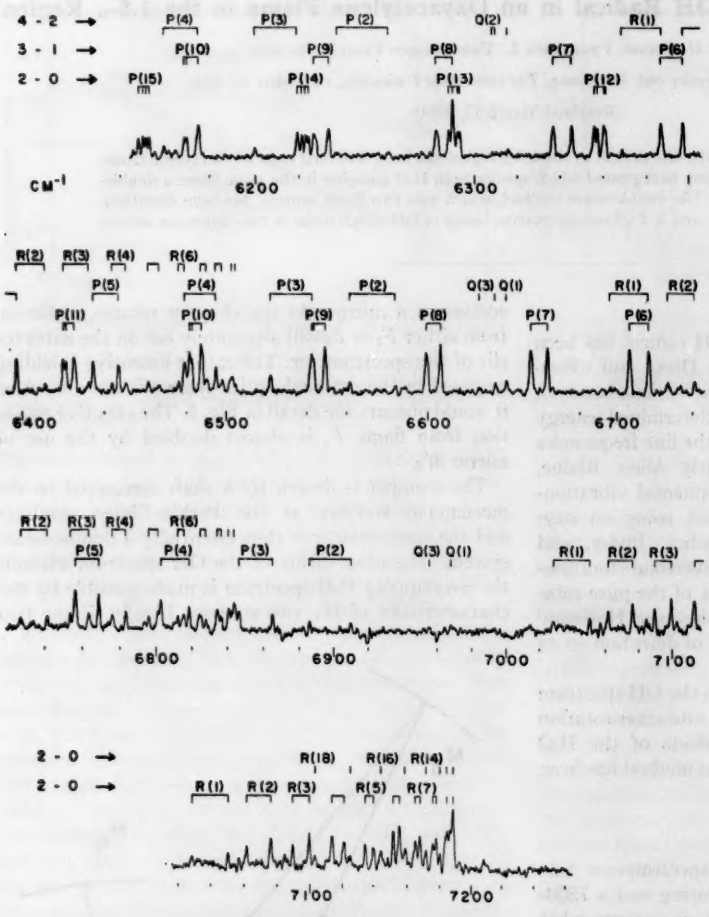

FIG. 2. Spectrum of the OH radical in an oxyacetylene flame in the 1.5-μ region.

sources were identical and radiation from similar areas of them were to fall on the entrance slit of the spectrometer, no signal would be recorded, provided the phasing of the mechanical rectifier and mirror chopper were correct.

The OH spectrum can be observed by taking advantage of the physical characteristics of the oxyacetylene flame. An oxygen-rich flame is used as the strong source of OH radiation in position F_1. Radiation from a portion of this flame just above the inner cone is made to fall on the spectrometer slit. This portion of the flame is especially rich in OH. The intensity of the H_2O spectrum is much less sensitive to the fuel-to-oxidant ratio and flow rates and also to the area within a given flame from which the radiation is obtained. A flame less rich in oxygen is used in position F_2. In a flame of this type the inner cone is much larger in comparison to the rest of the flame. Radiation from a mid position of the inner cone is made to fall on the entrance slit. This source is a much weaker source of OH radiation.

The flames are produced by small hand torches mounted on Lab-Jacks. Rather small openings in the radiation shields together with accurate torch-height adjustment make it possible to use small regions in either flame as the respective sources. Flow gauges are used to determine the amounts of fuel and oxidant used.

The source system makes it possible to have the flame F_2 supply H_2O radiation which will balance out the H_2O radiation of the strong OH source F_1. In the observation of the present bands the adjustment is made so that the radiation from F_2 minimizes some strong H_2O line near the OH 2-0 band head without significantly reducing the band head itself. The recorded spectrum is shown in Fig. 2.

RESULTS

The vibration-rotation bands of OH are complicated by a nonzero orbital angular momentum $\Lambda=1$, resulting in $^2\Pi$–$^2\Pi$ transitions. Furthermore, the electron spin is one-half. Each of these facts leads to a doubling

of the rotational-term values. Hill and Van Vleck[5] treated the intermediate case between Hund's cases A and B and obtained theoretical term values of the form

$$f_1(K)=B_v\{(K+1)^2-\Lambda^2 -\tfrac{1}{2}[4(K+1)^2+Y_v(Y_v-4)\Lambda^2]^{\frac{1}{2}}\}-D_vK^2(K+1)^2,$$

when $K=J-\frac{1}{2}$;

$$f_2(K)=B_v\{K^2-\Lambda^2+\tfrac{1}{2}[4K^2+Y_v(Y_v-4)\Lambda^2]^{\frac{1}{2}}\} -D_vK^2(K+1)^2,$$

when $K=J+\frac{1}{2}$.

This notation, with some variation, has been commonly used in recent literature. The Λ-type doubling which splits each $f_i(K)$ term into two terms may be expressed as

$$f_i'(K)-f_i(K)=q_vK(K+1).$$

The general selection rules are $\Delta J=0,\pm1$; $\Delta K=0,\pm1$; $+\rightarrow-$, $-\rightarrow+$. This allows 24 branches all together, usually subdivided into 12 main branches and 12 satellite branches. The main branches are those for which $\Delta J=\Delta K$, and the satellite branches are those for which $\Delta J\neq\Delta K$, and the satellite branches are, in general, much weaker than the main branches. The 12 main branches are

$$\begin{aligned}
P_1(K)&=f_1(K-1)-f_1(K) && (J-1\rightarrow J)\\
P_1'(K)&=f_1'(K-1)-f_1'(K) && (J-1\rightarrow J)\\
P_2(K)&=f_2(K-1)-f_2(K) && (J-1\rightarrow J)\\
P_2'(K)&=f_2'(K-1)-f_2'(K) && (J-1\rightarrow J)\\
Q_1(K)&=f_1(K)-f_1'(K) && (J\rightarrow J)\\
Q_1'(K)&=f_1'(K)-f_1(K) && (J\rightarrow J)\\
Q_2(K)&=f_2(K)-f_2'(K) && (J\rightarrow J)\\
Q_2'(K)&=f_2'(K)-f_2(K) && (J\rightarrow J)\\
R_1(K)&=f_1(K+1)-f_1(K) && (J+1\rightarrow J)\\
R_1'(K)&=f_1'(K+1)-f_1'(K) && (J+1\rightarrow J)\\
R_2(K)&=f_2(K+1)-f_2(K) && (J+1\rightarrow J)\\
R_2'(K)&=f_2'(K+1)-f_2'(K) && (J+1\rightarrow J).
\end{aligned}$$

In Fig. 2, $P(K)$, $Q(K)$, and $R(K)$ stand for groups of four lines each. Thus $P(K)$ includes $P_1(K)$, $P_1'(K)$, $P_2(K)$, and $P_2'(K)$ while $R(K)$ and $Q(K)$ include similar groups of four lines indicated in the preceding equations. $P_1(K)$ and $P_1'(K)$ remain close together, as do $P_2(K)$ and $P_2'(K)$ when compared with the spacing between $P_1(K)$ and $P_2(K)$, hence the former are more difficult to resolve. Only for high K values could the P lines be split into four distinct lines. The R lines were never resolved into more than two components, $R_1(K)$ and $R_2(K)$, the Λ-type doubling being too weak. For high K values, $K>8$, all four components were so close together that only one $R(K)$ line was observed. The Q lines are so weak that only a few scattered lines could be identified.

The 2–0, 3–1, and 4–2 band heads in Fig. 2 occur at 7187.7, 6844.5, and 6504.7 cm^{-1}, respectively, in good agreement with the frequencies predicted by Dieke and Crosswhite.[1] In fact, all line frequencies calculated from the spectrum are in agreement with the predicted line frequencies of Dieke and Crosswhite to within the accuracy of our measurements. The individual line frequencies are not tabulated.

A comparison of Fig. 2 with a single-flame record like that of Benedict, Plyler, and Humphreys[2] indicates the effectiveness of the phase-discrimination method. Such a comparison shows that the H_2O intensity is weak below 6400 cm^{-1} but that from there to 7200 cm^{-1} it increases so much that a strong line like the 2–0 band head at 7187.7 cm^{-1} can hardly be identified in a single-flame record. However, only traces of H_2O emission exist in the double-flame record of Fig. 2 as can be seen by looking at the region just to the right of the 2–0 band head. In a single-flame record, such a region contains H_2O lines as strong as the 2–0 band head. In a double-flame record it is possible for H_2O lines to appear as small negative deflections. The negative deflections in Fig. 2 between 6800 and 7000 cm^{-1} are strong H_2O lines.

A few line intensities are disturbingly weak or strong and deserve special consideration. The H_2O emission should have practically no effect on OH lines when two flames are used. However, since no portion of the instrument was evacuated, atmospheric H_2O absorption could give rise to a reduction in intensity of lines. On this assumption, the frequencies of OH lines whose intensities seemed insufficient were compared with H_2O absorption-line frequencies and intensities as given by Nelson.[6] For example, the $R_1(4)$ line at 7120.6 cm^{-1} is somewhat weaker than the $R_2(4)$ line in Fig. 2. A rather intense atmospheric H_2O absorption line at 7120.3 cm^{-1} as reported by Nelson seems to explain this apparent lack of normal intensity. Other similar cases lead one to conclude that H_2O absorption does reduce the intensity of some lines. A line that appears too strong does so merely because another line occurs near the same frequency. For instance, the apparently strong 2–0 $P_1(13)$ line at 6290.0 cm^{-1} includes the 3–1 $P_2(8)$ line.

[5] E. L. Hill and J. H. Van Vleck, Phys. Rev. 32, 250 (1923).

[6] R. C. Nelson, Summary Rept. No. 4, Northwestern University, Evanston, Illinois.

Radial Distribution Functions from the Born-Green Integral Equation

A. A. BROYLES

The RAND Corporation, Santa Monica, California

(Received February 12, 1960)

Comparisons are made between solutions to the Born-Green integral equation and radial distribution functions obtained by the Monte Carlo method by Wood and Parker for the Lennard-Jones potential. It is observed that multiplying the particle separation distance in the Born-Green case by a constant factor improves the agreement for loops beyond the first.

I. INTRODUCTION

THE equation of state of a classical monatomic fluid may be readily obtained if the radial distribution function is known. The most practical procedure for determining this distribution function accurately for high densities or low temperatures employs a Monte Carlo method. A recent paper by Wood and Parker[1] presents their results for particles in a fluid interacting by means of the Lennard-Jones potential,

$$\phi(r)=4\epsilon[(a/r)^{12}-(a/r)^{6}], \tag{1}$$

where r is the separation distance between a pair of particles.

They also make a comparison with the results of Kirkwood, Lewinson, and Alder[2] using the Born-Green integral equation. Unfortunately, the Born-Green calculations were done for a modified Lennard-Jones potential having a hard core whose radius is equal to the radius at which the Lennard-Jones potential is zero [$r=a$ in Eq. (1)]. Such a core is large enough to noticeably affect the radial distribution function. The solutions to the Born-Green equation described here were obtained for the unmodified Lennard-Jones potential and were extended to lower specific volumes v than those of footnote reference 2.

Although the Monte Carlo procedure is probably the best way to compute accurate distribution functions, there still remains the possibility that solving the Born-Green integral equation can produce solutions more rapidly. For this reason, it might be worth considering the Born-Green solutions as aids to interpolating between radial distribution functions obtained by the Monte Carlo method. An effort was made here to present the Born-Green solution in such a manner that the agreement between it and the Monte Carlo solution was improved. This was done by altering the radius scale of the Born-Green solution.

It is also possible that this comparison of the two methods may suggest a way of correcting the Born-Green integral equation itself to give a better radial distribution function. Such a correction would involve improving upon the superposition approximation.

The Born-Green equation was preferred over the Kirkwood equation because it can be reduced to one involving a double integral while the Kirkwood equation required a triple integral. No reason other than numerical simplicity can be given for preferring it over the many other equations that now exist.

II. NUMERICAL PROCEDURE

The Born-Green equation was solved in the form

$$f(r)=(n\pi/r)\int_0^\infty \exp[-\beta\phi(s)+f(s)]\beta\phi'(s)\times$$

$$\int_{r-s}^{r+s}[s^2-(y-r)^2]y\{\exp[-\beta\phi(y)+f(y)]-1\}dyds, \tag{2}$$

where the radial distribution function g is given by

$$g(r)=\exp[-\beta\phi(r)+f(r)], \tag{3}$$

n is the particle density, and β is the reciprocal of the temperature multiplied by the Boltzmann constant.

The solution was obtained by iteration. A guess, f_1, was substituted for f where it appears under an integral sign in Eq. (2). A new function f_2 was then obtained by integration. These two f's were then used to compute g's from Eq. (3) and a new g, g_3, obtained from these using the linear combination

$$g_3=\alpha g_2+(1-\alpha)g_1. \tag{4}$$

Equation (3) was then used to obtain the new guess f_3 from g_3.

It was discovered that, for a fixed α, continued iteration by the above procedure caused g to approach its final value exponentially with the iteration number j. Thus we have

$$g^{(j)}\approx g^{(\infty)}+Ae^{-\alpha j} \tag{5}$$

provided $g^{(j)}$ is near enough to $g^{(\infty)}$. This equation may be used to show that a $g^{(j)}$, behaving in such a manner,

[1] Wood and Parker, J. Chem. Phys. **27**, 720 (1957).

[2] J. G. Kirkwood, V. A. Lewinson, and B. J. Alder, J. Chem. Phys. **20**, 929 (1952).

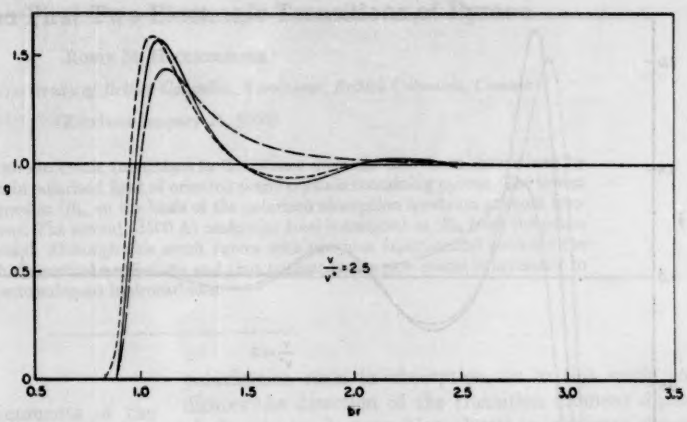

FIG. 1. The radial distribution function g vs br for $v/v^* = n^{-1} = 2.5$ from the Monte Carlo method (solid curve) and the Born-Green equation (short-dashed curve). The function $e^{-\beta\phi}$ vs br (long-dashed curve). The parameter b is a^{-1} for the Monte Carlo and $e^{-\beta\phi}$ curves and is $0.97a^{-1}$ for the Born-Green curve.

can be used to calculate $g^{(\infty)}$ from the relation

$$g^{(\infty)} = g^{(j)} + [g^{(j+1)} - g^{(j)}]/(1-R), \tag{6}$$

where

$$R = [g^{(j+1)} - g^{(j)}]/[g^{(j)} - g^{(j-1)}]. \tag{7}$$

This extrapolation procedure became particularly valuable when it was discovered that R seemed to be independent of r.

It was further discovered that $g^{(j)}$ settled more rapidly to a smooth approach to $g^{(\infty)}$ such as that in Eq. (5) when α in Eq. (4) was small. It should be emphasized that Eqs. (5) and (6) did not apply unless $g^{(j)}$ was close enough to $g^{(\infty)}$.

Although the foregoing procedure was adopted here, it is not at all clear but what less calculating time would have been required if Eq. (2) had been "linearized" on the assumption that the guess f_1 was not far from the true solution. The resulting linear equation could then have been solved by standard techniques for such equations. Iteration would still have been necessary but each succeeding guessed value of f would have been determined in a more sophisticated way than that of Eq. (4).

III. ACCURACY

The difficulty of obtaining a solution increases as v/v^* decreases. For this reason, the accuracy with which solutions were determined decreased with decreasing v/v^*. Nevertheless, the author is convinced that the solution presented in Fig. 3 for $v/v^* = 1.0$ lies within 1% of a true solution of the Born-Green equation for points to the right of the first $g=1$ point. In order to ensure such an accuracy, it is necessary to make certain that (1) the interval in r is small enough to allow the numerical integration in Eq. (2) to be performed accurately and (2) a sufficient number of iterations of the type described in Sec. II were carried out.

To check the interval size, a comparison was made between solutions obtained with intervals of 0.05 and 0.025 in r. The largest differences found between the two solutions for points to the right of the first $g=1$ point amounted to slightly more than 1%. Since errors for such numerical calculations usually increase with the *square* of the interval for small errors, it seems reasonable to assume that the solution obtained at an interval of 0.025 in r is well within 1% of the limit as Δr approaches zero.

Any three successive iterations could be used to extrapolate $g^{(\infty)}$ with the aid of Eqs. (6) and (7). The last two extrapolated $g^{(\infty)}$'s obtained at the interval of 0.025 in r, differed by less than 0.2% for all points to the right of the first $g=1$ point. The $g^{(j)}$'s themselves differed from extrapolated $g^{(\infty)}$'s by only about 0.4%. These iterations were performed with an α of 0.25. It is interesting to compare $g^{(j)}$ and $g^{(\infty)}$ at an earlier iteration where they differed by about 2%. The $g^{(\infty)}$ extrapolated from these iterations differed from $g^{(\infty)}$ computed from the last iterations by only about 0.4%. It is concluded that the error due to the failure to iterate an infinite number of times must be less than 1%.

IV. RESULTS AND DISCUSSION

The results of the numerical procedures described in Sec. II are presented in Figs. 1–3 along with the Monte Carlo radial distribution functions obtained for the same potential in footnote reference 1. All cases are for a value of $\beta\epsilon$ equal to $(2.74)^{-1}$. The unit of r was chosen to be the a in the Lennard-Jones potential of Eq. (1). The v/v^* used by Wood and Parker is equal to $n^{-1}a^{-3}$. Of course, $a=1$ in our units. The function $e^{-\beta\phi}$ is also plotted for comparison.

It is interesting to note that loops to the right of the first one are very similar for the two methods when r for the Born-Green solution is multiplied by a scaling factor. It should be emphasized, however, that this scaling factor is no help at all in describing the shape of the curve to the left of the second crossing of the $g=1$ line. Since this left region is likely to be most important for computing thermodynamic quantities, the scaling factor is of little value for such calculations.

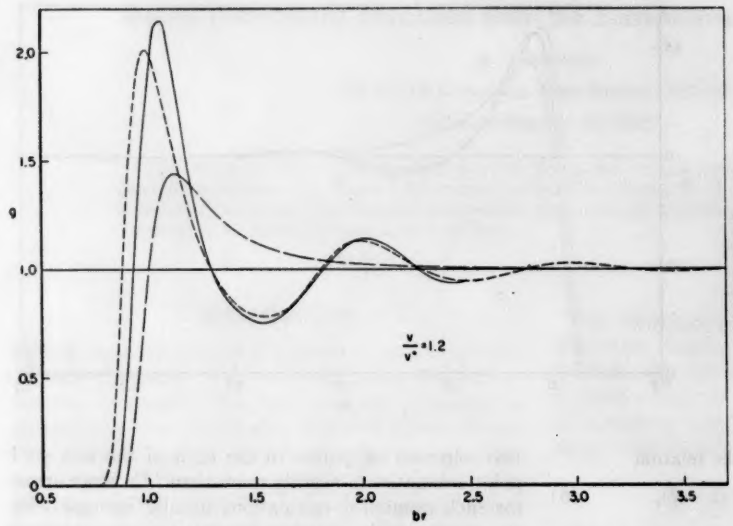

FIG. 2. The radial distribution function g vs br for $v/v^* = \pi^{-1} = 1.2$ from the Monte Carlo method (solid curve) and the Born-Green equation (short-dashed curve). The function $e^{-\beta\phi}$ vs br (long-dashed curve). The parameter b is a^{-1} for the Monte Carlo and $e^{-\beta\phi}$ curves and is $0.916a^{-1}$ for the Born-Green curve.

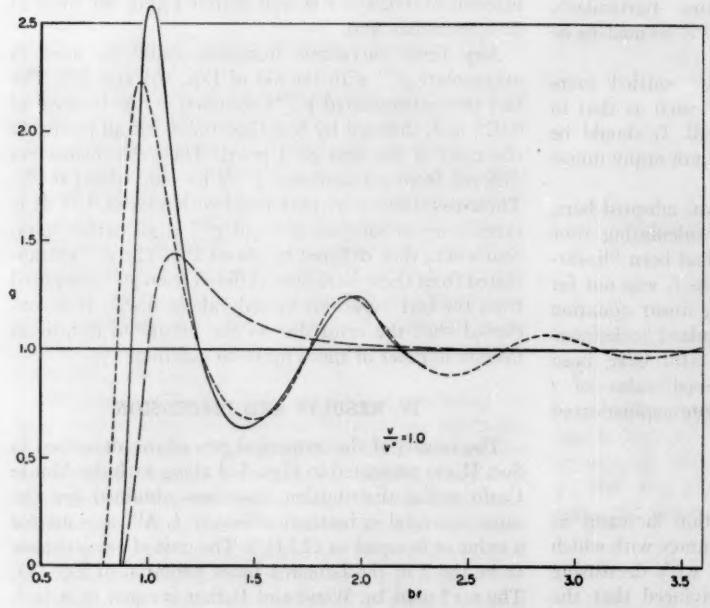

FIG. 3. The radial distribution function g vs br for $v/v^* = \pi^{-1} = 1.0$ from the Monte Carlo method (solid curve) and the Born-Green equation (short-dashed curve). The function $e^{-\beta\phi}$ vs br (long-dashed curve). The parameter b is a^{-1} for the Monte Carlo and $e^{-\beta\phi}$ curves and is $0.898a^{-1}$ for the Born-Green curve.

It does, however, provide a means of obtaining approximately the Monte Carlo results from the Born-Green solution for loops to the right of this second point of $g=1$ when v/v^* is less than 1.0. Since the scaling factor is a function of v/v^*, it must be interpolated for values not computed here.

Calculations are currently in progress for the case in which v/v^* is 0.90. Although the final results are not yet available, it seems rather certain that a solution of the Born-Green equation does exist here, even though the crystal structure is already apparent in the Monte Carlo radial distribution function.

V. ACKNOWLEDGMENTS

Very helpful information about the Monte Carlo work was obtained in a conversation and correspondence with W. W. Wood. The coding of this problem for the RAND electronic computer (Johnniac) was carried out by C. L. Lowery who is responsible for several helpful suggestions for the numerical procedure.

Polarization of the First Two Electronic Transitions of Pyrene

ROBIN M. HOCHSTRASSER

Chemistry Department, The University of British Columbia, Vancouver, British Columbia, Canada

(Received January 21, 1960)

The polarization of the first two electronic transitions in the pyrene molecule have been determined by measuring the absorption spectra in polarized light of oriented single crystals containing pyrene. The lowest molecular level (3700 A) is assigned as $^1B_{3u}$ on the basis of the polarized absorption spectrum at room temperature of pyrene in phenanthrene. The second (3500 A) molecular level is assigned as $^1B_{2u}$ from the polarized spectrum of pyrene in dibenzyl. Although this result agrees with previous experimental evidence the assignments are at variance with theoretical predictions and thus suggest that a new model is necessary to predict the molecular levels of pericondensed hydrocarbons.

INTRODUCTION

IN many cases the symmetry assignments of the molecular levels of aromatic hydrocarbons cannot be deduced directly from measurements of the polarization ratio. For example naphthalene,[1] anthracene,[2] and pyrene[3] are in this category. This situation arises because of crystal-induced mixing of electronic states of different polarization caused by the interactions between molecules in the unit cell.[4] The result of such interactions is that the measured polarization ratio is frequently quite different from that calculated from an oriented gas model and is often a function of wavelength. McClure demonstrated that a molecule dissolved in a suitable matrix crystal behaved more like an oriented gas molecule.[5] The first two states of naphthalene were assigned by examining the spectrum of small quantities of naphthalene in single crystals of durene. Later the lowest state of anthracene was assigned using a dilute solid solution of anthracene in phenanthrene.[6]

The true assignment of the electronic states of pyrene is particularly interesting because it is not yet certain whether the numerous theories which have been used to successfully predict the energy levels and polarizations of the electronic states of catacondensed hydrocarbons are applicable to pericondensed systems. This paper is concerned with the polarized absorption spectra of pyrene in suitable crystal matrices at room temperature and it is shown that this approach can decide on the symmetry of the two lowest electronic states of pyrene. The earlier and more detailed experiments of McClure[5] and Sidman[6] were concerned with vibrational analyses at very low temperatures. Although experiments at room temperature may not be as convincing as those at 20°K it appears to be possible to measure some further properties of the dissolved molecule at the elevated temperature. For example, a measurement of the polarization ratio in absorption, as in this work, indicates the direction of the transition moment dipole of the electronic transition. Further, accurate determinations of this ratio may provide new information regarding the orientation of the solute molecules in the crystal matrix.

PREPARATION AND PROPERTIES OF THE MIXED CRYSTALS

A dilute crystalline solid solution of pyrene in phenanthrene was prepared by slow recrystallization from the melt. When a small crystal was melted between quartz disks, large monocrystalline areas could be developed. The *ab* face of the crystal was developed parallel to the face of the disk. Phenanthrene is known to contain anthracene in substitutional solid solution and the procedure for removing this impurity is lengthy.[7] In this work it was found that the presence of anthracene did not interfere with the absorption measurements. The anthracene absorption bands could be used to monitor the pyrene absorption in each polarization and hence prove that the pyrene molecules were in true solid solution. The absorption spectrum of the phenanthrene crystal is known[8] and though the crystal structure has not been unambiguously determined the similarity of the phenanthrene and anthracene crystals can provide additional information. The long molecular axis must lie nearly along the *c* direction of the crystal and the short molecular axis should make an angle of approximately 35° with the *b* crystal axis and lie along the *ab* plane. This should result in a polarization ratio D_b/D_a of 2.04:1 for transitions polarized along the short molecular axis while long-axis-polarized transitions should be more strongly absorbed in the *a* polarization.

The amount of pyrene in the crystals was about 0.1% and a comparison of the relative optical density of the pyrene and anthracene peaks indicated that the pyrene to anthracene ratio was around 50 moles/mole. The extinction coefficients in liquid solution were used for this calculation. The phenanthrene absorption started

[1] D. S. McClure and O. Schnepp, J. Chem. Phys. **23**, 1575 (1955).
[2] D. P. Craig and P. C. Hobbins, J. Chem. Soc. **1955**, 539, 2302.
[3] J. Ferguson, J. Chem. Phys. **28**, 765 (1958).
[4] D. P. Craig, Revs. Pure and Appl. Chem. **3**, 207 (1953).
[5] D. S. McClure, J. Chem. Phys. **22**, 1668 (1954).
[6] J. W. Sidman, J. Chem. Phys. **25**, 115 (1956).
[7] W. E. Bachmann, J. Am. Chem. Soc. **57**, 555 (1935).
[8] D. S. McClure, J. Chem. Phys. **25**, 481 (1956).

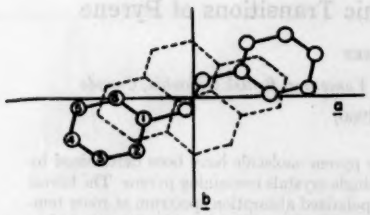

FIG. 1. The orientation of a dibenzyl molecule with respect to the a and b crystallographic axes. The most probable relative orientation of the pyrene molecule is indicated by the dashed line.

to appear at around 2650 A so it was necessary to use another host crystal to examine the higher electronic states of pyrene. It was assumed that the pyrene molecules occupied the positions in the phenanthrene lattice which would produce the least distortion of the crystal. This would have occurred only if a pyrene molecule had its long axis parallel to the corresponding molecular axis of the phenanthrene molecules.

To examine the next electronic state of pyrene (occurring in liquid solution at 3000–3600 A) it was necessary to obtain a host crystal which was transparent in this spectral region, and whose crystal structure was known. Biphenyl, durene, and naphthalene were tried without success. In each of these cases large single crystals could be grown yet no pyrene absorption was detected even in the thickest crystals (2–3 mm).

It was possible to obtain solid solutions of pyrene in dibenzyl. The polarization properties and microscopic examination of these crystals showed that they were true monocrystals with pyrene in solid solution. The mixed crystals showed a strong blue fluorescence which was evenly distributed throughout the crystal. Again it was reasonable to assume that the pyrene molecules occupied positions at least distortion in the dibenzyl lattice, that is, the long axis of pyrene parallel to the long molecular axis of dibenzyl. Dibenzyl forms needle-like crystals when solidified from the melt and samples suitable for spectroscopic examination could be obtained by repeated melting and recrystalization between pressed quartz disks. In this way the ab plane of the crystal was developed parallel to the face of the disks.

The a and b crystallographic axes were located by examining each of the crystals under the polarizing microscope.

Crystal Structure of Dibenzyl

The dibenzyl crystal structure has been determined by Robertson[9] and subsequently reexamined and refined by Jeffrey.[10] The crystal is monoclinic. The unit cell contains two centrosymmetric molecules related by the space group $2_1/a$. The benzene rings are planar to within 1°. The unit cell has the dimensions $a=12.77$ A, $b=6.12$ A, $c=7.7$ A, and $\beta=116°$.

[9] J. M. Robertson, Proc. Roy. Soc. (London) **A150**, 348 (1935).
[10] G. A. Jeffrey, Proc. Roy. Soc. (London) **A188**, 222 (1947).

The location of a dibenzyl molecule referred to the a and b crystallographic axes is given in Fig. 1 and the most probable position of the pyrene molecules is also indicated. The short molecular axis of pyrene was taken to be parallel to the C_2—C_8 line and the long molecular axis parallel to C_1—C_4 in the dibenzyl molecule. In Table I, ψ and χ are the inclinations to the a and b crystal axes of the lines associated with the benzene rings.

The polarization ratio D_a/D_b is defined as the ratio of the optical density when the electric vector of the incident light is parallel to the a axis relative to that when it is parallel to the b axis of the crystal. On the basis of an oriented gas model the expected ratios D_a/D_b for transitions polarized along the short and long molecular axes of pyrene are 0.422 and 9.0, respectively. Thus the presence of long-axis-polarized transitions should result in a marked pleochroism normal to the ab face of the crystal.

The lowest singlet-singlet transition of the dibenzyl crystal was examined by Coffman and McClure[11] and it was shown that this transition is short-axis polarized. There was no pleochroism and it was not possible to distinguish between the a- and b-polarized spectra. Thus it may be assumed that any marked deviation from a unit polarization ratio indicates a long-axis-polarized transition.[12] Restrictions such as these do not exclude the possibility of transitions polarized perpendicular to the plane of the aromatic ring but transitions of this type will not be considered feasible as all $\pi\rightarrow\pi^*$ transitions must give rise to excited states which are totally symmetric to reflection in the molecular plane. Hence the transition moments must always be in the plane of the aromatic ring.[13]

Determination of the Absorption Spectra

The spectra were recorded on a Hilger medium quartz spectrograph. The standard housing was replaced by a

TABLE I. The direction cosines[a] of the molecular axes of pyrene to the dibenzyl crystal axes.

Crystal axis	Short molecular axis	Long molecular axis
a	0.525	0.810
b	0.705	0.235

[a] The values in the table are $\cos\psi$ and $\cos\chi$ where the molecular axes make angles ψ and χ with the a and b crystal axes, respectively.

[11] R. Coffman and D. S. McClure, Can. J. Chem. **36**, 48 (1958)
[12] These authors quote a value of 0.65 for D_a/D_b calculated from an oriented gas model for the short axis polarized transitions in dibenzyl. This figure is the ratio of the direction cosines $\cos\psi/\cos\chi$ whereas the optical density ratio D_a/D_b is given by $\cos^2\psi/\cos^2\chi$.
[13] Recently R. Williams [J. Chem. Phys. **30**, 233 (1959)] has observed from polarized fluorescence measurements that the lowest triplet state of phenanthrene is polarized perpendicular to the molecular plane. As he points out such is possible only if there is some mixing with the σ states of the molecule which are however at much higher energy than the π states.

1P28 photomultiplier which was driven by the automatic scanning attachment. The photocurrents were amplified on a Keithley micromicroammeter the output of which was connected to a pen recorder. The light source was an air-cooled Osram HB160 high-pressure xenon arc which had a stabilized power supply. After passage through a water filter, parallel light fell normal to the *ab* face of the crystal. The crystal was placed over a small hole in order that the incident light intensity could be measured simply by removing the crystal and replacing it by two quartz disks of the same thickness as those containing the crystal. The analyzer was a Wollaston prism placed between the crystal and the slit of the spectrometer. The Wollaston prism could be rotated with the result that the *a*- and *b*-polarized light beams were interchanged at the slit. Both the *a*- and *b*-polarized absorptions were measured with and without the crystal in the light beam and optical densities at each wavelength calculated.

The total (unpolarized) spectra were recorded on the Cary model 14 spectrophotometer in convergent light. Consistently lower optical densities were obtained on this instrument. Thus the observed polarized optical densities are upper limits of the true optical density of the pyrene solid solution.

RESULTS

Pyrene in Phenanthrene

The polarized absorption spectrum of a single crystal *a*—axis vertical and light normal to *ab* face, is shown in Fig. 2. This spectrum was recorded at room temperature and both the *a* and *b* absorptions are shown. The polarization ratio was $D_b/D_a=1.7$ and this ratio is independent of wavelength in the range 3550–3807 A. Nor was the value of D_a/D_b considerably different from crystal to crystal, the lowest value being 1.6 and the highest 1.8. The constancy of the ratio D_a/D_b with wavelength was accurate to within 5%.

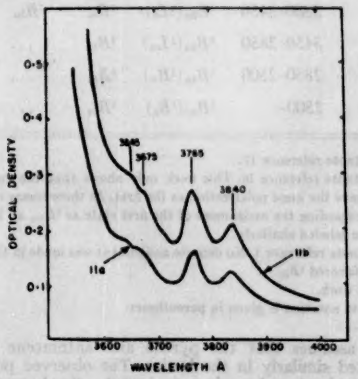

FIG. 2. The polarized absorption spectrum of pyrene in phenanthrene || *a*: the electric vector parallel to the *a* axis; || *b*: the electric vector parallel to the *b* axis.

TABLE II. The absorption spectrum of pyrene and anthracene in phenanthrene at room temperature.

Observed bands	Assignment		Observed red shift
A±2	Substance	A[a]	cm^{-1}±25
3840	Anthracene	3745	660[b]
3765	Pyrene	3715	350
3675	Pyrene	3620	270
3645	Anthracene	3545	770
	or		
	Pyrene[c]	3620	190

[a] Wavelengths of maximum absorption in methyl alcohol-ethyl alcohol (see footnote reference 14).

[b] Sidman (see footnote reference 5) measured a shift of 615 cm^{-1} for the anthracene 0-0 transition between methanol-ethanol and anthracene in phenenthrene at 20°K.

[c] It is not immediately obvious which of these is correct but either choice supports the arguments in the text.

The band at 3840 A was the first and most intense maximum of the lowest singlet-singlet transition of anthracene.

This band is present in the spectrum of phenanthrene without added pyrene and corresponds to the 3780 A peak (liquid solution) of anthracene. The red shift amounts to 370 cm^{-1} in going from isooctane solution to the solid solution in phenanthrene. The remaining anthracene peaks were hidden under the pyrene absorption which has its first maximum at 3765 A. Table II lists the wavelengths of the maxima and inflections of the spectra in Fig. 2; each was identified with a band of either pyrene or anthracene in liquid solution at room temperature. The red shifts between liquid and solid solution were surprisingly large and were probably indicative of strong interactions of the host molecules with the oriented impurities. The large increase of optical density at wavelengths below 3600 A was due to the onset of phenanthrene absorption. The 0–0 transition of the lowest singlet transition of the phenanthrene crystal lies at about 3500 A.

Pyrene in Dibenzyl

Absorption Spectrum at Room Temperature

Figure 3 shows the polarized absorption spectrum of an oriented single crystal of dibenzyl containing a small amount of pyrene. The apparent absorption at the tail (~4000 A) was due to reflected light but this did not amount to much of the total absorption in the region 2400–3500 A. The first singlet transition of pyrene (*A* in Fig. 3) was barely distinguishable in this spectrum, but the second, more intense transition that commences at around 3400 A (*B*) was clearly defined. The positions of the main peaks were 3400, 3250, 3100, and 3000 A while in methanol-ethanol at 18°C the first four peaks occur at 3335, 3180, 3050, and 2920 A.[14]

[14] E. Clar, *Aromatische Kohlenwasserstoffe* (Springer-Verlag, Berlin, 1952), p. 324.

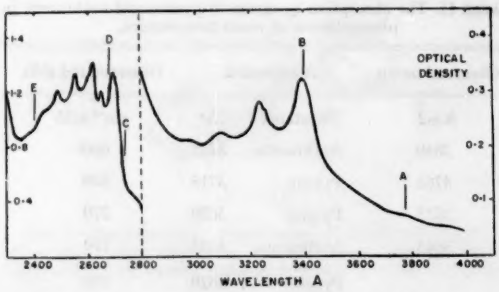

FIG. 3. The polarized absorption spectrum of pyrene in dibenzyl. The *a*- and *b*-polarized absorptions were nearly indistinguishable, as discussed in the text.

The polarization ratio, D_b/D_a, varied slightly from crystal to crystal. For a crystal containing 0.25 mole % pyrene the ratio D_b/D_a was about 1.3 at each of the peaks. For another crystal, which contained 0.05 mole % pyrene, the ratio was 2.0 at each of the peaks. The *a*- and *b*-polarized spectra were identical in shape so only one curve is shown on Fig. 3. At shorter wavelengths than 3000 A the ratio D_b/D_a was not significantly different from unity, in agreement with Coffman and McClure. Below 2800 A, the onset of the third pyrene transition (C), most of the light was absorbed by dibenzyl so even a large pleochroic effect due to the dissolved molecule would not have been apparent in this region. Thus these spectra could not be used to examine the third transition.

DISCUSSION

Lowest Electronic State of Pyrene

The polarized absorption spectrum of pyrene in phenanthrene has clearly indicated that the electronic transition commencing at about 3800 A involves a transition moment which is directed along the short molecular axis of pyrene. As no other transitions are known to occur at lower energies than this it will be assumed to be the lowest singlet-singlet transition of pyrene. The pyrene molecule belongs to the point group D_{2h} and the allowed transitions are to states with symmetry $^1B_{2u}$ or $^1B_{3u}$ (ground state $^1A_{1g}$). These transitions should be associated with long- and short-axis transition moments, respectively. Thus the following considerations enabled the characterization of the first singlet transition as $^1B_{3u} \leftarrow {}^1A_{1g}$.

(1) The polarization ratio D_b/D_a is predicted to be 2.04 for short-molecular-axis transitions and the observed value of 1.7 was close to this.

(2) The transition moment was in the same crystal direction as that for anthracene *present in the same crystal lattice* which shows that the pyrene molecule was in true solid solution and that the transition moment was directed along the same molecular axis as for anthracene.[15] The 3800 A state of anthracene is known to be short-axis polarized.[5]

Second Electronic State of Pyrene

Absorption to this state commenced at about 3500 A. As for the lowest state the polarization ratio of an oriented single crystal is a good criterion of the symmetry of the electronic transition. The *b*-polarized absorption was always greater than the *a* absorption although in other respects the *a* and *b* spectra were identical. This was to be expected for short-axis-polarized transitions only. In the dibenzyl crystal the ratio D_a/D_b is unity for the first transition and from other considerations the transition moment may be assigned along the short axis. Thus the observed spectra of pyrene in dibenzyl confirm that the two transition moments were along the *same crystal direction* and that both are short-axis-polarized transitions. The second electronic transition of pyrene is therefore $^1B_{3u} \leftarrow {}^1A_{1g}$.

Comparison with Theory

Table III gives the theoretical predictions for the electronic states of pyrene and also the experimental assignments. The assignments which arise from this work are in agreement with those of Williams[16] but are at variance with all the theoretical predictions.[17] Therefore it appears that the free electron model and the perimeter model which have been demonstrated to predict accurately the molecular levels of catacondensed hydrocarbons may not be extended to pyrene, which is a pericondensed hydrocarbon. Even the theoretical predictions of the energy of the molecu-

TABLE III. A comparison of the theoretical and experimental symmetries of the molecular levels of pyrene.

Electronic state	Absorption region A	Symmetry of molecular level			
		Calc.[a]	Exptl[b]	Exptl[c]	Exptl[d]
1st	3800–3450	$^1B_{3u}(^1L_b)$[e]	$^1B_{3u}$	$^1B_{3u}$	$^1B_{3u}$
2nd	3450–2850	$^1B_{2u}(^1L_a)$	$^1B_{3u}$	...	$^1B_{2u}$
3rd	2850–2500	$^1B_{3u}(^1B_a)$	$^1B_{3u}$	...	...
4th	2500–	$^1B_{2u}(^1B_b)$	$^1B_{3u}$	...	...

[a] See footnote reference 17.

[b] See footnote reference 16. This work only shows that the 2nd, 3rd, and 4th states have the same polarization as the first. As there seems to be general agreement regarding the assignment of the first state as $^1B_{3u}$, all levels in this column were labeled similarly.

[c] See footnote reference 3. No definite assignment was made in this work but the results favored $^1B_{3u}$.

[d] Present work.

[e] The Platt notation is given in parentheses.

[15] This assumes that the pyrene and anthracene molecules are oriented similarly in the lattice. The observed polarization properties of properly oriented crystals of phenanthrene or dibenzyl-containing pyrene clearly justify this assumption.

[16] R. Williams, J. Chem. Phys. 26, 1186 (1956).

[17] N. S. Ham and K. Ruedenberg, J. Chem. Phys. 25, 13 (1956).

lar levels in pyrene do not agree well with the experimental values. The discrepancy arises because the calculated ^1L_b–^1B_b splitting by configuration interaction was much too great in the case of pyrene. This was already pointed out by Hamm and Ruedenberg.[17]

The absorption spectrum of crystalline pyrene was not easily interpreted as both the polarization ratio and the measured Davydov splitting were found to lie between the values calculated for $^1B_{2u}$ and $^1B_{3u}$ molecular levels.[3] However the polarization ratio favored a $^1B_{3u}\leftarrow{}^1A_{1g}$ transition, although this ratio varied with temperature.

In the pyrene crystal strong crystal-induced mixing of the electronic states probably occurs. Ferguson's work shows that the polarization ratio in the lowest state markedly changes with wavelength indicating that vibrational-electronic interactions were occurring with a *nearby* state of *different* polarization. The fourth state appears to be too distant in energy, the third state has been shown by Williams to have the same polarization as the first.[16] The second also has the same polarization as the first as has been shown in this work. In the fluorescence experiments of Williams it was possible that the source (Hg 2537 A) used to excite the third transition also excited a considerable fraction of the molecules into the fourth molecular level. The absorption bands of these states overlap quite considerably even at −170°C. So the assignment of the third and fourth states should be confirmed in absorption. It should be made clear that because of crystal interactions Ferguson[3] was unable to definitely assign the first state. Williams[16] made no attempt to assign the state but only to show the *relative symmetries* of the first four states. Consequently this work contains the new results: (a) *strong indication* of the symmetry of the *first two molecular levels*, (b) confirmation of Ferguson's "mixing" conclusions, and (c) confirmation of the validity of William's fluorescence experiments for the *first two states* of pyrene.

The molecular orbitals of catacondensed hydrocarbons differ only in *angular* nodal properties. Platt has shown that pericondensed hydrocarbons such as pyrene acquire radial nodes as the orbital energy is increased.[18] However, inclusion of Platt's idea into the configuration-interaction treatment of Ham and Ruedenberg still predicts the order of the levels as ^1L_b, ^1L_a, ^1B_b, ^1B_b for pyrene. A simple Hückel-orbital calculation[19] yielded the same results.[20] It is clear that the degenerate singlet levels are split too far apart by the free electron network configuration interaction. It may be that the particular aspect of the theory requires adjustment to suit the pericondensed systems.

ACKNOWLEDGMENT

The author would like to express his thanks to Dr. D. S McClure for criticizing the manuscript.

[18] J. R. Platt, J. Chem. Phys. **22**, 1448 (1954).
[19] Compare C. A. Coulson and H. C. Longuet-Higgins, Proc. Roy. Soc. (London) **A191**, 39 (1947).
[20] J. R. Rowlands (private communication).

Distribution Functions of a Fluid in an External Potential Field: Application to Physical Adsorption

WILLIAM A. STEELE AND MARVIN ROSS

Department of Chemistry, The Pennsylvania State University, University Park, Pennsylvania

(Received December 17, 1959)

The thermodynamic properties of a fluid in an external potential field are expressed in terms of the spatial distribution functions appropriate to the fluid. Several methods of computing these distribution functions are given: integro-differential equations analogous to the Born-Green-Yvon equations; integral equations analogous to the Kirkwood-Salsburg equations; and two approximate methods of computation based on a perturbation approach. The applicability of these methods of calculation to various aspects of the problem of physical adsorption is discussed.

1. INTRODUCTION

IN recent years, a great deal of attention has been given to the computation of the spatial distribution functions of uniform fluids and to the calculation of the thermodynamic properties of fluids in terms of these functions.[1] However, little consideration has been given to a similar treatment of the properties of a fluid in an external potential field. In this paper, formal equations are written down which give the thermodynamic properties of such a fluid in terms of the distribution functions of the fluid at given T, μ, and external field.

The equations presented here have obvious applications to fluids in gravitational or centrifugal fields. It is also possible to treat many physical adsorption systems as examples of fluids which are in an external field due to the field of force near the surface of an adsorbent. Previous work which has used this approach to the problem has been carried out by Wheeler,[2] Ono,[3] and Freeman and Halsey.[4] However, the results of these treatments are expressed in terms of cluster integral expansions of the distribution functions and are thus of little practical use at high densities. In the present work, formal equations are given for the number-density distribution function which are applicable at all densities, and some methods for computing these functions are outlined.

2. THERMODYNAMIC PROPERTIES

We shall treat a one-component fluid with two-body central forces in an external field which is a function of position only. In this case, the total potential energy of a system of N atoms is given by

$$U(\mathbf{r}_1, \cdots, \mathbf{r}_N) = \sum_{i=1}^{N} u_s(\mathbf{r}_i) + \sum_{1 \le i < j \le N} u(r_{ij}), \qquad (2.1)$$

where $u_s(\mathbf{r}_i)$ is the energy of the ith atom at position $\mathbf{r}_i$ due to the external field, and $u(r_{ij})$ is the mutual interaction energy of atoms i and j in the fluid a distance r_{ij} apart. $\rho^{(n)}(\mathbf{r}_1, \cdots, \mathbf{r}_n)$ is defined in the usual way:

$$\rho^{(n)}(\mathbf{r}_1, \cdots, \mathbf{r}_n) = [N!/(N-n)!] \times \frac{\int \cdots \int_V \exp(-U(\mathbf{r}_1, \cdots, \mathbf{r}_N)/kT) d\mathbf{r}_{n+1} \cdots d\mathbf{r}_N}{Z} \qquad (2.2)$$

$$Z = \int \cdots \int_V \exp(-U(\mathbf{r}_1, \cdots \mathbf{r}_N)/kT) d\mathbf{r}_1 \cdots d\mathbf{r}_N. \qquad (2.3)$$

An expression for E_a, the total energy of a fluid in an external field, is obtained by differentiating the log of the partition function Q with respect to $1/T$:

$$Q = Z/N!\Lambda^{3N}, \qquad \Lambda = h/(2\pi mkT)^{\frac{1}{2}}. \qquad (2.4)$$

The result of this differentiation is written as

$$E_a = 3NkT/2 + \int_V \rho^{(1)}(\mathbf{r}_1) u_s(\mathbf{r}_1) d\mathbf{r}_1 + \tfrac{1}{2} \iint_V \rho^{(2)}(\mathbf{r}_1, \mathbf{r}_2) u(r_{12}) d\mathbf{r}_1 d\mathbf{r}_2. \qquad (2.5)$$

Since $\rho^{(1)}$ depends on $\mathbf{r}_1$, and $\rho^{(2)}$ depends on $\mathbf{r}_1$ and $\mathbf{r}_2$, the partial integration used to simplify the analogous expression for the uniform fluid[1] cannot be used here.

The pressure of a nonuniform fluid will now be considered. As is well known, the pressure of a fluid depends upon the gradient of the external field, which ordinarily depends on direction. The partition function of a one-component system is related to the external forces on the system by the equation

$$d(kT \ln Q) = SdT + \sum_i \mathbf{X}_i \cdot d\mathbf{x}_i + \mu dN, \qquad (2.6)$$

where $\mathbf{X}_i$ is the ith generalized force on the system and $\mathbf{x}_i$ is the extensive variable appropriate to $\mathbf{X}_i$. Here, it is most convenient to consider the forces corresponding to the three diagonal elements of the pressure tensor. For simplicity, the derivation will be shown for the xx element only. $\bar{P}_{xx}$ is then defined as the force in the x

[1] T. L. Hill, *Statistical Mechanics* (McGraw-Hill Book Company, Inc., New York, 1956), Chap. 6.
[2] A. Wheeler, American Chemical Society National Meeting, Atlantic City, New Jersey, September, 1949.
[3] S. Ono, J. Phys. Soc. (Japan) **6**, 10 (1951); **8**, 173 (1953).
[4] M. P. Freeman and G. D. Halsey, Jr., J. Phys. Chem. **59**, 181 (1955).

direction on unit area perpendicular to the x direction averaged over the entire volume of the fluid. In a system with dimensions L_x, L_y, L_z, the differential extensive variable associated with $\bar{P}_{xx}$ is $L_yL_zdL_x$, and $\bar{P}_{xx}$ is given by

$$\bar{P}_{xx}=kT/L_yL_z(\partial \ln Q/\partial L_x)_{N,T,L_y,L_z}. \quad (2.7)$$

Following the method of Born and Green[5], we substitute a new set of variables into Eq. (2.3),

$$x_k=L_xx_k', \qquad y_k=L_yy_k', \qquad z_k=L_zz_k'; \quad (2.8)$$

$\ln Z$ can now be differentiated with respect to L_x:

$$\partial \ln Z/\partial L_x=N/L_x-(L_xL_yL_z)^N/ZkT\int_0^1\cdots\int_0^1(\partial U/\partial L_x)\times\exp(-U(\mathbf{r}_1,\cdots\mathbf{r}_N)/kT)dx_1'\cdots dz_N' \quad (2.9)$$

$$\partial U/\partial L_x=1/L_x\sum_{i=1}^{N}(\partial u_s(\mathbf{r}_i)/\partial x_i)x_i+1/L_x\sum_{1\le i<j\le N}(\partial u(r_{ij})/\partial r_{ij})x_{ij}^2/r_{ij}. \quad (2.10)$$

When Eq. (2.10) is substituted in (2.9), and the integration variables are changed to their original form, $\bar{P}_{xx}$ is given by

$$\bar{P}_{xx}=NkT/V-1/V\int_V[\partial u_s(\mathbf{r}_1)/\partial x_1]x_1\rho^{(1)}(\mathbf{r}_1)d\mathbf{r}_1-1/2V\iint_V[\partial u(r_{12})/\partial r_{12}][x_{12}^2/r_{12}]\rho^{(2)}(\mathbf{r}_1,\mathbf{r}_2)d\mathbf{r}_1d\mathbf{r}_2. \quad (2.11)$$

The set of extensive variables used here is by no means unique. For instance, in many treatments of physical adsorption, the extensive variables conjugate to the generalized forces have been chosen to be V and $\mathfrak{A}$, the volume and area of the adsorbed phase. If the adsorbent has macroscopic area and negligible curvature, and the z direction is defined to be perpendicular to the surface of the adsorbent, it is easy to show that $\bar{P}_{zz}$ is the pressure to be associated with V, and that $\bar{P}_{xx}=\bar{P}_{yy}$. Furthermore, the intensive variable associated with $\mathfrak{A}$ is given by $L_z(\bar{P}_{xx}-\bar{P}_{zz})$ where L_z is the thickness of the adsorbed phase. This quantity is often called ϕ, the spreading pressure.

3. MEAN FORCE EQUATIONS

In this section, an integro-differential equation for $\rho^{(n)}$ is given which is analogous to the Born-Green-Yvon equation for a uniform fluid.[5] This equation is obtained by writing down the expression for $\mathbf{F}_n(\mathbf{r}_1)$, the mean force on particle 1 with particles 1 to n fixed at positions $\mathbf{r}_1,\cdots\mathbf{r}_n$. This force is due to the external field as well as the other molecules in the fluid and is given by

$$\mathbf{F}_n(\mathbf{r}_1)=-\nabla_1\{u_s(\mathbf{r}_1)+\sum_{i=2}^{n}u(r_{1i})+\sum_{j=n+1}^{N}\langle u(r_{1j})\rangle\}, \quad (3.1)$$

where ∇_1 denotes the gradient with respect to $\mathbf{r}_1$ and $\langle\ \rangle$ indicates an average over all configurations of atoms $n+1,\cdots,N$. Equation (3.1) can also be written as

$$-\mathbf{F}_n(\mathbf{r}_1)=\nabla_1[u_s(\mathbf{r}_1)+\sum_{i=2}^{n}u(r_{1i})]+\int_V\nabla_1u(r_{1,n+1})\rho^{(n+1)}(\mathbf{r}_1,\cdots,\mathbf{r}_{n+1})d\mathbf{r}_{n+1}. \quad (3.2)$$

Since $\mathbf{F}_n(\mathbf{r}_1)$ is also equal to $kT\nabla_1\ln\rho^{(n)}(\mathbf{r}_1,\cdots,\mathbf{r}_n)$, the final equation for $\rho^{(n)}$ is

$$-kT\nabla_1\ln\rho^{(n)}(\mathbf{r}_1,\cdots,\mathbf{r}_n)=\nabla_1[u_s(\mathbf{r}_1)+\sum_{i=2}^{n}u(r_{1i})]+\int_V\nabla_1u(r_{1,n+1})\rho^{(n+1)}(\mathbf{r}_1,\cdots,\mathbf{r}_{n+1})d\mathbf{r}_{n+1}. \quad (3.3)$$

The corresponding equation for $\rho^{(2)}$ in an uniform fluid has been solved by invoking the superposition approximation.[6] If it is assumed that this approximation is equally valid for a nonuniform fluid, the equation for $\rho^{(2)}$ becomes

$$-kT\nabla_1\ln\rho^{(2)}(\mathbf{r}_1,\mathbf{r}_2)=\nabla_1[u_s(\mathbf{r}_1)+u(r_{12})]+\int_V\nabla_1u(r_{13})\frac{\rho^{(2)}(\mathbf{r}_2,\mathbf{r}_3)\rho^{(2)}(\mathbf{r}_1,\mathbf{r}_3)}{\rho^{(1)}(\mathbf{r}_1)\rho^{(1)}(\mathbf{r}_2)\rho^{(1)}(\mathbf{r}_3)}d\mathbf{r}_3. \quad (3.4)$$

It is clear that it is still impractical to attempt to solve Eq. (3.4) without further simplification. Further discussion of this equation will be given in the section on perturbation calculations.

4. GRAND CANONICAL ENSEMBLE

Equation (3.3) combined with the thermodynamic equations (2.5) and (2.11) is sufficient, in principle, to compute the properties of interest in a nonuniform fluid. However, it is clear that such computations can be carried out only with great difficulty, particularly where a rapidly varying external potential is found, as is the case in physical adsorption. By the use of the grand canonical ensemble, relations can be derived between the distribution functions and the activity (or active number density) z which may be more readily usable than the equations resulting from the canonical ensemble.

Ono[3] has previously made use of the grand canonical ensemble in order to derive expressions for the properties of a system in an external field in terms of a cluster expansion of the distribution functions. Here, a partial cluster expansion similar to that presented by Kirkwood and Salsburg[7] will be given.

[5] M. Born and H. S. Green, *A General Kinetic Theory of Liquids* (Cambridge University Press, New York, 1949).

[6] J. G. Kirkwood, J. Chem. Phys. **3**, 300 (1935).

[7] J. G. Kirkwood and Z. Salsburg, Discussions Faraday Soc. **15**, 28 (1953).

The equation for $\rho^{(n)}(\mathbf{r}_1\cdots\mathbf{r}_n)$ in terms of Ξ, the grand partition function, is

$$\rho^{(n)}(\mathbf{r}_1\cdots\mathbf{r}_n)$$
$$=\Xi^{-1}\sum_{N\geq n}\frac{z^N}{(N-n)!}\int\cdots\int_V \exp(-U_N/kT)d\mathbf{r}_{n+1}\cdots d\mathbf{r}_N, \tag{4.1}$$

where $U_N=U(\mathbf{r}_1\cdots\mathbf{r}_N)$.

U_N is now written in the form

$$U_N=U_n^{(1)}(\mathbf{r}_1\cdots\mathbf{r}_n)+\sum_{j=N+1}^{N}u(r_{1j})+U_{N-1}(\mathbf{r}_2\cdots\mathbf{r}_N) \tag{4.2}$$

$$U_n^{(1)}(\mathbf{r}_1\cdots\mathbf{r}_n)=u_s(\mathbf{r}_1)+\sum_{j=2}^{n}u(r_{1j}). \tag{4.3}$$

The equation for $\rho^{(n)}$ is now

$$\rho^{(n)}(\mathbf{r}_1,\cdots,\mathbf{r}_n)$$
$$=\frac{\exp[-U_n^{(1)}(\mathbf{r}_1,\cdots,\mathbf{r}_n)/kT]}{\Xi}\sum_{N\geq n}\frac{z^N}{(N-n)!} \tag{4.4}$$
$$\int\cdots\int_V\exp(-U_{N-1}(\mathbf{r}_2,\cdots,\mathbf{r}_N)/kT)\prod_{\sigma=n+1}^{N}(1+f_{1\sigma})d\mathbf{r}_{1\sigma},$$

where

$$f_{1\sigma}=\exp[-u(r_{1\sigma})/kT]-1. \tag{4.5}$$

An expression for $\rho^{(n)}$ can now be derived following the method of Kirkwood and Salsburg. The result is written as

$$\rho^{(n)}(\mathbf{r}_1,\cdots,\mathbf{r}_n)=z\exp\{-[u_s(\mathbf{r}_1)+\sum_{i=2}^{n}u(r_{1i})]\,kT\}\{\rho^{(n-1)}(\mathbf{r}_2,\cdots,\mathbf{r}_n)$$
$$\times\sum_{l\geq 1}1/l!\int\cdots\int_V \mathrm{K}_l(1,n+1,\cdots,n+l)\rho^{(n+l-1)}(\mathbf{r}_2,\cdots,\mathbf{r}_{n+l})d\mathbf{r}_{n+1}\cdots d\mathbf{r}_{n+l}\}, \tag{4.6}$$

where

$$K_l=\prod_{\sigma=n+1}^{n+l}f_{1\sigma}.$$

5. PERTURBATION METHODS

It is possible to give an approximate treatment of many systems of interest by means of perturbation calculations. For instance, the change in free energy of a uniform fluid when a small external field is imposed can be computed. Alternatively, it is possible to consider the unperturbed fluid to be an ideal gas in an external field and to compute the perturbation of this system due to two body and higher interactions in the gas. It is obvious that the latter approach must reduce to a cluster expansion of the free energy similar to those already given by previous workers.[2-4] Zwanzig[8] has computed the change in configurational free energy of a system at constant N, V, T when the two-body interactions in a uniform fluid are altered. His treatment is readily adapted to the problem of a uniform fluid in a small external potential field. The configurational free energy of the fluid A_c is first written as

$$\exp(-A_c/kT)=1/N!\int\cdots\int_V$$
$$\times\exp[-U_0(\mathbf{r}_1,\cdots,\mathbf{r}_N)/kT]$$
$$\times\exp[-U_s(\mathbf{r}_1,\cdots,\mathbf{r}_N)/kT]d\mathbf{r}_1,\cdots,d\mathbf{r}_N, \tag{5.1}$$

where U_0 is the potential energy of the fluid in the absence of the external field, and U_s is the perturbation energy due to the external potential. If the change in free energy A_c-A_0 is written as a power series in $1/kT$, and $\exp[-U_s(\mathbf{r}_1,\cdots,\mathbf{r}_N)/kT]$ is expanded, the coefficients of the series for the free energy change can be written down. The final result is given by

$$A_c-A_0=\omega_1-\omega_2/kT+0/(kT)^2, \tag{5.2}$$

where

$$\omega_1=\sum_{i=1}^{N}\langle u_s(\mathbf{r}_i)\rangle_0=\rho_0\int_V u_s(\mathbf{r}_1)d\mathbf{r}_1, \tag{5.3}$$

$$\omega_2=\sum_{i=1}^{N}\sum_{j=1}^{N}\langle u_s(\mathbf{r}_i)u_s(\mathbf{r}_j)\rangle_0-\omega_1^2=\rho_0^2\int\int_V[g_0(\mathbf{r}_1,\mathbf{r}_2)-1]u_s(\mathbf{r}_1)u_s(\mathbf{r}_2)d\mathbf{r}_1d\mathbf{r}_2+\rho_0\int_V[u_s(\mathbf{r}_1)]^2d\mathbf{r}_1, \tag{5.4}$$

where $\langle\ \rangle_0$ denotes an ensemble average over the unperturbed ensemble, ρ_0 is the number density of the unperturbed fluid, and $g_0(\mathbf{r}_1,\mathbf{r}_2)$ is the radial distribution function of the unperturbed fluid.

In order to give a complete description of the thermodynamic properties of a system treated in such a manner, it is also necessary to compute the number density of the system. Two alternate perturbation calculations of the number density will be given. The first of these is appropriate to systems in which the density of the unperturbed fluid can take on any value as long as the compressibility is small compared to $1/u_s(\mathbf{r}_i)\rho_0$. The second is appropriate to systems in which the density of the fluid in the external field is not greatly different from that of an ideal gas in the same field. The latter case has been treated rigorously by

[8] R. Zwanzig, J. Chem. Phys. **22**, 1420 (1954).

means of the cluster integral expansion.[2-4] It is anticipated that the rather laborious cluster integral computations of $\rho^{(1)}(\mathbf{r}_i)$ may be partially avoided by use of the approximate expressions derived here.

An expression for the perturbation of the nth-order distribution function of a fluid at constant z, V, T can be obtained from Eq. (4.1). The total potential energy U is written as U_0+U_s in this equation, and $\exp(-U_s/kT)$ is expanded as a power series in $1/kT$. The final result can be written as

$$\rho^{(n)}(\mathbf{r}_1,\cdots,\mathbf{r}_n)=\frac{\rho_0^{(n)}(\mathbf{r}_1,\cdots,\mathbf{r}_n)\{1-\sum_{i=1}^{n}u_s(\mathbf{r}_i)/kT\}-\int_V[u_s(\mathbf{r}_{n+1})/kT]\rho^{(n+1)}(\mathbf{r}_1,\cdots,\mathbf{r}_{n+1})d\mathbf{r}_{n+1}+0/(kT)^2}{1-\rho_0\int_V[u_s(\mathbf{r}_1)/kT]d\mathbf{r}_1+0\ (kT)^2} \tag{5.5}$$

$$=\rho_0^{(n)}(\mathbf{r}_1,\cdots,\mathbf{r}_n)\{1-\sum_{i=1}^{n}u_s(\mathbf{r}_i)/kT\}-\int_V[u_s(\mathbf{r}_{n+1})/kT][\rho_0^{(n+1)}(\mathbf{r}_1,\cdots,\mathbf{r}_{n+1})-\rho_0\rho_0^{(n)}(\mathbf{r}_1,\cdots,\mathbf{r}_n)]d\mathbf{r}_{n+1}+0/(kT)^2. \tag{5.6}$$

An expression for $\rho^{(1)}(\mathbf{r}_1)$ correct to terms in $1/kT$ can now be written as

$$\rho^{(1)}(\mathbf{r}_1)/\rho_0=1-u_s(\mathbf{r}_1)/kT-\rho_0\int_V[u_s(\mathbf{r}_2)/kT][g_0(\mathbf{r}_1,\mathbf{r}_2)-1]d\mathbf{r}_2. \tag{5.7}$$

The integrals in Eqs. (5.4) and (5.7) can be evaluated approximately by expanding $u_s(\mathbf{r}_2)$ in a Taylor series around $u_s(\mathbf{r}_1)$:

$$u_s(\mathbf{r}_2)=u_s(\mathbf{r}_1)+\mathbf{r}_{12}(\partial u_s(\mathbf{r}_1)/\partial_{\mathbf{r}_{12}})+\cdots. \tag{5.8}$$

When atom 1 is not too close to the boundary of V,

$$\int_V\mathbf{r}_{12}[g_0(\mathbf{r}_1,\mathbf{r}_{12})-1]d\mathbf{r}_{12}=0$$

because of symmetry. We obtain

$$A_c-A_0=\rho_0\int_V u_s(\mathbf{r}_1)d\mathbf{r}_1-\kappa_0\rho_0^2\int_V[u_s(\mathbf{r}_1)]^2d\mathbf{r}_1+\cdots \tag{5.9}$$

$$\rho^{(1)}(\mathbf{r}_1)/\rho_0=1-u_s(\mathbf{r}_1)\kappa_0\rho_0\cdots, \tag{5.10}$$

where κ_0 is the isothermal compressibility of the unperturbed fluid. It can be shown that the higher-order terms in A_c-A_0 and $\rho^{(1)}(\mathbf{r}_1)/\rho_0$ contain higher powers of the compressibility, as well as derivatives of the compressibility with respect to V. (Terms containing integrals over higher-order terms in the series of Eq. (5.8) must also appear.)

The alternate expressions for $\rho^{(1)}$ and $\rho^{(2)}$ which are appropriate to a nearly ideal gas can be derived by writing these quantities as power series in $1/kT$ and solving Eqs. (3.3) and (3.4) for the coefficients. The distribution functions are written

$$\rho^{(1)}(\mathbf{r}_1)=\exp[-u_s(\mathbf{r}_1)/kT+\phi_1(\mathbf{r}_1)/(kT)^2+\phi_2(\mathbf{r}_1)/(kT)^3\cdots] \tag{5.11}$$

$$\rho^{(2)}(\mathbf{r}_1,\mathbf{r}_2)=\rho^{(1)}(\mathbf{r}_1)\rho^{(1)}(\mathbf{r}_2)g_0(r_{12})\exp[\lambda_1(\mathbf{r}_1,\mathbf{r}_2)/(kT)^2\cdots]. \tag{5.12}$$

The exponentials in these equations are expanded, and the resulting expressions are substituted into Eq. (3.3) for $\rho^{(1)}$ and Eq. (3.4) for $\rho^{(2)}$. After some manipulations, the results are

$$-\nabla_1[\phi_1(\mathbf{r}_1)+\phi_2(\mathbf{r}_1)/kT\cdots]=\rho_0\int_V\nabla_1u(r_{12})g_0(r_{12})\{-u_s(\mathbf{r}_2)/kT+1/(kT)^2\times\{[u_s(\mathbf{r}_2)]^2/2+\phi_1(\mathbf{r}_2)+\lambda_1(\mathbf{r}_1,\mathbf{r}_2)\}\cdots\}d\mathbf{r}_2, \tag{5.13}$$

$$\nabla_1(\phi_1(\mathbf{r}_1)+\lambda_1(\mathbf{r}_1,\mathbf{r}_2)/kT\cdots)=\rho_0\int_V\nabla_1u(r_{13})g_0(r_{23})g_0(r_{13})\{u_s(\mathbf{r}_3)/kT\cdots\}d\mathbf{r}_3. \tag{5.14}$$

$g_v(r_{ij})$ is now written in terms of the expansion in powers of $1/kT$ which has been used by Kirkwood, Lewinson, and Alder:[9]

$$g_0(r_{ij})=g_{00}(r_{ij})+g_{00}(r_{ij})e\psi_1(r_{ij})/kTr_{ij}\cdots, \tag{5.15}$$

where $g_{00}(r_{ij})$ is the hard-sphere radial distribution function for a uniform fluid with density ρ_0, and ϵ is the parameter indicating the depth of the modified Lennard-Jones potential energy curve used by Kirkwood, Lewinson, and Alder.

When terms containing equal powers of $1/kT$ in Eqs. (5.13) and (5.14) are equated, the coefficients

[9] J. G. Kirkwood, V. A. Lewinson, and B. J. Alder, J. Chem. Phys. **20**, 929 (1952).

ϕ_i and λ_i are given by

$$\phi_1(\mathbf{r}_1)=\rho_0\int_0^{\mathbf{r}_1}\int_V \nabla_1 u(r_{12})\,u_s(\mathbf{r}_2)\,g_{00}(r_{12})\,d\mathbf{r}_2 d\mathbf{r}_1 \qquad (5.16)$$

$$\phi_2(\mathbf{r}_1)=\rho_0\int_0^{\mathbf{r}_1}\int_V \nabla_1 u(r_{12})\,g_{00}(r_{12})\{u_s(\mathbf{r}_2)\,e\psi_1(r_{12})/r_{12}$$
$$+[u_s(\mathbf{r}_2)]^2/2+\phi_1(\mathbf{r}_2)+\lambda_1(\mathbf{r}_1,\mathbf{r}_2)\}d\mathbf{r}_2 d\mathbf{r}_1, \qquad (5.17)$$

$$\lambda_1(\mathbf{r}_1,\mathbf{r}_2)=\rho_0\int_0^{\mathbf{r}_1}\int_V \nabla_1 u(r_{13})\,u_s(\mathbf{r}_3)\,g_{\omega}(r_{13})$$
$$\times[g_{00}(r_{23})-1]d\mathbf{r}_3 d\mathbf{r}_1, \qquad (5.18)$$

etc., where the origin of the coordinate axes has been placed at some point where $u_s(\mathbf{r}_i)$ is zero, and $u(r_{ij})$ is the modified Lennard-Jones potential function. The ϕ_i and λ_i can be computed by using the values of the functions $g_{0\omega}(r_{12})$ and $\psi_1(r_{12})$ which have been tabulated by Kirkwood *et al.* for various values of ρ_0.[9,10]

It is particularly easy to evaluate the integrals in Eqs. (5.16)–(5.18) if it is assumed that $u(r_{ij})$ is a hard-sphere potential (i.e., ϵ is taken to be zero) and that $u_s(\mathbf{r}_i)$ can be written in terms of the series of Eq. (5.8). For instance, it is easy to show that $\phi_1(\mathbf{r}_1)$ can be written as

$$\phi_1(\mathbf{r}_1)=\rho_0\int_0^{\mathbf{r}_1}[\partial u_s(\mathbf{r}_1)/\partial \mathbf{r}_{12}]d\mathbf{r}_1\int_V \mathbf{r}_{12}\nabla_1 u(r_{12})\,g_{00}(r_{12})\,d\mathbf{r}_{12} \qquad (5.19)$$

where terms in the third and higher derivatives of $u_s(\mathbf{r}_1)$ have been dropped. When these integrations are performed, the result is

$$\phi_1(\mathbf{r}_1)=2u_s(\mathbf{r}_1)\,(p_{00}v/kT-1), \qquad (5.20)$$

where p_{00} is the pressure of the hard-sphere fluid at density ρ_0. The quantity $p_{00}v/kT-1$ has been tabulated by Kirkwood, Maun, and Alder.[10]

6. APPLICATION TO PHYSICAL ADSORPTION

Probably the most intensively studied examples of fluids in external potential fields have been those of physical adsorption of gases on solids. Theoretical treatments of this problem have generally used detailed models as starting points.[11] If it is assumed that a physically adsorbed phase is a fluid in an external potential field, then the formalism given in this paper is appropriate to the problem, under the restrictions that the two-body forces in the fluid are not altered by the presence of the solid, and that the thermodynamic properties of the solid are not altered by the presence of the fluid. In this case, the external potential field is equal to the change in potential energy when a semi-infinite slab of adsorbate at given μ and T is replaced by solid adsorbent.[11a]

The results of most experimental investigations of adsorption systems are reported in terms of "amount adsorbed" as a function of the pressure, and isosteric heats as a function of the amount adsorbed. The isosteric heat is defined as the partial molar heat of desorption, and is easily computed from $E_{gas}-E_a$ where E_a is given by Eq. (2.5). Several definitions of "amount adsorbed" are possible[12]: the most natural definition for the present treatment is the Gibbs definition of amount adsorbed as the surface excess N_a-N_0 where N_a is the amount of adsorbate in the container at given T and P, and N_0 is the amount of adsorbate which would be held in the container if the solid did not interact with the adsorbate. It is obvious that

$$N_a-N_0=\int_V[\rho^{(1)}(\mathbf{r}_1)-\rho_\omega]d\mathbf{r}_1. \qquad (6.1)$$

Note that some ambiguity remains as to the location of the dividing surface which defines V, the volume available to the adsorbate. It appears that no completely satisfactory definition of V can be given. In this work, the dividing surface between solid and gas phase will be defined to be the locus of the points where the gas-surface interaction energy is zero (i.e., passes from repulsive to attractive). Although this definition has the disadvantage that it makes V dependent upon the nature of the gas, it has several advantages since V is now a mathematically well-defined quantity which does not depend on temperature. Also, in this way, the large positive contributions to $u_s(\mathbf{r}_i)$ which would make the perturbation approach of Sec. 5 unusuable are eliminated. The use of this definition should introduce a negligible error, since $\rho^{(1)}(\mathbf{r}_1)$ must be roughly equal to or less than ρ_0 in the volume of space where $u_s(\mathbf{r}_i)$ is repulsive, and thus gives an extremely small contribution to N_a-N_0.

$\rho^{(1)}$ and $\rho^{(2)}$ can be computed as a function of z using Eq. (4.6). Since z is generally known from the pressure or density of the gas in equilibrium with the adsorbed phase, the thermodynamic properties of the system can be obtained in this way. As an example, of this method of computation, a derivation of the Langmuir equation for a monatomic adsorbate will now be given. First, expressions for $\rho^{(1)}$ and $\rho^{(2)}$ as a function of z are

[10] J. G. Kirkwood, E. K. Maun, and B. J. Alder, J. Chem. Phys. **18**, 1040 (1950).

[11] T. L. Hill, Advances in Catalysis **4**, 211 (1951); (a) In order to define the external field in this way, it is necessary to assume that $g(\mathbf{r}_1,\mathbf{r}_2)=1$ for all positions of atom 1 in the adsorbate and atom 2 in the slab of fluid which is replaced by adsorbent.

[12] T. L. Hill, J. Phys. Chem. **63**, 456 (1959).

written down:

$$\rho^{(1)}(\mathbf{r}_1)=z\exp[-u_s(\mathbf{r}_1)/kT]\Big\{\Big[1+z\int_V f_{12}\exp[-u_s(\mathbf{r}_2)/kT]d\mathbf{r}_2+z^2\iint_V f_{12}f_{23}$$

$$\times\exp\{-[u_s(\mathbf{r}_2)+u_s(\mathbf{r}_3)]/kT\}d\mathbf{r}_2d\mathbf{r}_3+\cdots\Big]+\tfrac{1}{2}\iint_V f_{12}f_{13}\rho^{(2)}(\mathbf{r}_2,\mathbf{r}_3)d\mathbf{r}_2d\mathbf{r}_3+\cdots\Big\} \quad (6.2)$$

$$\rho^{(2)}(\mathbf{r}_2,\mathbf{r}_3)=z\exp\{-[u_s(\mathbf{r}_2)+u(r_{23})]/kT\}\{\rho^{(1)}(\mathbf{r}_3)\cdots\}. \quad (6.3)$$

In this derivation, the usual statistical version of the Langmuir model[13] is equivalent to making the assumptions that: the adsorbent surface is made up of N_s identical cells of volume V_s; inside these cells, $u_s(\mathbf{r}_i)$ has a finite value, and outside, it is plus infinity; these cells are so located and of such dimensions that $u(r_{ij})$ is zero when i and j are in different cells and plus infinity when i and j are in the same cell. When these restrictions are applied to Eq. (6.3), it is apparent that $\rho^{(2)}(\mathbf{r}_i,\mathbf{r}_j)$ is zero when atoms i and j are in the same cell. Furthermore, all terms containing $f_{12}f_{13}\cdots f_{1n}$ are zero except when atoms 1, 2, 3, $\cdots n$ are all in the same cell. In this way, it can be shown that

$$\rho^{(1)}(\mathbf{r}_1)=z\exp[-u_s(\mathbf{r}_1)/kT]\Big[1+\sum_{n=1}^{N_s}\Big\{-z\int_{V_s}\exp[-u_s(\mathbf{r}_i)/kT]d\mathbf{r}_i\Big\}^n\Big]. \quad (6.4)$$

It is clear that $\rho^{(1)}(\mathbf{r}_1)$ is zero except when atom 1 is in one of the N_s cells. Thus we can write

$$N_a=\int_V\rho^{(1)}(\mathbf{r}_1)d\mathbf{r}_1$$

$$=zN_s\int_{V_s}\exp[-u_s(\mathbf{r}_1)/kT]d\mathbf{r}_1\Big\{1+z\int_{V_s}\exp[-u_s(\mathbf{r}_i)/kT]d\mathbf{r}_i\Big\}^{-1}. \quad (6.5)$$

The constant p_0 is now defined as

$$p_0^{-1}=1/kT\int_{V_s}\exp[-u_s(\mathbf{r}_i)/kT]d\mathbf{r}_i. \quad (6.6)$$

Since $z=p_{\text{gas}}/kT$ for an ideal gas, the isotherm equation which results is identical to the Langmuir equation:

$$N_a/N_s=p/p_0(1+p/p_0)^{-1}. \quad (6.7)$$

It is interesting to note that $(p_0/kT)^{-1}$ is here given in terms of a cell integral rather than the conventional ratio of atomic partition functions[13] and is seen to be closely related to the cell-free volume of the Lennard-Jones-Devonshire theory of liquids.[14]

Halsey and co-workers[15] have carried out extensive measurements of the interaction of gases with surfaces at high temperatures and low gas densities, and have interpreted these results in terms of the appropriate second and third gas-surface virial coefficients. The expression for $\rho^{(1)}(\mathbf{r}_1)$ given in Eq. (5.11) leads to the exact gas-surface second virial coefficient if all the ϕ_i are set equal to zero, and leads to approximate values for higher virial coefficients if the ϕ_i are computed from Eqs. (5.16) and (5.17). Freeman[16] has shown that there is a considerable disagreement between experimental values of the third virial coefficient and the third virial coefficient computed for a $r^{-3}-r^{-9}$ gas-solid potential function and a $r^{-6}-r^{-12}$ gas-gas potential curve. This disagreement was tentatively interpreted as having been caused by changes in the two-body gas-gas forces in the vicinity of a solid surface. However, the laborious computations required for a rigorous evaluation of the third virial coefficients precluded any consideration of the variations in the gas-solid potential curve due to the periodicity of the solid lattice.[17] It is hoped that the use of the expressions given for $\rho^{(1)}$ in Eqs. (5.11), (5.16), and (5.17) will facilitate an approximate evaluation of the magnitude of this effect, as well as enabling the calculations of $\rho^{(1)}$ to be carried to higher densities than those amenable to treatment in terms of second and third virial coefficients.

Another group of physical adsorption systems which can be treated by the perturbation methods of Sec. 5 is composed of thick adsorbed films at temperatures and pressures close to the condensation point of the bulk liquid adsorbate. Experimental measurements on such systems are often interpreted in terms of the Frenkel-

[13] R. Fowler and E. A. Guggenheim, *Statistical Thermodynamics* (Cambridge University Press, New York, 1939), p. 424.
[14] Footnote reference 1, p. 376.
[15] W. A. Steele and G. D. Halsey, Jr., J. Chem. Phys. **22**, 979 (1954); M. P. Freeman and G. D. Halsey, Jr., J. Phys. Chem. **59**, 181 (1955); G. Constabaris and G. D. Halsey, Jr., J. Chem. Phys. **26**, 1433 (1957).
[16] M. P. Freeman, J. Phys. Chem. **62**, 729 (1958).
[17] W. A. Steele and G. D. Halsey, Jr., J. Phys. Chem. **59**, 57 (1955).

Halsey-Hill isotherm equation.[11] It is possible to derive this equation from Eq. (5.9) and (5.10), and to write down some higher order correction terms to the original Frenkel-Halsey-Hill equation. First, $\mu_{ac}-\mu_{lc}$ must be computed where μ_{ac} and μ_{lc} are the configurational contributions to the chemical potentials of the adsorbed phase and the bulk liquid, respectively. An isotherm equation is then obtained by setting $\mu_{ac}-\mu_{lc}=RT\ \ln p/p_0$, where p_0 is the vapor pressure of bulk liquid. Now

$$\mu_{ac}-\mu_{lc}=[\partial(A_c-A_0)/\partial N]_{V,\mathfrak{A},T}$$

$$=[\partial(A_c-A_0)/\partial L_z]\left[\int_{\mathfrak{A}}\rho^{(1)}(L_z,\mathfrak{A})d\mathfrak{A}\right]^{-1}. \quad (6.8)$$

Equation (5.9) is now written as

$$A_c-A_0=\rho_0\int_0^{L_z}\int_{\mathfrak{A}}u_s(z,\mathfrak{A})d\mathfrak{A}dz$$

$$-\kappa_0\rho_0^2\int_0^{L_z}\int_{\mathfrak{A}}[u_s(z,\mathfrak{A})]^2d\mathfrak{A}dz. \quad (6.9)$$

If $\mathbf{u}_s(z)$ is defined to be the perturbation energy at a given distance from the surface averaged over the entire surface, it follows that

$$\mathfrak{A}^{-1}[\partial(A_c-A_0)/\partial L_z]$$

$$=\rho_0\bar{u}_s(L_z)-\kappa_0\rho_0^2[\bar{u}_s(L_z)]^2+\cdots. \quad (6.10)$$

Equations (6.10) and (5.10) are now substituted into (6.8):

$$\mu_{ac}-\mu_{lc}=u_s(L_z)\frac{1-\kappa_s\bar{u}_s(L_z)\rho_0+\cdots}{1-\kappa_0\bar{u}_s(L_z)\rho_0+\cdots}. \quad (6.11)$$

Since the first-order change in the density of the fluid is canceled by the second-order change in A_c-A_0, it can be concluded that the assumption of zero compressibility which is generally made in the derivation of the Frenkel-Halsey-Hill isotherm is unnecessarily restrictive. Several further approximations must be made in order to obtain the final equation. These assumptions are taken to be that: (a) the thickness of the adsorbed film is proportional to the amount adsorbed; (b) $\bar{u}_s(L_z)$ is proportional to L_z^{-3}; (c) the properties of the bulk liquid persist unchanged up to the gas-liquid interface, (d) higher terms in Eq. (6.11) are negligible; (e) the first two terms in the Taylor series expansion of $u_s(\mathbf{r}_1)$ must give an adequate representation of $u_s(\mathbf{r}_1)$. Singleton and Halsey[18] have discussed deviations of experimental isotherms from the Frenkel-Halsey-Hill isotherm in terms of an "incompatibility parameter" which is roughly a measure of the mismatch between solid-adsorbent and liquid-adsorbate lattice spacings. It can be easily shown that this mismatch is important when the lattice spacing of the solid is comparable to or larger than the most probable separation distance of atoms in the liquid. When this is the case, assumptions *b* and *e* will cease to be applicable at small L_z. Furthermore, if $u_s(\mathbf{r}_i)$ and $g_0(r_{ij})$ are known, correction terms comparable to an "incompatibility parameter" can be computed from Eqs. (5.7) and (5.2).

It is interesting to note that experimental evidence has been obtained which indicates that physical adsorption of gases on solids at temperatures equal to or higher than the boiling points of the bulk adsorbate proceeds in a nonsitewise manner. Results of measurements of the adsorption of several different rare gases on a nearly uniform surface show that the densities of the monolayers are characteristic of liquidlike packing, rather than of adsorption on a fixed number of sites.[19] Other measurements of the adsorption of helium on a nearly uniform surface over a wide range of temperatures show that the apparent monolayer density calculated from sitewise models is a fairly strong function of temperature,[20] a result which is not possible with a fixed number of sites. Indeed, many measurements of monolayer volumes of different substances at different temperatures on the same adsorbent have shown that the number of molecules held in the first adsorbed layer is not at all constant. Since these surfaces are frequently rough on an atomic scale (i.e., heterogeneous), these results are often explained as being due to a change in the number of available sites as the size or shape of the adsorbate molecule is changed. However, the work reported in footnote references 19 and 20 was carried out using adsorbents with nearly uniform surfaces. The most reasonable explanation for the continued observance of varying monolayer densities over uniform surfaces appears to be that adsorption in these systems is not strictly sitewise, but is mobile, or very nearly so. It is anticipated that Eqs. (6.2) and (6.3) may be of considerable use in the general treatment of the properties of thin films with horizontal interactions, particularly since the series in these equations converge most rapidly when the number of nearest neighbors to a given atom in the film is small.

[18] J. H. Singleton and G. D. Halsey, Jr., Can. J. Chem. **33**, 184 (1955).

[19] J. G. Aston and J. Greyson, J. Phys. Chem. **61**, 613 (1957).

[20] M. Ross, Ph.D. thesis, Pennsylvania State University, June, 1960.

Energy of Interaction of Two Helium Atoms

NEAL MOORE*

Sloane Physics Laboratory, Yale University, New Haven, Connecticut

(Received February 22, 1960)

The interaction energy of two helium atoms in the ground state is calculated as a function of internuclear separation. Use is made of a variational trial state function developed in analogy with Hirschfelder and Linnett's treatment of the hydrogen-hydrogen interaction. The results are in good agreement with the best previous treatments in the repulsive region as well as with the results of Rosen, Margenau, and Page in the neighborhood of the van der Waals minimum; in addition, information is obtained concerning the instantaneous mutual polarization of the two atoms.

IN recent years several attempts at calculating the interaction energy of two normal helium atoms as a function of the distance of nuclear separation have been made.[1-5] The present paper summarizes the results of a further, somewhat lengthy variational computation of this type. Fundamentally, the purpose of the paper is to show that a single state function for the system can be employed to produce rather good values of interaction energy over a wide range of internuclear distances. Beyond this, it is hoped that the evaluation of the parameters involved in such a state function will shed some light on the nature of the physical process being investigated.

A traditional treatment of the problem[6] begins with a state function represented by the Pauli determinant:

$$\psi=C\begin{vmatrix} a(1)\alpha(1) & a(1)\beta(1) & b(1)\alpha(1) & b(1)\beta(1) \\ a(2)\alpha(2) & a(2)\beta(2) & b(2)\alpha(2) & b(2)\beta(2) \\ a(3)\alpha(3) & a(3)\beta(3) & b(3)\alpha(3) & b(3)\beta(3) \\ a(4)\alpha(4) & a(4)\beta(4) & b(4)\alpha(4) & b(4)\beta(4) \end{vmatrix}, \quad (1)$$

where C is a normalization constant. The letters a and b designate $1s$ hydrogen energy eigenfunctions containing the atomic number Z as a variable parameter. The four numbers refer to the electrons belonging to the two atoms, while α and β denote the usual spin functions. The coordinate system to be used is sketched in Fig. 1. The nuclei are separated by the distance R. It is clear that with such a coordinate system

$$x_{ai}=x_{bi}, \quad y_{ai}=y_{bi}, \quad \text{and} \quad z_{ai}=z_{bi}+R$$

for the ith electron. Thus the literal subscripts are of importance only in connection with the z coordinates.

It is known that if one wishes to find the interaction potential at relatively large R, in the vicinity of the weak van der Waals minimum, the Pauli determinant will not suffice. The spherically symmetric $1s$ atomic orbitals employed in it do not have sufficient flexibility to allow for the instantaneous mutual polarization of the two atoms, which is responsible for the van der Waals attraction. Consequently the determinant alone can offer only repulsion, the energy remaining positive for all values of the internuclear separation.

Difficulties of a similar nature had been encountered by Hirschfelder and Linnett[7] in their treatment of hydrogen-hydrogen interaction; they were surmounted by including polarization terms with adjustable coefficients in the trial function, these coefficients being taken as the variational parameters. Until more recently,[8] the quality of the results obtained in this way for the $^3\Sigma$ state of the hydrogen molecule at intermediate R had not been equaled by other investigations.

Therefore, we chose to construct a variation function for the helium-helium problem which would be analogous to that of Hirschfelder and Linnett. The manner in which this could be done is not unique; nevertheless, the most direct way in which to proceed seems to be as follows. The term corresponding to the principal diagonal in the Pauli determinant is modified so as to become

$$\begin{aligned} &a(1)\alpha(1)a(2)\beta(2)b(3)\alpha(3)b(4)\beta(4) \\ &\quad\times[1+\gamma Z^2(x_{a1}x_{b3}+x_{a1}x_{b4}+x_{a2}x_{b3}+x_{a2}x_{b4}) \\ &\quad+\gamma Z^2(y_{a1}y_{b3}+y_{a1}y_{b4}+y_{a2}y_{b3}+y_{a2}y_{b4}) \\ &\quad+\delta Z^2(z_{a1}z_{b3}+z_{a1}z_{b4}+z_{a2}z_{b3}+z_{a2}z_{b4})]; \quad (2) \end{aligned}$$

in order to maintain the antisymmetrization, the other terms must be similarly modified. γ, δ, and Z are to be the variational parameters in our problem; more will be said about Z later.

The added terms involving γ and δ are those which will allow for the instantaneous mutual polarization of

* This work was supported by Air Force Contract and by the National Science Foundation's Fellowship Program.

[1] P. Rosen, J. Chem. Phys. **18**, 1182 (1950).

[2] V. Griffing and J. F. Wehner, J. Chem. Phys. **23**, 1024 (1955).

[3] M. Sakamoto and E. Ishiguro, Prog. Theoret. Phys. **15**, 37 (1956).

[4] N. Lynn, Proc. Phys. Soc. **72**, 201 (1958).

[5] T. Hashino and S. Huzinaga, Prog. Theoret. Phys. **20**, 631 (1958).

[6] L. Pauling and E. Wilson, *Introduction to Quantum Mechanics* (McGraw-Hill Book Company, Inc., New York, 1935), p. 361.

[7] J. O. Hirschfelder and J. W. Linnett, J. Chem. Phys. **18**, 130 (1950).

[8] A. Dalgarno and N. Lynn, Proc. Phys. Soc. **69**, 821 (1956).

TABLE I. Polarization parameters vs internuclear distance.

R(A)	γ	δ
0.6270	−0.00497	+0.00180
1.097	−0.00654	0.00906
1.568	−0.00378	0.00767
1.882	−0.00246	0.00531
2.195	−0.00161	0.00340
2.509	−0.00110	0.00225
2.744	−0.000841	0.00171
3.136	−0.000565	0.00113
3.606	−0.000371	0.000741
∞	0	0

the atoms; we shall therefore refer to γ and δ as the "polarization parameters." The fact that only two such quantities are needed (rather than three) follows from the equivalence of the x and y directions in this problem. Although the introduction of the added terms is desirable on physical grounds, the calculation is now much more complicated, for one must deal with a state function containing 24×13 terms, instead of merely the original 24.

The polarization parameters relate the coordinates of an electron on one atom to those of an electron on the other atom; that is, they are a measure of electronic repulsions as the two atoms approach one another. Since there can be no correlation of electronic motions when the atoms are infinitely far apart, γ and δ should vanish under these conditions. But if $\gamma=\delta=0$, the function reduces to the original determinant; consequently the total energy of the two isolated atoms will still be given by the well-known expression[9] $2Z^2-(27/4)Z$, which has a minimum for $Z=(27/16)$. The magnitudes of γ and δ then increase as the atoms are brought closer together, as can be seen in Table I. For given coordinate magnitudes, the fact that γ is negative means that one of the terms involving γ in the state function will be largest when an electron on one atom and an electron on the other atom are on *opposite* sides of the z axis joining the nuclei; but, this is just the phenomenon of polarization. On the other hand, Table I shows that δ is always positive, which means that for a given pair of electrons (one belonging to each atom), there is a tendency for one and only one electron to be "between" the nuclei. A negative value for δ would have favored a crowding of electrons into this region, with a resultant lowering of potential energy and hence increased attraction, which could hardly be expected in the case of helium. However, a defect of the present function, not encountered for hydrogen, arises as follows. We have just seen that the x (or y) coordinates of a pair of electrons, one on each atom, tend to have opposite signs; this conclusion holds for *any* of the four possible pairs. The inevitable consequence is that both electrons of the *same* atom tend to be near one another, a situation which seems undesirable on physical grounds. It is hoped that the chosen variation function will have other merits sufficient to offset this disadvantage; in practice, of course, the fact that all the integrals which arise may be evaluated exactly, as is indeed the case in the present formulation, is a noteworthy characteristic.

Having selected this modified Pauli determinant with added polarization terms as our trial state function Ψ, the next step is to form the quantum mechanical expression for the total energy E of the system[10]:

$$E=\int\Psi^*H\Psi d\tau \Big/ \int\Psi^*\Psi d\tau. \tag{3}$$

We shall employ the usual atomic units, measuring energies in terms of the quantity e^2/a_0 (where e is the electronic charge and a_0 is the first Bohr radius for hydrogen), and distances in units a_0. By utilizing these conventions, the Hamiltonian H may be written:

$$H=-\tfrac{1}{2}\sum_{i=1}^{4}\nabla_i^2-2\sum_{i=1}^{4}\left(\frac{1}{r_{a_i}}+\frac{1}{r_{b_i}}\right)+\tfrac{1}{2}\sum_{i,j=1,(i\neq j)}^{4}\frac{1}{r_{ij}}+\frac{4}{R}. \tag{4}$$

We now wish to evaluate the integrals in the numerator and denominator of the energy expression. The problem is considerably simplified through the use of spin orthogonality. Each term in Ψ (or Ψ^*) contains as a factor a product of four spin functions of the type

$$\alpha(1)\beta(2)\alpha(3)\beta(4).$$

By permuting the arguments, six possible spin functions are thus obtained; integration over the spin coordinates may be performed at once. Each of the six products will occur 4×13 times in the 24×13 terms of the modified determinantal expansion. For a particular term in the energy numerator (or denominator), one such product of four spin factors will arise from Ψ and another from Ψ^*; unless the two are identical, spin orthogonality will destroy the contribution of that term. Therefore in this manner precisely five-sixths of the otherwise possible terms are eliminated.

Next, it is noticed that the Hamiltonian is Hermitian. Furthermore, it is symmetric in the four electrons and the two nuclei. Bearing these facts in mind, many terms can be combined so as to simplify the energy

[9] H. Margenau and G. Murphy, *Mathematics of Physics and Chemistry* (D. Van Nostrand Company, Inc., Princeton, New Jersey, 1956), 2nd ed., p. 382.

[10] This avoids the uncertainties inherent in many perturbation schemes; see H. Margenau and P. Rosen, J. Chem. Phys. **21**, 394 (1953).

expression greatly. Let us define

$$A\equiv 1+\gamma Z^2(x_1x_3+x_1x_4+x_2x_3+x_2x_4)+\gamma Z^2(y_1y_3+y_1y_4+y_2y_3+y_2y_4)+\delta Z^2(z_{a1}z_{b3}+z_{a1}z_{b4}+z_{a2}z_{b3}+z_{a2}z_{b4}),$$

$$A'\equiv 1+\gamma Z^2(x_1x_3+x_1x_2+x_3x_4+x_2x_4)+\gamma Z^2(y_1y_3+y_1y_2+y_3y_4+y_2y_4)+\delta Z^2(z_{a1}z_{b3}+z_{a1}z_{b2}+z_{b3}z_{a4}+z_{b2}z_{a4}),$$

$$B\equiv 1+\gamma Z^2(x_1x_3+x_1x_4+x_2x_3+x_2x_4)+\gamma Z^2(y_1y_3+y_1y_4+y_2y_3+y_2y_4)+\delta Z^2(z_{b1}z_{a3}+z_{b1}z_{a4}+z_{b2}z_{a3}+z_{b2}z_{a4}),\quad \text{etc.} \quad (5)$$

(The primes are formed by interchanging electrons 2 and 4, and B differs from A by an exchange of the nuclei.)

By virtue of the Hermiticity of H, we can put

$$\int[a(1)a(2)b(3)b(4)A]H[b(1)b(2)a(3)a(4)B]d\tau$$

equal to

$$\int[b(1)b(2)a(3)a(4)B]H[a(1)a(2)b(3)b(4)A]d\tau$$

as a typical example of one kind of combination. For another, using the invariance of H under interchange of electrons and the fact that our labeling of the electrons in a given integral is quite arbitrary, one may equate

$$\int[a(1)a(2)b(3)b(4)A]H[b(1)b(2)a(3)a(4)B]d\tau$$

and

$$\int[a(1)b(2)b(3)a(4)A']H[b(1)a(2)a(3)b(4)B']d\tau.$$

Also, it is clear that similar relations will hold for

$$\int\Psi^*\Psi d\tau.$$

Taking all possible interchanges into account, one finds that the numerator of the energy expression may be written:

$$\int\Psi^*H\Psi d\tau = \int[a(1)a(2)b(3)b(4)A]H[a(1)a(2)b(3)b(4)A]d\tau + \int[a(1)a(2)b(3)b(4)A]H[b(1)b(2)a(3)a(4)B]d\tau - 2\int[a(1)a(2)b(3)b(4)A]H[a(1)b(2)b(3)a(4)A']d\tau. \quad (6)$$

The normalizing factor

$$\int\Psi^*\Psi d\tau$$

consists of a similar sum of three integrals, but without the operator H in the integrand.

Even though symmetry relations have greatly simplified the problem, the full expansion of the products in the numerator will still yield a sum of several thousand terms, to which attention will now be turned. Each of the terms in this sum is a product of basic integrals involving the four electrons. The tabulation of integrals from the Hirschfelder-Linnett hydrogen calculation is needed here in its entirety, but in addition a number of other, more complicated integrals arise in this problem from the $1/r_{ij}$ terms in the Hamiltonian. A complete list of all necessary integrals is given in Table II. For convenience and consistency, the notation of Preuss[11] has been used throughout the table, with but one exception. Most of the integrals (Coulomb, exchange, ionic, etc.) are proportional to Z; in addition, the Z used by Preuss differs from ours by a factor of two. With this slight change, the integrals for principal quantum number $n=2$ become identical with ours. Again, as a matter of convenience, we have chosen to redefine the notation for the integrals so that the symbols will be independent of Z, thereby displaying explicitly the dependence of the energy upon Z. In order to cover a wide range of R, it was necessary to extend the numerical tables of Preuss somewhat; because of the assumed equality of Z for the two nuclei, it was possible to do this in a reasonable amount of time without having to neglect or approximate any integrals. In this respect, the works of Kotani[12] and Roothaan[13] were of considerable help. Over much of the range of R, numerical values for all the integral designations can be taken directly from the tables of Preuss.

The only problem remaining is then to express the energy as a function of the basic integrals, a procedure which is algebraically straightforward but tedious. Most of the elements of the Hamiltonian present no difficulty; upon writing out the many terms in

$$\int\Psi^*H\Psi d\tau,$$

it is readily apparent that each one may be expressed as a product of basic integrals for the four electrons. If E_0 is the energy of an isolated helium atom, for the

[11] H. Preuss, *Integraltafeln zur Quantenchemie* (Springer-Verlag, Berlin, 1956).

[12] M. Kotani, A. Amemiya, E. Ishiguro and T. Kimura, *Table of Molecular Integrals*, Maruzen Co. Ltd. (1955).

[13] C. C. J. Roothaan, *Tables of Two-Center Coulomb Integrals*, Special Tech. Rept., Laboratory of Molecular Structure and Spectra, 1955.

TABLE II. Basic integrals.

(a) Simple integrals

$$\int \frac{a(1)^2}{r_{a1}} d\tau_1 = Z.$$

$$Z^2 \int \frac{a(1)^2}{r_{a1}} z_{a1}^2 d\tau_1 = \tfrac{1}{2} Z.$$

$$Z^4 \int \frac{a(1)^2 b(2)^2}{r_{a1}} (x_1 x_2 + y_1 y_2)^2 d\tau_{12} = Z.$$

$$\left(Z^2 \int a(1)^2 x_1^2 d\tau_1 = Z^2 \int a(1)^2 y_1^2 d\tau_1 = Z^2 \int a(1)^2 z_{a1}^2 d\tau_1 = 1. \right)$$

$$\int a(1) b(1) d\tau_1 = S_{kk}.$$

$$-Z^2 \int a(1) b(1) z_{a1} z_{b1} d\tau_1 = S_{ss}.$$

$$Z^2 \int a(1) b(1) x_1^2 d\tau_1 = Z^2 \int a(1) b(1) y_1^2 d\tau_1 = S_{xx}.$$

$$\int \frac{a(1)^2}{r_{b1}} d\tau_1 = 2ZK_{kk}.$$

$$Z^2 \int \frac{a(1)^2}{r_{b1}} z_{a1}^2 d\tau_1 = 2ZK_{ss}.$$

$$Z^4 \int \frac{a(1)^2 b(2)^2}{r_{b1}} (x_1 x_2 + y_1 y_2)^2 d\tau_{12} = 4ZK_{xx}.$$

$$Z \int \frac{a(1)^2}{r_{b1}} z_{a1} d\tau_1 = 2ZK_{ks}.$$

$$\int \frac{a(1) b(1)}{r_{a1}} d\tau_1 = 2ZJ_{kk}.$$

$$-Z^2 \int \frac{a(1) b(1)}{r_{a1}} z_{a1} z_{b1} d\tau_1 = 2ZJ_{ss}.$$

$$Z^4 \int \frac{a(1) b(1) a(2) b(2)}{r_{a1}} (x_1 x_2 + y_1 y_2)^2 d\tau_{12} = 4ZS_{xx} J_{xx}.$$

TABLE II.—*Continued*

(A number of simple integrals which clearly vanish because of an odd integrand are not included here.) Also, putting $q=ZR$, we have

$$Z\int a(1)b(1)z_{a1}d\tau_1\left(=-Z\int a(1)b(1)z_{b1}d\tau_1\right)=\tfrac{1}{2}qS_{kk}.$$

$$Z\int\frac{a(1)b(1)}{r_{a1}}z_{a1}d\tau_1=(2Z/3)qJ_{kk}.$$

$$Z\int\frac{a(1)b(1)}{r_{b1}}z_{a1}d\tau_1=(4Z/3)qJ_{kk}.$$

$$\int\frac{a(1)^2a(2)^2}{r_{12}}d\tau_{12}=\tfrac{5}{8}Z.$$

$$Z^2\int\frac{a(1)^2a(2)^2}{r_{12}}x_1^2\ (\text{or } y_1^2, \text{ or } z_{a1}^2)d\tau_{12}=\tfrac{7}{16}Z.$$

$$Z^2\int\frac{a(1)^2a(2)^2}{r_{12}}x_1x_2\ (\text{or } y_1, y_2, \text{ or } z_{a1}z_{a2})d\tau_{12}=\tfrac{7}{96}Z.$$

(b) Coulomb integrals

$$\int\frac{a(1)^2b(2)^2}{r_{12}}d\tau_{12}=2ZC_{kkkk}.$$

$$-Z^2\int\frac{a(1)^2b(2)^2}{r_{12}}z_{a1}z_{b2}d\tau_{12}=2ZC_{sskk}.$$

$$Z^2\int\frac{a(1)^2b(2)^2}{r_{12}}(x_1x_2+y_1y_2)d\tau_{12}=4ZC_{xxkk}.$$

$$Z^4\int\frac{a(1)^2b(2)^2}{r_{12}}z_{a1}^2z_{b2}^2d\tau_{12}=2ZC_{zzzz}.$$

$$Z^4\int\frac{a(1)^2b(2)^2}{r_{12}}(x_1x_2+y_1y_2)^2d\tau_{12}=4Z(C_{xxxx}+C_{xxx'x'}).$$

$$-Z^4\int\frac{a(1)^2b(2)^2}{r_{12}}(x_1x_2+y_1y_2)z_{a1}z_{b2}d\tau_{12}=4ZC_{xxzz}.$$

$$Z\int\frac{a(1)^2b(2)^2}{r_{12}}z_{a1}d\tau_{12}=2ZC_{skkk}.$$

$$Z^2\int\frac{a(1)^2b(2)^2}{r_{12}}z_{a1}^2d\tau_{12}=2ZC_{sksk}.$$

TABLE II.—*Continued.*

(b) Coulomb integrals

$$Z^2\int\frac{a(1)^2b(2)^2}{r_{12}}x_1^2d\tau_{12}\left(=Z^2\int\frac{a(1)^2b(2)^2}{r_{12}}y_1^2d\tau_{12}\right)=2ZC_{xkxk}.$$

$$-Z^3\int\frac{a(1)^2b(2)^2}{r_{12}}z_{a1}^2z_{b2}d\tau_{12}=2ZC_{zzzk}.$$

$$Z^3\int\frac{a(1)^2b(2)^2}{r_{12}}z_{a1}x_1x_2d\tau_{12}=2ZC_{xxzk}.$$

(c) Exchange integrals

$$\int\frac{a(1)b(1)a(2)b(2)}{r_{12}}d\tau_{12}=2ZA_{kkkk}.$$

$$-Z^2\int\frac{a(1)b(1)a(2)b(2)}{r_{12}}z_{a1}z_{b2}d\tau_{12}=2ZA_{zzkk}.$$

$$Z^2\int\frac{a(1)b(1)a(2)b(2)}{r_{12}}(x_1x_2+y_1y_2)d\tau_{12}=4ZA_{xxkk}.$$

$$Z^4\int\frac{a(1)b(1)a(2)b(2)}{r_{12}}z_{a1}z_{b1}z_{a2}z_{b2}d\tau_{12}=2ZA_{zzzz}.$$

$$Z^4\int\frac{a(1)b(1)a(2)b(2)}{r_{12}}(x_1x_2+y_1y_2)^2d\tau_{12}=4Z(A_{xxxx}+A_{xxx'x'}).$$

$$-Z^4\int\frac{a(1)b(1)a(2)b(2)}{r_{12}}z_{a1}z_{b2}(x_1x_2+y_1y_2)d\tau_{12}=4ZA_{xxzz}.$$

$$Z\int\frac{a(1)b(1)a(2)b(2)}{r_{12}}z_{a1}d\tau_{12}=2ZA_{zkkk}.$$

$$-Z^2\int\frac{a(1)b(1)a(2)b(2)}{r_{12}}z_{a1}z_{b1}d\tau_{12}=2ZA_{zkzk}.$$

$$Z^2\int\frac{a(1)b(1)a(2)b(2)}{r_{12}}x_1^2d\tau_{12}=2ZA_{xkxk}.$$

$$-Z^3\int\frac{a(1)b(1)a(2)b(2)}{r_{12}}z_{a1}z_{b1}z_{a2}d\tau_{12}=2ZA_{zzzk}.$$

$$Z^3\int\frac{a(1)b(1)a(2)b(2)}{r_{12}}z_{a1}x_1x_2d\tau_{12}=2ZA_{xxzk}.$$

TABLE II.—*Continued.*

(d) Ionic (hybrid) integrals

$$\int \frac{a(1)^2 a(2) b(2)}{r_{12}} d\tau_{12} = 2ZL_{kkkk}^{-}.$$

$$-Z^2 \int \frac{a(1)^2 a(2) b(2)}{r_{12}} z_{a1} z_{b2} d\tau_{12} = 2ZL_{kkss}^{-}.$$

$$Z^2 \int \frac{a(1)^2 a(2) b(2)}{r_{12}} (x_1 x_2 + y_1 y_2) d\tau_{12} = 4ZL_{kkss}^{-}.$$

$$Z \int \frac{a(1)^2 a(2) b(2)}{r_{12}} z_{a1} d\tau_{12} = 2ZL_{skkk}^{-}.$$

$$Z^2 \int \frac{a(1)^2 a(2) b(2)}{r_{12}} z_{a1}^2 d\tau_{12} = 2ZL_{sksk}^{-}.$$

$$Z^2 \int \frac{a(1)^2 a(2) b(2)}{r_{12}} x_1^2 d\tau_{12} = 2ZL_{xkxk}^{-}.$$

$$-Z^3 \int \frac{a(1)^2 a(2) b(2)}{r_{12}} z_{a1}^2 z_{b2} d\tau_{12} = 2ZL_{skss}^{-}.$$

$$Z^3 \int \frac{a(1)^2 a(2) b(2)}{r_{12}} z_{a1} x_1 x_2 d\tau_{12} = 2ZL_{xxsk}^{-}.$$

$$Z \int \frac{a(1)^2 a(2) b(2)}{r_{12}} z_{a2} d\tau_{12} = 2ZL_{kskk}^{-}.$$

$$-Z^2 \int \frac{a(1)^2 a(2) b(2)}{r_{12}} z_{a2} z_{b2} d\tau_{12} = 2ZL_{ksks}^{-}.$$

$$Z^2 \int \frac{a(1)^2 a(2) b(2)}{r_{12}} x_2^2 d\tau_{12} = 2ZL_{kxkx}^{-}.$$

$$-Z^3 \int \frac{a(1)^2 a(2) b(2)}{r_{12}} z_{a1} z_{a2} z_{b2} d\tau_{12} = 2ZL_{ksss}^{-}.$$

$$Z^3 \int \frac{a(1)^2 a(2) b(2)}{r_{12}} x_1 z_{a2} x_2 d\tau_{12} = 2ZL_{kxsx}^{-}.$$

(Corresponding integrals in y can be written for those given here in terms of x.)

(The bar following the last subscript of L indicates that only this subscript corresponds to a function centered on atom b.)

interaction energy $\Delta E = E - 2E_0$ one finally obtains

$$\Delta E = \frac{aZ+bZ^2+c\gamma Z+d\gamma\delta Z+e\delta Z+f\delta Z^2+g\gamma^2 Z+h\gamma^2Z^2+i\delta^2Z+j\delta^2Z^2}{k+l\delta+m\gamma^2+n\delta^2}+2Z^2-\tfrac{27}{4}Z-2(\tfrac{27}{16})^2+\tfrac{27}{4}(\tfrac{27}{16}), \qquad (7)$$

where

$$a=(4k/q)+16(1-S_{kk}^2)(2S_{kk}J_{kk}-K_{kk})-S_{kk}^2(\tfrac{11}{2}-\tfrac{27}{4}S_{kk}^2)+4(2-S_{kk}^2)C_{kkkk}-4(1-3S_{kk}^2)A_{kkkk}-16S_{kk}L_{kkkk},$$

$$b=4S_{kk}(1-S_{kk}^2)(S_{kk}-2J_{kk}),$$

$$c=16[(2-S_{kk}^2)C_{\pi\pi kk}-(1-2S_{kk}^2)A_{\pi\pi kk}-2S_{kk}L_{kk\pi\pi}],$$

$$d=4[-4(2-S_{kk}^2)C_{\pi\pi o o}+4(1-2S_{kk}^2)A_{\pi\pi o o}+4qS_{kk}(S_{kk}C_{\pi\pi ok}-2S_{kk}A_{\pi\pi ok}+L_{\pi\pi ok}+L_{ko\pi\pi})+q^2S_{kk}^2(C_{\pi\pi kk}-2A_{\pi\pi kk})],$$

$$e=(4l/q)+8[-(2-S_{kk}^2)C_{ookk}+(1-2S_{kk}^2)A_{ookk}+2S_{kk}L_{kkoo}+qS_{kk}(qL_{kkkk}-2S_{kk}K_{ko}-2qJ_{kk}[1-2S_{kk}^2]$$
$$+S_{kk}C_{okkk}-4S_{kk}A_{okkk}+L_{okkk})+\tfrac{1}{4}q^2S_{kk}^2(C_{kkkk}-2A_{kkkk}+\tfrac{11}{8}-4K_{kk}+16S_{kk}J_{kk}-\tfrac{27}{4}S_{kk}^2)],$$

$$f=8qS_{kk}[qS_{kk}^3-\tfrac{1}{4}qS_{kk}+\tfrac{3}{2}qJ_{kk}(1-\tfrac{7}{2}S_{kk}^2)],$$

$$g=4\{(m/q)+2(2-S_{kk}^2)(C_{\pi\pi\pi\pi}+C_{\pi\pi\pi'\pi'}-4K_{\pi\pi})-2(1-2S_{kk}^2)(A_{\pi\pi\pi\pi}+A_{\pi\pi\pi'\pi'}-8S_{\pi\pi}J_{\pi\pi})$$
$$+2(2-S_{\pi\pi}^2)(C_{kkkk}-4K_{kk})-2(1-2S_{\pi\pi}^2)(A_{kkkk}-8S_{kk}J_{kk})+\tfrac{85}{24}-\tfrac{19}{4}S_{kk}^2-\tfrac{11}{4}S_{\pi\pi}^2+\tfrac{27}{2}S_{kk}^2S_{\pi\pi}^2$$
$$+8C_{\pi k\pi k}-4S_{kk}S_{\pi\pi}C_{\pi\pi kk}-4A_{\pi\pi kk}(1-2S_{kk}S_{\pi\pi})+16S_{kk}S_{\pi\pi}A_{\pi k\pi k}-8(S_{kk}+S_{\pi\pi})L_{kk\pi\pi}-8S_{kk}L_{\pi k\pi k}-8S_{\pi\pi}L_{k\pi k\pi}\}$$

$$h=8[S_{kk}^2+S_{\pi\pi}^2-4S_{kk}^2S_{\pi\pi}^2-2S_{kk}J_{kk}(1-2S_{\pi\pi}^2)-4S_{\pi\pi}J_{\pi\pi}(1-2S_{kk}^2)],$$

$$i=2\{(2n/q)+2(2-S_{kk}^2)(C_{oook}-4K_{oo})-2(1-2S_{kk}^2)(A_{oook}-8S_{oo}J_{oo})+2(2-S_{oo}^2)(C_{kkkk}-4K_{kk})$$
$$-2(1-2S_{oo}^2)(A_{kkkk}-8S_{kk}J_{kk})+\tfrac{85}{24}-\tfrac{19}{4}S_{kk}^2-\tfrac{11}{4}S_{oo}^2+\tfrac{27}{2}S_{kk}^2S_{oo}^2+8C_{okok}-4S_{kk}S_{oo}C_{ookk}$$
$$+4A_{ookk}(1+2S_{kk}S_{oo})+16S_{kk}S_{oo}A_{okok}-8S_{kk}L_{ookk}-8S_{oo}L_{kkoo}-8S_{kk}L_{okok}-8S_{oo}L_{kook}-4qA_{okkk}$$
$$+qS_{kk}[-4S_{kk}C_{ookk}-4S_{oo}C_{kkko}+8S_{oo}A_{okkk}+8S_{kk}A_{ookk}-4L_{okkk}-4L_{kooo}-4L_{kokk}-4L_{okoo}+8qJ_{kk}$$
$$+8K_{ko}(S_{kk}+S_{oo})]+q^2S_{kk}^2[-C_{okok}-C_{ookk}+2A_{ookk}+2A_{okok}+2qA_{okkk}-\tfrac{15}{8}+\tfrac{27}{32}q^2S_{kk}^2+\tfrac{27}{4}S_{kk}S_{oo}$$
$$+2K_{kk}+2K_{oo}-24S_{oo}J_{kk}-8S_{kk}J_{oo}-4q^2S_{kk}J_{kk}]\}$$

$$j=4[S_{kk}^2+S_{oo}^2-4S_{kk}^2S_{oo}^2-2S_{kk}J_{kk}(1-2S_{oo}^2)-4S_{oo}J_{oo}(1-2S_{kk}^2)]$$
$$+2qS_{kk}[qS_{kk}-\tfrac{1}{2}q^3S_{kk}^3+\tfrac{29}{3}qS_{kk}S_{oo}J_{kk}-4q^2S_{kk}^2S_{oo}+4qS_{kk}^2J_{oo}-\tfrac{8}{3}qJ_{kk}(1-\tfrac{1}{2}q^2S_{kk}^2)],$$

$$k=(1-S_{kk}^2)^2,$$

$$l=q^2S_{kk}^2(1-2S_{kk}^2),$$

$$m=4(2-S_{kk}^2-S_{\pi\pi}^2+2S_{kk}^2S_{\pi\pi}^2),$$

$$n=2(2-S_{kk}^2-S_{oo}^2+2S_{kk}^2S_{oo}^2-\tfrac{1}{2}q^2S_{kk}^2+\tfrac{1}{8}q^4S_{kk}^4+q^2S_{kk}^3S_{oo}),$$

$[q=ZR.$

The coefficients here given are functions of q alone because of the way in which the integrals were defined. The numerical tables of integrals refer to discrete values of q. It is then necessary to compute all the coefficients for several appropriate choices of q; in principle, at each q the energy should be minimized with respect to the three variational parameters. In practice, of course, the form of our function makes this difficult to do. However, simpler calculations of a similar nature made by previous authors indicate that the variation of Z is not likely to be important anyway; adopting $Z=(27/16)$, which minimizes the energy of an isolated atom, will also be very nearly the best choice of Z that we could make here. Numerical work by the present author testifies to the validity of this assumption.

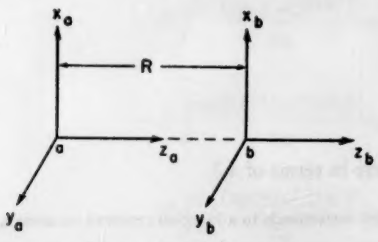

FIG. 1. Coordinate system.

The trial function now depends only on the polarization parameters; since the energy of the isolated atoms

TABLE III. He—He interaction energy vs internuclear distance.

R(A)	Interaction Energy (e^2/a_0) Present paper	Pauli determinant	Rosen[a]	Hashino and Huzinaga[b]
0.6272	+0.9103	+0.9133	+1.360	+0.7958
1.097	0.1123	0.1152	...	...
1.568	0.01317	0.01424	0.0221	0.01232
1.882	0.002822	0.003296	0.00577	0.002507
2.195	0.0005339	0.0007334	0.00147	0.0004012
2.509	0.00006573	0.0001551	0.000371	0.00003644
2.744	−0.00000476	0.00004703	...	...
3.136	−0.00001682	0.00000617	0.0000242	...
3.606	−0.00000910	0.00000076	...	...
∞	0	0	0	0

[a] See footnote 1.
[b] See footnote 5.

is obviously independent of these quantities, the direct minimization of the interaction ΔE will be equivalent to that of the total energy. But the presence of the parameters in the normalizing factor of the denominator still complicates the matter. We bypass this difficulty by making a good guess as to the magnitude of γ and δ and noting that only the variation of the numerator will be at all significant, an assumption which is supported by the resulting calculation. With this simplification, one is left with the equations

$$\partial(\Delta E)/\partial\gamma = 0 \doteq cZ + d\delta Z + 2g\gamma Z + 2h\gamma Z^2$$

and

$$\partial(\Delta E)/\partial\delta = 0 \doteq d\gamma Z + eZ + fZ^2 + 2i\delta Z + 2j\delta Z^2, \quad (8)$$

which are simultaneous linear equations in γ and δ. The common solution of these equations yields the values in Table I. Once these have been found, substitution in Eq. (7) produces ΔE, which is presented as a function of R in Table III.

For purposes of comparison, the interaction energy as computed from the original Pauli determinant is also given in Table III, along with other theoretical curves. It is observed that the curve of the present paper exhibits a van der Waals minimum, a property not always found in other calculations. In this region, the data differ by only a few percent from the combined values of Page,[14] Margenau,[15] and Rosen (see Fig. 2).[1] At smaller R, all well-known theoretical curves are in reasonably good agreement (See Fig. 3). There the introduction of polarization terms does not depress ΔE by any significant fraction. Nevertheless, our interaction energies are somewhat lower than those of Rosen, or even of Sakamoto and Ishiguro[3]; however, they are

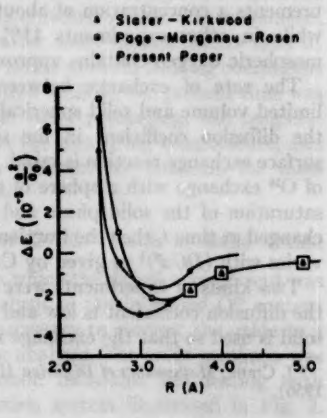

FIG. 2. He-He interaction potential-attractive region. Slater & Kirkwood data are from Phys. Rev. 37, 682 (1931).

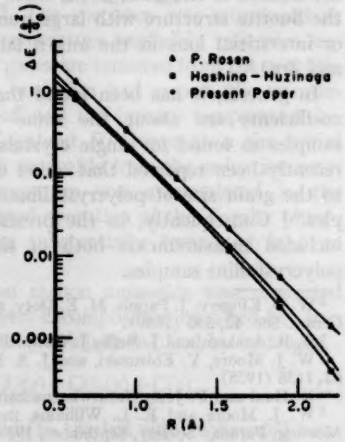

FIG. 3. He-He interaction potential-repulsive region.

[14] C. H. Page, Phys. Rev. 53, 426 (1938).
[15] H. Margenau, Phys. Rev. 56, 1000 (1939).

not quite so low as the value of Hashino and Huzinaga.[5] The fact that the latter are lower than ours does not imply, of course, that they are more nearly correct, but of all similar calculations, those of Hashino and Huzinaga come closest to agreeing with the experimental scattering data of Amdur and Harkness.[16]

In conclusion, we can state that our primary goal, which was to describe the entire range of the He—He interaction in terms of parameters which are physically meaningful, has been fulfilled. The results of this calculation agree rather well with others over a wider range of internuclear separation than is usually considered. In addition, it is felt that the polarization parameters clarify the physical situation to some extent.

[16] I. Amdur and A. L. Harkness, J. Chem. Phys. **22**, 664 (1954).

ACKNOWLEDGMENTS

Finally, the author would like to express his gratitude to Dr. Henry Margenau for generous encouragement and advice during the course of this investigation. We are also indebted to Nils Tongring for several pertinent references.

THE JOURNAL OF CHEMICAL PHYSICS VOLUME 33, NUMBER 2 AUGUST, 1960

Self-Diffusion of Oxygen in Single Crystal and Polycrystalline Aluminum Oxide

Y. OISHI AND W. D. KINGERY

Ceramics Division, Department of Metallurgy, Massachusetts Institute of Technology, Cambridge, Massachusetts

(Received December 21, 1959)

The self-diffusion coefficient of oxygen has been determined as a function of temperature in single crystal and polycrystalline aluminum oxide at temperatures up to 1780°C. The rate of exchange between a gas phase and solid particles was measured, utilizing the stable isotope, O^{18}. In single crystals of aluminum oxide intrinsic diffusion occurs in a high temperature region, depending on temperature as $D=1.9\times10^{2}\exp(-152\,000/RT)$. At temperatures below about 1600°C variable results were obtained depending on impurity content and previous heat treatment. For one set of samples experimental results could be represented as $D=6.3\times10^{-3}\exp(-57\,600/RT)$. The diffusion coefficient of oxygen in polycrystalline samples is about two orders of magnitude larger than that found for the single crystals, and has a somewhat smaller activation energy. With the polycrystalline oxide, variable results were also observed at lower temperatures.

I. INTRODUCTION

IN part because of the availability of radioisotopes' there have been extensive investigations of cation diffusion coefficients in a number of oxide systems. In contrast, reported measurements of oxygen diffusion are limited to $Zr_{0.85}Ca_{0.15}O_{1.85}$[1] and UO_2,[2] both having the fluorite structure with large numbers of vacancies or interstitial ions in the anion lattice, Cu_2O,[3] CdO,[4] and ZnO.[5]

In general, it has been found that cation diffusion coefficients are about the same in polycrystalline samples as found for single crystals. However, it has recently been reported that anion diffusion is related to the grain size of polycrystalline alkali halide samples.[6,7] Consequently, in the present study we have included measurements both of single crystals and polycrystalline samples.

[1] W. D. Kingery, J. Pappis, M. E. Doty, and D. C. Hill, J. Am. Ceram. Soc. **42**, 393 (1959).
[2] A. B. Auskern and J. Belle, J. Chem. Phys. **28**, 171 (1958).
[3] W. J. Moore, Y. Ebisuzaki, and J. A. Sluss, J. Phys. Chem. **62**, 1438 (1958).
[4] R. Haul and P. Just, Naturwissenschaften **45**, 435 (1958).
[5] W. J. Moore and E. L. Williams, paper No. 6, Kingston Meeting, Faraday Society, September, 1959 (to be published).
[6] J. F. Laurent and J. Bénard, J. Phys. Chem. Solids **3**, 7 (1957).
[7] J. F. Laurent and J. Bénard, J. Phys. Chem. Solids **7**, 218 (1958).

II. EXPERIMENTAL

(a) General Technique

The rate of exchange between a gas phase and solid particles was followed using gas enriched with the stable isotope O^{18}. Gas used for exchange measurements was obtained by electrolysis of water enriched in O^{18}, obtained from the Isotope Division, Atomic Energy Research Establishment, Harwell, England, or from the Weizmann Institute of Science, Israel. In some measurements a concentration of about 1.6% O^{18} was used while in other experiments 11% O^{18} was used (atmospheric oxygen contains approximately 0.21% O^{18}).

The rate of exchange between a gas solution of limited volume and solid spherical particles is fixed by the diffusion coefficient in the solid as long as the surface exchange reaction is rapid. If M_∞ is the amount of O^{18} exchange with a sphere of radius a at complete saturation of the solid phase and M_t the amount exchanged at time t, then the fractional exchange M_t/M_∞, varies with $(Dt/a^2)^{\frac{1}{2}}$ as given by Crank.[8]

Two kinds of experiments were tried. In most cases the diffusion coefficient is low and a limited amount of solid is used so that the exchange results in no appreci-

[8] J. Crank, *Mathematics of Diffusion* (Clarendon Press, Oxford, 1956).

able depletion of the O^{18} concentration in the gas phase. In these cases (the majority) the amount of exchange was measured by determining the O^{18} content of the solid. When the fractional exchange is small, the diffusion coefficient is given by[8]:

$$D=(\pi/36t)a^2(M_t/M_\infty)^2 \qquad (1)$$

In other cases where the diffusion coefficient is larger or more solid is used, the change in O^{18} concentration in the gas phase can be followed directly by determining it at various time intervals during a constant temperature run. After calculating the percentage of O^{18} taken up at complete saturation, the diffusion coefficient can be determined from the fractional exchange at time, t.[8]

(b) Exchange Apparatus

Exchange experiments were carried out in the furnace arrangement illustrated in Fig. 1. The sample was heated in a platinum, 90 Pt-10 Rh, or 60 Pt-40 Rh susceptor suspended in a water-cooled Vycor enclosure. The susceptor was surrounded by a platinum radiation shield, and the sample was held in a small crucible centered in the susceptor so that it was heated by radiation. This arrangement allowed the attainment of temperatures up to 1780°C for periods of several hours in an oxidizing atmosphere. Cooling of the enclosure prevented any exchange between the gas phase and wall during the experiments. During the higher temperature runs, some of the platinum-rhodium vaporized after long times; in order to prevent this from causing errors in temperature measurements, a magnetic shutter arrangement was used on the sighting window through which the temperature was measured with an optical pyrometer. The susceptor was provided with a platinum gauze double bottom filled with 90 Pt-10 Rh wire in order to obtain satisfactory preheating of the gas coming in contact with the sample.

The volume of the gas phase was 322 cc and the oxygen pressure employed in all the experiments reported here was fixed at 152 mm Hg.

In operation, the furnace containing the sample was assembled, evacuated, enriched oxygen was introduced, and the temperature for most measurements held at 1100°C for 40 min to insure uniform starting conditions. For measurements below 1300°C, the preheat time was reduced to 5–10 min. After preheating, the temperature was increased to the measuring temperature, and samples of the gas collected at intervals for mass spectrometric analysis.

(c) Determination of O^{18}/O^{16} Ratio in Solid Oxide

For experiments in which the diffusion coefficient was determined from analysis of the increased O^{18} content of the solid, it was necessary to convert the oxide to a suitable gas phase for analysis. The oxide specimen was first reduced to carbon monoxide by heating with graphite in the reaction system illustrated in Fig. 2.

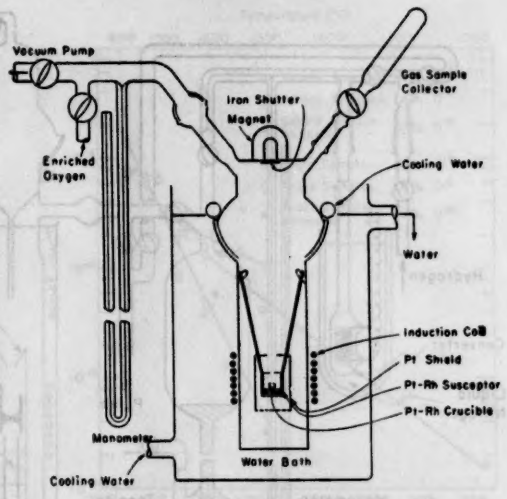

FIG. 1. Oxygen isotope exchange apparatus.

The specimen of about 6 mg was crushed and ground in a boron carbide mortar with about 3 mg of graphite powder which had been previously heated *in vacuo* at 1760°C for 50 hr to remove absorbed gases. The oxide-graphite mixture was wrapped in platinum foil and introduced into the reaction chamber after outgassing. The reaction chamber consisted of a graphite crucible heated by high-frequency induction in a water-cooled enclosure. After evacuating the furnace, hydrogen gas was introduced, and the temperature of the graphite crucible raised to 1760°C and then evacuated until no gas evolution was observed for at least fifteen minutes. (Hydrogen gas was introduced to prevent oxidation of molybdenum parts by gases released from graphite during initial heating.) The oxide-graphite sample was introduced by dropping into the platinum funnel illustrated in Fig. 2. The specimen was introduced at 1200°C. At this temperature negligible reduction occurs, but absorbed gases are removed from the graphite powder. After gas evolution had ceased, the vacuum pump was closed off and the furnace temperature increased to 1700°C—about 50° lower than the initial outgassing. Carbon monoxide from the reduction reaction at this temperature was accumulated in the converter by repeated operation of the Toepler pump. The reduction was substantially completed in 5 to 10 min.

The accumulated carbon monoxide was converted into CO_2 by catalytic decomposition on a red-hot iron wire which had been previously reduced by hydrogen,

$$2CO(g)=CO_2(g)+C(s). \qquad (2)$$

As equilibrium tends to the left side at elevated temperatures, the heated iron coil gives a rapid reaction rate but a small conversion ratio. In order to get a substantial amount of carbon dioxide, the bulb was im-

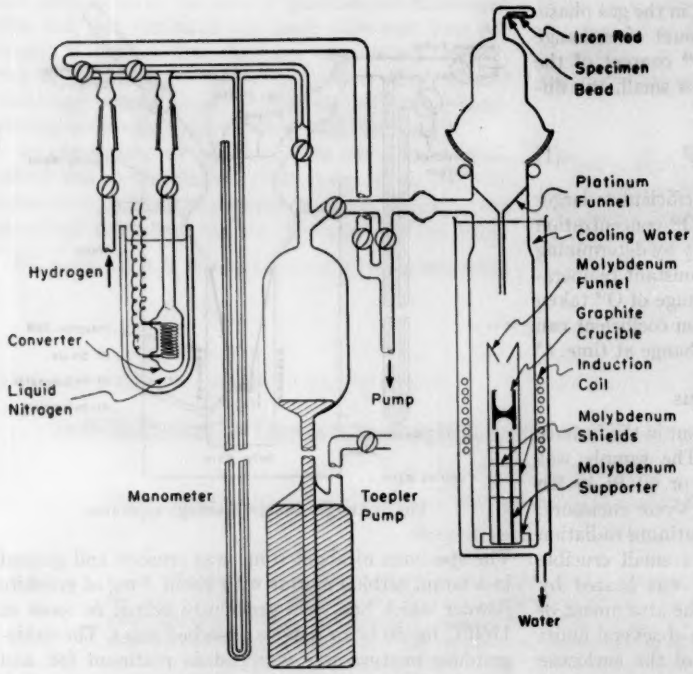

FIG. 2. Apparatus for reducing oxide to CO and then converting CO to CO_2.

mersed in a liquid nitrogen bath; solid carbon dioxide formed on the bulb wall and allowed the reaction to proceed. The conversion reaction was continued until no further decrease in the pressure was observed. This required 2 to 4 hr, depending on the surface condition of the iron wire.

The bulb (under liquid nitrogen) was connected to the Toepler pump by opening the stopcock after completion of the conversion reaction. This eliminated unconverted carbon monoxide and any other noncondensable gases that might have been taken in with the sample during the reduction procedure.

(d) Mass Spectrometric Analysis

The amount of O^{18} exchange was determined from mass spectrometric analysis of the O_2^{34}/O_2^{32} ratio or the CO_2^{46}/CO_2^{44} ratio, depending on the experimental method. For the measurements, a Consolidated Nier Isotope Ratio mass spectrometer (Model 21–201) was used. The O^{18} concentration changes determined were mostly of the order of 10^{-4}, while the O^{18}/O^{16} ratio of the original specimen was about 0.0021. Accordingly, special precautions were necessary to obtain sufficient accuracy in the mass spectrometric analysis; it was found that the precision of the instrument depended critically on the method of operation. Using a standard sample of carbon dioxide as a comparison standard for instrument calibration, maintaining a strictly constant room temperature, taking the same ion current for standard and unknown, and allowing equilibrium to be achieved for each measurement, a precision within less than 2×10^{-6} was achieved for repeated determinations of the O^{18}/O^{16} ratio of the order of 2×10^{-3}.

(e) Alumina Samples Studied

Single crystal samples were prepared from Linde Company sapphire obtained as 0.030-in. dia spheres (used in this form) and as single crystal rods (crushed and used as 200–230 mesh grain). Polycrystalline samples were prepared from Linde alumina powder which was pressed and sintered at 1900°C and then crushed to form 60–65 mesh grain. Some of this was used as such; some was made into spherical particles by dropping through a three-phase carbon arc, as described by Kingery and Berg.[9] Minor impurity content as indicated by spectrographic analysis is shown in Table 1.

Spherical samples are advantageous in that the surface-volume ratio is fixed and the relations in Eq. (1) apply directly. For irregular particles the exchange rate depends on the surface-volume ratio. Effects of local surface irregularities predominate in the initial stages of the exchange reactions; when a substantial amount of material is exchanged, these effects are washed out and shape differences of the same order of magnitude as the particle size become important. In the present nonspherical samples the surfaces are

[9] W. D. Kingery and M. Berg, J. Appl. Phys. 26, 1205 (1955).

smooth, but the grains are irregular in shape. Microscopic observations indicated that the ratio of maximum diameter to minimum diameter for a typical grain was about 3 to 1. For calculations, an equivalent spherical diameter was used which gave the same surface-volume ratio as observed microscopically. All samples are sufficiently close to spherical in shape that this value is within ten per cent of the average of the largest and smallest dimension.

III. RESULTS AND DISCUSSION

A large number of individual experiments was carried out, with the objective of determining the effect of temperature on the diffusion coefficient of oxygen in both single-crystal and polycrystalline aluminum oxide. Diffusion coefficients were small (10^{-16}–10^{-13}), measurements were made at high temperatures (up to 1780°C), and in most cases repeated measurements of an identical sample were not possible since the solid was used up on the isotope analysis. Many sources of error contributed to a lack of experimental precision. Precision of time measurements, temperature measurements, gas container reliability and spectroscopic analysis combined to give an estimated over-all precision of a few percent for each exchange determination.

The experimental results showed a range up to ±100% for any particular temperature. Prior heat treatment was found to have a marked effect on experimental results. This may have resulted from the removal of impurities, changes in stoichiometry, removal of dislocations and subgrain boundaries, or other effects. The importance of prior thermal treatment was not recognized until late in the program. Consequently, the major source of variation in the experimental data was differences in the starting material and in prior heat treatments.

(a) Single-Crystal Samples

Experimental measurements for single-crystal samples were made with 0.030-in. diam spheres and with crushed grain passed through 200–230 mesh screens; microscopic measurements gave an equivalent spherical diameter of 0.0098 cm for the grain.

Unless otherwise indicated, samples were first heated to about 1100°C for 40 min and then raised to the test temperature in 2 to 3 min. The measured exchange was always an order of magnitude greater than that found in a blank test. In a few cases the samples were heated in air at 1900°C prior to carrying out the exchange measurements; these experiments are identified as "annealed" samples.

TABLE I. Spectrographic analysis for minor impurities.

Impurity	Sapphire spheres	Sapphire grain	Polycrystalline spheres
Mg	<0.01%	<0.01%	<0.01%
Ca	<0.01	<0.01	<0.01
Fe	nil	<0.01	<0.01
Ga	nil	nil	<0.01
Mn	nil	<0.01	nil
Si	<0.01	<0.01	<0.01

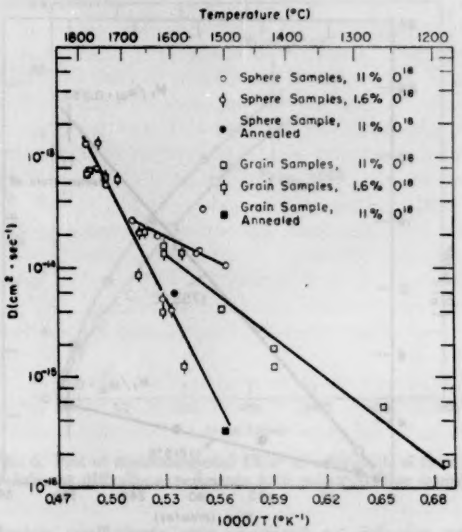

FIG. 3. Experimental results for oxygen self-diffusion in single-crystal 0.030-in. diam spheres and single-crystal grains of Al_2O_3. See text for complete sample description.

At temperatures above about 1650°C reasonably good agreement was obtained between experimental results with different samples and different heat treatments. At lower temperatures, as shown in Fig. 3, there were large discrepancies between different samples and samples with different prior heat treatment. The "annealed" samples fell on a straight line with the high-temperature measurements, and some of the other samples did also. Some, however, gave measured diffusion coefficients substantially higher than this value. In other experiments with single crystals of aluminum oxide[10] it was observed that extended heating at a temperature of 1750°C or above was necessary to give stable electrical property measurements. The conductivity decreased during this first heating and subsequently remained constant. The effect of heating could result from various causes, and the reason for the spread in the values of the diffusion coefficient measured at the lower temperatures has not been determined. However, the lower curve in Fig. 3 apparently corresponds to the intrinsic oxygen diffusion coefficient while impurity or structure sensitive diffusion is observed in some samples at the lower temperatures.

Most of the measurements reported here were determined by analysis of the solid phase, so that the

[10] J. Pappis and W. D. Kingery (to be published).

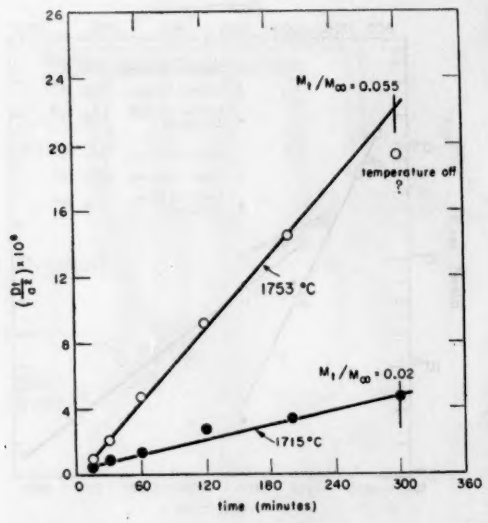

FIG. 4. Plot of nondimensional Dt/a^2 as a function of time for two different diffusion experiments with single-crystal grains.

constancy of the diffusion coefficient with time or with amount of diffusion was not determined. In order to ensure that the temperature dependence would be independent of any such variation, experiments were carried out to give an exchange of about 5–10% of the sample for the crushed grain and about 0.1–2% of the sample for the spheres. These values correspond to an O^{18} penetration of about 10 μ and 1 μ.

Two samples of 100–120 mesh single-crystal grains were studied by taking gas samples for analysis to obtain a concentration-time curve. In order to obtain sufficient concentration changes for precise measurements, these experiments were carried out with gas enrichments of 11% O^{18} and 7% O^{18}. Results were evaluated in terms of the (Dt/a^2) vs time plots illustrated in Fig. 4. For both samples the data fell on a straight line, corresponding to diffusion-controlled exchange with a constant diffusion coefficient. A small change in the rate of initial temperature rise or in the time to reach uniform temperature can account for the 1715°C experiment's not passing through the origin. In the upper line, the temperature dropped during the last 30 min of the test so that the last point is doubtful. In both of these measurements the temperature was sufficient to cause some sintering which restricts the gas flow from the interior of the sample, leading to a depletion of O^{18} content and a decrease in the apparent diffusion coefficient. Sintering would also cause a small decrease in surface area, leading to a smaller observed diffusion coefficient, but these effects seem doubtful. In general, our data indicate a diffusion-controlled exchange with a constant diffusion coefficient, but a more rapid exchange in the immediate vicinity of the surface cannot be ruled out.

The experimentally determined intrinsic self-diffusion coefficient of oxygen in single-crystal Al_2O_3 (least-mean-squares solid line for lower points in Fig. 3) can be represented as:

$$D=1.9\times10^3\exp(-152\,000\pm25\,000/RT). \quad (3)$$

The straight line portion of the lower-temperature data for one set of crushed grain samples gives:

$$D=6.3\times10^{-8}\exp(-57\,600/RT). \quad (4)$$

The low-temperature portion of the curve for a set of spherical samples does not cover a sufficiently wide temperature region to estimate an activation energy.

These results are of particular interest in that this is the first case in which an oxide system has shown an intrinsic and an extrinsic range for measured diffusion coefficients. The activation energy for the extrinsic region can be attributed to ion mobility in this system. This value is about 1.4 times the values reported for Cl^- in NaCl[6,11]; this ratio does not seem unreasonable in view of the increased valence of oxygen ion compared to the chlorine ion. Similarly, the ratio of the activation energy for the extrinsic anion mobility in $Zr_{0.85}Ca_{0.15}O_{1.85}$ and CaF_2[12] is about a factor of 1.5–2.

The high-temperature part of the diffusion curve could correspond either to the formation of Frenkel defects (equal numbers of vacant oxygen sites and interstitial oxygen ions) or Schottky defects (vacancies in both the anion and cation lattices). In view of the close-packed arrangement of oxygen ions in the aluminum oxide structure, the latter seems more probable and we can write for the intrinsic diffusion coefficient:

$$D=D_0\exp-(\tfrac{3}{5}E+U)/RT, \quad (5)$$

where E is the energy required to form an oxygen ion vacancy plus two-thirds of an aluminum ion vacancy necessary for electrical neutrality, and U is the activation energy for ion mobility. In this case $E=5/3(152-58)=157$ kcal/mole is the energy required to form Schottky defects in the aluminum oxide lattice. This value is about three times that found for sodium chloride and seems a not unreasonable value.

For the Eyring equation,

$$D=\lambda^2(kT/h)\exp(\Delta S^*/R)\exp(-\Delta H^*/RT) \quad (6)$$

in the range of intrinsic diffusion, taking a jump distance of 2.94 A corresponding to the oxygen-oxygen separation in the structure, $\Delta S^*=20$ cal/deg and $\Delta H^*=148$ kcal/mole. The entropy value is not sufficiently precise for any detailed interpretation, but is not inconsistent with the formation and mobility of Schottky defects at the higher temperatures. For the extrinsic data, we calculated from, from Eq. (4), $\Delta S^*=-28$ cal/deg and $\Delta H^*=54$ kcal/mole. The apparent negative entropy of activation for anion diffusion is

[11] D. Patterson, G. S. Rose, and J. A. Morrison, Phil. Mag. 46, 393 (1955).
[12] R. W. Ure, Jr., J. Chem. Phys. 26, 1363 (1957).

also observed for some of the alkali halides.[6,7] As suggested by Birchenall,[13] a transmission coefficient of $\frac{1}{4}$ should probably precede Eq. (6) for diffusion where the diffusing ion moves through a close array of neighbors into a normally unoccupied interstitial site and then passes through another array to reach a new equilibrium position, as has been discussed by Laurent and Bénard.[5]

Any detailed discussion of the activation process and mechanism of oxygen mobility is obviously speculative on the basis of the present data. Added information with regard to effects of impurities, dislocation structure, thermal treatment, transport number measurements, etc., would be most desirable. As discussed in the preceding paragraphs, however, experimental data are in satisfactory agreement with reasonable hypotheses. It should not be inferred that these hypotheses are proved by the present data.

(b) Polycrystalline Samples

Experimental diffusion coefficients for polycrystalline alumina were considerably higher than the values found for single crystals, as shown in Fig. 5. In addition, as shown in Fig. 6, a definite decrease in the apparent

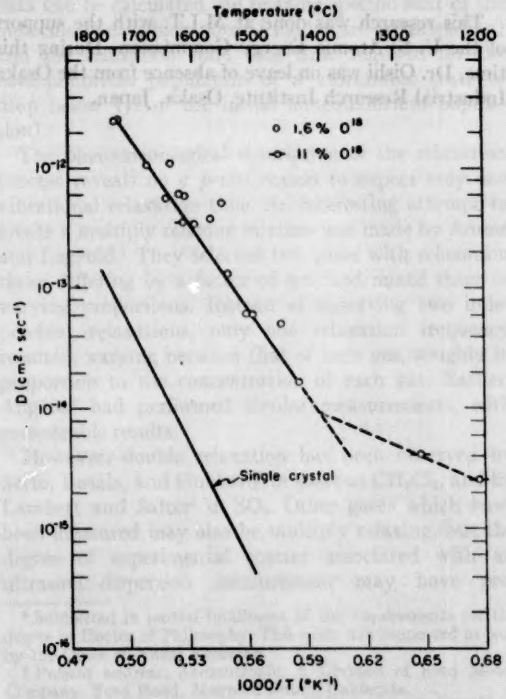

FIG. 5. Experimental results for oxygen self-diffusion coefficients in polycrystalline alumina (lower line is result for single crystals).

[13] C. E. Birchenall, Contract Report AF 18 (600)-967, AFOSR-TR-59-43 (1959).

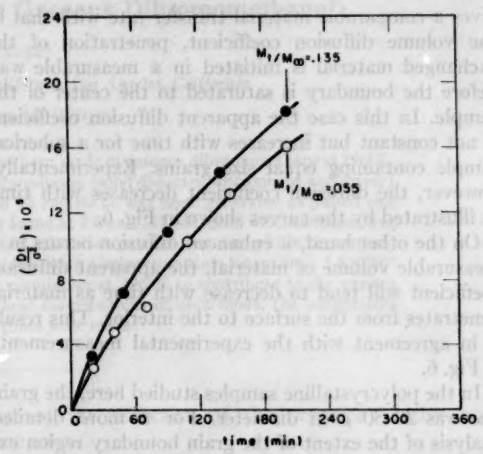

FIG. 6. Plot of nondimensional Dt/a^2 as a function of time for two different diffusion experiments with polycrystalline samples.

diffusion coefficients was observed as diffusion progressed. In order to have comparable results for analysis of the temperature dependence, experimental measurements were carried out to give a fractional exchange of 1–2% in all cases. This corresponds to the initial part of the curves illustrated in Fig. 6.

In the temperature range above about 1450°C, the experimental results can be represented by the relationship:

$$D = 2.0 \exp(-110\,000 \pm 15\,000/RT) \qquad (7)$$

At lower temperatures the experimental measurements departed from this relationship as shown in Fig. 5.

There are several possible explanations for the higher diffusion coefficients found in a polycrystalline sample. In the Fisher analysis[14] it is assumed that boundary diffusion is substantially more rapid than volume diffusion, but that the capacity of the boundaries for absorbing material is negligible compared to that of the grain. Consequently, diffusion occurs along the grain boundaries and spreads out to the volume of the crystals. In contrast, for alkali halides, Laurent and Bénard[7] found that the diffusion coefficient for anions in polycrystalline samples is larger than that in single crystals by virtue of enhanced diffusion adjacent to boundaries. This is equivalent to having boundary regions with a capacity for exchange as well as an enhanced diffusion coefficient.

In the case where the grain boundaries have rapid diffusion rates but no capacity for exchange, the diffusion coefficient is independent of time and has the same activation energy as observed for volume diffusion, as long as the rate of boundary diffusion is several orders of magnitude greater than that for volume diffusion. If the boundary diffusion coefficient

[14] J. C. Fischer, J. Appl. Phys. **22**, 74 (1951).

gives a comparable material transfer rate with that of the volume diffusion coefficient, penetration of the exchanged material is initiated in a measurable way before the boundary is saturated to the center of the sample. In this case the apparent diffusion coefficient is not constant but increases with time for a spherical sample containing equal size grains. Experimentally, however, the diffusion coefficient decreases with time as illustrated by the curves shown in Fig. 6.

On the other hand, if enhanced diffusion occurs in a measurable volume of material, the apparent diffusion coefficient will tend to decrease with time as material penetrates from the surface to the interior. This result is in agreement with the experimental measurements in Fig. 6.

In the polycrystalline samples studied here, the grain size was 20–30 μ in diameter. For a more detailed analysis of the extent of the grain boundary region exchange capacity, it would be desirable to have penetration-concentration curves for the exchange reaction as well as measurements for a variety of grain sizes.

IV. SUMMARY

Experimental methods have been devised for determining oxygen self-diffusion in oxides at temperatures up to 1780°C for diffusion coefficients as low as 10^{-16} cm^2/sec. For these measurements, O^{18} stable isotope tracers were employed.

Oxygen diffusion coefficients in single-crystal Al_2O_3 have been determined over the temperature range 1360–1780°C. Experimental measurements indicated an intrinsic diffusion coefficient with an activation energy of 152 kcal/mole. At temperatures below 1650°C the measurements of diffusion gave variable results depending on prior heat treatment and impurity concentration corresponding to impurity-controlled or structure-sensitive diffusion. The experimental activation energy for diffusion of one set of samples in this region was 57.6 kcal/mole. From these results we tentatively calculate the energy required for the formation of intrinsic imperfections in the aluminum oxide lattice as being about 157 kcal/mole of oxygen ion vacancies and associated aluminum ion vacancies.

The oxygen diffusion coefficient in polycrystalline aluminum oxide is nearly two orders of magnitude larger than that observed for single-crystal samples. The time dependence of measured diffusion coefficients suggests that there is enhanced diffusion in a boundary region having an appreciable capacity for exchange. The activation energy observed for polycrystalline alumina at temperatures above 1450°C is 110 kcal/mole. At lower temperatures variable results were obtained, presumably corresponding to impurity-controlled or structure sensitive diffusion.

ACKNOWLEDGMENT

This research was done at M.I.T. with the support of the U. S. Atomic Energy Commission. During this time, Dr. Oishi was on leave of absence from the Osaka Industrial Research Institute, Osaka, Japan.

Multiple Vibrational Relaxation in Gaseous Dibromomethane*

NORMAN J. MEYER†

Department of Physics, University of California, Los Angeles, California

(Received December 14, 1959)

Ultrasonic-dispersion and absorption measurements have been made in gaseous dibromomethane at 296°K, and at pressures between 0.5 and 15 mm Hg. Wide-band transducers (solid dielectric microphone and driver) were used. A continuous selection of frequencies between 13 and 80 kc was used, generated as pulsed sine waves. Independent vibrational relaxation processes were found at 7.0 and 125 Mc/atm, with corresponding relaxation times of 3.02×10^{-6} and 0.146×10^{-6} sec. A third relaxation process was not within the experimental range of the apparatus, and occurs below 0.1 Mc/atm, with a relaxation time longer than 1.8×10^{-6} sec. Seven of the nine vibrational modes have sufficient population at 296°K to contribute to the various relaxation processes. Primarily based upon the specific heat contributions of each mode, the assignments of the various modes relaxing at the different relaxation times were made.

INTRODUCTION

A LARGE number of acoustic experiments have been performed in polyatomic gases to explore the intermolecular collision process. The experiment usually performed measured an anomalous dispersion in the speed of sound or an anomalous sound absorption. The experimental results yielded the following quantities: relaxation frequency, percent dispersion, and maximum coefficient of absorption per wavelength. From these data can be calculated the relaxing specific heat of the molecule (i.e., which normal modes are participating) and the relaxation time (the time required for the nonequilibrium population of a vibrational state to drop below $1/e$ of the initial nonequilibrium population).

The phenomenological description of the relaxation process reveals no *a priori* reason to expect only one vibrational relaxation time. An interesting attempt to create a multiply relaxing mixture was made by Amme and Legvold.[1] They selected two gases with relaxation times differing by a factor of ten, and mixed them in varying proportions. Instead of observing two independent relaxations, only one relaxation frequency resulted, varying between that of each gas, roughly in proportion to the concentration of each gas. Earlier, Angona[2] had performed similar measurements, with comparable results.

However, double relaxation has been observed by Sette, Busala, and Hubbard[3] in gaseous CH_2Cl_2, and by Lambert and Salter[4] in SO_2. Other gases which have been measured may also be multiply relaxing, but the degree of experimental scatter associated with an ultrasonic-dispersion measurement may have prevented the detection of the presence of this phenomenon.

On the basis of the theoretical analysis of the chloromethanes by Tanczos[5] and the similar treatment of SO_2 by Dickens and Linnett,[6] CH_2Br_2 appeared to have the necessary vibrational energy-level characteristics (Fig. 1 and Table I) to exhibit more than one relaxation process.

EXPERIMENTAL APPARATUS

The method used here for performing the acoustic experiment was the "direct method"—measuring sound absorption (and speed) as the source is moved away from the receiver. Additionally, the technique of pulsed sine wave signals had these advantages: reduced heating of the gas due to a shortened duty cycle, and facility in identifying the direct sound signal from the various reflected waves. By performing measurements in the far field, i.e., at source-receiver separations large

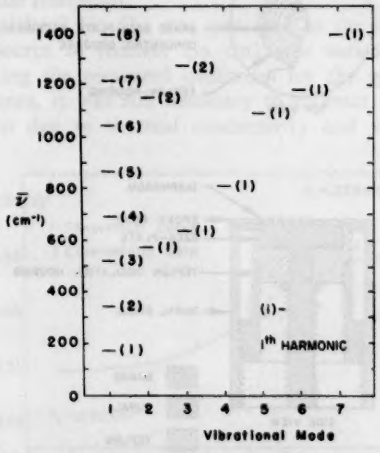

FIG. 1. Vibrational wave numbers for gaseous dibromomethane.

* Submitted in partial fulfillment of the requirements for the degree of Doctor of Philosophy. This work was supported in part by the Office of Naval Research.

† Present address: Aeronutronic, A Division of Ford Motor Company, Ford Road, Newport Beach, California.

[1] R. Amme and S. Legvold, J. Chem. Phys. **26**, 514 (1957).

[2] F. A. Angona, J. Acoust. Soc. Am. **25**, 1111 (1953).

[3] D. Sette, A. Busala, and J. C. Hubbard, J. Chem. Phys. **23**, 787 (1955).

[4] J. D. Lambert and R. Salter, Proc. Roy. Soc. (London) **A243**, 78 (1957).

[5] F. I. Tanczos, J. Chem. Phys. **25**, 439 (1956).

[6] P. G. Dickens and J. W. Linnett, Proc. Roy. Soc. (London) **A243**, 94 (1957).

TABLE I. Vibrational frequencies,[a] specific heats, and limiting speeds of sound in CH_2Br_2 at 296°K.

Mode	ν_i (cm^{-1})	C_i/R
1	174	0.9417
2	576	0.5405
3	637	0.4742
4	810	0.3133
5	1091	0.1416
6	1183	0.1064
7	1388	0.0534
8	2988	0.0001
9	3061	0.0001
C_{vib}/R	2.5713	
C_{vo}/R	5.5713	
C_{po}/R	6.5713	
γ_0	1.1795	
V_0	1.292×10^4 cm/sec	
V	1.374×10^4 cm/sec	

$R=8.317\times10^7$ erg/°K mole
$C_{v\infty}/R=3.0000$
$C_{p\infty}/R=4.0000$
$\gamma_\infty=1.3333$

[a] J. M. Dowling and A. G. Meister, J. Chem. Phys. 22, 1042 (1954).

compared with $\pi a^2/\lambda$, where a is the driver's radiating-surface radius, and λ is the wavelength of the sound signal, the sound field was effectively that due to a "pulsating point source," producing a spherically divergent sound field.

The transducers employed in this experiment, the condenser type with solid dielectric,[7] were identical (Fig. 2). A sheet of gold-plated Mylar, 0.25 mils thick, was stretched over and bonded to a hollow dural

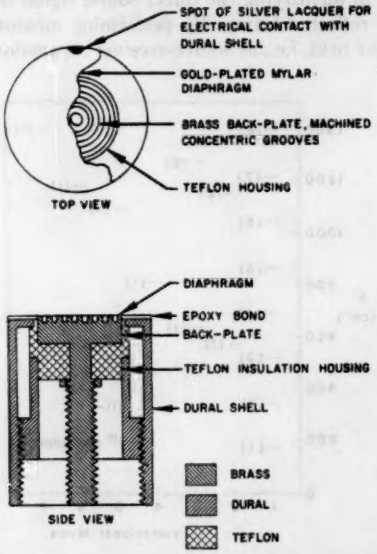

FIG. 2. Transducer assembly.

[7] W. Kuhl, G. R. Schodder, and F. K. Schröder, Acustica 4, 519 (1954).

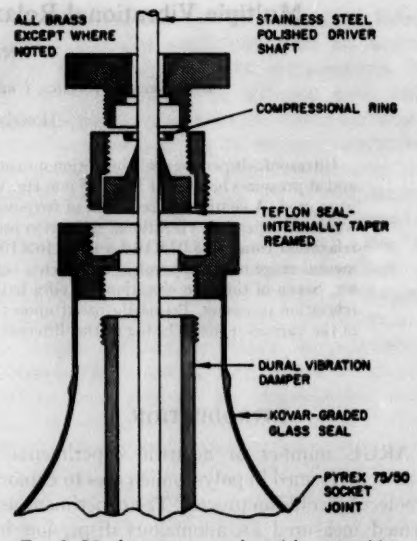

FIG. 3. Moving vacuum seal on drive assembly.

cylinder. The brass backplate, insulated by a Teflon housing, had concentric circular grooves cut into it. Tensioning of the diaphragm was achieved by advancing the backplate into the Mylar side of the diaphragm. The dural shell and the gold plating on the diaphragm served as the ground side of the condenser.

The speaker was mounted at the end of a 30-cm long precision-ground stainless-steel tube (Fig. 3), terminated by a Kovar metal-glass vacuum seal, and containing an insulated inner wire carrying the electrical signal (the shell of the speaker and the steel tube were the grounded return lead). The steel shaft passed through a Teflon sleeve compressed tightly about the shaft, acting as a moving vacuum seal. Positioning of the speaker was effected by a rack-and-pinion, manually

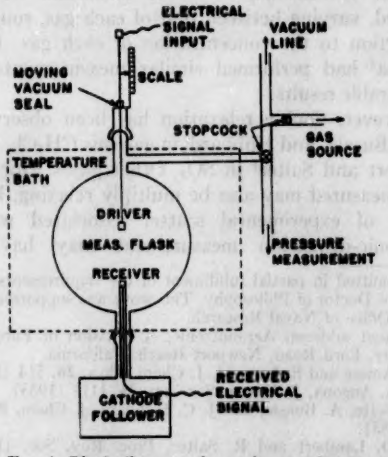

FIG. 4. Block diagram of experimental layout.

operated drive affixed to the topmost end of the steel tube; a vernier attached to this extension of the tube moved over a fixed rule. The position of the speaker could be measured to ±0.01 cm.

The measuring flask was a 12-liter Pyrex sphere (Fig. 4) fitted with a ball-and-socket joint at each end of a vertical diametral line. Through the upper end, the movable driver assembly was inserted. At the bottom of the flask, the stationary microphone assembly was supported, with the microphone facing upward (inside the flask).

A block diagram of the electrical system is shown in Fig. 5. To generate the pulsed sine wave signal, an internally triggered GR unit pulser was used to drive a blocked Hartley oscillator. This stable oscillator was continuously tunable over a frequency range of 13–310 kc. This signal was then fed into the driver unit, which was supplied with a 200-v dc polarizing voltage.

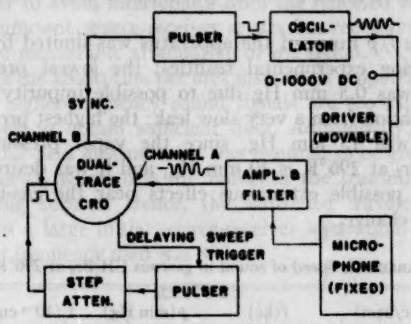

FIG. 5. Block diagram of signal generation, detection, and display.

The received signal was amplified, filtered, and presented on one channel of a dual-trace plug-in unit of a Tektronix type-545 oscilloscope. The CRO sweep was synchronized by the driving GR unit pulser. Simultaneously presented on the CRO through the other channel input was a square wave, generated by another GR unit pulser. This pulser was triggered through the oscilloscope delaying sweep, providing variable time positioning of this comparison signal. Attenuators controlled the comparison signal height in 0.1-db steps. The comparison signal was also conveniently used as a marker on the received signal for velocity and period measurements.

The CH_2Br_2 was Eastman No. 1903, highest purity. This substance is a colorless liquid with a vapor pressure of 40 mm Hg at 296°K. The manufacturer guarantees a 98% purity and further indicates that the purity exceeds 99% since the liquid remained colorless. A schematic diagram of the experimental layout is shown in Fig. 4. The dibromomethane was admitted to an evacuated storage flask in liquid form. The flask was then cooled and evacuated to reduce the presence of noncondensible vapors. A stopcock was opened between the storage flask and the evacuated measuring vessel

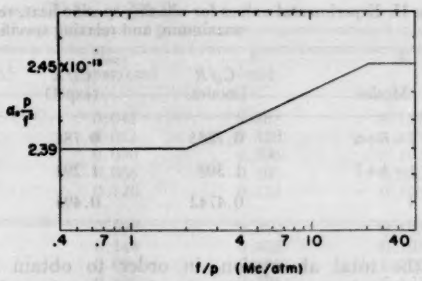

FIG. 6. Variation of absorption due to viscosity and thermal conductivity over relaxation region.

until the desired pressure was reached. After completing the measurements, the measuring vessel was again evacuated. A water bath controlled the temperature of the measuring flask to ±0.1°C.

EXPERIMENTAL MEASUREMENTS

Preliminary measurements to evaluate the apparatus and the method were made on dry N_2, due to its ease in handling and its having been extensively studied. The measuring apparatus was carefully cleaned and dried, and repeatedly flushed with the gas under study and evacuated to reduce residual impurities.

Absorption measurements were made by recording signal level (in db) as the source was moved away from the receiver. The sound intensity level I may then be represented by

$$I = I_0/r^2 \exp(-\alpha_c + \mu/\lambda)r, \qquad (1)$$

where I_0 is a reference sound intensity level, α_c is the intensity coefficient of absorption due to classical effects (discussed below), and μ is the intensity coefficient of absorption per acoustic wavelength due to molecular relaxation.

Signal level (in db) was measured as the distance from source to receiver (in cm) was varied. After correcting the measured quantities for the spherical divergence, it was still necessary to subtract the absorption due to thermal conductivity and viscosity

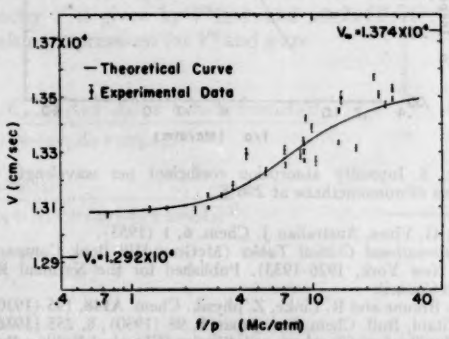

FIG. 7. Speed of sound in gaseous dibromomethane at 296°K.

TABLE II. Experimental values for relaxing specific heat, relaxation time, relaxation frequency, limiting speed of sound, absorption maximum, and relaxing specific heat of modes (computed from Table I).

Modes	C_i/R (modes)	C_i/R (exptl)	τ (10^{-6} sec)	μ_m (nepers/wavelength)	f_m (Mc/atm)	V_0 (10^4 cm/sec)
2+5+6	0.7885	0.784	>180	...	<0.1	1.292
1+4+7	1.308	1.294	3.02	0.195	7.0	1.308
3	0.4742	0.493	0.146	...	125	1.350

from the total absorption, in order to obtain the attenuation due to the vibrational effects alone. The expression for the classical intensity absorption coefficient is given by

$$\alpha_c=(4\pi^2RT/V^3M)\eta\{\tfrac{4}{3}+(k_TM/\eta)[(\gamma-1)/\gamma C_v]\}f^2/p, \quad (2)$$

where R=universal gas constant, M=molecular weight of CH_2Br_2, f=sound frequency, p=ambient pressure, k_T=coefficient of thermal conductivity, η=coefficient of shear viscosity, C_V=specific heat at constant volume, V=speed of sound, $\gamma=C_p/C_v$.

A thorough search of the literature failed to reveal any measurements of η and k_T in gaseous CH_2Br_2 near 296°K. It was necessary, therefore, to approximate these values from data available[8–12] particularly from those of related substances. The values used were

$$k_T=10\times10^{-6}\text{ cal/cm sec °C},$$

$$\eta=120\ \mu\text{ poise}.$$

α_c is a function of the relaxation-dependent variables C_v, V, and γ, and $\alpha_c p/f^2$ will not remain constant at f/p values near a relaxation frequency. Substitution of the experimentally determined values of C_v, V and γ into Eq. (2) permitted Fig. 6, an approximate classical correction curve, to be drawn.

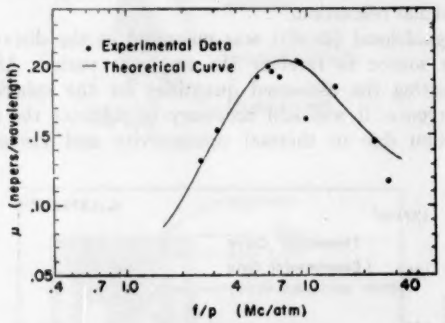

FIG. 8. Intensity absorption coefficient per wavelength in gaseous dibromomethane at 296°K.

Speed-of-sound measurements were made by recording the time required for the acoustic signal to traverse equal-distance increments. The set of distance and time measurements was then subjected to a least-squares fit of the data to a straight line, the slope of which yielded the speed of sound. The vertical spread of each point in Fig. 7 represents the standard deviation of the slope.

The f/p range of the apparatus was limited by the following experimental realities: the lowest pressure used was 0.5 mm Hg due to possible impurity contamination from a very slow leak; the highest pressure used was 15 mm Hg, since the vapor pressure of CH_2Br_2 at 296°K is 40 mm Hg, and it was desired to avoid possible extraneous effects near the gas-liquid phase change.

TABLE III. Speed of sound in gaseous CH_2Br_2 at 296°K.

f/p (Mc/atm)	f(kc)	p(mm Hg)	V(10^{-4} cm/sec)
0.73	14.3	14.8	1.307
1.28	24.9	14.8	1.310
1.58	30.8	14.8	1.310
2.24	43.6	14.8	1.308
2.24	43.6	14.8	1.309
2.62	34.1	9.9	1.310
2.62	34.1	9.9	1.314
3.16	41.1	9.9	1.314
3.62	21.9	4.6	1.318
4.38	13.8	2.4	1.329
5.53[a]	33.5	4.6	1.323
7.04	22.2	2.4	1.331
7.1	26.1	2.8	1.325
8.64	13.7	1.2	1.329
9.0	33.0	2.8	1.325
9.0	33.0	2.8	1.330
9.0	21.4	1.8	1.334
9.2	21.7	1.8	1.342
9.85[a]	31.1	2.4	1.338
10.5	13.8	1.0	1.326
14.2	33.6	1.8	1.345
14.3	22.6	1.2	1.349
17.0	13.7	0.6	1.331
22	34.7	1.2	1.357
23.1	30.4	1.0	1.351
25.8	34.0	1.0	1.347
28	22.1	0.6	1.349
28	22.1	0.6	1.353

[a] Two measurements.

[8] R. G. Vines, Australian J. Chem. **6**, 1 (1953).
[9] *International Critical Tables* (McGraw-Hill Book Company, Inc., New York, 1926–1933). Published for the National Research Council.
[10] J. Braune and R. Linke, Z. physik. Chem. **A148**, 195 (1930).
[11] Titani, Bull. Chem. Soc. Japan **5**, 98 (1930); **8**, 255 (1933).
[12] *Handbook of Chemistry and Physics* (Chemical Rubber Publishing Company, Cleveland, Ohio, 1958).

TABLE IV. Intensity absorption of gaseous CH_2Br_2 at 296 °K.

f/p (Mc/atm)	freq. (kc)	press (mm Hg)	α_{meas} (neper/cm)	α_{corr} (neper/cm)	λ (cm)	μ
2.6	34.1	9.9	0.384	0.042	0.385	0.132
3.2	41.1	9.9	0.546	0.062	0.320	0.155
5.5	33.5	4.6	0.576	0.090	0.396	0.192
6.2	21.9	2.7	0.396	0.066	0.605	0.200
6.5	39.6	4.6	0.710	0.126	0.335	0.196
7.1	26.1	2.8	0.466	0.090	0.510	0.192
9	33.0	2.8	0.620	0.144	0.405	0.193
9.2	21.7	1.8	0.414	0.096	0.616	0.202
14.3	22.6	1.2	0.470	0.160	0.596	0.185
23.1	30.4	1.0	0.670	0.344	0.444	0.145
28	22.1	0.6	0.496	0.304	0.611	0.117

The lowest frequency used was 13 kc. The decreasing sound absorption at low frequencies requires the initial distance measurement to be made at a larger distance in order to avoid interference from the reflected wave, with sufficient source-receiver separation remaining to observe measurable attenuation of the signal.

Since the absorption per unit distance is proportional to f^2, higher-frequency sound signals are too rapidly absorbed to obtain sufficient data. Additionally, the initial far-field measurement was required to be greater than $\pi a^2/\lambda$, where a is the radius of the transducer's radiating surface. Hence, the shortened wavelength dictates a large initial source-receiver separation. The highest frequency used was 80 kc.

RESULTS

By inspection of the experimental values for the speed of sound shown in Fig. 7 it can be seen that a relaxation process is completed without reaching either the higher or lower asymptotes. Therefore, there exists a minimum of three relaxation times, $\tau_1>\tau_2>\tau_3$, in gaseous dibromomethane, the middle region being the one explored in this experiment.

A careful examination of the data indicates that τ_1 is much larger than τ_2. Therefore, any dispersion or absorption due to relaxation processes at τ_1 has no measurable effect in the f/p range of this experiment. This permits an estimate of the upper limit of the lowest relaxation frequency of 0.1 Mc/atm, and hence $\tau_1>1.8\times10^{-6}$ sec.

To compute C_1, the specific heat relaxing at τ_1, the expressions applicable to a single relaxation process were used. From Vigoureux,[13] the velocity dispersion and the absorption coefficient maximum (μ_{m_1}) may be related by

$$\pi\left(\frac{V_{\infty 1}}{V_{01}}-\frac{V_{01}}{V_{\infty 1}}\right)=\mu_{m_1}=\frac{\pi C_1}{[(C_{p_0}-C_1)(C_{v_0}-C_1)C_{p_0}C_{v_0}]^{\frac{1}{2}}}, \quad (3)$$

where C_{p0}, C_{v0}, and V_{01} are found in Table I, and $V_{\infty 1}$ is determined from Fig. 7 to be 1.308×10^4 cm/sec. From Eq. (3), C_1/R is then found to be 0.784,

Further examination of the experimental results leads to the conclusion that τ_3 is not greatly different from τ_2; that is, the two relaxation times are sufficiently close to each other to require the use of equations describing overlapping relaxation "zones." C_2 and C_3, relaxing at τ_2 and τ_3, are determined in the following manner. It can be shown[14] that the frequency-dependent specific heat C_{23} may be written

$$C_{23}=C_{v\infty}+C_2/(1+i\omega\tau_2)+C_3/(1+i\omega\tau_3). \quad (4)$$

If Eq. (4) is substituted into the expression for the speed of sound, a complex quantity V^2 results:

$$V^2=\frac{(C_{23}+R)}{C_{23}}\frac{RT}{M}=A+iB, \quad (5)$$

From Eq. (5), Vigoureux[13] has shown that the phase velocity V is given by $V^2\cong A$, and $\mu\cong 2\pi(B/A)$. The resulting expressions for V^2 and μ are

$$\left(\frac{V}{V_\infty}\right)^2=C_{v\infty}\frac{(1+1/\gamma_\infty)(A_2+A_3)+C_{v\infty}/R+R/C_{p\infty}[(A_2+A_3)^2+(\omega\tau_2A_2+\omega\tau_3A_3)^2]}{(C_{v\infty}/R+A_2+A_3)^2+(\omega\tau_2A_2+\omega\tau_3A_3)^2}, \quad (6)$$

$$\mu=\frac{2\pi(\omega\tau_2A_2+\omega\tau_3A_3)}{(C_{p\infty}/R+A_2+A_3)(C_{v\infty}/R+A_2+A_3)+(\omega\tau_2A_2+\omega\tau_3A_3)^2}, \quad (7)$$

where

$$A_i=(C_i/R)/(1+\omega^2\tau_i^2), \qquad i=2, 3.$$

[13] P. Vigoureux, *Ultrasonics* (John Wiley & Sons, Inc., New York, 1951).
[14] K. F. Herzfeld, "Relaxation phenomena in gases," *Thermodynamics and Physics of Matter*, edited by F. D. Rossini (Princeton University Press, Princeton, New Jersey, 1955), p. 667.

The quantities which are needed in order to plot Eqs. (6) and (7) are the vibrational specific heats and the relaxation times. Since $C_{v1b}=C_1+C_2+C_3$, and the first two values are known, then the determination of either C_2 or C_3 fixes the other. The best fit of the experimental data was achieved by use of the values listed in Table II. The experimental data points are presented in Tables III and IV, and the respective resulting curves are plotted in Figs. 7 and 8. The relaxation frequency, f_{mi}, corresponding to the absorption peak, μ_{mi}, was computed from

$$f_{mi}=(2\pi\tau_i)^{-1}\left(\frac{C_{v0i}C_{p0i}}{C_{v\infty i}C_{p\infty i}}\right)^{\frac{1}{2}},\ i=1,\ 2,\ 3,$$

where the subscript 0 or ∞ indicates low or high asymptotic value of specific heat, respectively,

The assignment of modes in Table II was made largely on a curve-fitting basis. It is noted, for example, that mode 1 should probably have the shortest relaxation time (certainly shorter than mode 3). In the absence of other information, the modal assignments may be regarded as a "possibility," and other theoretical and experimental investigations are invited.

CONCLUSIONS

Three separate relaxation times were found to exist in gaseous dibromomethane. The middle and part of the high-frequency relaxation regions were measured. Relaxation processes involving modes 2, 5, and 6 (see Table I) occur in the f/p region below the experimental range. Hence, no conclusion could be drawn as to the possibility of these modes having independent relaxation times. A direct measurement, though not possible on this apparatus, would certainly be of interest.

Since CH_2Br_2 is multiple relaxing, the variation of relaxation time with either temperature or controlled impurity addition could be readily investigated.

Investigation of the dihalogenated methane series as a group would be of interest; CH_2I_2 has not as yet been investigated.

ACKNOWLEDGMENTS

The author wishes to thank Professor I. Rudnick and Professor R. W. Leonard for their supervision of this work, and for their extensive technical guidance.

THE JOURNAL OF CHEMICAL PHYSICS VOLUME 33, NUMBER 2 AUGUST, 1960

Interaction Energies for the H-H_2 and H_2-H_2 System*

JOSEPH T. VANDERSLICE AND EDWARD A. MASON

Institute for Molecular Physics, University of Maryland, College Park, Maryland

(Received March 3, 1960)

Interaction energies for the H-H_2 and H_2-H_2 systems have been obtained by a semiempirical perfect-pairing procedure used previously. The results have been compared with interaction energies obtained from other sources and the agreement among the different curves is reasonably good. A brief discussion of the previous applications of this semiempirical scheme to other systems is included.

INTRODUCTION

A CALCULATION of the transport properties of a gas presupposes a knowledge of the interaction energies between the various species present in the gas. Hydrogen gas at temperatures of several thousand degrees will contain not only hydrogen molecules but also a fair amount of ground-state hydrogen atoms. Consequently, the atom-atom, atom-molecule, and molecule-molecule interactions must be known if one wants to obtain reliable results from a transport-property calculation. Hydrogen should serve as a particularly simple example for the calculation of transport properties of hot gases, and its transport properties are of some current interest for their own sake.[1]

As two ground-state hydrogen atoms approach one another, they can interact along either one of two potential curves, corresponding to the $^1\Sigma_g^+$ and $^3\Sigma_u^+$ spectroscopic states of molecular hydrogen. Reasonably accurate curves for these interactions are known,[2–5] but the curves for the interactions such as H-H_2 and H_2-H_2 are not well known over a range of distance corresponding to interaction energies of about a volt or less. This latter range is the important one in determining high-temperature properties.

Previously we have used the valence-bond scheme of perfect pairing[6] to generate atom-molecule and mole-

* This research was supported in part by the National Aeronautics and Space Administration.

[1] J. J. Newgard and M. Levoy, Sci. American **200**, 46 (1959).

[2] J. T. Vanderslice, E. A. Mason, W. G. Maisch, and E. R. Lippincott, J. Mol. Spectroscopy **3**, 17 (1959).

[3] H. M. James, A. S. Coolidge, and R. D. Present, J. Chem. Phys. **4**, 187 (1936).

[4] A. Dalgarno and N. Lynn, Proc. Phys. Soc. (London) **A69**, 821 (1956).

[5] R. J. Fallon, E. A. Mason, and J. T. Vanderslice, Astrophys. J. **131**, 12 (1960).

[6] C. A. Coulson, *Valence* (Oxford University Press, London, 1952), pp. 166–171.

cule-molecule interactions from a knowledge of atom-atom interactions. The results so obtained agreed well with the available experimental data.[7–10] It seemed reasonable to suppose that we might use the same semiempirical procedure to calculate the interaction energies for the H-H_2 and H_2-H_2 systems from a knowledge of the H-H interactions. These systems also serve as an especially simple case for the further testing of this semiempirical scheme. Curves for these interactions have been obtained and are compared with results obtained by other methods.

METHOD AND RESULTS

The perfect-pairing procedure yields for the interaction energy of a system[6]

$$V=\sum_{\substack{\text{paired}\\\text{orbitals}}} J_{ij}-\tfrac{1}{2}\sum_{\substack{\text{nonpaired}\\\text{orbitals}}} J_{ij}-\sum_{\substack{\text{orbitals with}\\\text{parallel spins}}} J_{ij}, \qquad (1)$$

if one neglects Coulombic terms which should be small at large distances. Here J_{ij} is the exchange integral involving the orbitals i and j. Equation (1) immediately yields for the interaction energies between two ground-state H atoms

$$V(^1\Sigma)=+J,$$
$$V(^3\Sigma)=-J. \qquad (2)$$

For the interaction between H atoms in *different* molecules, however, where spins are randomly oriented with respect to one another, one obtains

$$V(\mathrm{H}\cdots\mathrm{H})=-\tfrac{1}{2}J. \qquad (3)$$

Following the procedure we have used in the past,[7–10] we evaluated J from a knowledge of the interaction curve for the $^3\Sigma$ state, and used this same J to obtain

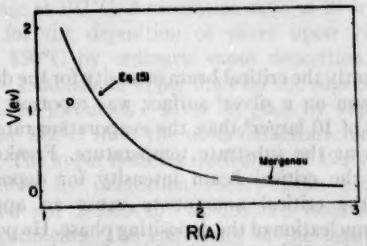

FIG. 1. Interaction energies for the H-H_2 system. The curve indicated by Eq. (5) was calculated by the perfect-pairing procedure. The two curves at larger distances are Margenau's calculated curves for the linear and triangular configurations, the upper curve being due to the linear one. The circle corresponds to a point on the H-H_2 curve obtained from scattering data on the H^--H_2 system.

[7] J. T. Vanderslice, E. A. Mason, and E. R. Lippincott, J. Chem. Phys. **30**, 129 (1959).
[8] J. T. Vanderslice, E. A. Mason, and W. G. Maisch, J. Chem. Phys. **31**, 738 (1959).
[9] J. T. Vanderslice, E. A. Mason, and W. G. Maisch, J. Chem. Phys. **32**, 515 (1960).
[10] J. T. Vanderslice and E. A. Mason, Revs. Modern Phys. **32**, 417 (1960).

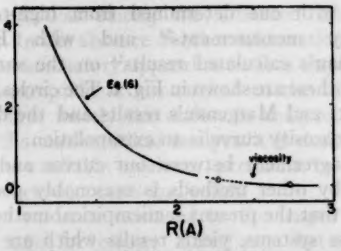

FIG. 2. Interaction energies for the H_2-H_2 system. The curve indicated by Eq. (6) was calculated by the perfect-pairing procedure. The curve marked "viscosity" was obtained from high-temperature viscosity measurements. The dashed part of this latter curve is an extrapolation. The circles are Evett and Margenau's calculated results.

$V(\mathrm{H}\cdots\mathrm{H})$ by Eq. (3). We have taken the expression for $V(^3\Sigma)$ from footnote reference 5. This yields

$$V(\mathrm{H}\cdots\mathrm{H})=30.21e^{-3.013r}\ \text{ev}, \qquad 0.8\ \text{A}<r<2.1\ \text{A}. \qquad (4)$$

The interaction between an atom and a molecule or between molecules is then, consistent with the perfect-pairing approximation, just the sum of all the separate interactions. The results of course depend on the relative orientations of the approaching species. Many times, it is useful to have potentials averaged over orientations for purposes of comparison with experimental results. The methods of averaging have been summarized previously for cases where all orientations are equally probable.[7] Application of this procedure gives for the H-H_2 interaction,

$$\langle V(R)\rangle=61.5e^{-2.952R}\ \text{ev}, \qquad 0.86\ \text{A}<R<2.12\ \text{A}, \qquad (5)$$

and for the H_2-H_2 interaction,

$$\langle V(R)\rangle=116.5e^{-2.959R}\ \text{ev}, \qquad 0.91\ \text{A}<R<2.14\ \text{A}, \qquad (6)$$

where R is the distance between the centers of mass of the species.

These curves are plotted in Figs. 1 and 2, respectively. The H-H_2 curve can be compared with the first-order perturbation results of Margenau,[11] who calculated the interaction energy for both the linear and triangular cases. His results are shown in Fig. 1. Equation (5) can also be compared with one point (indicated by the circle in Fig. 1) on the H-H_2 curve obtained indirectly from the scattering of H^- ions in H_2.[12] It is seen to fall below the curve given by Eq. (5). There are two likely reasons for this. First, this point is not unambiguously determined because of the difficulty in interpreting the experimental results.[12] Secondly, our averaging assumes that all orientations are equally probable, which is certainly not the case at distances of the order of 1 A.

The H_2-H_2 potential can be compared at larger dis-

[11] H. Margenau, Phys. Rev. **66**, 303 (1944); **64**, 131 (1943).
[12] E. A. Mason and J. T. Vanderslice, J. Chem. Phys. **28**, 1070 (1958).

tances with one determined from high-temperature viscosity measurements[13] and with Evett and Margenau's calculated results[14] on the same system. Both of these are shown in Fig. 2. The circles correspond to Evett and Margenau's results and the dashed part of the viscosity curve is an extrapolation.

The agreement between our curves and those obtained by other methods is reasonably good and indicates that the present semiempirical method, at least for these systems, yields results which are reliable to within a factor of 2 or better.

DISCUSSION

The interaction energies for the H-H_2 and H_2-H_2 systems obtained here offer a better check of this semiempirical scheme than the other systems on which it has been tried, namely, N_2-N_2, O_2-O_2, and N_2-O_2.[7–10] The reason for this is that cross terms arise out of Eq. (1) for many-electron systems. We argued qualitatively, that these should be small for the systems we considered and neglected them. Actually, there were not sufficient data at the time to evaluate them and this necessitated their neglect. In the present case, such terms do not arise. Furthermore, the exchange terms which do arise for the present cases are of s character and the relative orientation of the molecules do not affect their values. If the exchange terms involve p orbitals, then the exchange terms do depend on relative orientation and this does introduce some error.[9]

In conclusion then, we feel that the calculation of the interaction energies for the H-H_2 and H_2-H_2 systems by this semiempirical perfect pairing scheme offers a good test for the method. The results seem to indicate that this scheme will yield values for the interaction energies which are reliable to within a factor of 2 or better.

[13] E. A. Mason and W. E. Rice, J. Chem. Phys. **22**, 522 (1954).
[14] A. A. Evett and H. Margenau, Phys. Rev. **90**, 1021 (1953).

THE JOURNAL OF CHEMICAL PHYSICS VOLUME 33, NUMBER 2 AUGUST, 1960

Interaction of Condensable Gases with Cold Surfaces

G. W. Sears and J. W. Cahn
General Electric Research Laboratory, Schenectady, New York

(Received August 10, 1959)

Deposition from a molecular beam onto a cold target surface only occurs when the beam pressure is many orders of magnitude larger than the vapor pressure of the depositing phase at the substrate temperature. The critical beam pressure for deposition has been interpreted as a critical supersaturation for heterogeneous nucleation of a condensed phase. It is shown that the critical beam pressure is much too large to be accounted for as a critical value for nucleation if the adsorbate temperature and the substrate temperature are alike. The interpretation of critical deposition phenomena as a nucleation event must include the additional assumption that the adsorbate temperature is somewhat higher than the substrate temperature.

INTRODUCTION

WHEN a molecular beam of a condensable vapor is allowed to impinge upon a cold target surface, condensation does not occur when the beam pressure[1] just slightly exceeds the vapor pressure of the condensed vapor phase. Condensation only occurs when the beam pressure is many orders of magnitude greater than the vapor pressure of the condensate at the target temperature. This behavior is in marked contrast to condensation behavior during ordinary sublimation processes where very small supersaturations are required to condense the sublimate.

Recently the critical beam intensity for the deposition of sodium on a silver[2] surface was reported to be 19 powers of 10 larger[3] than the evaporation rate of solid sodium at the substrate temperature. Frenkel[4] interpreted the critical beam intensity for deposition as being the critical amount to cause an appreciable rate of nucleation of the depositing phase. He postulated that the deposition occurred through the intermediation of an adsorbed layer of beam molecules on the target surface. He assumed that a steady-state concentration of adsorbed atoms was formed at the substrate temperature and that nucleation occurred when the surface concentration exceeded a critical value. The mechanism is analogous to the mechanism of crystal growth by two-dimensional nucleation.

[1] In accord with the literature in this field, we define beam pressure in terms of the beam flux and the substrate temperature. This pressure differs from the actual momentum transfer per unit area by the square root of the ratio of beam to substrate temperatures. This definition has the advantage that saturation ratio in terms of a ratio of flux to and from the substrate is given directly by the ratio of the beam pressure so defined to the equilibrium vapor pressure of the deposit at the substrate temperature.

[2] The silver surface in the reported experiment was unquestionably contaminated with adsorbed gases.
[3] L. Yang, C. E. Birchenall, G. M. Pound, and M. T. Simnad, Acta Met. **2**, 462 (1954).
[4] J. Frenkel, Z. Physik **26**, 117 (1924).

Although this model rationalized the existence of a critical beam intensity for deposition, it fails to account for the tremendous ratios of critical beam intensity to evaporation rate per unit area for the condensed phase at the substrate temperature.

It is the purpose of the present paper to define a simple, but critical, modification of Frenkel's mechanism to account for the huge critical beam intensities for deposition. Implicit in Frenkel's assumption of the identity of the substrate temperature and the adsorbate temperature is the more basic assumption that the relaxation time for energy interchange between adsorbate atoms and substrate is very short compared to half-life for evaporation of the adsorbed atom. The present treatment recognized that energy interchange between adsorbate and substrate is not instantaneous. The true critical supersaturation for deposition is the ratio of impingement rate to evaporation rate of condensate phase at the adsorbate temperature, not the reported ratio of impingement rate to *evaporation rate at the substrate temperature*. With this small modification Frenkel's suggestion of nucleation-controlled deposition becomes completely valid. In addition some new predictions about the beam deposition process become apparent.

DISCUSSION

A. Discrepancies in Critical Saturation Ratios

Since data are available for the deposition of silver on a glass surface both from an atomic beam and from whisker-growth experiments, a comparison will be made for this substance.

Yang and co-workers[5] have reported a critical saturation ratio of $>2.6\times10^{12}$ for the condensation of silver from an atomic beam at 700°C impinging upon a glass surface at 192°C. A saturation ratio of 10 or less is required for the deposition of silver upon vitreous silica[6] at 850°C by ordinary vapor deposition. It is possible to establish an upper limit for the supersaturation required to nucleate silver on glass by vapor deposition at 192°C from the observed saturation ratio at 850°C. The upper limit for nucleation at 192°C as an extrapolation by nucleation theory from 850°C is 7×10^{5} and not $>2.6\times10^{12}$ as deduced from atomic-beam experiments. The continuity of the main arguments will be maintained by treating the extrapolation in Appendix A.

B. Nature of Gas-Solid Interaction

The mathematical analysis will be formulated by treating the adsorbed atoms as a thermodynamic phase and by assigning a temperature to the adsorbate between that of the substrate and of the furnace. This procedure makes the assumption that the kinetic-energy distribution among the adsorbed atoms is Maxwellian. In the absence of other information this is considered a satisfactory approximate. It is emphasized that this assumption is not critical to the following arguments; it is merely the easiest to analyze. Before presenting the mathematical analysis it is desirable to consider the available evidence pertinent to energy interchange between gases and solids.

No direct evidence exists as to the length of the relaxation time for energy interchange between an adsorbed condensable vapor and the substrate. However, thermal-accommodation coefficient measurements furnish some information about the rate of energy interchange between an adsorbed layer of noncondensable vapor and a metal substrate. If a metal filament is maintained at a temperature T_s, while surrounded by a volume of gas at a temperature T_0, while the desorbing gas molecules have a temperature T_1, the thermal accommodation efficient χ is defined as

$$\chi=(T_s-T_1)/(T_s-T_0). \tag{1}$$

The accommodation coefficient for helium on clean tungsten[7] is 0.06 and for neon on tungsten is 0.08.[8]

If every impinging atom was temporarily adsorbed these measurements imply that the adsorbate temperature was much less than the substrate temperature. Although the assumption that all impinging atoms are temporarily adsorbed before reevaporation has not been demonstrated specifically for these two systems it is almost certainly true.

Experiments on the reflection of molecular beams can be used to distinguish between direct reflection and adsorption followed by reevaporation. Specular reflection can not involve temporary adsorption, and diffuse reflection according to the cosine law almost certainly involves temporary adsorption. Knauer and Stern[9] have studied the reflection of H, H_2, He, Ne, Ar, and CO_2 at cleaved surfaces of NaCl crystals and have found strong specular reflection for the first three gases. The observation of specular reflection is limited to about six or eight systems.

Wood[10] observed a cosine law for the reflection of molecular beams of mercury and cadmium from glass. Knudsen[11] confirmed the cosine law for mercury reflected from a glass surface. Taylor[12] found the complete absence of specular reflection and an accurate cosine law for the reflection of a cesium beam from cleaved surfaces of NaCl and LiF at 500°C.

For neon impinging upon a tungsten surface it is likely that all atoms are temporarily adsorbed and that the adsorbed layer fails to come to thermal equilibrium with the substrate before reevaporation occurs. The available evidence supports this interpretation.

[5] L. Yang, M. T. Simnad, and G. M. Pound, Acta Met. **2**, 470 (1954).
[6] G. W. Sears, Acta Met. **3**, 367 (1955).
[7] J. K. Roberts, Proc. Roy. Soc. (London) **A129**, 146 (1930).
[8] J. K. Roberts, Proc. Roy. Soc. (London) **A152**, 445 (1935).
[9] F. Knauer and O. Stern, Z. Physik **53**, 779 (1929).
[10] R. W. Wood, Phil. Mag. **30**, 300 (1915); and **32**, 364 (1916).
[11] M. Knudsen, Ann. Phys. **48**, 1113 (1915).
[12] J. B. Taylor, Phys. Rev. **35**, 375 (1930).

Evidence for a significantly different substrate and adsorbate temperature may be derived from the discrepancy between reported critical saturation ratios from atomic-beam experiments and values extrapolated from crystal-growth observations. The reported saturation ratio α_r in the adsorbed layer is given by

$$\alpha_r=\dot{N}_i/\dot{N}_e(T_s), \tag{2}$$

where $\dot{N}_i$ is the measured impingement rate and $\dot{N}_e$ (T_s) is the evaporation rate of the condensed phase at the substrate temperature. The true saturation ratio α_t in the adsorbed layer is given by

$$\alpha_t=\dot{N}_i/\dot{N}_e(T_a), \tag{3}$$

where $\dot{N}_e$ (T_a) is the evaporation rate of the condensed phase at the adsorbate temperature. It follows that the true saturation ratio for the condensation of a molecular beam is less than the reported critical saturation ratio. The longer the half-life for energy interchange between adsorbate and substrate, the higher the adsorbate temperature and in turn the lower the true critical supersaturation for deposition. Conversely, an adsorbate having a very long half-life for reevaporation will essentially attain the temperature of the substrate material.

Equation (7) may conveniently be rewritten as

$$\alpha_t=p_i/p_0(T_a), \tag{4}$$

where p_i is the impinging beam pressure and p_0 (T_a) is the vapor pressure of the condensed phase at the adsorbate temperature. From Eqs. (2) and (8) it is possible to estimate the temperature of the adsorbed film of silver on glass when the glass is at 192°C and the beam temperature is 700°C. The adsorbate temperature must be that at which the true saturation ratio as given by Eq. (8) equals the critical saturation ratio as given by Eq. (A2). The adsorbate temperature is the value at which $\alpha_t=\alpha_c$.

In the experiments of Yang *et al.*[6] the beam pressure was 10^{-6} of the vapor pressure of silver at 700°C. An adsorbate temperature of 300°C would give a saturation ratio of 10^6, which would be adequate for an appreciable rate of nucleation of solid silver. From Eq. (5) the thermal accommodation coefficient for silver on glass is found to be 0.8.

Mathematical Analysis

Since the beam temperature as it affects the adsorbate temperature is an important parameter in the deposition behavior of hot condensable vapors on cold surfaces, some of the determining factors will be examined. In thermal accommodation coefficient measurements, cold gases impinge upon hot surfaces. In this case a kinetically determined adsorbate temperature is stable. A momentary increase in the adsorbate temperature would decrease the heat transfer to the adsorbed layer from the substrate and increase its evaporation rate to return it to the original state.

However, when hot gases impinge on a cold surface, the two factors, heat transfer and evaporation rate, are always opposed. More than one stable steady-state solution, as well as unstable ones, become possible. That is, there might be a steady state in which the adsorbate is at a high temperature and the impinging atoms reevaporate quickly before losing much energy to the substrate as well as a steady state characterized by a lower temperature and a higher surface concentration of adsorbate.

A simple kinetic model will now be constructed for determining the thermodynamic state of the adsorbate. First consider a steady-state energy balance. The rate of energy gain from the beam $\dot{U}_1$ is given by

$$\dot{U}_1=\dot{N}_iC(T_b-T_a), \tag{5}$$

where T_b is the beam temperature and C is the heat capacity of the vapor. If it is assumed that the rate of energy loss from the adsorbed layer to the substrate $\dot{U}_2$ is proportional to the fractional coverage θ and the temperature difference between adsorbate and substrate it can be written that

$$\dot{U}_2=k_1\theta(T_a-T_s), \tag{6}$$

where k_1 is the proportionality constant.

Next consider the mass balance at steady state. The rate of evaporation is set equal to the impingement rate. If small fractional coverages are considered it follows that

$$\dot{N}_i=k_e\theta, \tag{7}$$

where k_e is the evaporation rate constant from the adsorbed layer and will be assumed to depend only on the adsorbate temperature. Combining Eqs. (7) and (8) gives

$$\dot{U}_2=k_1\dot{N}_i(T_a-T_b)/k_e, \tag{8}$$

where steady state corresponds to $\dot{U}_1=\dot{U}_2$.

If k_e is of the form

$$k_e=A_0\exp(-Q/RT_a), \tag{9}$$

then the shape of $\dot{U}_2$ is determined as a function of the substrate temperature. If $RT_s>Q/2$, $\dot{U}_2$ is a monotonic increasing function of T_a without inflection. If $Q/4<RT_s<Q/2$, $\dot{U}_2$ is still monotinic increasing but has an inflection point. For $RT_s<Q/4$, $\dot{U}_2$ has a maximum and a minimum. The possibility of three solutions to $\dot{U}_1=\dot{U}_2$ must be considered. Figure 1 gives $\dot{U}_2$ in terms of $k_1\dot{N}_iQ/AR$ as a function of the adsorbate temperature for various substrate temperatures relative to Q/R. Since $\dot{U}_1$, in these units, is a straight line with slope $-AC/k_1$ intersecting the ordinate at $T_b(R/Q)$, the solutions of $\dot{U}_1=\dot{U}_2$ are determined by RT_b/Q, RT_s/Q, and AC/k_1. The first two

are experimental variables; the last is determined by the choice of the system. Figure 2 gives the solution of $\dot{U}_1=\dot{U}_2$ for $RT_s/Q=0.1$ and $AC/k_1=500$ for various values of RT_b/Q. At high beam temperatures only a solution corresponding to a low thermal-accommodation coefficient exists. At low temperatures there also is only one solution corresponding to a thermal accommodation coefficient close to unity. At intermediate temperatures both of these solutions are possible, and in addition, another solution, intermediate in χ, exists. This latter solution is unstable; the instability can be verified by considering a small fluctuation.

If the beam temperature was raised from a low value, it would be expected that the steady state would follow the low-temperature branch into the region where two stable solutions exist. At a critical temperature, the adsorbate temperature would be expected to jump to the value characteristic of the high-temperature branch. The reverse would be true if the beam temperature was lowered from a high temperature. It might be expected that two possible steady states might exist over a range of beam temperature dependent upon the thermal history. It is conceivable for domains at both temperatures to coexist in the intermediate region.

Since both $\dot{U}$'s are proportional to the beam intensity $\dot{N}_1$, the solutions for T_a are independent of beam intensity with this model. The thermal-accommodation coefficient can be expressed as a function of the rate

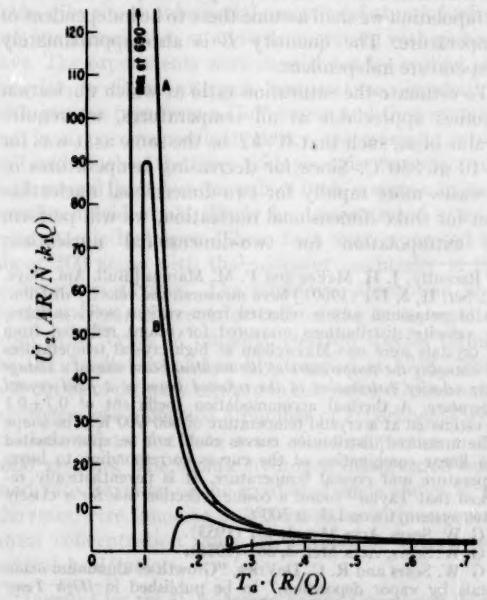

FIG. 1. $\dot{U}_2$, the rate of heat transfer from adsorbate to substrate, in units of $\dot{N}_1k_1Q/AR$ as a function of adsorbate temperature for four substrate temperatures [see Eqs. (8) and (9)]. Temperatures are in units of Q/R. Curves A, B, C, and D are for substrate temperatures of 0.08, 0.10, 0.15, and 0.25 in these units.

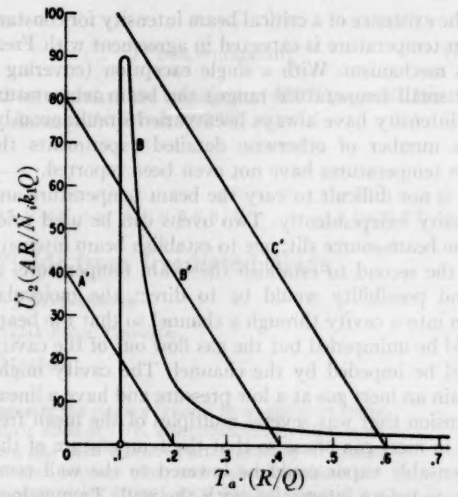

FIG. 2. $\dot{U}_1$, the rate of heat transfer from beam to adsorbate, again in units of $\dot{N}_1k_1Q/AR$, is plotted against adsorbate temperature in units of Q/R for the special case $AC/k_1=200$. Curves A', B', and C' correspond to beam temperatures of 0.2, 0.4, and 0.6, respectively, in these units. Curve B of Fig. 1 is shown. The intersections represent possible steady states $\dot{U}_1=\dot{U}_2$.

constants for evaporation and heat transfer from the adsorbed layer by combining Eqs. (1), (6), and (8).

$$\chi=[1+(Ck_a/k_1)]^{-1}. \tag{10}$$

Thus an empirical determination of the thermal-accommodation coefficient will allow an evaluation of T_a as well as of the quotient Ck_a/k_1 as a function of T_a. This quotient also equals the ratio of the half-lives for energy exchange and reevaporation. A measurement of χ as a function of temperature will permit an evaluation of the $\dot{U}_1$ and the $\dot{U}_2$ curves.

This model of thermal-accommodation coefficients is valid not only for adsorbed condensable gases prior to nucleation, but to adsorbed noncondensable gases as well. The critical assumption is that every molecular impact leads to a temporary adsorption as opposed to specular reflection. A modified analysis must be made if a fraction of the impacts lead to temporary adsorption.

DISCUSSION

It is predicted for constant beam intensity and fixed substrate temperature that there is a *critical beam temperature* above which nucleation will not occur and below which nucleation will occur. In contrast Frenkel's[4] theory requires no effect of beam temperature on the condensation behavior. So great has been the influence of Frenkel's treatment that beam temperature has usually been ignored by experimenters. In addition it is expected under some conditions that a thermal hystersis will be observed in these phenomena. The behavior should depend upon how the beam and/or substrate temperatures were reached.

The existence of a critical beam intensity for constant beam temperature is expected in agreement with Frenkel's mechanism. With a single exception (covering a very small temperature range) the beam temperature and intensity have always been varied simultaneously. In a number of otherwise detailed experiments the beam temperatures have not even been reported.

It is not difficult to vary the beam temperature and intensity independently. Two ovens can be used prior to the beam-source slit, one to establish beam intensity and the second to establish the beam temperature. A second possibility would be to direct the molecular beam into a cavity through a channel so that the beam would be unimpeded but the gas flow out of the cavity would be impeded by the channel. The cavity might contain an inert gas at a low pressure and have a linear dimension that was several multiples of the mean free path in inert gas phase so that the temperature of the condensable vapor could be lowered to the wall temperature before interaction with the wall. Tremendous supersaturations could be attained without homogeneous nucleation in the vapor phase. The pressure of the condensable vapor would be small as compared to the inert gas pressure so that vapor molecule-wall collisions would occur to the exclusion of vapor molecule self collisions.

The present discussion is pertinent both to the nucleation of a condensed phase by the impingement of a molecular beam upon a cold surface and to the condensation of a chemically unstable species (e.g., free radicals) onto a cold surface. In this instance a third rate process is involved. Not only must the thermal energy of free radicals impinging upon a condenser surface be dissipated to the substrate to cause nucleation, but the faster the energy is dissipated the higher is the probability of obtaining condensed free radical as opposed to condensed free-radical reaction products.

A final application of the mechanism of the present paper is involved in the thermal decomposition of a gas impinging at a hot surface. If the impinging molecules reevaporate before approaching the temperature of the hot surface, they may never be thermally decomposed before reevaporating.

SUMMARY

It has been recognized that the energy interchange between an adsorbed layer and its substrate must occur at a finite rate. When a hot gas impinges upon a cold surface the adsorbed layer must be characterized by a temperature between that of the beam and the substrate. This feature of the interaction between a condensable molecular beam and a cold target surface accounts for the huge reported supersaturations necessary for deposition on the target surface. It also leads to a relation between thermal accommodation coefficients and the ratio of the half-lives for reevaporation from the adsorbed layer and for energy interchange between the adsorbate and substrate. These conclusions are of importance to the condensation of free radicals at very low temperatures as well as to the thermal decomposition of molecules at hot surfaces. Critical experiments have been suggested.[13]

APPENDIX A

In order to compare observations on nucleation of solid obtained from whisker-growth[14–16] experiments with those obtained from the beam experiments, a long extrapolation is required.

In the whisker growth experiments at 850°C, it was observed that below a supersaturation of 10, whiskers of silver[6] nucleated on the vitreous silica substrate and grew without thickening by two-dimensional nucleation of new layers. At supersaturations of 10 or greater, whiskers began to thicken and equiaxed deposits were observed on the substrate. We thus can take a supersaturation of 10 at 850°C as adequate for nucleation and growth of deposit.

From classical nucleation theory[17–21] we have for the rate of nucleation

$$N^0 = B \exp(-W/kT), \qquad \text{(A1)}$$

where W is the work of forming a critical nucleus and is either inversely proportional to $RT \ln\alpha$ for two-dimensional nucleation of new layers, or inversely proportional to $(RT \ln\alpha)^2$ for three-dimensional heterogeneous nucleation of new crystals. W is also a function of the various surface energies and the geometry of the nucleation site, but for the present purposes of our extrapolation we shall assume these to be independent of temperature. The quantity B is also approximately temperature independent.

To estimate the saturation ratio at which nucleation becomes appreciable at all temperatures, we require a value of α_c, such that W/kT be the same as it was for $\alpha = 10$ at 850°C. Since for decreasing temperatures α_c increases more rapidly for two-dimensional nucleation than for three-dimensional nucleation, we will perform the extrapolation for two-dimensional nucleation,

[13] Recently, J. H. McFee and P. M. Marcus [Bull. Am. Phys. Soc., Ser. II, 5, 171 (1960)] have measured the velocity distribution of potassium atoms reflected from various solid surfaces. The velocity distributions measured for beams reflected from LiF crystals were non-Maxwellian at high crystal temperatures and *changing the temperature of the incident beam caused a change in the velocity distribution of the reflected beam at a fixed crystal temperature.* A thermal accommodation coefficient of 0.7±0.1 was estimated at a crystal temperature of 600–900°K. The shape of the measured distribution curves could not be approximated by a linear combination of the curves corresponding to beam temperature and crystal temperature. It is parenthetically remarked that Taylor[12] found a cosine reflection law for a closely related system, Ce on LiF at 500°C.

[14] G. W. Sears, Acta Met. 1, 457 (1953).

[15] G. W. Sears, Acta Met. 3, 361 (1955).

[16] G. W. Sears and R. C. DeVries, "Growth of aluminum oxide crystals by vapor deposition," to be published in *High Temperature Chemistry* in Advances in Chem.

[17] W. Kossel, Nachr. Ges. Wiss. Gottingen 135 (1927).

[18] I. Stranski, Z. physik Chem. 136, 259 (1928).

[19] R. Becker and W. Döring, Ann. Phys. 24, 719 (1935).

[20] J. Frenkel, J. Phys. U.S.S.R. 9, 3921 (1945).

[21] G. W. Sears and R. C. DeVries, J. Chem. Phys. 32, 93 (1960).

although it is highly unlikely that two-dimensional nucleation is required for a beam deposit which can hardly be expected to have perfect surfaces. We thus obtain as an upper limit for the critical saturation for nucleation at any temperature $T<850°C$ the expression

$$T^2 \ln\alpha_c = \text{constant} \qquad \text{(A2)}$$

and we evaluate the constant at 850°C, $\alpha_c=10$. We thus obtain $\alpha_c \leq 7\times10^5$ at 192°C.

THE JOURNAL OF CHEMICAL PHYSICS VOLUME 33, NUMBER 2 AUGUST, 1960

Atomic and Molecular Hydrogen Yields from Irradiated Acids

RALPH LIVINGSTON AND A. J. WEINBERGER

Oak Ridge National Laboratory, Oak Ridge, Tennessee*

(Received March 21, 1960)

The paramagnetic-resonance method has been used to measure the yields of atomic hydrogen from many concentrations of aqueous sulfuric, phosphoric, and perchloric acids at 77°K after irradiation with gamma rays. The yields of molecular hydrogen (and oxygen) have also been measured after similarly irradiated acids were warmed and the gases collected. The correspondence between atom and molecule yields is discussed. In sulfuric and phosphoric acids the atom and molecule yields depend upon whether the acid is a glassy or crystalline solid at the time of irradiation. Prolonged irradiation of 0.129-mole-fraction sulfuric acid (glassy) gives a saturation concentration of 3.4×10^{18} hydrogen atoms per gram. The corresponding number for 0.125-mole-fraction perchloric acid is 2.9×10^{19}. The seavenging effects of nitric acid and hydrogen peroxide on the atomic and molecular hydrogen yields for 0.129-mole-fraction sulfuric acid have been measured and are discussed. The corresponding effect of nitric acid on the atom yield from perchloric acid is presented.

INTRODUCTION

IT has been shown[1,2] that various substances, particularly solutions of sulfuric, perchloric, and phosphoric acids, give rise to substantial amounts of atomic hydrogen upon irradiation at a low temperature with gamma rays. The experiments were carried out by cooling the samples to liquid-nitrogen temperature, irradiating with gamma rays from a Co^{60} source and then examining in a paramagnetic-resonance spectrometer while still cold. Each of the three acids gave rise to a spectrum with several lines, but one pair of lines, common to each irradiated acid, could clearly be demonstrated to arise from atomic hydrogen. These lines were separated by about 500 gauss with the midpoint essentially at the free-electron g value. The remaining absorption lines in the spectra, different for each of the acids, resulted from other types of unpaired-electron species formed by the irradiation and stably trapped at 77°K. They will not be of primary concern in this paper. Once atomic hydrogen was identified a number of experiments were carried out[2] to elucidate some of its properties in the solid systems. The atomic hydrogen disappeared upon moderate warming of the irradiated acids above 77°K; the rates were found to be second order with respect to atom concentration, and the activation energy was several kcal/mole.

These findings suggest that the disappearance of hydrogen might be diffusion limited, and that H atoms might be combining to form molecular hydrogen. Of course, second-order kinetcis could be explained in a number of other ways, for example, by the reaction of one H atom with any other species formed in 1:1 correspondence with it. Inasmuch as molecular hydrogen is usually a product from irradiated hydrogenous materials (especially aqueous systems), it was decided to carry out assays to see if there was any correspondence between atom yields and molecule yields. The experiments have been done with a large range of aqueous concentrations of sulfuric, perchloric, and phosphoric acids. The general plan has been to cool the samples to 77°K, to irradiate with gamma rays from Co^{60} and to assay the atomic hydrogen formed using the paramagnetic-resonance method. Larger samples, prepared and irradiated in a similar manner, were warmed and melted and the gases collected and assayed for molecular hydrogen (and oxygen) by conventional vacuum-line techniques. The absolute radiation chemical yield of molecular products could be carried out in a straightforward manner and expressed in the conventional units of G, the number of molecules formed per 100 ev of gamma-ray energy absorbed by the sample. The paramagnetic-resonance assays of the atomic-hydrogen content of the cold samples posed special problems and were carried out in two steps. The first step was to make relative assays by comparing the atomic-hydrogen absorption lines from a number of samples. One concentration of sulfuric acid was chosen

* Operated for the U. S. Atomic Energy Commission by the Union Carbide Corporation.

[1] R. Livingston, H. Zeldes, and E. H. Taylor, Phys. Rev. **94**, 725 (1954).

[2] R. Livingston, H. Zeldes, and E. H. Taylor, Disc. Faraday Soc. **19**, 166 (1955).

as the reference substance, and all assay data on the three acids were taken relative to this one reference. The final step, involving many more uncertainties than the relative assays, was to make an absolute measurement of the atomic-hydrogen yield from the reference substance.

EXPERIMENTAL METHODS

The sulfuric-, phosphoric-, and perchloric-acid samples were prepared from reagent-grade acids, the concentrations being ascertained by titration. In the case of phosphoric acid, concentrations higher than the readily available 85 % acid were needed, and these were prepared by heating the acid to 135°C for several hours.

The molecular yields were determined on 5-cc samples which were weighed into Pyrex glass ampoules of about 10-cc volume. Each ampoule was sealed to a high-vacuum system and the sample outgassed by intermittent boiling and evacuating. All distillate was collected on a cold finger and returned to the ampoule so that the concentration would remain unchanged. The ampoule was then sealed and cooled to liquid-nitrogen temperature. Both glassy and polycrystalline samples could be prepared from certain concentrations of the acids. Whenever glassy samples were needed, the ampoules were quenched from room temperature to liquid-nitrogen temperature. The methods of preparing crystalline samples varied but, in general, were to cycle the sample temperature to initiate crystal centers, allow to stand at an intermediate temperature (say, dry-ice temperature) and then to cool slowly to liquid-nitrogen temperature. Some difficulty with ampoule breakage was encountered in preparing glassy samples; laying the cylindrical ampoule on its side while cooling helped considerably.

Ampoules were irradiated in a Dewar filled with liquid nitrogen in a nominal 1000-currie Co^{60} gamma-ray source. The dose rate was measured with a ferrous sulfate dosimeter[3] taking $G=15.6$. At the start of the work the dose rate, in terms of energy absorbed per gram of water, was 8.5×10^{17} ev/min and 40-min irradiation times were nominally used. The various measurements were made over a period of a few years, and the irradiation time was later increased to compensate for source decay. Following irradiation, the gas assays for hydrogen and oxygen were made by breaking the warmed ampoule in a high-vacuum system, collecting total gas that was noncondensible with liquid nitrogen by use of a Toeppler pump, and, finally, making conventional volume-pressure measurements accompanied by combustion over a platinum filament.

Atomic-hydrogen assays, relative to a reference sample of H_2SO_4, were made with a simple paramagnetic-resonance spectrometer operating at 9000 Mc and employing oscilloscope display and 60-cps field modulation. The cavity was a transmission type operating in the TE_{101} mode; coaxial-cable connections were made to it; and it was totally immersed in liquid nitrogen with provision for introducing samples from outside through a connecting tube. Relative assays were carried out by preparing a series of acid samples (usually 10 to 15 samples), irradiating them simultaneously at 77°K in a uniform-flux region of the Co^{60} source and then comparing the higher-field atomic-hydrogen lines in the spectrometer. A sample of 0.129-mole-fraction H_2SO_4 frozen quickly to a glass was always included as the reference. The operation of the spectrometer was highly standardized; a long warmup period was used, the magnetic-field sweep was metered and held constant, the power level was adjusted to give constant, metered detector-crystal current which was low enought not to give saturation effects, and the oscilloscope was used essentially as a null device. The latter was accomplished by inserting an accurate potentiometer (Helipot) ahead of the oscilloscope and by adjusting it to give a standard signal height on the oscilloscope. The potentiometer readings were then inversely proportional to signal strength, but correction factors were needed for variations in line width. These corrections were obtained by photographing the oscilloscope traces (Polaroid-Land camera) and deducing the line widths from enlargements of the photographs. These corrections, generally, were small.

Consideration was given to sample preparation and positioning in the cavity. All samples for H assays were contained in thin-wall spherical bulbs blown on the end of $\frac{1}{16}$-in. diam glass melting-point capillaries. In an initial experiment, assay results were compared for sulfuric-acid samples of the same concentration but contained in bulbs of different sizes and irradiated different lengths of time. All comparisons were consistent (total spread of values within ±10 %) provided the insertion depths of the samples in the cavity were adjusted within a small range which gave maximum signal strength. An intermediate sample-bulb diameter, nominally 0.188 in. with volumes always within several percent of 0.055 ml, was selected for all subsequent work.

It has been shown[2] that a small amount of atomic hydrogen is formed from water adsorbed on Pyrex glass when the glass is irradiated at 77°K. In the present experiments the amount of atomic hydrogen from this source was negligibly small primarily because of the short irradiation times. There is no other paramagnetic-resonance absorption from irradiated glass in the region of the atomic-hydrogen lines.

Originally it was hoped that 20% accuracy could be achieved in the relative assays. Generally, this appears to have been obtained. Comparisons with the reference were usually made at the start and end of an experiment. The results undoubtedly could have been improved by making more frequent and painstaking intercompari-

[3] C. J. Hochanadel and J. A. Ghormley, J. Chem. Phys. **21**, 880 (1953).

sons, but this did not seem warranted in the present study.

Samples for atomic-hydrogen assays were usually not outgassed, but some experiments bearing on this point will be discussed later. Both glassy and crystalline samples were studied, and these were prepared by cooling in much the same way as for the samples used in gas assays. In some cases, however, crystallization of the samples was initiated by innoculation with a tiny amount of separately prepared seed crystals. All irradiations were carried out with the same dose rate used in the gas-assay work.

The absolute assay of the atomic hydrogen in irradiated 0.129-mole-fraction glassy sulfuric acid at 77°K was carried out by making comparisons with α,α-diphenyl-β-picrylhydrazyl (DPPH). Six single-crystal samples of DPPH were weighed on a microbalance; their nominal weights were two each of 20, 50, and 100 μg. The areas of the absorption lines were compared at room temperature and found to be consistent with the weighings. The four smaller samples were subsequently used for the assays.

Two sets of experiments were made. In the first assay one sample of acid in the usual spherical bulb was irradiated 60 min at 77°K and the two atomic-hydrogen lines compared with the lines from each of the four DPPH crystals at 77°K. The areas of both atomic-hydrogen lines as well as the DPPH samples were measured. The DPPH samples were positioned in the cavity at the point where the center of a spherical acid sample was normally located. In the second set of assays three samples of acid, irradiated 90 min, were cross compared with the four DPPH crystals. This time the DPPH crystals were mounted in small capillaries which were inserted into and centered in spherical bulbs of the acid. These were cooled to 77°K but not irradiated. Two of the three acid samples that were irradiated had similar capillaries with small crystals of DPPH inserted. In this way essentially identical cavity loading was obtained when making the comparisons.

The precision of all absolute assays was regarded as fair, but there were a number of systematic errors which makes it difficult to estimate the expected accuracy. For example, DPPH contains benzene of crystallization,[4] one molecule of benzene per molecule of DPPH. Some benzene, however, is easily lost from the crystal and a small error could result from the molecular weight used. The Lorentz shape of the DPPH line is of concern since a moderate error can result from a portion of the area not being observed; this area would be present in the flanks of the absorption line and lost in the base line. Another serious source of error in making the comparisons was the fact that DPPH was concentrated at a point in the cavity while the acid samples were distributed over a volume. Even though the spherical acid samples could be moved slightly in the cavity without affecting the results of the relative assays, any movement of the DPPH sample did cause the line intensity to vary. Locating the DPPH at the center of the acid sample was probably a good compromise, but a moderate systematic error is probably present. The final assay values are probably good to about 50%. For these reasons, comparisons of yields between the three acids, as well as between different concentrations of the same acid, may be made more reliably (20%) than the estimated error in the absolute yields would indicate (50%).

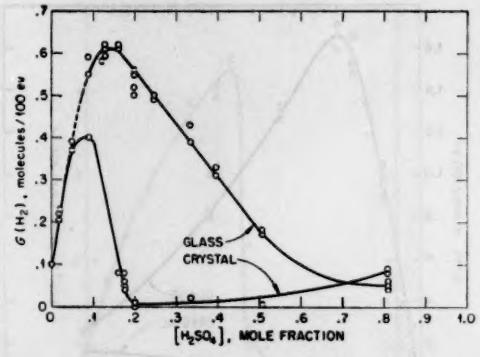

FIG. 1. Molecular-hydrogen initial yields from aqueous sulfuric acid irradiated at 77°K with gamma rays and then warmed.

SULFURIC ACID

As shown in Fig. 1 there is a large variation in the molecular hydrogen yield from sulfuric acid depending upon whether it was irradiated as a glassy or crystalline solid. Visual inspection of the samples studied indicated formation of excellent glasses from 0.51 mole fraction down to 0.09 mole fraction, but attempts to prepare glasses by rapidly quenching lower concentrations to 77°K gave samples that were certainly part crystalline (indicated by the dotted portion of the glass curve of Fig. 1). In the limit of zero acid mole fraction (ice) the sample was entirely crystalline, and the yield $G(H_2) = 0.10$ was the same as that obtained by Ghormley and Stewart[5] in ice irradiated at 77°K. Concentrated sulfuric acid (0.81 mole fraction) did not form completely clear glasses, but the samples for which points are given on the glass curve of Fig. 1 were regarded as being largely glasslike in nature. Some of the points on the crystal curve of Fig. 1 represent unique, solid compounds. These are the monohydrate of sulfuric acid (0.5 mole fraction), the dihydrate (0.33 mole fraction), and ice. Samples of glassy 0.20-mole-fraction acid were irradiated for $\frac{1}{2}$, 2, and $2\frac{1}{2}$ times the normal integrated dose. The yields for the higher doses were slightly low but are included in Fig. 1.

There is a striking similarity between the atomic-hydrogen yields obtained on samples at 77°K as shown

[4] M. Sternberg, Compt. rend. **240**, 990 (1955).

[5] J. A. Ghormley and A. C. Stewart, J. Am. Chem. Soc. **78**, 2934 (1956).

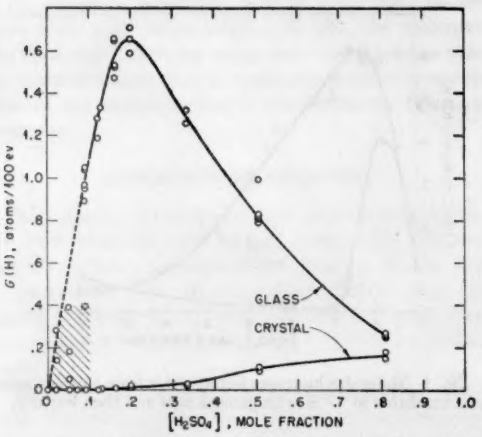

FIG. 2. Atomic-hydrogen initial yields from aqueous sulfuric acid irradiated with gamma rays and examined at 77°K.

in Fig. 2 and the molecular yields (Fig. 1). The dotted portion of the glass curve below 0.09-mole-fraction acid, as in Fig. 1, indicates attempts to prepare glassy samples that actually turned out to be part crystalline. In the limit of zero acid concentration (ice) no atomic hydrogen is stably trapped[2] at 77°K. The low-concentration portion of the crystal curve is shaded to indicate a region over which highly irreproducible results were obtained. Mixed crystals are obtained over the indicated concentration range. Usually no atomic hydrogen was observed in irradiated crystalline samples at 77°K for these concentrations, but a few samples did show a moderate yield.

The atomic-hydrogen data of Fig. 2 are for air-saturated acid since the method of sample preparation was not well suited for outgassing. A pertinent experiment was, however, made an 0.129-mole-fraction sulfuric acid. Three glassy samples of this concentration were irradiated simultaneously and compared. One sample was air saturated, the second was purged of dissolved gases and saturated with oxygen, and the third was purged and saturated with argon. No significant variation in the atomic-hydrogen yield was observed. Although this is the only concentration for which a test was made for the effect of dissolved oxygen, the similarity of the curves of Figs. 1 and 2 suggests the presence of dissolved oxygen to be unimportant in its effect on the atom yields. The major region of departure of the two sets of curves appears in the low-concentration region, and this will be separately discussed later.

Many of the glassy samples were very highly strained, and if they were touched with a sharply pointed rod they violently fractured and became opaque. One sample of irradiated 0.129-mole-fraction acid was "popped" and fractured in this way. The atomic-hydrogen content was found to be unchanged.

Glassy 0.129-mole-fraction sulfuric acid was used as the reference sample for making relative atomic-hydrogen-yield measurements. The absolute assay of four samples of this concentration gave yields of 1.24, 1.12, 1.52, and 1.43. The average value of $G(H)=1.33$ was used in plotting the data of Fig. 2 on an absolute basis. As indicated earlier, there is considerable uncertainty in the absolute assay, but the striking correspondence between Figs. 1 and 2, indicates that one of the predominant reactions by which hydrogen atoms disappear on warming is combination to form hydrogen molecules. Essentially all of the observed hydrogen gas may be accounted for in this way.

It has recently been shown[6] that atomic hydrogen is stably trapped in ice irradiated and examined at 4°K. The ice was irradiated with electrons from a 40-Mev linear accelerator, and the yield of atomic hydrogen was approximately 0.5 atom per 100 ev. Upon warming the ice, the atomic hydrogen disappeared at some temperature below 77°K. It is apparent from these results that if a lower temperature had been used in the present experiments the atom-yield curve (Fig. 2) would intersect zero acid mole fraction (ice) at a non-zero value. No accuracy estimates were given for the value of $G(H)\approx 0.5$. The number is about twice that needed to bring the curve of Fig. 2 into excellent correspondence with Fig. 1 in the low-concentration region.

When gas assays were made on the irradiated and subsequently melted acid samples the amount of oxygen formed was also measured. The oxygen yields are given in Fig. 3. The yields are very much smaller than the corresponding hydrogen yields, but similarly shaped curves are obtained. Again, the yields from crystalline samples were much lower than from glassy samples. No oxygen was obtained from ice irradiated at 77°K, which is in agreement with the results of Ghormley and Stewart.[5]

In obtaining the atomic-hydrogen yields of Fig. 2 some consideration was given to how much total dose could be accumulated before the atom concentration vs dose curve showed departure from linearity (initial yield). Most of the data of Fig. 2 were obtained with total doses less than 10^{20} ev/g. A number of points on the glassy curve were also obtained in duplicate experiments where the total doses differed by a factor of two; no significant change in G value was observed. In the

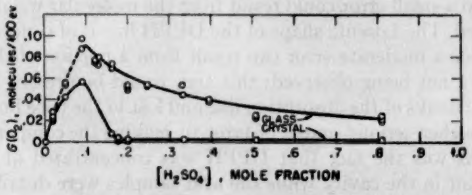

FIG. 3. Molecular-oxygen initial yields from aqueous sulfuric acid irradiated at 77°K with gamma rays and then warmed.

[6] L. H. Piette, R. C. Rempel, H. E. Weaver, and J. M. Flournoy, J. Chem. Phys. **30**, 1623 (1959).

case of some of the crystalline samples, however, the yield was so small that substantially longer irradiation times were used. The values may be subject to a moderate percentage error, but these yields were so small that the error would hardly show in the low-yield crystal data of Fig. 2. In addition, a study of saturation was made with 0.129-mole-fraction acid irradiated as a glassy solid. The results are given in Fig. 4. The points of the curve were obtained on a relative basis by comparing samples which had been irradiated different lengths of time in the same radiation flux. The graph was plotted on an absolute basis using the absolute assay result $G(H)=1.33$ for this acid concentration. The saturation concentration of H atoms (Fig 4) is about 3.4×10^{18} atoms/g for 0.129-mole-fraction acid (specific gravity = 1.344). This amounts to about 0.01% of the hydrogen of the sample converted to trapped atoms. Whether or not the molecular-hydrogen production shows a similar saturation behavior has not been determined.

The line widths for atomic hydrogen in the samples used for Fig 4 showed a small broadening in the most heavily irradiated cases; this was presumably caused by contribution to the width from electron-magnetic-dipole interactions. The widths after the shorter irradiations which were normally used in assays appeared to be largely caused by neighboring nuclear magnetic dipoles (protons). In the most dilute acid (0.02 mole fraction) the line was about 4.8 gauss full width at half height, and the width uniformly dropped to 3.6 gauss for the most concentrated acid (0.81 mole fraction). This uniform sharpening of the line in progressing to the more concentrated acids probably reflects the uniform decrease in magnetic-nucleus (proton) concentration of the samples.

PERCHLORIC ACID

In contrast to the sulfuric acid results (Fig. 1) the molecular-hydrogen yields from degassed perchloric

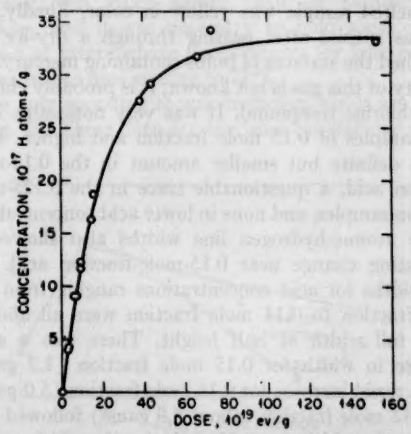

FIG. 4. The saturation of atomic hydrogen upon prolonged gamma irradiation of 0.129-mole-fraction sulfuric acid at 77°K.

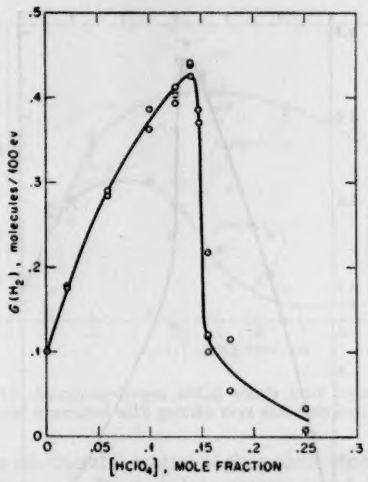

FIG. 5. Molecular-hydrogen initial yields from aqueous perchloric acid irradiated at 77°K with gamma rays and then warmed.

acid solutions did not depend upon whether the samples were glassy or crystalline at the time of irradiation. The yields are given in Fig. 5. The glasses, however, were not so clear and so well defined as those made with sulfuric acid. Most often, attempts to prepare a glassy sample by rapid quenching in liquid nitrogen gave a white, opaque solid. In a few cases clear or slightly translucent solids were obtained. The molecular-hydrogen yields from such samples were essentially the same as the yields from carefully and slowly crystallized samples of the same concentration. The yield curve (Fig. 5) is quite different from that for either glassy or crystalline sulfuric-acid samples (Fig 1). The most striking feature of Fig. 5 is the very large change of yield with concentration in the vicinity of 0.15-mole-fraction acid.

The corresponding atomic-hydrogen yields obtained with irradiated samples at 77°K are given in Fig. 6. Again, no difference in yield was observed between glassy and polycrystalline samples. Somewhat better-looking glasses were obtainable for the atom-yield work since the samples were very small compared to those used for gas assays and could be much more rapidly quenched to 77°K. The yields were initially determined relative to that of 0.129-mole-fraction sulfuric acid. The graph was plotted on an absolute basis using the assay result for this concentration of sulfuric acid as described earlier.

The similarity of the atom-yield curve (Fig 6) and the molecule-yield curve (Fig 5) is apparent. The rapid change of yield with concentration appears in the vicinity of 0.15 mole fraction for both curves. The molecule-yield curve starts at the appropriate $G(H_2)=0.1$ for ice while the atom-yield curve starts as zero since H atoms are not stably trapped in ice at 77°K. If the temperature had been lower the curve would have

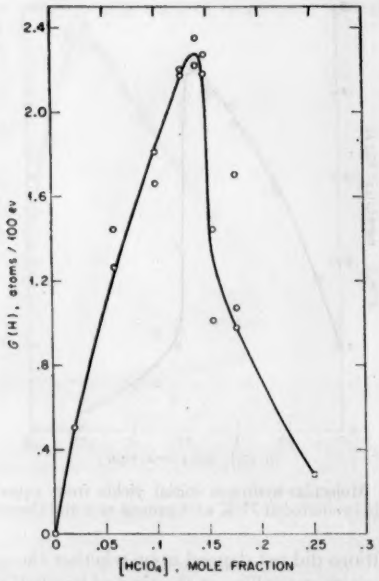

FIG. 6. Atomic-hydrogen initial yields from aqueous perchloric acid irradiated with gamma rays and examined at 77°K.

started at a higher value following the discussion given with the sulfuric-acid results. The absolute yield of atomic hydrogen for most of the intermediate concentrations is roughly twice that needed to account for all of the molecular hydrogen found after melting.

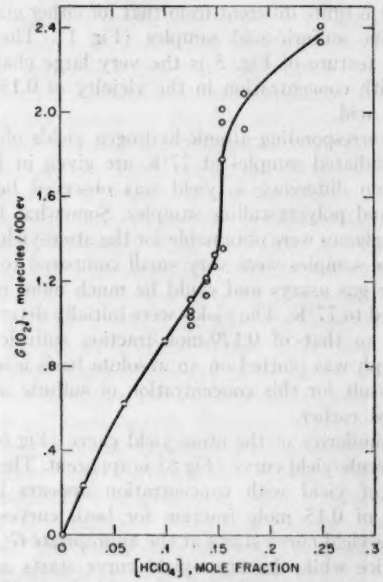

FIG. 7. Molecular-oxygen initial yields from aqueous perchloric acid irradiated at 77°K with gamma rays and then warmed.

The molecule yields were obtained from degassed samples while the atom yields were obtained with air-saturated samples. Air-, oxygen-, and argon-saturated samples of perchloric acid (0.140 mole fraction) were irradiated and compared for atomic-hydrogen content using the same procedure as for the sulfuric-acid sample previously discussed. Here, also, no significant variation in yield was observed.

Molecular-oxygen yields obtained after melting are given in Fig. 7. The yields are generally very high with a sharp break in the yield curve in the vicinity of 0.15-mole-fraction acid. In making the gas assays definite evidence was obtained for another gaseous species in addition to hydrogen and oxygen. This third species was noted in several ways in the more concentrated acid samples. The samples were yellow after melting. In the gas-collection operations preparatory to making the actual assay, it was noted that solid (ice) collected at

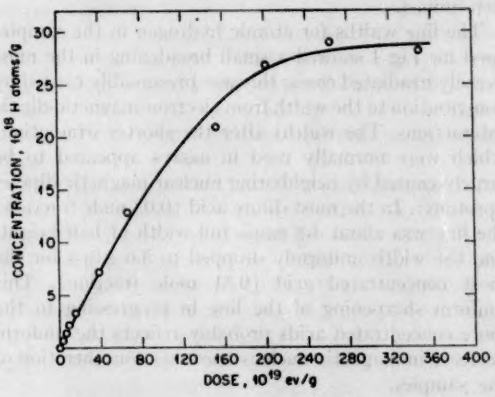

FIG. 8. The saturation of atomic hydrogen upon prolonged gamma irradiation of 0.125-mole-fraction perchloric acid at 77°K.

liquid-nitrogen temperature from the vapor phase over the melted sample was yellow in color. Finally, this gaseous species after passing through a dry-ice trap tarnished the surfaces of bulbs containing mercury. The identity of this gas is not known; it is probably chlorine or a chlorine compound. It was very noticeable in all acid samples of 0.15 mole fraction and higher. There was a definite but smaller amount in the 0.14-mole-fraction acid, a questionable trace in the 0.125-mole-fraction samples, and none in lower acid concentrations.

The atomic-hydrogen line widths also showed an interesting change near 0.15-mole-fraction acid. The line widths for acid concentrations ranging from 0.02 mole fraction to 0.14 mole fraction were all about 4 gauss full width at half height. There was a slight increase in width for 0.15 mole fraction (4.2 gauss) then a rapid increase for 0.16 mole fraction (5.0 gauss) and 0.18 mole fraction (about 5.8 gauss) followed by a decrease in width for 0.25 mole fraction (4.8 gauss).

A series of experiments showing the saturation of

atomic-hydrogen concentration with radiation dose was carried out for 0.125-mole-fraction $HClO_4$ in the same way as for H_2SO_4. The results are given in Fig. 8 which may be compared with the corresponding curve for 0.129-mole-fraction H_2SO_4 (Fig. 4). The saturation concentration of 2.9×10^{19} atoms/g is almost an order of magnitude higher than that found in the sulfuric acid. At saturation about 0.07% of all of the bound hydrogen initially present was converted to stably trapped atoms. This does not represent the total unpaired-electron content since paramagnetic species other than atomic hydrogen were known to be present in high concentrations. The atomic-hydrogen line widths increased greatly with the higher doses indicated in Fig. 8. The most heavily irradiated sample had a full width at half height 3.2 times that of the lightly irradiated samples, an increase from about four to 13 gauss. The width increase was likely caused by electron dipole-dipole interactions between hydrogen atoms as well as between hydrogen atoms and other paramagnetic species. The three most heavily irradiated samples of Fig. 8 showed a noticeable width increase and intensity decrease with progressive dose such that the integrated areas remained little changed. This suggests that even after saturation of the atomic hydrogen the concentration of other unpaired-electron species might still be increasing with increasing dose.

ORTHOPHOSPHORIC ACID

Molecular-hydrogen yields from phosphoric-acid solutions after low-temperature irradiation followed by melting are given in Fig. 9. The yields depended upon whether the acid was irradiated as a glassy solid or polycrystalline solid as indicated in the two plotted curves. Solutions of 0.1-mole-fraction acid always appeared to give crystalline solid upon cooling while concentrations from about 0.2 to 0.35 mole fraction could only be prepared as glasses. The formation of crystals, generally, was much slower than for sulfuric acid solutions, and it was necessary to hold some of the samples at intermediate temperatures for long periods of time before final cooling to 77°K.

The corresponding atomic-hydrogen yields are given in Fig. 10. These data are the least satisfactory of all;

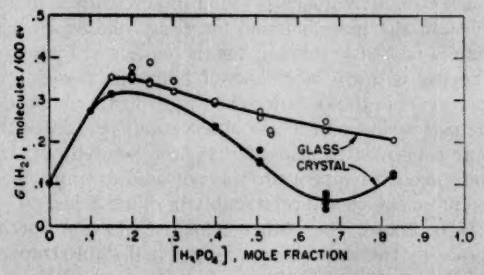

FIG. 9. Molecular-hydrogen initial yields from aqueous phosphoric acid irradiated at 77°K with gamma rays and then warmed.

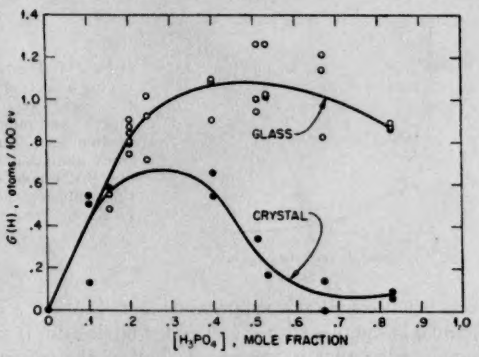

FIG. 10. Atomic-hydrogen initial yields from aqueous phosphoric acid irradiated with gamma rays and examined at 77°K.

there is considerable scatter of the points, especially for the glass curve. Nevertheless, a pronounced difference in yield was observed depending upon whether the sample was irradiated as a glassy or crystalline solid. It appears that the amount of stably trapped atomic hydrogen at 77°K is well in excess of that needed to account for all of the hydrogen gas found after melting. This is especially true of the data obtained with glassy samples; the yields for the crystalline curves of Figs. 9 and 10 are in much closer quantitative correspondence.

The yields of molecular oxygen after melting were very small. A yield in the vincinity of 0.01 molecule/100 ev was found for concentrations around 0.1 to 0.2-mole-fraction acid while other concentrations gave essentially zero yield. The yields of oxygen were far too small to allow a valid comparison between crystalline and glassy samples. The atomic-hydrogen line widths varied very little with concentration; most observed line widths ranged from 4.5 to 5 gauss full width at half-height.

SCAVENGER EXPERIMENTS

At the time some of the properties of atomic hydrogen in solid acids were studied,[2] it was also found (but not published) that certain substances, such as hydrogen peroxide and nitric acid, added to sulfuric acid before irradiation would greatly suppress the yield of stably trapped atomic hydrogen. A more detailed examination of a few scavengers has now been made. Nitric acid added to sulfuric acid not only reduces the yield of atomic hydrogen but the molecular-hydrogen yield as well. These results are summarized in Fig. 11. The indicated weight percentages were obtained by adding concentrated nitric acid (70%) to 0.129-mole-fraction sulfuric acid; since the amounts added were small, the sulfuric-acid concentration remained essentially unchanged. All samples were quickly frozen to give clear glasses, and were then irradiated and assayed as indicated earlier. Relative yields are given in Fig. 11; the absolute yields corresponding to 100% are $G(H_2)=0.61$ and $G(H)=1.3$. Whereas large amounts of nitric acid reduce the atom yield to zero (Fig. 11), the molecule

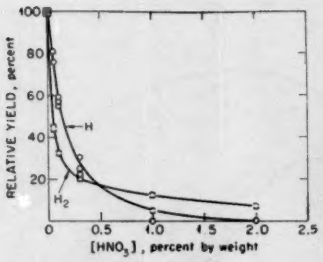

FIG. 11. The scavenging effect of nitric acid on the atomic- and molecular-hydrogen yields from gamma-irradiated 0.129-mole fraction sulfuric acid at 77°K.

yield is not completely suppressed; there is about a 7% residual in samples with 2% of added nitric acid. It was stated earlier that it appears that all of the collected hydrogen after melting originated essentially from atoms stably trapped at the low temperature. The results embodied in Fig. 11 support this general view, but the inability to scavenge all of the molecular hydrogen at concentrations where the atomic hydrogen is completely scavenged suggests that several percent of the molecular hydrogen is formed by processes not involving atoms that can be stably trapped at 77°K. It is not known if the nitric acid itself participates in these other processes.

The addition of a small amount of nitric acid has a much greater effect on the molecule yield than on the atom yield (Fig. 11). This result is consistent with the view that upon irradiation the atoms move from their original sites in the solid and find their way to a trapping site in the cold matrix. The atom-yield curve is then a measure of the probability that an atom will meet a scavenger molecule before it finds a trapping site. This process represents the first part of the life history of a hydrogen atom in these experiments. The second part occurs when the sample is warmed; the atoms start to diffuse and there is a probability that a scavenger molecule will be encountered before another hydrogen atom is encountered. The molecule-yield curve would thus represent the combined probabilities of scavenging up to the time of trapping and during diffusing upon warming. Molecular-oxygen yields were also determined, and these were found to rise from $G(O_2)=0.075$ with no added nitric acid to 0.29 for 2% nitric acid.

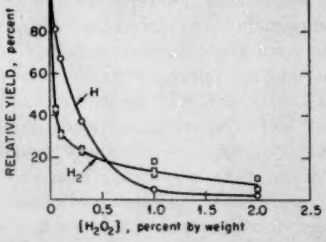

FIG. 12. The scavenging effect of hydrogen peroxide on the atomic and molecular hydrogen yields from gamma-irradiated 0.129-mole-fraction sulfuric acid at 77°K.

Similar scavenging experiments were carried out with hydrogen peroxide. The results are summarized in Fig. 12. Comparison with Fig. 11 indicates that H_2O_2 and HNO_3 when plotted on a weight basis show similar scavenging effects. On a molecule basis HNO_3 is somewhat more effective than H_2O_2. The molecular-oxygen yields were very high, increasing to $G(O_2)\approx 7$ for 2% hydrogen peroxide. One experiment was carried out with HNO_3 as a scavenger in 0.125-mole-fraction $HClO_4$. Only the effect on the atomic-hydrogen yield was measured as indicated in Fig. 13. Comparison with Fig. 11 shows HNO_3 to be much less effective as a scavenger in the $HClO_4$ solution than in the H_2SO_4. This result is consistent with the view that atoms move to trapping sites. The saturation curves for the same acid concentrations as given in Figs. 4 and 8 show that much more atomic hydrogen can be trapped in the $HClO_4$ than in the H_2SO_4. This indicates that the density of trapping sites is very much higher in $HClO_4$; the probability of an atom encountering a scavenger

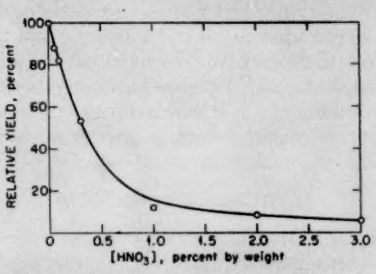

FIG. 13. The scavenging effect of nitric acid on the atomic-hydrogen yield from gamma-irradiated 0.125-mole-fraction perchloric acid at 77°K.

molecule before it finds a trapping site would then be much less in $HClO_4$ than in H_2SO_4.

DISCUSSION AND SUMMARY

There is a striking correspondence between measured hydrogen-atom and molecule yields in sulfuric, perchloric, and phosphoric acids. Although the absolute assay for atomic hydrogen is subject to considerable error, the correspondence appears to be essentially stoichiometric for a range of concentrations of sulfuric acid and crystalline phosphoric acid. About twice as much atomic hydrogen is found in perchloric acid and substantially more is found for glassy phosphoric acid than is needed to account for the molecular hydrogen. The use of nitric acid and of hydrogen peroxide as scavengers in the sulfuric-acid system further bears out the correspondence. These observations pertain to the more concentrated acids. It has been pointed out that a low enough temperature was not used to trap hydrogen atoms in ice and presumably in dilute acids.

It is known that other unpaired electron species (probably free radicals) are formed and stably trapped at 77°K in addition to the atomic hydrogen as evidenced by their paramagnetic-resonance spectra. Their nature

is different in each of the three acids, and their concentrations are often much greater than that of atomic hydrogen. One would expect these species and possibly others not seen by the paramagnetic-resonance method to be extremely reactive with hydrogen atoms. This may explain the fate of the surplus atomic hydrogen over that needed to account for the molecular hydrogen which was found, for example, with perchloric acid. In other cases it is difficult to understand why the hydrogen atoms seemingly combine to form hydrogen molecules more readily than they combine with the high concentration of other reactive species. For example, in the sulfuric-acid system the correspondence between atom and molecule yields for many acid concentrations is not far from being stoichiometric. Upon warming the irradiated acids the atomic hydrogen disappears at a much lower temperature than the other paramagnetic species. In principle it should be possible to measure the concentration of paramagnetic species before and after the atomic hydrogen is made to disappear. Measurements of this kind have not been made except in a cursory examination of sulfuric acid where no profound change in concentration of nonhydrogen-atom species was observed. We are at a loss to explain this seeming lack of reactivity of hydrogen atoms with species other than themselves. Steric effects and conceivably activation energies may be involved. In sulfuric-acid systems an important consideration may be the observation[7] that molecular hydrogen does not react with OH radical in 0.4*M* acid (liquid) and Allen's proposal[8] that the OH radical has formed complexes with the acid. Thus one paramagnetic, reactive species is traded off for another paramagnetic species that may be less amenable to reaction. Of course, the atomic hydrogen is affected by added molecules of scavenger, but the amounts added are relatively very large. An interesting steric effect follows from the liquid model of Eyring, Ree, and Hirai[9] where dislocations in liquids (and glasses) are considered. These dislocations are of atomic dimensions in cross section, and it has been proposed that they are the trapping site for hydrogen atoms. The atoms might then find each other by diffusing along highly directed paths.

In describing the results of scavenger experiments the adoption of a simple model of movement of atoms to stable trapping sites followed by subsequent diffusion and reaction after warming was in qualitative accord with the findings. Figure 8 shows that the saturation concentration of hydrogen atoms after prolonged irradiation of 0.125-mole-fraction perchloric acid was 2.9×10^{19} atoms/g. Let us regard this as being the number of trapping sites in a gram of unirradiated acid. This assumes the number of sites created by the irradiation to be relatively unimportant. If enough scavenger, say nitric acid, is added to the perchloric acid to drop the atom yield to one-half, the number of molecules of scavenger should equal the number of trapping sites. This view is certainly crude for it assumes that an atom will be trapped with the same cross section as it would have for reaction with a scavenger molecule. Figure 13 shows that 0.33% nitric acid will drop the atom yield to one-half. This amounts to 3.1×10^{19} molecules/g. The remarkable closeness of the two numbers must be fortuitous in view of the crudeness of the model. Similar considerations for 0.129-mole-fraction sulfuric acid scavenged with nitric acid give 3.4×10^{18} sites from the saturation curve (Fig. 4) and 13.3×10^{18} sites from the scavenger curve (Fig. 11). Although the agreement is only within a factor of four the combined results on the two acids are impressive enough to make it worthwhile pursuing the model further. This could be done by studying saturation curves for other acid concentrations and also the effects of many different scavengers. There will be differences in reaction cross sections of scavengers as already indicated for nitric acid and hydrogen peroxide in Figs. 11 and 12.

Sulfuric acid, and to a lesser extent phosphoric acid, showed a pronounced change in both molecular- and atomic-hydrogen yield depending upon whether the sample was a glassy or crystalline solid at the time of irradiation. A similar effect has been seen[10] in the photolysis of glassy and crystalline ethyl iodide. The effect might result from a difference in caging at the initial site of formation of the atom or a difference in the availability or density of trapping sites. In any case, it is likely that more atoms are created than eventually appear in the measurements; one way in which the surplus might be lost is back reaction. If the effect resulted from the relative abundances of trapping sites it would follow that such sites are much more abundant in the glassy material. Here again, additional experiments would be of interest, particularly saturation curves and the effects of scavengers on glassy and crystalline acids of the same concentration.

Comparisons of yields in the solid acids with liquids is not straightforward. Hydrogen atom yields have been deduced[11] for water and 0.8*N* sulfuric acid ($\approx$0.01 mole fraction) using scavenger techniques, and values of $G(H)=2.78$ and $G(H)=3.70$, respectively, have been reported. Unfortunately, these compositions are in the region where a low enough trapping temperature was not used in the present experiments. However, these results suggest that atom yields deduced from scavenger experiments on the more concentrated acids (liquids) would be much higher than the yields directly measured in the present study. This is consistent with the previous discussion. Mahlman[12] has measured molecular-hydrogen yields from sulfuric-acid solutions

[7] T. J. Sworski, J. Am. Chem. Soc. **78**, 1768 (1956).
[8] A. O. Allen, Radiation Research **1**, 85 (1954).
[9] H. Eyring, T. Ree, and N. Hirai, Proc. Natl. Acad. Sci. U. S. **44**, 683 (1958).
[10] R. H. Luebbe, Jr., and J. E. Willard, J. Am. Chem. Soc. **81**, 761 (1959).
[11] T. J. Sworski, J. Am. Chem. Soc. **76**, 4687 (1954).
[12] H. A. Mahlman (personal communication).

up to $36N$ and has found $G(H_2)=0.45$ for dilute acids up to $4N$ (≈ 0.04 mole fraction) with a gradual drop to $G(H_2)=0.05$ for $36N$ acid. Although the limiting value for the most concentrated acid is like that given for the glass curve of Fig. 1 there is great departure for the more dilute acid. In the solution experiments bromide ion was added to protect the molecular hydrogen from OH attack, a common practice in such solution studies. The mechanism of formation of final products often depends strongly on diffusional processes; thus, it should not be unexpected to find differences in yields when solids and liquids are compared.

THE JOURNAL OF CHEMICAL PHYSICS VOLUME 33, NUMBER 2 AUGUST, 1960

Microwave Spectrum of $CFCl_3$†

MAURICE W. LONG, QUITMAN WILLIAMS, AND T. L. WEATHERLY

Georgia Institute of Technology, Atlanta, Georgia

(Received December 28, 1959)

A calculation has been made for the hyperfine spectrum of the $J=1\rightarrow 2$ transition for symmetric-top molecules having three identical nuclei of spin $\frac{3}{2}$. Measurements on the $J=1\rightarrow 2$ through $J=6\rightarrow 7$ transitions of $CFCl_3$ are described and the results are used to determine the molecular structure, the quadrupole coupling constant with respect to the molecular symmetry axis, and the centrifugal distortion coefficients. The $J=1\rightarrow 2$ transition of $CHCl_3$ has been measured and the results are compared with those for $CFCl_3$ and with previous work on $CHCl_3$.

INTRODUCTION

AN investigation[1] was made on the microwave spectrum of $CFCl_3$ and the results were compared with those obtained for $CHCl_3$. The purpose was to study the hyperfine splitting produced by three identical nuclei of spin $\frac{3}{2}$ and to determine the molecular dimensions of $CFCl_3$. The hyperfine spectra due to the quadrupolar interaction are very complex; the complexity increases rapidly with increase in J. For this reason the spectrum was investigated at the lowest practical frequency, even though line strengths decrease rapidly with decrease in frequency. The weakest line measured was at 9875 Mc and it has a calculated intensity of 3.9×10^{-11} cm^{-1}.

The hyperfine splitting produced by three identical nuclei with quadrupole moments has been investigated by Bersohn[2] who obtained matrix elements for the interactions and by Mizushima and Ito[3] who used Bersohn's work to calculate the effect of quadrupole interaction on the $J=0\rightarrow 1$ rotational transition for a molecule with three identical nuclei with spins of 1, $\frac{3}{2}$, 2, and $\frac{5}{2}$. Also, a theoretical investigation of the expected hyperfine structure of ND_3 (three nuclei of spin 1) was undertaken by Hadley.[4] The first experimental work reported was that of Kojima *et al.*[5] who applied the theoretical calculations of Mizushima and Ito to the $J=0\rightarrow 1$ rotational transition of $CHBr_3$. The spectrum reported was proved later[6] to be of spurious origin. Wolfe measured the $J=2\rightarrow 3$ spectrum of $CHCl_3$[35] and calculated[7] a theoretical spectrum by use of the procedure outlined by Bersohn. More recently Herrmann[8] made measurements on ND_3 and compared these with the theoretical work of Hadley.

CALCULATED SPECTRA

Frequencies of absorption lines for the $J\rightarrow J+1$ transition may be expressed as

$$f=2(J+1)(B-D_{JK}K^2)-4D_J(J+1)^3+\Delta\nu_Q. \quad (1)$$

Terms of Eq. (1) involving D_{JK} and D_J represent the effects of centrifugal distortion, and $\Delta\nu_Q$ represents the frequency shift resulting from nuclear quadrupole interaction. The selection rule for K is $\Delta K=0$, but $K=0$ components were not detected with the Stark modulation spectrograph used. The $J=1\rightarrow 2$ hyperfine spectrum caused by nuclear quadrupole interaction was calculated because it was the simplest spectrum that could be observed experimentally.

The frequencies and relative intensities of the $J=1\rightarrow 2$, $K=1$, $\Delta F=\pm 1$ transitions were calculated[9] by a method similar to that outlined by Wolfe[7] for the $J=2\rightarrow 3$ transition. The calculation results in 11 energy levels for $J=1$ and 16 for $J=2$. There are a total of 99

† Supported in part by the Office of Naval Research.

[1] A preliminary report of this work was published by M. W. Long, J. Q. Williams, and T. L. Weatherly in Bull. Am. Phys Soc. Ser. II, **4**, (1959).

[2] R. Bersohn, J. Chem. Phys. **18**, 1124 L (1950).

[3] M. Mizushima and T. Ito, J. Chem. Phys. **19**, 739 (1951).

[4] G. F. Hadley, J. Chem. Phys. **26**, 1482 (1957).

[5] S. Kojima, K. Tsukada, S. Hagiwara, and M. Mizushima, J. Chem. Phys. **20**, 804 (1952).

[6] G. Hermann, J. Chem. Phys. **22**, 2093 L (1954).

[7] P. N. Wolfe, J. Chem. Phys. **25**, 976 (1956).

[8] G. Herrmann, J. Chem. Phys. **29**, 875 (1958).

[9] M. W. Long, Ph.D. thesis, Georgia Institute of Technology 1959; also available in form of T.R. No. 1, Contract No. Nonr-991(07), ASTIA No. 216 615, June, 1959.

TABLE I. Hyperfine components for the $J=1\rightarrow2$, $K=1$ spectrum of a symmetric top containing three identical nuclei with spin $\frac{3}{2}$.

$\Delta\nu_Q/eQV_{zz}$	Intensity	$\Delta\nu_Q/eQV_{zz}$	Intensity
−0.44241	0.24	0.00354	0.32
−0.41325	0.08	0.00426	0.50
		0.00495	0.01
−0.37522	0.17	0.01835	0.01
−0.35664	0.08	0.02068	0.14
−0.34627	0.00	0.02378	0.10
−0.34207	0.24	0.03292	0.18
−0.31711	0.01	0.04262	0.23
		0.04988	0.26
−0.29678	0.00	0.05294	0.27
−0.28396	0.14	0.05355	0.02
−0.25875	0.04	0.06302	0.03
−0.25024	0.01	0.06371	0.00
−0.23802	0.10	0.06428	1.32
−0.23166	0.01	0.06428	0.52
−0.21709	0.14	0.06429	1.25
−0.21382	0.37	0.06785	0.02
−0.20406	0.14	0.08609	0.21
−0.20064	0.12	0.08617	0.17
		0.08755	0.03
−0.19999	0.19	0.09593	0.04
−0.19434	0.03		
−0.18165	0.01	0.10670	0.01
−0.18165	0.00	0.10739	0.08
−0.16708	0.12	0.10949	0.10
−0.15571	0.35	0.11624	0.10
−0.14188	0.01	0.11786	0.08
−0.14137	0.06	0.11786	0.01
−0.14068	0.00	0.14226	0.61
−0.13377	0.01	0.15950	0.02
−0.12144	0.09	0.16117	0.03
−0.11221	0.08	0.16941	0.04
−0.11152	0.01	0.17093	0.06
		0.17500	0.07
−0.09820	0.21	0.17855	0.06
−0.08884	0.10	0.18928	0.17
−0.07908	0.00		
−0.07837	0.12	0.21434	0.01
−0.07546	0.35	0.22558	0.02
−0.07501	0.20	0.22627	0.23
−0.06333	0.01	0.22817	0.15
−0.06071	0.25	0.24286	0.60
−0.06071	0.52	0.24821	0.08
−0.06071	2.37	0.25355	0.10
−0.05713	0.08	0.27185	0.07
−0.05665	0.29	0.28450	0.06
−0.04208	0.06		
−0.03883	0.02	0.31786	0.10
−0.03743	0.01	0.30672	0.01
−0.02907	0.67	0.33756	0.06
−0.02907	0.05	0.35950	0.30
−0.01549	0.00	0.39073	0.01
−0.00023	0.15		
		0.41267	0.35

hyperfine components but many of them are relatively weak. The increase in frequency, $\Delta\nu_Q$, in terms of eQV_{zz} and the relative intensity of these hyperfine components are listed in Table I. The data in Table I are normalized so that they can be applied to other symmetric tops containing three identical nuclei with spin $\frac{3}{2}$. These hyperfine components indicate two major prominences shifted in frequency by $-0.0607\ eQV_{zz}$ and $+0.0643\ eQV_{zz}$. A spectrum was calculated by using a half-width for individual components, in terms of the experimentally determined value of eQV_{zz}, which gives line widths comparable to measured widths. Figure 1 shows the sums of intensities at intervals of 0.001 eQV_{zz}. These intensities were summed by assuming that each component is Gaussian in shape and has a width between one-half intensity points of 0.015 eQV_{zz}.

The predicted frequencies for the $J=2\rightarrow3$ transition are based on the calculations of Wolfe. Figures 2 and 3 give the frequencies and intensities for the $J=2\rightarrow3$, $K=1$, and $K=2$ transitions, respectively. These frequencies were obtained from the calculations of Wolfe[10] by simply multiplying his data by -2.8688, the

[10] P. N. Wolfe, Ph.D. thesis, Ohio State University, 1955, Tables 18 and 19.

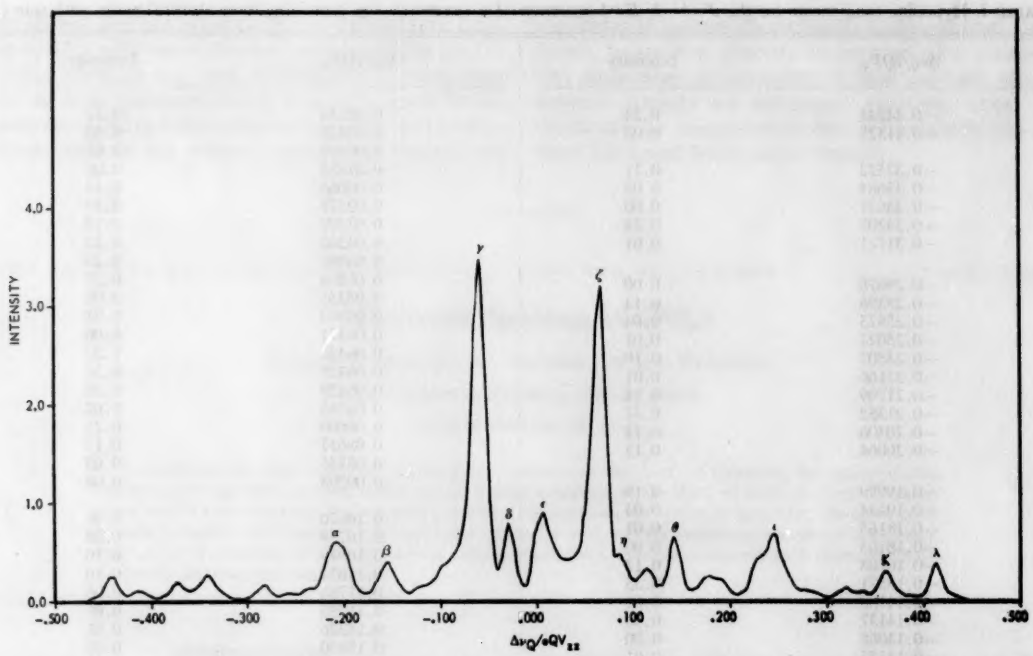

FIG. 1. Predicted hyperfine spectrum of $J=1\rightarrow 2$, $K=1$.

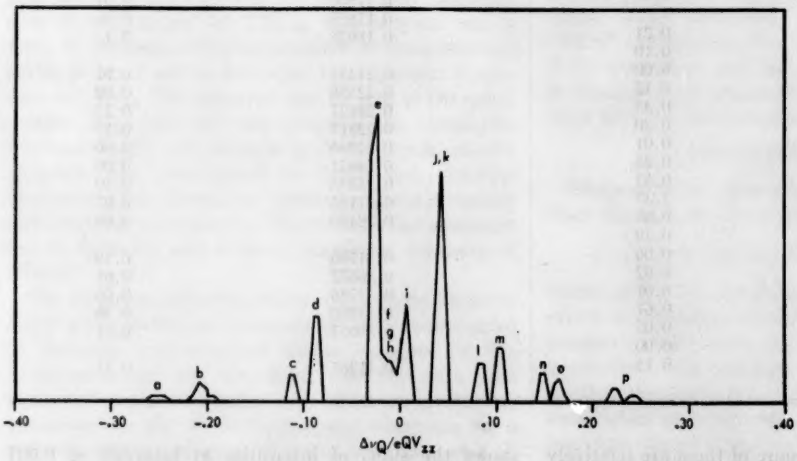

FIG. 2. Predicted hyperfine spectrum for $J=2\rightarrow 3$, $K=1$.

constant[11] which converts frequencies which are given in terms of the quadrupole coupling constant with respect to the bond axis, to frequencies given in terms of the quadrupole coupling constant with respect to the molecular symmetry axis, eQV_{zz}. Figures 2 and 3 show the sums of line intensities at intervals of 0.005 eQV_{zz}, each sum containing all components which lie within 0.005 eQV_{zz} of its center. The summation of components within 0.005 eQV_{zz} provides theoretical spectra of finer detail than was used by Wolfe; this was required to obtain comparable widths for the measured and predicted spectra shown in Fig. 6.

Wolfe also determined an expression for the frequency shift of the most intense hyperfine component for any $J\rightarrow J+1$ transition. He found that the most intense

[11] The sign for $G(JK)$ is incorrect in Eq. 3 of reference 7; it is given correctly in Eq. 17 of reference 10. Because of the error in Eq. 3, the sign is also incorrect in Eq. 6 of reference 7. These differences in sign were confirmed by personal communication with the author.

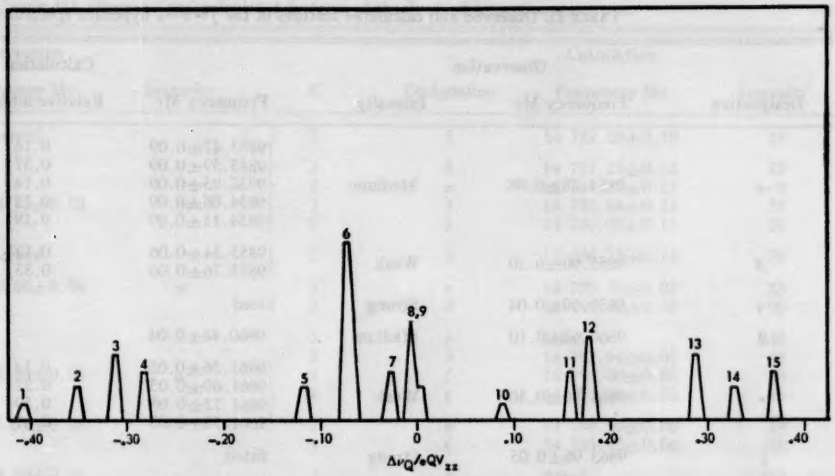

FIG. 3. Predicted hyperfine spectrum for $J=2\rightarrow3$, $K=2$.

component belongs to the set $K=1$ and is specified by $F=J+7/2\rightarrow J+9/2$. His expression, when modified to be in terms of the quadrupole coupling constant eQV_{zz}, is

$$\Delta\nu_Q=\beta(J)eQV_{zz}$$

where

$$\beta(J)=-\tfrac{3}{4}\frac{(J+1)(J+2)+(4J+7)}{(2J+5)(2J+3)(J+2)(J+1)}. \quad (2)$$

Here $\Delta\nu_Q$ is the frequency by which the most intense hyperfine component of the $J\rightarrow J+1$ transition is shifted because of quadrupole interaction. The $J=0\rightarrow1$ transition, having only $K=0$ components, does not satisfy this relation.

OBSERVATIONS AND ANALYSES

The $CFCl_3$ employed as a sample was purchased from The Matheson Company, Inc. This gas has the trade name of "Freon 11" and reportedly has a purity of 99.9%. An 85-kc Stark spectrograph was employed with a 3-in. × 1½-in. × 12-ft absorption cell for the lower transitions and with a 1-in. × ½-in. × 20-ft absorption cell for the higher transitions. The cells were operated at dry-ice temperature and the Stark fields used were between 160 and 640 v/cm. Frequency was determined approximately by a cavity wave meter and then more precisely with a secondary frequency standard. Markers from the frequency standard were beat against the klystron source and the difference frequency was measured with a calibrated HRO communications receiver.

$J=1\rightarrow2$ Spectrum of $CFCl_3$

Two relatively strong lines that are almost equal in intensity and several smaller lines, corresponding to the lines designated by Greek letters in Fig. 1, were observed. Based on about 30 measurements for each line taken at pressures of 30 μ or less, the two stronger lines were observed at 9859.30±0.04 and 9863.96±0.05 Mc. The indicated errors are probable errors under the assumption that the errors are normally distributed about the mean frequencies.

From Table I it is seen that the quadrupole interaction produces a shift in frequency of $-0.06071\ eQV_{zz}$ in the most intense line and $+0.06429\ eQV_{zz}$ in the other strong line; the difference in measured frequencies gives

$$eQV_{zz}=37.3\pm0.5 \text{ Mc.}$$

Comparisons between the calculated and observed frequencies are given in Table II. The relative intensities given in this table for prominences consisting of more than one line were taken from Table I.

The calculated intensity[9] of the most intense line, γ, for room temperature is 4.5×10^{-10} cm^{-1}. Other calculated intensities were obtained from the intensity of γ by using the relative intensities indicated by Fig. 1; these are included in Table II.

$J=2\rightarrow3$ Spectrum of $CFCl_3$

Figure 4 is typical of recordings made using pressures of 30 μ or less. Results of repeatedly measuring frequencies of the major prominences are given in Table III. Figure 5 illustrates a typical spectrum measured with pressures between 60 and 150 μ. The frequency of the second-strongest prominence, C of Fig. 5, corresponds to that of the strongest prominence, C, for the low-pressure case illustrated in Fig. 4. The largest prominence (E, F) of Fig. 5 corresponds to a frequency intermediate to prominences E and F of Fig. 4, indicating that the strongest high-pressure prominence contains components E and F. Figure 6 shows a comparison of the measured prominences C, D, E, F of Fig. 4 with the corresponding part of a composite spectrum composed of Figs. 2 and 3. The amount that the $K=2$ spectrum was shifted with respect to the $K=1$

TABLE II. Observed and calculated features of the $J=1\rightarrow2$ hyperfine spectrum.

	Observation		Calculation		
Designation	Frequency Mc	Intensity	Frequency Mc	Relative intensity	Intensity cm^{-1}
α	9853.68±0.08	Medium	9853.47±0.09 9853.59±0.09 9853.95±0.09 9854.08±0.09 9854.11±0.09	0.14 0.37 0.14 0.12 0.19	7.7×10^{-11}
β	9855.60±0.20	Weak	9855.34±0.06 9855.76±0.06	0.12 0.35	5.0×10^{-11}
γ	9859.30±0.04	Strong	fitted		4.5×10^{-10}
δ	9860.60±0.10	Medium	9860.48±0.04		9.5×10^{-11}
ϵ	9861.80±0.30	Weak	9861.56±0.05 9861.69±0.05 9861.72±0.05 9861.75±0.05	0.15 0.32 0.50 0.01	1.0×10^{-10}
ζ	9863.96±0.05	Strong	fitted		4.1×10^{-10}
η	9865.00±0.20	Weak	9864.78±0.05		5.9×10^{-11}
θ	9866.69±0.11	Medium	9866.85±0.07		8.6×10^{-11}
ι	9870.50±0.20	Medium	9870.62±0.10		8.6×10^{-11}
κ	9875.00±0.25	Weak	9874.96±0.16		3.9×10^{-11}
λ	9877.00±0.25	Weak	9876.94±0.18		5.0×10^{-11}

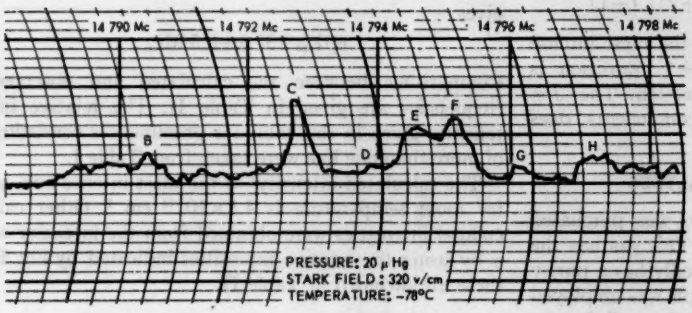

FIG. 4. $J=2\rightarrow3$ transition in $CFCl_3^{35}$ at 20-μ pressure.

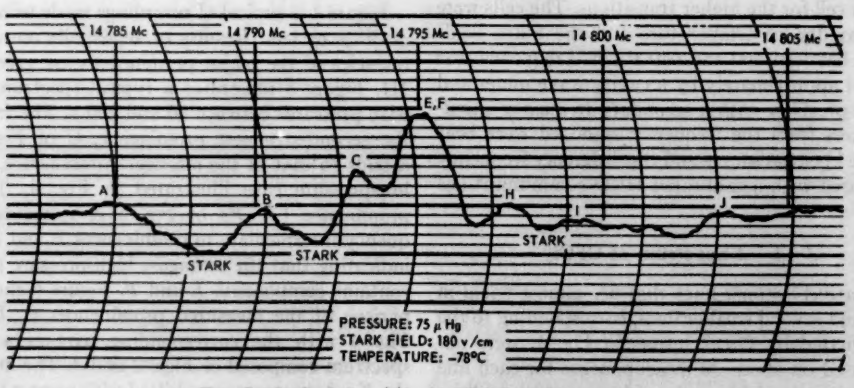

FIG. 5. $J=2\rightarrow3$ transition in $CFCl_3^{35}$ at 75-μ pressure.

TABLE III. Observed and calculated features of the J=2→3 hyperfine spectrum.

Observation			Calculation			
Designation	Frequency Mc	Intensity	K	Designation	Frequency Mc	Intensity
	Unobserved		2	1	14 782.08±0.19	19
			2	2	14 784.25±0.16	39
			1	*a*	14 784.37±0.13	9
A	14 784.75±0.10	m[a]	2	3	14 785.64±0.14	78
			1	*b*	14 786.02±0.11	26
	Unobserved		2	4	14 786.73±0.14	58
B	14 790.46±0.08	w	1	*c*	14 789.59±0.07	33
			1	*d*	14 790.52±0.07	99
			1	*e*	fitted	288
			2	5	14 792.94±0.07	39
C	14 792.80±0.06	s	1	*f*	14 793.00±0.06	59
			1	*g*	14 793.24±0.06	46
D	14 793.92±0.08	w	1	*h*	14 793.59±0.06	35
			1	*i*	14 793.95±0.06	118
E	14 794.66±0.08	s	2	6	fitted	214
F	14 795.26±0.08	s	1	*j*	14 795.14±0.07	195
			1	*k*	14 795.46±0.07	83
G	14 796.25±0.10	w	2	7	14 796.29±0.08	58
			1	*l*	14 796.84±0.08	46
			2	8	14 797.02±0.09	78
H	14 797.12±0.10	m	2	9	14 797.32±0.09	39
			1	*m*	14 797.77±0.09	65
I	14 799.50±0.30	w	1	*n*	14 799.28±0.11	34
			1	*o*	14 799.85±0.11	31
	Unobserved		2	10	14 800.58±0.11	19
	Unobserved		1	*p*	14 802.38±0.14	29
J	14 803.40±0.30	w	2	11	14 803.18±0.14	58
			2	12	14 803.98±0.15	97
	Unobserved		2	13	14 807.98±0.20	78
	Unobserved		2	14	14 809.45±0.21	39
	Unobserved		2	15	14 811.09±0.23	58

[a] Intensities are s, strong; m, medium; w, weak.

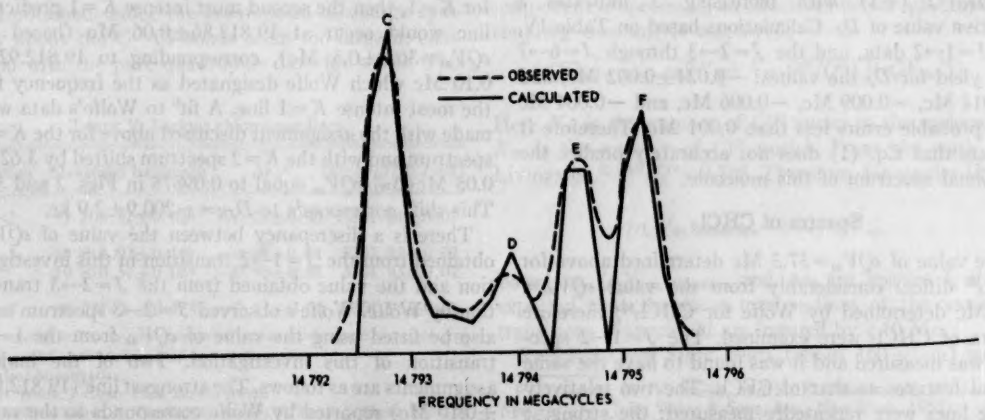

FIG. 6. Observed and calculated features of the $J=2\rightarrow3$ transition in $CFCl_3$.

TABLE IV. Frequencies of the strongest line in various spectra.

Transition	Measured frequency, f, of strongest line	$\beta(J)$	$\Delta\nu_Q$[a]	$(f-\Delta\nu_Q)/2(J+1)$
1→2	9 859.30±0.04	−0.0607	−2.26±0.03	2465.39±0.01
2→3	14 792.80±0.06	−0.0268	−1.00±0.01	2465.63±0.01
3→4	19 725.17±0.01	−0.0148	−0.55±0.01	2465.72±0.00
4→5	24 657.26±0.03	−0.0093	−0.35±0.00	2465.76±0.00
5→6	29 588.95±0.01	−0.0063	−0.23±0.00	2465.76±0.00
6→7	34 520.42±0.01	−0.0046	−0.17±0.00	2465.76±0.00

$\Delta\nu_Q=\beta(J)eQV_{zz}$, where $\beta(J)=-\frac{1}{2}\{[(J+1)(J+2)+(4J+7)]/(2J+5)(2J+3)(J+2)(J+1)\}$

[a] eQV_{zz}=37.3±0.5 Mc based on J=1→2 data.

spectrum corresponds to $D_{JK}=-196\pm6$ kc. Table III contains measured and calculated frequencies for all components included in Figs. 2 and 3; the general agreement in line structure indicates a valid assignment of components.

The calculated intensity for room temperature of the most intense line of the $J=2\rightarrow3$ spectrum is 2.5×10^{-9} cm^{-1}; the corresponding coefficient for the $J=1\rightarrow2$ transition is 4.5×10^{-10} cm^{-1}.

Other Transitions of $CFCl_3$

Measurements were made for the frequencies of the largest resolvable prominence at pressures of about 25 μ for each of the rotational transitions $J=3\rightarrow4$ to $J=6\rightarrow7$, inclusive. The measurements were used to assist in the assignment of the major prominences in the $J=2\rightarrow3$ hyperfine spectrum. The results were analyzed with Eq. (2), and are included in Table IV. Because the strongest component is expected to correspond to $K=1$, Eq. (1) may be expressed as

$$(f-\Delta\nu_Q)/2(J+1)=(B-D_{JK})-2D_J(J+1)^2. \quad (3)$$

If D_{JK} is assumed constant, the increasing value of $(f-\Delta\nu_Q)/2(J+1)$ with increasing J indicates a negative value of D_J. Calculations based on Table IV, the $J=1\rightarrow2$ data, and the $J=2\rightarrow3$ through $J=6\rightarrow7$ data yield for D_J the values: -0.024 ± 0.002 Mc, and -0.014 Mc, -0.009 Mc, -0.006 Mc, and -0.004 Mc with probable errors less than 0.001 Mc. Therefore it appears that Eq. (1) does not accurately predict the rotational spectrum of this molecule.

Spectra of $CHCl_3$

The value of $eQV_{zz}=37.3$ Mc determined above for $CFCl_3^{35}$ differs considerably from the value $eQV_{zz}=28.7$ Mc determined by Wolfe for $CHCl_3^{35}$; therefore spectra of $CHCl_3$ were examined. The $J=1\rightarrow2$ spectrum was measured and it was found to have the same general features as that of $CFCl_3$. The two relatively strong lines were repeatedly measured; the strongest line occurs at 13 204.32±0.04 Mc and the second-strongest line occurs at 13 208.89±0.05 Mc. In accordance with the discussion of the $J=1\rightarrow2$ spectrum for $CFCl_3$, these frequencies give $eQV_{zz}=36.6\pm0.5$ Mc for $CHCl_3^{35}$.

Experience with the analysis of the $J=2\rightarrow3$ spectrum of $CFCl_3$ had indicated that it would have been virtually impossible to analyze this spectrum without the value of eQV_{zz} from the $J=1\rightarrow2$ spectrum and without data from higher rotational transitions. On this basis Wolfe's frequency data were reviewed to ascertain if they represent a definite discrepancy with the $J=1\rightarrow2$ data.

Wolfe's measured $J=2\rightarrow3$ spectrum has two large prominences similar to C and E, F of Fig. 5 but with a smaller intensity difference. The frequencies of these lines are listed in Table V along with the most intense lines of the $J=1\rightarrow2$ spectrum and the unresolved peak frequency of the $J=6\rightarrow7$ spectrum. The trend of $(f-\Delta\nu_Q)/2(J+1)$ apparent for $CFCl_3$ in Table IV indicates that the line at 19 810.57 Mc in Table V would be the strongest line in a more completely resolved spectrum. That this can happen may be seen by a comparison of Figs. 4 and 5 for $CFCl_3$. If the frequency 19 810.57±0.05 Mc reported by Wolfe corresponds to the predicted most intense component for $K=1$, then the second most intense $K=1$ predicted line would occur at 19 812.86±0.06 Mc (based on $eQV_{zz}=36.6\pm0.5$ Mc), corresponding to 19 812.92±0.10 Mc which Wolfe designated as the frequency for the most intense $K=1$ line. A fit[9] to Wolfe's data was made with the assignment discussed above for the $K=1$ spectrum and with the $K=2$ spectrum shifted by 3.62±0.05 Mc ($\Delta\nu_Q/eQV_{zz}$ equal to 0.09878 in Figs. 2 and 3). This shift corresponds to $D_{JK}=-200.9\pm2.9$ kc.

There is a discrepancy between the value of eQV_{zz} obtained from the $J=1\rightarrow2$ transition in this investigation and the value obtained from the $J=2\rightarrow3$ transition by Wolfe. Wolfe's observed $J=2\rightarrow3$ spectrum can also be fitted using the value of eQV_{zz} from the 1→2 transition of this investigation. Two of the major assignments are as follows. The strongest line (19 812.92 ±0.10 Mc) reported by Wolfe corresponds to the sum of the strongest $K=2$ line (6 in Fig. 3) and the second

strongest $K=1$ line, (j, k in Fig. 2), and Wolfe's second-strongest line (19 810.57±0.05 Mc) corresponds to the strongest $K=1$ line (e in Fig. 2).

QUADRUPOLE COUPLING CONSTANTS

In order to compare the quadrupole coupling constant of $CFCl_3$[35] with that of other methyl chlorides, it is convenient to express the field gradient at the chlorine nucleus V_{zz} in terms of V_{aa}, where a is the C—Cl bond direction. If it is assumed that the field gradient is due entirely to a cylindrically symmetric charge distribution about the C—Cl bond, then[7] one obtains

$$V_{zz}=(\cos 2\alpha)V_{aa}=\tfrac{1}{2}(3\cos^2\beta-1)V_{aa},$$

where 2α is the angle Cl–C–Cl and β is the angle between a C—Cl bond and the molecular symmetry axis. The value 109°40′ for 2α gives

$$eQV_{aa}=-110.8\pm1.5 \text{ Mc}$$

for $CFCl_3$. Use of 110°55′ for the Cl–C–Cl angle[7] and $eQV_{zz}=36.6\pm0.5$ Mc, obtained in this investigation for $CHCl_3$, gives $eQV_{aa}=-102.5\pm1.4$ Mc. Table VI lists the quadrupole coupling constants obtained from both microwave spectra and pure quadrupole resonance studies for various methyl chlorides. Where necessary, the assumption of axial symmetry of charge about the C—Cl bond was made in order to obtain eQV_{aa}. There is a general agreement in the ratio of quadrupole coupling constant of $CFCl_3$ to that of $CHCl_3$ obtained from the pure quadrupole resonance data and the ratio of the much larger constants obtained in this investigation.

The discrepancy between the coupling constant obtained in this investigation for $CFCl_3$ and the constant obtained by Wolfe in an analysis of the $J=2\rightarrow3$ spectrum of $CHCl_3$ was particularly disturbing. The present investigation, however, indicates no definite discrepancies between eQV_{zz} for the $J=1\rightarrow2$ and the $J=2\rightarrow3$ spectra of $CFCl_3$ or $CHCl_3$. The values of eQV_{aa} obtained under the assumption of charge symmetry about the C—Cl bonds seem too large in comparison with the pure quadrupole data for solids. This seems to indicate that the usual assumption of charge symmetry about the C—Cl bond is not valid for the case of the three nuclei of $CFCl_3$ and $CHCl_3$.

TABLE V. Various chloroform lines.

Transition	Measured frequency	$\Delta\nu_Q$[a]	$(f-\Delta\nu_Q)/2(J+1)$
1→2	13 204.32±0.04[b]	−2.22±0.03	3301.64±0.01
2→3	19 812.92±0.10[c]	−0.98±0.01	3302.32±0.02
	19 810.57±0.05[c]	−0.98±0.01	3301.93±0.01
6→7	46 227.2 ±0.15[d]	−0.17±0.00	3301.96±0.01

[a] $eQV_{zz}=36.6\pm0.05$ Mc based on $J=1\rightarrow2$ data.
[b] Present investigation.
[c] P. N. Wolfe, J. Chem. Phys. 25, 976 (1956).
[d] R. R. Unterberger, R. Trambarulo, and W. V. Smith, J. Chem. Phys. 18, 565 (1950).

TABLE VI. The quadrupole coupling constant of Cl^{35} in various molecules.

Molecule	Gas eQV_{aa}	Solid $\lvert eQV_{aa}\rvert$
CH_3Cl	−75.50 Mc[a]	68.40 Mc[a]
CH_2Cl_2	−78.4±2[b]	72.47[a]
$CHCl_3$	−80.39±0.22[a]	76.98[a]
	−102.5±1.4[d]	
$CFCl_3$	−110.8±1.5[d]	79.63[a]
CCl_4		81.85[a]

[a] R. Karplus and A. H. Sharbaugh, Phys. Rev. 75, 889 (1949).
[b] R. J. Myers and W. D. Gwinn, J. Chem. Phys. 20, 1420 (1950).
[c] P. N. Wolfe, J. Chem. Phys. 25, 976 (1956).
[d] Present investigation.
[e] R. Livingston, J. Chem. Phys. 19, 1434 (1951).

STRUCTURE OF $CFCl_3$

The structure of $CFCl_3$ was determined from experimental $J=1\rightarrow2$ data for the most intense line of $CFCl_3$[35] and the most intense lines of the transitions $J_\tau=1_0\rightarrow2_1$ and $J_\tau=1_{-1}\rightarrow2_0$ for $CFCl_2$[35]Cl[37].

From the values of energy and the selection rules,[12] the frequencies corresponding to the $J=1\rightarrow2$ transitions for the asymmetric species are

$$f(1_1\rightarrow2_2)=A+B+2C+2[(B-C)^2+(A-C)(A-B)]^{\frac{1}{2}}$$
$$f(1_0\rightarrow2_1)=3A+B$$
$$f(1_{-1}\rightarrow2_0)=A+3B.$$

Previous data indicate that the most intense line in the $J=1\rightarrow2$ spectrum for $CFCl_3$[35], species I, is lowered by 2.26 Mc. To account for the shift in the most intense component of species II, an effective nuclear quadrupole coupling constant is employed,

$$(eQV_{zz})_{\text{effective}}=[N_{35}+N_{37}(Q^{37}/Q^{35})](eQV_{zz}/3).$$

Here N_{35} is the number of Cl^{35} nuclei in the molecule, N_{37} is the number of Cl^{37} nuclei. From the work of Livingston,[13] $Q^{37}/Q^{35}=0.788$. Therefore, for species II

$$(eQV_{zz})_{\text{effective}}=0.929eQV_{zz}.$$

Based on $(eQV_{zz})_{\text{effective}}$ and $\Delta\nu_Q$ for species I, it is expected that the most intense lines of the various transitions of species II are lowered by 2.10 Mc.

Relatively low Stark fields (about 160 v/cm) were

[12] W. Gordy, W. V. Smith, and R. F. Trambarulo, *Microwave Spectroscopy* (John Wiley & Sons, Inc., New York, 1953).
[13] R. Livingston, Phys. Rev. 82, 289 (1951).

TABLE VII. Observed and predicted $J=1\rightarrow2$ transitions in fluorotrichloromethane (Mc).

Species	f (Obs)	f (Predicted)
I	9859.30±0.04	$4B(\mathrm{I})-2.26$
II	9786.05±0.20	$3A(\mathrm{II})+B(\mathrm{II})-2.10$
	9656.62±0.10	$A(\mathrm{II})+3B(\mathrm{II})-2.10$

employed throughout this investigation. As a consequence, $K=0$ components were not observed since these possess no first-order Stark effect. The available Stark field was not large enough to observe the frequency $f(1_1\rightarrow2_2)$, which corresponds to $K=0$ in the limiting case of a symmetric top. Table VII gives the observed frequencies and corresponding frequency expressions in terms of rotational constants.

The data in Table VII yield

$$A(\mathrm{I})=B(\mathrm{I})=2465.39\ \mathrm{Mc}$$

$$A(\mathrm{II})=2463.22\ \mathrm{Mc}$$

$$B(\mathrm{II})=2398.50\ \mathrm{Mc}.$$

The molecular structure was calculated from the rotational constants by assuming the bond lengths and angles to be the same for $CFCl_3^{35}$ and $CFCl_2^{35}Cl^{37}$. This analysis gives

$$\mathrm{C—Cl}=1.76\ \mathrm{A}$$

$$\mathrm{C—F}=1.33\ \mathrm{A}$$

$$\mathrm{Cl—C—Cl}=109°40'.$$

Electron diffraction data[14] for this molecule indicate C—Cl: 1.76 A, C—F: 1.40 A and Cl—C—Cl: 111.5°. Although the C—F distance determined in this investigation does not agree with the electron diffraction results, it is in good agreement with most of the previously reported[15] microwave data below:

CF_3Cl^{35}:	1.32 A
CF_3Br^{79}:	1.33 A
CF_3I:	1.33 A
CF_3H:	1.332 A
CH_3F:	1.39 A.

CONCLUSIONS

Details of the measured $J=1\rightarrow2$ and the $J=2\rightarrow3$ hyperfine spectra for $CFCl_3^{35}$ and $CHCl_3^{35}$ match the predicted hyperfine spectra. Values of eQV_{aa}, calculated from experimentally determined values of eQV_{zz} for $CFCl_3$ and $CHCl_3$ by assuming extranuclear charge symmetry about the C—Cl bond, are large compared to values obtained for other molecules. This seems to indicate that the usual assumption of charge symmetry is not valid for $CFCl_3$ and $CHCl_3$.

Values of D_J obtained by assuming that D_{JK} is constant for $K=1$ are negative and not constant but appear to approach zero in the limit of large J. Changes of D_J with J might suggest a dependence of eQV_{zz} on J due to molecular distortion. However, relatively large changes in eQV_{zz} would be required to produce substantial changes in D_J and no such changes were observed for the $J=1\rightarrow2$ and $J=2\rightarrow3$ spectra.

To affect agreement of the eQV_{aa} calculated under the assumption of charge symmetry about the C—Cl bonds with values of eQV_{aa} given for other C—Cl bonds, eQV_{zz} must be decreased considerably. In contradistinction to this, calculations of D_J can be made nonnegative only through the assumption of a considerable increase in eQV_{zz}.

Because of the dependence of D_J on J under the assumption that D_{JK} is a constant, the usual centrifugal distortion theory for which the coefficients D_J and D_{JK} are constants can not be used to accurately predict the rotational spectra of $CFCl_3$ and $CHCl_3$.

[14] P. W. Allen and L. E. Sutton, Acta. Cryst. 3, 46 (1950).

[15] C. H. Townes and A. L. Schawlow, *Microwave Spectroscopy* (McGraw-Hill Book Company, Inc., New York, 1955), p. 55.

THE JOURNAL OF CHEMICAL PHYSICS VOLUME 33, NUMBER 2 AUGUST, 1960

Dissolution Kinetics at Dislocation Etch Pits in Single Crystals of Lithium Fluoride

M. B. Ives and J. P. Hirth

Metals Research Laboratory, Carnegie Institute of Technology, Pittsburgh, Pennsylvania

(Received February 29, 1960)

The kinetics of dissolution at dislocation etch pits on lithium fluoride in dilute aqueous solutions of ferric fluoride were studied by interferometric observations on etched surfaces.

The effects on dissolution of the variables time, temperature, undersaturation, crystal perfection, and crystal orientation were determined. It was found that dissolution was consistent with the mechanistic theories of crystal dissolution involving dissociation of lithium fluoride from monomolecular ledges on close-packed surfaces and subsequent diffusion into solution, if a time-dependent adsorption of inhibitor at the receding ledges is invoked.

I. INTRODUCTION

TWO avenues of approach to the theoretical description of crystal dissolution have been opened to date. The mechanistic approach was first rigorously applied by Burton, Cabrera, and Frank[1] (henceforward 'B-C-F') and has been since modified and extended by subsequent workers. More recently the phenomenological approach has resulted in the elegant topographical theory of Frank.[2,3]

Both approaches invoke Kossel's[4] concept of a surface structure of low-index facets separated by ledges of monomolecular height.[5] The ledges consist of segments lying in close-packed directions separated by kinks of monomolecular offset. These ledges are preferred sites for the removal of atoms from the crystal. Hence the process of dissolution consists of the recession of a train of monomolecular ledges on the crystal surface. The local rate of dissolution on a surface will be proportional to the product of the ledge velocity, v, and the concentration of ledges, k, in the same region. The detailed description of dissolution kinetics rests on developing the dependence of v on k. Frank[3] assumed a form for $v(k)$ and developed a topographical theory of crystal dissolution: B-C-F and later workers considered the ledge mechanism of dissolution and derived $v=v(k)$.

Qualitatively, the above ideas explain many observations of crystal dissolution. The topographical theory[3] has been quantitatively verified by Ives[6] for the macroscopic dissolution of lithium fluoride in acidic and aqueous etchants, and by Ives and Frank[7] in application to Batterman's[8] work on the dissolution of germanium in "Superoxol" etchant. However, quantitative data with which to test the ledge or microscopic-dissolution theories has been lacking. The present investigation was undertaken in an effort to obtain such quantitative data. The dissolution kinetics, at dislocation sites, of lithium fluoride in water were studied as a function of time, temperature, undersaturation, and inhibitor (or "poison") concentration. In the following the ledge theories are reviewed, and the results of the experiments compared with the predictions of the theories.

II. CURRENT THEORIES OF CRYSTAL DISSOLUTION

A. Topographical Theory

The topographical theory of Frank[3] in the form in which it has been elicited in detail is based on the condition that v is a function only of k (or is dependent on time only through orientation-independent factors). If this condition is fulfilled, the theory predicts that the trajectory of a given crystal orientation on the surface will be a straight line. Also, if the dissolution rate is measured normal to the crystal surface, and the reciprocal of this rate is plotted on a polar diagram as a function of orientation, the trajectory of a point of given orientation on the surface will be parallel to a normal to the polar diagram at the corresponding orientation. Thus, knowing the crystal shape as a function of dissolution time, one can construct the polar diagram of reciprocal dissolution rate and vice versa.

In this investigation the straight-line-trajectory condition was employed to test the applicability of the topographical theory. As will appear later, the trajectory condition was not fulfilled in dissolution at dislocation sites in lithium fluoride. The most likely cause for the inapplicability of the topographical model is that the dissolution at etch pits is time dependent. However, in order to test the feasibility of a time dependence, it was first necessary to develop the kinetics of dissolution predicted by the mechanistic approach first developed by B-C-F,[1] and since modified to other cases and conditions by the work of Cabrera and Levine[9] and that of Hirth and Pound.[10]

[1] W. K. Burton, N. Cabrera, and F. C. Frank, Phil. Trans. Roy. Soc. 243A, 299 (1951).

[2] F. C. Frank, "On the orientation-dependent solution of crystals" (to be published).

[3] F. C. Frank, *Growth and Perfection of Crystals* (John Wiley & Sons, New York, 1958), p. 411.

[4] W. Kossel, Nachr. Ges. Wiss. Göttingen 135 (1927).

[5] The rigorous three-dimensional Frank theory[2] makes no use of any ledge concept, showing that the theory is independent of the applicability of the concept. However, the two-dimensional approach does invoke the concept and it is this approach which is always referred to in the present context.

[6] M. B. Ives, Ph.D. thesis, University of Bristol, 1959.

[7] M. B. Ives and F. C. Frank, J. Appl. Phys. (to be published).

[8] B. W. Batterman, J. Appl. Phys. 28, 1236 (1957).

[9] N. Cabrera and M. M. Levine, Phil. Mag. 1, 450 (1956).

[10] J. P. Hirth and G. M. Pound, J. Chem. Phys. 26, 1216 (1957).

B. Ledge Mechanism

The principal controlling factors in the etching of lithium fluoride by a dilute solution of ferric fluoride in water are the diffusion field of dissolved lithium fluoride, and the inhibition afforded by the ferric ions. It is logical to suppose that the two factors each modify a different stage of the dissolution process. The poison will control the surface-reaction stage, the act of severing the chemical bonding of the ions of the crystal; the diffusion field will control the liquid-diffusion and surface diffusion stages, the process of transport of dissolved ions away from the crystal surface. Mathematically, then, the presence of surface inhibitor will adjust the boundary conditions for the diffusion problem and may, in the extreme, completely dominate the dissolution kinetics.

Complete diffusion control will be outlined first, and then the modification of such control by first a time-independent, and secondly a time-dependent ledge inhibition will be considered.

The symbols to be employed in the following treatment are: b=magnitude of Burgers vector of a dislocation, C=concentration, and C_0=saturation concentration of lithium fluoride in solution at temperature of process, D=diffusion coefficient of lithium fluoride, h=height of (monomolecular) ledges, J=atom (ion) flux, k=concentration of ledges, N_k=number of kinks per centimeter of ledge=$1/x_0$, n_s=concentration of adsorbed ions at crystal surface, q=flux of ledges, v=the velocity of a ledge, v_∞=steady-state ledge velocity, $\dot{w}$=rate of change of width of etch pit, $\bar{X}$=mean free path of diffusion, x_0=distance between successive kinks in ledge, y_0=distance between successive ledges=$1/k$, γ=specific interfacial free energy, δ=thickness of unstirred layer of solution adjacent to the crystal, σ=undersaturation of solute in etchant=$(C_0-C)/C_0$, Ω=atomic volume of dissolving ions $\simeq h^3$, μ=shear modulus of crystal, and ρ_c=radius of the critical-sized two-dimensional hole in a perfect crystal surface in equilibrium with a solution of undersaturation, σ.

C. Diffusion Control

The diffusion problem for the dissolution of crystals has been analyzed by B-C-F.[1] As noted above, they regard the crystal surface as close-packed regions bounded by ledges containing kinks. The sources of the ledges are either crystal edges, pits where a dislocation with a screw component normal to the surface intersects the surface, or holes nucleated in the close-packed surface. The kinks are sites of easiest transfer of a molecule from the crystal into solution because the least number of chemical bonds are broken in transfer at such a site. Hence atoms enter solution at kinks and diffuse into the undersaturated solution. B-C-F equate the sum of the steady-state hemispherical diffusion fluxes around the kinks in a ledge to the steady-state semicylindrical diffusion flux around the ledge; and the sum of the semicylindrical fluxes from the ledges to the planar diffusion flux into the solution through the unstirred layer of liquid adjacent to the surface.

At high undersaturation their treatment yields the steady-state velocity of a parallel train of ledges,

$$v_\infty = D(C_0-C)\Omega y_0/h\delta. \tag{1}$$

This relation demonstrates that in this case the step velocity continuously decreases with decreasing y_0; i.e., increasing step concentration, in agreement with the ideas expressed by Frank[3] for the dependence of step flux, q, on concentration, k, for a pure solvent in the absence of an inhibitor.

The above treatment assumes that the thickness of the unstirred layer, δ, is much greater than the steady-state ledge spacing, y_0. There is some reason to suppose, however, that the unstirred layer is only a few angstroms thick.[11] To accomodate these recent views it is necessary to obtain a solution to the diffusion equation when $\delta \lesssim y_0$.

Under this condition it is likely that motion of ions on the surface, rather than directly into the solution, will be the limiting step to the diffusion of matter from the ledges, leading to a solution similar to that of Hirth and Pound[10] for crystal evaporation. Their solution for the surface-diffusion problem gives the ledge velocity as a function of the hyperbolic tangent of the ledge spacing, namely,

$$v=[(2\bar{X}/h)\tanh(y_0/2\bar{X})]D\Omega(C_0-C)/\delta. \tag{2}$$

The ledge velocity, v, approaches its terminal value, v_∞, asymptotically as the hyperbolic tangent approaches unity as its argument increases beyond ~ 3. The crystal ledge therefore accelerates at small values of y_0 until the maximum, v_∞, is attained when $y_0/2\bar{X} \approx 3$. This limiting value is given by

$$v_\infty \approx D\Omega(C_0-C)y_0/3\delta h, \tag{3}$$

which is of the same form as (1).

This treatment, in which surface diffusion fluxes have a significant role, in essence differs from the B-C-F treatment only in describing the dissolution processes prior to the attainment of a steady state, which may in fact never obtain. If y_0 at the source exceeds $6\bar{X}$, the ledges will maintain a constant spacing and will move at a steady-state velocity given by Eq. (2). However, if y_0 at the ledge source is less than $6\bar{X}$, the ledges will accelerate as dissolution proceeds; the ledge spacing at a fixed distance from the source will continuously decrease. Thus in such a circumstance a steady state is only approached asymptotically.

The spacing y_0^0 at the ledge source at the center of an etch pit can be estimated as follows. B-C-F have shown that the ledge emanating from a screw dislocation will wind into a spiral as dissolution proceeds until the curvature at the center of the spiral reaches the critical

[11] A. Carlson, reference 3, p. 421.

value $1/\rho_c$. The spacing at the spiral center is then given by B-C-F as

$$y_0^0 = 4\pi\rho_c,^{12} \quad (4)$$

where ρ_c is given by

$$\rho_c = -\gamma\Omega/kT\ln(C/C_0). \quad (5)$$

After combining (4) and (5), we see that the slope of the etch pit at the ledge source is

$$h/y_0^0 = hkT\ln(C_0/C)/4\pi\gamma\Omega. \quad (6)$$

Again, if y_0^0, given by Eq. (4), exceeds $6\bar{X}$, the ledges will maintain a constant spacing, and the slope of the pit sides will remain constant at the value given by Eq. (6). If y_0^0 is less than $6\bar{X}$, then the ledges will accelerate, and the slope of the pit side will become less steep as the distance from the source increases, approaching a limiting value $h/6\bar{X}$. Thus a measurement of pit slope is a criterion for distinguishing between volume-diffusion and surface-diffusion control.

The spacing, y_0^0, at an edge-dislocation source depends on the hole-nucleation probability at the dislocation, since no perpetuating ledges are associated with an edge dislocation.[13] Nucleation of edge-dislocation etch-pit attack, i.e., of holes at a dislocation, has been studied by Cabrera and Levine,[9] who determine the condition that the radius of the critical nucleus is real, as

$$-\ln(C/C_0) < 2\pi^2\Omega\gamma^2/kT\mu b^2. \quad (7)$$

Taking $\Omega = 10^{-22}$ cm^3, $\gamma = 177$ ergs cm^{-2},[14] $T = 300°$K, $\mu = 5.4\times10^{11}$ d/cm^2, and $b = 4\times10^{-8}$ cm, the critical concentration ratio is $C_n/C_0 = 0.2$. For $C_n < 0.2\ C_0$ there is no barrier to nucleation at edge dislocations, and the kinetics of ledges emanating from such a source will be analogous to the kinetics treated above. For concentration ratios greater than C_n/C_0, nucleation of ledges at the source will be required and the resulting ledge spacing will be too large to produce a microscopically observable etch pit. Note that because of the dependence of spiral ledge spacing on concentration, Eq. (4), the spacing of ledges emanating from a screw dislocation will also become very large at concentration ratios smaller than the critical ratio C_n/C_0.

For these kinetic relations to apply to etch-pit formation, it is necessary that dissolution of the main close-packed surface be negligible. Applying standard nucleation theory,[15] the critical concentration ratio for appreciable nucleation of holes of monomolecular depth in the close-packed surface is

$$\ln[C_{hole}/C_0] = \pi h\gamma^2\Omega/k^2T^2[-(\Delta G_D^*/kT) + \ln(4\pi\rho_c\nu\Omega C_0^2)], \quad (8)$$

where ΔG_D^* is the activation energy for diffusion of lithium ions in solution. Taking the same values for Ω, T, and γ as above and $h = 4\times10^{-8}$ cm, $\nu = 10^{13}$ sec^{-1}, $C_0 = 1.5\times10^{-3}$ g ml^{-1}, and $\Delta G_D^* = 0.2$ ev, $C_{hole}/C_0 = 2\times10^{-5}$. For concentration ratios less than 2×10^{-5}, nucleation on the close-packed surface would occur. However as soon as dissolution had occurred a diffusion gradient into the solution would be set up and the effective concentration ratio at the interface would be increased to a value greater than 2×10^{-5}, so that etching of the close-packed crystal surface because of two-dimensional nucleation can be neglected. Previous results on the dissolution of LiF[6,7] justify such an assumption.

D. Part Poison, Part Diffusion Control

It is now necessary to consider how the ferric-fluoride "poison" will modify the dissolution kinetics. The presence of a poison at the crystal surface affects only two of the parameters in Eqs. (3)–(8), namely the surface free energy γ, and the effective saturation concentration C_0.

Inhibitor deposited at a crystal ledge will lower the free energy of the ledge and hence adjust γ to some lower value, γ'. This reduction of free energy is significant once monolayer (or, in this case, monoledge) adsorption is attained, whence Gibbs' adsorbed layer starts to form. Since the equilibrium crystal slope [Eq. (6)] is inversely proportional to the surface free energy, the presence of inhibitor can produce an increase in slope.

The second possible effect is to hinder dissociation of a lithium-fluoride molecule from a ledge so that the concentration of solute maintained at a kink is reduced. This necessitates the substitution of $C_0' < C_0$[16] in (3) and (6), effectively reducing the undersaturation of the solvent for a given concentration of solute.

The ledge-velocity and crystal-slope relations are

[12] Cabrera and Levine[9] have revalued this relation to $y_0^0 = 19\rho_c$, but the absolute value is not important here.

[13] By edge dislocation we refer to a dislocation with no component of its Burger's vector normal to the surface. Because of line tension, dislocation lines are likely to be normal to the surface, so this use of "edge" dislocation corresponds to the usual definition.

[14] Condition (7) is markedly dependent on the value adopted for γ. The above value was chosen as follows. The only experimental datum for γ (vapor-crystal) is the tentative result of J. J. Gilman (to be published), based on cleavage experiments, indicating that the maximum value of γ (vapor-crystal) is 300 to 400 ergs/cm^2. The experimental value of γ (vapor-liquid) at the melting point is 249 ergs/cm^2 [Jaeger, Z. anorg. und allgem. Chem. **101**, 1 (1917)]. Now it is expected that γ (vapor-crystal) > γ (vapor-liquid) [see A. S. Skapski, Acta Met. **4**, 576 (1956)], so γ (vapor-crystal) is supposed to be bounded by the limits 300 to $400 > \gamma$ (vapor-crystal) ≥ 249 ergs/cm^2.

We have observed experimentally that the contact angle, θ, of water on a freshly cleaved (100) surface of lithium fluoride is $0° < \theta < 10°$ at room temperature. Taking γ (vapor-crystal) $\geq$ 249 ergs/cm^2, one finally obtains γ (crystal-solution) $\geq \gamma$ (vapor-crystal) $-\gamma$ (vapor-water) $\cos 5° = 249 - 72 = 177$ ergs/cm^2.

[15] M. Volmer, *Kinetic der Phasenbildung* (Theodor Steinkopff Verlag, Dresden, 1939).

[16] This is a nonequilibrium condition arising from partial interface control during dissolution. For growth the nonequilibrium condition would be $C_0' > C_0$. In any case C_0' is likely to be a function of C, T, and t. As will be shown later it appears that C_0' is approximately independent of C in the range of C covered in the present experiments.

TABLE I. Part poison, part diffusion-controlled dissolution of lithium fluoride at crystal dislocation sites.

Kinetic relation	Theoretical predictions	Experimental confirmation
(i) $v \propto \tanh[f(y_0)]$	Ledges accelerate at small values of y_0, until maximum, v_∞, is approached (unless ledge spacing at source, y_0°, is less than $6\bar{X}$).	Yes. Observe convex pit profiles (Fig. 4).
(ii) $h/y_0^\circ \neq f(t)$	(a) Eventual attainment of a constant crystal slope at pit source with time, and therefore, (b) linear growth of pit with time.	Yes, at long times. Yes (Fig. 5).
(iii) $v_\infty \propto (C_0'-C)y_0$	$v \to 0$, $y_0 \to \infty$, as $C \to C_0'$, i.e., the inability to produce crystal dissolution when $C \to C_0'$.	Yes, if $C_0' \approx 0.2\ C_0$. (Fig. 6).
(iv) $h/y_0^\circ \propto \ln C_0'/C$	Pit slope at source decreases with decreasing undersaturation of lithium fluoride.	Not observed (Fig. 7).
(v) $h/y_0^\circ \propto 1/\gamma'$	Reduction of surface free energy, γ, by an increase of inhibitor (FeF_3) concentration will produce an increase in the steady-state slope at the pit center.	Yes (Fig. 8), but to a maximum asymptotically.

thereby amended, and will now be represented by the following:

$$\text{Ledge velocity} = v \approx 2\bar{X} \tanh(y_0/2\bar{X}) D\Omega(C_0'-C)/h\delta, \qquad (2')$$

which, in time, approximates to a steady-state value,

$$v_\infty \approx D\Omega(C_0'-C)y_0/3\delta h; \qquad (3')$$

Slope at the pit source, given by

$$h/y_0^0 = hkT \ln(C_0'/C)/4\pi\gamma'\Omega. \qquad (6')$$

With these equations, the dissolution properties of dislocation etch pits may be predicted. Table I summarizes the most significant predictions.

E. Other Considerations

The nucleation conditions, represented by C_n/C_0 and C_{hole}/C_0 will be increased by a reduction of γ because of adsorption of inhibitor. Pit nucleation thereby occurs at a lower undersaturation (higher concentration ratio). Surface (hole) nucleation would then occur at higher lithium-fluoride concentrations and would be responsible for the reduction of $\dot{w}$ at high concentrations. However, the continued etching (5 days) of a specimen in an etchant 20% saturated revealed no measurable dissolution of the {100} crystal surfaces, although etch pits were produced. We may therefore still infer that the surface dissolution by two-dimensional nucleation on close-packed planes occurs at concentrations too small to significantly affect the growth of etch pits in this work.

It is conceivable that a multiple adsorbed layer of ferric fluoride would form on the surface. This could result in a rate-controlling process of diffusion of lithium fluoride through such a layer. However, such a process would predict[3] either a constant pit slope, or a pit slope that increased with increasing distance from the pit center. Neither of these conditions was observed. The determination of ferric-ion adsorption at the lithium fluoride using a radioactive technique has been accomplished and confirms the view that a monolayer, or less, is adsorbed.

Also, one could argue that the concentration of LiF in the solution in the pit would increase as dissolution proceeded. This effect would predict a decrease in pit slope at the pit center as dissolution proceeded, again a situation that was not observed in experiment.

III. EXPERIMENT

A. Experimental Apparatus and Techniques

The Etchant

Gilman, Johnston, and Sears[17] have developed a simple etchant, consisting of a dilute solution of ferric fluoride in distilled water, which produces well-defined etch pits at dislocation-surface intersections on the {100} faces of lithium fluoride. They state that a solution containing 1.2 ppm ferric ion is optimum for producing pits with square surface intersections. In this work the optimum etch, denoted "W_F," was obtained by adding 2.5 ppm ferric ion as ferric fluoride to distilled water which had been slightly acidified to prevent the precipitation of ferric hydroxide. "W_F" was used throughout this work except for the experiments in which ferric-ion concentration was the independent variable.

Varying values of the solubility of lithium fluoride in water are quoted in the standard reference works. The results of Payne[18] were confirmed by the analytical staff of this laboratory, and were adopted for this work. It was also established that the presence of a few ppm of ferric ion did not affect the solubility of lithium fluoride in water.

The temperature of the etchant was maintained to within 0.1°C by immersion in a controlled-temperature

[17] J. J. Gilman, W. G. Johnston, and G. W. Sears, J. Appl. Phys. 29, 747 (1958).
[18] J. H. Payne, J. Am. Chem. Soc. 56, 947 (1937).

FIG. 1. {100} lithium-fluoride surface etched for 10 min in "W_F" etchant 7.5% saturated with lithium fluoride.

stirred water bath. It was found experimentally that the dissolution rate of lithium-fluoride crystals turned in a circle of 3 cm diameter was independent of linear velocity of the crystals in the range around 10 cm/sec, the velocity selected for all the following experiments.

Lithium Fluoride

The etching was performed on the {100} cleavage faces of optical-grade lithium-fluoride crystals, obtained from Taylor, Taylor and Hobson Ltd., England. This hard material is cleaved easily by a sharp steel chisel struck with a light blow. Before cleaving, crystals were lightly deformed to produce a controlled distribution of dislocation sites for subsequent etch-pit formation.

Interferometry

A Zeiss two-beam interference microscope was used to produce monochromatic interference fringes on the surfaces of etched crystals, enabling etch-pit profiles to be directly determined. The comparison mirror was maintained parallel to the surface being examined so that the interference pattern corresponded to a set of undistorted surface contours. Patterns were obtained by illumination with thallium light of 0.54-μ wavelength and were recorded at a magnification of 90× on Eastman Kodak Panatomic—X 35-mm film. A typical interference micrograph is presented in Fig. 1.

The emulsion density as a function of distance across a section of film was measured on a Jarrel-Ash table recording microphotometer linked with a strip-chart recorder, on which fringe spacings could be determined to within 0.15 μ.

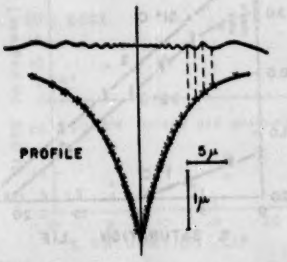

FIG. 2. Microphotometer record of a section of pit "A" in Fig. 1, and the (distorted) pit profile deduced.

Profile Determination

Profiles were directly determined on the same sheet as that on which emulsion density was plotted, as demonstrated on Fig. 2 for the density plot of the fringes on pit "A" in Fig. 1. For convenience the half-wavelength depth shift between successive fringe maxima was plotted as $\frac{1}{2}$ in. in depth on the profile plot, so that the depth magnification was 47 000× and the profile distorted vertically by a factor of 8.25. For deep pits, the fringes could not be clearly resolved over the entire pit. However, the microphotometer was sufficiently sensitive to record some periodic density fluctuation in such cases, e.g., the center of the trace in Fig. 2.

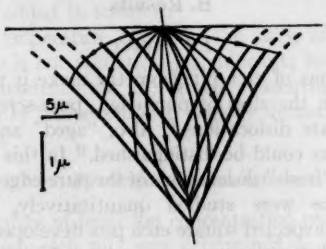

FIG. 3. Successive etch-pit profiles and orientation trajectories for a screw-dislocation etch pit. Profile distorted 8.25× for ease of interpretation.

To obtain a profile history of a particular pit, the profiles at successive etching times were superposed on one drawing. Pits at sites of edge dislocations, which are normal to the crystal surface, were superposed with pit centers aligned normal to the original surface; pits at screw dislocations, which intersect the crystal surfaces at 45°, were superposed with pit centers aligned along a line representing the dislocation line at 45° to the original surface. Orientation trajectories were constructed on the graphs of profile history as shown in Fig. 3.

Some profiles of dissolving crystal edges were also determined interferometrically. Also, pit widths were measured directly in the interference microscope using a micrometer eyepiece.

FIG. 4. {100} lithium-fluoride surface etched in "W_F" etchant (a) for 25 min; (b) for 150 min.

B. Results

Pit Shapes

Variations of etch-pit geometry make it possible to distinguish the sites of pure-edge, pure-screw, and of intermediate dislocations.[17] Also, "aged" and "fresh" dislocations could be distinguished.[17] In this investigation only "fresh" dislocations of the pure-edge and pure-screw type were studied quantitatively. Figure 1 shows the expected square etch pits developed at screw and edge dislocations at short etching times. After very long etching times the pits tended to develop rounded surface intersections as manifested by the bowing out of the fringes in Fig. 4(a). Even after very long etching times, however, asymmetry was maintained at screw-dislocation pit sites [Fig. 4(b)].

Orientation Trajectories

Typical trajectories, developed as outlined above, are shown in Fig. 3 for a screw pit. Edge-pit trajectories were similar in shape. It is apparent that straight-line trajectories are only followed by orientations near the pit edge. A statistical count on 20 pits showed that indeed straight trajectories are obtained near pit edges, and that inner-pit-orientation trajectories are curved. The curved trajectories tend to curve towards the pit center as illustrated by the example in Fig. 3.

Increase of Pit Widths

Pit widths were measured as a function of etching time as illustrated in Fig. 5. Each point on the graph is the average of 10 separate pit-width measurements which had a maximum deviation of ±5%. It can be seen that after long etching times, the velocity of pit widening, $\dot{w}$, was constant, but that initially $\dot{w}$ was greater as indicated by the positive intercepts of all the straight lines.

Each of the lines on Fig. 5 corresponds to one specimen on one etching run. The results show very little deviation at any one temperature, and a decrease in rate with decreasing temperature.

In this manner, values of $\dot{w}$ were obtained for crystals etched in solutions of varying undersaturations of lithium fluoride, and at the three temperatures noted above. For each etchant composition at least three

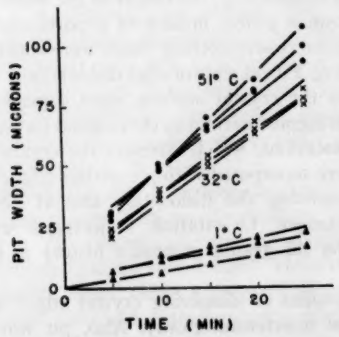

FIG. 5. Mean pit width as a function of total etching time in "W_F" etchant for the three temperatures shown.

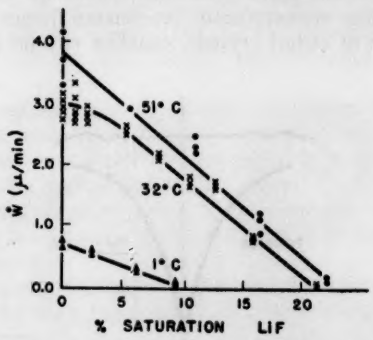

FIG. 6. Mean rate of increase of pit width, $\dot{w}$, as a function of saturation of lithium fluoride in "W_F" etchant at temperatures shown.

specimens were etched in fresh etchant baths, and the resulting $\dot{w}$ values plotted against percentage saturation of lithium fluoride in solution. The results are displayed in Fig. 6, where it is seen that increasing the concentration of fluoride in the etchant linearly reduced the rate of growth of the etch pits, until at approximately 25% saturation the rate was insufficient to produce pits in reasonable times. A sample was stirred in a 30% saturated lithium-fluoride etchant for a total of 21 hr, after which thorough examination revealed no etch pits of any kind, although some dissolution at the crystal edges occurred.

Etch-Pit Slopes

Pit slopes, measured relative to the (100) crystal surface, were determined by direct geometric measurement on the deduced profiles. Specific slope values were obtained at measured distances from the pit center, and also the mean slope of the whole pit was determined.

Each side of a pit at an edge dislocation is at an equal inclination to the surface, and hence the mean slope values could be obtained from any side of a number of such pits. The sides of the asymmetrical screw-dislocation pits, however, are not equally inclined and must be treated individually. In recording the slopes of screw pits, the slope of the steep side and of the shallow side were measured separately. The means of a number of each of the three types of slope were determined to represent the slope values under each set of dissolution conditions. Mean slope of a pit as a whole, and the specific slope at the pit center were both analyzed in this manner.

It was found that the central slope of the etch pits increased with prolonged dissolution, approaching a maximum asymptotically.

The variation of mean slope and of slope at the pit center with concentration of lithium fluoride in the etchant are shown in Fig. 7 for the three types of pit slope at 32°C etchant temperature. Only the points have been placed on the graph. The mean slope values presented in these diagrams were determined at etching times such that pits were of roughly the same width, except in the case of the crystals etched in solutions which produced a very small "$\dot{w}$" value. The graphs

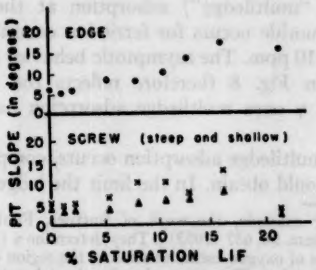

FIG. 7. Mean slope of etch pits as a function of saturation of lithium fluoride in "W_F" etchant after 25 min etching at 32°C.

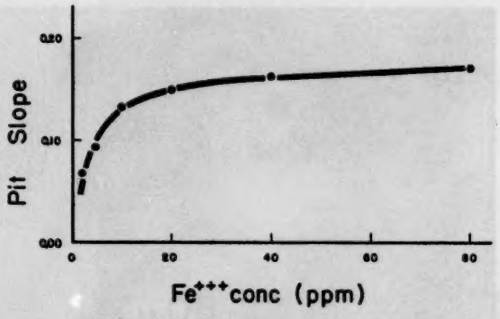

FIG. 8. Effect of Fe^{+++} concentration on the slope at the center of edge dislocation etch pits after 20 min etching at 32°C.

show that at low concentrations, the slope of the etch pits increased with concentration of lithium fluoride in the etchant at a rate which was approximately linear and about one degree of angle for each 30 ppm lithium fluoride added to solution.

The temperature effect on the slope of dislocation etch pits is not statistically significant; however there was a tendency at any given concentration for an increase in temperature to slightly decrease the mean pit slope.

Ferric-Ion Concentration

The effect of ferric-ion concentration on the slope of dislocation etch pits was determined as presented in Fig. 8. It is seen that as the quantity of ferric ion in solution was increased, the pit slope increased until it approached a steady value asymptotically. This maximum slope appears to be approximately 10 deg.

In addition to the effect on the slope values, an increase of ferric ions produced a rounding off of the pits. This is demonstrated by the microphotographs of Fig. 9, which show the shape of typical pits produced by an etchant containing (a) twice, and (b) four times, the optimum ferric-ion concentration.

The growth of the pits, measured in terms of $\dot{w}$, is also modified by excess ferric ions. As the concentration of ferric fluoride in the etchant is increased, the rate of pit growth significantly decreases.

IV. DISCUSSION

The experimental observations are compared with the theoretical predictions in Table I. It is readily seen that the comparison is a good one, but for a few notable exceptions, the most important of which concerns the dependence of pit slope on undersaturation.

To reconcile this it is necessary to invoke the concept of a time dependence in the kinetics of dissolving crystal ledges. In the present dissolution system the steady-state velocity of ledges is controlled by both the diffusion fields and the inhibiting poison. It is clearly conceivable that the latter does not necessarily assert a constant restraint on a particular step as it travels

FIG. 9. Effect of Fe^{+++} concentration on the shapes of etch pits etched at 32°C for 20 min in ferric-fluoride solutions containing (a) twice the optimum concentration of Fe^{+++}; (b) four times the optimum concentration of Fe^{+++}.

outward from the source. For a square (or circular) ledge, the rate of increase of ledge per unit length of the complete ledge is inversely proportional to the width (or radius) of the continuous ledge, $(dl/l)/dr=1/r$.

Therefore, if the rate of poison accumulation from solution (in atoms/cm²/sec) is a constant, there will be a consequent time dependence of adsorption of poison at a ledge. For steps near the dislocation line, the rate of ledge-length increase per unit length is very large, while at large radii this increase is reduced. Therefore it is probable that the poison cannot inhibit each step equally, since there will be some ledges that are increasing in length at too great a rate to allow uniform inhibition, while others are expanding slowly enough for inhibition to be completely effective. Thus as the distance of a ledge from the source increases, the adsorption at the ledge will increase and asymptotically approach a limiting value. Because, as noted above, increasing adsorption decreases γ to γ' and C_0 to C_0', the latter being a less marked effect, this time dependence of adsorption will result in a time dependence in $\gamma'(t)$ and $C_0'(t)$. Hence in Eq. (6′) the slope at the source will be determined by the values at the source $\gamma'(t_0)$ and $C_0'(t_0)$, which do not correspond to the limiting values $\gamma'(t_\infty)$ and $C_0'(t_\infty)$.

Invoking this concept of time dependence, it is possible to rationalize the pit slope vs LiF concentration results. The principal effect of increasing the concentration of lithium fluoride in the etchant is to decrease the dissolution rate by reducing the ledge velocity [Eqs. (2′), (3′)]. So, assuming the inhibitor to be deposited on the surface at a constant rate, the adsorption at the source will be greater at the more slowly moving ledges, $\gamma'(t_0)$ will be less, and the slope [Eq. (6′)] greater. Also, the velocity of a given ledge [Eq. (3′)] will decrease as $C_0'(t_0)$ decreases to $C_0'(t_\infty)$, so that one would expect a concave-orientation trajectory in such a case, as is observed in Fig. 3.

Thus the time dependence of the inhibition at a ledge explains both the dependence of slope on undersaturation and the inapplicability of the topographical theory in the case of dislocation etch pits. Because this time dependence is only a source effect it would be expected that there is no such time dependence for dissolution ledges emanating from crystal edges, where the ledge length remains constant as dissolution proceeds. It has previously been shown[6] that dissolution at crystal edges is in agreement with the Frank topographical theory, consistent with the above model for time-dependent dissolution.

The asymptotic nature of the pit-slope–ferric-ion relation (Fig. 8) is a consequence of the asymptotic nature of interfacial free energy with increasing inhibition. While monolayer (monoledge) adsorption obtains, the decrease of free energy with concentration of inhibiting species should follow the Gibbs adsorption law. This should produce a slope dependence on poison concentration having a continuously positive second derivative, which if pursued to the limit of saturation would produce an infinite slope. However, it has been recognized (although never experimentally substantiated) that the free-energy change will deviate from the Gibbs law at high concentration, and become small once multilayer adsorption takes place.[19] Thus, it is indicated that the onset of multilayer (or more correctly "multiledge") adsorption at the ledges of lithium fluoride occurs for ferric-ion concentrations of from 5 to 10 ppm. The asymptotic behavior of the slope relation in Fig. 8 therefore reflects the asymptotic nature of γ once multiledge adsorption has been attained.

When multiledge adsorption occurs, complete poison control should obtain. In the limit the ledges would be

[19] See, for example, the work of Buttner, Funk, and Udin [J. Phys. Chem. **56**, 657 (1952)]. They determine γ (silver-vapor) as a function of oxygen contamination in the region of monolayer oxygen adsorption. The extrapolated value of oxygen pressure for $\gamma=0$ is about 10 orders of magnitude less than the dissociation pressure for silver oxide where one would expect γ to equal zero.

poisoned immediately as they were emitted at the source. The time dependence of the poisoning would then no longer exist. Ledges would be uniformly controlled by the inhibitor throughout their progress up the pit side, and a constant profile would result. Such limiting behavior is exhibited by the etch pits in Fig. 9(b).

Finally, consider the pit-width rate variation with lithium-fluoride concentration. In the absence of an inhibitor the dissolution rate will decrease linearly with concentration of lithium fluoride down to zero at $C=C_0$, as predicted by Eq. (3). When a poison is present, however, the decrease of step motion produced by the decreased undersaturation of lithium fluoride also leads to a more rapid approach of $C_0'(t)$ to $C_0'(t_\infty)$, as discussed above. In this case, the rate of change of width would decrease linearly and be represented by a line such as the complete line of Fig. 10, which extrapolates to zero growth rate at a concentration $C_0'<C_0$.

Equation (7) suggests that at $C_n \simeq 0.2C_0$, a concentration in the same range as the observed C_0', pit formation will cease completely, or in the case of screw dislocations, pits will become too shallow to observe. Therefore one would suppose that the $\dot{w}$ relation in the region of C_0' would be of the form shown in Fig. 10. This experiment was not sufficiently sensitive to detect any difference between C_0' and C_n. However, the present observations and those of Gilman *et al.*[17] support the view that C_n/C_0 is less than 0.25, because no observable dislocation pits could be produced for concentration ratios greater than 0.25.

V. CONCLUSIONS

Dissolution at dislocation etch pits in lithium fluoride dissolving in a dilute aqueous solution of ferric fluoride did not follow the kinetic laws predicted by the current topographical or mechanistic theories of crystal dissolution. The results were consistent with the mechanistic theory involving dissociation of lithium fluoride from monomolecular steps on lithium fluoride and subsequent diffusion into solution, if a time-dependent adsorption of ferric-fluoride "poison" at the receding monomolecular steps was invoked. Deviations from the topographical dissolution theory of Frank could also be explained by this time-dependent model. The experimental results could only be qualitatively compared with theoretical predictions because of the complexity of the time-dependent dissolution process.

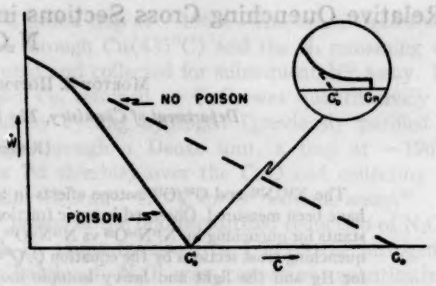

FIG. 10. Theoretical relationship between $\dot{w}$, rate of increase of pit width, and undersaturation with and without the presence of a poison.

VI. ACKNOWLEDGMENTS

This research was sponsored by the U.S. Office of Naval Research. The authors are grateful to Dr. E. S. Hodge of Mellon Institute, Pittsburgh, for the use of the microphotometric measuring equipment.

Relative Quenching Cross Sections in the Reaction of $Hg(6^3P_1)$ Atoms with Isotopic N_2O Molecules*

MORTON Z. HOFFMAN† AND RICHARD B. BERNSTEIN

Department of Chemistry, The University of Michigan, Ann Arbor, Michigan

(Received March 23, 1960)

The N^{14}/N^{15} and O^{16}/O^{18} isotope effects in the $Hg(6^3P_1)$-photosensitized decomposition of nitrous oxide have been measured. Observed isotopic fractionation factors, S^0 (interpreted in terms of ratios of rate constants for quenching by $N^{14}N^{14}O^{16}$ vs $N^{15}N^{14}O^{16}$, $N^{14}N^{15}O^{16}$, and $N^{14}N^{14}O^{18}$), are related to the ratio of isotopic quenching cross sections by the equation $Q/Q^* = S^0(\mu/\mu^*)^{\frac{1}{2}}$, where μ and μ^* are the collisional reduced masses for Hg and the light and heavy isotopic molecules, respectively. The quenching cross section ratio for $N^{14}{}_2O^{16}/N^{14}{}_2O^{18}$ was unity within the experimental uncertainty ($\pm 0.1\%$). The ratios for $N^{14}N^{14}O^{16}/N^{15}N^{14}O^{16}$ and $N^{14}N^{14}O^{16}/N^{14}N^{15}O^{16}$ differed from unity by $+0.98$ and $+0.44\%$, respectively. The order of the quenching cross sections for the isotopic nitrous oxide molecules is thus: $N^{15}N^{14}O^{16} < N^{14}N^{15}O^{16} < N^{14}N^{14}O^{18} \cong N^{14}N^{14}O^{16}$. The implications of the present observations are briefly discussed.

INTRODUCTION

WHEN $Hg(6^3P_1)$ atoms interact with molecules of a foreign gas, a transfer of energy may occur with the return of the Hg atoms to the ground state (6^1S_0) by means of a nonradiative transition. The $(6^3P_1) \rightarrow (6^1S_0)$ fluorescence is thus quenched. The theory[1] of the optical method of measuring effective quenching cross sections is well known.[2] Absolute values of quenching cross sections have been reported[2] but their accuracy is limited, perhaps[3] because of the variations in the optical systems used.

Attempts to correlate quenching cross sections in terms of a mechanism of energy transfer have been rather unsuccessful. Furthermore, the values obtained by the optical method represent effectively the sum of the cross sections for the $(6^3P_1) \rightarrow (6^1S_0)$ and $(6^3P_1) \rightarrow (6^3P_0)$ transitions.[4] If dissociation of the quenching molecule occurs, then the quenching cross section may be deduced by chemical means, thus yielding a value which refers to the $(6^3P_1) \rightarrow (6^1S_0)$ transition alone. Such chemical determinations are difficult, requiring a knowledge of the kinetics of the reaction, evaluation of the rate constant of the quenching step, and from this the effective quenching cross section.[5]

However, the determination of *relative* quenching cross sections may be accomplished more readily. Cline and Forbes[6] measured the rates of reaction of $Hg(6^3P_1)$ with O_2, H_2S, and N_2O and determined their relative quenching efficiencies; unfortunately, the reaction mechanisms were not considered in detail. Cvetanović[7] measured the quantum yield of N_2 and H_2 production for binary mixtures of N_2O and hydrocarbons and obtained quenching cross sections relative to n-C_4H_{10}. He also determined the relative efficiencies of quenching the $Hg(6^3P_1)$ to the ground state and the (6^3P_0) state. Relative quenching cross sections of ethylene oxide,[8] acetaldehyde,[9] and butylene oxide[10] were also measured.

As yet there is no quantitative theoretical interpretation which accounts for these relative values of quenching cross sections. It has been stated[11] "there is no simple way of predicting the efficiency of a physical quenching process, but that a potential-energy surface must be constructed for each case under consideration." This statement, of course, could be extended to "chemical quenching" wherein the quenching molecule dissociates.

In order to aid in the understanding of the energy transfer mechanism, one may consider the relative quenching cross sections of *isotopic* molecules, whose potential energy curves are essentially identical. Such measurements have been reported for H_2–D_2,[12] NH_3–ND_3,[12] H_2O–D_2O,[12] and PH_3–PD_3[13] using the optical technique. The precision of the optical method is insufficient for use with isotopes other than deuterium.

In the present work, the relative quenching cross sections of isotopic N_2O have been measured by chemical means. The isotopic fractionation in the photosensitized decomposition has been measured, from

* The authors appreciate financial support from the U. S. Atomic Energy Commission, Division of Research, and the Michigan Memorial-Phoenix Project.

† Taken from work performed in partial fulfillment of the requirements for the Ph.D. degree of M.Z.H. Receipt of fellowships from the Michigan Memorial-Phoenix Project and the National Science Foundation are gratefully acknowledged.

[1] M. W. Zemansky, Phys. Rev. **36**, 919 (1930).

[2] For a review of the quenching of Hg-resonance radiation, see (a) A. C. G. Mitchell and M. W. Zemansky, *Resonance Radiation and Excited Atoms* (Cambridge University Press, Cambridge, England, 1934); (b) W. A. Noyes, Jr., and P. A. Leighton, *The Photochemistry of Gases* (Reinhold Publishing Corporation, New York, 1941); (c) K. J. Laidler, *The Chemical Kinetics of Excited States* (Clarendon Press, Oxford, England, 1955).

[3] W. A. Noyes, Jr., J. Am. Chem. Soc. **53**, 514 (1931).

[4] B. de B. Darwent and F. G. Hurtubise, J. Chem. Phys. **20**, 1684 (1952).

[5] Footnote reference 2(c), p. 97.

[6] J. E. Cline and G. S. Forbes, J. Am. Chem. Soc. **63**, 2152 (1941).

[7] R. J. Cvetanović, J. Chem. Phys. **23**, 1208 (1955).

[8] R. J. Cvetanović, Can. J. Chem. **33**, 1684 (1955).

[9] R. J. Cvetanović, Can. J. Chem. **34**, 775 (1956).

[10] R. J. Cvetanović and L. C. Doyle, Can. J. Chem. **35**, 605 (1957).

[11] Footnote reference 2(c), p. 106.

[12] M. G. Evans, J. Chem. Phys. **2**, 445 (1934).

[13] H. W. Melville, J. L. Bolland, and H. L. Roxburgh, Proc. Roy. Soc. (London) **A160**, 406 (1937).

which ratios of quenching cross sections for the various isotopic (N^{15} and O^{18}) species of N_2O have been evaluated.

EXPERIMENTAL

Nitrous oxide, containing natural-abundance nitrogen and oxygen isotopes, (Matheson Company, stated purity: >98.0%) was purified by repeated distillations from −160° to −196°C; the middle fractions were collected and stored over mercury at room temperature. The vapor pressure at the triple point and the infrared spectrum agreed well with the literature.[14,15]

For certain experiments dealing with the N^{14}/N^{15} isotope effect, isotopically labeled nitrous oxides were used. They were prepared from the appropriately labeled NH_4NO_3 by thermal decomposition.[16] The N^{15}-labeled ammonium nitrates had been prepared by the reaction of ammonia and nitric acid with subsequent evaporation to dryness and recrystallization from hot water. By using N^{15}-labeled HNO_3, $NH_4N^{15}O_3$ was produced and from it $NN^{15}O$ (sample *A*). By using N^{15}-enriched $(NH_4)_2SO_4$ (liberating the ammonia with NaOH), $N^{15}H_4NO_3$ was produced and from it $N^{15}NO$ (sample *B*). The atom fractions of N^{15} in samples *A* and *B* (as determined mass spectrometrically[17]) were nearly the same (4.3±0.1%).

A conventional vacuum apparatus was used. The reactants were continuously circulated through the illuminated zone (the "reactor") at a rate of 100 to 200 cc/min by a glass circulating pump[18] with a Teflon-covered magnetic bar and by convection using an auxiliary heater. The reactor was constructed of Vycor (type 7910), 30 mm o.d. and 26 mm i.d. Concentric with this tubing was an inner wall (24 mm o.d.). The reaction zone thus consisted of an annulus, 13 cm long with a width of 2 mm. This Vycor is transparent only for λ>2100 A and served as a filter to remove the 1849-A Hg line. Liquid mercury was present in the closed loop through which the gases circulated.

The 2537-A radiation was supplied by a Hanovia Company low-pressure Hg arc (helix). An aluminum reflector was used. The lamp and reaction zone were cooled by a stream of air at 25±3°C. The lamp surrounded the reaction zone with a clearance of 1–2 mm.

The nitrous oxide was metered into the reaction loop and the decomposition followed manometrically for a time (ca 1 hr) corresponding to a small (<0.15) fraction of reaction. The reaction mixture, containing unreacted N_2O, N_2, O_2, and traces of higher oxides of nitrogen,[19] was separated by passage through a trap at −78°C into a trap at −196°C. The volatile gases were cycled through Cu(435°C) and the N_2 remaining was measured and collected for subsequent N^{15} assay. The product O_2, retained as CuO, was quantitatively removed by cycling hydrogen (previously purified by passage through a Deoxo unit, a trap at −196°C, and a Pd thimble) over the CuO and collecting the resulting H_2O at −196°C for O^{18} isotopic assay.[20]

By means of the photosensitized reduction of N_2O in excess H_2 (time required: ca 1 hr),[21] the nitrogen in each batch of N_2O was converted quantitatively (±1%) to N_2 and the oxygen to H_2O, yielding "reference samples" for isotopic analysis.

The mass spectrometer was a Nier-type double-beam isotope-ratio instrument. N^{15} analyses were performed by alternating samples with tank N_2 and recording the ratio of the 29/28 peaks for tank vs sample. During every series a "reference sample" was measured. The isotopic fractionation factor S is defined

$$S=\frac{[(N^{15}N^{14})/(N^{14}N^{14})]_{ref}}{[(N^{15}N^{14})/(N^{14}N^{14})]_{sample}}.$$

The usual small correction of S to zero extent of reaction was made using the standard logarithmic formula[22] $S^0=\ln(1-f)/\ln(1-f/S)$, where f=fraction of substrate reacted. For $f\lesssim 0.1$ (the usual case), the simplified form[22] was used: $S^0-1=(S-1)(1+f/2)$.

The H_2O samples were equilibrated[23] with CO_2 for 3–5 days at 25°C. The CO_2 was freed of H_2O by distillation and collected for O^{18} assay; the mass-spectrometric procedure was similar to that described for N^{15}. The ratio of the 46/44 peaks was measured for CO_2 from the equilibration with H_2O from the decomposition reaction and from the "reference samples," all compared with tank CO_2. From the ratio of $(46/44)_{sample}/(46/44)_{tank}$ for the CO_2 samples, the atom fraction of O^{18} in the "unknown" water was calculated using the simplified form[24] of the Dostrovsky-Klein formula.[25] The O^{18} isotopic fractionation factor, S, is defined $S=(Z_0)_{ref}/(Z_0)_{sample}$ where Z_0 is the atom fraction of O^{18} in the water before equilibration. The usual small correction to zero extent of reaction was applied to this value of S.

RESULTS

The qualitative aspects of the reaction reported by Cvetanović[19] have been confirmed. The ratio of N_2 to O_2 produced was in the range 2.00–2.08 (i.e., a slight deficiency in O_2). Small amounts of HgO, which deposited on the wall of the reactor, were removed before each experiment by flaming. The rate of N_2 production was not consistent, varying over a threefold range;

[14] H. Hoge, J. Research Natl. Bur. Standards **34**, 281 (1945).
[15] G. Herzberg, *Infrared and Raman Spectra* (D. Van Nostrand Company, Inc., Princeton, New Jersey, 1951), p. 277.
[16] L. Friedman and J. Bigeleisen, J. Chem. Phys. **18**, 1325 (1950).
[17] In the case of $NN^{15}O$, for example, the 4.3 at. % N^{15} would be distributed as follows, in terms of all the molecules: $N^{15}NO$=0.4%, $NN^{15}O$=3.9%, and NNO=95.7%.
[18] Adapted from the design of M. M. Benarie, I. Amariglio, and M. Mokady, J. Sci. Instr. **35**, 70 (1958).
[19] R. J. Cvetanović, J. Chem. Phys. **23**, 1203 (1955).
[20] Typical quantities of H_2O obtained were in the range of 6.5–15 mg.
[21] H. A. Taylor and N. Zwiebel, J. Chem. Phys. **14**, 539 (1946).
[22] H. Friedman, R. B. Bernstein, and H. E. Gunning, J. Chem. Phys. **23**, 109 (1955).
[23] M. Cohn and H. C. Urey, J. Am. Chem. Soc. **60**, 679 (1938).
[24] R. B. Bernstein, J. Chem. Phys. **23**, 1797 (1955).
[25] I. Dostrovsky and F. S. Klein, Anal. Chem. **24**, 414 (1952).

TABLE I. Observed isotope effects in the Hg-photosensitized decomposition of N_2O.

Set	Experiment	P_0 (mm Hg)	Isotope fractionation S^0 (N^{14}/N^{15})	Isotope fractionation S^0 (O^{16}/O^{18})
A.	NN*O (4.3 at. % N^{15})	503	1.0134	
		503	1.0153	
		506	1.0133	
			Av 1.0140±0.0009[a]	
B.	N*NO (4.3 at. % N^{15})	299	1.0188	
		304	1.0184	
		322	1.0185	
			Av 1.0186±0.0001[a]	
C.	NNO (natural isotopic abundance: 0.4 at. % N^{15})	224	1.0164	
		230	1.0172	
		243	1.0169	
		310	1.0171	
		312	1.0172	
		325	1.0173	
		595	1.0170	
			Av 1.0170±0.0002[a]	
D.	NNO (natural isotopic abundance: 0.2 at. % O^{18})	237		1.0196
		237		1.0195
		322		1.0187
		322		1.0220
		502		1.0182
		530		1.0192
				Av 1.0195±0.0008[a]

[a] Average deviation from the mean.

this difficulty had been previously noted[19] and had been attributed to a variable decrease in the Hg-vapor concentration (and thus the light absorbed) during the early stages of reaction.

Table I summarizes the isotopic fractionation data at various initial pressures P_0.

DISCUSSION

Cvetanović[19] concluded that the primary step in the quenching of $Hg(6^3P_1)$ atoms (Hg′) to the ground state by N_2O produced N_2+O and that all the product nitrogen was formed in that step. The fate of the O atom was not certain but there was strong indication that atom recombination occurred. The fact that nearly stoichiometric amounts of O_2 are produced and that N_2O is not attacked by O atoms[26] lends strength to this supposition.

The relevant isotopic reactions[27] can be written

1. $Hg'+NNO \rightarrow N_2+O+Hg$
2. $Hg'+N^*NO \rightarrow N^*N+O+Hg$
3. $Hg'+NN^*O \rightarrow NN^*+O+Hg$
4. $Hg'+NNO^* \rightarrow N_2+O^*+Hg$
5. $O+O+M \rightarrow O_2+M$
6. $O^*+O+M \rightarrow O^*O+M.$

[26] G. B. Kistiakowsky and G. G. Volpi, J. Chem. Phys. **27**, 1141 (1957).

[27] The symbols N and N* represent N^{14} and N^{15}, respectively, while O and O* refer, respectively, to O^{16} and O^{18}.

Assuming negligible extent of reaction and tracer isotopic level, the fractionation factors may be related to appropriate ratios of rate constants 1–4, as follows.

The atom fraction of O^{18} in the oxygen atoms produced in steps 1 and 4 is directly measured by the O^{18}-atom fraction in the product O_2 (and thus in the H_2O assayed) so that

$$k_1/k_4 = S_{14}^0 \text{ (for } O^{16}/O^{18}). \qquad (1)$$

Thus from the data of set D in Table I, $k_1/k_4 = 1.0195 \pm 0.0008$.

From the kinetic equations (1–3), the over-all N^{14}/N^{15} isotope effect (corrected to zero extent of reaction), S^0, may be approximated by

$$(S^0-1) = Y(S_{12}^0-1)+(1-Y)(S_{13}^0-1), \qquad (2)$$

where $Y = (N^*NO)/(N^*NO+NN^*O)$; $S_{12}^0 = k_1/k_2$; $S_{13}^0 = k_1/k_3$.

S_{12}^0 and S_{13}^0 represent so-called "intermolecular isotope effects" which refer to the relative probability for rupture of the NN—O bond in a molecule of $N^{14}N^{14}O$ vs a molecule containing an N^{15} atom.

For the N^{15}-labeled nitrous oxides (4.3 at. % N^{15}),[28] using the data of sets A and B (Table I), the simultaneous solution of Eq. (2) yields $S_{12}^0 = 1.0191$ and $S_{13}^0 = 1.0136$.

Using these values in Eq. (2) for N_2O of natural N^{15} abundance (where $Y = 0.5$), a calculated value of $S^0 =$

[28] The value of Y for sample A is: $Y = (0.004)/(0.004+0.039) = 0.093$; for sample B, $Y = (0.039)/(0.039+0.004) = 0.907$.

1.0163 is obtained, which agrees well with the observed value of 1.0170 (set C, Table I).

The isotopic rate-constant ratios thus determined may be related to ratios of isotopic quenching cross sections by the equation[7]

$$q \equiv Q/Q^* = S^0(\mu/\mu^*)^{\frac{1}{2}}, \qquad (3)$$

where Q and Q^* are the isotopic quenching cross sections and S^0 is the appropriate ratio of rate constants; μ and μ^* are the collisional reduced masses for Hg and the light and heavy isotopic molecules, respectively. Table II expresses the results as relative quenching cross sections (q) for the isotopic nitrous oxides.

These results should aid in elucidating the nature of the quenching process. The potential energy diagram of nitrous oxide, formulated[29] on the basis of the uv absorption spectrum, has led to the postulate[19] that the quenching step involves the transfer of 4.86 ev to ground-state N_2O ($^1\Sigma$) to form an electronically excited repulsive state (which could be $^1\Sigma$, $^3\Sigma$, $^1\Pi$, $^1\Delta$, or $^3\Pi$) immediately leading to dissociation. The *over-all* process is thus[19] $Hg(6^3P_1)+N_2O(^1\Sigma)\rightarrow N_2(^1\Sigma)+O(^3P$, or $^1D)+Hg(6^1S_0)$. In addition, the infrared spectra of the N^{15}-labeled nitrous oxides have been measured (and vibrational analyses carried out),[30–32] so that the electronic ground-state vibrational levels for all isotopic modifications are reasonably well known.

An attempt to interpret the order of the isotopic quenching cross sections by analogy with the theory of the isotope effect in photolysis[33] was unsuccessful. Here it was assumed that the transfer of the quantum of energy from the Hg′ to the N_2O results in a vertical electronic transition from the ground-state zero-point level to the upper repulsive state. The observed order of the isotopic cross sections ($N^{14}N^{14}O^{16} \leqq N^{14}N^{14}O^{18} > N^{14}N^{15}O^{16} > N^{15}N^{14}O^{16}$) would thus imply that the zero-point levels were in the same order. This is not in agreement with the order obtained from the calculated[31] zero-order frequencies, $N^{14}N^{14}O^{16} > N^{15}N^{14}O^{16} > N^{14}N^{14}O^{18} > N^{14}N^{15}O^{16}$, nor with that from the contribution to the zero-point energy of the presumably important antisymmetric stretching mode (ω_3): $N^{14}N^{14}O^{16} > N^{14}N^{14}O^{18} > N^{15}N^{14}O^{16} > N^{14}N^{15}O^{16}$.

It is, however, believed that observations on isotope effects in quenching cross sections should serve as valuable constraints in connection with any future theoretical treatment of intermolecular energy transfer in the quenching process.

TABLE II. Relative quenching cross sections (q) for isotopic N_2O molecules.

Isotope effect considered	Isotopic molecules compared	q	Percent isotope effect[a] $100(q-1)$
O^{16}/O^{18}	$\frac{N^{14}N^{14}O^{16}}{N^{14}N^{14}O^{18}}$	1.0011	0.11±0.10
N^{14}/N^{15}	$\frac{N^{14}N^{14}O^{16}}{N^{15}N^{14}O^{16}}$	1.0098	0.98±0.10
	$\frac{N^{14}N^{14}O^{16}}{N^{14}N^{15}O^{16}}$	1.0044	0.44±0.10
	$\frac{N^{14}N^{14}O^{18}}{N^{15}N^{14}O^{16}}$	1.0054	0.54±0.10

[a] The uncertainties listed refer to the over-all estimated probable errors.

ACKNOWLEDGMENT

The authors thank J. N. Doshi for his assistance with the mass spectrometric analyses.

[29] M. Zelikoff, K. Watanabe, and E. C. Y. Inn, J. Chem. Phys. **21**, 1643 (1953).
[30] W. S. Richardson and E. B. Wilson, Jr., J. Chem. Phys. **18**, 694 (1950).
[31] J. Bigeleisen and L. Friedman, J. Chem. Phys. **18**, 1656 (1950).
[32] G. M. Begun and W. H. Fletcher, J. Chem. Phys. **28**, 414 (1958).
[33] A. A. Gordus and R. B. Bernstein, J. Chem. Phys. **30**, 973 (1959).

Heterogeneous Reactions Studied by Mass Spectrometry. I. Reaction of $B_2O_3(s)$ with $H_2O(g)$*

DAVID J. MESCHI, WILLIAM A. CHUPKA, AND JOSEPH BERKOWITZ

Argonne National Laboratory, Lemont, Illinois

(Received December 23, 1959)

Knudsen effusion and mass-spectrometric techniques were employed in studying the gaseous species in thermodynamic equilibrium with condensed boric oxide and water vapor in the temperature range from 1060° to 1450°K. Water vapor was introduced into a Knudsen cell containing B_2O_3, and the vapor effusing from the cell was analyzed mass spectrometrically. The ions H_2O^+, HBO_2^+, $H_3BO_3^+$, and $(HBO_2)_3^+$ were observed. Of the various boron-containing species in equilibrium with the system, the one present in largest amounts was found to be HBO_2. $\Delta H_0°$ for the reaction

$$\tfrac{1}{2}H_2O(g)+\tfrac{1}{2}B_2O_3(s)\rightarrow HBO_2(g)$$

was calculated to be 47.6±2.0 kcal/mole. The data pertaining to the trimer $(HBO_2)_3$ are rather poor, but, in the temperature range covered, its concentration was less than 1% of that of the monomer HBO_2, and at the highest temperature (1450°K) was approximately equal to the concentration of H_3BO_3. A crude calculation of the heat of formation of the trimer by means of the third law gives $\Delta H_0°(f)\approx-540\pm10$ kcal/mole.

INTRODUCTION

SOME years ago Margrave and his co-workers investigated the vaporization of B_2O_3 in the presence of H_2O,[1] and concluded from their data that the vaporization proceeded mainly by means of the reaction: $\frac{1}{2}H_2O(g)+\frac{1}{2}B_2O_3(s \text{ or } l)\rightarrow HBO_2(g)$. This qualitative conclusion was based on the observation that the evaporation rate increased as the square root of the water vapor pressure. In the work presented here, quantitative measurements of the gaseous species involved in the vaporization are in agreement with this conclusion, and permit the calculation of thermodynamic values pertaining to the reaction given above. It was also possible to determine what other species contributed to the vaporization.

The equilibrium vapor from a Knudsen cell was collimated into a molecular beam and allowed to pass through the ionizing region of a mass spectrometer. The ions thus formed were analyzed mass spectrometrically. With B_2O_3 vapor as a standard, the identity and concentration of the vapor species in the cell could then be determined from the relative intensities of the ion currents. Any error introduced in the estimation of the relative ionization cross sections is small enough that it does not seriously affect the accuracy of the derived thermodynamic values. In this method no assumptions regarding the nature of the vaporizing species are required, but it is necessary to assume that the species in the vapor are in equilibrium with each other and with any other phases present. The validity of this assumption can be tested by determining $\Delta H_T°$ for the reaction in question by two independent methods and comparing the values thus obtained. These quantities should, of course, also be in agreement with previously determined values. The data pertaining to the trimer are the least satisfactory in this regard.

EXPERIMENTAL DETAILS

The experimental procedure for studying the H_2O–B_2O_3 system is essentially the same as that described previously,[2] except that the Knudsen cell containing the B_2O_3 was modified to allow the introduction of water vapor from a reservoir outside the mass spectrometer. The modified cell is schematically illustrated in Fig. 1.

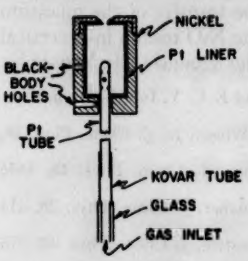

FIG. 1. Gas-inlet Knudsen cell.

The inner liner of the cell is made of platinum as is the vapor introduction tube. The tube was soldered to the liner with palladium, which melts at 1550°C and so set an upper limit to the temperature range covered in the experiment. A Kovar tube fit snugly over the platinum tube and was in turn sealed to a glass tube leading to an exterior vacuum line. Water vapor from a reservoir was introduced into the system through a needle valve, which regulated the rate of flow. The pressure of the water vapor on the mass-spectrometer side of the needle valve was read by means of a small McLeod gauge. The Knudsen cell and ion source of the mass spectrometer were located in separate, differentially pumped chambers. This differential pumping made it

* Work performed under the auspices of the U. S. Atomic Energy Commission. Presented at the American Chemical Society meeting, April 1959, Boston, Massachusetts.

[1] J. L. Margrave, J. Phys. Chem. **60**, 715 (1956).

[2] W. A. Chupka and M. G. Inghram, J. Phys. Chem. **59**, 100 (1955); W. A. Chupka, J. Berkowitz, and C. F. Giese, J. Chem. Phys. **30**, 827 (1959).

possible to introduce noncondensable gases into the Knudsen cell at pressures as high as several mm Hg without exceeding the limit of operating pressure in the ion source region. Temperatures were read by means of a Leeds and Northrup optical pyrometer, and the readings were corrected for emissivity and window transmission.

RESULTS

Preliminary scans of the mass spectrum showed peaks corresponding to the ions H_2O^+, HBO_2^+, $B_2O_3^+$, $H_3BO_3^+$, and $(HBO_2)_3^+$. Intensity measurements of some or all of these peaks were made at ten temperatures between 1061° and 1451°K. The H_2O pressure was varied between 0.05 and 0.14 mm on the McLeod gauge.

Boron has an isotopic constitution of approximately 20% mass 10, and 80% mass 11. Thus, except in the cases of very low intensity, there were several masses from which to choose in making measurements. For HBO_2^+ the mass 43 position was found to be cleaner and freer from residual background than the mass 44 position, and so all the measurements for this species were made at that mass position. For other boron-containing species, the measurements were taken at the mass position corresponding to the most abundant isotopic combination, that is, mass 70 for B_2O_3, mass 132 for $(HBO_2)_3$, and mass 62 for H_3BO_3. In the case of H_2O^+, the trouble encountered was that of too high an intensity rather than discrimination from the background. This difficulty was circumvented by using the mass 20 position, which corresponded to the ion $(H^1_2O^{18})^+$, and which constitutes some 0.204% of the total H_2O^+ current. For each of these ions, the amount actually coming out of the cell was determined by operation of a movable slit plate in a manner previously described.[2]

Throughout these measurements an ionizing potential of 75 v was used. This potential is high enough to cause fragmentation of the molecules, so there was an *a priori* possibility that a substantial portion of the HBO_2^+ ions were coming from the fragmentation of other species, such as the trimer, $(HBO_2)_3$. However, in view of the low intensities of the other ion peaks this is extremely unlikely, and the dependence of the HBO_2^+ ion intensity on the $\frac{1}{2}$ power of the H_2O concentration, rather than the $\frac{3}{2}$ power, makes it effectively impossible. The appearance potential of the HBO_2^+ ion was also measured and found to be 12.6±0.2 v.

The temperatures at which these measurements were made were too low to permit calibration by the effusion of a known quantity of silver in the usual manner.[2] Instead the $B_2O_3^+$ ion intensity was calibrated against the known vapor pressure of B_2O_3 at various temperatures.[3–5] From these calibrations and estimated relative ionization cross sections, the vapor pressures of other vapor species could be calculated from the magnitudes of the corresponding ion currents. The one exception to this was H_2O, which was calibrated independently.

At normal temperatures the water vapor pressure as read on the McLeod gauge is somewhat higher than that in the Knudsen cell because of the flow impedance of the intervening system. However, heating the cell causes a rise in pressure in the cell itself. In the limiting case of very low pressures, for which the mean-free path of the molecules is larger than the dimensions of the apparatus, calculations showed that these two effects would almost cancel at temperatures in the range 1000–1100°C. At the pressures used in these experiments the mean-free paths were actually of the same order as the dimensions of the apparatus or smaller, but the calculations are still a reasonable approximation to the actual state of affairs. It also happens that in the temperature range mentioned only a very small fraction of the water is used up in reactions. Thus, it was possible to calibrate H_2O^+ ion current directly against the McLeod gauge at these lower temperatures and obtain a calibration that could be used to determine the actual H_2O pressure in the cell at higher temperatures. Calibrations of this sort were made at 1141°, 1136°, and 1061°K, with respective H_2O pressures of 0.14, 0.06, and 0.055 mm. The results obtained agreed to within 20%. When the H_2O pressure calculated by this method was checked against pressures obtained from the B_2O calibration as described above, the two agreed to within 20% or so, which is well within the usual estimated error of a factor of two in the relative ionization cross sections for such dissimilar molecules.

The relative ionization cross sections used in these calculations were

$$H_2O: HBO_2: B_2O_3: H_3BO_3: (HBO_2)_3 = 1:2:4:3:6.$$

MONOMER HBO_2

Under the conditions of this experiment the vapor species present in largest amounts were HBO_2 and H_2O. The reaction of greatest interest consequently was

$$\tfrac{1}{2}\,H_2O(g)+\tfrac{1}{2}\,B_2O_3(l)\rightarrow HBO_2(g). \qquad (1)$$

Another reaction of interest is the similar one:

$$\tfrac{1}{2}\,H_2O(g)+\tfrac{1}{2}\,B_2O_3(g)\rightarrow HBO_2(g). \qquad (2)$$

An advantage of this latter reaction is that the equilibrium constant is dimensionless, and so is free from some errors in calibration. As a check on the experimentally determined thermodynamic quantities, the quantities pertaining to reaction (2) can be subtracted from those of reaction (1), whereupon the results should be simply half the enthalpy of sublimation for B_2O_3.

Measured data and calculated quantities pertaining to reactions (1) and (2) are listed in Table I.

The values of $\Delta H_T°$ listed in the table were calculated by means of the relation: $\Delta H° = T\Delta S° + \Delta F°$, where

[3] Soulen, Sthapitanonda, and Margrave, J. Phys. Chem. 59, 132 (1955).
[4] Speiser, Naiditch, and Johnston, J. Am. Chem. Soc. 72, 2578 (1950).
[5] A. W. Searcy and C. E. Myers, J. Phys. Chem. 61, 957 (1957).

TABLE I. B_2O_3—H_2O system.

Temp °K	Relative ion currents Mass 20 H_2O^+	Mass 43 HBO_2^+	Mass 70 $B_2O_3^+$	Log K (1)[a]	Log K (2)[a]	$\Delta H_T°$ (1)[a]	$\Delta H_{298}°$ (1)[a]	$\Delta H_T°$ (2)[a]	$\Delta H_{298}°$ (2)[a]	Relative ion currents Mass 132 $(HBO_2)_3^+$	Mass 62 $H_2BO_3^+$
1061	1.32×10^5	2.78×10^6		−4.146		42.6	47.8				
1141	3.85×10^5	1.99×10^6		−3.509		41.7	47.3				
1184	1.31×10^5	1.96×10^6		−3.273		41.8	47.6				
1214	3.30×10^5	5.28×10^6		−3.038		41.5	47.4			5.84×10^4	
1273	9.9×10^4	5.52×10^6		−2.731		41.5	47.6			2.27×10^4	
1323	1.32×10^5	1.57×10^7	1.61×10^6	−2.378	0.822	40.6	46.9	−1.6	−2.2	1.13×10^5	
1332	3.30×10^5	2.75×10^7	1.80×10^6	−2.238	0.842	40.2	46.2	−1.5	−2.4	2.13×10^5	
1357	4.51×10^4	1.08×10^7	3.68×10^6	−2.277	0.714	41.2	47.5	−0.9	−1.7	5.06×10^4	
1423	1.32×10^5	3.69×10^7		−1.960		40.9	47.5				
1451	2.2×10^4	2.34×10^7	2.25×10^7	−1.803	0.812	40.5	47.2	−1.6	−2.8	1.77×10^5	1.15×10^5

[a] The parenthesized subscript (1) refers to the reaction $\frac{1}{2}H_2O(g)+\frac{1}{2}B_2O_3$(l or s)$\rightarrow HBO_2(g)$; subscript (2) refers to the reaction $\frac{1}{2}H_2O(g)+\frac{1}{2}B_2O_3(g)\rightarrow HBO_2(g)$. Mean value of $\Delta H_{298}°(1)=47.3\pm2$ kcal/mole; $\Delta H_0°(1)=47.6\pm2$ kcal/mole. Mean value of $\Delta H_{298}°(2)=-2.3\pm2$ kcal/mole; $\Delta H_0°(2)=-2.1\pm2$ kcal/mole. $2[\Delta H_0°(1)-\Delta H_0°(2)]=99.4\pm6$ kcal/mole.

$\Delta F°=-RT\ln K$. The entropy change $\Delta S°$ for each of the two reactions was calculated from tabulated values for $H_2O(g)$, $B_2O_3(g)$ and $B_2O_3(l)$ are from Report No. AR-1S-59 of the Dow Chemical Company[6]; those for $HBO_2(g)$ are from White.[7] Because of its use of entropies, this method of calculating $\Delta H_T°$ is usually referred to as the "third law" method.

Values of $\Delta H_{298}°$ were gotten from the $\Delta F_T°$ by use of the free-energy functions, $(F_T°-H_{298}°)/T$. These were taken from the same sources. From the individual values, a mean value of $\Delta H_{298}°$ was calculated, which was corrected to 0°K to give $\Delta H_0°$.

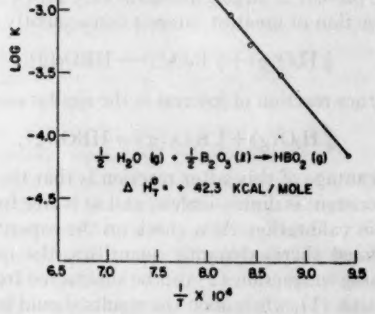

FIG. 2. Plot of log$K$ vs $1/T$ for reaction:

$\frac{1}{2}H_2O(g)+\frac{1}{2}B_2O_3(l)\rightarrow HBO_2(g)$.

As discussed above, twice the difference $[\Delta H_0°(2)-\Delta H_0°(1)]$ should be the heat of sublimation of B_2O_3 at 0°K. This quantity turns out to be 99±6 kcal/mole, as compared with the 94.5±2.0 kcal/mole listed by White.[7]

In Fig. 2, the values of log$K$ for reaction (1) are plotted against $1/T$. As calculated from the slope of the plot by means of the relation $\partial(\ln K)/\partial(1/T)=-\Delta H°/R$, the enthalpy change $\Delta H_T°$ was found to be 42.3±2 kcal/mole, in good agreement with the values of ΔH_T in Table I. This supports the assumption that reactions (1) and (2) are at equilibrium in the cell.

TRIMER $(HBO_2)_3$

The data pertaining to the trimer $(HBO_2)_3$ are considerably cruder than those for the monomer. Ion currents pertaining to this species are also listed in Table I. The ion of mass 132 constitutes 53.54% of the total $(HBO_2)_3^+$ ion current.

A plot of log$K$ vs $1/T$ for the reaction $\frac{3}{2}H_2O(g)+\frac{3}{2}B_2O_3(l)\rightarrow(HBO_2)_3(g)$ shows a slope corresponding to a positive $\Delta H_T°$, whereas third law calculations of this value give a negative value. This discrepancy may arise from lack of equilibrium at lower temperatures, that is, the partial pressure of the trimer may be too low at these temperatures. The most reliable values then would be those calculated by means of the third law from the data taken at the highest temperature.

There is also some error arising from uncertainty in the H_2O pressure, which appears to the $\frac{3}{2}$ power in the expression for K for the reaction given. An alternative reaction $H_3BO_3(g)+B_2O_3(l)\rightarrow(HBO_2)_3(g)$, does not

[6] Dow Chemical Company Rept. No. AR-1S-59, *Thermodynamic Properties of Combustion Products* (April 1, 1959).
[7] David White (private communication).

explicitly depend on the H_2O pressure and so is less likely to be in error. It also has the advantage of avoiding calibration errors, because it is dimensionless and involves only the ratio of ionization cross sections. For these reasons this latter reaction was used for the determination of thermodynamic quantities pertaining to the trimer.

Measurements made at 1451°K, the highest temperature, give a value of $K \approx 0.9$ for this reaction. From this value and tabulated data,[6,7] calculations give $\Delta H_{1451}° \approx -3$ kcal/mole, $\Delta H_{298}° \approx -2$ kcal/mole, and a heat of formation for the trimer: $\Delta H_{298}°(f) = -540 \pm 10$ kcal/mole.

It should be noted that the tabulated thermodynamic quantities used in the calculations are based on a ring structure for the trimer.

CONCLUSION

The main boron-containing gaseous species in equilibrium with $B_2O_3(l)$ and $H_2O(g)$ in the temperature range 1061° to 1451°K was found to be HBO_2. The trimer of this molecule was also present in the vapor to the extent of less than 1%. Measurements pertaining to this trimer, particularly at the lower temperatures, leave much to be desired. Certainly this very interesting species should be investigated more closely.

THE JOURNAL OF CHEMICAL PHYSICS VOLUME 33, NUMBER 2 AUGUST, 1960

Heterogeneous Reactions Studied by Mass Spectrometry. II. Reaction of $Li_2O(s)$ with $H_2O(g)$*

JOSEPH BERKOWITZ, DAVID J. MESCHI, AND WILLIAM A. CHUPKA
Argonne National Laboratory, Lemont, Illinois

(Received December 23, 1959)

The reaction of water vapor with lithium oxide was studied by a mass-spectrometric technique. In the temperature range 1100–1400°K and with water vapor pressures of the order of 0.1 mm, the major reaction product in the vapor phase was LiOH. Smaller amounts of $Li_2(OH)_2$ and traces of $Li_3(OH)_3$ were measured. Various equilibria among the above species were studied with the use of isotopic substitution for lithium and hydrogen. The decomposition of lithium hydroxide was studied in the temperature range 500–600°K. Structural parameters and vibrational frequencies were estimated and thermodynamic functions were calculated for the LiOH and $Li_2(OH)_2$ molecules. The following heats of reaction, which are consistent within experimental error, were then determined:

$Li_2O(s)+H_2O(g) \rightarrow 2LiOH(g)$	$\Delta H_{1200}° = 79.0 \pm 2.0$ kcal
$Li_2O(s)+H_2O(g) \rightarrow Li_2(OH)_2(g)$	$\Delta H_{1250}° = 15.0 \pm 2.0$ kcal
$Li_2(OH)_2(g) \rightarrow 2LiOH(g)$	$\Delta H_{1200}° = 60.0 \pm 3.0$ kcal
$2LiOH(s) \rightarrow Li_2O(s)+H_2O(g)$	$\Delta H_{500}° = 30.4 \pm 1.0$ kcal
$2LiOH(s) \rightarrow Li_2(OH)_2(g)$	$\Delta H_{800}° = 45.0 \pm 3.0$ kcal.

I. INTRODUCTION

THE composition of the vapor phase in equilibrium with a condensed phase of alkali-metal hydroxide has been reported recently by Porter and Schoonmaker.[1a–e] For each of the systems NaOH, KOH, RbOH, and CsOH, mass-spectrometric analysis of the ions formed by electron impact of the vapor molecules produced peaks corresponding to the ions $(M_2OH)^+$, $(MOH)^+$, and M^+, where M is the alkali-metal atom involved. When the same procedure was employed for LiOH, the heating "furnace filaments were attacked and destroyed during outgassing" [1a] and "the background pressure in the vacuum system was too high to permit operation of the mass spectrometer."[1a] Hence, no lithium-hydroxide vapor molecule could be identified in these experiments. The analysis of the other hydroxide molecules was complicated by three factors:

(1) The fragmentation pattern of the molecules $M_2(OH)_2$ (The progenitor of the $[M_2OH]^+$ ion) and MOH was not known accurately.

(2) The activity of the molten alkali hydroxides was evidently reduced by the magnesium-oxide container material.[1b]

(3) The molecular parameters of the molecules involved (moments of inertia, frequencies of vibration) were either unknown or poorly known, making the application of the third law of thermodynamics tenuous.

* Work performed under the auspices of the U. S. Atomic Energy Commission.

[1a] R. C. Schoonmaker and R. F. Porter, J. Chem. Phys. **31**, 830 (1959).

[1b] R. C. Schoonmaker and R. F. Porter, J. Chem. Phys. **28**, 454 (1958).

[1c] R. F. Porter and R. C. Schoonmaker, J. Chem. Phys. **28**, 168 (1958).

[1d] R. F. Porter and R. C. Schoonmaker, J. Phys. Chem. **62**, 486 (1958).

[1e] R. F. Porter and R. C. Schoonmaker, J. Phys. Chem. **62**, 234 (1958).

Porter and Schoonmaker studied the equilibria

$$NaOH(l) \rightarrow NaOH(g) \quad (1)$$

and

$$2NaOH(l) \rightarrow Na_2(OH)_2(g) \quad (2)$$

by observing the change in equilibrium constants for each of the reactions (1) and (2) with changing temperature.[1b] From Clausius-Clapeyron curves they obtained

$$\Delta H_{660°K}° \text{ [reaction (1)]} = 41 \pm 3 \text{ kcal/mole}$$

$$\Delta H_{660°K}° \text{ [reaction (2)]} = 28 \pm 3 \text{ kcal/mole.}$$

Hence, for the reaction

$$2NaOH(g) \rightarrow Na_2(OH)_2(g) \quad (3)$$

they obtained

$$\Delta H_{660}° = -54 \pm 5 \text{ kcal/mole.}$$

By studying the equilibrium constants corresponding to reaction (3) in a mixed hydroxide system, e.g., NaOH–KOH, these authors then obtained differences in dimerization energies of each of the hydroxides KOH, RbOH, and CsOH relative to the "slope" value for NaOH. These results were compared to the corresponding dimerization energies of alkali-halide dimers, specifically alkali-fluoride dimers,[2] and the trends were shown to be similar, i.e., decreasing dimerization energy from the sodium to the cesium compound. The absolute values of all the hydroxide dimerization energies, however, were subject to the error in slope determination for reactions (1) and (2).

The difficulty associated with studying LiOH, as implied by the above authors, was a reaction competitive with reactions of type (1) and (2), for LiOH, i.e.,

$$2LiOH(s) \rightarrow Li_2O(s) + H_2O(g). \quad (4)$$

As a consequence of some modifications in experimental apparatus (to be described below) the present authors considered it feasible to study the $Li_2O(s)$–$H_2O(g)$ system, effectively producing reaction (4) in reverse, but with a reduced partial pressure of H_2O. In this way, it was hoped that: (a) lithium-hydroxide molecular species could be identified in the vapor phase; and (b) thermodynamic data could be obtained for lithium hydroxide independent of information on the other alkali hydroxides.

II. EXPERIMENTAL ARRANGEMENT

Two types of experiments were performed:

(1) Identical in form to the experiments of Porter and Schoonmaker.[1a–e] Lithium hydroxide or deuteroxide is placed in a platinum cell having a 1-mm orifice, the cell placed in a tantalum oven and the assembly heated by radiation from tungsten filaments. The vapor effusing through the orifice is collimated, and the resulting molecular beam is bombarded by a transverse electron beam in an ionization chamber. The ions produced are accelerated, focused, and mass analyzed by a mass spectrometer quite similar to that described by Porter and Schoonmaker.[1a–e] One major improvement, previously described[3] is the separate pumping of the Knudsen-cell chamber and the ionization region which are separated by an adjustable shutter plate. This innovation permitted the mass spectrometer to be operated even with relatively high water vapor pressure in the Knudsen cell and (as will be seen later) made possible a rather crucial experiment.

(2) A platinum cell was designed for introduction of vapor from an external source directly into the cell. The schematic arrangement is described in Fig. 1 of Part I of this series [J. Chem. Phys. **33**, 530 (1960), preceding article]. A conventional gas metering system external to the mass spectrometer culminates in 5-mm glass tubing, which is joined to Kovar metal. The Kovar-metal tubing fits snugly over the platinum tubing which is palladium—soldered to the platinum cell. The tubing system is joined to the mass spectrometer assembly by a Kovar-glass seal.

Most of the experiments were performed with a 1mm orifice in the Knudsen cell. In one experiment, however, the orifice was reduced to 0.3 mm to check the approach to equilibrium.

It was found convenient at various times to use the following isotopic species:

LiOH	(normal isotopic composition)
Li^6OD	($Li^6/Li^7 \cong 12.5$; D/H$\sim$5)
Li_2^6O	($Li^6/Li^7 \cong 12.5$)
H_2O	(normal isotopic composition)
D_2O	(D/H$\sim$5).

Temperature was measured by a Leeds and Northrup optical pyrometer for $T \sim 1000°C$, and with a Pt–Pt, 10% Rh thermocouple for $T \sim 300°C$.

III. EXPERIMENTAL DATA

The chronological sequence of experiments will be presented below:

1. $Li_2^6O + H_2O$

Several experiments were performed with these components, following method (2) of the section on experimental arrangements. A typical mass spectrum obtained at $T = 1350°K$ and a partial pressure of H_2O equal to 0.16 mm Hg is shown in Table I. It should be noted that the magnitude of the H_2O ion peak was monitored on mass 20, corresponding to $(H_2O^{18})^+$, because the mass 18 peak was too intense for the electron multiplier detector system.

[2] R. C. Schoonmaker and R. F. Porter, J. Chem. Phys. **30**, 283 (1959).

[3] W. A. Chupka, J. Berkowitz, and C. F. Giese, J. Chem. Phys. **30**, 827 (1959).

TABLE I. Mass spectrum of $Li_2^6O(s)-H_2O(g)$ experiment.

$T=1350°K$ Identification	$P_{H_2O}=0.16$ mm Hg Mass	Ionizing-electron energy = 75 ev Ion intensity (arbitrary units)
H_2O^{18}	20	1.76×10^5
Li^6OH	23	9.18×10^7
Li_2^6OH	29	2.42×10^6
$Li_2^6(OH)_2$	52	6.6×10^4
Li^6	6	2.47×10^6

TABLE II. Mass spectrum of $Li_2^6O(s)-D_2O$ experiment.

$T=1220°K$ Identification	$P_{D_2O}=0.13$ mm Hg Mass	Ionizing-electron energy = 75 ev Ion intensity (arbitrary units)
D_2O	20	6.86×10^7
Li^6OD	24	2.40×10^7
Li_2^6OD	30	1.40×10^6
$Li_2^6(OD)_2$	54	3.96×10^5

Figure 1 is a graph of $\log_{10}K$ vs $1/T$ for the reaction

$$Li_2O(s)+H_2O(g)\rightarrow 2LiOH(g).$$

The partial pressure of H_2O was maintained at 0.04 mm Hg for one set of experiments, and 0.16 mm Hg for the other. The slopes of the individual lines yield

$$\Delta H_{1300°K}^\circ = 79\pm3 \text{ kcal/mole and}$$

$$\Delta H_{1200°K}^\circ = 77\pm3 \text{ kcal/mole}$$

for 0.04 mm Hg and 0.16 mm Hg experiments, respectively.

2. $Li_2^6O+D_2O$

Heavy water was introduced as a reactant partially to check the mass assignments, and partially to shift the important peaks to more convenient masses. $(LiOH)^+$, which previously might have been confused with an Na^+ impurity, was now definitely established. $(Li_2OH)^+$ was shifted from mass 29 (which normally has a fairly high background due to residual gas) to mass 30, permitting greater accuracy of measurement. A similar adjustment holds for the shift of $(H_2O)^+$ from mass 18 to mass 20. A typical mass spectrum for this experiment, corresponding to $T=1220°K$ and $P_{D_2O}=0.13$ mm Hg, is reproduced in Table II.

As mentioned above, the D_2O experiment permitted more accurate measurement of the ion peak attributable to dimer, i.e., $(Li_2OH)^+$ vs $(Li_2OD)^+$. Hence, this experiment has been chosen to present graphs involving dimer formation. In Fig. 2, $\log K$ vs $1/T$ is plotted for

$$Li_2O(s)+D_2O(g)\rightarrow Li_2(OD)_2(g).$$

The slope of this curve corresponds to

$$\Delta H_{1250°K}^\circ = 14\pm2 \text{ kcal/mole.}$$

In Fig. 3, $\log K$ vs $1/T$ is plotted for

$$Li_2(OD)_2(g)\rightarrow 2LiOD(g).$$

The slope of the line yields

$$\Delta H_{1300°K}^\circ = 58\pm3 \text{ kcal/mole.}$$

This latter reaction was examined exhaustively for both the H_2O and D_2O experiments. The absolute equilibrium constants, (see experiment 3 below) temperatures and experimental conditions are summarized for this reaction, as well as two others, in Tables III–V.

3. $Li_2^6O+D_2O$

Orifice area reduced by a factor of 1/10

Because it was felt that a gas-introduction experiment might not attain equilibrium readily, the approach to equilibrium was examined by changing the ratio of effusion area to reaction area by a factor of 10. Under these conditions, no dimer molecule could be observed, and in general the ion intensities were reduced relative to background. However, the $(D_2O)^+$ and $(LiOD)^+$ ion peaks could be measured. As a typical result, corresponding to $T=1240°K$, $P_{D_2O}=0.16$ mm Hg, one obtains the results shown in Table VI.

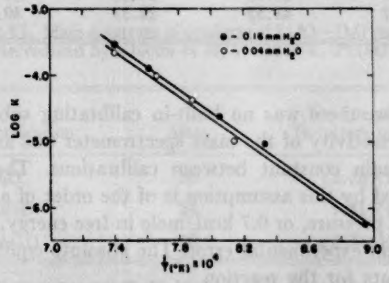

FIG. 1. Plot of $\log K$ vs $1/T$ for the reaction $Li_2O(s)+H_2O(g)\rightarrow 2LiOH(g)$.

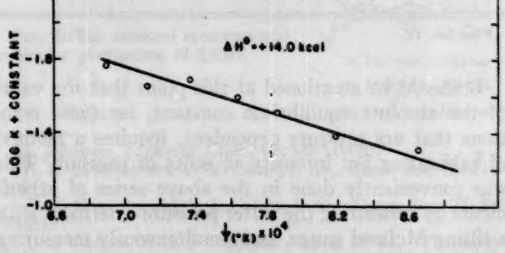

FIG. 2. Plot of $\log K$+constant vs $1/T$ for the reaction $Li_2O(s)+D_2O(g)\rightarrow Li_2(OD)_2(g)$.

TABLE III. Equilibrium constants and derived thermodynamic quantities[a] for the reaction $Li_2(OH)_2(g) \rightarrow 2\,LiOH(g)$.

T°K	$P(H_2O)$ mm Hg	K_{eq} atm^{-1}	log K	ΔF_T° kcal	$T\Delta S_T^\circ$ kcal	ΔH_T kcal	$-(\Delta F_T^\circ - \Delta H_0^\circ)$ kcal	ΔH_0 kcal
1350	0.16	108.2	2.03423	12.561	51.651	64.212	52.576	65.137
1306	0.16	255	2.40654	14.376	50.137	64.513	50.892	65.278
1270	0.16	467	2.66932	15.506	48.857	64.363	49.505	65.011
1226	0.16	1432	3.15594	17.698	47.324	65.022	47.814	65.512
1152	0.16	6610	3.82020	20.129	44.698	64.827	44.953	65.082
1119	0.04	11530	4.06183	20.790	43.518	64.308	43.675	64.465
1241	0.04	695	2.84198	16.132	47.841	63.973	48.387	64.519
1314	0.04	316	2.49969	15.024	50.392	65.416	51.193	66.217
1182	0.04	1863	3.27021	17.680	45.755	63.435	46.117	63.797
1352	0.04	248	2.39445	14.808	51.278	66.536	52.647	67.455
1154	0.05 (D_2O)	3200	3.5051	18.50	44.77	63.27	45.03	63.53
1221	0.05 (D_2O)	827	2.9175	16.29	47.13	63.42	47.62	63.91
1274	0.05 (D_2O)	328	2.5159	14.66	48.99	63.65	49.66	64.32
1310	0.05 (D_2O)	140	2.1461	12.86	50.25	63.11	51.04	63.90
1357	0.05 (D_2O)	71.7	1.8555	11.52	51.92	63.44	52.84	64.36
1403	0.05 (D_2O)	32.5	1.5119	9.70	53.50	63.20	54.62	64.32
1448	0.05 (D_2O)	22.4	1.3502	8.94	55.02	63.96	56.33	65.27
1394	0.022 (D_2O)	60.5	1.7818	11.36	53.17	64.53	54.27	65.63
1410	0.110 (D_2O)	38.2	1.5821	10.20	53.76	63.96	54.88	65.08

[a] See Sec. IV.

TABLE IV. Equilibrium constants and derived thermodynamic quantities[a] for the reaction: $Li_2O(s) + H_2O(g) \rightarrow 2LiOH(g)$.

T°K	K_{eq} atm	log K	ΔF_T°	ΔS_T°	$T\Delta S_T^\circ$	ΔH_T	Remarks
1350	2.21×10^{-4}	−3.656	+22.55	+43.40	58.50	81.05	Used H_2O
1306	9.73×10^{-5}	−4.012	23.95	43.66	57.00	80.95	Used H_2O
1270	4.14×10^{-5}	−4.382	25.45	43.87	55.60	81.05	Used H_2O
1226	1.0×10^{-5}	−5.000	28.00	44.13	54.10	82.10	Used H_2O
1152	1.48×10^{-6}	−5.829	30.75	44.67	51.50	82.25	Used H_2O
1119	5.70×10^{-7}	−6.244	31.95	44.90	50.30	82.25	Used H_2O
1241	2.37×10^{-5}	−4.626	26.25	44.04	54.55	80.80	Used H_2O
1314	1.25×10^{-4}	−3.902	23.45	43.62	57.30	80.75	Used H_2O
1182	7.32×10^{-6}	−5.135	27.75	44.43	52.50	80.25	Used H_2O
1352	2.83×10^{-4}	−3.548	21.95	43.39	58.50	80.45	Used H_2O
1154	3.78×10^{-6}	−5.4225	28.65	44.64	51.60	80.25	Used H_2O
1221	2.6×10^{-5}	−4.585	25.60	44.16	53.90	79.50	Used H_2O
1274	9.21×10^{-5}	−4.036	23.52	43.85	55.85	79.37	Used H_2O
1310	2.29×10^{-4}	−3.640	21.80	43.64	57.10	78.90	Used H_2O
1357	6.66×10^{-4}	−3.177	19.70	43.36	58.75	78.45	Used H_2O
1403	1.30×10^{-3}	−2.886	18.57	43.09	60.45	79.02	Used H_2O
1448	2.38×10^{-3}	−2.623	17.38	42.85	61.95	79.33	Used H_2O
1240	2.3×10^{-5}	−4.638	26.30	44.05	54.55	80.85	Decreased orifice by 1/10

[a] See Sec. IV.

TABLE V. Equilibrium constants and derived thermodynamic quantities[a] for the reaction: $2LiOD(s) \rightarrow Li_2(OD)_2(g)$.

T°K	K atm	log K	ΔF_T°	ΔH_T	$T\Delta S_T^\circ$	ΔS_T°
598.0	5.99×10^{-9}	−8.22257	22.50	45.90	23.40	39.141
559.5	5.18×10^{-9}	−8.28567	21.22	43.55	22.33	39.855

[a] See Sec. IV.

It should be mentioned at this point that the value of the absolute equilibrium constant, for those reactions that are pressure dependent, requires a method of calibrating ion intensity in units of pressure. This was conveniently done in the above series of experiments by measuring the water pressure externally with a tilting McLeod gauge, and simultaneously measuring the intensity of the appropriate ion peak corresponding to $(H_2O)^+$ or $(D_2O)^+$. However, in experiments 4 and 5 below, there was no built-in calibrating substance. The sensitivity of the mass spectrometer was assumed to remain constant between calibrations. The error incurred by this assumption is of the order of a factor of 2 in pressure, or 0.7 kcal/mole in free energy, which is within experimental error. The absolute equilibrium constants for the reaction

$$Li_2{}^6O(s) + D_2O(g) \rightarrow 2LiOD(g)$$

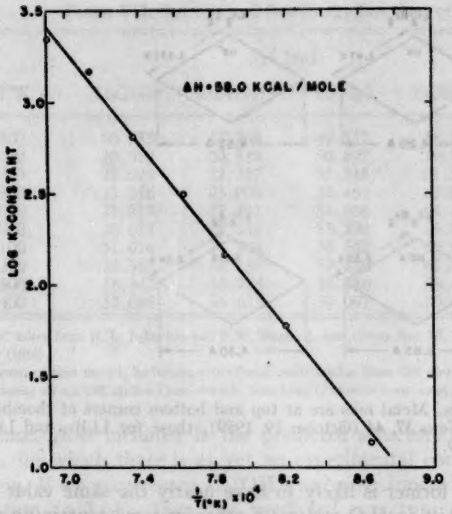

FIG. 3. Plot of $\log K$+constant vs $1/T$ for the reaction $Li_2(OD)_2(g) \rightarrow 2LiOD(g)$.

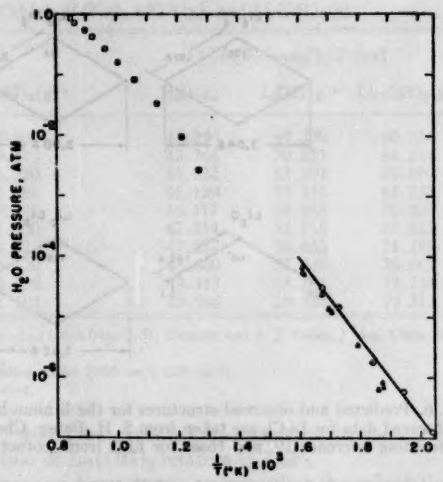

FIG. 4. Plot of $\log K$ vs $1/T$ for the reaction $2LiOH(s) \rightarrow Li_2O(s)+D_2O(g)$ including the following data: △—Gregory and Mohr; □—Johnston; ○—present work.

using the two orifice sizes (i.e., orifice diameters of 1 and 0.3 mm, respectively) were

$$K_{1211°K} = 2.6\times10^{-6} \text{ atm} \qquad (\text{diam} = 1.0 \text{ mm})$$

$$K_{1240°K} = 2.3\times10^{-6} \text{ atm} \qquad (\text{diam} = 0.3 \text{ mm})$$

and for the corresponding reaction using H_2O instead of D_2O,

$$K_{1241°K} = 2.37\times10^{-6} \text{ atm}.$$

4. $2LiOH(s) \rightarrow Li_2O(s)+H_2O(g)$

The background intensity at masses 18 and 29 nullified this experiment.

5(a). $2Li^6OD(s) \rightarrow Li_2{}^6O(s)+D_2O(g)$

(b). $2Li^6OD(s) \rightarrow Li_2(OD)_2(g)$

The shifting of the mass peaks made possible by substitution of the deuterium isotope enabled both these experiments to be performed. The variation of $\log K$ with $1/T$ for experiment 5(a) is shown in Fig. 4, together with the results of Gregory and Mohr[4] and Johnston.[5] From the current data, the slope yields

$$\Delta H_{600}° = 30.4\pm1 \text{ kcal/mole for 5(a)}.$$

For the reaction of 5(b) only a few experimental points could be taken, corresponding to the highest temperature attainable without excessive water volatilization. At 598°K, the equilibrium constant for reaction of 5(b) was equal to 5.99×10^{-9} atm.

TABLE VI. Mass spectrum of products of $Li_2{}^6O$—D_2O reactions, orifice area reduced by a factor of 10, $T = 1240°K$, $P(D_2O) = 0.16$ mm Hg.

Identification	Mass	Ion intensity (arbitrary units)
D_2O	20	2.58×10^{5}
LiOD	24	1.31×10^{5}
Li_2OD	30	$<5.5\times10^{4}$

[4] N. W. Gregory and R. H. Mohr, J. Am. Chem. Soc. 77, 2142 (1955).

IV. CALCULATIONS

In order to employ the third law of thermodynamics in the analysis of the above results, entropy and free-energy functions must be obtained for the pertinent reactants and products, i.e., $Li_2O(s)$, $LiOH(s)$, $H_2O(g)$, $LiOH(g)$, and $Li_2(OH)_2(g)$. The first three present little difficulty. Johnston and Bauer[6] have reported the standard entropy of $Li_2O(s)$ and $LiOH(s)$ at $T = 298°K$. Shomate and Cohen[7] have obtained $S_T - S_{298}$ for these same species. For $H_2O(g)$ we may employ various sources, of which one of the most recent is the tabulation of Gordon.[8]

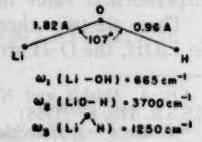

FIG. 5. The assumed structure and molecular parameters of LiOH.

[5] J. Johnston, Z. physik. Chem. 62, 330 (1908).
[6] H. L. Johnston and T. W. Bauer, J. Am. Chem. Soc. 73, 1119 (1951).
[7] C. H. Shomate and A. J. Cohen, J. Am. Chem. Soc. 77, 285 (1955).
[8] J. S. Gordon, WADC Technical Report 57-33, "Thermodynamics of high-temperature gas mixtures and application to combustion problems," Wright Air Development Center (1957).

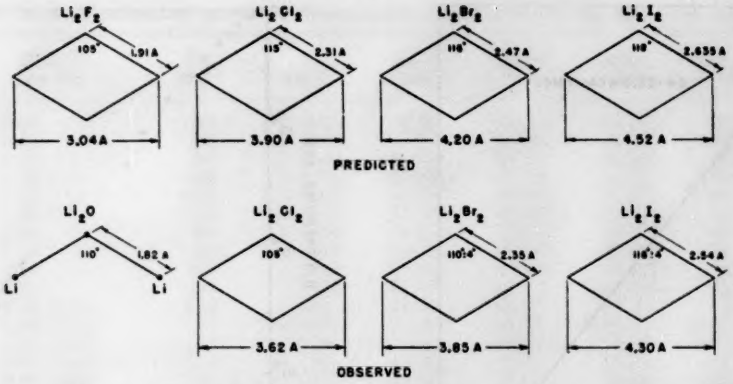

FIG. 6. Predicted and observed structures for the lithium-halide dimers. Metal ions are at top and bottom corners of rhombus. The observed data for Li_2Cl_2 are taken from S. H. Bauer, Chem. Engr. News 37, 44 (October 19, 1959), those for Li_2Br_2 and Li_2I_2 from footnote reference 19, and those for Li_2O from footnote reference 9.

In evaluating $S_T°$ and $-(F_T°-E_0°)/T$ for LiOH(g), it was recognized that H_2O has a bent structure with bond angle of approximately 105°, and Li_2O(g) was also recently shown to have a bent structure,[9] with bond angle of ca 110°. The Li—O bond distance was taken as that reported by electron-diffraction experiments[9] on Li_2O, (1.82 A), and the O—H bond length to be that in H_2O (0.96 A).[10] For the estimate of vibrational frequencies of LiOH(g), as well as $Li_2(OH)_2$, the analogy of gaseous hydroxides to gaseous-alkali halides is invoked. The experiments of Porter and Schoonmaker[1a,2] and Spinar,[11] point up the similarity between alkali fluorides, in particular, and alkali hydroxide. Until recently, no experimental results were available for the vibration frequency of LiF or the corresponding mode in LiOH. Vidale[12] has now obtained the infrared spectrum of LiF, and reports $\omega_e=906.2\pm1.5$ cm^{-1} and $r_e=1.545\pm0.006$ A. Ionic-model calculations, which have been shown to be generally adequate for predicting the vibration frequency of diatomic-alkali halides,[13,14] predict a frequently of 650–750 cm^{-1} for LiF. Since the internuclear distance Li–O in LiOH is likely to be larger than that observed in LiF, the vibration frequency predicted by ionic-model calculations is believed to be a closer approximation to the Li–OH stretch than the observed experimental value for LiF.

There are two other vibration frequencies to consider in LiOH, the O–H stretch and Li–O–H bending mode. The former is likely to have nearly the same value it exhibits in H_2O and most other systems containing an O–H group, i.e., approximately 3700 cm^{-1}.[15] The H–O–H bending motion in H_2O has a frequency of 1654 cm^{-1}, that in D_2O is 1210 cm^{-1}.[16] The motion corresponds to two protons (or two deuterons) vibrating against one another, with little motion on the part of the oxygen. The force constant for this bending motion is rather similar, for as diverse a pair of compounds as H_2O and F_2O.[17] The difference in frequency between H_2O and D_2O is almost entirely a reduced mass effect. If we assume a similar situation to hold for the LiOH bond, we obtain

$$\omega_{Li-O-H}/\omega_{H-O-H}=M_{H+}M_{Li}/2M_{Li},$$

and

$$\omega_{Li-O-H}\cong1250\text{ cm}^{-1}.$$

The results of these considerations are summarized in Fig. 5.

With $Li_2(OH)_2$(g) the arguments must be multiplied manyfold. At the outset one is faced with the problem of choosing a molecular configuration. If we again appeal to the apparent similarity of alkali halides and hydroxides in forming dimeric species, we might get some clue by comparison with known alkali-halide dimer structures. Until recently, these were only calculations based on an ionic model.[14,18] Now, however, electron-diffraction experiments from two independent sources[19,20] tend to verify the structure predictions. In Fig. 6, the predicted structures of Li_2Cl_2, Li_2Br_2, and Li_2I_2 are compared with the available experimental

[9] P. A. Akishin and N. G. Rambidi, Doklady Akad. Nauk S.S.S.R. 118, 83 (1958).
[10] G. Herzberg, *Molecular Spectra and Molecular Structure. II. Infrared and Raman Spectra* (D. Van Nostrand Company, Inc., Princeton, New Jersey), p. 489.
[11] L. H. Spinar, thesis, "Vaporization of alkali metal hydroxides," University of Wisconsin, Department of Chemistry, 1958, p. 45.
[12] G. Vidale, General Electric Technical Information Series No. R59SD359, Aerophysics Research Memo No. 32, Aerosciences Laboratory, 3750 "D" Street, Philadelphia, Pennsylvania.
[13] E. S. Rittner, J. Chem. Phys. 19, 1030 (1951).
[14] J. Berkowitz, J. Chem. Phys. 29, 1386 (1958).
[15] Footnote reference 10, p. 161.
[16] G. Gompertz and W. J. Orville-Thomas, J. Phys. Chem. 63, 1331 (1959).
[17] Footnote reference 10, pp. 170, 187.
[18] C. T. O'Konski and W. I. Higuchi, J. Chem. Phys. 23, 1175 (1955).
[19] P. A. Akishin and N. G. Rambidi, Vestnik Moskov. Univ. Ser. Mat. Mekh. Astron. Fiz. i Khim. 13, No. 6, 223–30 (1958).
[20] S. H. Bauer, Chem. Eng. News 37, 44 (October 19, 1959).

TABLE VII. Entropy and free-energy functions of $Li_2O(s)$, $LiOH(s)$, $H_2O(g)$, $LiOH(g)$, and $Li_2(OH)_2(g)$.

	$S_T°$ (eu)					$-(F_T°-E_0°)/T$ (eu)		
T°K	$Li_2O(s)$[a]	$LiOH(s)$[a]	$H_2O(g)$	$LiOH(g)$[b]	$Li_2(OH)_2(g)$[c]	$H_2O(g)$	$LiOH(g)$[b]	$Li_2(OH)_2(g)$[c]
500	16.785	17.268	49.332	58.540	75.105	41.290	49.220	60.234
600	20.010	20.139	50.892	59.949	79.419	42.764	50.873	63.254
700	22.699	22.727	52.248	61.599	83.070	44.024	52.302	65.899
800	25.218	25.098	53.462	63.062	86.284	45.129	53.558	68.232
900	27.513	27.297	54.568	64.371	89.221	46.117	54.688	70.405
1000	29.673	29.357	55.590	65.559	91.900	47.014	55.718	72.423
1100	31.676	31.304	56.542	66.641	94.329	47.837	56.662	74.289
1200	33.561	33.157	57.438	67.639	96.620	48.600	57.537	76.063
1300	35.347	34.928	58.286	68.664	98.938	49.313	58.351	77.734
1400	37.048	36.632	59.091	69.620	101.105	49.984	59.121	79.313

[a] $S_{298}°$ taken from H. L. Johnston and T. W. Bauer, J. Am. Chem. Soc. 73, 1119 (1951). S_T-S_{298} taken from C. H. Shomate and A. J. Cohen, J. Am. Chem. Soc. 77, 285 (1955).

[b] Assuming bent model, including vibrational contribution from OH stretching and bending modes (3700 cm^{-1}, 1250 cm^{-1}).

[c] Includes all six OH modes (two stretch, four bend); assume *trans* configuration, i.e., $\sigma=2$.

evidence. Also included is the predicted structure of Li_2F_2, for which there is as yet no experimental comparison. If we may regard $Li_2(OH)_2$ as being similar in structure to Li_2F_2, then the predicted structure of Li_2F_2 may serve as a basis. The predicted Li—F bond length in the dimer is 1.91 A. The experimental Li—O bond length in Li_2O is 1.82 A. Comparison of alkali-halide bond lengths in going from monomer to dimer shows ca 10% stretching. In this instance, we choose Li–O≅1.90 A. The O–Li–O angle, if analogous to the F–Li–F angle, would be expected to be less than 105°, since the experimental trend from Li_2F_2, Li_2Br_2, Li_2Cl_2 is 116°, 110°, and 105°. It would seem reasonable to choose O–Li–O≅100°. This leaves undetermined the position of the protons. If they are symmetrically placed above and below the plane of the rhombus, or if they extend away from the plane along the line connecting the oxygen nuclei, the symmetry number of the resultant molecule in phase space is 4. If, on the other hand, the protons assume a *trans* configuration above and below the plane, the symmetry number is 2. In this instance it is difficult to find a convincing argument in favor of either configuration. The subsequent analysis assumes the transconfiguration, recognizing that an uncertainty of $R\ln 2$ has been incorporated in the calculations.

In order to estimate the vibrational contribution, one again appeals to the similarity between alkali fluorides and hydroxides. The A_g', B_{2u}, and B_{3u} vibrational frequencies for Li_2F_2 were estimated by Berkowitz[14] using an ionic model and normal coordinate analysis. Subsequently[21] the A_g, B_{1g} and B_{1u} modes have also been estimated on this basis. These calculated frequencies have been applied directly to the $Li_2(OH)_2$ molecule. If, for the moment, the OH radical is considered a mass point, then there is no mass correction in going from Li_2F_2 to $Li_2(OH_2)$. Also, the available evidence indicates that: (1) the calculated frequencies for alkali fluorides are somewhat smaller than experimentally observed; and (2) the bulkier OH, substituted for F, would be expected to lower the frequencies of vibration of $Li_2(OH)_2$ relative to Li_2F_2.

Hence, we have reason to hope that the calculations of dimer frequencies for Li_2F_2 may be more accurately applied to $Li_2(OH)_2$.

One must now take account of the proton vibrations by adding 2 O–H stretches and 4 O–H bends to the dimer vibrations. A summary of the assumed molecular configuration and vibrational frequencies of $Li_2(OH)_2$ is shown in Fig. 7. In Table VII, the thermodynamic functions of the species considered in this section have been tabulated. In addition to the assumptions described in this section, the harmonic oscillator-rigid rotor approximation has also been employed.

V. CONCLUSIONS

We assume in the tabulation below that the difference of reaction energy for hydrogen- and deuterium-bearing molecules is within the experimental error.

Slope Measurements

$$Li_2O(s)+H_2O(g)\rightarrow 2LiOH(g)$$
$$\Delta H_{1300}°=78\pm 3 \text{ kcal/mole}$$

$$Li_2O(s)+H_2O(g)\rightarrow Li_2(OH)_2(g)$$
$$\Delta H_{1250}°=14\pm 2 \text{ kcal/mole}$$

$$Li_2(OH)_2(g)\rightarrow 2LiOH(g)$$
$$\Delta H_{1300}°=58\pm 3 \text{ kcal/mole}$$

$$2LiOH(s)\rightarrow Li_2O(s)+H_2O(g)$$
$$\Delta H_{500}°=30.4\pm 1 \text{ kcal/mole}$$

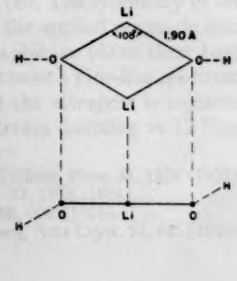

FIG. 7. The assumed structure and molecular parameters of $Li_2(OH)_2$. The vibrational frequencies were estimated to be (in cm^{-1}) 465, 365, 407, 385, 441, 448, 3700(2), 1250(4). The first six frequencies were taken to be equal to those for Li_2F_2 (footnote reference 21). The latter two are the O—H stretching and bending frequencies as explained in Sec. IV.

[21] J. Berkowitz, J. Chem. Phys. (to be published).

Absolute Pressure and Third Law Calculations

$Li_2O(s)+H_2O(g)\rightarrow 2LiOH(g)$

$\Delta H_{1300}^\circ = 80\pm 2$ kcal/mole

$Li_2O(s)+H_2O(g)\rightarrow Li_2(OH)_2(g)$

$\Delta H_{1500}^\circ = 16\pm 4$ kcal/mole

$Li_2(OH)_2(g)\rightarrow 2LiOH(g)$

$\Delta H_{1300}^\circ = 64\pm 4$ kcal/mole

$2LiOH(s)\rightarrow Li_2(OH)_2(g)$

$\Delta H_{600}^\circ = 45\pm 3$ kcal/mole

VI. DISCUSSION

The experimental results presented have evidently proven the existence of lithium-hydroxide molecules. From Tables I and II it may be deduced that ions were produced from LiOH, $Li_2(OH)_2$, and $Li_3(OH)_3$ molecules by the processes:

(a) $LiOH+e\rightarrow(LiOH)^++2e$

(b) $Li_2(OH)_2+e\rightarrow(Li_2OH)^++OH+2e$

(c) $Li_3(OH)_3+e\rightarrow Li_3(OH)_2^++OH+2e$.

Appearance-potential measurements and pressure and temperature variation have all tended to confirm these assignments.

The thermodynamic data inferred from the variety of experiments presented herein is generally self-consistent, with the exception of the dimerization reaction $2LiOH(g)\rightarrow Li_2(OH)_2$. The slope measurement for this reaction requires accurate measurement of two peaks simultaneously; one of these intensities is squared in the equilibrium constant.

The absolute pressure method requires a knowledge of the calibration constant relating ion intensity to pressure. Also, the entropy and free-energy functions calculated for LiOH(g) and $Li_2(OH)_2(g)$ are subject to doubt because in both cases a model had to be assumed. The LiOH structure may possibly be linear, tending to make slope and third law measurements agree. A similar effect could be obtained if $Li_2(OH)_2$ had a greater vibrational contribution to entropy. One may safely say that even with this reaction the agreement is within the experimental error.

It is of interest to compare the dimerization energy above with the results of Porter and Schoonmaker for the other alkali hydroxides, viz.,

ΔH_{dimer} (NaOH) $=54\pm 5$

KOH $=48\pm 5$

RbOH $=45\pm 5$

CsOH $=40\pm 5$.

As was mentioned earlier, these results are all based on a slope determination for NaOH, and hence are subject to that error plus the cumulative relative energy errors. Hence, although the slope measurements in the present case (LiOH) would seem to conform more readily to the trend of the Porter and Schoonmaker values, the error in both determinations is large enough to make the third law value of LiOH dimerization almost equally probable.

The ion peak attributable to $Li_3(OH)_2^+$ was too small in magnitude to permit thermodynamic investigation, although it was sufficiently intense and reproducible to firmly establish the presence and approximate partial pressure of $Li_3(OH)_3$ in the vapor.

Paramagnetic-Resonance Study of Hyperfine Interactions in Single Crystals Containing α,α-Diphenyl-β-Picrylhydrazyl

ROBERT W. HOLMBERG AND RALPH LIVINGSTON

Oak Ridge National Laboratory, Oak Ridge, Tennessee*

AND

WILLIAM T. SMITH, JR.

Department of Chemistry, University of Tennessee, Knoxville, Tennessee

(Received March 7, 1960)

α,α-Diphenyl-β-picrylhydrazyl, with and without N^{15}, contained in single crystals of the corresponding hydrazine has been studied by the paramagnetic-resonance method. All resolved hyperfine effects arise from the two hydrazyl nitrogen atoms. The tensors describing the hyperfine interaction for each nitrogen and the principal-axes directions have been deduced. The tensors have been interpreted on the basis of an s-p model with the following electron densities: for the α nitrogen $a_s^2=0.011$ and $a_p^2=0.263$ with the two parts having the same sign of spin density; for the β nitrogen $a_s^2=0.024$ and $a_p^2=0.396$ or $a_s^2=0.010$ and $a_p^2=0.605$. The two choices for the β nitrogen arise from an ambiguity in interpreting the hyperfine tensor, but with either choice the two parts have the same sign of spin density.

INTRODUCTION

THE stable free radical that has most frequently been observed by the paramagnetic-resonance method is undoubtedly α,α-diphenyl-β-picrylhydrazyl (DPPH). The first observation[1] was made on a polycrystalline powder, and a single, sharp absorption line was seen with a g value very close to that of the free electron. The sharpness of the line and lack of hyperfine structure was attributed to exchange interactions; this interpretation has been borne out in many later studies. Subsequently, others have investigated single crystals of DPPH, and a very small aniostropy in g value[2] and line width[3] have been reported. The closeness of the g value to that of the free electron is typical of the more complex free radicals which exhibit essentially complete quenching of orbital angular momentum.

A number of solution studies, usually in benzene, have been made. If the solution is sufficiently dilute so that exchange and dipole-dipole interactions are greatly reduced, then a nearly resolved five-line spectrum can be observed.[2] The spectrum arises from hyperfine interactions of the electron with the two hydrazyl nitrogen nuclei.[2,4] Each N^{14} nucleus ($I=1$) gives a triplet splitting which, in general, gives a composite spectrum of nine lines. The five lines have been interpreted as arising from the special case of essentially equal coupling of the two nitrogen nuclei which causes some of the nine lines to be superimposed within the limits of the resolution of the observed pattern. More recently a detailed analysis of the five-line spectrum in dilute solution has been made,[5] and the ratio of the couplings of the two nuclei has been reported to be 0.82. Only hyperfine effects arising from the contact hyperfine interaction are seen in solution.[6] No information is obtained on the dipolar contributions; their effects are averaged out by the tumbling motions in solution.

In the present study both the isotropic contact hyperfine interaction and the anisotropic dipolar interaction have been measured in single crystals containing DPPH. Normal DPPH, both hydrazyl nitrogens being N^{14}, and labeled DPPH, one of the nitrogens being N^{15}, have been used. The β position (Fig. 1) was labeled with N^{15}. The single crystals studied were diamagnetic α,α-diphenyl-β-picrylhydrazine ($DPPH_2$) containing a small amount of DPPH. (The formula of $DPPH_2$ differs from that of DPPH in that its extra hydrogen atom is located on the β nitrogen.) Both DPPH[7] and $DPPH_2$[8] grown from benzene solutions are monoclinic with two molecules in the unit cell plus two molecules of benzene; however, their space groups are different. DPPH has space group Pa while $DPPH_2$ has $P2_1$ (monoclinic angle 111° 14′). An x-ray diffraction examination of crystals of $DPPH_2$ containing small amounts of DPPH showed no change from that of pure $DPPH_2$. Hyperfine interactions from the two N^{14} nuclei of the hydrazyl, in general, would give a spectrum of nine lines. This would be doubled to 18 lines because there are two molecules in the unit cell. The symmetry of the dilute crystals is such that if the applied magnetic field is parallel to the crystallographic ac plane then both molecules appear alike, and at most a nine-line spectrum would be expected. If one of the nitrogens is replaced by N^{15} ($I=\frac{1}{2}$) a six-line spectrum doubling to 12 lines

* Operated for the U. S. Atomic Energy Commission by the Union Carbide Corporation.

[1] (a) A. N. Holden, C. Kittel, F. R. Merritt, and W. A. Yager, Phys. Rev. 77, 147 (1950); (b) C. H. Townes and J. Turkevich, Phys. Rev. 77, 148 (1950).

[2] C. A. Hutchison, Jr., R. C. Pastor, and A. G. Kowalsky, J. Chem. Phys. 20, 534 (1952).

[3] G. Berthet, Compt. rend. 240, 57 (1955).

[4] H. S. Jarrett, J. Chem. Phys. 21, 761 (1953).

[5] R. M. Deal and W. S. Koski, J. Chem. Phys. 31, 1138 (1959).

[6] S. I. Weissman, J. Chem. Phys. 22, 1378 (1954).

[7] M. Sternberg, Compt. rend. 240, 990 (1955).

[8] R. D. Ellison and R. W. Holmberg, Acta Cryst. 13, 446 (1960).

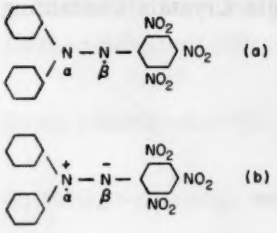

FIG. 1. α,α-Diphenyl-β-picrylhydrazyl. Two resonant structures are indicated.

(since there are two molecules) would be expected. This type of spectra has been observed. Their measurement has allowed the elements of a phenomenological hyperfine-interaction tensor to be evaluated for each nitrogen. These elements have then been interpreted in terms of s and p atomic orbitals for each nitrogen.

EXPERIMENTAL

Single crystals of $DPPH_2$ weighing up to $\frac{1}{2}g$ and containing small amounts of DPPH were grown from benzene solution by a slow-evaporation method and also by a thermal-gradient method. The latter was more generally successful. Typically, a gram of $DPPH_2$ and 20 mg of DPPH in 10 ml of benzene were placed in a 15-ml test tube. The lower part of the tube was heated to about 60°C and, with luck, after several days well-developed single crystals formed in the upper, room-temperature, portion of the tube. The crystals contained approximately 0.1% DPPH. The DPPH labeled with N^{15} had to be synthesized. The starting material was 98% N^{15} as nitric acid as obtained from the Oak Ridge National Laboratory Isotope Division. The acid was converted to dry $NaN^{15}O_3$. The nitrite was prepared from the nitrate by heating with granular lead for 16 hr at 375°C under an argon atmosphere and was recovered by leaching of the matrix with water. This was followed by the preparation[9] of α,α-diphenylhydrazine-β-N^{15} which in turn was converted[10] to $DPPH_2$ and then to DPPH. In growing crystals from solution, both the $DPPH_2$ and DPPH had to be labeled.

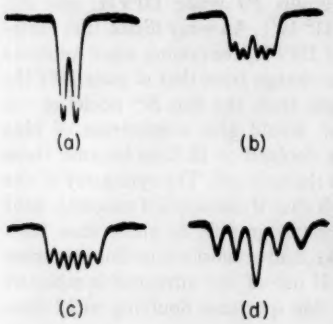

FIG. 2. Spectra of a single crystal containing N^{15}-labeled DPPH; the magnetic field was parallel to the ac plane. The field directions relative to the c axis were (a) 70°, (b) 45°, (c) 40°, and (d) 0°.

[9] A. Murray and D. L. Williams, *Organic Syntheses with Isotopes* (Interscience Publishers, Inc., New York, 1958), p. 1830.

[10] R. H. Poirier, E. J. Kahler, and F. Benington, J. Org. Chem. 7, 1435 (1952).

If the $DPPH_2$ was not N^{15} labeled rapid exchange of the β hydrogen completely destroyed the labeling.

The crystal habit was determined by comparing interfacial angles, measured with an optical goniometer, with those calculated from the cell parameters determined by x rays.[8] Usually the 100 and 001 faces were well developed and measurements with the magnetic field parallel to these planes could be conveniently carried out by laying the crystal on the appropriate surface in the bottom of the microwave cavity. For measurements parallel to the ac plane the crystal was cemented to a rod which was then inserted into the microwave cavity.

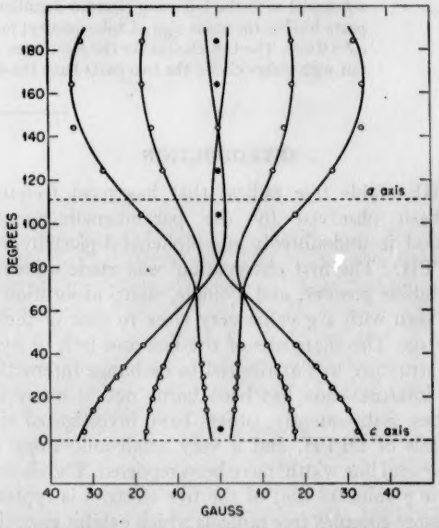

FIG. 3. Measured values and calculated curves for the hyperfine separations in a single crystal containing N^{15}-labeled DPPH; the magnetic field was parallel to the ac plane. The solid circles are measurements of unresolved lines.

A simple 9000-Mc paramagnetic-resonance spectrometer was used. It employed a rectangular cavity operating in the TE_{101} mode, 60-cps field modulation, and oscilloscope presentation of the spectrum. The magnetic-field direction could be altered by rotating the magnet. Fields were measured with a proton-magnetic-resonance probe. Most measurements were made at room temperature; some were made at 77°K to improve the signal intensity. Comparisons of the spectra at the two temperatures were made, and no significant change in line spacing or width could be observed. The lines at the lower temperature could, however, be much more readily power saturated.

Measurements were made with the normal (N^{14}—N^{14}) and labeled (N^{14}—N^{15}) crystals and in each case with the field at a number of settings parallel to the ac, ab, and bc crystallographic planes. Resolved hyperfine components had a full width at a half-height of about seven gauss. For many orientations this

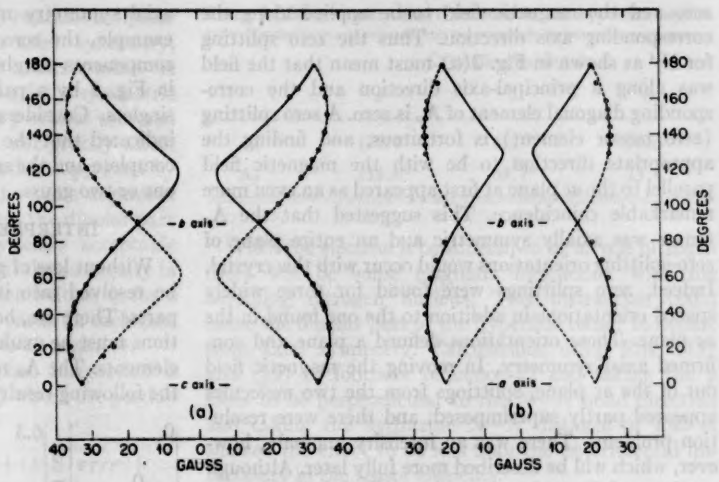

FIG. 4. Measured values and calculated curves for the over-all hyperfine separations in a single crystal contining N^{15}-labeled DPPH. The solid and dotted curves represent the two symmetry-related molecules. (a) The field was parallel to the *bc* plane. (b) The field was parallel to the *ab* plane.

exceeded the spacings between components and, consequently, the number of resolved data was quite limited. The N^{14}—N^{15} crystals gave spectra with fewer hyperfine components; resolved patterns could be seen over a greater range of angles. These data were used to evaluate the hyperfine tensor elements. Measured values obtained from the N^{14}—N^{14} crystals at a number of orientations were in excellent agreement with the N^{14}—N^{15} results. The use of N^{15} not only facilitated resolution of the spectra but also allowed an unambiguous assignment of the two hyperfine tensors to the appropriate nitrogens. The most useful data were obtained for the magnetic field parallel to the *ac* plane for the N^{14}—N^{15} crystals. Typical spectra are shown in Fig. 2, and measured values are given in Fig. 3. At most, only six lines appear. For one orientation [Fig. 2(a)] the hyperfine interaction for the N^{14} is zero and only the doublet for the N^{15} remains. Upon changing the orientation each component splits into a triplet, and contributions of both nitrogens to the hyperfine pattern are seen. Measured values for other planes are shown in Fig. 4. Only the outermost lines were sufficiently well resolved to be measured accurately.

The appropriate spin Hamiltonian to which the data were fitted is

$$\mathcal{H} = -g\beta[\mathbf{H}\cdot\mathbf{S}+\mathbf{S}\cdot\mathbf{A}_\alpha\cdot\mathbf{I}_\alpha+\mathbf{S}\cdot\mathbf{A}_\beta\cdot\mathbf{I}_\beta], \qquad (1)$$

where β is the Bohr magneton, H the applied magnetic field, S and I the electron- and nuclear-spin operators in units of $\hbar$, A the hyperfine tensor, and g refers to the electron. The subscripts α and β refer to the two nitrogens as labeled in Fig. 1. It was found, experimentally, that the anisotropy in the electron g value was negligibly small. It centered at about $g=2.003$ with a variation of approximately ± 0.001. This is similar to that observed[2] in concentrated single crystals of DPPH. Accordingly, the Zeeman energy of the electron was regarded as isotropic and the hyperfine interactions were treated as a small perturbation. The spacings of hyperfine components from the unperturbed line position (center of symmetric hyperfine multiplet) are given by

$$\Delta H = m_{I\alpha}(\hat{H}\cdot\mathbf{A}^2\cdot\hat{H})_\alpha^{\frac{1}{2}}+m_{I\beta}(\hat{H}\cdot\mathbf{A}^2\cdot\hat{H})_\beta^{\frac{1}{2}}, \qquad (2)$$

where ΔH is the spacing in magnetic-field units, m_I is the nuclear magnetic quantum number, $\hat{H}$ is a unit vector in the direction of the applied field, $\mathbf{A}^2=\mathbf{A}\cdot\mathbf{A}$ is a rank-two symmetric tensor and the allowed transitions have been taken to be for $\Delta m_I=0$. In a principal-axis system Eq. (2) becomes

$$\Delta H = m_{I\alpha}[\sum_i h_i^2 A_{ii}^2]_\alpha^{\frac{1}{2}}+m_{I\beta}[\sum_j h_j^2 A_{jj}^2]_\beta^{\frac{1}{2}}, \qquad (3)$$

where the h's are direction cosines of the applied magnetic field with respect to the principal axes, and the A's are written in component form. $(A_{ii}^2)=(A^2)_{ii}$. It is apparent that no information on the absolute or relative signs of the principal values of A can be deduced from Eq. (3); the spectra depend upon their *magnitudes*. In addition to separate tensors for each nitrogen, from the symmetry of $DPPH_2$ one would expect a second pair of tensors corresponding to the second molecule in the unit cell. Only the tensors for one molecule need be determined since those for the other molecule can be obtained by the appropriate symmetry operation, a twofold rotation about the *b* crystallographic axis.

In general the fitting of data is a 12-parameter problem, six parameters for each tensor. One approach would be to choose an arbitrary axis system, deduce the elements of $\mathbf{A}^2$ using Eq. (2), diagonalize and then deduce the diagonal elements of A. Fortunately, there are simplifying features that allowed one of the tensors to be determined directly in diagonal form. From Eq. (3) it is apparent that the only way a zero hyperfine splitting can occur is for a principal value to be

zero and the magnetic field to be applied along the corresponding axis direction. Thus the zero splitting for N^{14} as shown in Fig. 2(a) must mean that the field was along a principal-axis direction and the corresponding diagonal element of $\mathbf{A}_\alpha$ is zero. A zero splitting (zero tensor element) is fortuitous, and finding the appropriate direction to be with the magnetic field parallel to the *ac* plane at first appeared as an even more remarkable coincidence. This suggested that the $\mathbf{A}_\alpha$ tensor was axially symmetric and an entire plane of zero-splitting orientations would occur with this crystal. Indeed, zero splittings were found for three widely spaced orientations in addition to the one found in the *ac* plane. These orientations defined a plane and confirmed axial symmetry. In moving the magnetic field out of the *ac* plane, splittings from the two molecules appeared partly superimposed, and there were resolution problems. There was an intensity anomaly, however, which will be described more fully later. Although spacings of hyperfine lines from each molecule appeared normal, one molecule gave lines with only about one-third the intensity of the other. Good measurements could be made by confining observations to the strong family of lines. A strong doublet (each component threefold degenerate) was observed superimposed on a family of six very much weaker lines. The symmetry axis was overdetermined in this way and found to make angles of 126°, 62°, and 36° with the *a*, *b*, and *c* crystallographic axes, respectively. From the principal-axes directions and from the data of Fig. 3 the only nonzero element of $\mathbf{A}_\alpha$ was easily evaluated to be 18.7. Deducing the elements of $\mathbf{A}_\beta$ proceeded in a more conventional manner. Only over-all splittings of the hyperfine pattern were needed. The elements were deduced by using the values for $\mathbf{A}_\alpha$, the data of Figs. 3 and 4, and Eq. (2).

The magnitudes of the tensor elements are

$$\mathbf{A}_\alpha = \begin{vmatrix} 0 & & \\ & 0 & \\ & & 18.7 \end{vmatrix} \quad \text{and} \quad \mathbf{A}_\beta = \begin{vmatrix} 5.8 & & \\ & 5.8 & \\ & & 27.5 \end{vmatrix}.$$

Both are axially symmetric, and the principal-axes directions (symmetry axes) are given in Table I for one of the two molecules in the unit cell. The angle between the two symmetry axes is 13° with an estimated uncertainty of ±2°. The elements of the tensors are in units of gauss and refer to N^{14}. The tensor deduced for $N^{15}(\mathbf{A}_\beta)$ has been converted to the appropriate N^{14} value by multiplying each element by $|g_{14}|/|g_{15}| = 0.7129$. This facilitates comparisons between the two nitrogens. Although it is difficult to estimate errors in the tensor elements, spectra calculated from the two tensors and the principal-axes directions agree with the measured values to within a gauss. This is indicated in Figs. 3 and 4. Small deviations of the two tensors from axial symmetry might fit the data equally well. For example, the zero elements of $\mathbf{A}_\alpha$ represent hyperfine components merging to a true singlet. This is illustrated in Fig. 2 by a pair of triplets collapsing to a pair of singlets. Consideration of line widths and intensities indicated that the merging of lines was, indeed, quite complete and the small elements of $\mathbf{A}_\alpha$ could not exceed one or two gauss.

INTERPRETATION AND DISCUSSION

Without loss of generality, the hyperfine tensors may be resolved into isotropic and anisotropic (traceless) parts. There are, however, ambiguities since the resolutions must be made for all combinations of signs of the elements. The $\mathbf{A}_\alpha$ tensor gives the least ambiguity with the following result:

$$\begin{vmatrix} 0 & & \\ & 0 & \\ & & 18.7 \end{vmatrix} = \begin{vmatrix} 6.3 & & \\ & 6.3 & \\ & & 6.3 \end{vmatrix} + \begin{vmatrix} -6.3 & & \\ & -6.3 & \\ & & 12.5 \end{vmatrix}. \quad (4)$$

The only other choice is with the sign of every element of each tensor reversed. The simplest and most obvious model for describing the tensors is a combination of *s* and *p* atomic orbitals. The choice of signs made in Eq. (4) gives both parts a positive spin density. The only other choice would be for both parts to be negative. The three possible resolutions of $\mathbf{A}_\beta$ are

$$\begin{vmatrix} 5.8 & & \\ & 5.8 & \\ & & 27.5 \end{vmatrix} = \begin{vmatrix} 13.0 & & \\ & 13.0 & \\ & & 13.0 \end{vmatrix} + \begin{vmatrix} -7.2 & & \\ & -7.2 & \\ & & 14.5 \end{vmatrix} \quad (5)$$

$$\begin{vmatrix} -5.8 & & \\ & -5.8 & \\ & & 27.5 \end{vmatrix} = \begin{vmatrix} 5.3 & & \\ & 5.3 & \\ & & 5.3 \end{vmatrix} + \begin{vmatrix} -11.1 & & \\ & -11.1 & \\ & & 22.2 \end{vmatrix} \quad (6)$$

$$\begin{vmatrix} 5.8 & & \\ & -5.8 & \\ & & 27.5 \end{vmatrix} = \begin{vmatrix} 9.1 & & \\ & 9.1 & \\ & & 9.1 \end{vmatrix} + \begin{vmatrix} -3.3 & & \\ & -14.9 & \\ & & 18.3 \end{vmatrix}. \quad (7)$$

The third resolution given by Eq. (7) contains a dipolar tensor that departs greatly from axial symmetry, and for this reason is physically unacceptable. A quenched p orbital should give an axially symmetric tensor. It will later be shown that a p orbital centered on the adjacent nitrogen atom will not greatly affect the tensor elements. This view is further supported by the elements found for $\mathbf{A}_\alpha$ where the same argument applies and where, without ambiguity, the dipolar part is axially symmetric. For the physically acceptable choices, Eqs. (5) and (6), there is still the ambiguity in the signs of each element. The choice written is for a positive spin density for the s and p parts. In each case the other choice requires both parts to be negative.

The detailed form of the hyperfine interaction is given by the Hamiltonian of Eq. (1) where the portion $\mathbf{S}\cdot\mathbf{A}\cdot\mathbf{I}$ is given by

$$\mathbf{S}\cdot\mathbf{A}\cdot\mathbf{I}=\{(8\pi/3)\mathbf{S}\,|\Psi(0)|^2-(\mathbf{S}/r^3)+(3\cdot\mathbf{S}\cdot\mathbf{r}\mathbf{r}/r^5)\}\cdot g_N\beta_N\mathbf{I}. \quad (8)$$

As indicated in Eq. (1), there will be two terms of this form, one for each nitrogen, where β_N is the nuclear magneton and g_N is the appropriate nuclear gyromagnetic ratio. The eigenvalues have been discussed elsewhere.[11] If we use the same nomenclature for an $s-p$ model, the tensor elements, as defined in this paper, are

$$A_s=a_s^2(8\pi/3)\,|\Psi_s(0)\,|^2g_N\beta_N \quad (9)$$

$$A_p=\tfrac{4}{5}a_p^2\langle 1/r^3\rangle_p g_N\beta_N, \quad (10)$$

where A_s is an element of the isotropic part of the tensor and A_p is one of the elements of the dipolar tensor, and a_s^2 and a_p^2 are the probabilities of having the electron on the nitrogen in question in the s and p states, respectively. The element given for A_p in Eq. (10) is the unique one which corresponds to the applied magnetic field being along the symmetry axis of the quenched p lobe ($\theta=0°$ in the nomenclature of footnote reference 11).

The significance of the zero splitting (zero tensor element) was discussed above in terms of the phenomenological treatment. In terms of a detailed treatment using s and p states it can be seen[11] that the field at the nuclear position from an electron in an s state is always along the externally applied field direction. On the other hand, the contribution from a p state at the nuclear position will always have a perpendicular component unless the externally applied field is along the symmetry axis (0°) or perpendicular to the symmetry axis (90°). The s and p parts can only cancel for these two angles, and only if there is the appropriate admixture. The cancellation can only occur at 90° if the two parts have the same sign of spin density (the case for DPPH) and at 0° for opposite signs.

[11] H. Zeldes, G. T. Trammell, R. Livingston, and R. W. Holmberg, J. Chem. Phys. **32**, 618 (1960).

TABLE I. The symmetry-axes directions for the hyperfine tensors.

	Crystallographic axis		
	a	b	c
$\mathbf{A}_\alpha$	126.5°	61.7°	36.3°
$\mathbf{A}_\beta$	118.0°	68.7°	23.4°

When the electron is considered to be on one nitrogen there will be some magnetic interaction with the adjoining nitrogen nucleus. This interaction could cause the dipolar part of the hyperfine tensor to depart from axial symmetry. Calculations using Eqs. (15) and (19) of footnote reference 12 and taking the p lobes to be perpendicular to the N—N bond direction and taking the hydrazine N—N distance of 1.45 A showed the effect to be less than the experimental uncertainty in the tensor elements.

The value used for $|\Psi_s(0)|^2$ was 32.0×10^{24} cm^{-3} as deduced from Hartree[13] wave functions for a $2s$ electron on N(^4S). The corresponding value for $\langle 1/r^3\rangle$ for a $2p$ electron was 22.5×10^{24} cm^{-3}. This is an 8% increase from the value deduced from the Hartree function as discussed by Dousmanis.[14] This value was used for interpreting $\mathbf{A}_\beta$. In interpreting $\mathbf{A}_\alpha$ the electron is regarded as being on the α nitrogen with resonant structures of the type indicated in Fig. 1(b). To account for the decrease in screening because of the positive formal charge on the α nitrogen the value of $\langle 1/r^3\rangle$ was increased by a factor of 1.30 as indicated by Townes and Schawlow.[15]

Using the preceding values, we obtain the following results: For the α nitrogen $a_s^2=0.011$ and $a_p^2=0.263$. The spin densities of the two parts have the same sign. The total electron density on this nitrogen is 0.274 of which 4% is s character. For the nitrogen in the β position there are two choices: $a_s^2=0.024$ and $a_p^2=0.396$ or $a_s^2=0.010$ and $a_p^2=0.605$. For either choice, the spin densities of the s and p parts have the same sign. The total electron density on this nitrogen is 0.420 or 0.615 of which 5.7% or 1.6%, respectively, is s character. With either choice the electron density on the β nitrogen is greater than that on the α nitrogen indicating that a resonant structure of the type given in Fig. 1(a) predominates. This is the structure a chemist would normally write for DPPH. The foregoing values are substantially different from those calculated by a molecular-orbital method[16] which gave densities for the unpaired electron of 0.1416 and 0.1518 for the α and β nitrogens.

[12] G. T. Trammell, H. Zeldes, and R. Livingston, Phys. Rev. **110**, 630 (1958).

[13] D. R. Hartree and W. Hartree, Proc. Roy. Soc. (London) **A193**, 299 (1948).

[14] G. C. Dousmanis, Phys. Rev. **97**, 967 (1955).

[15] C. H. Townes and A. L. Schawlow, *Microwave Spectroscopy* (McGraw-Hill Book Company, Inc., New York, 1955), p. 239.

[16] R. Bersohn, Arch. sci. (Geneva) **11**, 12 (1958).

There are other magnetic nuclei in the system that can interact with the unpaired electron. These are the hydrogens and nitrogens attached to the aromatic rings. There were no experimental indications of splittings from these nuclei. The approximate 7-gauss line width of a resolved hyperfine component indicates these interactions to be weak; moreover, a substantial part of the width could arise from intermolecular magnetic dipole-dipole interactions. This is consistent with the electron being rather highly localized on the two hydrazyl nitrogens where either 0.694 or 0.889 total electron density is found depending on the choice made for the β nitrogen.

In the experimental discussion it was pointed out that a line-intensity anomaly was present. The hyperfine lines from one molecule in the unit cell were about three times as intense as those from the other molecule. The spacings were not anomalous. The effect could not be attributed to any asymmetry in the experimental configuration, and we are forced to conclude that there are different numbers of DPPH molecules in each of the two cell positions. This is inconsistent with the space group for $DPPH_2$. Only small amounts of DPPH were contained in the $DPPH_2$ crystals and distortions may have been present that were not observed in the x-ray-diffraction work. Since DPPH has a different space group than $DPPH_2$ there must ultimately be a change as one is added to the other to form a solid solution. Presumably, even with small amounts of added DPPH, the host lattice does not accommodate it well, and there are distortions not seen by x rays at such low concentrations; the "symmetry-related positions" are not occupied with equal probability. This may be related to the finding that 2% DPPH (compared to $DPPH_2$) had to be placed in solution to obtain a crystal containing only 0.1% DPPH.

It was hoped that a comparison of spectra calculated from the isotropic part of the hyperfine interactions [Eqs. (4)–(6)] with observed spectra in solution would remove the ambiguity in the resolution of A_β. Although one choice is favored, some doubt remains. In making the comparisons the over-all splitting from first to fifth component of the five-line solution spectra is used. Although a number of studies of the solution spectrum have been published, most authors have not stated measured values of the splitting. The first value reported[2] gave the separation between components as approximately 10 gauss or an over-all separation as approximately 40 gauss. We have remeasured this value for DPPH in benzene solution (0.002 and 0.005 M) and carbon-disulfide solution (0.005 M) with and without the solutions being saturated in $DPPH_2$. The spectra were essentially the same in all cases with an over-all splitting of 34 ± 1 gauss. There is some uncertainty due to lack of complete resolution, but we use this number for comparisons. The isotropic part of A_α is 6.3 [Eq. (4)] while the two choices for A_β are 13.0 and 5.3 [Eqs. (5) and (6)]. With the larger value for the isotropic part of A_β a seven-line spectrum would be expected in solution with an over-all splitting of 38.6 gauss. The ratios of interactions for the two nitrogens is 0.48. The over-all splitting is only a little large, but the other features are in complete disagreement with the observed solution spectrum. With the smaller value for the isotropic part of A_β a five-line spectrum would be expected with a ratio of interactions for the two nitrogens of 0.86 to be compared with the value of 0.82 recently deduced[5] from solution studies. Although this agreement is excellent, the calculated splitting is 23.2 gauss, which is quite small. These findings give some preference to the smaller value for the isotropic part of A_β. This is the choice that gave $a_s^2=0.010$, $a_p^2=0.605$, a combined density of 0.615 for the β nitrogen and a combined density of 0.889 for the two nitrogens. An examination of the results show that the isotropic parts of the interactions, the only parts observed in solution, represent a minor portion of the electron density. The small amount of s admixture might vary with the environment of the DPPH, which casts some doubt on the validity of comparing values in the solid with those in solution. Finding the same values in a few different solutions was reassuring, but, perhaps, it would be more significant to make the present measurements with different host crystals.

Proton-Transfer Studies by Nuclear Magnetic Resonance. I. Diffusion Control in the Reaction of Ammonium Ion in Aqueous Acid*

MERLE T. EMERSON,† ERNEST GRUNWALD,†‡ AND ROBERT A. KROMHOUT§

Florida State University, Tallahassee, Florida

(Received February 15, 1960)

Rate constants were determined by precise nuclear-magnetic-resonance techniques for the reactions:

$$NH_4^+ + H_2O \xrightarrow{k_4} NH_3 + H_3O^+;\quad NH_3 + H_3O^+ \xrightarrow{k_{-4}} NH_4^+ + H_2O;$$

and

$$NH_4^+ + NH_3 \xrightarrow{k_5} NH_3 + NH_4^+$$

in aqueous acid at 25°C. For 0.25–3.00M NH_4Cl, k_{-4} and k_5 were 4.3×10^{10} sec$^{-1}M^{-1}$ and 1.17×10^{9} sec$^{-1}M^{-1}$ respectively, independent of NH_4Cl concentration. Both rate constants increase on addition of KCl. The rate constant, k_4, was 24.6 sec^{-1} at zero ionic strength and decreased sharply with NH_4Cl concentration. The values of K_A needed in the kinetic analysis were measured also. The reaction of NH_4^+ with H_2O was investigated also in 50–60 wt % H_2SO_4-H_2O mixtures, where the half-life for isotopic exchange was between two and 20 minutes. The data allowed us to estimate the rate constant $(1/\tau_D+1/\tau_R)$ for the rupture of the $H_3N\cdots HOH$ hydrogen bond, by diffusion (D) or rotation (R). The value obtained was 51×10^{10} sec^{-1}. Using Einstein's theory of Brownian motion, the value of $1/\tau_D$ was estimated to be 34×10^{10} sec^{-1}, leaving 17×10^{10} sec^{-1} for $1/\tau_R$, of which 12×10^{10} and 5×10^{10} sec^{-1} are the contributions due to the rotation of H_2O and NH_3, respectively. The probability that NH_3 rotates during an encounter is therefore fairly small.

The order of magnitude of k_{-4} and k_5 suggests that these reactions are diffusion controlled. Upon applying the Debye-Smoluchowski theory to calculate the frequency of encounters, we found that k_{-4} is consistent with reaction occurring whenever H_3O^+ and NH_3 are next-nearest neighbors. The steric factor for this reaction appears to be unity. Since the data in strong acid suggest that rotation of a molecule during an encounter is improbable, we conclude that the reactants are oriented during their approach so that the unshared electrons of the NH_3 face an acidic hydrogen. To interpret k_5, we assume a mechanism in which NH_3 and NH_4^+ become next-nearest neighbors by simple diffusion; the jump to a nearest-neighbor site then requires a somewhat higher activation energy than simple diffusion because NH_3 must displace a tightly bonded water molecule. The reaction with rate constant k_4 is activation controlled. The negative salt effect on k_4 suggests diffusion of charge in the transition state.

INTRODUCTION

WITH the advent of isotopic-tracer and nuclear-magnetic-resonance (NMR) techniques, the proton-transfer reactions of ammonium salts in acidic solutions have received considerable attention.[1–7] In particular, Meiboom and co-workers,[3–4] using NMR techniques, have established the major mechanisms for proton exchange in aqueous acid. Stimulated by their work, we have begun a study of the dependence of these rates on the acid and base strength of the proton donor and acceptor. As a first step, we have reinvestigated, with improved precision, the reactions of ammonium ion in water over a wide range of acid concentrations.

Ammonium ion is a logical starting point for such a study, not only because it is the simplest member of the series, but also because the acids and bases of the ammonia system resemble, with respect to structure and size, those of the water system. Thus NH_4^+ and NH_3 may be expected to fit into the quasi-crystalline lattice of liquid water without seriously disrupting its structure. For this reason one may hope that precise rate constants for the reactions of ammonium ion may be relatively easy to interpret. In particular, one may be able to determine which of the reactions are diffusion controlled, and also predict the mean lives for the different molecular processes that can occur during an encounter. Moreover, the availability of physical data for these systems facilitates any calculations that may be necessary.

EVALUATION OF RATE CONSTANTS

Two different methods were used for measuring rate constants, depending on the half-life for the reaction. For half-lives in the range 0.1–0.001 sec, which were observed for solutions of ammonium ion in the pH range 1–4, the half-widths of the NMR lines were used. For half-lives greater than two minutes which were observed in strongly acid solutions, the rate of exchange of NH_3D^+ with solvent of normal isotopic composition was followed by measuring the intensity of the proton peak of the ammonium ion.

Rate Constants from Half-Widths

Typical NMR spectra for ammonium chloride in aqueous acid are shown in Fig. 1. The resonance of the

* Supported by the Air Force Office of Scientific Research.

† Department of Chemistry.
‡ Alfred P. Sloan Fellow, 1959.
§ Department of Physics.

[1] (a) R. A. Ogg, Discussions Faraday Soc. 17, 215 (1954); (b) R. A. Ogg and J. D. Ray, J. Chem. Phys. 26, 1339, 1340, 1515 (1957).

[2] E. Grunwald, A. Loewenstein, and S. Meiboom, J. Chem. Phys. 25, 382 (1956); 27, 630 (1957).

[3] A. Loewenstein and S. Meiboom, J. Chem. Phys. 27, 1067 (1957).

[4] S. Meiboom, A. Loewenstein, and S. Alexander, J. Chem. Phys. 29, 969 (1958).

[5] (a) C. G. Swain and M. M. Labes, J. Am. Chem. Soc. 79, 1084 (1957); (b) C. G. Swain, J. T. McKnight, and V. P. Kreiter. *ibid.* 79, 1088 (1957).

[6] L. Kaplan and K. E. Wilzbach, J. Am. Chem. Soc. 76, 2593 (1954).

[7] A. I. Brodskii and L. V. Sulima, Doklady Akad. Nauk S.S.S.R. 74, 513 (1950).

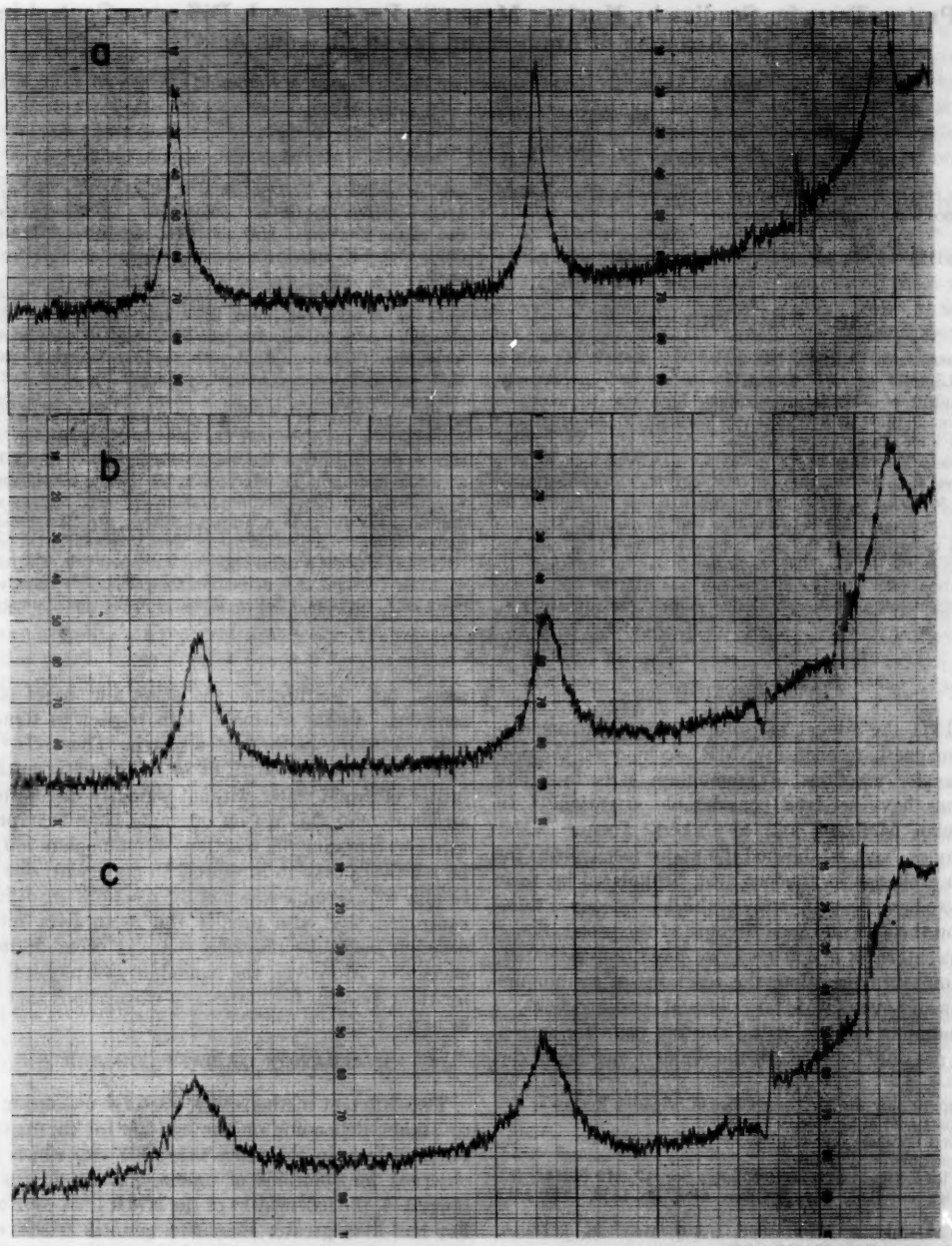

FIG. 1. Experimental NMR spectra of the NH_4^+ triplet for 0.5M ammonium chloride at the following H^+ concentrations: (a) $1.18\times10^{-1}M$; (b) $4.70\times10^{-1}M$; (c) $2.35\times10^{-3}M$.

protons on the ammonium ion is a triplet due to the spin-spin coupling to the N^{14} nucleus. As the hydrogen-ion concentration $[H^+]$ decreases, the lines become broader, indicating that the rate of proton exchange increases. If δ is the full width of the line at half-maximum ("half-width"), measured in cps, and if δ is much less than the triplet splitting, then

$$\pi\delta=(1/T_2)+(1/\tau) \qquad (1)$$

where $1/\pi T_2$ is the half-width in the absence of exchange, and τ is the average time that a proton is bonded to nitrogen of a given spin state (given I_z).

When δ is plotted vs $(1/H^+)$, straight lines are obtained, as shown in Fig. 2. The intercepts are appreciably greater than the value of $1/\pi T_2$ obtained for pure water. Moreover, they vary with salt concentration, indicating that there is also an exchange mechanism which is not proportional to $(1/H^+)$.

We have analyzed both slopes and intercepts on the assumption that the reactions occurring are those found by Meiboom and co-workers.[2-4] These are as follows:

$$H_3\overset{\oplus}{N}H + NH_3 \xrightarrow{k_6} H_3N + \overset{\oplus}{H}NH_3 \qquad (2)$$

$$H_3\overset{\oplus}{N}H' + O(H)-H^* + NH_3 \xrightarrow{k_7} H_3N + H'-O-H^*\overset{\oplus}{N}H_3 \qquad (3)$$

$$H_3\overset{\oplus}{N}H + OH_2 \underset{k_{-4}}{\overset{k_4}{\rightleftarrows}} H_3N + \overset{\oplus}{H}OH_2 \qquad (4)$$

$$H_3\overset{\oplus}{N}H + OH^- \underset{k_{-5}}{\overset{k_5}{\rightleftarrows}} H_3N + HOH. \qquad (5)$$

Reactions (4) and (5) may involve one or several intermediary water molecules, similar to reaction (3).

The rate constant k_6 has been measured by Eigen and Schoen[8]; it is $3.0\times10^{10}M^{-1}$ sec^{-1} at 20°. However, under our experimental conditions, the hydroxide concentration is so small that this reaction accounts for less than 0.5% of the observed rate of exchange. This reaction is therefore neglected. In addition, Meiboom and co-workers[4] have shown that k_7 is only 8% of k_6 at 21°. Since extensive data for $CH_3NH_3^+$ indicate that k_7/k_6 is quite independent of temperature[2] and concentration,[9] we shall accept this value in our analysis.

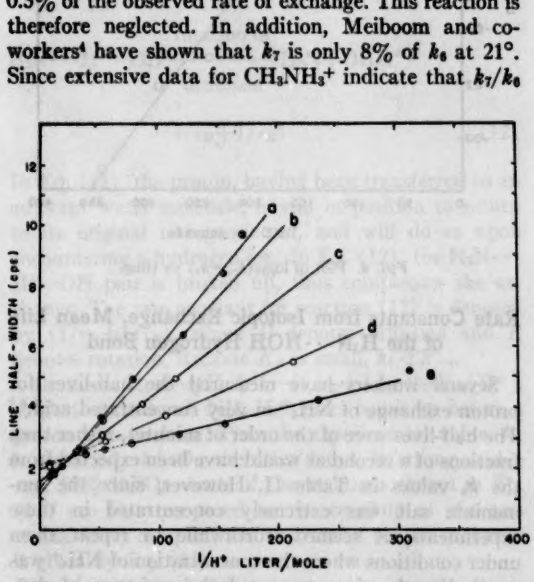

FIG. 2. Plots of δ vs $1/H^+$ for solutions of ammonium chloride containing (a) 2.99M; (b) 2.05M; (c) 1.01M; (d) 0.50M; (e) 0.25M ammonium chloride.

[8] M. Eigen and J. Schoen, Z. Elektrochem. 59, 483 (1955); Z. physik. Chem. (Frankfurt) 3, 126 (1955).

TABLE I. Determination of k_6 for aqueous solutions of ammonium chloride at 25±0.5°.

$[NH_4Cl]$ (M)	KCl (M)	η/η_0[a]	$K_A\times10^{10}$ (M)	$(k_6+\frac{3}{4}k_7)\times10^{-9}$ (M^{-1} sec^{-1})	$k_6\times10^{-9}$ (M^{-1} sec^{-1})
0.25	...	0.997	5.26	1.27	1.13
0.50	...	0.994	4.71	1.39	1.22
1.01	...	0.991	4.07	1.31	1.17
2.00	...	0.988	3.11	1.25	1.11
2.99	...	0.993	2.29	1.35	1.20
2.00	1.00	0.98	1.89	1.63	1.45
1.00	2.00	0.99	1.56	1.91	1.70
1.00	0.58	0.98	3.21	1.47	1.31
1.01	0.88	0.97	2.71	1.61	1.43
1.00	1.32	0.97	2.30	2.16	1.92

[a] Relative viscosity, based on data in the *International Critical Tables*.

Upon using appropriate statistical factors,[4] Eq. (6) is obtained:

$$\pi\delta = T_2^{-1} + \tfrac{1}{2}k_4 + [(k_6/6)+(k_7/4)][K_A(NH_4^+)/H^+]. \qquad (6)$$

From the slope of the experimental plot of δ vs $1/H^+$, the value of $(k_6/6+k_7/4)$ may be calculated if K_A is known. Since k_7 is about 8% of k_6, k_6 can be obtained. The results for solutions containing NH_4Cl and KCl are shown in Table I. The values of K_A were measured potentiometrically[10a] at 25° and are represented satisfactorily[10b] by Eq. (7):

$$\log K_A = -9.246 - 0.132[NH_4Cl] - 0.198[KCl]. \qquad (7)$$

In the absence of KCl, k_6 appears to be independent of $[NH_4Cl]$. The average value is $(1.17\pm0.04)\times10^9M^{-1}$ sec^{-1} at 25°.

According to Eq. (6), the intercepts, $\pi\delta_0$, of the plots of $\pi\delta$ vs $(1/H^+)$ are equal to $(1/T_2+k_4/4)$. Experimental values are shown in Table II. For solutions containing only NH_4Cl, the values of $\pi\delta_0$ decrease sharply with increasing $[NH_4Cl]$, in contrast to k_6 which was constant for the same solutions (Table I). It is shown in the Appendix that the decrease is not due to a change in $1/T_2$. We conclude, therefore, that k_4 is decreasing. In view of the similarity of the reactants involved in reactions (2) and (4), we would have expected very similar ionic-strength effects unless there were an important difference in reaction mechanism. Since k_6 is greater than k_4 by eight orders of magnitude, it seems plausible to suppose that reaction (4) is activation controlled, but that (2) is diffusion con-

[9] E. Grunwald, P. J. Karabatsos, R. A. Kromhout, and E. L. Purlee, J. Chem. Phys. 33, (1960), this issue, following paper.

[10] (a) A. L. Bacarella, E. Grunwald, H. P. Marshall, and E. L. Purlee, J. Org. Chem. 20, 747 (1955); (b) $\log K_A^0 = -9.246$ from R. G. Bates and G. Pinching, J. Am. Chem. Soc. 72, 1393 (1950). Equation (7) fits our data with a standard error of 0.013 logarithmic unit.

TABLE II. Determination of k_4 and k_{-4} for aqueous solutions of ammonium chloride at 25±0.5°.

[NH_4Cl] (M)	[KCl] (M)	$\pi\delta_0$ (sec^{-1})	K_A (M)	k_4[a] (sec^{-1})	$k_{-4}\times10^{-10}$ ($sec^{-1}\,M^{-1}$)
0.25	...	6.47	5.26	22.7	4.32
0.50	...	5.90	4.71	20.4	4.33
1.01	...	4.74	4.07	15.8	3.88
2.00	...	4.37	3.11	14.3	4.60
2.99	...	3.27	2.29	9.9	4.32
2.00	1.00	3.24	1.89	9.8	5.19
1.00	2.00	3.20	1.56	9.6	6.15
1.00	0.58	4.81	3.21	16.0	4.98
1.01	0.88	3.96	2.71	12.6	4.65
1.00	1.32	4.56	2.30	15.0	6.52

[a] $1/T_2$=0.80.

trolled. Some support for this hypothesis may be obtained from the data as follows:

Given k_4 and K_A, k_{-4} may be calculated from Eq. (8). A rough calculation shows that k_{-4} is even greater than k_6:

$$K_A=k_4/k_{-4}. \tag{8}$$

If the latter is diffusion controlled, it is reasonable to assume that the former is also. We shall assume, therefore, that salt effects on k_{-4} parallel those on k_6. Then for the solutions for which k_6 is constant, k_{-4} should also be constant, and $\pi\delta_0$ should vary linearly with K_A as shown in Eq. (9):

$$\pi\delta_0=k_{-4}K_A/4+1/T_2. \tag{9}$$

Values of $\pi\delta_0$ for solutions containing only NH_4Cl are plotted vs K_A in Fig. 3 and fall on a straight line, as predicted by Eq. (9). The intercept in Fig. 3, 0.80 sec^{-1}, is in good agreement with the value 0.7–1.0 sec^{-1} found for $1/T_2$ of NH_4^+ in the absence of exchange (see Appendix). Using this intercept, values of k_4 and k_{-4} were calculated for each solution and are shown in Table II. For solutions containing only NH_4Cl, the average value of k_{-4} is $4.3\pm0.2\times10^{10}$ sec^{-1} liters mole^{-1} at 25°. As a further check on the internal consistency of this scheme, it is worth noting that the calculated values of k_{-4} for solutions containing KCl increase with KCl concentration in much the same way as do the corresponding values of k_6 listed in Table I, in support of the assumptions.

Using 4.3×10^{10} for k_{-4}, k_4 at zero ionic strength is calculated via Eqs. (7) and (8) as 24.6 sec^{-1} at 25°. The decreasing values of k_4 with increasing electrolyte concentration are consistent with a reaction mechanism in which the ionic charge of NH_4^+ becomes more diffuse in the transition-state complex. At first sight it may seem surprising that one can measure rate constants as large as 10^{10} $sec^{-1}M^{-1}$ with good accuracy by this technique. The reason is that in these acidic solutions, the concentration of one of the reactants, NH_3, is extremely small.

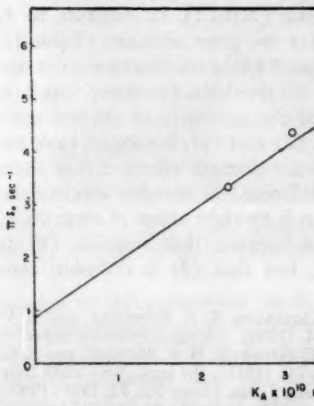

FIG. 3. Plot of $\pi\delta_0$ vs K_A.

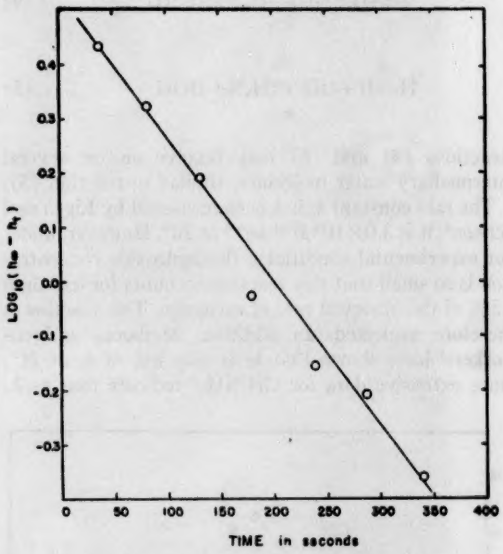

FIG. 4. Plot of $\log_{10}(h_\infty-h_t)$ vs time.

Rate Constants from Isotopic Exchange. Mean Life of the $H_3N\cdots HOH$ Hydrogen Bond

Several workers have measured the half-lives for proton exchange of NH_4^+ in very concentrated acid.[6,7] The half-lives were of the order of minutes, rather than fractions of a second as would have been expected from the k_4 values in Table II. However, since the ammonium salt was extremely concentrated in these experiments, it seemed worthwhile to repeat them under conditions where the concentration of NH_4^+ was small. We therefore measured the exchange of deuterated ammonium sulfate with H_2SO_4-H_2O mixtures of normal isotopic composition. Details of measurement are presented in the experimental section of this paper. Relevant kinetic expressions have been derived

TABLE III. Data for isotopic exchange of $(ND_4)_2SO_4$ with H_2SO_4-H_2O mixtures at 25.0°.

Wt % H_2SO_4	Density (25°)	η/η_0	h_0[a]	$(ND_4)_2SO_4$ (M)	$k_e\times10^3$ (sec^{-1})	$(1/\tau_D+1/\tau_R)$[b] (sec^{-1})
49.14	1.3827	3.71	1950	0.211	6.8[c]	49×10^{10}
49.14	1.3827	3.71	1950	0.112	6.4	46×10^{10}
58.37	1.4760	5.4	18600	0.209	0.57	57×10^{10}

[a] Acidity function, from footnote reference 11(b).
[b] $K_A^0=5.68\times10^{-10}$.
[c] Experimental value obtained at 24°, corrected to 25° by adding 10%.

by Swain and Labes,[5a] whose symbols we shall employ. The experimental rate constant, k_e, for the exchange in our case is equal to

$$k_e=(1/t)\ln[(h_\infty-h_0)/(h_\infty-h_t)] \qquad (10)$$

where h_t is the peak height of a particular NH_4^+-triplet line at time t. A representative experimental plot is shown in Fig. 4. The experimental results are summarized in Table III. The measured half-lives range from two to 20 minutes, which is consistent with the previous work.

The large decrease in the rate of exchange, which is not predicted by Eq. (6), can be explained by a mechanism first suggested by Swain.[5] It is helpful to represent the proton transfer as occurring in two steps:

$$H_3\overset{\oplus}{N}H^*\cdots OH_2 \underset{k'_{-4}}{\overset{k'_4}{\rightleftarrows}} H_3N\cdots H^*\text{—}OH+H^+ \qquad (11)$$

$$H_3N\cdots H^*\text{—}OH \xrightarrow[\text{diffusion}]{\text{rotation or}} H_3N+OHH^* \qquad \cdot(1/\tau_D+1/\tau_R) \qquad (12)$$

In Eq. (11), the proton, having been transferred to an adjacent water molecule, is still in position to return to its original nitrogen atom, and will do so upon encountering a hydrogen ion. In Eq. (12), the $H_3N\cdots H^*$—OH pair is broken up, thus completing the exchange. The rate constant for reaction (12) is denoted by $(1/\tau_D+1/\tau_R)$, where D denotes diffusion and R denotes rotation. Because K_A is small, $k_4'\ll k'_{-4}$.

In dilute acid—pH 1-4—$(1/\tau_D+1/\tau_R)\gg k'_{-4}[H^+]$, so that virtually all NH_3-H_2O pairs break up before a proton goes back on. Thus the experimental value, k_4, is essentially k_4'. On the other hand, in strong acid—say, 50% H_2SO_4—both of the reactions shown in Eq. (11) are fast compared to the breakup of the ammonia-water complex, and the rate of proton exchange is given by Eq. (13):

Rate of proton exchange

$$=(1/\tau_D+1/\tau_R)[H_3N\cdots H^*\text{—}OH]. \qquad (13)$$

The concentration of the $H_3N\cdots H^*$—OH pair is related to the *formal* concentration of ammonia $[NH_3]$, by

$$\frac{[H_3N\cdots H^*\text{—}OH]}{[NH_3]}=\frac{k'_{-4}[H^+]}{k'_{-4}[H^+]+(1/\tau_D+1/\tau_R)}. \qquad (14)$$

By supposition, $k'_{-4}H^+\gg(1/\tau_D+1/\tau_R)$ in strong acid. Hence we may replace the concentration of the complex by the formal concentration of ammonia in Eq. (13). The latter is related to the acidity of the medium as follows:

$$[NH_3]=K_A^0[NH_4^+]/h_0 \qquad (15)$$

where K_A^0 is the acid dissociation constant of NH_4^+ in water at infinite dilution (5.68×10^{-10} at 25°), and $h_0=\text{antilog}_{10}[-H_0]$, the acidity function of Hammett and Deyrup.[11] Thus we obtain Eq. (16) for the rate of proton exchange for protons:

$$\frac{\text{Rate of proton exchange}}{[NH_4^+]}=\frac{(1/\tau_D+1/\tau_R)K_A^0}{h_0}. \qquad (16)$$

Since the experimental rate constant k_e refers to D—H exchange, $(1/\tau_D+1/\tau_R)$ is computed by the following method. The experimental rate constant is corrected for the deuterium isotope effect by multiplying by $\sqrt{2}$.[12a] Since diffusion and rotation depend on the viscosity of the medium, the result is corrected to the viscosity of pure water by multiplying by η/η_0. Finally, there is a statistical factor of four.[5a,12b] Thus,

$$(1/\tau_D+1/\tau_R)=(\eta/\eta_0)(4\sqrt{2}k_eh_0/K_A^0). \qquad (17)$$

The values of $(1/\tau_D+1/\tau_R)$ obtained in this way are listed in Table III. It is seen that the values are constant, within ±10%, for a tenfold variation in h_0 and a nearly twofold variation in concentration and viscosity. This must be regarded as excellent confirmation of the theory, especially in light of the fact that the h_0 function is unmistakably different from other functions of acid composition.

[11] (a) L. P. Hammett and A. J. Deyrup, J. Am. Chem. Soc. **54**, 2721 (1932); (b) M. A. Paul and F. A. Long, Chem. Revs. **57**, 1 (1957).

[12] (a) Swain and co-workers[5] found, for the analogous reaction in methanol, $k_e(T-H)/k_e(D-H)=(\frac{1}{2})^{\frac{1}{2}}$; (b) Using Swain's notation, a, the molar concentration of N—H+N—D bonds, $=4[NH_4^+]$; furthermore, at our concentratoins, $a<0.02b$, the molar concentration of O—H+O—D bonds.

TABLE IV. Diffusion constants in water at 25°.

Species	$D\times10^5$ (cm²/sec)	Footnote reference
H_2O	2.44	16
NH_3	2.39	17
H_3O^+	9.31[a]	16
NH_4^+	1.96[a]	16
OH^-	5.29[a]	16

[a] At infinite dilution.

DISCUSSION

Reaction of H_3O^+ with NH_3

The magnitude of k_{-4} and the nature of the salt effects suggest that the reaction of hydronium ion with ammonia is diffusion controlled. In their studies of the related second-order reaction of H_3O^+ with OH^-, Eigen and DeMaeyer[13] were quite successful in predicting the rate constant for this diffusion-controlled process by applying the Smoluchowski-Debye[14,15] equation, which may be written in the form (18) for reactions involving two ions, and (19) for reactions involving a nonelectrolyte.

$$k_{SD}=8\pi N_0 qP(D_1+D_2)/1000(1-e^{-2q/\sigma}) \quad (18)$$

$$k_S=4\pi P(D_1+D_2)\sigma N_0/1000 \quad (19)$$

where

D_1, D_2 = diffusion coefficients, in cm²/sec

σ = effective collision diameter, in cm

N_0 = Avogadro's number, 6.02×10^{23}

P = steric factor

q = $z_1z_2e^2/2\epsilon kT$

z_1, z_2 = charge numbers

e = electronic charge

ϵ = dielectric constant

k = Boltzmann's constant.

The equations differ from those given by Debye in the inclusion of a steric factor, P. Except for this factor, Eq. (19) is equivalent to Smoluchowski's original equation.[14]

Treating σ as an unknown parameter, and assuming that P is unity, Eigen and De Maeyer obtained the value $\sigma=7.5\pm2$ A for the reaction of H_3O^+ with OH^-, which is of a reasonable magnitude if this reaction involves the *hydrated* ions.

The Smoluchowski-Debye theory has the advantage of making use of experimentally determined diffusion coefficients, thereby avoiding the necessity for calculating the rate constant entirely from first principles. Thus the theory may be expected to be more successful than one which is completely dependent upon theoretical assumptions. Furthermore, Smoluchowski has shown that the solvent medium need not be a continuum, but that the same result is obtained if Brownian movement involves a series of "jumps" of equal length, as would be the case if one adopts a cell model of the liquid state. However, the "jumps" are thought to take place with equal probability in all directions. Owing to the short range of the quasi-crystalline order of liquids, this is probably a fair approximation for encounters at next-nearest-neighbor distances or longer. Thus, if reaction were to proceed by a mechanism involving an intermediary water molecule [such as that shown in Eq. (3)], and if such a reaction were to take place at each encounter, Eq. (19) should give fairly accurate rate constants. However, one would expect the equation to give less accurate results for reactions involving nearest neighbors.

Diffusion constants for the species involved in our systems are summarized in Table IV.[16,17] Upon applying Eq. (19) to the reaction of H_3O^+ with NH_3, taking $k_{-4}=4.3\times10^{10}$ and $P=1$, we obtain $\sigma=4.85$ A. This distance is remarkably close to the average next-neighbor distance of 4.75 A in liquid water.[18] This is a very plausible value for σ, especially if one pictures the hydrated hydrogen ion as $H_9O_4^+$, as proposed by Eigen and De Maeyer.[13]

The question arises, however, whether it is reasonable to assume that the steric factor, P, is unity. If we adopt a rigid, icelike model in which twelve water molecules occupy next-nearest-neighbor sites and are in turn hydrogen bonded appropriately to the four water molecules in the first shell, then proton transfer can occur only from two of these—the starred positions in Fig. 5. Thus, one would expect a steric factor of 2/12, unless some molecular processes occur which cause the

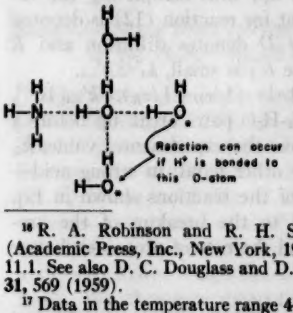

FIG. 5. Model showing the steric factor in the reaction of H_3O^+ with NH_3.

[13] M. Eigen and L. De Maeyer, Proc. Roy. Soc. (London) **A247** 505 (1958).

[14] (a) M. V. Smoluchowski, Physik. Z. **17**, 557, 585 (1916); (b) Z. physik. Chem. **113**, 35 (1924).

[15] P. Debye, Trans. Am. Electrochem. Soc. **82**, 265 (1942).

[16] R. A. Robinson and R. H. Stokes, *Electrolyte Solutions* (Academic Press, Inc., New York, 1955), p. 317, Chap. 6, Table 11.1. See also D. C. Douglass and D. W. McCall, J. Chem. Phys. **31**, 569 (1959).

[17] Data in the temperature range 4–17° were fitted to the equation $\log D_{NH_3}=-0.802-1139/T$, from which the value at 25° was calculated. Data taken from Landolt-Börnstein. *Physikalisch-Chemische Tabellen* (Verlag-Julius-Springer, Berlin, 1923), p. 246.

[18] J. Morgan and B. E. Warren, J. Chem. Phys. **6**, 666 (1938); G. W. Brady and W. J. Romanow, *ibid.* **32**, 306 (1960).

effective steric factor to approach unity. The most probable of these are (i) the rotational relaxation time of the molecules is short compared to the average duration of an encounter, or (ii) the diffusing molecules are oriented by the molecular fields as they approach each other.

Concerning the first possibility, the values of $(1/\tau_D+1/\tau_R)$ for the $H_3N\cdots H^*$—OH complex given in Table III are illuminating. If Einstein's theory of the Brownian movement is applied to the diffusion of a molecule to an adjacent site,[19] $1/\tau_D$ can be calculated. The mean time required for the diffusion of a molecule through a distance s in an arbitrary direction is $s^2/6D$, where D is the macroscopic diffusion coefficient. Thus, for the separation of the $H_3N\cdots H^*$—OH complex,

$$1/\tau_D \approx 6(D_{H_2O}+D_{NH_3})/s^2 \qquad (20)$$

where s is the distance to an adjacent site, 2.92 A.[18] Thus, $1/\tau_D \approx 34\times10^{10}$ sec^{-1} at 25°. Using the data in Table III, $1/\tau_R$ is then 17×10^{10} sec^{-1} at 25°. If the rate constant for rotation of the water molecule in the complex is the same as in pure water, or 12×10^{10} sec^{-1},[20] then, by difference, the rate constant for the rotation of the ammonia molecule is 5×10^{10} sec^{-1}. Allowing about 40% for the error in this treatment, the rate constant for the rotation of the ammonia molecule may be as large as 20×10^{10} sec^{-1}. This indicates that the probability that an ammonia molecule will rotate during an encounter is 60% or less.

In an encounter between *hydronium* ion and ammonia, the corresponding probability is likely to be even smaller: The rate constant for diffusion is greater, and the proton is being transferred, thus shortening the effective encounter time. The rate constant for rotation is likely to be less because of the strong force field of the hydronium ion. Therefore a mechanism involving the rapid rotation of NH_3 during an encounter is extremely improbable. Most likely, the diffusing molecules acquire the correct orientation for reaction as they approach each other.

There is also the possibility that the steric factor is less than unity and that the hydrated proton is larger than $H_9O_4^+$. Thus Hasted and Roderick[21] have inferred from the dielectric properties of hydrochloric acid that the proton may "irrotationally" bind as many as 10 water molecules.

Reaction of NH_4^+ with NH_3

This reaction must necessarily involve nearest neighbors. Using diffusion constants as given in Table IV, a collision diameter of 2.92 A, and $P=1$, the rate constant calculated from Eq. (19) is 9.6×10^9 sec$^{-1}M^{-1}$. However, this number is not the actual rate constant if the proton is transferred from one nitrogen atom to the other more than once during an encounter. If this exchange occurs many times during an encounter, there is a 50% chance that the proton ends up on the original nitrogen atom, resulting in a statistical factor of $\frac{1}{2}$ and a calculated rate constant of 4.8×10^9 sec$^{-1}M^{-1}$. Furthermore, if orienting effects are absent as the molecules approach one another, and if rotation of the molecules in an encounter can be neglected, there is an additional steric factor of $\frac{1}{4}$ because only one of the four sites around the ammonia molecule is adjacent to an unshared pair of electrons. Thus, the predicted rate constant is 1.2×10^9, in excellent agreement with the experimental value of 1.17×10^9 for k_8.

Surprisingly, the same simple method of calculation, when applied to the direct proton transfer between $CH_3NH_3^+$ and CH_3NH_2, again yields values which are in excellent agreement with observation. In this system, k_8 is found to be 4.0×10^8 sec$^{-1}M^{-1}$.[9] Using the values[22] $D_{CH_3NH_3^+}=1.56\times10^{-5}$, $D_{CH_3NH_2}=1.99\times10^{-5}$, and $\sigma=4.28$ A, and $P=1$, we obtain $k_8=11.5\times10^9$ sec$^{-1}M^{-1}$ from Eq. (19). If the exchange occurs many times during an encounter, this should again be multiplied by a statistical factor of $\frac{1}{2}$. In order to estimate the steric factor, we divide the surface of $CH_3NH_3^+$ into six nearly equivalent zones, corresponding to the positions of the six hydrogen atoms. For $CH_3NH_3^+$, three of these six zones are reactive; for CH_3NH_2, only one is reactive. Thus the predicted rate constant is $1/2\times3/6\times1/6\times11.5\times10^9$, or 4.8×10^8. This is within 20% of the experimental value.

We believe, however, that these excellent agreements are probably fortuitous. The water molecules in the first hydration shell of these ions are bound relatively tightly, and are less free to migrate independently than are the molecules in liquid water. The discussion of the detailed reaction mechanism is simplest for NH_4^+. There is strong evidence that NH_4^+ and the four water molecules in its first hydration shell form a single kinetic unit.[18,20] The activation energy for the motion of an ammonia molecule from site to site is therefore expected to be lower when the motion takes place in pure water than when the ammonia molecule ends up in a site adjacent to an NH_4^+ ion. Moreover, on account of the high activation energy, the ammonia molecule is not likely to "jump" unless it is oriented so that the unshared pair faces the NH_4^+ ion, thus reducing the activation energy by hydrogen-bond formation. The steric factor would then be unity. After the ammonia

[19] A. Einstein, *Investigations on the Theory of the Brownian Movement* (Methuen and Company, Ltd., London, 1926). Einstein's equation is not directly applicable to displacements of the order of molecular dimensions, but is likely to be a good approximation in view of Smoluchowski's arguments [footnote reference 14(a), p. 557–558].

[20] G. H. Haggis, J. B. Hasted, and T. J. Buchanan, J. Chem. Phys. **20**, 1452 (1952).

[21] J. B. Hasted and G. W. Roderick, J. Chem. Phys. **29**, 17 (1958).

[22] $D_{CH_3NH_2}$ is estimated on the basis that $D_{CH_3NH_2}-D_{CH_3NH_3^+}=D_{NH_3}-D_{NH_4^+}$. $D_{CH_3NH_3^+}$ is calculated from the limiting equivalent conductance of $CH_3NH_3^+$. For σ we have taken the diameter of the CH_3NH_2 molecule, which was estimated from the partial molar volume in water [A. Kanitz, Z. physik. Chem. **A22**, 344 (1897)], assuming random packing of spheres [R. H. Stokes and R. A. Robinson, Trans. Faraday Soc. **53**, 301 (1957)].

molecule has entered the first shell surrounding the NH_4^+ ion, it will be bound at least as tightly as a water molecule, and the duration of an encounter between NH_4^+ and NH_3 is proportionately long. Thus it is probable that the proton is transferred back and forth a number of times before the two molecules separate.

According to the preceding mechanism, it is difficult to decide whether this reaction should be classified as diffusion controlled or activation controlled. If it is true that proton transfer occurs at each encounter, the reaction might properly be called diffusion-controlled. However, if the ammonium ion with its first hydration shell is regarded as a single kinetic entity, the rate-determining step is not diffusion, but the displacement of a water molecule in this shell by an ammonia molecule.

The mechanism of reaction (3), which involves an intermediary water molecule, will be discussed in a subsequent paper.[9]

EXPERIMENTAL PART

Reagents and Solutions

All reagents used in this work were analytical grade, neutral, and had the correct equivalent weights. Doubly distilled water was used as the solvent for all solutions. The final distillation was from a $KMnO_4$ solution and was carried out in an all-glass apparatus. Stock solutions of KCl and NH_4Cl were used to prepare all other solutions by quantitative dilution. The concentrations of the stock solutions were determined by potentiometric titration of the chloride ion with standard $AgNO_3$ solution.

Solutions of different hydrogen ion concentrations were prepared by weighing a predetermined amount of constant-boiling HCl into a 25-ml volumetric flask, adding the required volumes of the stock solutions of ammonium and potassium chloride, and diluting to 25 ml. This technique can be used up to pH 3 to obtain hydrogen-ion concentrations with a precision of 0.1%. In order to check the accuracy of these values, the pH was checked potentiometrically for a series of solutions. The check was very good. When it was necessary to extend the pH range above pH 3, the potentiometric method was used.

The values of K_A listed in Table I were measured by the method of Bacarella, Grunwald, Marshall, and Purlee.[10a] At first, measurements were carried out in an open cell. The emf of the cell when the solution contained excess base tended to drift in a direction which indicated that free ammonia was being lost. To eliminate this experimental difficulty, a completely closed cell was constructed in the following way: Two female ball joints of sufficient size to accommodate the electrodes were sealed onto a 30-ml flask. The electrodes were then sealed into the male part of the joint by epoxy resin. When the joints were assembled, the electrodes were positioned so that they extended into the reaction flask. The joints, when properly greased, did not allow any ammonia to escape; thus the drifting emf was stabilized. The solutions used for the measurement of K_A were selected from the solutions prepared for the NMR work and had a pH of about 1.

NMR Line-Width Measurements

A Varian 40.0-Mc high-resolution NMR spectrometer was used for the NMR work. Since temperature-controlled sample-probe equipment was not available, all spectra were taken at room temperature. However, air conditioning allowed the temperature of the probe to be maintained at 25±0.5° C during any experiment, as measured by a thermocouple junction located in the probe. In preparing the spectrometer for a run, special care was taken to obtain a very stable magnetic field, with as high homogeneity as possible, in order to reduce the $1/T_2$ factor. The day-to-day changes in resolution were quite small; thus $1/T_2$ remained practically constant for all runs.

In the measurement of the line half-widths, the 54.3-cps peak-to-peak separation of the proton resonance lines of the NH_4^+ triplet was taken as an internal standard. The latter was measured independently (by linear interpolation between side bands produced by superposition of a known audio frequency), and was found not to change with concentration or pH. In measuring the line half-widths, the average half-width of two adjacent triplet lines (in mm) was divided by the peak-to-peak separation of these lines (in mm), and the ratio multiplied by 54.3 cps. A number of measurements were made in this way for each solution, and the average line width for each solution recorded. The average deviation for a series of measurements on one solution was typically about 10%.

Measurement of Slow Exchange Rates

Deuterated ammonium sulfate was prepared for use in these measurements in the following way: Reagent-grade ammonium sulfate was dissolved in hot water, and enough ethanol was added to produce a cloudy solution. Hot water was then added to this mixture drop by drop until the solution cleared. On cooling, this solution yielded beautiful crystals of ammonium sulfate. The deuteration was effected by dissolving 2 g of the dry purified sample in 10 ml of 99.9% D_2O. This mixture was then flash-evaporated to dryness under reduced pressure, yielding small crystals which would dissolve rapidly in the sulfuric acid solutions.

Stock solutions of sulfuric acid having the desired composition were made up from reagent-grade concentrated sulfuric acid and doubly distilled water. The weight percentages of H_2SO_4 in these solutions were calculated from the solution densities and later checked by acid-base titration. These two methods gave results which agreed to 0.1%.

Since the time factor was important in these kinetic measurements, the solutions on which the measurements were made had to be prepared as quickly as possible and gotten into the spectrometer before too much of the reaction had taken place. This was accomplished as follows: 10-ml aliquot portions of the stock acid solution were placed in stoppered 50-ml flasks. Samples of the deuterated ammonium sulfate, ranging from 0.15 to 0.30 g, were weighed into clean, dry weighing bottles. The final reaction mixture was made up by dumping the weighed salt sample into a sample of the acid solution. The precise amount of salt transferred to the solution could be determined from the weights of the sample bottle before and after dumping the sample; however, the final weighing need not be done until after all of the rate data have been taken. Using crystals obtained by flash-evaporation, solution was complete in about one minute.

The amount of exchange was followed by observing the peak height of a member of the NH_4^+ triplet as a function of time. The peak heights were compared with that of a reference sample, to compensate for changes in the performance of the equipment. The reference sample was undeuterated ammonium sulfate of the same concentration and in the same solvent as the reaction mixture. For reactions having half-lives of about 2 min, the reference peak height was measured before the reaction was started, and again after the reaction was completed. For the slower reactions, the reference peak height was measured periodically. About one half-life passed before peaks of the same shape as that of the reference peak were obtained. The reaction was then followed for six half-lives. Typical data are shown in Fig. 4.

APPENDIX

The question arises as to how much the proton resonance lines of NH_4^+ are broadened by transitions among different spin states of the N^{14} nucleus. If such broadening were significant, and if it were a function of salt concentration, the calculation of k_{-4} via Eq. (9), as given in Table II, would be in error. Jardetzky and Wertz[23] have shown that in aqueous solutions of sodium ion, the Na^{23} resonance line is not broadened appreciably by the addition of other electrolytes except at high concentrations where the formation of new species, such as ion pairs, produces electric field gradients at the Na^{23} nucleus. Thus, for example, the line width in 6*N* NaCl was the same as at high dilution. We have similarly observed that the proton resonance triplet of $(CH_3)_4N^+$ ion in sulfuric acid-water mixtures is not noticeably broadened at acid concentrations below 6*M*.

[23] O. Jardetzky and J. E. Wertz, J. Am. Chem. Soc. **82**, 318 (1960).

TABLE V. Half-widths of NH_4^+ proton resonance lines in sulfuric acid-water mixtures.

H_2SO_4 (wt%)	Half-width (sec^{-1})	$k_4\sqrt{2}$[a] (sec^{-1})	$1/T_2$[b] (sec^{-1})
80	1.68	0.00	5.3
65.2	0.79	0.00	2.4_8
49.6	0.55	0.01	1.7_0
34.2	0.55	0.31	1.4_3
28.9	0.67	0.95	1.1_5
0.0	...	...	(0.8)[c]

[a] Rate constant for proton-proton exchange. Calculated from Eq. (17).
[b] $[\pi \cdot (\text{half-width}) - k_4\sqrt{2}.]$
[c] Extrapolated.

Data for the half-width of the proton resonance lines of NH_4^+, obtained in 25–80 wt % H_2SO_4—H_2O, are shown in Table V. In this system we have independent measurements of the precise rate of exchange, using deuterium-labeled ammonium salts (Table III). The half-width can therefore be corrected objectively for the broadening due to exchange, leading by difference to the effective value of $1/T_2$ due to all other causes. As shown in Table V, the latter increases with acid concentration in a typical manner, slowly at low concentrations and more rapidly at high concentrations. The effective value of $1/T_2$ extrapolated to zero acid concentration is about 0.8 sec^{-1}. This is in perfect agreement with the value obtained for $1/T_2$ from the plot of $\pi\delta_0$ vs K_A in Fig. 3.

The electrolyte used in the experiments reported in Table II is monovalent and at lower ionic strengths than even that of 25% sulfuric acid. We would therefore expect no significant increase in $1/T_2$ above the value for infinitely dilute ammonium ion.

Proton-Transfer Studies by Nuclear Magnetic Resonance. II. Rate Constants and Mechanism for the Reaction $CH_3NH_3^+ + OH_2 + NH_2CH_3$ in Aqueous Acid*

ERNEST GRUNWALD,‡ PHOTIOS J. KARABATSOS,† ROBERT A. KROMHOUT,§ AND E. LEE PURLEE†

Florida State University, Tallahassee, Florida

(Received February 15, 1960)

Rate constants were measured by precise nuclear-magnetic-resonance techniques for the reactions

$$CH_3\underset{-}{\overset{+}{N}}H_3 + NH_2CH_3 \xrightarrow{k_6} CH_3\underset{-}{N}H_2 + H\overset{+}{N}H_2CH_3,$$

$$CH_3\underset{-}{\overset{+}{N}}H_3 + OH_2 + NH_2CH_3 \xrightarrow{k_7} CH_3\underset{-}{N}H_2 + HOH + H\overset{+}{N}H_2CH_3,$$

in aqueous acid at 25°. The ratio k_6/k_7 remained virtually constant between 1.7 and 8.1M concentration of CH_3NH_3Cl. The rate constants were inversely proportional to the viscosity of the solution, and were extrapolated on this basis to infinite dilution to yield the values $k_6^0 = 4.0\times10^8$ sec^{-1} M^{-1} and $k_7^0 = 5.3\times10^8$ sec^{-1} M^{-1} at 25°. Acid dissociation constants, densities, and viscosities for 1.7 to 9M solutions of CH_3NH_3Cl in water were measured also. Measurements of the water activity of these solutions showed that the mean ionic molal activity coefficients of CH_3NH_3Cl were virtually constant over the entire range. The magnitude of k_7, as well as the constancy of k_7/k_6, indicated that the most probable rate-determining step for the reaction with rate constant k_7 is proton transfer from a water molecule in the solvation shell of $CH_3NH_3^+$ to a molecule of CH_3NH_2, to produce the triple ion,

$$CH_3\underset{-}{\overset{+}{N}}H_3 \cdot \overset{-}{O}H \cdot H\underset{-}{\overset{+}{N}}H_2CH_3.$$

IT has recently been shown that proton transfer from alkylammonium ion to alkylamine in aqueous solution can occur by a mechanism in which one or several water molecules intervene between the proton donor and acceptor[1–3]:

$$R_3\underset{-}{\overset{+}{N}}H^* + OH + NR_3 \xrightarrow{k_7} R_3\underset{-}{N} + H^*\overset{H}{O} + H\overset{+}{N}R_3. \quad (1)$$

This reaction mechanism is of special interest because of the information it might yield concerning the nature of the solvation shells of the substances involved.

We now report a study of reaction (1) in acidic aqueous solutions of methylamine hydrochloride. In this study, the concentration of CH_3NH_3Cl is allowed to vary widely, from 1.7 to 8.1M, so that the H_2O/CH_3NH_3Cl molar ratio decreases from 28 to 3.6, and the water activity of the solution, from 0.936 to 0.593.

Methylamine hydrochloride was chosen for study because the rate of reaction (1) is nearly equal to that of the competing direct reaction, (2),

$$R_3\underset{-}{\overset{+}{N}}H + NR_3 \xrightarrow{k_6} R_3\underset{-}{N} + H\overset{+}{N}R_3, \quad (2)$$

so that both rates can be measured with good accuracy.[1] By comparing the rate constants for reaction (1) with those for reaction (2), we hoped to be in a better position to separate kinetic effects due to the changing reaction medium from those caused by the changing water activity.

Reactions (1) and (2) are the major proton-transfer processes in aqueous acid. There are, however, a number of additional reactions which contribute as much as several percent to the total rate and which must be considered in a precise analysis. These reactions, and the symbols employed for their rate constants,[4] are shown in Table I. In addition, several physical properties of the solutions were measured: the viscosity, density, water activity, mean ionic-activity coefficient of CH_3NH_3Cl, and the acid-dissociation constant of methylammonium ion.

EXPERIMENTAL PART

Reagents and Solutions

Reagent-grade methylamine hydrochloride was recrystallized three times from pure ethyl alcohol and dried *in vacuo* at 25°. Equivalent weight 67.53±0.07 (calc, 67.52).

Constant-boiling hydrochloric acid, prepared according to Foulk and Hollingsworth,[5] served as acidimetric standard. Its titer was confirmed by Volhard and potentiometric titrations with standard silver nitrate.

* Supported by the U. S. Air Force Office of Scientific Research.

† Department of Chemistry.

‡ Alfred P. Sloan Fellow, 1959.

§ Department of Physics.

[1] E. Grunwald, A. Loewenstein, and S. Meiboom, J. Chem. Phys. **25**, 382 (1956); **27**, 630 (1957).

[2] A. Loewenstein and S. Meiboom, J. Chem. Phys. **27**, 1067 (1957).

[3] S. Meiboom, A. Loewenstein, and S. Alexander, J. Chem. Phys. **29**, 969 (1958).

[4] The symbols are consistent with those used by Meiboom and coworkers,[1–3] except that k_4 and k_{-4} are used by us as pseudo-first-order rate constants, whereas Meiboom's k_4 and k_{-4} have been divided by 55.5, the water concentration, and are second-order rate constants.

[5] C. W. Foulk and H. Hollingsworth, J. Am. Chem. Soc. **45**, 1220 (1923).

All solutions were prepared using doubly distilled water and stored in polyethylene bottles. Since methylamine hydrochloride is hygroscopic, its concentration in the solutions was determined by titration with silver nitrate.

Solutions of methylamine hydrochloride containing a known hydrogen ion concentration (usually about 0.01M) were obtained by quantitative addition of constant-boiling HCl to the CH_3NH_3Cl solutions. In several cases, a check of HCl concentration was made by titrating potentiometrically the acidic solutions with standard NaOH to an end point where HCl is neutralized but CH_3NH_3Cl is not. This procedure would also detect the presence of acidic or basic impurities in the water or CH_3NH_3Cl reagent used in preparing the solutions. The two acid titers generally agreed to 2 % or better. On this basis, the maximum amount of basic impurity in the CH_3NH_3Cl reagent was estimated as 0.01 mole %.

Acid Dissociation Constants

We use K_A to denote the acid dissociation "constant" in terms of molar concentrations, and K_A° to denote the thermodynamic constant in terms of activities. Since the rate measurements were made in acidic solutions in which the concentration of free amine was extremely small, the K_A measurements were made under conditions as nearly comparable as possible. A Beckman model-GS pH meter and glass and calomel electrodes were used. First, known weights of CH_3NH_3Cl solution and of standard HCl were added to the cell, and the emf measured. Next, a measured weight of standard NaOH was added—sufficient to neutralize all the HCl and 0.5–10 % of the CH_3NH_3Cl—and the emf was again measured. Concentration of the NaOH was adjusted so that dilution was slight. Thus the liquid junction potential remained demonstrably constant, and the H^+ concentration of the partially neutralized solution could be computed.[6] Values of K_A obtained in this way were constant to 10% or better in the range of neutralization, 0.5–10%. In several experiments, excess acid was added at the conclusion of the experiment and the calculated pH was recovered, proving that there had been little loss of volatile amine.

Densities and Viscosities

Densities and viscosities were measured by standard techniques.

Water Activities

Water activities over the solutions of CH_3NH_3Cl were measured at 25.00° by the dynamic vapor-pressure method, using the apparatus described by Bacarella.[7] The carrier gas was pure nitrogen.

[6] A. L. Bacarella, E. Grunwald, H. P. Marshall, and E. L. Purlee, J. Org. Chem. **20**, 747 (1955).

[7] A. L. Bacarella, A. Finch, and E. Grunwald, J. Phys. Chem. **60**, 573 (1956).

TABLE I. Summary of rate processes in dilute aqueous acid.

Reaction	Rate constant
$R_3NH^+ + OH_3$	k_4 (sec^{-1})
$R_3N + HOH_3^+$	k_{-4} ($sec^{-1}\ M^{-1}$)
$R_3NH^+ + OH^-$	k_5 ($sec^{-1}\ M^{-1}$)
$R_3N + H_3O$	k_{-5} (sec^{-1})
$R_3NH^+ + NR_3$	k_6 ($sec^{-1}\ M^{-1}$)
$R_3NH^+ + OH_3 + NR_3$	k_7 ($sec^{-1}\ M^{-1}$)

In the calculation of the water activity, the gas phase was treated as an ideal gaseous solution.

Kinetic Measurements

Rates of exchange were measured by the nuclear-magnetic-resonance (NMR) technique, as described previously.[1] A Varian Associates high-resolution NMR spectrometer was used at 40.0 Mc. Rate constants were derived from (i) the shape of the CH_3 quadruplet; (ii) the half-width of the water line; and (iii) the shape and half-width of the NH_3 triplet (Fig. 1). Effective values of T_2 required for (i) were obtained before and after each experiment from the decay envelopes of the "wiggles" following rapid passage through an unbroadened water line, or from the half-width of such a line. Half-widths were measured by the side-band technique, in which values were obtained by linear interpolation between two side bands of known separation. The frequency of the generator used to produce the side bands was determined by counting its sinusoidal output for a given period of time. For example, the half-width of the water line was measured by generating 10-cycle side-bands on either side of the water line. The linear separation of the side bands was divided into the linear half-width of the water line, and the ratio multiplied by the 20-cycle separation of the side bands.

All experiments were conducted in an air-conditioned room. The temperature in the magnet gap was constant to 0.1° during each run, and was 25±0.5° in all experiments. The pH of the solutions was measured potentiometrically immediately before each run, employing the same apparatus and method as in the K_A determinations. The sample holders were made from carefully cleaned Pyrex glass tubing. They were rinsed several times with the solution to be measured prior to final insertion of the sample, to guard against possible changes in the pH of the samples, and were then sealed.

RESULTS

Acid Dissociation Constants

The experimental results are shown in Table II. Several features are noteworthy. First, the plot of $\log K_A$ vs $[CH_3NH_3Cl]$ is linear over a much smaller range of concentration than is the corresponding plot

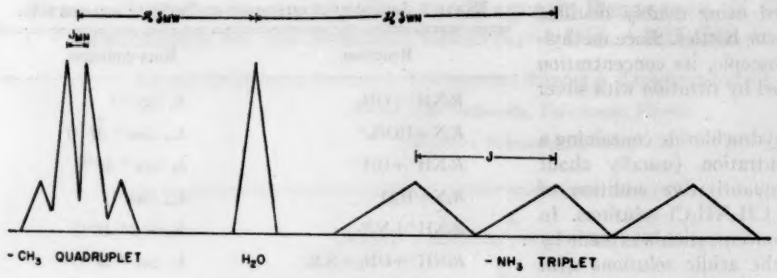

FIG. 1. Schematic diagram of NMR spectrum of CH_3NH_3Cl in aqueous acid at low pH. ν_0=40.0 Mc.

for ammonium chloride,[8] and the magnitude of the initial slope is much greater. The data at concentrations up to 0.0969M are represented well within their experimental error by the equation,

$$\log K_A = -10.616 - 0.710\,[CH_3NH_3Cl]. \quad (3)$$

The slope of −0.710 in Eq. (3) may be compared with the analogous slope of −0.132 for NH_4Cl. However, the large salt effect described by Eq. (3) is consistent with reports of similarly large salt effects on the K_A of several alkylammonium ions when KCl is added.[9] Apparently it is not always a good approximation to assume that K_A values obtained at 0.05 or 0.1M ionic strength are equal to K_A^0 for acids of this charge type.

Our value of K_A^0 agrees satisfactorily with that obtained by Everett and Wynne-Jones[9] in another careful series of measurements.

Densities and Viscosities

The densities of aqueous solutions of methylamine hydrochloride at 25° are given with an accuracy of 0.2% by the equation

$$d = 0.9970 + 0.0090\,[CH_3NH_3Cl] \quad (4)$$

where the molar concentration, $[CH_3NH_3Cl]$, may be as high as 9M.

Relative (to pure water) viscosities were measured at 25° for several aqueous solutions of methylamine hydrochloride. The results are as follows: molar concentrations, η/η_0; 1.78, 1.092±0.014; 4.98, 1.415±0.015; 9.01, 2.148±0.004. Values of η/η_0 at other concentrations were obtained by interpolation of these data on a smooth graph.

TABLE II. Acid dissociation constant of methylammonium ion at various CH_3NH_3Cl concentrations, water, 25.00°.

CH_3NH_3Cl (M)	$10^{11}K_A$ (M)	CH_3NH_3Cl (M)	$10^{11}K_A$ (M)
0.0142	2.46[a]	2.02	1.07
0.0352	2.22[a]	3.50	0.80[a]
0.0698	2.16[a]	4.53	0.63
0.0969	2.07[a]	8.19	0.31
1.06	1.46[a]	8.29	0.25[a]
1.13	1.34		

[a] Measured by M. L. Kaplan.

[8] M. T. Emerson, E. Grunwald, and R. A. Kromhout, J. Chem. Phys. **33**, 547 (1960), preceding paper, this issue.

[9] D. F. Everett and F. K. Wynne-Jones, Proc. Roy. Soc. (London) **A177**, 499 (1941).

Water Activities and Activity Coefficients

Experimental values of the water activity, a_1, are shown in Table III.

Mean molal ionic activity coefficients, γ_2 of CH_3NH_3Cl were obtained from these data by means of the thermodynamic equation,

$$\ln m_2\gamma_2 - \ln m_2^\circ\gamma_2^\circ = \int_{\ln a_1^\circ}^{\ln a_1} (27.751/m_2)\,d\ln a_1, \quad (5)$$

where m_2 is the molality. In this equation, m_2° is the solute molality at the beginning of our experimental range, that is, at 7.0 molal. The estimation of γ_2° presented a problem. We finally decided that, since the activity coefficients of CH_3NH_3Cl[10] closely resemble those of CsCl[11] in the range where both are known (0–1m), we could approximate γ_2° by using the known value for CsCl at 7m.[11] Thus we obtained $\gamma_2^\circ = 0.487$ for 7m CH_3NH_3Cl. Values at other rounded concentrations are shown in Table IV. It is seen that γ_2 is quite constant, decreasing by only 10% between 7 and 19m. In order to have a better understanding of the magnitude of deviations from ideal solute behavior in these solutions, we have also computed γ_{ideal} for a hypothetical ideal 1–1 electrolyte, using the equation,

$$\gamma_{ideal} = 1/(1+0.036m_2). \quad (6)$$

TABLE III. Water activities in CH_3NH_3Cl solutions at 25°C.

Molarity	Molality	a_1
0.00	0.00	1.0000
4.98	7.05	0.780_2
6.97	11.84	0.639_7
7.12	12.26	0.640_2
8.99	19.07	0.539_8
9.06	19.36	0.514

[10] H. Jones, F. J. Spuhler, and W. A. Felsing, J. Am. Chem. Soc. **64**, 965 (1942).

[11] (a) R. A. Robinson and D. A. Sinclair, J. Am. Chem. Soc. **56**, 1830 (1934); (b) R. A. Robinson and H. S. Harned, Chem. Revs. **28**, 453 (1941).

As shown in Table IV, γ_2/γ_{ideal} is also quite constant, increasing by only 20% in this wide concentration range.

Chemical Shifts and Spin-Spin Couplings

A schematic diagram of the NMR spectrum of CH_3NH_3Cl in aqueous solution at low pH is shown in Fig. 1. Numerical values of the frequency separations indicated in this figure are listed in Table V. It is worth noting that δ_{MN} changes much less with CH_3NH_3Cl concentration than does either δ_{MW} or δ_{WN}. The relatively large standard deviations of J, δ_{WN} and δ_{MN} are due to the considerable width of the NH_3 "lines."

Measurement of (k_6+k_7)

By methods identical with those reported previously,[1] we deduced from the shape of the CH_3 quadruplet[12] a pseudo-first-order rate constant,

$$k \equiv \text{rate of exchange}/[CH_3NH_3^+]. \qquad (7)$$

According to the reactions listed in Table I, k is given as a function of other variables in Eq. (8)

$$k = k_4 + \{k_5K_w + (k_6+k_7)K_A[CH_3NH_3^+]\}/[H^+]. \qquad (8)$$

In principle, all rate constants are functions of the CH_3NH_3Cl concentration; k_4 was estimated as follows: On the basis of data for the reaction of NH_3 with H_3O^+,[8] it is probable that the analogous reaction of CH_3NH_2 with H_3O^+ is diffusion controlled, and that k_{-4} is not highly sensitive to concentration. We therefore assumed that $k_4 = k_{-4}K_A$, with k_{-4} constant as given in Table VI. k_4, estimated in this way, ranged from 4 to 0.05% of k. Next, the average value of $k_5K_w + (k_6+k_7)K_A[CH_3NH_3^+]$ was calculated from the variation of $(k-k_4)$ with $[1/H^+]$. Finally, (k_6+k_7) was computed, using the reasonable estimate of k_5 in Table VI which is consistent with the experimental value of k_5 for the reaction of NH_4^+ with OH^-.[13] The term, k_5K_w, was in every case less than 4% of $(k_6+k_7)K_A[CH_3NH_3^+]$. The results are shown in Table VII, together with interpolated values of K_A and η/η_0, based on data reported in preceding sections. The table shows that (k_6+k_7) decreases to approximately one-half its maximum value in this concentration range, but that $(k_6+k_7)\,\eta/\eta_0$ appears to be constant within experimental error. We tried the factor η/η_0 because we hoped that reactions with specific rates as high as these might be diffusion controlled, but admit that the correlation may be fortuitous. At any rate, we appear to have a useful function for extrapolation to infinite dilution, and have tentatively adopted the average value of $(k_6+k_7)\eta/\eta_0$, 9.35 ± 0.55, as the best estimate of (k_6+k_7) at zero ionic strength. The fact that (k_6+k_7) is constant, after correction for the change in viscosity of the medium, is consistent with data for the corresponding reactions in the NH_4Cl system.[8]

TABLE IV. Mean molal ionic activity coefficients of concentrated aqueous solutions of CH_3NH_3Cl at 25°.

m_2	γ_2 (±0.03)	γ_{ideal}[a]	γ_2/γ_{ideal}
7	(0.487)	0.799	0.61
9	0.51	0.755	0.67
11	0.51	0.721	0.71
13	0.50	0.681	0.73
15	0.49	0.649	0.75
17	0.47	0.620	0.76
19	0.45	0.594	0.76

[a] Equation (6).

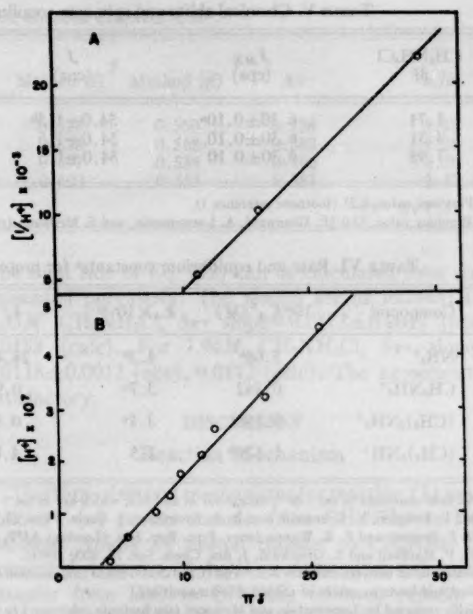

FIG. 2. Experimental plot of water line width in 7.94M aqueous solution of CH_3NH_3Cl at 25°. (a) $\pi\delta$ vs $[1/H^+]$ for "initial broadening"; (b) $\pi\delta$ vs $[H^+]$ for "final narrowing."

Measurement of k_7/k_6

In order to separate (k_6+k_7) into the individual rate constants, we have measured the exchange broadening of the water line. We define a quantity p by

$$p = \frac{k_5K_w + k_7K_A[CH_3NH_3^+]}{k_5K_w + (k_6+k_7)K_A[CH_3NH_3^+]} \qquad (9)$$

from which the ratio k_7/k_6 can be deduced since the small term k_5K_w is already known ($k_5Kw = 0.00038$, on the basis of Table VI). This quantity may be measured by two different methods: (i) from the "initial broadening" of the water line at relatively high $[H^+]$ concen-

[12] *Tables of Exchange Broadened N-M-R Multiplets* (The Weizmann Institute of Science, Rehovoth, Israel, 1958).
[13] M. Eigen and J. Schoen, Z. Elektrochem. 59, 483 (1955).

TABLE V. Chemical shifts and spin-spin couplings for the system CH_3NH_3Cl-H_2O at 25°. ν_0=40.0 Mc.

CH_3NH_3Cl M	J_{MN} (cps)	J (cps)	$\delta_{MW}\nu_0$ (cps)	$\delta_{WN}\nu_0$ (cps)	$\delta_{MN}\nu_0$ (cps)
1.71	6.30±0.10[a]	54.0±1.5[b]	85.2±0.2	104.4±1.0	189.6±1.0
4.31	6.30±0.10	54.0±1.5	...	109.2±1.5	...
7.95	6.30±0.10	54.0±1.5	76.0±0.3	117.1±1.5	193.1±1.5

[a] Previous value, 6.21 (footnote reference 1).
[b] Previous value, 53.0 [E. Grunwald, A. Loewenstein, and S. Meiboom (private communication)].

TABLE VI. Rate and equilibrium constants[a] for proton transfer reactions of alkylammonium ions in water at 25°.

Compound	$10^{10}K_A^\circ(M)$	$k_{-4}\times10^{-10}$	k_4°	$k_5\times10^{-10}$	$k_{-5}\times10^{-8}$	$k_6\times10^{-8}$	$k_7\times10^{-8}$
NH_4^+	5.68[b]	4.3[b]	24.4	3.0[g]	5[g]	11.5[b]	0.9[b,j]
$CH_3NH_3^+$	0.242	3.7[c]	0.90	3.7[h]	120	4.0	5.3
$(CH_3)_2NH_2^+$	0.168[c]	3.1[c]	0.52	...	...	0.5[i]	7.3[f]
$(CH_3)_2NH^+$	1.57[c,d]	2.5	4.0[f]	...	...	0.0[i]	4.0[f]

[a] All rate constants in $sec^{-1}M^{-1}$, except for k_4 and k_{-5}, which are in sec^{-1} (see footnote 4).
[b] M. T. Emerson, E. Grunwald, and R. A. Kromhout, J. Chem. Phys. 33, (1960), preceding paper, this issue.
[c] D. F. Everett and F. K. Wynne-Jones, Proc. Roy. Soc. (London) A177, 499 (1941).
[d] H. P. Marshall and E. Grunwald, J. Am. Chem. Soc. 76, 2000 (1954).
[e] Interpolated between data for NH_4^+ and $(CH_3)_2NH^+$. Since this reaction is diffusion controlled (see footnote reference b to this table), the interpolation seems justified and leads to values of the expected magnitude.
[f] Value reported by Loewenstein and Meiboom (see footnote reference i to this table), corrected from 22° to 25° by multiplying by 1.30.
[g] At 20°, see footnote reference 13.
[h] E. Grunwald, A. Loewenstein, and S. Meiboom, J. Chem. Phys. 25, 382 (1956); 27, 630 (1957).
[i] A. Loewenstein and S. Meiboom, J. Chem. Phys. 27, 1067 (1957).
[j] S. Meiboom, A. Loewenstein, and S. Alexander, J. Chem. Phys. 29, 969 (1958).

TABLE VII. Measurement of (k_6+k_7) for CH_3NH_3Cl in water at 25°.

$[CH_3NH_3Cl]$	$k_5k_W+(k_6+k_7)K_A[CH_3NH_3^+]$ (M sec^{-1})×10^3	$10^{11}K_A$(M)	$10^8(k_6+k_7)$ ($sec^{-1}M^{-1}$)	η/η_0	$10^8(k_6+k_7)\eta/\eta_0$ ($sec^{-1}M^{-1}$)
1.71	18.7±0.5	1.18	9.0	1.05	9.5
3.33	22.6±2.1	0.82	8.2	1.21	9.9
4.46	18.5±1.3	0.635	6.3	1.35	8.6
5.52	18.8±0.8	0.504	6.6	1.50	9.9
6.43	15.3±0.8	0.416	5.6	1.64	9.2
7.57	10.0±1.2	0.328	3.9	1.85	7.2
8.12	12.8±1.5	0.291	5.3	1.96	10.2
					Av 9.3_5±0.5_5

trations; (ii) from the "final narrowing" of the water line at relatively low $[H^+]$ concentrations.

The first of these methods has already been described. If δ is the full width of the water line at half of maximum height (half-width), then it can be shown that, as $\pi\delta$ approaches the unbroadened line width, $1/T_2$, its value is given in good approximation by

$$\pi\delta = T_2^{-1} + (m_2k_4/111.0) + p\frac{m_2\{k_5K_w+(k_6+k_7)K_A[CH_3NH_3^+]\}}{111.0[H^+]}. \quad (10)$$

In this equation, m_2 is the molality of methylamine hydrochloride, and $m_2/111.0$ is one-half the molar ratio, $[CH_3NH_3^+]/[H_2O]$. Thus, according to (10), the plot of $\pi\delta$ vs $[1/H^+]$ should be linear in the region of initial broadening. The slope of this line, in conjunction with the data listed in the second column of Table VII, permits evaluation of p. A typical experimental plot is shown in Fig. 2(a).

The second method utilizes the region of pH in which the exchange is fast enough for the H_2O and NH_3 proton resonances to have coalesced into a single, slightly broadened line. A method of obtaining rate constants for this limiting case of "final narrowing" has been described by Anbar, Loewenstein, and Meiboom[14] for the simple case of two proton lines. Using the simplified method of McConnell[15] for the special case of slow passage and negligible saturation, we have derived limiting expressions for the half-width of the single line resulting from the coalescence of the H_2O line and the

[14] M. Anbar, A. Loewenstein, and S. Meiboom, J. Am. Chem. Soc. 80, 2630 (1958).
[15] H. McConnell, J. Chem. Phys. 28, 430 (1958).

TABLE VIII. Measurement of k_7/k_6 for aqueous CH_3NH_3Cl, 25°.

$[CH_3NH_3^+]$ M	$m_2/111$	pH range Method (i)	pH range Method (ii)	p Method (i)	p Method (ii)	Av	k_7/k_6
1.78	0.0180	2.5–4.6	6.3–7.2	0.525	0.550	0.538	1.15
1.80	0.0182	2.5–4.8	6.0–6.4	0.598	0.568	0.583	1.38
4.31	0.0521	2.8–4.0	6.1–7.0	0.597	0.534	0.566	1.30
7.94	0.1344	3.7–4.3	6.3–8.0	0.609	0.565	0.587	1.42
							Av 1.31

NH_3 triplet, assuming that the only mechanisms of exchange are those listed in Table I, and that k_4 may be neglected at high pH. Expressed in terms of rate constants and quantities defined in Fig. 1, the final result is as follows:

$$\pi\delta = T_2^{-1} + \{(3\delta_{WN}\nu_0^2/p)[111.0/(111.0+3m_2)]^2 + 2J^2\} \times \{3m_2[H^+]/(111.0+3m_2)\} \times \{k_5K_w + (k_6+k_7)K_A[CH_3NH_3^+]\}^{-1}. \quad (11)$$

According to this equation, $\pi\delta$ is proportional to $[H^+]$, and the slope, in conjunction with data listed in Tables V and VII, permits evaluation of p. Typical data are shown in Fig. 2(b).

Results obtained by both methods are summarized in Table VIII. The p values are accurate to about 10%. The excellent agreement of results obtained by the two different methods indicates that the reactions listed in Table I correctly describe the proton transfer over a range of more than 5 pH units, from 2.5 to 8.0. Moreover, p is virtually independent of the CH_3NH_3Cl concentration, increasing by at most 20% over the entire range.

The values of k_7/k_6 were obtained from the p values by solving Eq. (9). These values, too, increase only insignificantly with concentration. Using their average, and data presented in the preceding section, we estimate that $k_6 = 4.0\times10^8$, and $k_7 = 5.3\times10^8$ sec^{-1} M^{-1}, for $CH_3NH_3^+$ in water at 25° and infinite dilution.

Confirmation from NH_3 Triplet

Although the consistency of p obtained by the two methods is already a strong indication of the correctness of our kinetic scheme, we thought it worthwhile to obtain further confirmation from the half-widths of the NH_3 triplet. The significance of this check has been discussed previously.[1] The method is closely analogous to that employed in the case of ammonium ion,[16] but is less precise because of the broad and complex nature of these lines even in the absence of exchange.[1] However, the plots of half-width vs $[1/H^+]$ for these lines were linear in the range of "initial broadening," pH 2.5–4.0, and the slopes were calculated by weighted least squares (weighting factor $=[H^+]$.) If the kinetic scheme is correct,[1,16] we see

$$3\pi\cdot\text{slope} = k_5K_w + (k_7+\tfrac{3}{2}k_6)K_A[CH_3NH_3^+]. \quad (12)$$

[16] Footnote reference 8, Eq. (6).

The right side of Eq. (12) can be calculated from data presented previously. The results are as follows: For $4.35M$ CH_3NH_3Cl, $3\pi\cdot$ slope $= 0.0173\pm0.0017$ (obs), 0.0158 (calc). For $7.94M$ CH_3NH_3Cl, $3\pi\cdot$ slope $= 0.0118\pm0.0012$ (obs), 0.0112 (calc). The agreement is satisfactory.

DISCUSSION

Reaction Mechanism

The three simplest mechanisms for reaction (1) are as follows[1]: (a) proton transfer from $CH_3NH_3^+$ to H_2O, followed rapidly by proton transfer to CH_3NH_2; (b) concerted transfer of both protons; and (c) proton transfer from H_2O to CH_3NH_2, followed rapidly by release of a proton from $CH_3NH_3^+$. Regarding mechanism (a), the specific rate for proton transfer from $CH_3NH_3^+$ to H_2O, $k_4°$, is 0.9 sec^{-1} (Table VI). It is difficult to see how this specific rate could be greatly accelerated by the presence of a CH_3NH_2 molecule in a site adjacent to the water molecule. This mechanism may therefore be ruled out.

In mechanism (b), the rate-determining step is either the reorientation of the water molecule(s) between the methylammonium ion and methylamine so as to permit the concerted proton transfer, or it is the proton transfer itself. In the former, the rate should depend on the extent of the required reorientation. If the latter, the contribution to the activation energy due to the proton transfer from the ion to water should be greater than that due to the transfer from water to the amine, since in the corresponding bimolecular processes, the activation energies are in this sequence (in Table VI, compare $k_4°$ with k_{-5}). Thus, if the proton transfer itself were rate determining, the rate constant for the concerted process should parallel the acid strength. In either case, k_7 should be *greater* for NH_4^+ than for $CH_3NH_3^+$: NH_4^+ and NH_3 fit substitutionally into the water structure,[17] so that concerted proton transfer is possible with a minimum of reorientation; and NH_4^+ is the stronger acid. In fact, k_7 is *smaller* for NH_4^+ than for $CH_3NH_3^+$ (Table VI), contrary to this prediction.

[17] There is evidence which suggests that the effect of NH_4^+ on the quasi-crystalline structure of water is very small. The viscosity B coefficient of NH_4^+ is -0.007 at 25°, which, according to the theory of Cox and Wolfenden, means that NH_4^+ produces a very slight increase in the structural temperature of the water in its cosphere. See W. M. Cox and J. H. Wolfenden, Proc. Roy. Soc. (London) **A145**, 486 (1934); R. W. Gurney, *Ionic Processes in Solution* (McGraw-Hill Book Company, Inc., New York, 1953), Chap. 9.

In mechanism (c), the electrostatic field of the ion is expected to increase the acid strength of adjacent water molecules by at least three orders of magnitude. For example, K_{A1}/K_{A2} for $H_3{}^+NCH_2CH_2N^+H_3$ is 1000 in water at 20°.[18] The increase in acid strength of the water facilitates the proton transfer to amine, and the observed magnitude of k_7 is reasonable relative to the values of k_{-5} listed in Table VI.[1,18b] Since the field produced by the ion at the nearest water molecule is the same for $NH_4{}^+$ and $CH_3NH_3{}^+$, the rate should parallel the base strength of the proton-accepting amine, as observed. Thus mechanism (c) is most consistent with the experimental facts.

Interpretation of k_7/k_6

Between the concentrations of 1.7 and 8*M* the molar ratio of water to CH_3NH_3Cl changes so markedly that the observation of near constancy of k_7/k_6 nevertheless requires a complex interpretation. At low concentrations, CH_3NH_3Cl is a strong electrolyte. But at higher concentrations, and especially at 8*M*, we must assume that ionic association is considerable. The smallness of the increase in γ_2/γ_{ideal} between 5 and 9*M* (7 and 19 molal, Table IV) shows that the desolvation of the ions, which is inevitable at the highest concentrations, is compensated almost exactly by ion-ion interactions, largely of short range. It seems reasonable to infer that the interaction energy of an ion with an adjacent water molecule is similar to that with an adjacent counterion. In further support of this view, the association constant of CsCl, as deduced from conductance data, is close to 0.8.[19] If the similarity of activity coefficients between 0 and 1*m* implies similarity of association constants, the value for CH_3NH_3Cl must be of the same order of magnitude. In view of this evidence, it is surprising that the difference, δ_{MN}, between the chemical shifts of the methyl and NH_3 protons does not change by more than 0.09±0.05 ppm (3.5 cps, Table V) over the entire concentration range.

According to the transition-state theory, the rate constant for reaction (1) may be formally represented as a function of electrolyte concentration:

$$k_7 = k_7{}^\circ y_{BH^+} y_B a_1 / y_{\pm 7}, \qquad (13)$$

where BH^+ denotes the alkylammonium ion, B its conjugate base, $\pm$ the transition-state complex, y the molar activity coefficient of the species indicated,[20] and $k_7{}^\circ$ the rate constant in water at infinite dilution. Since the water activity a_1 appears to the first power, Eq. (13) contains the assumption that only one water molecule participates. This is reasonable if reaction proceeds by mechanism (c). The activity coefficients are unknown, *a priori*, but many of the unknown factors cancel out in the ratio, k_7/k_6.

Let us first consider reaction (2) at fairly low concentrations where ionic association may be neglected. If the rate-determining step is the displacement of a water molecule by a molecule of amine in the solvation shell of BH^+,[8] reactions (1) and (2) are kinetically of the same order, and

$$k_7/k_6 = (k_7{}^\circ/k_6{}^\circ)(y_{\pm 6}/y_{\pm 7}). \qquad (14)$$

In Eq. (14), the factors a_1, y_{BH^+}, and y_B have canceled out. In addition, $y_{\pm 6}/y_{\pm 7}$ depends largely on the distribution of electric charge in the two transition states since the transition states are structural isomers, and non-Coulombic terms largely cancel out. According to mechanism (c), charge is generated in reaction (1), whereas charge is not generated in reaction (2).

$$BH^+ + OH_2 + B \xrightarrow[\text{mechanism (c)}]{\text{reaction (1)}} BH^+ \cdot OH^- \cdot BH^+.$$

Hence $y_{\pm 6}/y_{\pm 7}$, and therefore k_7/k_6, may be expected to *increase* with electrolyte concentration.

At high concentrations, one must allow for the possibility that chloride ions rather than water molecules occupy some of the sites adjacent to the $NH_3{}^+$ group. Formally, this complication is handled as follows: Let α=fraction of nearest-neighbor sites occupied by water molecules. Since reaction (1) takes place only when there is a water molecule, we may write,

$$k_7 = \alpha k_7'. \qquad (15)$$

On the other hand, reaction (2) can occur whenever BH^+ and B become nearest neighbors, regardless of the prior composition of the solvation shells. If the pairwise interaction energies of $BH^+ - H_2O$ and $BH^+ - Cl^-$ are comparable, it is likely that Cl^- is displaced by amine at a rate comparable to that of the displacement of a water molecule.

In terms of α, we may write

$$k_6 = \alpha k_6' + (1-\alpha) k_6'' \qquad (16)$$

where $\alpha k_6'$ is due to the displacement of H_2O, and $(1-\alpha)k_6''$ is due to all other displacements. Equations (15) and (16) lead to the expression

$$k_7/k_6 = (k_7'/k_6')/\{1 + (1-\alpha)k_6''/\alpha k_6'\}. \qquad (17)$$

Because of the charge generation in reaction 1, k_7'/k_6' may be expected to increase with electrolyte concentration, as before. But this increase can now be compensated by the increasing value of $(1-\alpha)k_6''/\alpha k_6'$, so that k_7/k_6 could remain nearly constant, as observed.

In conclusion, we have shown that the mechanisms we have assumed for reactions (1) and (2) are not inconsistent with the observed near constancy of k_7/k_6. As long as $(1-\alpha)k_6''$ is not small compared to $\alpha k_6'$,

[18] (a) G. Schwarzenbach, Helv. Chim. Acta **16**, 522 (1933); (b) for a theoretical discussion, see F. H. Westheimer and M. W. Shookhoff, J. Am. Chem. Soc. **61**, 555 (1939).

[19] R. L. Kay, J. Am. Chem. Soc. **82**, 2099 (1960).

[20] *Molar* activity coefficients y are used rather than *molal* activity coefficients γ, since the rate constants are expressed in molar concentration units.

k_7'/k_6' must be assumed to increase with electrolyte concentration, making it probable that the transition state for reaction (1) is more polar than that for reaction (2). This conclusion is not altered if the mechanism of reaction (2) is such that the rate-determining step is the proton transfer itself rather than the final step in the diffusion process. Equation (14) must then be replaced by

$$k_7/k_6=(k_7^\circ/k_6^\circ)a_1(y_{\pm6}/y_{\pm7}),$$

where a_1 decreases with increasing electrolyte concentration, thus forcing $y_{\pm6}/y_{\pm7}$ again to increase. Although many problems remain, mechanism (c) does seem to be the most likely mechanism for reaction (1).

THE JOURNAL OF CHEMICAL PHYSICS VOLUME 33, NUMBER 2 AUGUST, 1960

Nucleation and Growth of Mercury Crystals at Low Supersaturation

G. W. Sears

General Electric Research Laboratory, Schenectady, New York

(Received March 21, 1960)

In the present paper it is shown that mercury crystals can be nucleated on a cold glass surface at a much lower supersaturation than has been previously reported. The role of ambient temperature in the growth process is described. It is established that the growth habit is intrinsic to the pure mercury and is not characteristic of a growth modification by foreign gases.

INTRODUCTION

THE habit of mercury crystals grown on a cold glass surface from a supersaturated vapor may be altered by merely chainging the ambient temperature surrounding the growth surface. With an ambient temperature of about 25°C, very thin mercury platelets can be grown[1] at supersaturations of about fifteen hundred. If the ambient temperature is maintained at −50°C, mercury whiskers[2,3] can be grown at a supersaturation of about one hundred.

The growth mechanisms for both the whisker and platelet habits are well accounted for.[2-4] They are based upon the screw-dislocation mechanism of crystal growth[5] and are not unique to mercury. The general validity of the mechanisms has been established in studies of the growth of a variety of crystalline whiskers and platelets.[6-9]

The growth of mercury whiskers has been more recently studied by Honjo and co-workers electron microscopically[10] and by Gomer[11,12] using field emission microscopy. Gomer was able to obtain independent evidence for the existence of an axial screw dislocation in growing mercury whiskers. In addition, he studied the surface diffusion process in some detail.

In the present paper it will be shown by a new observational method that mercury whiskers grow at an ambient temperature of 25°C as well as at −50°C in a like region of supersaturation. The role of the ambient temperature is to determine the axial temperature gradient in the whiskers. Thus a lower ambient temperature leads to longer whiskers. In addition the nucleation of mercury crystals was observed at much lower supersaturations than previously reported. The crystals nucleated at a supersaturation of only 7 had a good thermal connection between the growing surfaces and the glass substrate, as opposed to either whiskers or platelets.

Although the growth behavior of mercury whiskers and platelets has been satisfactorily rationalized, the nucleation events leading to the growth habits are not well understood. Heterogeneous nucleation of parent nuclei must occur at supersaturations insufficient to cause an appreciable rate of two-dimensional nucleation. The nucleation process will be discussed in the present report.

EXPERIMENTAL

The crystal-growth experiments were carried out in the system illustrated in Fig. 1. Mercury vapor was supplied by a thermostatted reservoir of liquid mercury. The vapor was allowed to flow through a capillary leak into the growth chamber. The growth chamber was continuously pumped, but the pumping speed could be changed by a factor of 20 with the cutoff valve.

The liquid-mercury reservoir was constructed with a thin flat bottom so that the temperature of the mercury could be changed quickly. The auxilliary vacuum

[1] M. Volmer and I. Estermann, Z. Physik **7**, 13 (1921).
[2] G. W. Sears, Acta Met. **1**, 457 (1953).
[3] G. W. Sears, Acta Met. **3**, 361 (1955).
[4] G. W. Sears, J. Chem. Phys. **25**, 637 (1956).
[5] F. C. Frank, Discussions Faraday Soc. **5**, 48, 67 (1949).
[6] G. W. Sears, Acta Met. **3**, 367 (1955).
[7] C. R. Morelock, "Growth of sub-micron whiskers" (to be published).
[8] W. W. Webb and W. D. Forgeng, J. Appl. Phys. **28**, 1, 449 (1959).
[9] R. C. DeVries and G. W. Sears, J. Chem. Phys. **31**, 1256 (1959).
[10] G. Honjo, N. Kitamura, K. Shimaoka, and K. Mihama, J. Phys. Soc. Japan **11**, 527 (1956).
[11] K. Gomer, J. Chem. Phys. **28**, 458 (1958).
[12] R. Gomer, J. Chem. Phys. **26**, 1333 (1957).

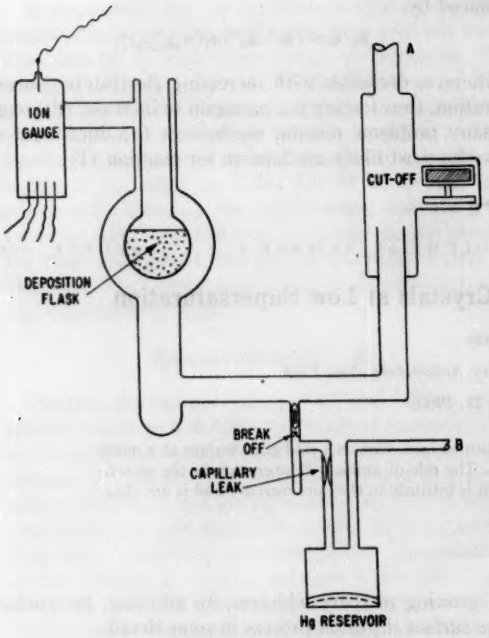

FIG. 1. Crystal-growth apparatus.

line *B* allowed continuous pumping of noncondensable gases from the reservoir while the pumping speed for mercury vapor by that line was effectively zero. The pressure on noncondensable gases was in this way maintained 10^{-4} times lower than the pressure of mercury vapor in the reservoir chamber.

The crystal-growth apparatus of Fig. 1 is shown in relation to the entire vacuum line as a block diagram in Fig. 2. The growth chamber, the associated ion gauge, and the cutoff were arranged so that they could be baked in a furnace. The bakeouts were at 500°C and usually for 24-hr periods. Bakeouts were continued until the background pressure with ion gauges outgassed fell to 10^{-10} mm as measured by inverted ion gauge. The ion gauges were outgassed by electron bombardment. The mercury reservoir was torched to outgas the liquid mercury. Some distillation into line *B* occurred. Since the pumping speed for mercury in this line was negligible, the distillation was unimportant. After the final bakeout the breakoff seal was opened and mercury vapor was pumped through the capillary and growth vessel.

The mercury pressure during a condensation experiment was continuously recorded. The positive-ion current from the ion gauge was amplified with the amplifier circuit of a DPA-38 ion-gauge control circuit. The output voltage was recorded with a G.E. photoelectric recorder-potentiometer type. During the outgassing procedure the positive-ion signal was measured with a Millivac micromicroammeter MV-11C.

The pressure of mercury vapor in the growth region was adjusted to the desired value by altering the temperature of the mercury reservoir. Only short-time temperature control was needed, so a Dewar of water served as a constant-temperature bath.

The mercury pressure in the growth vessel was maintained at some value less than 50 times the vapor pressure at −63°C since the nucleation and growth of mercury crystals on glass was not believed to occur under these circumstances. The pressure was established by the rate at which mercury flowed into the growth region through the capillary tubing and by the pumping speed out of the growth region.

As soon as the growth surface reached −63°C the cutoff was closed and the pressure began to rise to the new steady-state level. As the pressure increased, a supersaturation was attained sufficient to cause a rapid rate of nucleation and growth of mercury crystals on the cold glass surface. At this pressure the cold surface began to act as a pump for mercury vapor. The pressure reached a maximum and then decreased, as shown by curve C in Fig. 4 for a typical experiment. In the absence of a cold surface the pressure-time curve corresponded to Fig. 3. When the condensation surface was illuminated with a microscope light after growth the pressure increased sharply and dropped again.

Surprisingly, the height of the maximum in the pressure-time curve was found to depend on the length of time that the growth surface was exposed to a supersaturation of less than 50. A comparison of pressure-time curves proved to be a sensitive method of detecting nucleation that occurred before the cutoff was closed. In Fig. 4, pressure vs time curves after cutoff are shown for an initial pressure of 6×10^{-7} mm. Curve A was measured after a 9-min exposure to the initial pressure, curve B after a 24-min exposure, and curve C after 64 min. It is apparent that the pumping speed of the growth surface becomes significant at a lower supersaturation, the longer its exposure to mercury vapor at 6×10^{-7} mm. For the 64-min preliminary exposure the steady-state pressure fell just detectably during the exposure period.

With an initial pressure of 2.5×10^{-7} mm corresponding to a supersaturation of 7, a small amount of nuclea-

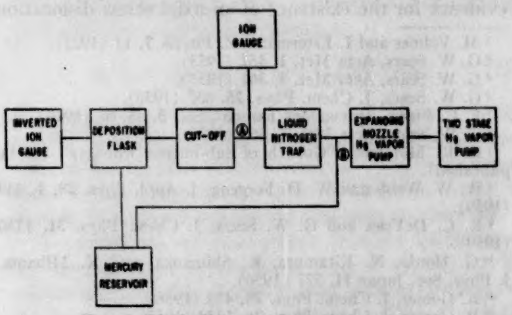

FIG. 2. Block diagram of vacuum system.

ation could be detected after 24 min exposure. The pressure-time maximum fell appreciably below the curve corresponding to 2.5-min preliminary exposure. No detectable decrease of initial pressure was observed before closing the cutoff.

Crystals grown after long exposure periods to an initial low supersaturation gave a contrasting result to those grown with very short exposure periods when illuminated with a microscope light. The pressure increase was almost undetectable when the growth surface was illuminated.

DISCUSSION

A. Rate of Pressure Variation

The steady-state pressure in the growth chamber in the absence of condensation is given by

$$P_1 = P_0 S_0 / S_1, \qquad \text{(A1)}$$

where P_0 is the pressure of mercury in the revervoir, S_0 is the volume rate of flow into the growth chamber from the reservoir and S_1 is the pumping speed out of the growth chamber.

The pressure-time curve after closing the cutoff is a solution of the differential equation

$$dP/dt + \{(S_2 + S_c)/V\} P = P_0 S_0 / V \qquad \text{(A2)}$$

subject to the boundary condition that $P = P_1$ when $t = 0$, where V is the volume of the region behind the cutoff and S_2 is the pumping speed past the cutoff, and S_c is the pumping speed of the growing crystals. The pumping speed of the deposition surface is again

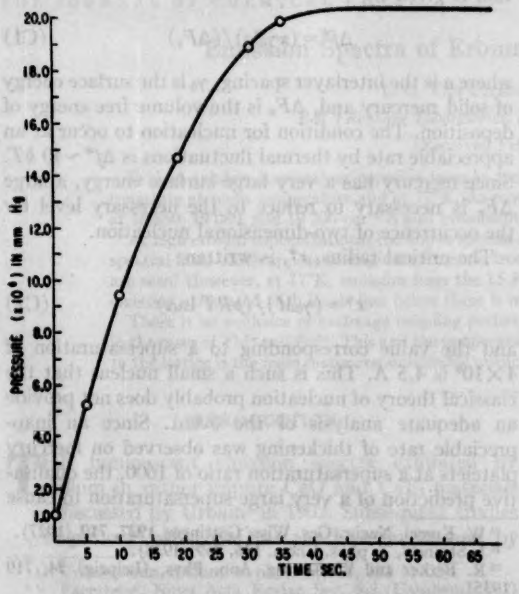

FIG. 3. Pressure vs time without cold finger.

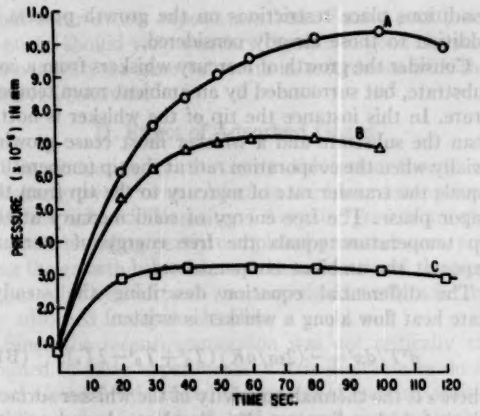

FIG. 4. Pressure vs time curves. *A*: Preliminary exposure 9 min at 6.5×10^{-7} mm; *B*: Preliminary exposure 24 min at 6.2×10^{-7} mm; *C*: Preliminary exposure 64 min at 6.2×10^{-7} mm.

some function of time, the functionality depending upon the exposure time to and the magnitude of the preliminary supersaturation.

In the absence of a cold surface $S_c(t) = 0$ and the solution of Eq. A is written

$$P = (P_0 S_0 / S_2)\{1 + [S_2/S_1) - 1] \exp(-S_2 t/V)\}. \qquad \text{(A3)}$$

Since $S_c \cong 0$ at $t = 0$ for the reported experiments, the initial slope of the pressure-time curves is independent of prenucleation and is given by

$$[dP/dt]_{t=0} = P_0 S_0 / V. \qquad \text{(A4)}$$

On the other hand, the maximum pressure P^* is directly dependent on $S_c(t^*)$, the pumping speed of the deposition surface at the time corresponding to the maximum pressure, and

$$P^* = P_0 S_0 \{S_2 + S_c(t^*)\}^{-1}. \qquad \text{(A5)}$$

Since $S_c(t^*)$ is dependent upon the area of growing crystal, any pretreatment that increases the number and/or size of the growing crystallites will decrease the height of the maximum in the pressure-time curve. The increased sensitivity has allowed a demonstration that mercury crystals may be nucleated upon a glass surface at a saturation ratio of only 8, an order of magnitude smaller than previously reported.

B. Temperature Gradients in Growing Whiskers

When a whisker grows from a surface at a given temperature but surrounded by a 2π solid angle of a different ambient temperature, the temperature of the whisker tip[13] differs from the substrate temperature. The thermal gradients in whiskers grown under these

[13] These gradients are of particular importance in a general technique for whisker growth developed by C. R. Morelock[10] in which small temperature differences are maintained between the source and growth region by taking advantage of steady-state radiant heat flow.

conditions place restrictions on the growth process in addition to those already considered.

Consider the growth of mercury whiskers from a cold substrate, but surrounded by an ambient room temperature. In this instance the tip of the whisker is hotter than the substrate and a whisker must cease growing axially when the evaporation rate at the tip temperature equals the transfer rate of mercury to the tip from the vapor phase. The free energy of solid mercury at the tip temperature equals the free energy of mercury vapor at the ambient temperature.

The differential equation describing the steady-state heat flow along a whisker is written

$$d^2T/dx^2 = -(2\epsilon\sigma/aK)(T_1^4+T_0^4-2T_4), \quad \text{(B1)}$$

where ϵ is the thermal emissivity of the whisker surface, a is the whisker diameter, K is the thermal conductivity of mercury, T_1 is the ambient temperature, and T_0 is the substrate temperature. The temperature $T(x)$ is bounded by T_0 and the melting temperature of mercury.

For the growth conditions $T_1=298°K$ and $T_0=210°K$ Eq. (B1) is approximated by the equation

$$d^2T/dx^2 = -1.5\epsilon\sigma T_1^4/aK. \quad \text{(B2)}$$

The right-hand side of Eq. (B2) differs by 10% from the right-hand side of Eq. (B1). Integrating Eq. (B2) yields

$$T-T_0 = (1.5\epsilon\sigma T_1^4/2aK)(2lx-x^2) \quad \text{(B3)}$$

under the approximation that $dT/dx=0$ at $x=1$. From Eq. (B3) the maximum length l^* to which a whisker can grow before reaching the melting temperature of mercury T_{Hg} at its tip is approximated by

$$l^* \approx \{[2aK(T_{Hg}-T_0)]/1.5\epsilon\sigma T_1^4\}.^{\frac{1}{4}} \quad \text{(B4)}$$

Introducing numerical values $K=6\times10^{-2}$ w/cm²/sec/deg/cm and $\epsilon=0.3$ yields

$$l^*=125\ \mu \qquad a=10^{-6}\text{ cm}$$
$$l^*=380\ \mu \qquad a=10^{-5}\text{ cm}$$
$$l^*=1230\mu \qquad a=10^{-4}\text{ cm}.$$

The reported absence of mercury whisker growth in original experiments with a room-temperature ambient[2] is consistent with the very short length, l^*, for 0.01-μ diam whiskers and the observational method. The burst of pressure observed in current experiments upon illumination with a microscope light is accounted for by the associated rise in temperature and vapor pressure at the whisker tips. The absence of a pressure burst upon illumination of crystals grown after nucleating at very low supersaturations qualitatively indicates a much more equiaxed morphology.

In the present experiments there was a steady influx of mercury vapor into the growth vessel, and a decreasing pressure of mercury as the pumping speed of the deposition surface increased. Thus the maximum length attainable by a whisker was determined in that the vapor pressure of mercury at the tip temperature could not exceed the pressure of mercury in the growth vessel. In the original experiments[2,3] the pumping speed of mercury to the growth finger was so large compared to the deposition rate that the pressure of the parent phase was very nearly equal to the vapor pressure of mercury in the source reservoir.

During a 64-min exposure of a $-63°C$ Pyrex surface to 6×10^{-7} mm pressure of mercury vapor, the pressure diminished by about 10^{-8} mm. An upper limit to the mass of condensed mercury is derived from the final condensation rate and the final pressure. No more than 0.4 μg of solid mercury could have condensed. The effect of these crystallites caused a marked decrease in the height of the pressure-time maximum.

C. Nucleation of Mercury Crystals on Glass

It was previously deduced that different parent nuclei were required to account for the whisker[3] vs platelet[4] growth habits. It was not understood why whiskers were not formed with a 25°C ambient temperature. Since they do indeed form the observations are now consistent with the theory.

The necessity for a screw-dislocation mechanism for mercury whisker growth was dependent upon a calculation based on the classical theory of two-dimensional nucleation.[14-17] It was estimated that an appreciable rate of two-dimensional nucleation should require a supersaturation of 4×10^6.[2]

The free-energy barrier to two-dimensional nucleation is given by

$$\Delta f^* = (\pi\gamma_0^2 a)/(\Delta F_v) \quad \text{(C1)}$$

where a is the interlayer spacing, γ_0 is the surface energy of solid mercury and, ΔF_v is the volume free energy of deposition. The condition for nucleation to occur at an appreciable rate by thermal fluctuations is $\Delta f^* \sim 40\ kT$. Since mercury has a very large surface energy, a large ΔF_v is necessary to reduce to the necessary level for the occurrence of two-dimensional nucleation.

The critical radius, r^*, is written

$$r^* = (\gamma_0 M)/(\rho RT \ln\alpha) \quad \text{(C2)}$$

and the value corresponding to a supersaturation of 4×10^6 is 4.5 A. This is such a small nucleus that the classical theory of nucleation probably does not provide an adequate analysis of the event. Since an inappreciable rate of thickening was observed on mercury platelets at a supersaturation ratio of 1600, the qualitative prediction of a very large supersaturation to cause

[14] W. Kossel, Nachr. Ges. Wiss. Göttingen **1927**, 719 (1927).
[15] I. Stranski, Z. phys. Chem. **136**, 259 (1938).
[16] R. Becker and W. Doring, Ann. Phys. (Leipzig) **24**, 719 (1935).
[17] J. Frenkel, J. Phys. U.S.S.R. **9**, 3, 921 (1945).

an appreciable rate of two-dimensional nucleation is empirically verified.

The heterogeneous nucleation of mercury crystals on glass at small supersaturations insufficient to two-dimensionally nucleate mercury on mercury is accounted for by assuming that a few singular surfaces exist such that the surface free energy of the nucleation site plus the surface free energy of solid mercury is greater than the interfacial free energy between the two phases.

The nuclei which formed at low supersaturations are accounted for by assuming the existence of very narrow cracks in the glass surface.[18] Volmer[19] recognized that stable nuclei of a low-temperature phase can be retained above the transformation temperature in cavities in the substrate. Turnbull[20] has presented a formal analysis of phase stability of embryos retained in cavities of specific shapes. He ascribed the effect of thermal history on the kinetics of freezing to the retention of solid embryos above the melting temperature. The existence of fine cracks whose walls preferentially wet solid mercury offers an explanation for nucleation of mercury crystals at very low supersaturations. If several nuclei formed in a given crack they would generate a system of dislocations so that further growth could occur at low supersaturations. Finally such a set of nuclei should yield mercury crystals in good thermal contact with the glass substrate in accordance with the observed behavior.

D. Effect of Adsorbed Gases

The deduction of the screw-dislocation theory of whisker growth[2,3] was subject to the basic assumptions that the only addition sites for crystal growth are the steps surrounding partly completed growth layers, and that the growth behavior was characteristic of the pure vapor-solid system and was not significantly affected by adsorbed foreign molecules.

Since the second assumption was not critically examined in early experiments[2-4] it is desirable to do so now. Gomer[11,12] described the growth of mercury whiskers in a baked, sealed off, and gettered system by electron field emission microscopy. The vacuum conditions were imputed to be very good, but were not directly measured. In the present experiments it has been demonstrated that mercury whiskers can be grown in the presence of a partial pressure of no more than 10^{-10} mm of total foreign gases. These whiskers were detectable by radiating with a microscope light in about 100 sec. After fifteen minutes they became visible to the eye with 25× magnification. In a hundred seconds the total quantity of impinging foreign-gas molecules was 0.003 monolayer. It seems unreasonable to ascribe the growth behavior to adsorbed gases as opposed to the screw-dislocation-mechanism.

[18] J. E. Gordon, D. M. Marsh, and M. E. Parratt, Proc. Roy. Soc. (London) A249, 65 (1959).
[19] M. Volmer, *Kinetik der Phasenbildung* (Theodor Steinkopff-Verlag, Dresden, 1939), p. 103.
[20] D. Turnbull, J. Chem. Phys. 18, 198 (1950).

THE JOURNAL OF CHEMICAL PHYSICS VOLUME 33, NUMBER 2 AUGUST, 1960

Emission Spectra of Erbium in the Scheelite Structure

L. G. VAN UITERT AND R. R. SODEN
Bell Telephone Laboratories, Inc., Murray Hill, New Jersey

(Received February 8, 1960)

Erbium exhibits luminescent emission from excited states at 15 300, 18 400, and 24 500 cm^{-1} in calcium tungstate at room temperature and at 77°K. At room temperature, emission from thermally excited states at 18 830, 19 080, and 19 200 cm^{-1} is also prominent.

At high erbium concentrations, the above spectra are essentially quenched at room temperature and new spectral lines which appear to originate from electronic levels just below the 18 400- and 24 500-cm^{-1} states are seen. However, at 77°K, emission from the 15 300, 18 400- and 24 500-cm^{-1} states is again strong and emission associated with levels just below these is no longer observed.

There is no evidence of exchange coupling preferentially quenching the higher-energy emission states as in the cases of Tb^{3+} and Eu^{3+}. This and the temperature dependencies observed suggest that thermal coupling to the lattice is the main factor responsible for quenching the emission of $Na_{0.5}Er_{0.5}WO_4$.

INTRODUCTION

THE luminescent emission spectra exhibited by erbium in rather impure CaO and CaF_2 materials re discussed by Urbain[1] in 1902. Subsequent studies Fagerberg[2] using CaO as the host lattice and by Chatterjee[3] employing CaF_2 greatly clarified the earlier data. Urbain reported the presence of line emission groups for erbium around 5500 and 4100 A with some question as to the dependability of the latter. Fagerberg found an additional group around 6600 A in CaO. This group was also found in carefully prepared CaF_2 by Chatterjee. However, he did not find an emission group

[1] G. Urbain, Ann. d chim. et phys. (8) 18, 222 (1902).
[2] S. Fagerberg, Nova Acta Regiae Soc. Sci. Upsaliensis (47) 7 (1931).
[3] N. Chatterjee, Z. Phys. 113, 96–114 (1939).

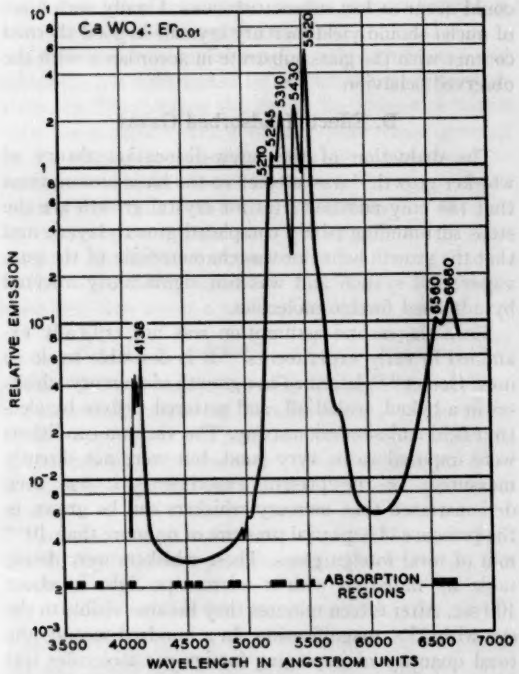

FIG. 1. Intensity of emission plotted on a logarithmic scale vs wavelength in Angstrom units for calcium tungstate containing 1 formula percent erbium excited by 3660-A radiation.

around 4100 A. From a study of the infrared absorption spectra of erbium, Gobrecht[4] was able to assign the 6600-A group emission to transitions within the ground-state multiplet ($^4I_{9/2} \rightarrow {}^4I_{15/2}$) and the 5500-A group emission to transitions from an excited state external to the ground multiplet to the $^4I_{15/2}$ ground term. The purpose of the present work is to demonstrate the presence of still other emission states for erbium in calcium tungstate and some of their concentration and temperature dependencies.

MATERIALS

Crystals having the scheelite structure and the compositions $Ca_{1-2x}Na_xEr_xWO_4$ where $x=0.5$, 0.25, 0.1, 0.03, 10^{-2}, 10^{-3}, 10^{-4}, 3×10^{-5}, and 10^{-5} were prepared employing a $Na_2W_2O_7$ flux as previously described.[5]

MEASUREMENTS

Measurements were made employing a Gaertner high-dispersion spectrometer adapted with an AMINCO photomultiplier microphotometer using a 1P22 tube. Ten-mil slit widths were employed at the entrance and exit to the spectrometer. The system was calibrated against a tungsten lamp to give relative values of brightness of the emitting surface in units of power per unit wavelength range.

Emission was excited by illuminating a sample 1 in. long by ½ in. wide by ¼ in. deep with a 3660-A rich H4 spotlight through a Corning 5874 filter. Mercury lines at 4047 and 4080 A were deducted from the spectra. All of the intensity measurements are relative to 100 for the 5450-A peak of a comparable sample of $Na_{0.5}Tb_{0.5}WO_4$ in keeping with previous intensity measurements.[6,7]

MULTIPLE EMISSION LEVELS

The photomultiplier response to the emission of $Ca_{0.98}Na_{0.01}Er_{0.01}WO_4$ vs wavelength in Angstrom units is shown in Fig. 1. The group centered about 6600 A is the one due to the transition ($^4I_{9/2} \rightarrow {}^4I_{15/2}$) originating from the upper level of the ground multiplet[4] at about 15 300 cm^{-1}. The peak marked 5430 and the members of the same group on its long-wavelength side in Fig. 1 are the ones due to transitions from an electronic state at about 18 400 cm^{-1} to the $^4I_{15/2}$ ground state.[4]

The three peaks just to the high-frequency side of the 5430 peak vary markedly in their intensities with temperature. When the samples under consideration are cooled to the temperature of liquid nitrogen (77°K) these peaks are no longer seen. They correspond to excited states at 19 200, 19 080, and 18 830 cm^{-1}. These states are within the vibration energy range[8] of the tungstate ion (850 cm^{-1}) from the emission level at 18 400 cm^{-1}.

The additional group of emission lines centered about 4100 A, evident in these tungstates, are due to transitions from about 24 500 cm^{-1}. The photomultiplier response shows peaks at 4138, 4121, 4106, 4082, 4070, and 4056 A. The five high-frequency peaks probably correspond to the 5430 peak in its group. At a higher resolution, D. L. Wood of these Laboratories found that the latter does separate into five peaks. The above enumerated emission levels correspond to known absorption levels as shown by the data of Prandtl and Scheiner[9,10] for $ErCl_3$ solutions and indicated as blocked areas below the curve in Fig. 1.

CONCENTRATION EFFECTS

The intensities of the several definable peaks within the 5200- to 5600-A range in Fig. 1 vary markedly relative to each other with concentration. Figure 2 shows the emission profiles for a number of the members of the series $Ca_{1-2x}Na_xEr_xWO_4$. In this figure, the 5430 peaks are chosen as a common reference. The intensity of emission of each, relative to the $Na_{0.5}Tb_{0.5}WO_4$ reference taken as 100, is indicated to the left of its

[4] H. Gobrecht, Ann. Physik **5**, 755 (1938).
[5] L. G. Van Uitert and R. R. Soden, J. Appl. Phys. **31**, 328–30 (1960).
[6] L. G. Van Uitert and R. R. Soden, J. Chem. Phys. **32**, 1161 (1960).
[7] L. G. Van Uitert and R. R. Soden, J. Chem. Phys. (to be published).
[8] C. L. Schafer and F. Matosii, *Das Ultrarot Spectrum* (Verlag-Julius-Springer, Berlin, 1930), p. 334.
[9] W. Prandtl and K. Scheiner, Z. anorg. Chem. **221**, 107 (1934) and **226**, 207 (1937).
[10] K. H. Hellwege, Naturwissenschaften **34**, 225–32 (1947).

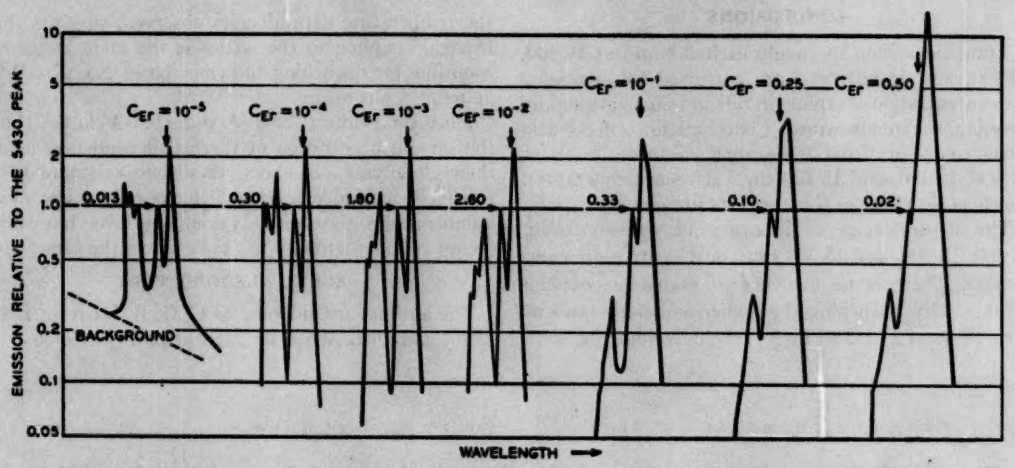

FIG. 2. Intensity of emission plotted on a logarithmic scale vs wavelength for the members of the series $Ca_{1-2x}Na_xEr_xWO_4$ indicated (details in text).

group. The concentration of erbium (C_{Er}) for each composition is indicated directly above its curve, and the position of the wavelength 5500 A is indicated for each curve by an arrow (↓).

The first five curves show that the thermally excited peaks change from an arrangement wherein they are roughly equal in intensity to the 5430 peak with the 5210 peak dominant to one where they fall off in intensity rapidly with increasing frequency as the concentration of erbium is increased. The last three curves show that a peak at 5570 A becomes dominant over the normally stronger 5520 peak at high erbium concentrations. A similar circumstance occurs for the high-frequency group where a peak at 4142 A becomes dominant over the 4138 peak.

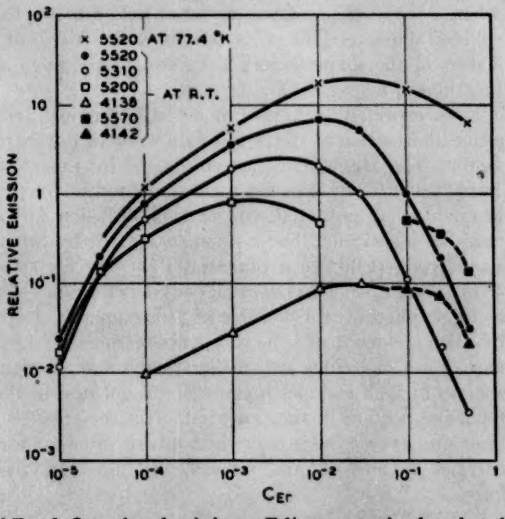

FIG. 3. Intensity of emission vs Er^{3+} concentration for selected lines of the erbium spectra. $C_{Er}=Er^{3+}$ ions per formula volume of $CaWO_4$.

The relative intensities at room temperature of a number of these peaks as a function of C_{Er} are shown in Fig. 3. C_{Er} is in units of the number of erbium ions per formula volume of calcium tungstate. The data for the 5430 peak parallels that for the 5520 peak but is omitted for clarity as its line crosses the 5310 curve twice (refer to Fig. 2). The dependence of the intensity of the 5520 peak upon concentration at 77°K is also shown.

The curves for the thermally excited states show increased divergence from each other and the curve for the 5520 peak with increased concentration. Above $C_{Er}=10^{-3}$ the emission falls off as the square of the concentration—a relationship which parallels the random probability of erbium ions occurring in neighboring calcium sites. The emission observed from $Na_{0.5}Er_{0.5}WO_4$ at room temperature is relatively weak and as mentioned above is dominated by transitions from states which are not as critically dependent upon C_{Er} as those which are dominant at 77°K for low values of C_{Er}. However, emission from the latter states increases markedly when $Na_{0.5}Er_{0.5}WO_4$ is cooled to 77°K and the peaks which are dominant at room temperature are no longer seen. At the lower temperature the intensities of emission shown by the 5430 and 5520 peaks are increased by a factor of about 200. Under these conditions they compare favorably to the emission from the optimum compositions at room temperature. $Na_{0.5}Er_{0.5}WO_4$ is an exception to the generalization[11] that of the rare earths only the compounds of samarium through dysprosium luminesce in the nondilute form.

[11] P. Pringsheim, *Fluorescence and Phosphorescence* (Interscience Publishers, Inc., New York, 1949), p. 458.

CONCLUSIONS

Transitions from thermally excited states at 19 200, 19 080, and 18 830 cm^{-1} are quenched by increasing the concentration of erbium in calcium tungstate and by lowering the temperature. Concentration effects also quench emission from the normal electronic levels at 24 500, 18 400, and 15 300 cm^{-1} at room temperature. However, in all cases these spectra are strong at 77°K.

The dependencies of intensity of emission from 24 500, 18 400, and 15 300 cm^{-1} on C_{Er} are quite comparable. There is no evidence of exchange coupling preferentially quenching the higher emission states as in the cases of Tb^{3+} and Eu^{3+}. This, in conjunction with the temperature dependencies observed, suggests that thermal coupling to the lattice is the main factor responsible for quenching the emission of $Na_{0.5}Er_{0.5}WO_4$ at room temperature.

Since the peaks at 5570 A and 4142 A do not show the same concentration or thermal dependences as do their close-lying neighbors, they may originate from relatively forbidden levels which are only a few wave numbers below the ordinarily dominant levels but which do not couple thermally to the lattice in the same way.

ACKNOWLEDGMENTS

The authors are indebted to C. G. B. Garrett, A. D. Liehr, and D. L. Wood for their helpful discussions.

THE JOURNAL OF CHEMICAL PHYSICS VOLUME 33, NUMBER 2 AUGUST, 1960

Thermal-Diffusion-Column Shape Factors for the Lennard-Jones (12-6) Potential*

B. B. McINTEER AND M. J. REISFELD

Los Alamos Scientific Laboratory, University of California, Los Alamos, New Mexico

(Received February 1, 1960)

The theory of the hot-wire thermal-diffusion column as developed by Jones and Furry involves the shape factors h, k_c, and k_d, which are functions of the transport properties of the gas. The shape factors have been evaluated numerically for a gas whose molecules interact according to the Lennard-Jones (12–6) potential, given by $V(r)=4\epsilon[(\sigma/r)^{12}-(\sigma/r)^6]$. The results are tabulated for a range of kT/ϵ from 0.8 to 30 for temperature ratios as great as 6 and for ratios of column radii up to 100. These values are more accurate than those previously computed for potentials varying as r^{-5} (Maxwellian) and for $r^{-\infty}$ (rigid spheres).

The values for the constants are found to give good agreement with experimental data on the system He^3-He^4.

I. INTRODUCTION

THE theory of the thermal-diffusion column was given by Furry, Jones, and Onsager[1,2] in which they obtained the basic transport equation in terms of the column constants H, K_c, and K_d. These quantities depend strongly on the general force law between the molecules, as well as on the column dimensions and the operating temperatures. The Jones and Furry calculations were carried out for Maxwellian molecules, which possess an attractive force varying as the inverse fifth power of the separation. For these molecules, the viscosity and thermal conductivity, which appear in the expressions for the column constants, have a temperature dependence of T^n where $n=1$. The thermal-diffusion factor α was assumed to be constant.

Srivastava[3] recalculated the column constants for the extreme cylindrical case ($r_1 \gg r_2$) on the basis of $n=\frac{1}{2}$ and found improved agreement with experimental data.

It is the purpose of this paper to calculate values of H, K_c, and K_d on the basis of a molecular model which has proved successful in the prediction of transport properties of nonpolar molecules. This is the Lennard-Jones (12–6) potential given by

$$V(r)=4\epsilon[(\sigma/r)^{12}-(\sigma/r)^6], \qquad (1)$$

where ϵ is the depth of the potential well, and σ is the collision diameter [the value of r for which $V(r)=0$]. Tables of the shape factors h, k_c, and k_d are given as functions of kT_1/ϵ, T_2/T_1, and r_1/r_2.

It is expected that this model will provide more exact information as to the absolute value of the shape factors. The Maxwellian case considered by Jones and Furry is not likely to fit most gases, and indeed for this intermolecular potential, the thermal-diffusion factor vanishes identically. The $n=\frac{1}{2}$ case, treated by Srivastava, corresponds to a potential $V(r)=\infty$ for $r\leq\sigma$, $V(r)=0$ for $r>\sigma$. This potential considers the molecules as rigid spheres, with no force of attraction. As stated by Hirschfelder *et al.*[4] "···the cross-sections for Lennard-Jones molecules are smaller than those for rigid spheres at high energies because of the softness of the repulsive portion of the potential. Also the cross-sections are several times their rigid-sphere values at low energies because of the influence of the attractive forces."

[1] W. H. Furry, R. C. Jones, and L. Onsager, Phys. Rev. **55**, 1083 (1939).
[2] R. C. Jones and W. H. Furry, Revs. Modern Phys. **18**, 151 (1946); Phys. Rev. **69**, 459 (1946).
[3] R. C. Srivastava, Proc. Phys. Soc. (London) **B70**, 93 (1957).
[4] J. O. Hirschfelder, C. F. Curtiss, and R. B. Bird, *Molecular Theory of Gases and Liquids* (John Wiley & Sons, Inc., New York, 1954).

II. THEORY

On using the terminology of Jones and Furry, the basic equation for transport of isotopes is given by

$$\tau = Hc(1-c) - (K_c + K_d)\partial c/\partial z, \tag{2}$$

where τ is the net flow of an isotope past the point z of the column, c is its concentration, and H, K_c, and K_d (the column constants) are given by

$$H \doteq -(2\pi/Q_1^3)\int_{T_1}^{T_2} (\rho D\alpha/\lambda T)G(T)dT, \tag{3}$$

$$K_c = (2\pi/Q_1^7)\int_{T_1}^{T_2} (\rho D/\lambda)G^2(T)dT, \tag{4}$$

$$K_d = (2\pi/Q_1)\int_{T_1}^{T_2} \lambda\rho D r^2 dT. \tag{5}$$

Here, ρ, D, α, and λ are the density, diffusion coefficient, thermal-diffusion factor, and coefficient of thermal conductivity, respectively; and $2\pi Q_1$, the radial heat flow per unit length, is given by

$$Q_1 \ln(r_1/r_2) = \int_{T_1}^{T_2} \lambda dT. \tag{6}$$

The function $G(T)$ is the solution of

$$\frac{d}{dT}\frac{1}{\lambda r^2}\frac{d}{dT}\frac{\eta}{\lambda}\frac{d}{dT}\frac{1}{\lambda\rho^2}\frac{d}{dT}\left[\frac{\rho D}{\lambda}G(T)\right] = g\frac{d\rho}{dT}, \tag{7}$$

with boundary conditions $G(T_1)=G(T_2)=G'(T_1)=G'(T_2)=0$, where g is the gravitational acceleration and η is the coefficient of viscosity.

The transport properties for the Lennard-Jones potential are written in terms of the "collision integrals" $\Omega^{(i,j)}(kT/\epsilon)$, and are expressed below in terms of these integrals and in terms of the value of the transport properties at the temperature T_1 denoted by the subscript 1.[5]

In terms of the quantities θ and $\Omega^{(i,j)*}$, defined by $\theta = T/T_1$ with $1<\theta<\theta_0$, and $\Omega^{(i,j)*} = \Omega^{(i,j)}/\Omega_1^{(i,j)}$, the transport properties for isotopic mixtures are given by

$$\rho = \rho_1/\theta, \tag{8}$$

$$D = D_1\theta^{\frac{1}{2}}/\Omega^{(1,1)*}, \tag{9}$$

$$\eta = \eta_1\theta^{\frac{1}{2}}/\Omega^{(2,2)*}, \tag{10}$$

$$\lambda = \lambda_1\theta^{\frac{1}{2}}/\Omega^{(2,2)*}, \tag{11}$$

$$\alpha = \frac{15(6C^*-5)(2A^*+5)}{2A^*(16A^*-12B^*+55)}\frac{M_1-M_2}{M_1+M_2} = \frac{M_1-M_2}{M_1+M_2}\frac{\phi}{A^*}. \tag{12}$$

The A^*, B^*, and C^* are ratios of various $\Omega^{(i,j)}$; and M_1 and M_2 are the molecular weights of components 1 and 2. The assumption has been made that the heat capacity is independent of temperature.

Integration of Eq. (7) with T_1 as the lower limit gives, upon substitution of Eqs. (8) to (12),

$$(y^2/\theta^{\frac{1}{2}})\Omega^{(2,2)*}(d^2/d\theta^2)y^2\theta^{\frac{1}{2}}\Omega^{(2,2)*}(d/d\theta)(\Omega^{(2,2*)}/\Omega^{(1,1)*})\gamma(\theta) = \theta^{-1} + C_1, \tag{13}$$

with boundary conditions $\gamma(1)=\gamma(\theta_0)=\gamma'(1)=\gamma'(\theta_0)=0$.

In Eq. (13), the quantities y and $\gamma(\theta)$ are given by

$$y = r_1/r, \qquad 1 \le y \le y_0, \tag{14}$$

where $y_0 = y(\theta_0)$, and

$$\gamma(\theta) = (\eta_1 D_1/g\lambda_1^4 r_1^4 T_1^3\rho_1)G(T). \tag{15}$$

The annular heat flow Q_1 is given by

$$Q_1 = (\lambda_1 T_1/\ln y_0)\int_1^{\theta_0} \theta^{\frac{1}{2}} d\theta/\Omega^{(2,2)*} = (\lambda_1 T_1/\ln y_0)F(\theta_0). \tag{16}$$

Substitution of the preceding expressions into Eqs. (1)–(3) gives for the column constants

$$H = -\frac{2\pi}{6!}\frac{\alpha_1\rho_1^2 g r_1^4}{\eta_1}\times 6!\left[\frac{\ln y_0}{F(\theta_0)}\right]^3\int_1^{\theta_0}\frac{\phi}{\phi_1}\gamma(\theta)\frac{d\theta}{\theta}, \tag{17}$$

$$K_c = \frac{2\pi}{9!}\frac{\rho_1 g^2 r_1^8}{\eta_1^2 D_1}\times 9!\left[\frac{\ln y_0}{F(\theta_0)}\right]^7\int_1^{\theta_0}\frac{\Omega^{(2,2)*}}{\Omega^{(1,1)*}}\gamma^2(\theta)d\theta, \tag{18}$$

$$K_d = 2\pi\rho_1 D_1 r_1^2\times\left[\frac{\ln y_0}{F(\theta_0)}\right]\int_1^{\theta_0}\frac{\theta}{y^2\Omega^{(1,1)*}\Omega^{(2,2)*}}d\theta. \tag{19}$$

It is convenient to tabulate, instead of the preceding constants, the dimensionless shape factors h, k_c, and k_d, which depend upon the reduced temperature at the cold wall, kT_1/ϵ; the ratio of operating temperatures, θ_0; and the ratio of the column radii, y_0:

$$h(kT_1/\epsilon, \theta_0, y_0) = -6![\ln y_0/F(\theta_0)]^3\int_1^{\theta_0}(\phi/\phi_1)\gamma(\theta)(d\theta/\theta), \tag{20}$$

$$k_c(kT_1/\epsilon, \theta_0, y_0) = 9![\ln y_0/F(\theta_0)]^7\int_1^{\theta_0}(\Omega^{(2,2)*}/\Omega^{(1,1)*})\gamma^2(\theta)d\theta, \tag{21}$$

$$k_d(kT_1/\epsilon, \theta_0, y_0) = [\ln y_0/F(\theta_0)]\int_1^{\theta_0}\frac{\theta}{y^2\Omega^{(1,1)*}\Omega^{(2,2)*}}d\theta. \tag{22}$$

III. NUMERICAL RESULTS

The numerical integrations involved in solution of the shape factor equations were carried out on an IBM 704 computer. The values of $\Omega^{(i,j)}$ required were obtained from tabulated data for the Lennard-Jones (12–6) potential.[4] Intermediate values, not listed therein, were arrived at by linear interpolation of $\Omega^{(i,j)}$ against $\ln T^*$, where $T^* = kT/\epsilon$. The A^*, B^*, and C^* used in the evaluation of ϕ were obtained by linear interpolation against T^*. It was found that 64

[5] The $\Omega^{(i,j)}$ of our work correspond to the $\Omega^{(i,j)*}$, of reference 4.

TABLE I. Comparison of experimental and theoretical results (McInteer, Aldrich, and Nier).

	Hot-wire column		Coaxial column	
Pressure (atm)	7.8	9.7	7.8	9.7
H (exp) (liters STP/day)	16.5	24.8	257	400
H ($n=1$) (liters STP/day)	9.5	14.8	266	414
H (L-J 12-6) (liters STP/day)	12.1	18.8	258	399
$2A$ (exp) (cm^{-1})	>0.043[a]	...	0.017	0.012
$2A$ ($n=1$) (cm^{-1})	0.052	0.062	0.020	0.014
$2A$ (L-J 12-6) (cm^{-1})	0.061	0.061	0.015	0.010

[a] Evaluated from the observed separation of the column ($q \geq 5\times10^{9}$). Application of the formula $\ln q \leq 2AL$, where L (the length of the column)=254 cm, leads to the foregoing value.

intervals in a Simpson's-rule integration sufficed to determine the integral to 0.01%.

Equation (13) was integrated twice numerically and solved for

$$(d/d\theta)[\Omega^{(2,2)*}\gamma(\theta)/\Omega^{(1,1)*}].$$

This expression was then integrated numerically, yielding one more constant of integration, C_2. The application of the boundary conditions at $\theta=1$ causes the third and fourth constants to vanish. The constants C_1 and C_2 are evaluated by applying the conditions at $\theta=\theta_0$.

The value of $\gamma(\theta)$ was substituted into Eqs. (20) to (22) for the shape factors, which were then evaluated numerically as functions of $T_1^*=kT_1/\epsilon$, θ_0, and y_0. The range of T_1^* was 0.8 to 30.0. For each value of T_1^*, y_0 covered the range 1.10 to 100. Each y_0 corresponded to a number of θ_0 values which varied from 2.00 to 6.00 at intervals of 0.25. These parameters served to cover most situations of interest. A table of shape factors resulting from these computations is quite lengthy, and, therefore, has not been included in this article. Such a table has been compiled and published elsewhere.[6] These data are accurate to better than 1%.

TABLE II. Bowring A column—comparison of experimental and theoretical results.

	Experimental	Theoretical ($n=1$)	Theoretical (L-J 12-6)
H/P^2 (cc STP/sec-atm^2)	0.005±0.001	0.0076	0.0068
K_e/P^4 (cc STP cm/sec-atm^4)	0.0032±0.0008	0.0026	0.0050
K_d (cc STP cm/sec)	1.90±0.4	3.34	2.51
$a=HLP^2/K_e$ (atm^2)	727±30	1333	622
$b=K_dP^4/K_e$ (atm^4)	600±25	1265	500
a/b (atm^{-2})	1.21±0.05	1.05	1.24

[6] B. B. McInteer and M. J. Reisfeld, Los Alamos Scientific Laboratory Rept. LAMS-2413, October, 1959. Available by writing to Office of Technical Services, Department of Commerce, Washington 25, D.C.

TABLE III. Bowring B column—comparison of experimental and theoretical results.

	Experimental	Theoretical ($n=1$)	Theoretical (L-J 12-6)
H/P^2 (cc STP/sec-atm^2)	0.09±0.015	0.116	0.104
K_e/P^4 (cc STP cm/sec-atm^4)	0.26±0.04	0.394	0.344
K_d (cc STP cm/sec)	15.0±3	14.8	14.1
$a=HLP^2/K_e$ (atm^2)	155.5±1.0	134	136.4
$b=K_dP^4/K_e$ (atm^4)	57.0±3.0	38	40.8
a/b (atm^{-2})	2.73±0.1	3.6	3.34

IV. COMPARISON WITH EXPERIMENTAL RESULTS

The system He^3-He^4 should be predictable by these computations because of the agreement of the transport properties of this gas with the Lennard-Jones model.[4] Experimental data exist in the work of McInteer, Aldrich, and Nier[7] and in that of Bowring.[8]

The thermal-diffusion plant used by McInteer *et al.* consisted of three columns, the first two being coaxial tubes and the third a hot-wire column. In Table I is shown the comparison of their experimental results with the theoretical values predicted by both the $n=1$ Maxwellian model and the Lennard-Jones (12-6) potential. The value of $2A$ is the ratio $H/(K_e+K_d)$.

It is noted that the Lennard-Jones potential gives closer agreement with these experimental values of H than does the Maxwellian model. The values of $2A$ for the hot-wire column are low by comparison with either of the theoretical results. The coaxial-tube column shows good agreement with both the $n=1$ model and the Lennard-Jones potential.

The transport coefficients were evaluated from the

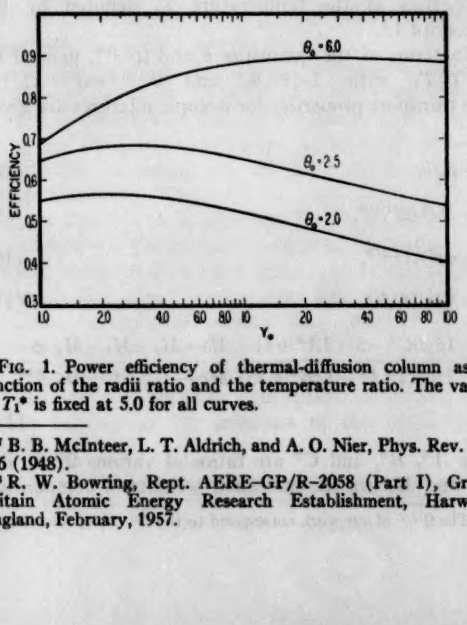

FIG. 1. Power efficiency of thermal-diffusion column as a function of the radii ratio and the temperature ratio. The value of T_1^* is fixed at 5.0 for all curves.

[7] B. B. McInteer, L. T. Aldrich, and A. O. Nier, Phys. Rev. **74**, 946 (1948).

[8] R. W. Bowring, Rept. AERE-GP/R-2058 (Part I), Great Britain Atomic Energy Research Establishment, Harwell, England, February, 1957.

equations according to the Lennard-Jones potential, with the exception of α_1, for which an experimental value of 0.059 exists.[9]

The second set of experiments was carried out on the system He^3-He^4 by Bowring and consisted of enrichment of atmospheric helium through two thermal-diffusion columns: one a hot-wire column denoted by A, and the other a coaxial-tube type denoted by B. A summary of the experimental results along with theoretical values computed on the basis of the Maxwellian model and the Lennard-Jones potential appear in Tables II and III. H, K_c, and K_d have their usual significance, and L is the length of the column in centimeters.

Considerable improvement in the theoretical prediction is obtained with use of a more realistic potential function, particularly for the hot-wire column A, for which the ratio $r_1/r_2 \gg 1$.

The auxiliary quantity $E=h^2 \ln y_0/k_c F(\theta_0)$ has been computed from the shape factors. This quantity, which represents the power efficiency of the column per unit length, is shown in Fig. 1 for $T_1^*=5.0$. It is seen that a larger power efficiency is obtained by increasing the temperature ratio θ_0, between the hot wire and the cold wall. However, for each value of θ_0, the efficiency may be maximized by selection of the optimal column geometry (y_0).

ACKNOWLEDGMENTS

The authors are grateful to Mrs. Leona Bordwell and to William Anderson of the Theoretical Division, who programed and performed the calculations on the IBM 704 computer at the Los Alamos Scientific Laboratory.

[9] B. B. McInteer, L. T. Aldrich, and A. O. Nier, Phys. Rev. 72, 510 (1947).

THE JOURNAL OF CHEMICAL PHYSICS VOLUME 33, NUMBER 2 AUGUST, 1960

On the Dynamical Theory of Diffusion in Crystals. V. Random-Walk Treatment of the Heat of Transport

ALAN R. ALLNATT* AND STUART A. RICE†

Department of Chemistry and Institute for the Study of Metals, University of Chicago, Chicago 37, Illinois

(Received February 29, 1960)

The heat of transport in a crystalline medium is calculated from the flux of matter in a combined temperature and concentration gradient. The use of a random-walk model leads to the prediction that the heat of transport is exactly equal to the activation energy for motion. This prediction is in excellent agreement with the measurements of Patrick and Lawson of vacancy motion in AgBr. The dynamical interpretation of the theory presented is briefly discussed.

I. INTRODUCTION

IF an otherwise homogeneous system has an internal concentration gradient there will arise a matter flux, proportional to the concentration gradient, which tends to remove the inequalities of concentration. If the same system is also subjected to a temperature gradient the net matter flux depends upon both the concentration and temperature gradients. The second matter flux, the thermal diffusion, is directly related to the transport of enthalpy in an isothermal system, owing to the flow of matter in response to a gradient of chemical potential. It is the purpose of this paper to calculate the heat of transport from simple considerations of the mechanism of diffusion.

There have been a number of studies of the relationship between the heat of transport and the parameters descriptive of self-diffusion, i.e., heat of activation,[1,2] heat of vacancy formation,[3] and so forth. Most of the arguments are based on models in which the atom absorbs energy at one temperature in one lattice plane and gives it up at some different temperature in a second lattice plane. Aside from the heuristic nature of the calculations we are unable to endow such models with any physical reality. In fact, the motion of any given atom is determined by the superposition and interaction of many normal modes of vibration. Since it is these very normal modes which must be used to define the thermodynamic variables describing the system, and since all but the highest-frequency normal modes involve the in-phase motion of numbers of adjacent atoms, the physical significance of the tempera-

* N.A.T.O. Fellow.
† Alfred P. Sloan Fellow.
[1] K. Wirtz, Physik. Z. 44, 221 (1943).
[2] R. E. Howard, J. Chem. Phys. 27, 1377 (1957).
[3] P. Shewmon, J. Chem. Phys. 29, 1032 (1958); S. Prager and H. Eyring, J. Chem. Phys. 21, 1347 (1953); I. Prigogine, L. de Brouckere, and R. Amand, Physica 16, 577 (1950); E. Dougherty and H. Drickamer, J. Phys. Chem. 59, 443 (1955); K. Wirtz and J. W. Hiby, Physik Z. 44, 369 (1943); see also R. Oriani in *Thermodynamic and Transport Properties of Gases, Liquids and Solids* (American Society Mechanical Engineers, New York 1959), p. 123.

ture at which an individual atom absorbs energy is obscure.

Although it represents a diversion from the main stream of this paper it is pertinent at this point to comment upon the earlier calculations. Wirtz[1] assumed that the motion of an atom is an activated process and that the total activation energy could be split into three contributions, each component being supplied at a different temperature. If the atom is assumed to jump from a site at temperature T to another site at temperature $T+\Delta T$, then Wirtz assumes that the motion requires an energy for moving the atom away from its neighbors, to be supplied at the temperature T, an energy to move the shell atoms and permit the diffusing atom to pass to the second site, to be supplied at the temperature $T+\frac{1}{2}\Delta T$, and an energy to form a vacancy at the second site, to be supplied at the temperature $T+\Delta T$. The result of the calculation is the prediction that the heat of transport is equal to the heat of activation to move the atom in the direction of its final position (not including shell-atom motions) minus the heat of vacancy formation. Similar models have been used by Prager and Eyring, Prigogine, de Brouckere and Amand, Dougherty and Drickamer, Wirtz, and Hiby and Howard.[2,3] The results of all of these calculations are the same in so far as physical content is concerned. They differ in minor detail owing to the use of still further simplifying assumptions.

We immediately note that the energetic quantities verbally defined in this model are very ambiguous. In the notation of Rice,[4] the prediction described above would be represented in the form $Q_1^*=U_0-\Delta H_v$, with U_0 the energy required to move the diffusing atom into the critical configuration independent of the positions of all the other atoms in the system. It is easy to see that U_0 is not the same as the activation energy for motion which is defined by $\Delta H_m^+=\Delta H^+-\Delta H_v$, since there are contributions in ΔH^+ from shell-atom motions and correlation effects. Nevertheless, despite this ambiguity of definition, Wirtz's analysis is often quoted as predicting that the heat of transport is the heat of activation for motion less the heat of vacancy formation. We shall see later that Wirtz's result is not in agreement with the available experimental evidence. The error in this treatment lies in the misunderstanding of the nature of the heat of transport which is defined as the energy that must be furnished the region of the origin of the flux of atoms in order to maintain an isothermal state. The heat of transport therefore is related to isothermal diffusion and depends upon the existence of suitable vacancies through the isothermal-diffusion coefficient and not separately, as assumed in the preceding theories.

A somewhat different calculation has been published by LeClaire[5] who assumes that the jump frequency and vacancy density depend only upon the local state of the lattice, in particular only upon the local temperature. By calculating the net flux of vacancies from the difference between the fluxes with and against the temperature gradient, it is concluded that the heat of transport is just the activation energy for motion.

In this communication we propose a much more general method of calculation than any discussed above. In fact, it is only in the last stage of the calculation that any reference to the crystalline state or to an activated process is made. Our method is fundamentally similar to the treatment of isothermal self-diffusion as a Markoffian process. Now, a treatment of the self-diffusion coefficient in a crystal is usually based on the Einstein relation

$$D=(\Gamma/2)\langle(\Delta x)^2\rangle, \tag{1}$$

valid for the isothermal case in which there is also no concentration gradient. The mean-square displacement $\langle(\Delta x)^2\rangle$ is geometrically linked with the crystal-lattice spacing while the jump frequency Γ can be related to the normal mode frequencies.[4]

Equation (1) is not valid when the environment of the labeled atom is asymmetric. For, if there is either a temperature or concentration gradient in the medium, the mean displacement $\langle\Delta x\rangle$ is nonvanishing. In the present communication we shall base our analysis of thermal diffusion on just this effect. That is, we consider the problem of the random walk of an atom in a crystal wherein the temperature and concentration gradients are nonvanishing. In this manner the flux of matter can be computed. Subsequent identification of the coefficients of the gradients in the matter-flux relationship with the corresponding coefficients in the irreversible thermodynamic formulation of the matter flux permits the unambiguous calculation of the heat transport. This method of calculation has advantages over those mentioned previously. We reserve for a subsequent paper the treatment and discussion of the dynamical basis of the heat of transport.

II. GENERAL CONSIDERATIONS

Consider an atom of species i undergoing a random walk in the presence of temperature and concentration gradients. Displacements will be measured relative to axes moving with the local velocity of the lattice. Let $K_i^{(1)}(x_i, t \mid x_i+\Delta x_i, t+\Delta t)$ be the relative probability density of finding an atom at the point $x_i+\Delta x_i$ at time $t+\Delta t$ if the atom was at the point x_i at time t. If $n_i(x_i, t)$ is the number density of molecules of species i at the point x_i at time t, then the conservation of matter requires that

$$n_i(x_i, t+\Delta t) = \int n_i(x_i-\Delta x_i, t)K_i^{(1)}(x_i-\Delta x_i, t \mid x_i, t+\Delta t)d(\Delta x_i)$$

$$\int K_i^{(1)}(x_i-\Delta x_i; t \mid x_i, t+\Delta t)d(\Delta x_i)=1. \tag{2}$$

[4] S. A. Rice, Phys. Rev. **112**, 804 (1958); O. P. Manley and S. A. Rice, Phys. Rev. **117**, 632 (1960).

[5] A. D. LeClaire, Phys. Rev. **93**, 344 (1954).

As in the original development of Einstein,[6] Eq. (2) can be converted into a differential equation by expanding both the right- and left-hand sides in powers of $-\Delta x_i$ and Δt, respectively, with the neglect of terms of order $(\Delta t)^2$ and $(\Delta x)^3$. The result of this operation is

$$n_i(x_i,t)+\frac{\partial n_i}{\partial t}(x_i,t)\,\Delta t = \int\left[n_i(x_i,t)-\frac{\partial n_i}{\partial x}\Delta x_i+\tfrac{1}{2}\frac{\partial^2 n_i}{\partial x^2}(\Delta x_i)^2\right] \times\left[K_i^{(1)}(x_i,t)\mid x_i+\Delta x_i,\,t+\Delta t) -\frac{\partial K_i^{(1)}}{\partial x}\Delta x_i+\tfrac{1}{2}\frac{\partial^2 K_i^{(1)}}{\partial x^2}(\Delta x_i)^2\right]d(\Delta x_i). \quad (3)$$

From the definition of the mean displacement $\langle\Delta x_i\rangle$ and the mean-square displacement $\langle(\Delta x_i)^2\rangle$

$$\langle\Delta x_i\rangle=\int K_i^{(1)}(x_i,t\mid x_i+\Delta x_i,t+\Delta t)\,\Delta x_i d(\Delta x_i)$$

$$\langle(\Delta x_i)^2\rangle=\int K_i^{(1)}(x_i,t\mid x_i+\Delta x_i,t+\Delta t)\,(\Delta x_i)^2 d(\Delta x_i) \quad (4)$$

and the use of the continuity equation

$$(\partial n_i/\partial t)=-(\partial/\partial x)(n_i v_i), \quad (5)$$

it is readily seen that

$$n_i v_i=(n_i\langle\Delta x_i\rangle/\Delta t)-(\partial/\partial x)[n_i\langle(\Delta x_i)^2\rangle/2\Delta t] \quad (6)$$

where v_i is the mean velocity of the species i relative to the lattice. The flux of component i relative to the lattice is therefore

$$J_i=n_i\left[\frac{\langle\Delta x_i\rangle}{\Delta t}-\frac{\partial}{\partial x}\frac{\langle(\Delta x_i)^2\rangle}{2\Delta t}-\frac{1}{n_i}\frac{\langle(\Delta x_i)^2\rangle}{2\Delta t}\frac{\partial n_i}{\partial x}\right]. \quad (7)$$

In an isothermal system without concentration gradients $\langle(\Delta x_i)^2\rangle$ is related to the self-diffusion coefficient as in Eq. (1). Under these conditions the mean-square jump length depends only upon the temperature and $(n-1)$ of the n components of the mixture. The n components chosen do not include the vacancies since the specification of the temperature, of $(n-1)$ composition variables, and the condition $\sum_i n_i+n_v=L$ with the total number density of lattice sites L a constant, suffices to determine the vacancy concentration n_v, provided the vacancies are everywhere in thermal equilibrium. In the more general case $\langle(\Delta x_i)^2\rangle$ may depend upon the gradients of temperature and concentration. This dependence must be at least of the second order since the inversion of the temperature gradient in a uniform system does not affect the heat of transport nor does the inversion of the direction of the concentration gradient in an isothermal system affect the ordinary diffusion coefficient. Thus the lowest-order dependence of the mean-square jump distance on ∇n and ∇T is of the form $(\nabla n)^2$, $(\nabla T)^2$ or $(\nabla n)(\nabla T)$. In the region where ∇n and ∇T are small these terms may be neglected and $\langle(\Delta x_i)^2\rangle$ expanded in terms of T and $(n-1)$ concentrations to give the relation

$$J_i=n_i\left[\frac{\langle\Delta x_i\rangle}{\Delta t}-\frac{1}{n_i}\frac{\partial n_i}{\partial x}\frac{\langle(\Delta x_i)^2\rangle}{2\Delta t}-\sum_{j=1}^{n-1}\frac{\partial}{\partial n_j}\left(\frac{\langle(\Delta x_i)^2\rangle}{2\Delta t}\right)\frac{\partial n_j}{\partial x} -\frac{\partial}{\partial T}\left(\frac{\langle(\Delta x_i)^2\rangle}{2\Delta t}\right)\frac{\partial T}{\partial x}\right]. \quad (8)$$

Consider now the vacancy mechanism for diffusion. The system under examination must contain at least two components: host atoms and vacancies. Then Eq. (8) becomes

$$J_1=-\frac{\langle(\Delta x_1)^2\rangle}{2\Delta t}\frac{\partial n_1}{\partial x} -n_1\left[\frac{\partial}{\partial T}\left(\frac{\langle(\Delta x_1)^2\rangle}{2\Delta t}\right)-\frac{\langle\Delta x_1\rangle}{\Delta t}\left(\frac{\partial T}{\partial x}\right)^{-1}\right]\frac{\partial T}{\partial x}. \quad (9)$$

The formal approach of irreversible thermodynamics leads to the following equation for the flux of atoms in a system composed only of atoms and vacancies,[7] when the vacancies are in local thermal equilibrium and jumps occur only by the vacancy mechanism:

$$J_1=-L_{11}[(kT/n_i)\nabla n_i+([Q_1^*-\Delta H_v/T)]\nabla T. \quad (10)$$

L_{11} is a phenomenological coefficient, Q_1^* is the heat of transport defined as the coefficient of proportionality between the "reduced" heat flux and the matter flux J_1, and ΔH_v is the enthalpy of formation of a vacancy. Direct comparison of Eqs. (9) and (10) leads to the identification

$$Q_1^*-\Delta H_v=kT^2\left[\frac{\partial}{\partial T}\ln\left(\frac{\langle(\Delta x_1)^2\rangle}{2\Delta t}\right)-2\frac{\langle\Delta x_1\rangle}{\langle(\Delta x_1)^2\rangle}\left(\frac{\partial T}{\partial x}\right)^{-1}\right]. \quad (11)$$

Consider now the case that the pure substance contains only atoms in lattice or interstitial positions and that diffusion may proceed only through the interstitial mechanism. The analog of (10) is

$$J_i=-L_{ii}[(kT/n_i)\nabla n_i+(Q_i^*/T)\nabla T], \quad (12)$$

where L_{ii} is a phenomenological coefficient, Q_i^* the heat of transport of the interstitial atoms, and n_i the concentration of interstitials. The same procedure which led to Eq. (11) gives in this case

$$Q_i^*=kT^2\left[\frac{\partial}{\partial T}\ln\left(\frac{\langle(\Delta x_i)^2\rangle}{2\Delta t}\right)-2\frac{\langle\Delta x_i\rangle}{\langle(\Delta x_i)^2\rangle}\left(\frac{\partial T}{\partial x}\right)^{-1}\right]. \quad (13)$$

[6] See for example, A. Einstein, *Theory of Brownian Motion* (Dover Publishers, New York, 1956).

[7] A. R. Allnatt and P. W. M. Jacobs (to be published).

This is valid whether the interstitials are in local thermodynamic equilibrium or not.

It is shown in the Appendix that

$$2kT^2[\langle \Delta x_1 \rangle / \langle (\Delta x_1)^2 \rangle](\partial T/\partial x)^{-1} = 2\Delta H_v$$

$$2kT^2[\langle \Delta x_i \rangle / \langle (\Delta x_1)^2 \rangle](\partial T/\partial x)^{-1} = 0 \qquad (14)$$

and

$$kT^2(\partial/\partial T)\ \ln[\langle (\Delta x_1)^2 \rangle / 2\Delta t] = \Delta H_m{}^+ + \Delta H_v$$

$$kT^2(\partial/\partial T)\ \ln[\langle (\Delta x_i)^2 \rangle / 2\Delta t] = \Delta H_m{}^+. \qquad (15)$$

Substitution of (14) and (15) into (11) and (13) leads to the relations

$$Q_1{}^* = \Delta H_m{}^+$$

$$Q_i{}^* = \Delta H_m{}^+ \qquad (16)$$

where $\Delta H_m{}^+$ is the heat of activation for motion of an atom. This is the same conclusion as was reached by LeClaire[5] by a less rigorous procedure.

III. DISCUSSION

Equation (16) is a formal expression of the intuitively appealing idea that the heat of transport is just the heat of activation for motion. That is, given the fact that the vacancy must be already formed before a jump can take place, the heat of vacancy formation is not "transported." The random-walk model on which Eq. (16) is based implies that an atom forgets from where it came before making another jump. This further implies that the excess energy required to produce an atomic jump is dissipated at the site into which the atom jumps. Although these deductions follow easily from the definition of the random walk, the corresponding connections with molecular dynamics are much more difficult to establish.

If we consider an ensemble of replicas of a crystal we may define the temperature at a given lattice point by the mean-square amplitude of vibration of an atom at that lattice point. Although it is easy to define the temperature in terms of the normal modes of vibration, the dynamical origin of the heat of transport is harder to interpret. Consider the mechanism by which an atomic jump occurs. In the analysis of Rice,[4] the motion of an atom is analyzed in terms of the superposition of normal modes. If the initial phases of the normal modes are randomly distributed, then after a certain interval of time the normal modes will come into phase and the amplitude of the atomic displacement at that time will be very large. In general, the only modes which will contribute to a diffusive motion are those which cause the atom and adjacent vacancy to move relative to one another. It is only the high-frequency vibrations which have this property, since the low frequencies, corresponding to long wavelengths, require the in-phase motion of large numbers of adjacent atoms. In an isothermal system the preceding analysis is clear and unambiguous. In a nonisothermal system, however, difficulties arise. For, if each of the atoms in the correlated motion which corresponds to a normal mode is at a different temperature, with the temperature defined as above by the mean-square atomic displacement, then the medium is dispersive with respect to the transmission of mechanical waves. We quote as an analogy the well-known fact that the propagation of sound in a medium with a temperature gradient leads to refraction and reflection under certain conditions. We may then anticipate that the normal mode distribution affecting the jump frequency of an atom into a vacancy will depend upon the temperature gradient in the volume element surrounding the atom-vacancy pair. Because only the high-frequency modes are of importance for diffusive motion, this volume will be small but finite. We now come to the crucial question of where the excess energy which leads to the atomic jump was before localization. From the preceding it appears clear that this energy was, owing to its distribution among the contributing normal modes, more or less uniformly spread over the volume element in question. In a certain sense, the energy is drawn from regions with a distribution of temperatures. We have no reason to believe that this distribution of energy was all to one side of the vacancy. Rather, it appears likely that the volume includes a region all around both atom and vacancy.

It is difficult to estimate the extent of anisotropy of the normal mode distribution in this region. To maintain a temperature gradient, the mean-square atomic amplitudes must be larger on one side of the vacancy than on the other. Such an effect can be obtained by superposing normal modes in different manners on the two sides of the vacancy. Because the superposition of modes is basically different from the isothermal case, it is not clear that the part of the amplitude of the jumping atom contributed by a given mode may not change, owing to changes in the mode projection along the given axis. Such an effect, due to local thermal expansion, might further enhance, or greatly detract from, the excess contribution due to increased vibrational amplitude. It is certain on physical grounds that the small anisotropy mentioned together with the anisotropy of the jump situation provide the necessary asymmetry for a nonvanishing heat of transport. Quantitative estimation from a molecular model seems to involve the combined difficulties of the theories of heat conduction and diffusion. If we turn to the question of energy dissipation at the site into which the atom jumps we are faced with a similar problem. The removal of energy by either flow through normal modes or interaction between normal modes suggests that the dissipated energy is also distributed in an approximately isotropic manner about the vacancy but with the small asymmetry of dominant importance. To further complicate the dynamical picture consideration must be given to the shell-atom motion and the accompanying energy localization required to permit the jumping atom to reach the vacancy.

We may also note that the heat of transport predicted in this paper is always positive. The analysis which we have given is designed to elucidate self-diffusion and is inapplicable in its present form to impurity diffusion. If a chemical or structural impurity is introduced into a lattice and the impurity is either a substitutional vacancy or an atom of smaller mass than a lattice atom, the frequencies of the continuum normal modes are displaced downwards $0(N^{-1})$ and some normal modes have their frequencies displaced upwards out of the band. The widely displaced frequencies correspond to localized normal modes with the atomic amplitudes due to such modes decreasing exponentially with distance from the defect. Oriani[8] has pointed out that the smaller the ratio of masses of the defect and normal lattice atom, the larger is the contribution of the localized mode to the diffusive motion. For a vacancy Oriani concludes that almost all the vibrational energy of the defect is drawn from the very high-frequency modes localized in the vicinity of the first shell of neighbors. Under these circumstances the jumping atom "takes with it" a sizable fraction of the activation energy and Q_1^* is necessarily positive. As the ratio of masses of the defect and normal lattice atom increases, the dominance of the localized modes decreases and the number of atoms whose motion is effectively correlated with the jumping impurity atom increases. Under these conditions the diffusive motion requires the superposition of many spatially extended normal modes, most of the activation energy comes from a relatively large region of the lattice, and once the defect has jumped most of the activation energy will be dissipated behind the interstitial atom. For this case Q_1^* is negative.

In summary then, the resolution of the difficulties posed above must lie in the small asymmetry of the energy distribution in the volume element discussed. Unlike the easily comprehended properties of a single-particle model, the transport of energy in a strongly interacting system is not an "all or nothing" process. When consideration is given to the definition of the normal modes in a system with a temperature gradient and to the asymmetry between the gathering and the dissipating of the excess energy caused by a shift in the center of the relevant volume element accompanying the shift in the vacancy position, it is indeed seen that there is a net flux of energy accompanying the diffusive jump. This energy flux is, however, not easily linked to simple models.

What then is the relevance of the calculation presented in this note. The basic features of the random-walk model are two in number: each particle moves by a sequence of independent steps, and the surroundings of the particle are at local thermodynamic equilibrium. It is therefore seen that the particle motion is determined by fluctuations in the medium. The model is a semimacroscopic analog of the dynamical model briefly discussed before. It is now possible to see why in the random-walk model the heat of transport is just the activation energy for motion, including the energy required for shell-atom motion. For, the assumption that the surroundings are at equilibrium implies that the energy distribution is approximately uniform. The localization of the energy necessary to move the shell atoms and its subsequent dissipation in a volume linearly displaced from the original volume must then contribute to the transport of energy. Because the steps are assumed independent the total activation energy for motion is transported. If the steps were not independent, or if the energy dissipation were isotropic only, a fraction of this energy would be transported.

There remains now the question of comparison between experiment and theory. The heat of transport has been determined for both vacancy and interstitial motion in AgBr by Patrick and Lawson.[8] For the case of the vacancy, the prediction that the heat of transport is the activation energy for motion is in quantitative agreement with experiment. For the case of the interstitial, the deduced heat of transport is about one-tenth the predicted value. It is interesting that the ratio of mobilities of the vacancy and interstitial calculated from the thermoelectric power and the theroretical predictions of this paper has the proper form, i.e., $\ln(\mu_v/\mu_i) \propto (1/T)$. However, the slope differs considerably from that obtained from the data of Tetlow.[9] This result may be rationalized when it is recognized that the environment of an interstitial is much more symmetric than the environment of a vacancy. Our qualitative arguments would then lead us to expect a less asymmetric distribution of energy, and thereby a smaller heat of transport. This is analogous to the observation that the correlation factor for interstitialcy self-diffusion is much smaller than that for vacancy self-diffusion.[10]

It is clear from the arguments of this paper that a detailed dynamical theory of the heat of transport must be based upon a careful examination of the normal modes, of the energy distribution, and of the energy flux of the crystalline medium. The identification of coefficients between the microscopic formulation of the heat or matter flux and the corresponding macroscopic formulation is in our opinion much to be preferred to model kinetic calculations.

Note added in proof. It is interesting to inquire whether or not the analysis of this paper casts any light on the fundamental problem of the introduction of irreversibility. It is not at present clear whether or not anharmonic forces are necessary for irreversibility, although it may be shown that they are sufficient.[12] For, if the mean time required for dispersal of the wave packet constituting the properly phased normal modes causing the diffusive jump is short relative to the time between jumps, the motion is irreversible by virtue of the dilution of the normal modes into the (infinite) reservoir. The question of the ratio of

[8] L. Patrick and A. W. Lawson, J. Chem. Phys. **22**, 1492 (1954).
[9] J. Teltow, Ann. Phys. **5**, 63 (1950).
[10] C. W. McCombie and A. D. Lidiard, Phys. Rev. **101**, 1210 (1956).
[12] S. A. Rice and H. L. Frisch, J. Chem. Phys. **32**, 1026 (1960).

the two times mentioned is at present unanswered. It can be shown[12] that in the presence of anharmonic forces two time scales are established, one for jumps between lattice sites and one for vibrations about a given lattice site. The calculations suggest that the dissipation of energy occurs almost entirely by relaxation of "recaptured" particles, little energy being lost in the transit across the barrier.

Of equal interest is the observation that Eq. (16) provides a criterion of the mechanism of irreversibility. The indicated relationship is just that expected if an atom jumps into a vacancy and dissipates its energy before jumping again. But this picture implies that the energy is given up rapidly in the time between jumps and therefore that the superposition of normal modes must dissipate rapidly relative to the time between jumps. Thus it is probable that the dominant source of irreversibility in vacancy motion is the very short lifetime of the wave packet leading to the jump. We have still not established the necessary considerations for irreversibility, but the sufficiency of the conditions quoted is clearly supported by the available experimental data.

IV. ACKNOWLEDGMENTS

We wish to thank Professor A. W. Lawson and Professor M. H. Cohen for helpful conversations.

APPENDIX

For the sake of simplicity we consider diffusion in a one-dimensional crystal with lattice spacing a. Let p_+ and p_- be the relative probabilities that when a jump is made it is by $+a$ and $-a$, respectively. Then

$$p_+ + p_- = 1. \tag{A1}$$

Consider jumps made from a plane at temperature T to adjacent planes at temperatures $T+\Delta T$ and $T-\Delta T$. For the case of vacancy diffusion the probabilities may be written

$$\begin{aligned} p_+ &= A n_{T+\Delta T}\Gamma' \\ p_- &= A n_{T-\Delta T}\Gamma' \end{aligned} \tag{A2}$$

where Γ' is the rate of jumping of an atom into an adjacent vacancy, A is a constant, and n_T the vacancy concentration at temperature T. From Eqs. (A1) and (A2) it is found that $A=(2n_T\Gamma')^{-1}$. The average displacement per jump is

$$\begin{aligned} d_1 &= a(p_+ - p_-) \\ &= a(n_{T+\Delta T} - n_{T-\Delta T})/2n_T \\ &= (a^2/n_T)(\partial n_v/\partial T)(\partial T/\partial x) \\ &= (a^2\Delta H_v/kT^2)(\partial T/\partial x). \end{aligned} \tag{A3}$$

If the value of $(p_+ - p_-)$ did not vary from lattice point to lattice point then for N jumps

$$\begin{aligned} \langle \Delta x_1 \rangle &= aN(p_+ - p_-) \\ &= (a^2 N\Delta H_v/kT^2)(\partial T/\partial x). \end{aligned} \tag{A4}$$

However, after N jumps the temperature will be

$$T + (\partial T/\partial x)\left(\sum_{i=1}^{N} d_i\right).$$

If we take as a first approximation that all the d_i are given by (A3) we have

$$d_{N+1} = (a^2\Delta H_v/kT^2)[1 + N(\partial T/\partial x)^2(a^2\Delta H_v/kT^3)]^{-2} \times (\partial T/\partial x).$$

On using suitable values of the parameters, we find the difference between d_{N+1} and d_1 due to the temperature gradient to be negligible so that $\langle \Delta X_1 \rangle$ is given by (A4) for vacancy diffusion.

Provided that p_+ and p_- are the same at every lattice position it can be shown (see, for example, LeClair[11]) that for N jumps in a one-dimensional lattice,

$$\langle (\Delta x_1)^2 \rangle = Na^2 + (\langle \Delta x_1 \rangle)^2, \tag{A5}$$

provided that $N \gg 1$. Further, it can readily be shown that this relation still holds to excellent approximation for the variations in the values of p_+, p_- encountered in practice in nonisothermal experiments. Solving Eqs. (A4) and (A5) we find

$$\langle (\Delta x_1)^2 \rangle = Na^2[1 + (Na^2\Delta H_v^2/k^2T^4)(\partial T/\partial x)^2].$$

The term involving the temperature gradient is again negligible, so that

$$\langle (\Delta x_1)^2 \rangle = Na^2. \tag{A6}$$

From equations (A4) and (A6) we have, therefore,

$$2kT^2[\langle \Delta x_1 \rangle / \langle (\Delta x_1)^2 \rangle](\partial T/\partial x)^{-1} = 2\Delta H_v. \tag{A7}$$

The corresponding equation for interstitial diffusion is zero. This is because $\langle \Delta X_i \rangle$ is zero since the interstitial atom has an equal probability of jumping in either direction, a vacant site being available on both sides.

If Γ is the mean jump frequency for the N jumps made in time t, then $N=\Gamma t$. We then have from Eq. (A6) that

$$kT^2(\partial/\partial T)\ \ln[\langle (\Delta x_1)^2 \rangle / 2\Delta t] = \Delta H_m^+ + \Delta H_v \tag{A8}$$

for the vacancy mechanism. The effect of the temperature gradient, which means that Γ varies from jump to jump is again found to be negligible in evaluating this expression. The result for the interstitial follows in the same manner.

[11] A. D. LeClaire, Phil. Mag. 3, 921 (1958).

Secondary Reactions in a Gas Discharge

IRENE B. ORTENBURGER AND MARTIN HERTZBERG*
Lockheed Missiles and Space Division, Palo Alto, California
AND
RICHARD A. OGG, JR.
Stanford University, Stanford, California

(Received February 22, 1960)

The pressure variations of H^+, H_2^+, H_3^+, He^+, and HeH^+ ions emanating from an electrodeless discharge in pure hydrogen and in mixtures of hydrogen and helium have been measured. Mass analysis was accomplished with a "strong-focusing" mass spectrometer. The analysis of the results in hydrogen are discussed, as well as the alternative mechanisms for hydrogen dissociation. From the results in hydrogen-helium mixtures, a value of 0.37 ± 0.15 has been obtained for the ratio k_2'/k_1'; where k_2' is the rate constant for reaction

$$He^+ + H_2 \rightarrow HeH^+ + H$$

and k_1' is the rate constant for the reaction

$$H_2^+ + H_2 \rightarrow H_3^+ + H.$$

In addition, a value of 0.016 ± 0.013 has been obtained for the ratio k_3'/k_2', where k_3' is the rate constant for the reaction

$$H_3^+ + He \rightarrow HeH^+ + H.$$

INTRODUCTION

EVER since the early experiments of Wood,[1] it has been known that atomic hydrogen could be produced in abundance inside a gaseous discharge. There have been two alternative mechanisms postulated to account for this dissociation. The first of these is a primary one involving the excitation of the hydrogen molecule by electron impact to the repulsive triplet state with subsequent dissociation into two hydrogen atoms, which recoil with excess kinetic energy.[2,3] The alternative is a secondary mechanism in which the H_2^+ ion, after formation by electron impact, subsequently reacts with a neutral H_2 molecule.[4] The "primary" mechanism may be written as the reaction,

$$H_2 + e^- \rightarrow 2H + e^-,$$

in which the hydrogen atoms formed are "hot"; their kinetic energy and the required dissociation energy coming from the impacting electron. The "secondary" mechanism may be written

$$H_2 + e^- \rightarrow H_2^+ + 2e^-$$
$$H_2^+ + H_2 \rightarrow H_3^+ + H$$
$$H_3^+ + e^- \rightarrow H_2 + H.$$

The net result of this chain is the dissociation of one hydrogen molecule for every molecular ion formed. From their experiments, Dorsch and Kallman[4] had concluded that the secondary mechanism was the dominant one. Subsequent investigations have not considered the secondary mechanism as significant. In fact, the yield of atomic hydrogen produced in a discharge has been used to obtain estimates of the sum of the cross sections for excitation of the hydrogen molecule to the forbidden triplet states: $^3\Sigma_u^+$ and $^3\Sigma_g$.[2,5] If the secondary reaction contributes to the atomic hydrogen yield, then the cross sections so measured would be too large by an undetermined amount.

One of the aims of the present experiment was to discriminate between these two mechanisms. In the experiment performed, hydrogen gas was subjected to an electrodeless radio-frequency discharge and the relative intensities of the ion products emanating therefrom were measured with a mass spectrometer. A second aim of the experiment involved a search for the H_4^{++} ion.[6,7] Since the mass-to-charge ratio of this ion coincided with that of the H_2^+ ion, it was necessary to use the deuterium isotope in order to detect its presence. The species H_2D^{++} and D_2H^{++} would be detected at 2.5 and 3.5 amu per electronic charge. Mixtures of hydrogen and deuterium were therefore used and an intensive search was made for these half-integral masses.

Reaction (3) is one of a class of ion-molecule reactions which have come under considerable study in recent years. Stevenson[8] and several other investi-

* Part of a dissertation submitted to the Department of Chemistry and Chemical Engineering in partial fulfillment of the requirements for the degree of Doctor of Philosophy in Chemistry.

[1] R. W. Wood, Proc. Roy. Soc. (London) **A97**, 455 (1920).

[2] H. S. W. Massey and E. H. S. Burhop, *Electronic and Ionic Impact Phenomena* (Clarendon Press, Oxford, England, 1952), p. 233.

[3] H. G. Poole, Proc. Roy. Soc. (London) **A163**, 404, 415, and 424 (1937).

[4] K. E. Dorsch and H. Kallman, Z. Physik **53**, 80 (1929).

[5] T. M. Shaw, J. Chem. Phys. **30**, 1366 (1959).

[6] R. A. Ogg, Jr., Report from the Symposium on Quantum Theory of Molecules, Stockholm and Uppsala, March 21–25, 1955.

[7] H. Shull and S. Hagstrom, J. Chem. Phys. **30**, 1314 (1959).

[8] D. P. Stevenson and D. O. Schissler, J. Chem. Phys. **29**, 294 (1958).

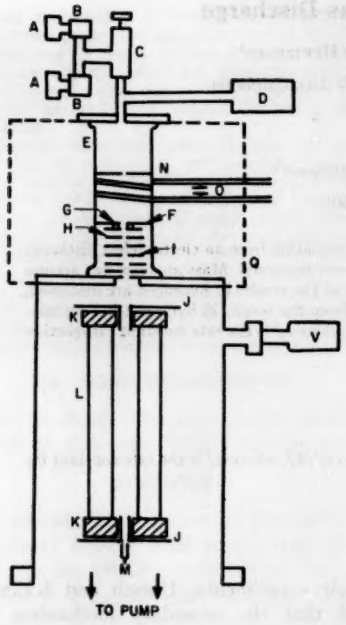

FIG. 1. Experimental arrangement. *A*: "quick connects" for calibrated leaks; *B*: bellows valves; *C*: throttle valve; *D*: manometer; *E*: discharge vessel; *F*: aperture plate; *G*: O-ring seal; *H*, *I*: collimating plates; *J*: entry aperture to spectrometer; *K*: Teflon holders for mass spectrometer electrodes; *L*: mass spectrometer rods; *M*: mass spectrometer collector; *N*: discharge coil; *O*: capacitor; *Q*: shield; *V*: ionization manometer.

gators[9,10] have measured the cross sections for a variety of such reactions and have generally found that, at low energies, they are between one and two orders of magnitude greater than the kinetic-theory collision cross sections. These results have been used to show that analogous reactions between the ions and the neutral components of the upper atmosphere exert a controlling effect on the composition of the ionic species present.[11] Such reactions have also been shown to exert a significant effect on the neutral species as well, providing a mechanism for dissociating molecular nitrogen in the ionosphere.

EXPERIMENTAL

A strong-focusing mass spectrometer, which has several advantages over existing instruments, was used to analyze the ion products. First described by W. Paul,[12–14] it utilizes purely electric fields to achieve the separation of ions. The operating principle is analogous to the magnetic strong-focusing used in high-energy accelerators, and hence it has been called the strong-focusing mass spectrometer. An article describing its characteristics in detail will be published elsewhere.

The experimental equipment used is shown schematically in Fig. 1. Gas was fed into the discharge chamber through calibrated leaks installed at points *A*. Gas flowed through the bellows valves *B* and throttle valve *C*. A mercury manometer *D* was used to observe the pressure. By using suitable combinations of calibrated leaks and apertures between the discharge and mass spectrometer, it was possible to adjust the discharge pressure, as read by *D*, over the range 1 to 1000 μ. The discharge tube consisted of an 8-in. length of 2-in. diam Pyrex pipe. The central region of the discharge tube was isolated by two $\frac{1}{4}$-in. thick Pyrex disks with holes in their centers. During operation, the discharge was confined to the central region between these disks. Power for the discharge was fed to the "tank coil" *N* and the capacitor *O* from a radio transmitter operating at 50 Mc. The apertures separating the discharge region from the analyzer region were drilled into plate *F*. A potential applied to plate *F* was used to vary the energy of the ions issuing from the discharge. After passing the collimating plates *I* and *H*, the ions entered the mass spectrometer through aperture *J*. Ions injected into the mass spectrometer were collected at *M*. An ionization manometer *V* was attached to the vacuum housing. A 700-liter/sec oil diffusion pump, a gate valve, a liquid-nitrogen cold-trap and a forepump completed the vacuum system.

RESULTS AND DISCUSSION

A. Hydrogen and Deuterium

Two mixtures, one containing three parts H_2 and one part D_2 and the other containing one part H_2 and three parts D_2 by volume, were obtained from the Stuart Oxygen Company. A sample spectrum from the latter mixture is shown in Fig. 2. The peak at mass 2 corresponds to the sum of contributions from H_2^+ and D^+, mass 3 to the sum HD^+ and H_3^+, mass 4 to the sum H_2D^+ and D_2^+, and mass 5 to the HD_2^+ ion.

Peaks corresponding to either H_3D^{++} or to D_3H^{++} were not observed at half-integral masses. They would have been observed if their intensities were as large as one part in 1000 of the total ion intensity. It is concluded that, if the H_4^{++} ion is a stable species, conditions in this discharge were not favorable for its formation.

B. Hydrogen

The results of the experiment in pure hydrogen are summarized in Fig. 3. The percentage of total ion current, plotted as a function of pressure in the range 0 to 500 μ, is shown. The data represent five distinct runs made at different times and, in some cases, under slight varying conditions as listed in the Table I.

[9] H. Gutbier, Z. Naturforsch. **12a**, 499–507 (1957).
[10] F. H. Field, J. L. Franklin, and F. W. Lampe, J. Am. Chem. Soc. **79**, 2419 (1957); **78**, 5697 (1956).
[11] M. Hertzberg, J. Geophys. Research **63**, 856 (1958).
[12] W. Paul and H. Steinwedel, Z. Naturforsch **8a**, 448 (1953).
[13] W. Paul and M. Raether, Z. Physik **140**, 262 (1955).
[14] W. Paul, H. P. Reinhard, and U. von Zahn, Z. Physik **152**, 143 (1948).

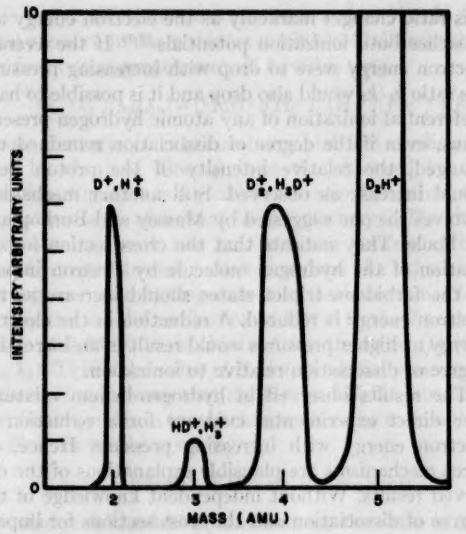

FIG. 2. Sample spectra obtained for a mixture of H_2 and D_2.

During these runs, the potential at plate F was made sufficiently negative so that the total unresolved ion current at the collector was approximately half the value observed when F was grounded. This insured a reasonably low value for the velocity of ions through the mass analyzer. The resolution was adjusted to a low value so that the peak shapes were nearly flat at the top. In Fig. 4, the results of this experiment are compared with those of Hogness and Lunn[15] and of Brasefield.[16] There is general agreement in the trend of the

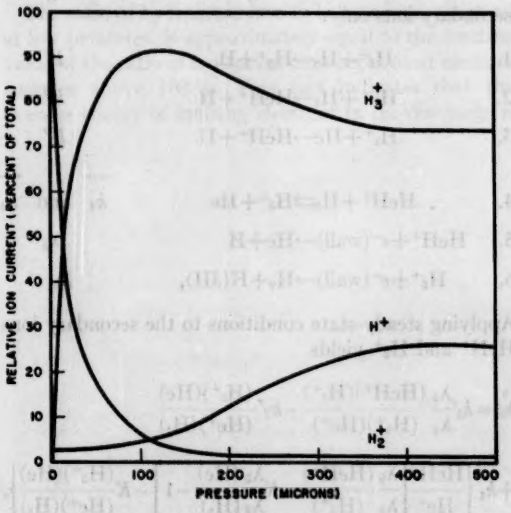

FIG. 3. Pressure variation of the relative ion current in pure hydrogen.

[15] T. R. Hogness and E. G. Lunn, Phys. Rev. **26**, 44 (1925).
[16] C. J. Brasefield, Phys. Rev. **31**, 52 (1928).

TABLE I.

Run No.	Aperture diam (in.)	Pressure range (μ)
1	0.010	3–1000
2	0.010	2–1000
3	0.010	50–900
4	0.032	5–150
5	0.070	2–15

curves with this study yielding results intermediate between those of the two earlier investigators. This is a reasonable result, considering the differences in the ion source used. Hogness and Lunn used an electron-bombardment source in which the ion energies were quite low, whereas Brasefield's source was a direct-current discharge and can be characterized by considerably larger energies. The radio-frequency source would be expected to contain ions whose average kinetic energy in the discharge are intermediate between those of the earlier investigators.

Let us consider the following reactions to be the only ones affecting the ionic species:

$$H_2+e^-\rightarrow H_2^++2e^-, \qquad k_1,$$
$$H_2^++H_2\rightarrow H_3^++H, \qquad k_2,$$
$$H+e^-\rightarrow H^++2e^-, \qquad k_3,$$
$$H_2^++e^-(\text{wall})\rightarrow H_2(2H), \qquad \lambda_2,$$
$$H_3^++e^-(\text{wall})\rightarrow H_2+H(3H), \qquad \lambda_3,$$
$$H^++e(\text{wall})\rightarrow H, \qquad \lambda_1.$$

Assuming steady-state conditions, we have

$$d(H_3^+)/dt=k_1(H_2)(e^-)-k_2(H_2)(H_2^+)-\lambda_2(H_2^+)=0,$$
$$d(H_3^+)/dt=k_2(H_2^+)(H_2)-\lambda_3(H_3^+)=0,$$
$$d(H^+)/dt=k_3(H)(e^-)-\lambda_1(H^+)=0,$$

where the k's refer to the rate constants for the reactions and the λ's may be considered loss coefficients for the ions. Assuming that ions are lost on single wall

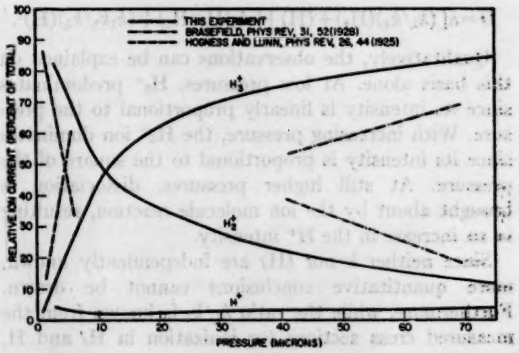

FIG. 4. Comparison of results of this experiment with those of earlier investigators.

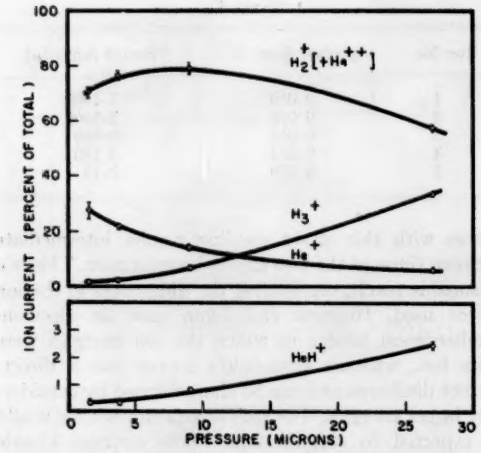

FIG. 5. Pressure variations of the relative ion currents in mixtures of hydrogen and helium.

collisions, the loss coefficient for a particular ion is essentially equal to the reciprocal of the average time required for an ion formed in the discharge to reach the wall. With typical ion velocities, λ is of the order of 10^5 sec^{-1}. Heterogeneous recombination at the wall would be the primary loss mechanism at low pressures and low degrees of ionization. At higher pressures, however, it may be necessary to consider loss by ion-electron recombination. The loss coefficient due to this process is $\alpha(\epsilon^-)$ where α is the recombination coefficient for the diatomic ions. In order for these two mechanisms to be comparable (ϵ^-) would have to be as large as 10^{13} cm^{-3}.[17] If we let $\lambda_1=\lambda_2=\lambda_3$, we obtain the following for the fraction of ions consisting of diatomic, triatomic, and atomic species, respectively:

$$f(H_2^+)=\lambda(k_1/k_3)(H_2)/D$$

$$f(H_3^+)=(k_1k_2/k_3)(H_2)^2/D$$

$$f(H^+)=[\lambda(H)+k_2(H)(H_2)]/D,$$

where

$$D=\lambda[(k_1/k_3)(H_2)+(H)]+k_2(H)(H_2)+(k_1k_2/k_3)(H)^2.$$

Qualitatively, the observations can be explained on this basis alone. At low pressures, H_2^+ predominates since its intensity is linearly proportional to the pressure. With increasing pressure, the H_3^+ ion dominates since its intensity is proportional to the square of the pressure. At still higher pressures, dissociation is brought about by the ion molecule reaction, resulting in an increase in the H^+ intensity.

Since neither λ nor (H) are independently known, more quantitative conclusions cannot be drawn. Furthermore, while the ratio k_1/k_3 is known from the measured cross sections for ionization in H_2 and H, this ratio changes markedly as the electron energy approaches both ionization potentials.[18,19] If the average electron energy were to drop with increasing pressure, the ratio k_1/k_3 would also drop and it is possible to have preferential ionization of any atomic hydrogen present. Thus, even if the degree of dissociation remained unchanged, the relative intensity of the proton peak would increase as observed. Still another mechanism involves the one suggested by Massey and Burhop and by Poole. They indicate that the cross section for excitation of the hydrogen molecule by electron impact to the forbidden triplet states should increase as the electron energy is reduced. A reduction in the electron energy at higher pressures would result in an increasing degree of dissociation relative to ionization.

The results observed in hydrogen-helium mixtures give direct experimental evidence for a reduction in electron energy with increasing pressure. Hence, all three mechanisms are plausible explanations of the observed results. Without independent knowledge of the degree of dissociation and the cross sections for impact dissociation relative to ionization, it is not possible to evaluate the relative importance of these three mechanisms.

C. Mixtures of Hydrogen and Helium

Mixtures of hydrogen and helium were also analyzed in the discharge. While masses 3, 4, and 5 can be assigned uniquely to H_3^+, He^+, and HeH^+, respectively, the peak at mass 2 represents the sum of contributions from H_2^+ and He^{++}. The relative intensity of these peaks plotted as a function of pressure for a 1:1 mixture are shown in Fig. 5. The data have been analyzed in terms of the following reactions involving the secondary ions only:

1.	$H_2^+ + H_2 \rightarrow H_3^+ + H$	k_1'
2.	$He^+ + H_2 \rightarrow HeH^+ + H$	k_2'
3.	$H_2^+ + He \rightarrow HeH^+ + H$	k_3'
4.	$HeH^+ + H_2 \rightleftarrows H_3^+ + He$	$\overrightarrow{k_4}$ and $\overleftarrow{k_4}$
5.	$HeH^+ + \epsilon^-(\text{wall}) \rightarrow He + H$	λ_5
6.	$H_3^+ + \epsilon^-(\text{wall}) \rightarrow H_2 + H(3H),$	λ_3.

Applying steady-state conditions to the secondary ions HeH^+ and H_3^+ yields

$$k_2'=k_1'\frac{\lambda_5}{\lambda_3}\frac{(HeH^+)(H_2^+)}{(H_3^+)(He^+)}-k_3'\frac{(H_2^+)(He)}{(He^+)(H_2)}$$

$$+\overrightarrow{k_4}\left\{\frac{HeH^+}{He^+}\left[\frac{\lambda_5}{\lambda_3}\frac{(HeH^+)}{(H_3^+)}-K\frac{\lambda_5}{\lambda_3}\frac{(He)}{(H_2)}-1\right]-K\frac{(H_3^+)(He)}{(He^+)(H_2)}\right\}.$$

[17] It will be assumed in the following discussion that the product $\alpha(\epsilon^-)$ is low enough so that recombination can be ignored.

[18] J. T. Tate and P. T. Smith, Phys. Rev. **39**, 270 (1932).

[19] W. L. Fite and R. T. Brackmann, Phys. Rev. **112**, 1141 (1958).

K is the equilibrium constant for reaction (4). As the total pressure in the system is diminished, all terms but the first two approach zero. If $k_3' \ll k_2'$, then

$$(k_2'/k_1')(\lambda_3/\lambda_5) = (HeH^+)(H_2^+)/(H_3^+)(He^+) = R.$$

Thus, the ratio of rate constants and loss coefficients may be obtained directly from the observed ion intensities. Figure 6 is a plot of the ratio R, against the partial pressure of helium in the discharge. The data were obtained with two mixtures, one containing one part hydrogen to one part helium and the other containing one part hydrogen to nine parts helium. Neglecting the small contribution of He^{++} to the 2 peak, a value of 0.48 ± 0.19 is obtained for the ratio $(k_2'/k_1')(\lambda_3/\lambda_5)$. This is the value of R at zero partial pressure of helium. If we assume that the H_3^+ and HeH^+ ions have identical energies in the discharge, then the ratio of loss coefficients will be given by

$$\lambda_5/\lambda_3 = VHeH^+/VH_3^+ = [M_3/M_5]^{\frac{1}{2}} = 0.775.$$

A value of 0.37 ± 0.15 is obtained for the ratio k_2'/k_1'. Gutbier has measured both rate constants separately. His result, 0.22, falls at the lower limit of our range.

If reaction (3) is not neglected as a possible source of HeH^+ ions, then one obtains the relation

$$k_2'/k_1' = (\lambda_5/\lambda_3)R - (k_3'/k_1')R'$$

where

$$R' = (H_2^+)(He)/(He^+)(H_2).$$

A plot of k_2'/k_1' vs R' has been used to obtain a value for k_3'/k_1'. We may therefore compare the rates of formation of HeH^+ ions via reaction (2) with the rate of formation via reaction (3). The ratio obtained for k_3'/k_2' is 0.016 ± 0.013.

The ratio of hydrogenic ions to helium ions, observed at low pressures, is approximately equal to the limiting value of the ratio of ionization cross sections at electron energies above 100 v. This fact indicates that the average energy of ionizing electrons in the discharge is at least this large. With increasing pressure, hence decreasing electron energy, this ratio increases rapidly, paralleling the increase in the ratio of ionization cross sections: Q_{H_2}/Q_{He}.

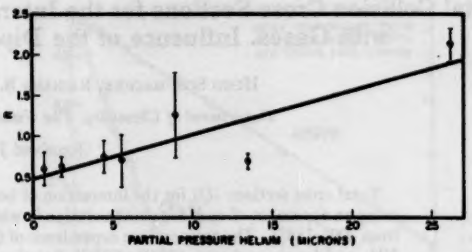

FIG. 6. Graph from which the ratio of rate constants k_2'/k_1' was obtained.

CONCLUSIONS

From an analysis of the ion products of a discharge in pure hydrogen, it has not been possible to discriminate between the two alternative mechanisms postulated to account for the dissociation of molecular hydrogen. A similar analysis in a mixture of hydrogen and deuterium has yielded values for the ratios of rate constants among several ion-molecule reactions in helium-hydrogen mixtures. A search for half-integral masses corresponding to the H_3D^{++} or D_3H^{++} ions in mixtures of hydrogen and deuterium have given negative results.

ACKNOWLEDGMENTS

The authors are indebted to Dr. F. S. Johnson, Dr. A. J. Dessler, Dr. W. B. Hanson, and Dr. D. Rapp for their helpful discussions; D. D. McKibbin, J. Drake, and D. Briglia for their contributions to the design of the mass spectrometer oscillator; and C. Searing, W. J. Page, and E. Arnold for their help in the construction of the equipment.

Total Collision Cross Sections for the Interaction of Molecular Beams of Cesium Chloride with Gases. Influence of the Dipole-Dipole Force upon the Scattering

HUGO SCHUMACHER, RICHARD B. BERNSTEIN, AND ERHARD W. ROTHE*

Department of Chemistry, The University of Michigan, Ann Arbor, Michigan

(Received January 22, 1960)

Total cross sections (Q) for the interaction of beams of CsCl with a number of molecules were measured using an apparatus of ca 4′ angular resolution in which the temperature of the scattering gas could be varied from 200°–735°K. The temperature dependence of Q was studied for Ar, CH_4, CH_2F_2, CHF_3, CF_4, NO, H_2S, NH_3, and for *cis*- and *trans*-CHCl=CHCl. Relative values of Q at 300°K were measured for eight additional gases.

The data were correlated using the Massey-Mohr theory, assuming an intermolecular potential $V(r) = -C/r^6$, so that $Q = b(C/v_r)^{2/5}$, where v_r is the relative velocity and b a known constant; the potential constant C was estimated from formulas for the dispersion, dipole-induced dipole, and dipole-dipole forces.

For the nonpolar gases the observed small temperature dependence of Q agrees within experimental error (±3%) with that expected from the temperature dependence of v_r. The theoretical values of Q differ by a nearly constant factor from the experimental results; thus relative cross sections (Q^*) are predicted with fair accuracy.

For the polar gases the Q's are large, decreasing significantly with increasing temperature. Because of the large dipole-dipole interaction, the approximate theoretical treatment (based on the limiting temperature-dependent dipole-dipole contribution to C) accounts only semiquantitatively for the observations.

INTRODUCTION

IN a previous paper[1] total collision cross sections (Q) for the interaction of atomic beams of K and Cs with a number of molecules (polar and nonpolar) were reported. The results were correlated with the Massey-Mohr theory[2] for an attractive intermolecular potential $V(r) = -C/r^6$.

The present paper describes experiments on the scattering of beams of the dipolar molecule CsCl. Studies with dipolar beam molecules are of interest because of the possibility of observing directly the influence of the dipole-dipole forces upon the scattering.

An approximate theoretical equation has been presented[1] for the estimation of elastic scattering cross sections for dipolar molecules. The assumptions in its development are such as to limit its applicability to cases where the interaction energy is small relative to kT, corresponding to low dipole moments and/or high temperatures. It will be seen that although the experimental results may be accounted for in a semiquantitative way by the limiting theory, considerable further theoretical development is needed before precise *a priori* calculations of cross sections can be made.

EXPERIMENTAL

The apparatus was that described by Rothe and Bernstein[1] (hereafter referred to as I) with the following modifications: The oven was supplied with additional heaters and surrounded by a water-cooled radiation shield. The oven slit was set at 0.005 cm. The scattering chamber (SC) was constructed of copper, with a Kovar-to-Pyrex seal leading to the external gas inlet system. It was attached to a Monel heater plate containing internal heating coils. This plate was itself in contact with a copper cooling plate through which liquid nitrogen could be passed. The SC was thermally insulated from its support by means of Vycor plates and rings. Three thermocouples located in suitable wells in the SC indicated that temperature gradients were negligible. Steady temperatures ranging from −130° to 465°C could readily be obtained; however, for other reasons the low-temperature limit of the experiments was set at 200°K.

The collimating slit on the SC was set at 0.005 cm. The calculated half-width of the unscattered beam at the detector (0.0025 cm diam) was 0.015 cm. The observed value varied somewhat with the temperature of the SC, but was in the range 0.02–0.03 cm. The resolution[3] of the apparatus is taken to be 4′ of arc (compared to 2′ with the arrangement used in I).

The Knudsen-gauge (KG) sensitivity was improved to a value of 2.0×10^{-6} mm Hg/mm scale deflection by increasing the heater temperature and the optical path. The working range of pressures in the SC was from 1×10^{-6} to 5×10^{-5} mm Hg. Since the SC was at a

* Present address: Physics Section, Convair San Diego, Division of General Dynamics Corporation, San Diego, California.

[1] E. W. Rothe and R. B. Bernstein, J. Chem. Phys. **31**, 1619 (1959). Errata are as follows: The exponent in Eq. (2) should read −17. The first bracket in Eq. (e) of Appendix II is to be deleted. A more correct estimate of the angular resolution is 2′ of arc (see footnote 3 of the present paper).

[2] H. S. W. Massey and C. B. O. Mohr, Proc. Roy. Soc. (London) **A144**, 188 (1934).

[3] P. Kusch (private communication, January 18, 1960) has developed an equation for calculating the efficiency of detection of scattering in terms of apparatus parameters, e.g., beam width and detector width. He suggests a reasonable definition of resolution as the minimum scattering angle for which the efficiency of detection of scattering is 50%. This criterion has been adopted here. *Note added in proof.* Application of this analysis to the experimental arrangements of two other previous workers (footnote references 2 and 10 of I) showed their resolution (at the 50% level) to be appreciably worse than their stated "resolution."

different temperature than the KG, the pressure readings required correction for the thermal transpiration effect, $P_{SC}=P_{KG}(T_{SC}/T_{KG})^{\frac{1}{2}}$. The ideal square root of T factor was used in view of calculations based on Liang's[4] empirical formula for thermal transpiration, using the present experimental parameters ($P<5\times10^{-5}$ mm, tubing diam 9 mm i.d., T_{SC} 200–735°K, and $T_{KG}=300$°K). The calculated factors agreed within 1% with the ideal $T^{\frac{1}{2}}$ factor used.

Larger liquid-nitrogen traps made it possible to maintain pressures $<3\times10^{-7}$ mm Hg in the oven chamber and $<2\times10^{-7}$ mm Hg in the detector chamber with both the oven and SC at high temperatures.

The operating procedure was similar to that described in I. Before each series of experiments with a new scattering gas, however, the SC was heated and thoroughly degassed. For each individual cross-section determination the beam intensity was measured for 20 or more values of the scattering gas pressure corresponding to 0–50% attenuation of the beam. Plots of $\log(I/I_0)$ vs P_{SC} were accurately linear in this range ($I/I_0>0.5$).

Argon was used as a standard "reference" gas; for comparison purposes the Q for argon was determined at least once during any series of measurements with another gas. In I, *relative* cross sections were reported (using argon as the reference). In the present work, whenever the argon cross section differed significantly from the "standard" argon curve (Fig. 2) all Q's of that series were adjusted accordingly (by amounts ranging from 0 to 14%). All data as reported are thus mutually consistent with the "standard" curve for argon.

MATERIALS

All scattering gases were purified (mostly by distillation) and were characterized before use. They are believed to contain less than 1% impurity. We used cp cesium chloride (Fairmount Chemical Company), stated to contain <0.5% impurity (most of which is KCl), for the beam. Based on the results of Kusch[5] it is unlikely that the abundance of dimeric or polymeric molecules in the beam is greater than 1–2%.

RESULTS

Figure 1 shows a typical plot of primary data. The calculation of the cross section from the slopes of such graphs is outlined in I.

The absolute cross sections for CsCl-argon are subject to uncertainty because of numerous sources of possible systematic errors.[1] For the earlier measurements[6] (Set A, beam temperature 876°K) the average value of Q for argon at 300°K was 395 A² with a maximum value of 450 A². However, for the subsequent, more

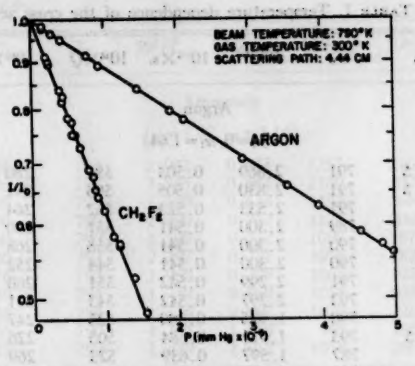

FIG. 1. Typical plot of primary data for CsCl scattering.

reliable determinations (Set B, beam temperature ca 790°K) most of the values for Q of argon at 300°K were between 540 and 560 A²; all of these determinations lay within a total range of 15%. All the data on the temperature dependence of the cross section as reported are consistent with the "Set B" measurements for argon.

Table I summarizes the results of the study of the influence of temperature on the scattering of CsCl beams by various polar and nonpolar gases. Here T_1 and T_2 represent the temperatures (°K) of the scattering gas and beam, respectively; $\bar{T}=2T_1T_2/(T_1+T_2)$, v_r (cm/sec) is the average relative velocity as defined in I, and Q (cm²) is the cross section. The potential constant C (erg cm⁶) is obtained[1] from the Massey-Mohr formula,

$$C=6.738\times10^{-20}v_r Q^{\frac{1}{2}}. \quad (1)$$

Listed in the table are the dipole moments μ (debyes) and polarizabilities α (A³) of the various gases [see Rothe (footnote 6) for sources of data].

Table II presents data on the relative cross sections for the scattering of CsCl beams by various nonpolar gases at 300°K. Set A summarizes the most reliable determinations from the earlier study.[6] The data of Set B are derived from Table I. The relative cross section Q^* is defined (as in I) by the ratio

$$Q^*=Q_{12}/Q_{Ar2}, \quad (2)$$

where Q_{12} and Q_{Ar2} are the total cross sections for the beam 2 with gas 1 and argon, respectively. The calculated relative cross sections are obtained from the equations [(6) and (7) of I] for the C_{ind} and C_{disp} terms, using the dipole moment of CsCl and the listed polarizabilities of the scattering gases.

The data are presented graphically in Figs. 2–12. Where different symbols for experimental points appear, they represent different series of measurements. Dashed lines through the data are "experimental," while solid lines show either the calculated fit to the data or the theoretical lines, as indicated. The dotted

[4] S. C. Liang, J. Phys. Chem. 57, 910 (1953).
[5] P. Kusch, J. Chem. Phys. 25, 860 (1956).
[6] E. W. Rothe, Ph.D. thesis, University of Michigan, 1959. Available from University Microfilms, Inc., Ann Arbor, Michigan.

TABLE I. Temperature dependence of the cross section for the scattering of CsCl beams (CsCl: $\mu_2=10.42$; $\alpha_2=5.912$).

T_1	T_2	$10^3/\bar{T}$	$10^{-5}\times v_r$	$10^{16}\times Q$	$10^{20}\times C$
		Argon			
		($\mu_1=0$, $\alpha_1=1.64$)			
223.5	791	2.869	0.503	585	280
227.5	791	2.830	0.505	593	291
263	791	2.533	0.523	562	264
300	789	2.300	0.541	551	260
300	790	2.300	0.541	558	268
300	790	2.300	0.541	544	252
300	791	2.299	0.542	551	260
300	793	2.297	0.542	543	251
381	790	1.945	0.580	525	247
390.5	793	1.911	0.584	505	226
520	787	1.597	0.639	523	269
531	791	1.573	0.644	500	243
555	791	1.533	0.654	510	258
635	784	1.425	0.685	504	263
699	791	1.347	0.710	498	264
731	782	1.323	0.721	486	252
					259 (av)
		Methane			
		($\mu_1=0$, $\alpha_1=2.56$)			
230	788	2.808	0.661	589	375
300	789	2.300	0.727	560	363
351	792	2.056	0.773	522	325
465	792	1.707	0.864	536	387
574	792	1.502	0.944	496	349
695	792	1.351	1.025	515	415
723	792	1.323	1.043	467	332
					364 (av)
		Carbon tetrafluoride			
		($\mu_1=0$, $\alpha_1=2.82$)			
214	792	2.968	0.433	786	505
300	792	2.298	0.456	734	448
406	792	1.863	0.483	686	401
530	792	1.575	0.512	740	513
537	788	1.566	0.513	727	492
616	792	1.443	0.532	741	536
667	792	1.380	0.543	663	414
					473 (av)
		Difluoromethane			
		($\mu_1=1.96$, $\alpha_1=2.69$)			
209.5	793	3.017	0.470	2600	10910
218	791	2.926	0.473	2667	11710
218	794	2.923	0.474	2572	10710
236	792	2.750	0.481	2669	11920
250	794	2.630	0.487	2789	13480
269	794	2.489	0.495	2487	10290
276	794	2.441	0.498	2616	11740
276.5	793	2.438	0.498	2547	10980
300	791	2.299	0.507	2330	8951
300	792	2.298	0.507	2344	9083
300	794	2.296	0.507	2412	9763
326	794	2.163	0.517	2175	7696
332	793	2.137	0.520	2214	8071
347	794	2.071	0.526	2088	7053
395	791	1.898	0.543	2040	6882
409	794	1.852	0.549	1962	6307
467	791	1.703	0.569	1983	6717
493	793	1.645	0.579	1936	6433
582.5	791	1.490	0.609	1937	6776
613	792	1.447	0.619	1818	5881
642	787	1.414	0.628	1818	5962
698	787	1.352	0.646	1757	5631
708	788	1.340	0.649	1903	6908
728	790	1.320	0.656	1677	5084
729.5	790	1.318	0.656	1735	5545
		Fluoroform			
		($\mu_1=1.64$, $\alpha_1=2.77$)			
201	794	3.117	0.444	2281	7431
221	791	2.894	0.450	2238	7180
222	794	2.882	0.451	2178	6724
246	794	2.662	0.459	1854	4574
266.5	794	2.506	0.465	1811	4376
300	794	2.296	0.476	1734	4011
300	794	2.296	0.476	1679	3703
331	794	2.140	0.485	1653	3633
388	794	1.918	0.503	1600	3466
501	793	1.628	0.535	1598	3680
619	791	1.440	0.567	1529	3493
702	790	1.345	0.588	1570	3871
730	790	1.318	0.595	1413	3010
		***cis*-Dichloroethylene**			
		($\mu_1=1.89$; $\alpha_1=8.08$)			
273	793	2.462	0.442	2818	12560
300	793	2.297	0.449	2766	12170
335	793	2.123	0.457	2661	11250
390	791	1.914	0.470	2579	10690
394	791	1.901	0.470	2615	11090
456	794	1.726	0.485	2403	9249
524	791	1.586	0.499	2379	9289
535	794	1.564	0.502	2370	9254
571	789	1.509	0.509	2242	8162
		***trans*-Dichloroethylene**			
		($\mu_1=0$, $\alpha_1=8.08$)			
273	795	2.460	0.443	1395	2167
300	795	2.296	0.449	1255	1689
331	795	2.140	0.456	1299	1871
397	795	1.888	0.472	1340	2088
474	795	1.684	0.489	1332	2133
528	794	1.577	0.501	1250	1864
563	793	1.519	0.508	1193	1684
					1928 (av)
		Nitric oxide			
		($\mu_1=0.16$, $\alpha_1=1.70$)			
213	792	2.979	0.534	750	554
213	792	2.979	0.534	737	531
262.5	792	2.536	0.565	642	398
300	792	2.298	0.588	602	352
300	794	2.296	0.588	608	361
373	792	1.972	0.630	578	341
427	792	1.802	0.660	573	349
445.5	792	1.754	0.669	545	313
545.5	792	1.548	0.720	540	329
581	792	1.492	0.737	542	340
637.5	791	1.416	0.764	554	371
689	788	1.360	0.787	538	356
730	790	1.318	0.805	522	337
735	790	1.313	0.807	482	278

TABLE 1 Continued.

T_1	T_2	$10^3/\bar{T}$	$10^{-5}\times v_r$	$10^{16}\times Q$	$10^{20}\times C$	T_1	T_2	$10^3/\bar{T}$	$10^{-5}\times v_r$	$10^{16}\times Q$	$10^{20}\times C$
Hydrogen sulfide ($\mu_1=1.02$, $\alpha_1=3.61$)						Ammonia ($\mu_1=1.47$, $\alpha_1=2.16$)					
197	794	3.168	0.508	1453	2750	204	793	3.082	0.623	1217	2168
226	794	2.842	0.525	1444	2800	226	791	2.845	0.644	1169	2029
260	794	2.553	0.544	1301	2241	259	794	2.560	0.675	1132	1960
300	794	2.296	0.567	1191	1868	300	790	2.300	0.712	1128	2049
429.5	793	1.794	0.633	1080	1635	300	790	2.300	0.712	1090	1879
549	791	1.542	0.689	993	1444	300	793	2.297	0.712	1078	1829
635	790	1.420	0.727	863	1070	376	793	1.960	0.775	1066	1936
727	788	1.322	0.765	793	913	459	794	1.719	0.839	1058	2059
						552	794	1.536	0.905	1070	2287
						705	790	1.342	1.005	946	1862
						717	792	1.329	1.012	1078	2603

TABLE II. Relative cross sections for scattering of CsCl beams by nonpolar molecules at 300°K.

Scattering gas	α_1	T_2	$10^3/\bar{T}$	$10^{-5}\times v_r$	Q_{obs}*	Q_{calc}*
			Set A			
Ar	1.64	876	2.237	0.555	(1.000)	(1.000)
He	0.206	876	2.237	1.32	0.37	0.32
Ne	0.408	876	2.237	0.68	0.60	0.55
Kr	2.49	876	2.237	0.475	1.35	1.24
Xe	4.02	876	2.237	0.446	1.55	1.51
H_2	0.806	876	2.237	1.816	0.52	0.46
D_2	0.796	876	2.237	1.313	0.55	0.52
SF_6	4.48	876	2.237	0.441	1.74	1.68
$SiCl_4$	11.27	876	2.237	0.434	2.24	2.34
			Set B			
Ar	1.64	790	2.300	0.541	(1.000)	(1.000)
CH_4	2.56	789	2.300	0.727	1.01	1.04
CF_4	2.82	792	2.298	0.456	1.33	1.37
trans-$C_2H_2Cl_2$	8.08	795	2.296	0.449	2.27	2.00

lines merely serve to connect different regions of the drawing.

DISCUSSION

A. Scattering by Nonpolar Gases

By inspection of Table I it is seen that the small observed temperature dependence of the cross section is entirely accounted for by the temperature dependence of v_r. The solid lines in Figs. 2–4 represent the calculated fit to the data (Q vs T_1) for Ar, CH_4, CF_4 and *trans*-CHCl=CHCl, based on Eq. (4) of I,

$$Q\sim(C/v_r)^{\frac{1}{2}}. \tag{3}$$

The temperature invariance of C [calculated from Q with Eq. (1)] is illustrated in Fig. 5 for Ar, Fig. 7 for CH_4 and CF_4, and Fig. 8 for *trans*-CHCl=CHCl.

It is of interest to compare these "observed" C values with those calculated[1]: $C_{calc}=C_{d\,isp}+C_{ind}$. Table III shows this comparison; the listed values of C_{obs} are the average C values from Table I.

The results are shown graphically in Figs. 5, 7, and 8 with C_{calc} indicated by a horizontal (solid) line.

In terms of the reverse calculation (i.e., Q from C_{calc}) for the worst case, CH_4, Q_{calc} differs from Q_{obs} by some 18%. Thus the agreement is fair, but there is much room for improvement. A discussion formulating possible sources for differences is presented in I.

B. Scattering by Polar Gases

The average potential for a system of two classically rotating ideal dipoles is given by the Keesom formula[7]:

$$\langle V(r)\rangle_{kv}=-2\mu_1^2\mu_2^2/3kTr^6 \tag{4}$$

valid in the limit when

$$(\mu_1\mu_2/r^3)/kT\ll 1 \tag{5}$$

(i.e., $T\to\infty$; μ_1, $\mu_2\to 0$; and/or $r\to\infty$).[8] For the molecular beam case it seems reasonable[6] to replace T by $\bar{T}=2T_1T_2/(T_1+T_2)$, so that

$$C_{d-d}=2\mu_1^2\mu_2^2/3k\bar{T}. \tag{6}$$

[7] W. Keesom, Physik. Z. **22**, 129 (1921).

[8] As noted in I, the condition for validity of Eq. (4) is equivalent to $r\gg r_{min}=(\mu_1\mu_2/kT)^{1/3}$. For $\mu_1=1$ debye, $\mu_2=10$ debyes, $T=300$°K, $r_{min}=6.2$ A. Thus the conditions are hardly satisfied for the present experimental situation.

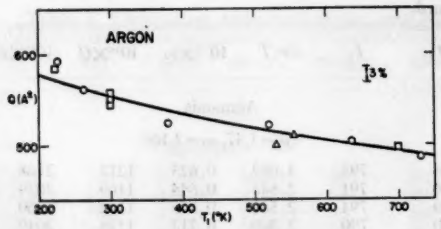

FIG. 2. Q vs temperature of scattering gas: —— calc fit.

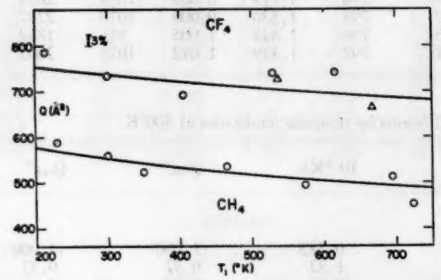

FIG. 3. Q vs temperature of scattering gas: —— calc fit.

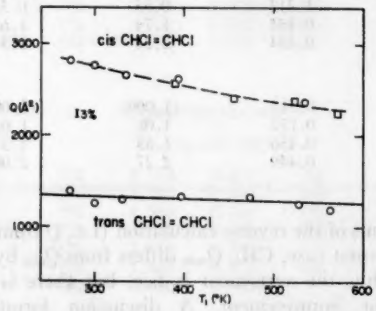

FIG. 4. Q vs temperature of scattering gas: —— calc fit; — — exptl.

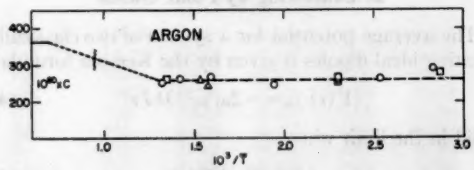

FIG. 5. C vs $1/\bar{T}$: —— theor; — — exptl.

TABLE III. C_{calc} vs C_{obs} for scattering by nonpolar molecules.

Molecule	$10^{60}\times[C_{disp}$	C_{ind}	C_{calc}	$C_{obs}]$
Ar	186	178	364	259
CH_4	267	277	544	364
CF_4	363	306	669	473
trans-CHCl=CHCl	835	878	1713	1928

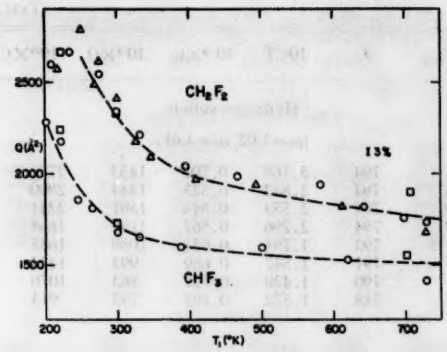

FIG. 6. Q vs temperature of scattering gas: — — exptl.

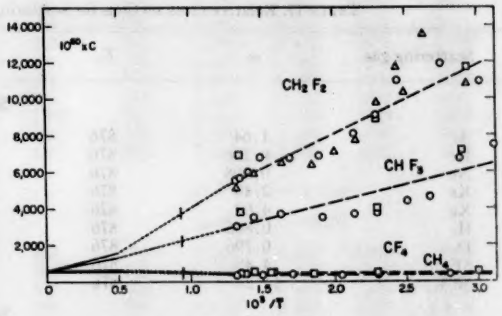

FIG. 7. C vs $1/\bar{T}$: —— theor; — — exptl.

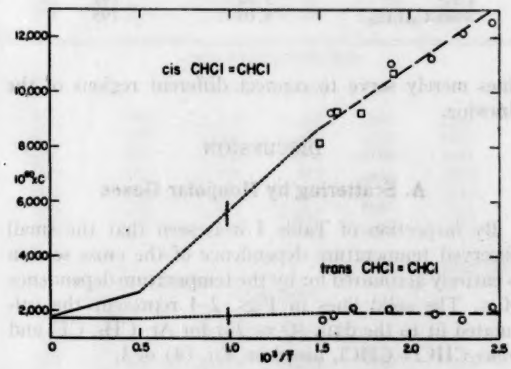

FIG. 8. C vs $1/\bar{T}$: —— theor; — — exptl.

Thus one may write a "limiting" equation,

$$C=C_{\infty}+\gamma/\bar{T}, \tag{7}$$

where

$$C_{\infty}=C_{disp}+C_{ind} \text{ and } \gamma=dC/d(1/\bar{T})=\tfrac{2}{3}\mu_1^2\mu_2^2/k. \tag{8}$$

For $\mu_2=10.42$ debyes, expressing μ_1 in debyes, $\bar{T}$ in °K, and C in erg-cm⁶, Eq. (7) becomes

$$C=C_{\infty}+5.244\times10^{-65}\mu_1^2/\bar{T}. \tag{9}$$

TABLE IV. Comparison of parameters for scattering by polar molecules.

Molecule	μ_1 (debyes)	$10^{60}\times$ [C_{disp}	C_{ind}	C_{∞}]	$10^{55}\times$ [γ_{calc}	γ_{obs}]
NO	0.16	202	185	387	0.13	(0.4)
H_2S	1.02	350	398	748	5.46	8.6
CHF_3	1.64	347	316	663	14.1	19.
CH_2F_2	1.96	326	314	640	20.1	37.
cis-$C_2H_2Cl_2$	1.89	835	899	1734	18.7	45.
NH_3	(1.47)	233	247	480	(11.3)	(0.0)

Table IV lists calculated values of C_{disp}, C_{ind}, C_{∞}, and γ. The slopes of the dashed lines drawn through the experimental points in Figs. 7, 8, 10, and 12 are listed for comparison. The solid lines near the intercepts (at $1/\bar{T}=0$) are *a priori* calculated lines based on the results given in Table IV.

For the first three (low-dipole) scattering gases, the discrepancy between the observations and the calculations is only moderate. For the next two (high-dipole) molecules, the cross sections and the "observed" C values are appreciably greater than calculated. This may indicate the departure from the limiting assumptions previously discussed.

The anomalous (small) temperature dependence of the C for NH_3 may possibly be associated with the inversion tunneling. Additional cross-section measurements with ND_3 and PH_3 would be desirable in order to clarify this point experimentally.

It is of interest to consider the possible origin of the difficulty with the high-dipole gases in terms of the other limiting situation (low temperature, small r) when the approaching dipoles "lock in" at close distances. Here the Keesom[7] potential becomes

$$V(r)=-C'/r^3, \quad \text{with} \quad C'=2\mu_1\mu_2, \tag{10}$$

independent of the temperature. Thus at a given r the potential is more negative. In addition, for this assumed potential the relation between Q and C' is not the same as that between Q and C [Eq. (3)], but rather

$$Q=1.788\times10^{28}(C'/v_r), \tag{11}$$

(upon evaluation of the Massey-Mohr equation for $s=3$) with the numerical constant consistent with the units employed here throughout. Sample calculations for typical cases show that the use of Eq. (11) yields calculated Q's considerably larger than obtained from Eq. (3), as expected, with a quite different temperature dependence.

A more rigorous theoretical approach is thus required in order to interpret more quantitatively the dipole-dipole scattering. The quantum mechanical

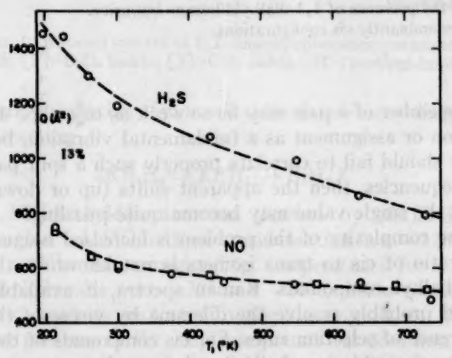

FIG. 9. Q vs temperature of scattering gas: — — exptl.

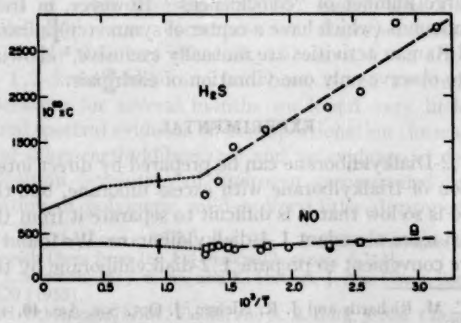

FIG. 10. C vs $1/\bar{T}$: —— theor; — — exptl.

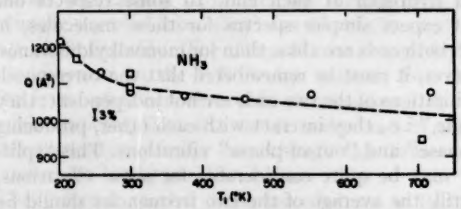

FIG. 11. Q vs temperature of scattering gas: — — exptl.

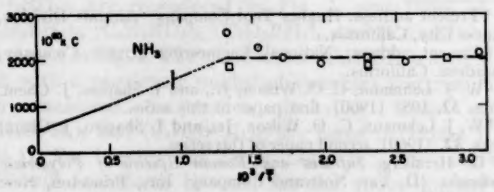

FIG. 12. C vs $1/\bar{T}$: —— theor; — — exptl.

treatment of scattering by an angle-dependent potential (together with the problem of rotational energy transfer) is, however, a formidable one, beyond the scope of the present work.

CONCLUSIONS

(1) The cross sections for the elastic scattering of CsCl beams by *nonpolar* molecules may be predicted with fair accuracy from the Massey-Mohr formula, using the Slater-Kirkwood approximation for the dispersion term and the Debye equation for the induction force.

(2) The influence of the dipole-dipole force upon the scattering is appreciable and may be directly observed. The scattering cross sections for the *dipolar* molecules are large and decrease significantly with increasing temperature.

(3) Owing to the large magnitude of the dipole-dipole interaction with the CsCl beams, the approximate theoretical treatment accounts only semiquantitatively for the experimental observations.

ACKNOWLEDGMENTS

Thanks are due to Fred A. Morse for his assistance with some of the measurements and calculations. The authors are grateful for financial support from the Alfred P. Sloan Foundation and the U. S. Atomic Energy Commission, Division of Research.

THE JOURNAL OF CHEMICAL PHYSICS VOLUME 33, NUMBER 2 AUGUST, 1960

Infrared Spectra of Alkyldiboranes. III. 1,2-Dimethyl- and 1,2-Diethyldiboranes

WALTER J. LEHMANN,* CHARLES O. WILSON, JR.,† AND I. SHAPIRO*

Research Laboratory, Olin Mathieson Chemical Corporation, Pasadena, California

(Received March 21, 1960)

The infrared spectra of three isotopic variants of 1,2-dimethyldiborane—$(CH_3B^{10}H_2)_2$, $(CH_3BH_2)_2$, $(CH_3BD_2)_2$—and of five 1,2-diethyldiboranes—$(C_2H_5B^{10}H_2)_2$, $(C_2H_5BH_2)_2$, $(C_2H_5BD_2)_2$, $(C_2D_5BH_2)_2$, $(C_2D_5BD_2)_2$—are reported and frequency assignments are made. 1,2-Dialkyldiboranes are very stable with respect to decomposition, but on prolonged standing rearrange to 1,1-dialkyldiboranes. Appearance of absorptions at ca 2100 and 1550 cm^{-1} is the first indication of the presence of 1,1-dialkyldiborane impurity. Although not conclusive, the evidence favors existence of predominantly cis configurations.

INTRODUCTION

In the monoalkyldiboranes[1,2] the vibrational character of diborane is partly preserved, in that one end of the molecule has retained both terminal hydrogens. This is not true in the 1,2-dialkyldiboranes, i.e., the sym-dialkyldiboranes, which have only a single terminal hydrogen at each end. In some respects one might expect simpler spectra for these molecules, in which both ends are alike, than for monoalkyldiboranes. However, it must be remembered that the corresponding vibrations of the two ends are not independent; they "couple," i.e., they interact with each other, producing "in-phase" and "out-of-phase" vibrations. This "splitting" may be quite considerable for some vibrations, but still, the average of the two frequencies should be relatively close to the value expected for the vibration of a single isolated unit.[3] Quite often the intensity of one member of a pair may be so weak as to escape detection or assignment as a fundamental vibration, but if we should fail to correlate properly such a split pair of frequencies, then the apparent shifts (up or down) from the single value may become quite puzzling.

The complexity of the problem is increased because the ratio of cis to trans isomers is not known in the 1,2-dialkyl compounds. Raman spectra, if available, would probably resolve the dilemma by virtue of the difference of selection rules. For cis compounds of this sort, e.g., *cis*-2-butene,[4] all vibrations are Raman active and all but one species (A_2) are infrared active, yielding a large number of "coincidences." However, in trans compounds (which have a center of symmetry) infrared and Raman activities are mutually exclusive,[3] allowing us to observe only one vibration of each pair.

EXPERIMENTAL

1,2-Dialkyldiborane can be prepared by direct interaction of trialkylborane with excess diborane, but the yield is so low that it is difficult to separate it from the much more abundant 1,1-dialkyldiborane. We found it more convenient to prepare 1,2-dialkyldiborane by the

* Present address: Hughes Tool Company—Aircraft Division, Culver City, California.

† Present address: National Engineering Science Company, Pasadena, California.

[1] W. J. Lehmann, C. O. Wilson, Jr., and I. Shapiro, J. Chem. Phys. **32**, 1088 (1960), first paper of this series.

[2] W. J. Lehmann, C. O. Wilson, Jr., and I. Shapiro, J. Chem. Phys. **32**, (1960), second paper of this series.

[3] G. Herzberg, *Infrared and Raman Spectra of Polyatomic Molecules* (D. Van Nostrand Company, Inc., Princeton, New Jersey, 1945).

[4] C. M. Richards and J. R. Nielsen, J. Opt. Soc. Am. **40**, 442 (1950).

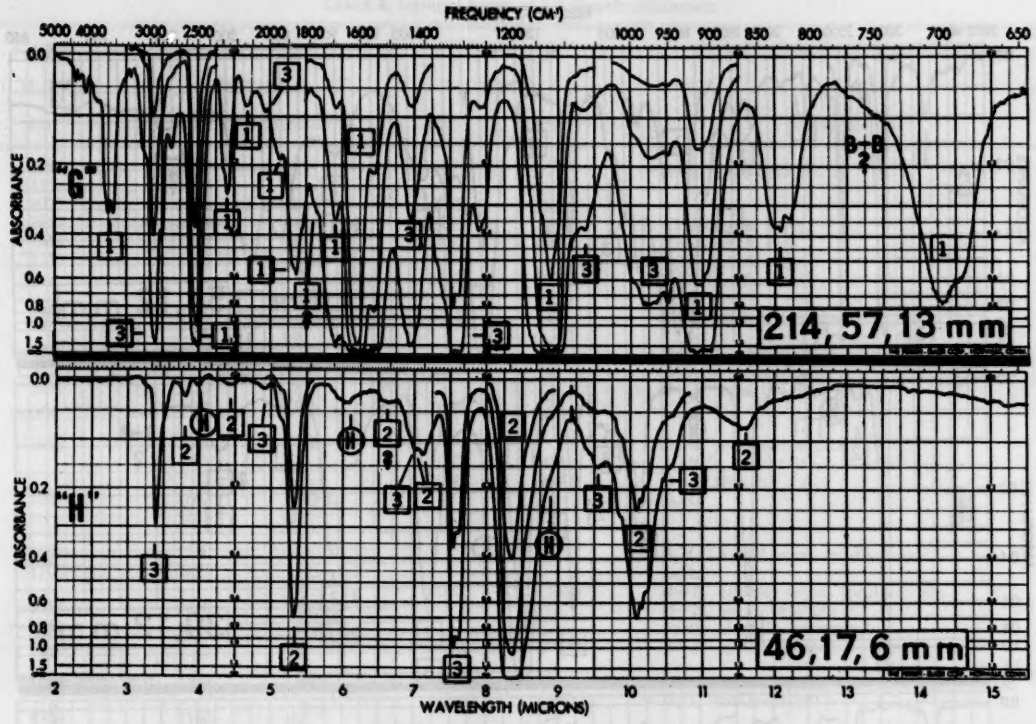

FIG. 1. Infrared spectra of 1,2-dimethyldiboranes; pressures reported for 5-cm cells. "G": $(CH_3BH_2)_2$; "H": $(CH_3BD_2)_2$. [1]:–B_2H_4 bands; [2]:–B_2D_4 bands; [3]:–CH_3 bands. (H): protium-impurity bands; B—B: stretching.

disproportionation of monoalkyldiborane[1,2] according to the reaction

$$2RB_2H_5 \rightleftarrows (RBH_2)_2 + B_2H_6.^5$$

1,2-Dimethyldiborane was purified by distillation through a −115°C bath and condensation in a −120°C bath, while the corresponding temperatures for 1,2-diethyldiborane were −72° and −80°C. Mass spectrometric analysis indicated negligible impurities. The vapor pressure of the ethyl compound was 36.4 mm at 0°C, in agreement with a previously reported value.[6]

Contrary to earlier reports,[7] our experience as well as that of other investigators[6] has shown that the 1,2-dialkyldiboranes decompose or disproportionate more slowly than any other alkyldiborane. Even after pure 1,2-dimethyldiborane had been stored at room temperature for several months we found very little infrared spectral evidence of disproportionation (formation of other methyldiboranes) and no evidence of decomposition (evolution of hydrogen accompanied by formation of polymeric solids). Very little disproportionation of 1,2-diethyldiborane was evident after two weeks storage at room temperature, but after several months most of the compound had rearranged to 1,1-diethyldiborane as well as small amounts of triethyldiborane and probably some monoethyldiborane. A similar result was obtained by heating a sample at 80°C for less than a half-hour. We surmise that the previously reported instability[7] was due to the catalytic effect of an impurity. The ultimate conversion of 1,2-dialkyldiborane to the 1,1- isomer and the fact that there is no evidence that this rearrangement is reversible indicate that the latter compound is more stable *thermodynamically*, even though the former can be stored for longer periods of time.

The infrared spectra were recorded on a Perkin-Elmer model 21 spectrophotometer equipped with sodium chloride optics. The spectra of $(CH_3BH_2)_2$ and $(CH_3BD_2)_2$ are reproduced in Fig. 1, and those of $(C_2H_5BH_2)_2$, $(C_2H_5BD_2)_2$, $(C_2D_5BH_2)_2$, and $(C_2D_5BD_2)_2$ are shown in Fig. 2. The spectrum of $(C_2H_5BH_2)_2$ agrees well with a previously published (weaker) spectrum.[6] Our measured frequencies, including those of $(CH_3B^{10}H_2)_2$ and $(C_2H_5B^{10}H_2)_2$, are listed in Tables I and II. For brevity, the designations "F", "G", and "H" will henceforth be used for the above methyl compounds, and "F_1" through "J_1" for the ethyl com-

[5] We use the form $(RBH_2)_2$ for the 1,2-dialkyldiboranes to distinguish them from the 1,1-dialkyldiboranes, $R_2B_2H_4$.

[6] I. J. Solomon, M. J. Klein, and K. Hattori, J. Am. Chem. Soc. **80**, 4520 (1958).

[7] H. I. Schlesinger, N. W. Flodin, and A. B. Burg, J. Am. Chem. Soc. **61**, 1078 (1939).

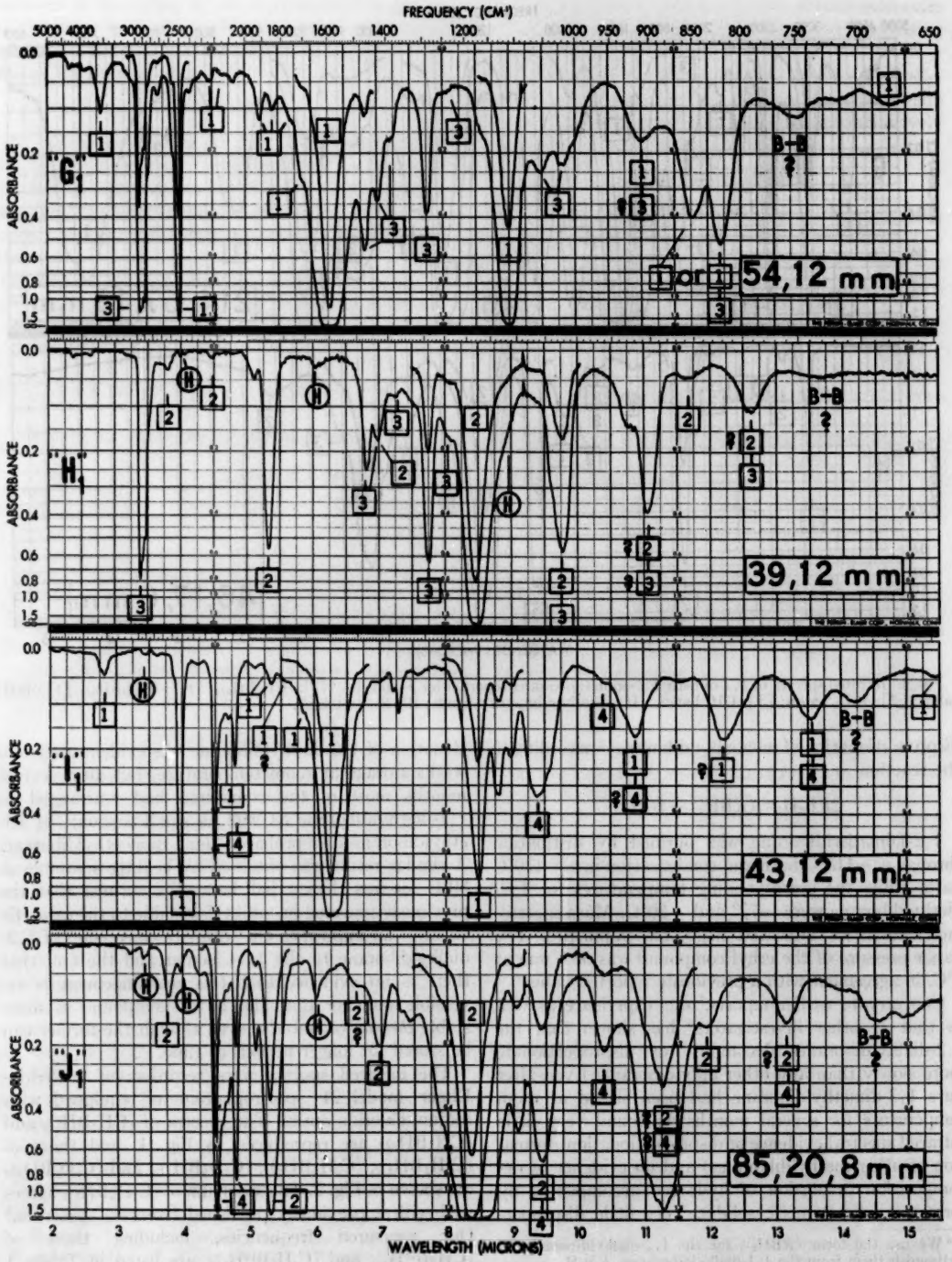

FIG. 2. Infrared spectra of 1,2-diethyldiboranes; pressures reported for 5-cm cells. "G_1": $(C_2H_5BH_2)_2$; "H_1": $(C_2H_5BD_2)_2$; "I_1": $(C_2D_5BH_2)_2$; "J_1": $(C_2D_5BD_2)_2$. [1]:—B_2H_4 bands; [2]:—B_2D_4 bands; [3]:—C_2H_5 bands; [4]:—C_2D_5 bands; (H) protium-impurity bands; B—B: stretching.

TABLE I. Infrared bands of 1,2-dimethyldiboranes.

"F" $(CH_3B^{10}H_2)_2$	"G" $(CH_3BH_2)_2$		"H" $(CH_3BD_2)_2$		
cm^{-1}	cm^{-1}	intensity[a]	cm^{-1}	intensity[a]	Assignment[b]
3636	3636	(31)			$-B_2H_4$ (combination)
3534	3546				
3077	3077	sh	3077	sh	
2958	2958	(140)	2958	(130)	CH_3 stretch. asym.
2841	2857	pip	2857	sh	CH_3 stretch. sym.
2755	2755	(15i)			$-B_2H_4$ (combination)
			2632	(12)	$-B_2D_4$ (combination)
2519	2519	(~450)	2512	(5)	B—H stretch. (protium imp. in "H")
	2299	sh			
2288	2268	(25)			$-B_2H_4$ (combination)
			2257	(4)	$-B_2D_4$ (combination)
2137	2137	(8)			B—H′ sym. in-phase
	2028	(9i)	2032	(7)	$-CH_3$
1955	1949	(18i)			B—H′ sym. out-of-phase
			1953	ssh	MeB_2D_5 and/or $Me_2B_2D_4$ imp.
			1880	(300)	B—D stretch.
1869	1862	(54) C?			$-B_2H_4$
	1835	sh			
1792	~1780	wsh			$-B_2H_4$ (B—H′ asym. out-of-phase?)
1706	1695	(125)			$-B_2H_4$
			1653	(15)b	B—H′ (single) asym. (protium imp.)
1615	1610	(2300)			B—H′ asym. in-phase
~1558	1555	(330i)			partly $Me_2B_2H_4$ impurity?
			1510	(15)b	B—D′ sym. in-phase?
1433	1437	(120)	1428	(52i)	CH_3 def. asym. and B—D′ sym. out-of-phase
			1404	(56i)	$-B_2D_4$ (combination)
1360	1360	sh			
1328	1328	(280)	1328	(~400)	CH_3 def. sym.
1316	1315	(250) B?	1316		
1269	1269	(35i)			
1258	1255	sh			
			1198	(1300)	B—D′ as. in-phase
(1160)	(~1163)	sh			BH in-plane bend.
1152	1143	A?			
(1138)	(1125)	(920)			
			1124	wvbsh	protium impurity
1129 A?	...	A?			
(1121)	(1115)	sh			
1081	1067	(35i)	1049	(66i)	CH_3 rock.
			1015	sh	
1010	998	sh	993–	(~300)	BD in-plane bend.
976	976	(75)	~985		CH_3 rock.
954	950	(71)	~952	sh	
924	~917–	(230)			BH bend. out-of-plane
915	~904				
			~865	(35)	$-B_2D_4$ (BD out-of-plane bend.?)
829	828	(36) A			$-B_2H_4$
758	746	bsh			B—B stretch.?
~690	~690	(72) A?			$-B_2H_4$

[a] Approximate intensities expressed as absorbance×10^4 divided by cell length in cm and sample pressure in mm. Abbreviations: w: weak, s: strong, sh: shoulder b: broad, v: very; i: apparent intensity increased by overlap with other band(s); A, B, C: apparent band types.
[b] B—H′ and B—D′ refer to bridge stretchings.

pounds (see headings of Tables I and II), continuing the scheme introduced for the monoalkydiboranes.[1,2]

Incidentally, the most sensitive areas for detection of 1,1-dimethyldiborane impurity in "G" are at 2100 and 1550 cm^{-1} (appearance of a shoulder), revealing the presence of a minimum of ca 2% of the 1,1- isomer, while the 2570-cm^{-1} region is not good for spotting less than ca 10% of this impurity. The corresponding sensitive frequencies for the ethyl compounds are 2080 and 1540 cm^{-1}.

ASSIGNMENTS

Simple comparison of the spectra enables us in many instances to assign bands to the molecular groups.

TABLE II. Infrared bands of 1,2-diethyldiboranes.

"F_1"	"G_1"		"H_1"		"I_1"		"J_1"		
$(C_2H_5B^{10}H_2)_2$	$(C_2H_5BH_2)_2$		$(C_2H_5BD_2)_2$		$(C_2D_5BH_2)_2$		$(C_2D_5BD_2)_2$		
cm^{-1}	cm^{-1}	intensity[a]	cm^{-1}	intensity[a]	cm^{-1}	intensity[a]	cm^{-1}	intensity[a]	Assignment[b]
3571	3546	(40)			3534	(20)			$-B_2H_4$ (combination)
							3106	(3)	
3077	3077	sh							
2950	2950	(600)	2958	(400)					CH_3 stretch. asym.
2915	2915	sh	2924	sh	2915	(5)b	2924	(6)	CH_2 stretch. asym.; protium imp. in "I_1" and "J_1"
2882	2882	sh	2882	sh			2882	sh	CH_3 stretch. sym.
2841	2841	wsh	2841	sh					CH_2 stretch. sym.
2730	2725	(27i)			2755	(5)b			$-B_2H_4$ (combination)
			2646	(15)			2646	(22)	$-B_2D_4$ (combination)
2577	2577	sh			2584	sh			$Et_2B_2H_4$ impurity
2512	2506	(670)	2506	(5)	2512	(400)	2519	(11)	B—H stretch; protium imp. in "H_1" and "J_1"
2421	2398	(26i)							
2342	2342	sh							
					2353	(10)b	2353	(12i)b	$-C_2D_5$
2257	2247	(18)							$-B_2H_4$ (combination)
			2247	(7)					$-B_2D_4$ (combination)
					2227	(300)	2227	(520)	CD_3 stretch. asym.
					2174	sh	2179	sh	CD_2 stretch. asym.
							2151	sh	
wb?	2137	w			2128	(60i)			B—H' sym. in-phase ("breathing")
					2083	(110)	2088	(200)	CD_3 and CD_2 stretch. sym. part. $Et_2B_2H_4$ imp.
~2105	2075	w							
			1961	(50i)			1961	(50i)	$Et_2B_2D_4$ imp.
					1953	(14)			
1927	1916	(46)			~1905	sh			B—H' sym. out-of-phase
			1876	(290)			1883	(360)	B—D stretch.
1852	1845	(20)			1869	(28)			$-B_2H_4$
1764	1760	wsh			1786	bsh			$-B_2H_4$ (B—H' asym. out-of-phase?)
1709	1706	sh			1709	sh			$-B_2H_4$
			1658	(15)			1661	(22)	B—H' (single) asym. (protium imp.)
1595	1595	(2000)			1600	(1350)			B—H' asym. in-phase
							1508	(16)b	B—D' sym. in-phase?
					1492	bsh			
1466	1466	(210i)	1468	(130)					CH_3 asym. and CH_2 def.
1426	1426	(125i)	1433	(95i)			1435	(47)	B—D' sym. out-of-phase
					1428	wb			
~1389	~1391	sh	1377	(65)					CH_3 def. sym.
					1389	(33i)			
					1374	(55)	1370	sh	
							1351	(33)	part. $(C_2D_5)_2B_2D_4$ imp.
			1333	bsh	1321	(20)			impurity?
1292	1289	(145)	1289	(330)					CH_2 wag. and/or twist.
1242	1242	bsh	1242	bsh			1266	sh	
			1183	(1400) A?			1198	(1600)	B—D' asym. in-phase
					1178	(380)			BH def. in-plane ("I_1")
	1175	sh							sl. B_2H_6 imp.
1168	1163	sh							sl. $Et_2B_2H_4$ imp.
					1136	(150)			also BH def. in-plane?
1122	1112	(750)							BH def. in-plane ("F_1" and "G_1")
					1111	(100i)	1102	(120i)	
					1066	(160)	1059	(160)	CD_3 asym. and CD_2 def. and BD def. in-plane
1060	1055	(93)							CH_3 rock.
1024	1020	(85)							
			1024	(300) A?					BD def. in-plane and/or B—C stretch.
					1047	sh			

TABLE II.—*Continued.*

"F_1"	"G_1"		"H_1"		"I_1"		"J_1"		
$(C_2H_5B^{10}H_2)_2$	$(C_2H_5BH_2)_2$		$(C_2H_5BD_2)_2$		$(C_2D_5BH_2)_2$		$(C_2D_5BD_2)_2$		
cm^{-1}	cm^{-1}	intensity[a]	cm^{-1}	intensity[a]	cm^{-1}	intensity[a]	cm^{-1}	intensity[a]	Assignment[b]
					962	sh	963	(50)	CD_2 rock.
			926	bsh					$Et_2B_2D_4$ imp.
							909	sh	
915	910	(63)			920	(80)			BH out-of plane bend.
			905	(200)			887	(320)	$-B_2D_4$? C—C stretch?
					866	wb			
			858	(25)b			838	(35i)	$-B_2D_4$ (BD out-of-plane bend?)
858	849	(150i)			818	(80)			$-B_2H_4$?
826	820	(195i)	794	(56)					CH_2 rock. ($-B_2H_4$ in "F_1", "G_1"?)
					738	(60)	760	(33)	CD_2 rock.
765	750	(45)	734	wb					B—B stretch?
							714	w	$(C_2D_5)_2B_2D_4$ imp.
					702	(40)	690	(33)	B—B stretch.?
725	717	w							
678	678	(35)			~640	...[c]			$-B_2H_4$
							667	(32)	

[a] Approximate intensities expressed as absorbance×10^3 divided by cell length in cm and sample pressure in mm. Abbreviations: w: weak, s: strong, sh: shoulder, b: broad, v: very; i: apparent intensity increased by overlap with other band(s); A, B, C: apparent band types.

[b] B—H′ and B—D′ refer to bridge stretchings.

[c] Beyond limit of chart.

However, particularly for these 1,2- compounds, many correlations are not immediately apparent and depend on a more detailed analysis. The final group assignments to $-B_2H_4$, $-B_2D_4$, $-CH_3$ or $-C_2H_5$, and $-C_2D_5$ are indicated by [1] to [4] in Figs. 1 and 2.

In general, the detailed assignments follow readily from comparison with the corresponding monoalkyldiboranes.[1,2] As expected, there are the fairly strong C—H (and C—D) stretching absorptions near 3000 (and 2100–2200) cm^{-1} and the very strong B—H′ (and B—D′) bridge stretching bands at 1600 (and 1200) cm^{-1}.

The 1,2-dialkyldiboranes can readily be distinguished[8] from the 1,1-dialkyldiboranes by their single strong B—H (and B—D) terminal stretching absorption at about 2510 (and 1880) cm^{-1}. For trans structures only the B—H (terminal) out-of-phase vibration is infrared active, but for cis compounds both the in-phase and out-of-phase vibrations are infrared active. Thus the shoulders at ca 2580 (and 1960) cm^{-1} might be assigned to the second B—H (and B—D) vibration. However, such large splitting of frequencies, ca 70–85 cm^{-1}, would indicate considerable coupling between the two ends of the molecule. We know that this situation does not exist, because deuterium substitution on only one end of the molecule does not appreciably affect the B—H vibration of the other end (see H, H_1, J_1). Similar lack of coupling has been observed in ethylenes.[9] As a consequence we conclude that the 2580- and 1960-cm^{-1} shoulders do *not* represent a second B—H or B—D vibration of 1,2-dialkyldiboranes, but rather are due to impurities, probably 1,1-dialkyldiborane.

The BH in-plane bending vibrations are located at ca 1110–1150 cm^{-1}. Their great intensity clearly links them with the stronger of the two bands in the same region in monoethyldiborane.[2] In the latter compound, the two bands in the 1150-cm^{-1} region were thought to belong to the BH and the BH_2 bendings, but there had been a tendency to assign the more intense member of that pair to the BH_2 deformation, in view of the great intensity of the BH_2 relative to HBD deformation in B_2H_5D.[10] It should be remembered, however, that in B_2H_5D the strong *A*-type 1178-cm^{-1} vibration actually represents BH_2 deformations in the *two* compounds present in the mixture—terminally and bridge-deuterated B_2H_5D. As in the monoalkyldiboranes, the BH frequency shifts *upward*, for some odd reason, in the carbon-deuterated compound ("I_1"). Other bands or shoulders in that region could possibly represent another of the BH bendings (if the compound is cis or if cis compound is present).

A small B^{10} shift of ca 10 cm^{-1} indicates that the boron atoms participate to some extent in the BH bending motion. Therefore, in considering the corresponding BD motion, the BH/BD frequency ratio should be less

[8] I. Shapiro, C. O. Wilson, Jr., and W. J. Lehmann, J. Chem. Phys. 29, 237 (1958).

[9] E. G. Hoffmann, Ann. Chem. Liebigs 618, 276 (1958).

than the "normal" 1.35 value.[8,10–12] Both the 1024- and 905-cm^{-1} absorptions in "H_1" would qualify (ratios of 1.09 and 1.23). It is conceivable that these bands represent the two BD bending vibrations. However, examination of "H" (where the only logical candidate is at 990 cm^{-1}) and comparison with monomethyl- and monoethyldiboranes (where ca 1050 cm^{-1} has been assigned to this vibration) persuades us to the former assignment only. In the completely deuterated compound, "J_1", this band seems to be hidden under a CD_3 vibration at 1059 cm^{-1}, although the intensity of that band does seem rather weak (as in $CD_3B_2D_5$ and $C_2D_5B_2D_5$).

The CH_3 asymmetric- and symmetric-deformation bands of the methyldiboranes are found as expected in the 1430- and 1325-cm^{-1} regions. It is not clear whether the latter bands appear as doublets, due to the two methyl groups, or whether we are observing poorly resolved rotational envelopes. The ethyl compounds have their CH_3 asymmetric and CH_2 deformations at ca 1470 (medium) and 1430 cm^{-1} (weak), and the symmetric CH_3 deformations at ca 1380 cm^{-1} (weak). The corresponding CD_3 asymmetric and CD_2 deformations in "I_1" and "J_1" are shifted to 1060 cm^{-1} (frequency ratio of ca 1.37). As for monoethyldiborane, we are unable to find an assignment in "I_1" and "J_1" for the CD_3 symmetric deformations.

The 1290 cm^{-1} bands with the 1240 cm^{-1} shoulders in the $-C_2H_5$ compounds represent CH_2 wagging and twisting modes. In monoethyldiboranes this frequency is less stable, varying from 1310 cm^{-1} in $C_2H_5B_2{}^{10}H_5$ to 1285 cm^{-1} in $C_2H_5B_2D_5$. In both boron-deuterated compounds this absorption is enhanced to more than double the intensity in the corresponding isotopically normal compounds. In the 1,2-diethyldiboranes, as for the monoethyldiboranes, no good assignment is found for the corresponding CD_2 vibrations.

Assignment of bands in the 900–920-cm^{-1} region to BH out-of-plane bending follows directly from comparison with the monoalkyldiboranes.

In monoethyldiboranes, CH_2 rocking was assigned to 826 ($C_2H_5B_2{}^{10}H_5$), 816 ($C_2H_5B_2H_5$), and 800 cm^{-1} ($C_2H_5B_2D_5$); CD_2 rocking, to 742 ($C_2D_5B_2H_5$) and 760 cm^{-1} ($C_2D_5B_2D_5$). The corresponding assignments in the 1,2-diethyldiboranes are thus reasonable: 826, 820, and 794 cm^{-1} to CH_2 rocking in "F_1", "G_1", and "H_1"; 738 and 760 cm^{-1} to CD_2 rocking in "I_1" and "J_1".

Although a number of fairly strong bands remain unassigned in the various spectra, their classification into groups [1] to [4] is not readily evident (see Figs. 1 and 2). This means that these bands are not really *characteristic* bands in the narrow sense of the word, but they nevertheless can be correlated with certain molecular vibrations. To arrive at assignments, extensive comparison is made with the monoalkyldiboranes[1,2] and other alkyldiboranes[13] as well as trialkylboranes.[14–16]

In the monomethyldiboranes CH_3-rocking motions have been assigned to the 950–975-cm^{-1} region. Similar bands are available for this assignment in compounds "F", "G", and "H". The $-CH_3$ bands in the 1050–1080-cm^{-1} region of "F", "G", and "H" have no analog in the monomethyldiboranes, but they appear in other alkyldiboranes[13] with increasing intensity. Hence, assignment to CH_3 rocking is reasonable.

In spectrum "G" there is a prominent *A*-type band at 828 cm^{-1}, having no obvious analog in "H". It possibly is a $-B_2H_4$ band of some sort and thus is related to either the 820- and 818- or the 849- and 818-cm^{-1} bands in "G_1" and "I_1", but the small B^{10}-isotope shift in "F" of only 1 cm^{-1} is puzzling. A similar situation exists for the 640–690-cm^{-1} bands.

The weak bands at about 750 cm^{-1} of the "G" and "G_1" could, in view of their relatively large B^{10}-isotope shifts of ca 15 cm^{-1}, represent B—B stretching across the double-hydrogen bridge. This frequency drops to 734 cm^{-1} in "H_1" and to 702 and 690 cm^{-1} in "I_1" and "J_1". No appropriate band is observed in "H". In $B_2{}^{10}H_6$, $B_2{}^{11}H_6$, $B_2{}^{10}D_6$, and $B_2{}^{11}D_6$ this frequency is[17] 816, 788, 721, and 712 cm^{-1}, respectively.

Weak absorptions in the 838–865 cm^{-1} region of the BD compounds are caused by some sort of $-B_2D_4$ motion, possibly BD out-of-plane bendings (BH/BD frequency ratios of 1.05 to 1.10).

The intense bands at 905 cm^{-1} in "H_1" and 887 cm^{-1} in "J_1" possibly are $-B_2D_4$ bands even though no counterpart is seen in "H". (It must be remembered that replacement of methyl groups by ethyls may alter the symmetry and thus affect the selection rules.) Possibly bands in the 887–920-cm^{-1} region of all the 1,2-diethyldiboranes could (additionally?) represent C—C stretching modes, assigned tentatively to 850–943 cm^{-1} in monoethyldiboranes.

CH_3- and CD_3-rocking modes follow almost exactly the pattern of the monoethyldiboranes. In "G_1" these are assigned to 1020 and 1055 cm^{-1} (ca 1015 and 1065 cm^{-1} in $C_2H_5B_2H_5$; B^{10}-isotope shift of ca 5 cm^{-1} in all cases). In "H_1", as in $C_2H_5B_2D_5$, these bands are masked by the more intense BD-bending absorption. In "I_1" and "J_1" we assign ca 963 cm^{-1} to CD_3 rocking (ca 945 cm^{-1} in $C_2D_5B_2H_5$ and $C_2D_5B_2D_5$).

---

[10] W. J. Lehmann, J. F. Ditter, and I. Shapiro, J. Chem. Phys. **29**, 1248 (1958).
[11] W. J. Lehmann, H. G. Weiss, and I. Shapiro, J. Chem. Phys. **30**, 1226 (1959).
[12] F. Halverson, Revs. Modern Phys. **19**, 87 (1947).
[13] W. J. Lehmann, C. O. Wilson, Jr., and I. Shapiro, J. Chem. Phys. (to be published as subsequent papers of this series).
[14] W. J. Lehmann, C. O. Wilson, Jr., and I. Shapiro, J. Chem. Phys. **28**, 777 (1958).
[15] W. J. Lehmann, C. O. Wilson, Jr., and I. Shapiro, J. Chem. Phys. **28**, 781 (1958).
[16] W. J. Lehmann, C. O. Wilson, Jr., and I. Shapiro, J. Chem. Phys. **31**, 1071 (1959).
[17] R. C. Taylor and A. R. Emery, Spectrochim. Acta **10**, 423 (1958).

As for the previous alkyldiboranes, no assignment is proposed for the B—C-stretching modes.

In each spectrum there remain some higher-frequency bands, most of which can readily be assigned to groups (see Figs. 1 and 2). They represent either combinations or overtones or additional bridge-stretching modes. The B—H′ (bridge) symmetric in-phase "breathing" vibration may be assignable to the 2128–2137 cm^{-1} bands. In that case, bands in "H" and "J_1" at ca 1510 may represent the corresponding B—D′ vibration; no such band is found in "H_1." The B—H′ symmetric out-of-phase vibrations are assigned to the 1905–1955-cm^{-1} region. The equivalent B—D′ bands are at 1428–1435 cm^{-1}, superimposed on CH deformations in "H" and "H_1". Very weak shoulders in the 1760–1792-cm^{-1} region may conceivably be identified with the B—H′ asymmetric out-of-phase vibration, although this vibration should be infrared inactive, at least in the methyl compounds. The related B—D′ vibration would be masked by the other bands. The very strong B—H′ and B—D′ asymmetric in-phase vibration has been discussed previously. A small amount of protium in the boron-deuterated compounds is responsible for the B—H′ (single) vibration of the B(HD)B bridges, at ca 1650 cm^{-1}.

MOLECULAR SYMMETRY

With the completed frequency assignment we can now examine whether our compounds are of the cis or the trans type. It might be argued that the relatively small number of infrared absorption bands is an indication that we are dealing with *trans*-1,2-dialkyldiboranes (in which only half the vibrations are infrared active), but we nevertheless feel more disposed to view the compounds as being predominantly of the cis type. A cursory comparison of a number of trans- and cis-disubstituted ethylenes[3,18–20] reveals that both members of a pair have approximately the same number of infrared bands. The small number of bands does, however, indicate that our compounds are composed predominantly of one isomer and not of a mixture of both.

We base our contention in favor of cis structures on the following arguments. In going from BH_2 deformation (scissors motion) in B_2H_6 to BH bending in our 1,2-dialkyldiboranes, the infrared band shifts from 1177 to ca 1112–1140 cm^{-1}. This relatively small shift parallels a similar shift from CH_2 deformation in C_2H_4 (1444 cm^{-1}) to CH bending in various cis-dialkylated ethylenes[21] (ca 1408 cm^{-1}), in contrast to trans-dialkylated ethylenes (ca 1300 cm^{-1}). Further support for cis structures is found in our somewhat hesitant assignments of B—H′ and B—H′ symmetric in-phase frequencies. These vibrational modes would definitely be infrared inactive in *trans*-di*methyl*diborane, and either active or inactive in *trans*-di*ethyl*diborane depending on the orientation of the ethyl groups.

If B—B (i.e., BH_2B) stretching bands are observed in the infrared spectrum—and we tentatively have assigned some bands to this vibration—this would be conclusive proof of the existence of cis isomers, at least for the methyl compounds.

In conclusion, it should be pointed out that the problem of molecular configuration, as well as a number of uncertainties in our assignments, will most likely be resolved when Raman spectra of these substances become available.

[18] J. Charette and M. de Hemptinne, Bull. classe sci., Acad. roy. Belg. 37, 436 (1951).

[19] N. Sheppard and G. B. B. M. Sutherland, Proc. Roy. Soc. (London) A196, 195 (1949).

[20] *Catalog of Infrared Spectral Data* (Carnegie Institute of Technology, Pittsburgh, Pennsylvania), Am. Petrol. Inst. Research Project 44.

[21] N. Sheppard and D. M. Simpson, Quart. Revs. (London) 6, 1 (1952).

Microwave Spectrum, Structure, and Dipole Moment of Formyl Fluoride*

OLIVER H. LEBLANC, JR.,† VICTOR W. LAURIE,‡ AND WILLIAM D. GWINN

Department of Chemistry, University of California, Berkeley, California

(Received March 22, 1960)

The microwave spectra of several isotopic species of formyl fluoride have been investigated in the region 11–46 kMc. Both parallel and perpendicular transitions have been assigned. The effective rotational constants for $HC^{12}OF$ are (Mc) $a=91153.6$, $b=11760.0$, $c=10396.8$; for $HC^{13}OF$, $a=88475.3$, $b=11755.2$, $c=10357.3$; for $DC^{12}OF$, $a=65090.1$, $b=11761.7$, $c=9941.7$. From these constants the structural parameters are calculated to be $r_{CF}=1.34_1$ A, $r_{CO}=1.18_3$ A, $r_{CH}=1.10_0$ A, $\angle FCO=122.7°$, $\angle HCF\approx 108°$, $\angle HCO\approx 129°$. Measurements of the Stark effect lead to a value of 2.02 ± 0.02 debyes for the dipole moment.

INTRODUCTION

THE formyl halides are the simplest members of the family of acyl halides, $RCOX$. The only one of the formyl halides which is relatively stable, however, is the fluoride, HCOF. This compound can be kept for long periods of time when stored at temperatures of the order of $-70°C$ but decomposes rapidly into HF and CO at room temperature.

Formyl fluoride is interesting both because of its relative instability and for its relationship to fundamental molecules such as formaldehyde and formic acid. A knowledge of its structure and dipole moment should provide some insight into the chemical bonding of elementary systems.

Infrared spectra have been reported by Morgan, Staats, and Goldstein,[1] and by Stratton and Nielsen.[2] An electron diffraction study by Jones, Hedberg, and Schomaker[3] has determined values for the heavy-atom structural parameters. The microwave study was undertaken to attempt a more accurate determination of the complete structure and to measure the dipole moment and its orientation in the molecule. Subsequently, Favero, Mirri, and Baker[4] reported a millimeter wave study of $HC^{12}OF$, but had insufficient data for an unambiguous structural determination and reported no quantitative dipole-moment data.

EXPERIMENTAL

Spectra were taken with the spectrographs both at Berkeley and at Harvard University. Detailed descriptions of these instruments have been given previously.[5,6]

Samples of HCOF and DCOF were prepared by a procedure similar to that described by Morgan *et al.*,[1] and were stored at dry-ice temperature. Infrared spectra of these samples were taken on a Perkin-Elmer model-21 spectrograph and were identical with those previously[1] reported. The microwave spectrum of $HC^{13}OF$ was observed with the species which was present in the HCOF sample in its natural abundance of 1%.

ASSIGNMENT OF SPECTRA

The spectra of formyl fluoride were observed in the region 11–46 kMc and are characteristic of a near-prolate rotor with both parallel and perpendicular transitions. Lines were generally quite intense and fairly narrow line widths could be attained. Assignments were made from the readily identifiable Stark patterns.

The observed frequencies of assigned lines are given in Table I together with the frequencies calculated from the constants listed in Table II. A certain amount of centrifugal distortion is apparent, but the rotational constants calculated from the observed lines of low J should be sufficiently accurate for the purposes of this work. The rotational constants of $HC^{12}OF$ are in reasonable agreement with those recently reported by Favero *et al.*,[4] from their high-frequency microwave study. No previous study of $DC^{12}OF$ or $HC^{13}OF$ has been reported.

STRUCTURE

The effective moments of inertia given in Table II are available for a determination of the structural parameters. Planarity for the equilibrium configuration is shown by the small positive value of $I_c^0-I_b^0-I_a^0$. For a completely rigid molecule this quantity vanishes for the planar case and is negative otherwise. The observed positive value arises from zero-point vibrations and is similar to values found for other planar molecules. Thus, there are two independent moments of inertia from each isotopic species or six independent

* This research was supported in part by a grant from the Sloan Foundation to the University of California, and by a grant extended Harvard University by the Office of Naval Research.

† National Science Foundation Predoctoral Fellow, 1955–1956. Present Address: General Electric Research Laboratory, Schenectady, New York.

‡ Work done in part at Harvard University while a National Science Foundation Predoctoral Fellow, 1955–1956.

[1] H. W. Morgan, P. A. Staats, and J. H. Goldstein, J. Chem. Phys. **25**, 337 (1956).

[2] R. F. Stratton and A. H. Nielsen, Bull. Am. Phys. Soc. Ser. II, **4**, 389 (1959).

[3] M. E. Jones, K. Hedberg, and V. Schomaker, J. Am. Chem. Soc. **77**, 5278 (1955).

[4] P. Favero, A. M. Mirri, and J. G. Baker, J. Chem. Phys. **31**, 566 (1959).

[5] G. L. Cunningham, Jr., A. W. Boyd, R. J. Myers, W. D. Gwinn, and W. I. LeVan, J. Chem. Phys. **19**, 676 (1951).

[6] K. B. McAfee, R. H. Hughes, and E. B. Wilson, Jr., Rev. Sci. Instr. **20**, 821 (1949).

data for the determination of the five structural parameters.

If the molecular plane is taken as the xz plane and the a principal axis as the z axis, $I_a=\Sigma m_i x_i^2$ and $I_b=\Sigma m_i z_i^2$. Here m_i is the mass of the ith atom, and x_i and z_i refer to the coordinates of that atom in the principal-axis system. Substitution for C^{12} by C^{13} and H by D should enable calculation of the coordinates of those atoms in the principal-axis system of $HC^{12}OF$.

TABLE I. Assigned transitions of formyl fluoride (Mc).

Transition	Obs freq[a]	Calc freq
$HC^{13}OF$		
$3_{03}\rightarrow 2_{12}$	11647.9	11647.1
$3_{13}\rightarrow 4_{04}$	12388.8	12391.9
$0_{00}\rightarrow 1_{01}$	22156.8	22156.8
$6_{16}\rightarrow 6_{15}$	28613.9	28614.7
$2_{02}\rightarrow 1_{11}$	35097.5	35097.4
$4_{14}\rightarrow 5_{05}$	36956.0	36962.1
$8_{17}\rightarrow 7_{26}$	39044.3	39038.5
$1_{11}\rightarrow 2_{12}$	42950.7	42950.4
$1_{01}\rightarrow 2_{02}$	44296.0	44296.1
$1_{10}\rightarrow 2_{11}$	45676.8	45676.8
$HC^{13}OF$		
$0_{00}\rightarrow 1_{01}$	22112.5	22112.5
$2_{02}\rightarrow 1_{11}$	32514.1	32514.1
$1_{11}\rightarrow 2_{12}$	44827.2	44827.2
$1_{10}\rightarrow 2_{11}$	45623.0	45622.9
$DC^{12}OF$		
$4_{14}\rightarrow 4_{13}$	18193.7	18196.1
$3_{13}\rightarrow 4_{04}$	37370.8	37370.8
$5_{14}\rightarrow 4_{23}$	40852.1	40842.9
$1_{11}\rightarrow 2_{12}$	41586.8	41586.8
$1_{01}\rightarrow 2_{02}$	43361.9	43361.7
$1_{10}\rightarrow 2_{11}$	45226.9	45226.9

[a] Accuracy is estimated to be ±0.1 Mc.

Then with the use of the C and H coordinates and the relations $I_a=\Sigma m_i x_i^2$, $I_b=\Sigma m_i z_i^2$, $\Sigma m_i x_i=0$, $\Sigma m_i z_i=0$, $\Sigma m_i x_i z_i=0$, the coordinates of the O and F atoms can be found. Coordinates calculated by this procedure are given in Table III under the heading "I" and the corresponding structure is given in Table IV. Unfortunately, the H and C atoms are close to the b principal axis and the moments of inertia are not very sensitive to their z coordinates. This is particularly noticeable for the H atom where zero-point effects make b_0 larger

TABLE II. Rotational constants (Mc) and moments of inertia[a] (amu A²) of formyl fluoride.

	$HC^{12}OF$	$HC^{13}OF$	DCOF
a	91153.6	88475.3	65090.1
b	11760.0	11755.2	11761.7
c	10396.8	10357.3	9941.7
I_a	5.5459	5.7138	7.7666
I_b	42.9875	43.0049	42.9810
I_c	48.6237	48.8091	50.8496
$I_c-I_b-I_a$	0.0903	0.0904	0.1020

[a] Conversion factor 5.05531×10^5 Mc amu A².

for DCOF than for HCOF, an impossible result for a rigid molecule. Thus it is clear that the z coordinate of the H atom is very small, but no precise determination can be made. By contrast with the z coordinate, the x coordinate of H is very well determined since there is a difference of 26 000 Mc between the a rotational constants of $HC^{12}OF$ and $DC^{12}OF$. Also, the x coordinate of C is reasonably well established by the $HC^{13}OF$ data. However, chiefly because of the uncertainty caused by vibration-rotation effects on the apparent z coordinate of the C atom, a structure calculated from the coordinates "I" of Table III is not as precise as might be desired. The electron diffraction study by Jones, Hedberg, and Schomaker[3] has measured the ratio of the CF distance to the CO distance rather accurately and reports $r_{CF}/r_{CO}=1.134\pm0.005$. If this relation is combined with the spectroscopic data, the coordinates listed under "II" in Table III are obtained. The corresponding structural parameters are given in Table IV. It is thought that the structure determined in this way is probably the best obtainable, since it fits the restraints of the most accurately determined parameters of both spectroscopic and electron-diffraction data. The apparently large differences between structures "I" and "II" are due in large measure to the difference of 0.015 A in the z coordinate for C. How-

TABLE III. Coordinates of atoms in principal-axis system of $HC^{12}OF$ (A).

	I	II
x_C	−0.413	−0.413
x_F	0.162	0.159
x_O	0.212	0.215
x_H	−1.502	−1.502
z_C	−0.134	−0.149
z_F	1.060	1.064
z_O	−1.158	−1.152
z_H	~0	~0

TABLE IV. Structures of formyl and acetyl fluoride.

	I	II	III[a]	IV[b]
r_{CF}(A)	1.325	1.341	1.351±0.013	1.348
r_{CO}(A)	1.200	1.183	1.192±0.011	1.181
r_{CH}(A)	1.098	1.100	...	...
∢ FCO	122.8°	122.7°	121.9±0.9°	121.3°
∢ HCF	~109°	~108°	...	110.4° (CCF)
∢ HCO	~128°	~129°	...	128.3° (CCO)

[a] Electron diffraction values for HCOF. See footnote reference 3.
[b] Microwave values for CH_3COF. See footnote reference 11.

ever, this amounts to a change of only 0.005 amu A² in the difference of the b effective moments of inertia, which is well within zero-point effects. Further, structure "I" gives a ratio for $r_{CF}/r_{CO}=1.104$ which is incompatible with the electron-diffraction data. Structure "II", on the other hand, is consistent within the estimated uncertainties with both the electron diffraction and the spectroscopic data. It is difficult to give precise values for the uncertainty in structure "II" but an estimate of ±0.01 A for bond distances and ±30′ for ∢ FCO seems reasonable. There is an uncertainty of 2–3 deg in the angles involving H, but the bond distance CH is fairly well established at 1.10 A, since the bond length does not depend very much on z_H.

The value of 1.18₃ A found for the C═O distance is considerably shorter than the values of 1.21 reported[7] for H_2CO and 1.20 for HCOOH.[8] The distance of 1.34₁ A for r_{CF} is also a sizable decrease from the value 1.385 A which is found[9] in CH_3F. It may be noted that the C═O stretching frequency[1] of 1834 cm⁻¹ for HCOF is higher than the frequencies of 1744 and 1740 cm⁻¹ found[10] for H_2CO and HCOOH.

Much the same situation has been found[11,12] for the homologous acetyl compounds. The corresponding structural parameters of CH_3COF, determined by Pierce and Krisher from microwave data, are very similar to those of HCOF, as is shown in Table IV.

TABLE V. Stark-effect coefficients for $HC^{13}OF$.

Transition	M	$\Delta\nu/E^2$(Mc/sec)/(statvolt²/cm²)
$0_{00}\rightarrow 1_{01}$	0	$3.60\pm0.03\times10^{-6}$
$1_{10}\rightarrow 2_{11}$	1	$-1.67\pm0.01\times10^{-6}$
$2_{02}\rightarrow 1_{11}$	0	$6.65\pm0.01\times10^{-6}$
$3_{03}\rightarrow 2_{12}$	0	$1.69\pm0.02\times10^{-6}$

DIPOLE MOMENT

Formyl fluoride has a component of dipole moment along both the a and the b axes. The Stark effect of the $0_{00}\rightarrow 1_{01}$, $1_{10}\rightarrow 2_{11}$, $2_{02}\rightarrow 1_{11}$, and $2_{12}\rightarrow 3_{03}$ transitions were used to determine the values of $|\mu_a| = 0.595\pm0.006$ debye and $|\mu_b| = 1.93_4\pm0.02$ debye; the resultant total dipole moment is 2.02±0.02 debye. The Stark effect was determined using a dc bias which was measured with a potentiometer. The electrode spacing of the absorption cell was calculated from the observed[13] Stark effect of OCS. Observed Stark coefficients are shown in Table V.

Since only the absolute values of the dipole-moment components can be determined, assumptions about the signs must be made before the orientation of the total dipole moment in the molecule can be inferred. If it is assumed that the O and F are negative relative to the C, the total dipole moment makes an angle of 41.0° with the C═O bond and 81.7° with the CF bond. It is interesting to note that the corresponding angles in CH_3COF are 42.1° and 79.2° although the total moment is 2.96 debyes.[11]

Favero *et al.*[4] have reported an anomalous doubling of the Stark effect for some high-frequency lines of $HC^{13}OF$. We have observed no anomalies.

ACKNOWLEDGMENTS

One of us (V.W.L.) would like to thank Dr. G. R. Wilkinson of King's College, London, for discussions and for allowing him to see preliminary high-resolution infrared values for some of the rotational constants of formyl fluoride during the summer of 1956. He would also like to thank Professor E. B. Wilson, Jr., in whose laboratories part of this work was carried out.

We are indebted to Professor Kenneth Hedberg for communications on the accuracy of the electron-diffraction work.

It is also a pleasure to acknowledge helpful discussions with Professor Rollie J. Myers.

[7] R. B. Lawrence and M. W. P. Strandberg, Phys. Rev. **83**, 363 (1951).
[8] G. Kwei and R. F. Curl, Jr., J. Chem. Phys. **32**, 1592 (1960).
[9] O. R. Gilliam, H. D. Edwards, and W. Gordy, Phys. Rev. **83**, 363 (1951).
[10] G. Herzberg, *Infrared and Raman Spectra* (D. Van Nostrand Company, Inc., Princeton, New Jersey, 1945).
[11] L. Pierce and L. C. Krisher, J. Chem. Phys. **31**, 875 (1959).
[12] L. C. Krisher and E. B. Wilson, Jr., J. Chem. Phys. **31**, 882 (1959).
[13] S. A. Marshall and J. Weber, Phys. Rev. **105**, 1502 (1957).

Paramagnetic-Resonance Absorption of Ions with Spin 5/2: Mn^{++} in Calcite

CHIHIRO KIKUCHI*

Department of Nuclear Engineering, University of Michigan, Ann Arbor, Michigan

AND

L. M. MATARRESE†

Solid State Division, Naval Research Laboratory, Washington 25, D. C.

(Received February 25, 1960)

The theory of the paramagnetic-resonance absorption of ions with $S=\frac{5}{2}$ in crystalline fields of trigonal symmetry is presented. The case of manganous ions in calcite ($CaCO_3$) is taken as an example. It is shown that the splitting of the fine-structure satellites into doublets first reported by Hurd, Sachs, and Hershberger [Phys. Rev. 93, 373 (1954)] can be accounted for by assuming that the manganous ions can occupy the two nonequivalent Ca^{++} sites at random. The maximum splitting was measured at X band and K band and found to be 19.3 ± 0.5 gauss. The value computed from the theory, assuming an ionic model, is 23.8 gauss. In addition, five pairs of weak lines were found, each pair occurring midway between adjacent hyperfine groups. The origin of these lines is uncertain. The applicability of the present theory to Al_2O_3:Fe, a zero-field maser material, and to the photosensitive Fe^{+++} center in CdS is pointed out.

INTRODUCTION

IN a paper on the paramagnetic-resonance absorption spectrum of Mn^{++} in single crystals of $CaCO_3$ of the calcite structure, Hurd, Sachs, and Hershberger[1] reported the splitting of the Mn^{++} fine-structure lines into doublets. According to their observations, the doublet separations depend upon the orientation of the applied magnetic field with respect to the crystal, the splitting being most pronounced at about 60° with respect to the trigonal c axis, and decreasing to zero at 0° and 90°. Furthermore, it was noted that the strong fine-structure lines are split into wider doublets than the weak ones.

The explanation of this effect was provided independently by one of the present authors[2] and by McConnell.[3] The doublet structure results from the difference in the crystalline electric fields at the two nonequivalent Ca^{++} sites occupied by the Mn^{++} ions. Because of the three-fold symmetry about the c axis, the crystalline electric field potential contains the non-axial harmonics $Y_{4\pm3}$ in addition to the axial harmonics considered by HSH. It will be the purpose of this paper to show that by including terms which transform like $Y_{4\pm3}$, it is possible to account for their results. Additional results have been reported by Kikuchi, Ager, and Matarrese.[4]

Although in the above references the problem of Mn^{++} ions in calcite was dealt with, the same general arguments are applicable to all paramagnetic ions of spin $\frac{5}{2}$ in a trigonal field. One example is Fe^{+++} in corundum ($\alpha-Al_2O_3$), a material which recently has attracted considerable attention because of its usefulness as a material for a zero-field maser.[5] Because the spin of Fe^{+++} is $\frac{5}{2}$, the Fe^{+++} ions occupying the nonequivalent Al^{+++} sites in corundum become distinguishable, in contrast to the Cr^{+++} ions, which are all magnetically equivalent because the spin is only $\frac{3}{2}$. Another example is the photosensitive iron center in CdS reported by Lambe, Baker, and Kikuchi.[6] In this case, the effects due to the crystalline electric field are large and the line width is narrow, so that the second-order splitting of the $-\frac{1}{2}\leftrightarrow\frac{1}{2}$ line is observed.

Thus, because of the growing interest in the problem of paramagnetic ions of spin $\frac{5}{2}$ in a field of trigonal symmetry, the present paper was undertaken to present some of the theoretical and experimental details which have hitherto not been published.

CALCIUM SITES

The rhombohedral unit cell of calcite is shown in Fig. 1. The crystal constants are $a_0=6.361$ A and $\alpha=46°6'$, and c_0'', the length of the unit cell along the trigonal c axis, is 17.020 A. The carbonates and calcium ions contained in a unit cell are designated by A, B, and P, Q, respectively. These ions lie in separate layers normal to the c axis, such that the stacking sequence is $BPAQ$, with spacing $c_0''/12$. The hexagonal prisms in Fig. 1 show the different arrangements of the carbonates about the P and Q calcium sites. In order to make clear the difference between the calcium sites, the top and bottom of each prism are shown in greater detail in Fig. 2. According to x-ray analysis, carbonate oxygens form an equilateral triangle with 1.26 A as the carbon-oxygen distance. Further, the carbonates

* Supported in part by Air Force Office of Scientific Research and Project Michigan.

† Part of the contribution of this author is based on work done at Lawrence Radiation Laboratory, Livermore, California, summer, 1959.

[1] F. K. Hurd, M. Sachs, and W. D. Hershberger, Phys. Rev. 93, 373 (1954); referred to hereafter as HSH.

[2] C. Kikuchi, Phys. Rev. 100, 1243 (1955).

[3] H. M. McConnell, J. Chem. Phys. 24, 904 (1956).

[4] C. Kikuchi, R. Ager, and L. M. Matarrese, Bull. Am. Phys. Soc. Ser. II, 3, 135 (1958).

[5] J. King and R. W. Terhune, J. Appl. Phys. 30, 1844 (1959).

[6] J. Lambe, J. Baker, and C. Kikuchi, Phys. Rev. Letters 3, 270 (1959).

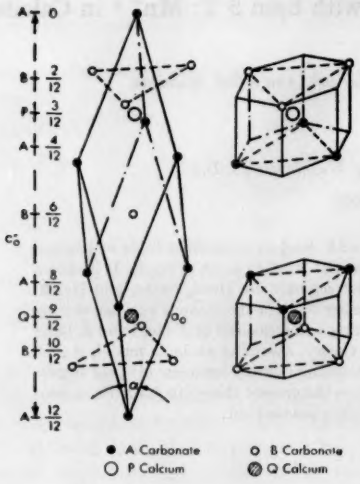

FIG. 1. Unit cell of calcite.

of type B are related to those of type A by an inversion with respect to the central carbon.

One can think of the nearest oxygens as being situated on the alternate vertices of a hexagonal prism. Then Fig. 2 shows that these prisms are different for the sites P and Q; if λ_1 is the angular displacement of the nearest oxygen with respect to the carbons, as shown in the figure, then the relative angular displacement of the two prisms is $2\lambda_1$. The crystalline electric fields at the sites P and Q can be thought of as consisting of contributions from the carbons and the first, second-, and third-nearest oxygens, each set of ions being situated on the alternate vertices of a hexagonal prism. Figure 3 shows two of these prisms. It can be seen that a reflection in the vertical reflection plane whose trace is shown in the figure changes a P site into a Q site.

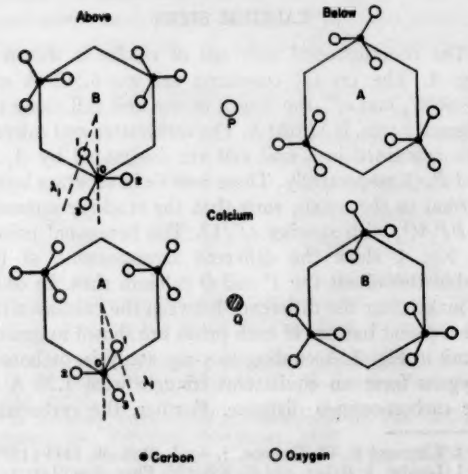

FIG. 2. Carbonates about Ca^{++} sites.

CRYSTALLINE ELECTRIC FIELD

The ions located at lattice sites produce an electrostatic field at the position of the electrons localized about the paramagnetic ions. The general form of the crystalline field potential that meets the requirements of crystal symmetry, namely that the field be (1) real, (2) invariant under rotation $\pm 2\pi/3$ about the c axis,

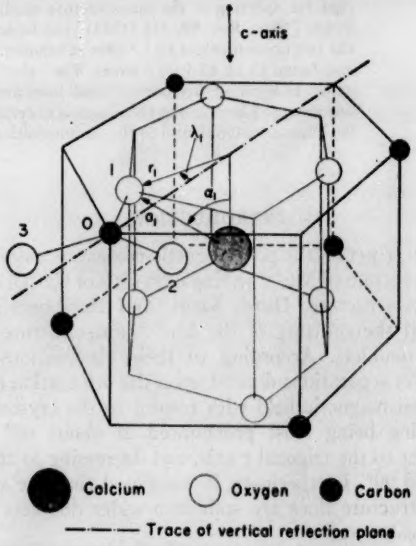

FIG. 3. Calcite hexagonal cell; a P site is shown.

and (3) invariant under rotation $\pi/3$ followed by reflection in a plane normal to the c axis, is given by

$$V=a_{20}Y_{20}+a_{40}Y_{40}+a_{43}Y_{43}+a_{4-3}Y_{4-3}+a_{60}Y_{60}+a_{63}Y_{63}+a_{6-3}Y_{6-3}+a_{66}Y_{66}+a_{6-6}Y_{6-6}+\cdots, \quad (1)$$

in which the Y_{lm} are spherical harmonics and

$$a_{l-m}=(-1)^m a_{lm}^*. \quad (2)$$

For rare-earth ions all of the above terms need to be taken into account; for the iron-group ions, the contribution from spherical harmonics of degree six and higher vanishes, so that the general form of the crystalline electric field can be written

$$V=a_{20}Y_{20}+a_{40}[Y_{40}+b_3Y_{43}-b_3^*Y_{4-3}]. \quad (3)$$

For calcite, if one considers the electrostatic field at the central ion due to the six nearest carbonates, it can be shown that

$$b_{\pm 3}=\frac{\sum_s (Z_s/a_s^5)\bar{P}_{4\pm 3}(\cos\alpha_s)\exp(\mp 3i\lambda_s)}{\sum_s (Z_s/a_s^5)\bar{P}_{40}(\cos\alpha_s)}, \quad (4)$$

in which the $\bar{P}_{lm}$ are the normalized associated Legendre

polynomials. The index s refers to the different hexagonal prisms delineated by the carbons and oxygens; Z_s is the charge assigned to the corner ion, and the quantities a_s, α_s, and λ_s are the coordinates of the ion, as exemplified in Fig. 3, for the prism of the first-nearest oxygens. As will be seen later, the parameter that enters directly into the expression for the doublet splitting is

$$b \equiv -(2i)^{-1}(b_3 - b_3^*), \tag{5}$$

so that

$$b = \frac{\sum_s (Z_s/a_s^5)\bar{P}_{43}(\cos\alpha_s)\ \sin 3\lambda_s}{\sum_s (Z_s/a_s^5)\bar{P}_{40}(\cos\alpha_s)}. \tag{6}$$

This equation gives us the opportunity to compare the value of b computed from crystallographic data with that obtained from the observed doublet splittings.

MATRIX ELEMENTS

Although the above expressions for the crystalline electric field are written in terms of Y_{lm}, these spherical harmonics are used merely to indicate the transformation properties of the crystalline electric field operator. To obtain the explicit expression for the spin operator, a scheme such as that suggested by Bleaney and Stevens[7] can be used. An alternative procedure is suggested by the property that the Y_{lm} transform like the operators $T_q^{(l)}$ generated by the process[8]

$$T_{q-1}^{(l)} = [l(l+1) - q(q-1)]^{-\frac{1}{2}}[S_-, T_q^{(l)}]. \tag{7}$$

If we set

$$T_2^{(2)} = 6^{-\frac{1}{2}} S_+^2, \tag{8}$$

then

$$T_{\pm 1}^{(2)} = \mp 6^{-\frac{1}{2}}(S_z S_\pm + S_\pm S_z),$$

$$T_0^{(2)} = [S_z^2 - \tfrac{1}{3}S(S+1)],$$

and

$$T_{-2}^{(2)} = 6^{-\frac{1}{2}} S_-^2. \tag{9}$$

Taking

$$T_4^{(4)} = \tfrac{1}{168}(70)^{\frac{1}{2}} S_+^4, \tag{10}$$

we get

$$T_{\pm 3}^{(4)} = \mp \tfrac{1}{8}(35)^{\frac{1}{2}} S_\pm^3 (2S_z \pm 3),$$

$$T_{\pm 2}^{(4)} = -\tfrac{1}{8}(10)^{\frac{1}{2}} S_\pm^2 [S(S+1) - 7S_z^2 \mp 14S_z - 9],$$

$$T_{\pm 1}^{(4)} = \mp \tfrac{1}{8}(5)^{\frac{1}{2}} S_\pm (2S_z \pm 1) \times [-3S(S+1) + 6 + 7S_z^2 \pm 7S_z],$$

$$T_0^{(4)} = \tfrac{1}{8}[35S_z^4 - 30S(S+1)S_z^2 + 25S_z^2 - 6S(S+1) + 3S^2(S+1)^2],$$

and

$$T_{-4}^{(4)} = \tfrac{1}{168}(70)^{\frac{1}{2}} S_-^4. \tag{11}$$

[7] B. Bleaney and K. W. H. Stevens, Repts. Progr. Phys. **16**, 108 (1953).

[8] G. Racah, Phys. Rev. **62**, 438 (1942).

The numerical values of some of the matrix elements, for $S=\frac{5}{2}$, are

$$\langle \pm\tfrac{5}{2} \mid T_0^{(4)} \mid \pm\tfrac{5}{2} \rangle = 15/2,$$

$$\langle \pm\tfrac{3}{2} \mid T_0^{(4)} \mid \pm\tfrac{3}{2} \rangle = -45/2,$$

$$\langle \pm\tfrac{1}{2} \mid T_0^{(4)} \mid \pm\tfrac{1}{2} \rangle = 30/2,$$

$$-\langle \tfrac{1}{2} \mid T_3^{(4)} \mid -\tfrac{5}{2} \rangle = \langle \tfrac{5}{2} \mid T_3^{(4)} \mid -\tfrac{1}{2} \rangle$$

$$= \langle -\tfrac{5}{2} \mid T_{-3}^{(4)} \mid \tfrac{1}{2} \rangle = -\langle -\tfrac{1}{2} \mid T_{-3}^{(4)} \mid \tfrac{5}{2} \rangle$$

$$= -(15/2)(14)^{\frac{1}{2}}$$

$$\langle \tfrac{3}{2} \mid T_3^{(4)} \mid -\tfrac{3}{2} \rangle = 0,$$

and

$$\langle \tfrac{3}{2} \mid T_4^{(4)} \mid -\tfrac{5}{2} \rangle = (15/2)(14)^{\frac{1}{2}}. \tag{12}$$

The crystalline electric potential, given by Eq. (3), can then be written

$$V = D[S_z^2 - \tfrac{1}{3}S(S+1)] - (2/45)a_0[T_0^{(4)} + b_3 T_3^{(4)} - b_3^* T_{-3}^{(4)}]. \tag{13}$$

The numerical coefficient and the sign in front of a_0 were chosen in such a way that, if the crystalline potential has cubic symmetry, the ground state consists of a doublet and a quartet, the former lying lower by $3a_0$. Equation (13) indicates that at zero magnetic field the ground state consists of three doublets at

$$E = \tfrac{1}{3}D - \tfrac{1}{2}a_0 \pm [(3D + \tfrac{1}{6}a_0)^2 + (14/9)a_0^2 \mid b_3 \mid^2]^{\frac{1}{2}} \tag{14}$$

and

$$E = -\tfrac{2}{3}D + a_0.$$

In the case of solely cubic symmetry, it can be shown[9] that $b_3 = (10/7)^{\frac{1}{2}} e^{i\lambda}$, in which λ is a phase factor that depends on the choice of coordinate axes. Taking $D=0$ and $b_3 = (10/7)^{\frac{1}{2}}$ in Eq. (14), we obtain a quartet at a_0 and a doublet at $-2a_0$.

It is noted that the expression given by Eq. (3) can be written as a sum of an axial and a cubic field, i.e.,

$$V = V_a + V_c, \tag{15}$$

in which

$$V_a = DY_{20} - (2/45)a_0[1 - \mid b_3 \mid (7/10)^{\frac{1}{2}}]Y_{40}, \tag{16}$$

$$V_c = -(2/45)a_0 \mid b_3 \mid (7/10)^{\frac{1}{2}} \times [Y_{40} + (10/7)^{\frac{1}{2}}(e^{i\lambda}Y_{43} - e^{-i\lambda}Y_{4-3})]. \tag{17}$$

The expression V_a given by Eq. (16) is frequently referred to as the "trigonal field," despite the fact that it possesses axial symmetry. The coefficients in Eqs. (16) and (17) are related to the a and F used by Bleaney and Trenam[10]; the exact relations are $a_0 = a - F$ and $\mid b_3 \mid (7/10)^{\frac{1}{2}} = a/a_0 = a/(a-F)$.

[9] L. M. Matarrese and C. Kikuchi, J. Phys. Chem. Solids **1**, 117 (1956).

[10] B. Bleaney and R. S. Trenam, Proc. Roy. Soc. (London) **A223**, 1 (1954).

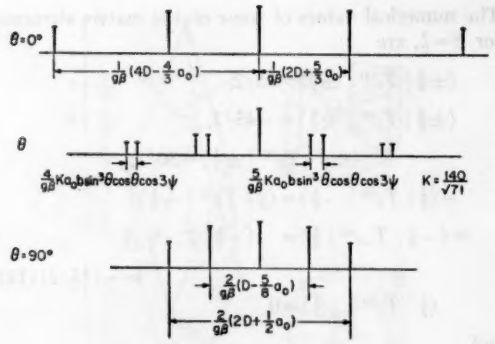

FIG. 4. Angular dependence of fine structure.

CRYSTALLINE ZEEMAN EFFECT

The expressions for the crystalline electric potential given by Eqs. (3) or (13) apply if the z axis is taken along the axis of threefold symmetry. Consequently, if the axis of quantization is taken along the magnetic field, it becomes necessary to calculate the crystalline field in terms of spherical harmonics defined in the new coordinate system. This can be done by rotating from the "crystal" into the "magnetic" coordinate system. Under this transformation each of the spherical harmonics will transform into a linear combination of spherical harmonics defined in the new coordinate system, i.e.,

$$Y_{lm}(\theta_e,\psi_e)=\sum_{m'}\gamma_{mm'}{}^{(l)}(\theta,\psi,\phi)\,Y_{lm'}(\theta_e',\psi_e'), \quad (18)$$

in which (θ,ψ,ϕ) are the Eulerian angles of the new coordinate system with respect to the old, and (θ_e',ψ_e') and (θ_e,ψ_e) are the spherical coordinates of the electron in the new and old coordinate systems, respectively. The transformation coefficients $\gamma_{mm'}{}^{(l)}$ can be expressed in terms of Jacobi polynomials.[11] However, in our present problem we shall be concerned only with the case $m'=0$, needed for the first-order perturbation calculation. The reason for this is that for Mn^{++} in calcite, when experiments are carried out at K band frequencies, the Zeeman term is large in comparison to the crystalline field terms. For $m'=0$, the Jacobi polynomials reduce to associated Legendre polynomials, so that the transformation coefficients can be written in the form:

$$m=0: \quad \gamma_{00}{}^{(l)}=[2/(2l+1)]^{\frac{1}{2}}\bar{P}_{l0}(\cos\theta),$$

$$m<0: \quad \gamma_{m0}{}^{(l)}=[2/(2l+1)]^{\frac{1}{2}}(-1)^{m}i^{-m}e^{im\psi}\bar{P}_{lm}(\cos\theta),$$

$$m>0: \quad \gamma_{m0}{}^{(l)}=[2/(2l+1)]^{\frac{1}{2}}(-1)^{m}i^{-m}e^{im\psi}\bar{P}_{l-m}(\cos\theta). \quad (19)$$

[11] E. Wigner, *Gruppentheorie und ihre Anwendung auf die Quantenmechanik der Atomspektren* (Friedrich Vieweg und Sohn, Braunschweig, 1951); now available in English translation (Academic Press, Inc., New York, 1959).

The diagonal elements of the spin Hamiltonian

$$\mathcal{H}=g\beta\mathbf{S}\cdot\mathbf{H}+A\mathbf{I}\cdot\mathbf{S}+V, \quad (20)$$

where the symbols have their usual significance, are given by

$$\langle Mm\,|\,\mathcal{H}\,|\,Mm\rangle=g\beta HM+AMm+D\gamma_{00}{}^{(2)}\langle M\,|\,Y_{20}'\,|\,M\rangle$$
$$-(2/45)a_0[\gamma_{00}{}^{(4)}+b_3\gamma_{30}{}^{(4)}-b_3{}^{*}\gamma_{-30}{}^{(4)}]\langle M\,|\,Y_{40}'\,|\,M\rangle. \quad (21)$$

(Note that g and A are here regarded as isotropic; experiment [1,4] shows this to be an excellent approximation.)

The paramagnetic-resonance absorption spectrum calculated from Eq. (21) for the special values of $\theta=0°$ and $\theta=90°$ consists of six groups of five lines each, i.e., one group for each value of m, the nuclear magnetic quantum number. The decomposition of each group into five lines, called the fine structure, is illustrated in Fig. 4. The figure also shows the appearance of the group at an arbitrary θ and how the strong and weak satellites of the central component are split into doublets, whereas the central component itself remains unchanged. We now proceed to an analysis of this doublet splitting.

As pointed out earlier, the nonequivalent sites in calcite have a common axis of threefold symmetry, but are displaced from each other by a rotation about the threefold axis. If the crystalline fields at the two sites, P and Q, are given by

$$V^{(P)}=DY_{20}-(2/45)a_0[Y_{40}+b_3{}^{(P)}Y_{43}-b_3{}^{*(P)}Y_{4-3}], \quad (22)$$

and

$$V^{(Q)}=DY_{20}-(2/45)a_0[Y_{40}+b_3{}^{(Q)}Y_{43}-b_3{}^{*(Q)}Y_{4-3}], \quad (23)$$

and furthermore, if the x axis is picked so as to lie in the vertical reflection plane as shown in Fig. 3, then

$$b_3{}^{(Q)}=b_3{}^{*(P)}, \quad (24)$$

since reflection in this plane changes a P site into a Q site. Equation (24) can also be verified by an application of Eq. (4). The difference in the crystalline field at sites P and Q leads to a splitting of the fine-structure lines into doublets. The separation of the components of a doublet is

$$\langle M\,|\,V^{(P)}-V^{(Q)}\,|\,M\rangle-\langle M-1\,|\,V^{(P)}-V^{(Q)}\,|\,M-1\rangle$$
$$=(2/45)a_0(b_3{}^{(P)}-b_3{}^{*(P)})(\gamma_{30}{}^{(4)}+\gamma_{-30}{}^{(4)})$$
$$\times[\langle M\,|\,Y_{40}'\,|\,M\rangle-\langle M-1\,|\,Y_{40}'\,|\,M-1\rangle]$$
$$=-(8/45)a_0b(105/\sqrt{7}!)\,\sin^3\theta\cos\theta\cos3\psi$$
$$\times[\langle M\,|\,Y_{40}'\,|\,M\rangle-\langle M-1\,|\,Y_{40}'\,|\,M-1\rangle]. \quad (25)$$

For the transitions $\pm1/2\leftrightarrow\pm1/2$ (central component), the quantity in the brackets is zero, but for the transitions $\pm1/2\leftrightarrow\pm3/2$, which yield the strong satellite lines, it is $75/2$; also, $\sin^3\theta\cos\theta$ is a maximum at $\theta=60°$.

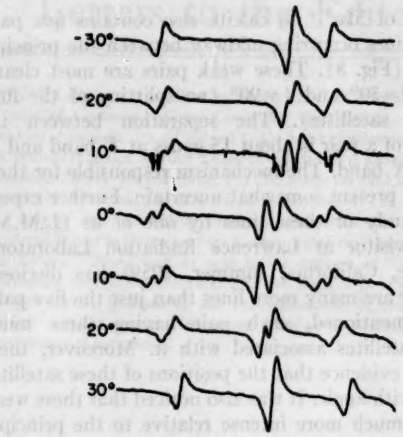

FIG. 5. Mn^{++} in calcite. Dependence of the doublet splitting on the azimuthal angle ψ. Note that the splitting is a maximum at 0°, but zero for $-30°$ and 30°.

Consequently, the expression for the numerical value of the doublet splitting at this angle becomes

$$\Delta(\pm 1/2 \leftrightarrow \pm 3/2) = (5/16)(105)^{\frac{1}{2}} \mid a_0 b \cos 3\psi \mid . \quad (26)$$

For the weak satellites ($\pm 3/2 \leftrightarrow \pm 5/2$) the quantity in the brackets is 60/2, so that the ratio of the strong to weak doublet splittings is 5:4, in agreement with the observations by HSH. Furthermore, the angular dependence of $\sin^3\theta \cos\theta$ shows that the doublet splitting should vanish for $\theta = 0$ and 90°. The dependence of the doublet splitting on the azimuthal angle ψ should be noted, being maximum and zero for $\psi = 0°$ and $\psi = 90°$, respectively. The case $\psi = 90°$ occurs when the magnetic field lies on the vertical reflection plane.

EXPERIMENTAL PROCEDURE AND RESULTS

To check the above results, a single crystal of natural calcite containing a small concentration (~0.04%) of manganese was examined in an X band electron-spin resonance spectrometer. The spectra of Fig. 5, which shows the azimuthal dependence of the doublet splittings, were obtained by placing a calcite crystal in a rectangular TE_{012}-mode cavity in such a way as to have the c axis and the microwave magnetic field both horizontal and parallel to each other. The magnet, on a rotating mount, was swung into an appropriate position, say 70°, with respect to the crystal c axis. The crystal itself was attached to a graduated dial so that the azimuthal angle could be read accurately. Figure 5 shows that the strong and weak doublets split and coalesce with a 60° azimuthal period, as expected from the $\cos 3\psi$ dependence. Figure 6 shows an enlarged recorder trace for $\theta = 70°$ and $\psi = 0°$. The maximum

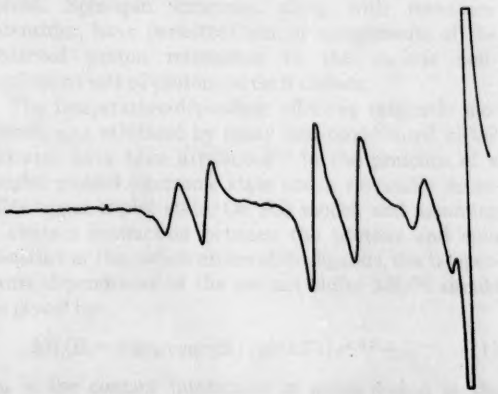

FIG. 6. Doublet splitting of the weak and strong satellites of the fine structure of Mn^{++} in calcite at $\theta = 70°$, $\psi = 0°$.

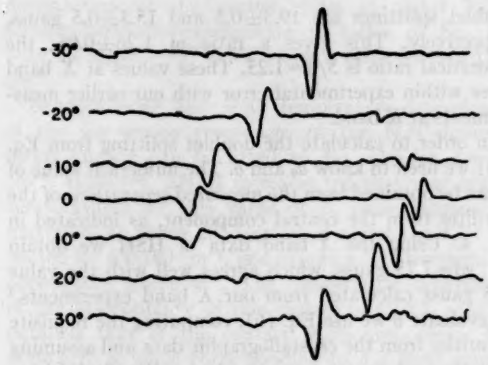

FIG. 7. Fe^{+++} in α-Al_2O_3. Dependence of the doublet splitting on the azimuthal angle ψ.

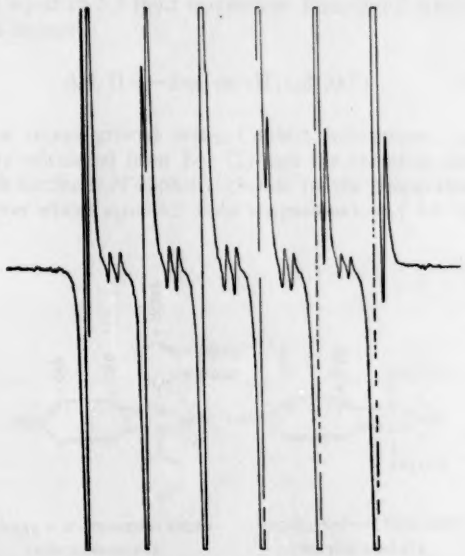

FIG. 8. Mn^{++} in calcite. The five pairs of weak lines between the hfs groups shown at high spectrometer gain.

doublet splittings are 19.3±0.5 and 15.3±0.5 gauss, respectively. This gives a ratio of 1.26±0.08; the theoretical ratio is 5/4=1.25. These values at X band agree within experimental error with our earlier measurements at K band.[4]

In order to calculate the doublet splitting from Eq. (26) we need to know a_0 and b. The numerical value of a_0 can be obtained from the measured separations of the satellites from the central component, as indicated in Fig. 4. Using the X band data of HSH we obtain $|a_0|g\beta=7.75$ gauss, which agrees well with the value 7.85 gauss calculated from our K band experiments.[4] To evaluate b we use Eq. (6), computing the requisite quantities from the crystallographic data and assuming that the calcite structure is ionic. We find $|b|=(68.1)(7!)^{-1}$. The computed maximum splitting for the strong doublet at $\theta=60°$, $\psi=0°$, is thus 23.8 gauss. This is to be compared with the experimental value quoted above, 19.3±0.5.

Figure 7 shows the azimuthal dependence of the absorption line of Fe^{+++} in Al_2O_3. This doublet structure occurs near 5100 gauss for $\theta=60°$ at 9.35 kMc.

OTHER RESULTS

During the course of these investigations, it was discovered that the paramagnetic-resonance absorption spectrum of Mn^{++} in calcite also contains five pairs of weak lines occurring midway between the principal hfs lines (Fig. 8). These weak pairs are most clearly seen at $\theta=30°$ and $\psi=90°$ (no splitting of the fine-structure satellites). The separation between the members of a pair is about 15 gauss at K band and 24 gauss at X band. The mechanism responsible for these lines is at present somewhat uncertain. Further experimental study of these lines by one of us (L.M.M., while a visitor at Lawrence Radiation Laboratory, Livermore, California, summer, 1959) has disclosed that there are many more lines than just the five pairs already mentioned, each pair having three much weaker satellites associated with it. Moreover, there was some evidence that the positions of these satellites changed with angle. It was also noticed that these weak pairs are much more intense relative to the principal hfs lines at X band than they are at K band, and that their relaxation times were somewhat longer than those corresponding to the main-spectrum lines. The study of these lines is still in progress and will be reported at a later date.

ACKNOWLEDGMENTS

It is a pleasure to acknowledge the technical assistance of Richard Ager and James E. King.

Letters to the Editor

THE Letters to the Editor section is subdivided into three parts entitled Communications, Comments and Errata, and Notes. These three sections are all subject to the same limitations on length. The textual material of each Letter is limited to a number of words equal to 950 minus the following: (a) 200 words for each average-sized figure; (b) 50 words for each displayed equation; (c) 7 words for each line of table including headings and horizontal rulings. No proof will be sent to the authors of "Communications" and "Comments and Errata." Proof will be sent to the authors of "Notes." The publication charge for Letters is $30 per page, with a minimum of $30 per Letter. If honored, the Institution will be entitled to 100 reprints without covers. See issues of May–September, 1957, for descriptions of categories.

Communications

Ligand Spin Densities and Magnetic Properties of Some Aminotroponeimine Chelates of Nickel

W. D. PHILLIPS AND R. E. BENSON

Central Research Department, Experimental Station, E. I. du Pont de Nemours and Company, Wilmington, Delaware

(Received May 23, 1960)

WE have observed large high and low field shifts in the proton magnetic resonance spectra of solutions of nickel aminotroponeimineates[1] (Fig. 1) that are attributed to isotropic contact proton hyperfine interactions in ground and thermally accessible triplet states. The proton relaxation times are sufficiently long in these chelates so that in many instances the proton spin-spin interactions of 6–12 cps can be resolved. Spin-spin structure, along with resonance intensities, have permitted unique assignments of the observed proton resonances to the various nonequivalent sets of protons of each chelate.

The temperature-dependent effective magnetic moments, μ_{eff}, exhibited by many four-coordinated nickel chelates have been attributed[2,3] to the presence of a singlet ground electronic state and a thermally accessible upper triplet state. On this model, and assuming a contact interaction between the protons and spin densities at the carbon atoms of the ligands, the temperature dependences of the contact shifts $\Delta H/H$ should be given[4] by

$$\Delta H/H = -2a_H(\gamma e/\gamma H)(g\beta/kT)(e^{\Delta/kT}+3)^{-1}. \quad (1)$$

a_H is the contact interaction in gauss and Δ is the singlet-triplet separation. Analysis of the temperature dependences of the proton shifts of nickel N,N′-dimethylaminotroponeimineate in terms of Eq. (1) over the range $-95°$ to $95°$ yields a value for Δ of 1990 cm^{-1}.

Between $-90°$ and $-50°$ temperature dependences of the six proton resonances of the N,N′-diphenyl nickel chelate can be fitted to Eq. (1) for $\Delta=780$ cm^{-1}. However, $\Delta H/H$ increases too slowly at higher temperatures for this value of Δ, passes through a maximum at about 20° instead of about the 420° expected for $\Delta=780$ cm^{-1}, and follows a $1/T$ temperature dependence above 40°. The temperature dependence of the susceptibility of this chelate in $CDCl_3$ solution parallels that of the contact shifts and, above 40°, approachs a value corresponding to 3.2 Bohr magnetons. This value of μ_{eff} is typical of that of four-coordinated square planar nickel chelates possessing triplet ground states.[5] Contact shifts at a given temperature for this chelate in $CDCl_3$ and CS_2 are different below 40° but are the same above this temperature. It is suggested, then, that the singlet-triplet separation for this chelate is both temperature and solvent dependent with Δ decreasing with increasing temperature until the ground state, singlet at low temperature, becomes triplet above about 20°. Other hydrogen bonding and more basic solvents, as well as spectral and susceptibility measurements, are being employed to further elucidate this behavior.

The proton shifts for nickel N,N′-diethylaminotroponeimineate (in which, incidentally, the separation between the CH_2 and H_γ proton resonances reaches 482 ppm at $-95°$) follow a $1/T$ temperature dependence in $CDCl_3$ between $-95°$ and 95°. μ_{eff} of this chelate in $CDCl_3$ between $-50°$ and 73° is constant and equal to 3.2 Bohr magnetons. Equation 2 applies to a molecule

$$\Delta H/H = -2a_H(\gamma e/\gamma H)(g\beta/3kT) \quad (2)$$

in a triplet ground state. Contact interactions, a_H, were calculated from Eq. (2) and the chemical shift data for the N,N′-diphenyl chelate (in the temperature region where $\mu_{eff}=3.2$ Bohr magnetons) and for the

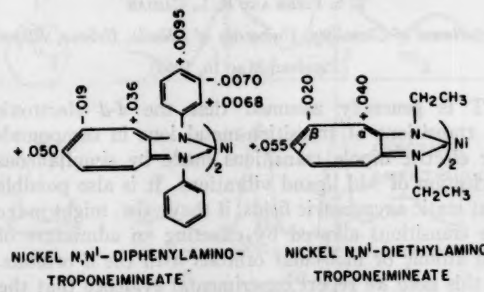

FIG. 1. Spin densities in two nickel aminotroponeimineates.

N,N′-diethyl chelate. Carbon spin densities, ρ_c, evaluated from $a_H = \frac{1}{2}Q\rho_c$ where a value of $Q = -22.5$ gauss was assumed for both the six- and seven-membered rings,[6] are shown in Fig. 1. It is seen that the signs of the spin densities alternate on the phenyl rings and on the five positions of the seven-membered ring that can be observed. When methyl is substituted for the para proton as in the N,N′-ditolyl chelate, the sign of $a_{p\text{-}CH_3}$ is positive and about 20% greater than the negative $a_{p\text{-}H}$. This observation is consistent with a direct mechanism for contact interactions proceeding via hyperconjugation that leads to similar signs for a_{CH_3} and ρ_c, and an indirect mechanism for contact interactions involving aromatic C—H fragments that leads to opposite signs for $a_{C\text{-}H}$ and ρ_c.[7] A similar effect was observed recently for paramagnetic acetylacetonates.[8]

Details of the magnetic resonance, as well as susceptibility and spectral studies of transition metal chelates of aminotroponeimines, will be reported shortly. Studies also are in progress on other nickel chelates such as those of bipyridyl and 1,10-phenanthroline for which similar large NMR shifts have been observed.

[1] W. R. Brasen, H. E. Holmquist, and R. E. Benson, J. Am. Chem. Soc. **82**, 995 (1960).
[2] G. Maki, J. Chem. Phys. **28**, 651 (1958); **29**, 162 (1958); **29**, 1129 (1958).
[3] C. J. Ballhausen and A. D. Liehr, J. Am. Chem. Soc. **81**, 538 (1959).
[4] H. M. McConnell and D. B. Chesnut, J. Chem. Phys. **28**, 107 (1958).
[5] J. B. Willis and D. P. Mellor, J. Am. Chem. Soc. **69**, 1237 (1947).
[6] H. M. McConnell and H. H. Dearman, J. Chem. Phys. **28**, 51 (1958).
[7] H. M. McConnell, J. Chem. Phys. **24**, 764 (1956); R. Bersohn, J. Chem. Phys. **24**, 1066 (1956); S. I. Weissman, J. Chem. Phys. **25**, 890 (1956); B. Venkataraman and G. K. Fraenkel, J. Chem. Phys. **24**, 737 (1958); A. D. McLachlan, Mol. Phys. **1**, 233 (1958).
[8] A. Forman, J. N. Murrell, and L. E. Orgel, J. Chem. Phys. **31**, 1129 (1959).

Polarized Visible Spectra of Crystalline Trisoxalatometallates: The Source of Intensity*

T. S. PIPER AND R. L. CARLIN

Department of Chemistry, University of Illinois, Urbana, Illinois

(Received May 16, 1960)

IT is generally assumed that the *d-d* electronic transitions of transition-metal ions in compounds are electric dipole transitions made by simultaneous excitation of odd ligand vibrations. It is also possible that static asymmetric fields, if they exist, might make the transitions allowed by effecting an admixture of odd atomic or molecular orbitals with the *d* orbitals. In this note we report experimental evidence that the transitions are indeed electric dipolar but are allowed by the purely electronic mechanism in the case of trisoxalatometallates.

We have obtained the absorption spectra of trivalent metal ions in the colorless diluent crystal $NaMgAl(C_2O_4)_3 \cdot 8H_2O$. This crystal[1] belongs to the space group $D_3{}^2$; the site symmetry at the trivalent metal ion is D_3, which is the same as that of the free ion $Al(C_2O_4)_3{}^{-3}$. The field is predominantly octahedral with the smaller trigonal component. This particular symmetry allows a unique test of theories of intensity Since a center of inversion is absent, the transitions are not forbidden by the Laporte rule. Nevertheless, the symmetry is high enough to afford the selection rules:

$$\overset{\sigma}{A_{1,2} \longleftrightarrow E}; \qquad \overset{\pi}{A_1 \longleftrightarrow A_2};$$

and

$$A_{1,2} \longleftarrow\!\!\!\!\!\!\mid\!\!\!\!\!\!\longrightarrow A_{1,2}.$$

Here $\sigma(\perp)$ or $\pi(\|)$ refer to the polarization of the electric vector of the light with respect to the C_3 axis.

The absorption maxima of the spin-allowed transitions are presented in Table I. The spectra were taken with the polarized incident light ray perpendicular to the hexagonal axis. The spectra with incident light parallel to the C_3 axis (axial spectra) are identical to the σ spectra but quite different from the π spectra; this proves that the electric dipole and not the magnetic dipole excites the transitions.[2]

The selection rules are well obeyed in the Cr^{+3} and Co^{+3} spectra. For ${}^4A_2 \rightarrow {}^4T_1$ of Cr^{+3}, the parallel component of the band is weak and diffuse and the ratio of extinction coefficients $\epsilon_{\|}/\epsilon_{\perp}$ is 0.06. For ${}^1A_1 \rightarrow {}^1T_2$ of Co^{+3}, $\epsilon_{\|}/\epsilon_{\perp}$ is 0.05. Since the electronic selection rules apply, we conclude that the coupling with vibrations is not important in determining the intensities. Nevertheless, the vibrations of the ligands (probably the even ones) are strongly excited; this is indicated by the breadth of the bands ($\Delta\nu_{\frac{1}{2}} \approx 3000$ cm^{-1}).[3] There is a greater breakdown of the selection rules in the spectra of V^{+3}; for ${}^3A_2 \rightarrow {}^3T_1$, $\epsilon_{\|}/\epsilon_{\perp}$ is 0.2. This is understandable

TABLE I. Spectra of M^{+3} in $NaMgAl(C_2O_4)_3 \cdot 8H_2O$ at 25°C.

Ion and ground state	Band maximum cm^{-1}	$\Gamma(D_3)$	$\Gamma(O_h)$
V^{+3}	16 667	${}^3A_1$	${}^3T_{2g}$
$3d^2({}^3A_2)$	16 920	${}^3E$	
	...	${}^3A_2$	${}^3T_{1g}$
	24 390	${}^3E$	
Cr^{+3}	17 316	${}^4A_1$	${}^4T_{2g}$
$3d^3({}^4A_2)$	17 620	${}^4E$	
	23 670	${}^4E$	${}^4T_{1g}$
	...	${}^4A_2$	
Co^{+3}	16 350	${}^1E$	${}^1T_{1g}$
$3d^6({}^1A_1)$	16 500	${}^1A_2$	
	23 400	${}^1E$	${}^1T_{2g}$
	...	${}^1A_1$	

because this band is a shoulder on an intense charge transfer band. The extinction coefficients for these oxalates are about 10 to 20 times greater than those of the hexaquo ion and hence some vibrational allowance of the same order of magnitude as in the hexaquo ions is not ruled out.

At 77°K the spin-forbidden transitions were observed. In particular, we mention the transition $^3A_2 \rightarrow {}^1A_1$ of V^{+3} observed as a weak line at 20 480 cm^{-1}; it is found in the axial and σ spectra but is completely absent in the π spectra. Thus, the transition is electric dipolar just as the spin-allowed transitions. Symmetry arguments predict the polarization and confirm that this transition is made possible by spin-orbit coupling of the $^1A_1$ state to triplet states. Since $\mathbf{l}\cdot\mathbf{s}$ transforms as A_2+E of D_3, the state $^1A_1$ is coupled only to the $^3A_2$ and ^3E states and the transition in question should be σ polarized.

* This research has been supported by the National Science Foundation.

[1] L. Frossard, Schweiz. mineral. petrog. Mitt. **36**, 1 (1956).

[2] E. V. Sayre, K. Sancier, and S. Freed, J. Chem. Phys. **23**, 2060 (1955).

[3] Because of this broadening, the trigonal splittings are not reliably obtained. However, the order of the bands is consistent with a negative trigonal splitting parameter K as is the fact that the ground state of V^{+3} is the $^3A_2$ component of $^3T_{1g}(O_h)$. See S. Sugano and Y. Tanabe, J. Phys. Soc. Japan **13**, 880 (1958).

Paramagnetic Resonance of Gamma-Irradiated Single Crystals of Ice at 77°K*

J. A. McMillan,† M. S. Matheson, and B. Smaller

Argonne National Laboratory, Argonne, Illinois

(Received June 8, 1960)

THE EPR spectrum of gamma-irradiated polycrystalline ice has been observed by several authors.[1–6] All have found a doublet, with a separation of 30 oe at 350 Mc/sec,[1] and 40 oe at 23[2–4] and 9 kMc/sec.[5,6] A broad hump at lower fields was also reported. First assumed to be due to H atoms,[1] the doublet was later speculatively attributed to OH since single crystals of irradiated ice showed some anisotropy.[2] This assumption is supported by some kinetic evidence.[5] The ground state of OH is, however, $^2\Pi_{\frac{3}{2}}$, and should therefore have a g value of $\frac{4}{3}$, while the observed one is approximately 2. This fact suggests that the orbital angular momentum is almost completely quenched. This is supported by the fact that NO trapped in an ice matrix[5] also shows resonance at $g=2$. Consequently, we undertook the problem of studying the anisotropy of the spectra of single crystals, irradiated and measured at 77°K, hoping to identify the paramagnetic species, its position and its orientation.

Single crystals of ice were grown following the technique of Jona and Scherrer,[7] cut in a cold box, irradiated at 77°K with total doses of approximately 10^{21} ev/cc, and then transferred to nonirradiated high purity silica tubes for measurement. The resonance was observed in a dual modulation equipment operating at 9.1 kMc/sec.[8] Special care was taken to keep the samples under liquid nitrogen, since the signals begin to disappear at over 90°K with a measurable rate.[5] The spectra were obtained with the c axis parallel and perpendicular to the axis of rotation, this latter always perpendicular to the static, and parallel to the microwave, magnetic fields. The parallel run showed sixfold symmetry. The perpendicular one showed one canonical orientation (c axis parallel to the static magnetic field) in which the doublet has the minimum separation (35.5 oe) and the maximum g value (2.0127), and two mirror planes (m_{I} and m_{II} in Fig. 1). The spectra show twelve-fold periodicity at the orientations of 15° to each mirror. These results are accounted for on the basis of a cylindrically symmetric radical: (1) having an unpaired electron interacting with a proton at approximately 1 A distance; (2) having its symmetry axis pointing toward any of the corners of the hexagon (0001); (3) having equal populations in these orientations, which are all perpendicular to the c axis of the parent crystal. The Hamiltonian Spin is then

$$\mathcal{H}=\beta\mathbf{S}\cdot\mathbf{g}\cdot\mathbf{H}+g\beta\mathbf{S}\cdot\mathbf{A}\cdot\mathbf{I}$$

where g and β are the g value and the magneton for the electron, and $\mathbf{A}=\mathbf{a}+\mathbf{B}$, $\mathbf{a}$ being the contact term and $\mathbf{B}$ the dipole-dipole interaction contribution to the hyperfine splitting, in magnetic field units. The experi-

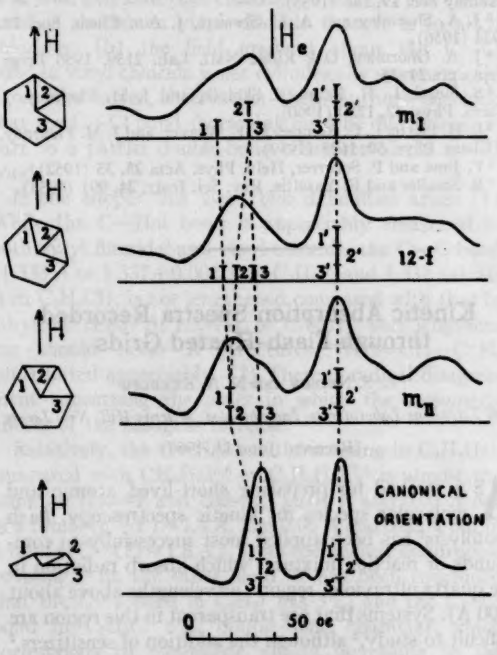

FIG. 1. Typical observed spectra and calculated lines for OH.

mental values are $g_{||}=2.0127$, $g_{\perp}=2.0077$; $a=41.3$ oe, $B_{||}=12$ oe, and $B_{\perp}=-6$ oe. The absolute g values are accurate to ± 0.001, their differences to ± 0.0003. Figure 1 shows typical observed spectra as well as those calculated on the basis of the above parameters. The authors believe that the strong dipolar field of the water molecules breaks down the Russell-Saunders coupling leading to spin-only paramagnetism.

The low field broad hump observed in polycrystalline samples resolves into at least two lines in the parallel run that also exhibit sixfold symmetry. This part of the spectrum can be accounted for on the basis of a radical having, if any, a very small contact term, and the following values of the g tensor: $g_{||}=2.00$ and $g_{\perp}=2.04$ with the z axis ($g_{||}$) oriented along every hydrogen bonding in the parent lattice. In view of these facts, we think that it could perhaps be identified with H_2O^+, although there is not enough evidence to support this or any other assumption.

Detailed results will be published at a later date.

We wish to acknowledge the United States Atomic Energy Commission for sponsoring this work and one of us, J. A. McMillan, thanks the John Simon Guggenheim Memorial Foundation for having awarded him a Fellowship.

* Based on work performed under the auspices of the U. S. Atomic Energy Commission.

† Guggenheim Fellow, on leave from Instituto de Física de San Carlos de Bariloche, Bariloche, Río Negro, Argentina.

[1] M. S. Matheson and B. Smaller, J. Chem. Phys. **23**, 521 (1955).
[2] R. Livingston, H. Zeldes, and E. H. Taylor, Discussions Faraday Soc. **19**, 166 (1955).
[3] J. A. Shormley and A. C. Stewart, J. Am. Chem. Soc. **78**, 2934 (1956).
[4] J. A. Ghormley, Oak Ridge Natl. Lab. 2159, 1956 Progr. Rept., pp. 21–23.
[5] S. Siegel, L. H. Baum, S. Skolnik, and J. M. Flournoy, J. Chem. Phys. **32**, 1250 (1960).
[6] L. H. Piette, L. C. Rempel, H. E. Weaver, and J. M. Flournoy, J. Chem. Phys. **30**, 1623 (1959).
[7] F. Jona and P. Scherrer, Helv. Phys. Acta **25**, 35 (1952).
[8] B. Smaller and E. Yasaitis, Rev. Sci. Instr. **24**, 991 (1953).

Kinetic Absorption Spectra Recorded through Flash-Heated Grids

L. S. Nelson and N. A. Kuebler

Bell Telephone Laboratories, Incorporated, Murray Hill, New Jersey

(Received June 13, 1960)

As a method for preparing short-lived atomic and molecular species for kinetic spectroscopy, flash photolysis[1] has been applied most successfully to compounds or reaction mixtures which absorb radiation in the quartz ultraviolet region (wavelengths above about 2000 A). Systems that are transparent in this region are difficult to study,[2] although the addition of sensitizers,[3] direct exposure to discharges,[4–6] and flash irradiation in the vacuum ultraviolet[7,8] have been used in some instances.

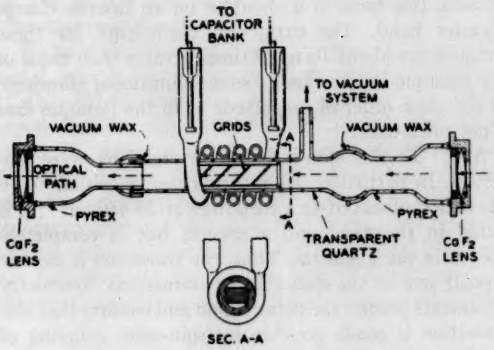

FIG. 1. Cell for kinetic absorption spectroscopy through flash-heated grids.

Here we describe a preparative technique that can produce similar instantaneous concentrations of intermediates thermally, without the need for photochemically active absorption—heterogeneous flash heating[9] of fine grids which are suspended in an absorption cell so that the background light passes through the grids before entering the spectrograph. The grids, each of which blocks 1–2% of the background light, are strongly heated by absorption of intense light pulses from sources similar to conventional flash photolysis discharge lamps. Some of our lamps deliver instantaneous optical fluxes of 10–15 kw cm^{-2}, which is above the range of many arc-imaging and solar furnaces.

If the grid windings have diameters smaller than 100μ we have estimated[9] that their temperatures can approach the brightness temperatures of the sources (usually about 5000°K). Vigorous thermal reactions such as vaporization or desorption from the grids themselves, or heating or pyrolysis of the solid, liquid or gaseous matrix in which they are immersed occur readily.

The short initiation times and the compact spatial arrangement possible with these reactions permit a record to be made of the kinetic absorption spectra of absorbing intermediates or products formed around the grids in a manner completely analogous to reactions initiated by flash photolysis. In effect, we have added a heterogeneous "sensitizer" to a nonabsorbing parent system in order to convert the optical energy from the lamp into chemical excitation.

We have used the cell shown in Fig. 1. It consists basically of an evacuable, transparent, fused quartz or Pyrex tube closed at each end with CaF_2 lenses to allow spectra to be recorded in the Schumann ultraviolet as well as the near-ultraviolet and visible regions of the spectrum. The lenses are held in high-alumina ceramic end plates, which insulate the cell from possible discharge effects due to nearby high voltage components. Surrounding the inner quartz tube is a five-turn spiral

fused quartz discharge lamp similar to Christie and Porter's lamp III[10] with MgO coated reflector. It is flashed at 112.5μf and up to 8 kv, with discharge times of about 300 μsec.

Time-delayed absorption spectra may be recorded in the region 1200–5000 A on 35 mm Eastman SWR film with a 2-meter normal incidence McPherson grating vacuum spectrograph[11] (dispersion 7.51 A mm^{-1}) using one 22 μsec flash from a Lyman source (3.75 μf, 10 kv) similar to that described by Thrush.[12] The delays were generated by the photocell-thyratron unit of Callomon and Ramsay.[13]

From one to six 25×35 mm grids were placed in an inclined position in the cell. They were wound with approximately 2 m of monofilament rayon pyrolyzed in N_2 at 950°C to give 0.01 mm diameter carbonaceous strands. Windings were 1 mm apart.

To illustrate the method, we have flash heated four grids in an evacuated cell. A number of sharp and diffuse features were observed in absorption with delays up to about one millisecond. The most prominent were: (1) eight sharp bands between 2609 and 2623 A that correspond within our limits of accuracy to emission bands of benzene[14] and seem to arise from vibrationally excited ground-state benzene; (2) a weaker, almost continuous absorption with a sharp edge at 2575 A and extending with steadily decreasing intensity to about 2605 A, which we have not as yet identified; (3) a heavy continuum below about 2000 A; and (4) acetylene bands between 2244 and 2275 A. No other features of the benzene absorption near 2500 A were detected. Within 20 sec after the preparative flash, the 2000 A absorption bands of benzene have appeared with moderate intensity, as well as a continuum below 1840 A presumably due also to benzene. Upon evacuation of the cell to 1 mm Hg, three sets of paired absorption bands of ethylene were observed at wavelengths below 1744 A. We have attributed the species mentioned above to processes accompanying further pyrolysis of the grid fibers.

When the products from the first flash were pumped from the cell and it was filled with 10 mm Hg of methane or deuteromethane, a second preparative flash (with the same grids which remain essentially intact) showed the previous features only faintly. With delays of about 100 μ sec, however, the absorption bands of CH_3 at 2158 and 2164 A[15] or CD_3 at 2142 and 2144 A[15] were observed. To the best of our knowledge, this is the first time methyl has been observed directly in a pyrolytic reaction.

It is felt that these preliminary experiments indicate the usefulness of this technique in the study of thermal reactions, either of the grids themselves, or of the transparent system in which the grids are immersed. It may be possible to use liquid and solid as well as gaseous matrices.

[1] R. G. W. Norrish and B. A. Thrush, Quart. Revs. (London) **10**, 149 (1956).
[2] R. G. W. Norrish, Proc. Chem. Soc. (London) **1958**, 247.
[3] R. G. W. Norrish, G. Porter and B. A. Thrush, Proc. Roy. Soc. (London) **A227**, 423 (1955).
[4] R. J. Dwyer, J. Chem. Phys. **7**, 40 (1939).
[5] L. S. Nelson and D. A. Ramsay, J. Chem. Phys. **25**, 372 (1956).
[6] J. A. Golden and A. L. Myerson, J. Chem. Phys. **28**, 978 (1958).
[7] H. Schuler and E. Krimmel, Z. Naturforsch. **12a**, 528 (1957).
[8] L. S. Nelson and D. A. Ramsay, J. Chem. Phys. **25**, 372 (1956).
[9] L. S. Nelson and J. L. Lundberg, J. Phys. Chem. **63**, 433 (1959).
[10] M. I. Christie and G. Porter, Proc. Roy. Soc. (London) **A212**, 390 (1952).
[11] J. A. Golden and A. L. Myerson, J. Opt. Soc. Am. **48**, 548 (1958).
[12] B. A. Thrush, Proc. Roy. Soc. (London) **A243**, 555 (1958).
[13] J. H. Callomon and D. A. Ramsay, Can. J. Phys. **35**, 129 (1957).
[14] J. B. Austin and I. A. Black, Phys. Rev. **35**, 452 (1930).
[15] G. Herzberg and J. Shoosmith, Can. J. Phys. **34**, 523 (1956).

Comments and Errata

Bond Lengths and Nuclear Quadrupole Coupling in Vinyl Halides

E. SPINNER

Department of Medical Chemistry, Australian National University, Canberra, A.C.T. Australia

(Received April 18, 1960)

A RECENT, very accurate study by Kivelson, Wilson, and Lide[1] has confirmed that: (a) the C—Cl bond is shorter in vinyl chloride than it is in alkyl chlorides; (b) the field gradient about the C—Cl bond in vinyl chloride is not cylindrically symmetrical.[2] From the latter observation these authors conclude that the C—Cl bond shortening must be due at least in part to a partial double-bond character of the C—Cl bond.

If one adopts this view, two difficulties arise: (1) While the C—Hal bond is appreciably shortened in both vinyl fluoride[3] and vinyl chloride, the C=C bond (1.333 A or 1.337±0.002 A in C_2H_3F, and 1.332±0.005 A in C_2H_3Cl), is not lengthened compared with that in ethylene[4] (1.337 A, 1.334 A, or 1344 A); such lengthening should occur if structures $^{+}Hal{=}CH{-}C^{-}H_2$ contributed appreciably. (2) There is radical disagreement concerning the order in which the mesomeric effects of the halogens increase.

Relatively, the C—Hal bond shortening in C_2H_3Hal, compared with CH_3Hal[5,6] or C_2H_5Hal,[7,8] is almost the same for Hal=F and Hal=Cl [0.04 A and 0.03 A out of a total r(C—F) ≈ 1.4 A, and 0.06 A and 0.05 A out of a total r(C—Cl) ≈ 1.8 A]. From the nuclear quadrupole coupling,[2b] on the other hand, it has been concluded that the C—I bond in C_2H_3I has 3%, and the C—Cl bond in C_2H_3Cl 6%, double-bond character, which corresponds to mesomeric effects increasing in the order I<Br<Cl<F. This order is in agreement with a

considerable amount of evidence,[9,10] but a variety of spectral data on halogenobenzenes have been regarded as evidence that the mesomeric effects of halogens increase in the order[11] F<Cl<Br<I; the dipole moment anomalies (interaction moments) observed for the *p*-nitrohalogenobenzenes[12] represent evidence for the latter order (if inductive interaction is small[12b]).

However, no partial double-bond character needs to be postulated for the C—Hal bonds in C_2H_3Hal. The pure single bond C—*X* in C_2H_3X should not be cylindrically symmetrical. The lack of cylindrical symmetry in the C—C bond in ethane has been referred to previously.[13] Repulsions between the C—H and the C—*X* bonding electrons in CH_3X cause the electron-density contour lines of the C—*X* bonding electrons to approach a triangular shape, as in (I), instead of being

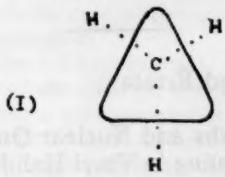

(I)

FIG. 1

circular. Similarly, in a planar trigonal molecule *ABCX*, repulsions between the *A*—*B* and *A*—*C* bonding electrons on the one hand and the *A*—*X* bonding electrons on the other cause the density contour lines of the latter latter electrons to approach an elliptical shape, as in (II).

(II)

FIG. 2

The cross section of a nucleus of finite quadrupole moment is also elliptical. In a molecule *ABCX*, such as vinyl-*X*, a corresponding coupling is to be expected if *X* possesses a nuclear quadrupole. The I nucleus in C_2H_3I being farther away from the C—H and the C=C bonds than is the Cl nucleus in C_2H_3Cl, the deviation from cylindrical symmetry in the electric field gradient should be smaller at the I than at the Cl nucleus (which is in agreement with observation).

The author attributes the shortening of the C—Hal bond in vinyl-Hal as compared with alkyl-Hal[14] to: (a) reduced intramolecular steric repulsions, resulting from a widening of the bond angles[15] from 109° to 120°; (b) intramolecular van der Waals-London attraction between the halogen atom and the remainder of the molecule, which is increased by the presence of the highly polarizable C=C bond.

[1] D. Kivelson, E. B. Wilson, and D. R. Lide, J. Chem. Phys. **32**, 205 (1960).

[2] (a) J. H. Goldstein and J. K. Bragg, Phys. Rev. **75**, 1453 (1949); (b) J. H. Goldstein, J. Chem. Phys. **24**, 106 (1956); A. Howe and J. H. Goldstein, J. Chem. Phys. **27**, 831 (1957).

[3] B. Bak, D. Christensen, L. Hansen-Nygaard, and J. Rastrup-Anderson, Spectrochim. Acta **13**, 120 (1958); H. W. Morgan and J. H. Goldstein, J. Chem. Phys. **30**, 1025 (1959).

[4] For original literature, see footnote reference 1.

[5] O. R. Gilliam, H. D. Edwards, and W. Gordy, Phys. Rev. **75**, 1014 (1949).

[6] S. L. Miller, L. C. Aamodt, G. Dousmanis, C. H. Townes, and J. Kraitchman, J. Chem. Phys. **20**, 1112 (1952).

[7] J. Kraitchman and B. P. Daily, J. Chem. Phys. **23**, 184 (1955).

[8] R. S. Wagner and B. P. Daily, J. Chem. Phys. **26**, 1588 (1957).

[9] C. K. Ingold, *Structure and Mechanism in Organic Chemistry* (Cornell University Press, Ithaca, New York, 1953) pp. 75, 89, 332.

[10] N. J. Leonard and L. E. Sutton, J. Am. Chem. Soc. **70**, 1564 (1948).

[11] W. W. Robertson and F. A. Matsen, J. Am. Chem. Soc. **72**, 5252 (1950); W. F. Forbes and A. S. Ralph, Can. J. Chem. **34**, 1447 (1956); W. F. Forbes and W. A. Mueller, *ibid.* **35**, 488 (1957); R. N. Jones, W. F. Forbes, and W. A. Mueller, *ibid.* **35**, 504 (1957); L. Goodman and H. Shull, J. Chem. Phys. **27**, 1388 (1957).

[12] J. W. Smith, *Electric Dipole Moments* (Butterworths Scientific Publications, Ltd., London, 1955), (a) p. 209, (b) p. 210.

[13] E. Gorin, J. Walter, and H. Eyring, J. Am. Chem. Soc. **61**, 1876 (1939); E. B. Wilson, Proc. Natl. Acad. Sci. U.S.A. **43**, 816 (1957).

[14] Concerning the analogous problem of the shortened C—N bonds in amides, see E. Spinner, Spectrochim. Acta **15**, 95 (1959).

[15] J. B. Conn, G. B. Kistiakowski, and E. A. Smith. J. Am. Chem. Soc. **61**, 1868 (1939); A. Burawoy, in *Contribution a l'Etude de la Structure Moleculaire* (Maison Desoer, Liège, 1948), p. 73.

Bond Lengths and Nuclear Quadrupole Coupling in Vinyl Halides

E. BRIGHT WILSON, JR.

Mallinckrodt Chemical Laboratories, Harvard University, Cambridge 38, Massachusetts

(Received May 2, 1960)

THE interesting comments of Spinner[1] concerning the interpretation of the bond lengths and quadrupole coupling data for vinyl chloride[2] point up the facts that present-day theoretical interpretations of such properties are far from being completely satisfactory or unambiguous and that the best that can be said for such concepts as conjugation, hybridization, etc., is that they have a rough predictive value for coarser effects even though they often either fail to predict correctly, or, more often, fail to provide any prediction at all for finer effects. Nevertheless, perhaps some comments on Spinner's criticisms are in order.

First of all, Mulliken[3] has discussed the criticism that no lengthening of the double bond involved in conjugation is observed and has pointed out that the best calculations show that only a small lengthening is to be expected, less than the present experimental uncertainties in the comparisons required. Secondly, possible disagreement in the order of the conjugative

effects among the halogens is not necessarily an argument against the existence of conjugation, but merely indicates that it is probably not the only effect involved.

The attempt to explain the observed lack of cylindrical symmetry of the C—Cl bond by arguing that single bonds are not normally cylindrical because of electron repulsions incurs certain difficulties. At one time this seemed to the present author[4] a possible explanation of barriers to internal rotation about single bonds, but further reflection showed that any such effect should tend to stabilize the wrong conformation, since the lowest energy would be expected for the maximum overlap of the bonding orbitals.

It is difficult in the absence of a satisfactory quantitative theory of nonbonded forces to comment on Spinner's last point.

Finally, although it is becoming highly probable that there is no simple explanation of all the variations of bond lengths, angles, dipole moments, etc., from one molecule to another, the concept of conjugation does permit some successful rough predictions, including also the existence of rather high barriers to internal rotation around single bonds with some supposed double-bond character. It would therefore seem premature to reject it entirely.

[1] E. Spinner, J. Chem. Phys. **32**, 000 (1960).
[2] D. Kivelson, E. B. Wilson, and D. R. Lide, J. Chem. Phys. **32**, 205 (1960).
[3] R. S. Mulliken, Tetrahedron **6**, 68 (1959).
[4] E. Bright Wilson, Jr., Proc. Natl. Acad. Sci. **43**, 816 (1957); see also Advances in Chem. Phys. **2**, 367 (1959).

Note on the Optical Absorption of $MnCl_2$ and $MnBr_2$

R. PAPPALARDO

Bell Telephone Laboratories, Inc., Murray Hill, New Jersey

(Received April 6, 1960)

AN interesting property of some of the excited electronic levels of $3d^5$ systems (Mn^{2+} and Fe^{3+}) is that their energy separation from the ground state is independent of crystal fields for cubic symmetry.[1] Low symmetry components of the crystal field do not affect, in a first order, the $^4A_{1g}$, $^4A_{2g}$, $_a{}^4E_g$, $_b{}^4E_g$ levels, while the $^4T_{2g}(de^3d\gamma^2)$ and $^4T_{1g}(de^3d\gamma^2)$ levels are influenced by such fields, in a first order, only via configuration mixing.[2,3] Hence, the study of the position of the $^4A_{1g}$, $^4A_{2g}$, and ^4E_g levels can supply information on the value, in solids, of Racah's parameters[4] of electrostatic interaction, which are closely related to the shape of the electronic cloud. An analysis of this kind has been done by Professor J. W. Stout[5] for the case of MnF_2 and by the writer[3] for the case of $MnCl_2$ and $MnBr_2$.

TABLE I. Transitions to excited levels of Mn^{2+} in $MnCl_2$: Experimental values[a] at 78°K and calculated values.

Calculation I: $B_0=700$ cm^{-1}; $C_0=3430$ cm^{-1}; $Dq=750$ cm^{-1}; $\epsilon=0.03$.[a]
Calculation II: $B=950$ cm^{-1}; $C=3280$ cm^{-1}; $Dq=830$ cm^{-1}; $\epsilon=0.13$.[b]

Excited Levels	Exper (10^3 cm^{-1})	Calc I (10^3 cm^{-1})	Calc II (10^3 cm^{-1})
$^4T_{1g}(^4G)$	18.5	18.5	17.9 [f]
$^4T_{2g}(^4G)$	22.0	21.8	22.6
$^4A_{1g}(^4G)$[c]	23.59	23.5[c]	23.5
$_a{}^4E_g(^4G)$[c]	23.825	23.7[c]	24.0
$^4T_{2g}(^4D)$[d]	26.75	26.5[c]	27.8
$_b{}^4E_g(^4D)$[c]	28.065	28.0	28.1
$^4T_{1g}(^4P)$[d]	36.5	34.0	31.3
$^4A_{2g}(^4F)$[c]	38.4	37.5[f]	34.2
$^4T_{1g}(^4F)$	40.65	39.0	42.2
$^4T_{2g}(^4F)$	42.37	42.0	42.2

[a] See footnote reference 3.
[b] See footnote reference 6.
[c] These levels have the same subshell configuration as the ground state.
[d] Idem, when configuration mixing is neglected.
[e] Assumed as starting points in the calculations.
[f] See footnote reference 3, App. 1.

In order to interpret the absorption spectrum of MnF_2, J. W. Stout used: (a) the values of Racah's parameters B and C which give the best fitting for the spectrum of the free ion; (b) the parameter Dq of crystalline cubic field; (c) the covalency parameter ϵ.[2]

In the case of MnF_2,[5] as well as in that of $MnCl_2$ and $MnBr_2$, Stout finds[6] an excellent agreement between prediction and experiment for the set of excited electronic levels of Mn^{2+} and also obtains a reasonable sequence of values for the covalency parameter ϵ going from the fluoride to the bromide. These results are quite satisfactory. On the other hand, it seems to us that the parameter ϵ, as used by Stout,[5,6] is more of a "complex formation" parameter than a covalency parameter. In it, in fact, are included the effects of various factors (finite size of the electronic cloud, for instance) which cause a deformation of the free ion electronic distribution when the same ion is present in a solid.

In the method we used[3] to interpret the spectrum of $MnCl_2$, an approximation was made to consider the covalency effects as a perturbation on the wave functions u and v already pertaining to Mn^{2+} in the solid state, in a purely ionic system. Both the Racah parameters and the covalency parameter corresponding to this ideal model were estimated by means of a self-consistent calculation. Because of it, we could ignore the values of the Racah's parameters for the free ion. So it is not surprising that our values B_0 and C_0 are not a good fit[6] for the free ion spectrum.

Since Professor Stout was so kind as to inform us of the results of his calculation[6] prior to their publication, it was thought convenient to extend the experimental study of $MnCl_2$ and $MnBr_2$ to the bands which have not as yet been reported.

A Cary Universal Spectrophotometer, Model 14, was

TABLE II. Transitions to excited levels of Mn^{2+} in $MnBr_2$: Experimental values[a] at 78°K and calculated values.

Calculation I: $B_0=700$ cm^{-1}; $C_0=3430$ cm^{-1}; $Dq=700$ cm^{-1}; $\epsilon=0.05$.[a]
Calculation II: $B=950$ cm^{-1}; $C=3280$ cm^{-1}; $Dq=940$ cm^{-1}; $\epsilon=0.15$.[b]

Excited Levels	Exper (10^3 cm^{-1})	Calc I (10^3 cm^{-1})	Calc II (10^3 cm^{-1})
$^4T_{1g}(^4G)$	18.45	18.74	16.5
$^4T_{2g}(^4G)$	21.65	21.78	21.5
$^4A_{1g}(^4G)$[c]	23.084	23.085[c]	23.0
$^4{}_aE_g(^4G)$[c]	23.55	23.15	23.6
$^4T_{2g}(^4D)$[d]	26.52	26.95	27.2
$^4{}_bE_g(^4D)$[c]	27.505	27.72	27.4
$^4T_{1g}(^4P)$[d]	29.95	31.62	31.6
$^4A_{2g}(^4F)$[c]	34.80	36.22	32.8
$^4T_{1g}(^4F)$	37.40	39.16	42.1
$^4T_{2g}(^4F)$	38.75	40.50	42.3

[a] See footnote reference 3.
[b] See footnote reference 6.
[c] These levels have the same subshell configuration as the ground state.
[d] Idem, when configuration mixing is neglected.
[e] Only experimental value used in the calculations.

used for this purpose. Thin plates of $MnCl_2$ and $MnBr_2$ were studied at room temperature and 78°K. For $MnCl_2$, we found, in the ultraviolet region, four additional bands superimposed on a stronger continuous absorption, very intense (optical density $D>4$) even for a sample 0.005-in. thick. The bands are located at 36 500 cm^{-1}, 38 400 cm^{-1}, 40 650 cm^{-1}, and 42 370 cm^{-1}.

In Table I are listed the complete set of observed bands for $MnCl_2$, the assignment to definite electronic levels, and the values of their energies as predicted (a) in footnote reference 3 and (b) by Stout in footnote reference 6. Apart from the differences in the predicted values obtained by the two methods, it is quite remarkable that the crystal field theory enables one to predict exactly the number of bands observed experimentally and also to estimate quite closely their energy.

For $MnBr_2$, the new bands found are: a bell-shaped broad band at 18 450 cm^{-1} and four bands in the ultraviolet region at 29 950 cm^{-1}, 34 800 cm^{-1}, 37 400 cm^{-1}, and 38 750 cm^{-1}. In Table II, we give a summary of predicted and experimental values of the bands of $MnBr_2$. We estimated the predicted values of the energies using the B_0 and C_0 values deduced from the treatment[3] of $MnCl_2$. The value of $\cos^2\psi=1-\epsilon$ was deduced from the position[3] of $^4A_{1g}$. Using this value for ϵ, a good fit was found for the rest of the spectrum when using the reasonable value $Dq=700$ cm^{-1} for the cubic field parameter.

Also in the case of $MnBr_2$, there is a satisfactory agreement of the predictions with experiment, although the agreement is not as good as for $MnCl_2$.

We think it rather unlikely that the Dq value for the bromide should be higher[6] than that of the chloride, since Br precedes Cl in Tsushida's spectrochemical series.[7]

The writer wishes to thank Dr. D. L. Wood of these Laboratories for useful comments on the manuscript. He is also grateful to Professor J. W. Stout for sending a copy of his article prior to its publication.

[1] Y. Tanabe and S. Sugano, J. Phys. Soc. Japan **9**, 753 (1954).
[2] S. Koide and M. H. L. Pryce, Phil. Mag. **3**, 607 (1958).
[3] R. Pappalardo, J. Chem. Phys. **31**, 1050, (1959).
[4] G. Racah, Phys. Rev. (a) **62**, 438 (1942); (b) **63**, 367 (1942); (c) **76**, 1352 (1949).
[5] J. W. Stout, J. Chem. Phys. **31**, 709 (1959).
[6] J. W. Stout, J. Chem. Phys. (to be published).
[7] R. Tsushida, Bull. Chem. Soc., Japan **13**, 388, 436, 471 (1938).

Potential Curves for N_2, NO, and O_2

JOSEPH T. VANDERSLICE, EDWARD A. MASON, AND WILLIAM G. MAISCH
Institute for Molecular Physics, University of Maryland, College Park, Maryland
AND
ELLIS R. LIPPINCOTT
Department of Chemistry, University of Maryland, College Park, Maryland

(Received June 7, 1960)

IN a series of articles[1-3] we have used the Rydberg-Klein-Rees[4] method to obtain potential-energy curves for the bound states of N_2, NO, and O_2. F. Gilmore[5] has pointed out that our working equations are in error. Equations (4), (5), and (6) of footnote reference

TABLE I. Potential energy of the $A\ ^3\Sigma_u^+$ state of O_2.

v	V(cm^{-1})	$r_{max}(A)$	$r_{min}(A)$	V(ev)	T_e+V(ev)
(a) Experimental data and vibrational assignments of Herzberg					
0	383.1	1.608	1.461	0.04751	4.5343
1	1127	1.683	1.421	0.1397	4.6265
2	1838	1.743	1.397	0.2279	4.7147
3	2513	1.798	1.380	0.3116	4.7984
4	3149	1.851	1.366	0.3905	4.8773
5	3742	1.906	1.353	0.4640	4.9508
6	4284	1.966	1.342	0.5313	5.0181
7	4770	2.034	1.333	0.5915	5.0783
8	5188	2.117	1.327	0.6433	5.1301
9	5524	2.231	1.322	0.6849	5.1717
(b) Experimental data from Herzberg and vibrational assignments of Broida and Gaydon					
0	397[a]	1.600	1.454	0.04923	4.4382
1	1172[a]	1.668	1.411	0.1453	4.5343
2	1916	1.723	1.385	0.2375	4.6265
3	2627	1.774	1.366	0.3257	4.7147
4	3302	1.823	1.350	0.4094	4.7984
5	3938	1.873	1.338	0.4883	4.8773
6	4530	1.926	1.327	0.5618	4.9508
7	5073	1.984	1.318	0.6291	5.0181
8	5559	2.052	1.311	0.6893	5.0783
9	5977	2.135	1.305	0.7411	5.1301
10	6313	2.247	1.300	0.7828	5.1717

[a] These values have been obtained by extrapolation.

1 should be replaced by:

$$f=(8\pi^2\mu c/h)^{-1}\sum_{i=1}^{n}(\omega x)_i^{-1}\ln W_i, \quad (1)$$

$$g=(2\pi^2\mu c/h)^{\frac{1}{2}}\sum_{i=1}^{n}\{2\alpha_i(\omega x)_i^{-1}\times[(U_n-U_{i-1})^{\frac{1}{2}}-(U_n-U_i)^{\frac{1}{2}}]+(\omega x)_i^{-\frac{1}{2}}[2B_i-\alpha_i(\omega x)_i^{-1}\omega_i]\ln W_i\}, \quad (2)$$

$$W_i=\left|\frac{[\omega_i^2-4(\omega x)_iU_i]^{\frac{1}{2}}-2(\omega x)_i^{\frac{1}{2}}(U_n-U_i)^{\frac{1}{2}}}{[\omega_i^2-4(\omega x)_iU_{i-1}]^{\frac{1}{2}}-2(\omega x)_i^{\frac{1}{2}}(U_n-U_{i-1})^{\frac{1}{2}}}\right|. \quad (3)$$

We have repeated the calculations for all the bound states previously reported for these molecules. The only differences in numerical results were found for the $A\,^3\Sigma_u^+$ and $B\,^3\Sigma_u^-$ states of O_2. Here the error is about 1% at the uppermost levels. For all other states, the results were essentially the same. The maximum differences found were two parts in the last figures in some of the states, and this occurred only at the uppermost levels. The new curves (calculated with the same data) for the $A\,^3\Sigma_u^+$ and $B\,^3\Sigma_u^-$ states are given in Tables I and II. None of the conclusions drawn are affected by these new results.

The authors are extremely grateful to Forrest Gilmore for informing them of their error before publication of his own work.

We have had a number of inquiries concerning the fitting of the vibrational-energy levels. This can be done in either of two ways. If G_v represents the vibrational energy, then $G_v/(v+\frac{1}{2})$ can be least-squared as a function of $v+\frac{1}{2}$ to yield ω_i and ωx_i, or ΔG_v can be least-squared as a function of $v+1$ to yield the two constants. However, if this latter method is used, the expression for G_v contains a constant A_i, i.e.,

$$G_v=A_i+\omega_i(v+\tfrac{1}{2})+(\omega x)_i(v+\tfrac{1}{2})^2.$$

The reason for this is that U and G_v must be measured from the same zero of energy. If this second procedure is used, then the above equations are formally the same except that U_n, U_i, and U_{i-1} are replaced by U_n-A_i, U_i-A_i, and $U_{i-1}-A_i$, respectively. This procedure has been used in the cases of N_2, NO, and O_2.

TABLE II. Potential energy of the $B\,^3\Sigma_u^-$ state of O_2.

v	$V(\text{cm}^{-1})$	$r_{max}(A)$	$r_{min}(A)$	$V(\text{ev})$	$T_e+V(\text{ev})$
0	348.2	1.683	1.531	0.04318	6.2187
1	1036	1.756	1.486	0.1285	6.3040
2	1701	1.813	1.459	0.2110	6.3865
3	2343	1.865	1.438	0.2905	6.4660
4	2960	1.914	1.420	0.3671	6.5426
5	3553	1.962	1.405	0.4405	6.6160
6	4114	2.009	1.392	0.5101	6.6856
7	4648	2.057	1.380	0.5764	6.7519
8	5149	2.112	1.373	0.6384	6.8139
9	5614	2.170	1.365	0.6961	6.8716
10	6043	2.232	1.356	0.7493	6.9248
11	6431	2.299	1.347	0.7975	6.9730
12	6777	2.379	1.344	0.8403	7.0158
13	7077	2.470	1.340	0.8776	7.0531
14	7332	2.576	1.336	0.9092	7.0847
15	7542	2.696	1.335	0.9352	7.1107
16	7711	2.865	1.334	0.9561	7.1316
17	7844	3.046	1.335	0.9726	7.1481
18	7946	3.274	1.342	0.9853	7.1608
19	8021	3.551	1.342	0.9946	7.1701
20	8074	3.909	1.348	1.0012	7.1767

[1] J. T. Vanderslice, E. A. Mason, and E. R. Lippincott, J. Chem. Phys. **30**, 129 (1959).
[2] J. T. Vanderslice, E. A. Mason, and W. G. Miasch, J. Chem. Phys. **31**, 738 (1959).
[3] J. T. Vanderslice, E. A. Mason, and W. G. Maisch, J. Chem. Phys. **32**, 515 (1960).
[4] (a) R. Rydberg, Z. Physik **73**, 376 (1931); (b) O. Klein, Z. Physik **76**, 226 (1932); (c) A. L. G. Rees, Proc. Phys. Soc. (London) **59**, 998 (1947); (d) J. T. Vanderslice, E. A. Mason, E. R. Lippincott, and W. G. Maisch, J. Mol. Spectroscopy **3**, 17 (1959).
[5] Present address: Rand Corporation, Santa Monica, California.

Note on Hurley's "Improved Molecular Orbitals and the Valence Bond Theory"*

P. PHILLIPSON AND R. S. MULLIKEN

Laboratory of Molecular Structure and Spectra, Department of Physics, University of Chicago, Chicago 37, Illinois

(Received June 13, 1960)

SOME time ago[1] we published the results of some calculations for H_2 which showed that the usual LCAO-MO wave functions of the lowest excited singlet and triplet states can be enormously improved by varying the orbital exponents (effective nuclear charges) ζ separately for the $\sigma_g 1s$ (i.e., $1s_a+1s_b$) and $\sigma_u 1s$ (i.e., $1s_a-1s_b$) MO's, instead of keeping them equal. For small and medium R values, we found that the energy is minimized for $\zeta_g>\zeta_u$. Independently and earlier, Huzinaga[2] arrived at the same conclusions. The emphasis in these calculations was on getting improved MO's, applicable of course primarily in the range of R values near R_e where wave functions of the MO type may be expected to be fairly good approximations.

As is well known, the usual LCAO-MO function with $\zeta=\zeta_g=\zeta_u$ is identical, for the $\sigma_g 1s\,\sigma_u 1s$, $^1\Sigma_u^+$ or V state, with the closed-shell H^- approximation to the $^1\Sigma_u^+$ VB function, namely $1s_a(1)1s_a(2)-1s_b(1)1s_b(2)$ times singlet spin function, for which the energy-minimizing ζ is 0.6875 for free H^-. As is also well known, the actual VB wave function for the V state must be a linear combination, whose coefficients vary with R, of the pure ionic $^1\Sigma_u^+$ function and the two covalent $^1\Sigma_u^+$ functions ($1s2s$ and $1s2p\sigma$) corresponding to one normal and one 2-quantum excited atom.[3] Since in zeroth approximation the potential energy curves be-

longing to the ionic and the two covalent functions must cross near 10 a.u., but must interact strongly near 10 a.u., the actual V state, though to a large extent ionic below 10 a.u., nust become pure covalent above 10 a.u. and dissociate to one normal and one excited H atom.

In our communication[1] we assumed without checking, that our two-parameter (ζ_g, ζ_u) variation function would tend as $R\to\infty$ toward the closed-shell H^- approximate pure ionic function. However, Hurley[4] has recently pointed out that our variation function for energy-minimizing values of ζ_g and ζ_u actually goes as $R\to\infty$ into a linear combination of an open-shell H^- pure ionic and a $1s2s$-like covalent function. Hurley has also pointed out[5] that on introducing an additional parameter (namely, the ratio of the ionic and covalent terms), the function goes over smoothly as $R\to\infty$ into a rather good approximation to a $1s2s$ covalent function. (Presumably, however, it should go into a $1s2hy$ function, where $2hy$ is a $2s-2p\sigma$ hybrid.)

While the indicated behavior of our function as $R\to\infty$ is very interesting, we feel that the main significance of our function is in the framework of MO theory, at small and moderate R values. But also, we have found, in calculations made subsequent to our original communication, that in a range of R values greater than R_e, but less than the crossing point of the pure ionic and covalent zeroth order potential energy curves near 10 a.u., the energy of our function is actually minimized with $\zeta_g=\zeta_u\approx 0.7$. In other words, the closed-shell ionic function is in this range the best wave function obtainable within the limitations of our two-parameter variation function. These calculations show that at 2.5 A (4.73 a.u.) the energy of our function is minimized with $\zeta_g=\zeta_u\approx 0.7$, but also indicate an incipient second minimum of *higher* energy for $\zeta_g\approx 0.9$, $\zeta_u\approx 0.5$. At 4.0 A (7.56 a.u.) we find two definite minima, one for $\zeta_g=\zeta_u\approx 0.7$, the second near $\zeta_g=0.1$, $\zeta_u=0.3$, but this time the second minimum is appreciably (0.15 ev) *lower* than the first.[6] In other words, the $R\to\infty$ asymptotic behavior described by Hurley has now begun to take over. Nevertheless, our results indicate that there is a definite range of R where the pure ionic function with $\zeta_g=\zeta_u$ represents the best approximation within the limitations of our variation function. Our calculations are being continued in order to explore more thoroughly the behavior of ζ_g and ζ_u for the two minima in this range and to delineate more precisely the boundaries of this range.

We wish to thank Dr. Hurley for his suggestions and enlightening communications with us.

* This work was assisted by a grant from the National Science Foundation to the University of Chicago.

[1] P. Phillipson and R. S. Mulliken, J. Chem. Phys. **28**, 1248 (1958).

[2] S. Huzinaga, Progr. Theoret. Phys. **19**, 125 (1957).

[3] For relevant calculations, see J. T. Lewis, Proc. Phys. Soc. (London) **68**, 632 (1955).

[4] A. Hurley, J. Chem. Phys. **32**, 301 (1960).

[5] This is implied in footnote reference 4 and was made clear in a private communication to us from Dr. Hurley.

[6] The energy at 4.0 A for $\zeta_g=\zeta_u=0.7$ is 10.79 ev, and not 10.98 ev as reported in footnote reference 1. This is to be compared with 10.64 ev with $\zeta_g=1.0$, $\zeta_u=0.3$.

Comment on the Homogeneous Exchange Reaction Between Hydrogen and Deuterium

A. Cimino, E. Molinari, and G. G. Volpi

Istituto di Chimica Generale ed Inorganica dell'Università di Roma, Centro per la Chimica Generale del C.N.R., Rome, Italy

(Received May 12, 1960)

In a recent theoretical paper by I. Shavitt[1] on the elementary reactions of the type $H+H_2=H_2+H$, existing experimental data are reviewed, including our previous work on the hydrogen-deuterium exchange.[2]

A comment seems appropriate on some remarks by Shavitt regarding the perturbing action of oxygen, since our experiments have been discussed further, together with additional data, in a previous paper.[3] At the same time we wish to correct a trivial arithmetical error present in our paper, which leads to an inconsistency, as pointed out by Shavitt.

In our paper[2] we stated that the experiments by Farkas and Farkas[4] (F and F), and by Van Meersche (VM)[5] were effected by the diffusion of oxygen through the walls of the reaction vessel. Shavitt comments on this point by remarking that some of the measurements of VM were obtained at temperatures low enough to exclude any oxygen diffusion through the walls. These measurements are in good agreement with VM's measurements at higher temperatures, as well as with F and F's measurements. It would therefore appear that oxygen diffusion at high temperature must be irrelevant for the exchange reaction. We wish to point out that a heterogeneous effect of the oxygen can actually be present at all temperatures. In order to eliminate the oxygen adsorbed on the walls, the reaction vessel must be outgassed at around 1100°C with a vacuum jacket around it. If this precuation is not taken, higher reaction rates are obtained, yielding, however, the same activation energy. The effect clearly showed up in our case[2] with a vessel which had been partially degassed; measurements were reproducible, and yielded the same activation energy, but higher exchange rates were observed than after further outgassing. The cause for the observed higher rates has been attributed by us to a higher stationary concentration of atoms. We recall that atoms are produced by a heterogeneous process. In addition to the above-mentioned effect, a heterogeneous production of HD molecules, characterized by an activation energy of about 17 kcal/mol, becomes increasingly important at lower temperatures.[3]

Thus, of the whole temperature interval studied by us (from 800 to 1010°K), only the interval 910 to 1010°K is free from heterogeneous production of HD molecules, and can be examined for the homogeneous reaction.

In our paper, the ratio k_3/k_4 between the velocity constants of the reactions $D+H_2$, and $H+D_2$, because of a trivial arithmetical error, was given as 1.6 at 1000°K. The value for k_3/k_4 should be corrected as 1.31. This correction leaves the values of the over-all rate a (Table I of footnote reference 2) unchanged within 2%. The ratio between the values of F and F and our values therefore remains 2. The same factor may be assumed for the *ortho-para* reactions, as already discussed.[2] The only values which are affected are the experimental k's for the exchange reaction.

We would like, however, to comment briefly on this point. It can be verified that in our kinetic treatment the expansion in series and the limiting condition (24), which allowed us to calculate the value of k_3/k_4, are in fact equivalent to imposing the additional condition $[H]/[D]=\text{const}=(K_{H_2}/K_{D_2})^{\frac{1}{2}}$ $(=1.31$ at 1000°K). In fact, substitution of $k_3/k_4=(K_1/K_2)^{\frac{1}{2}}=(K_{H_2}/K_{D_2})^{\frac{1}{2}}$ in the equation $[H]/[D]=(k_3[H_2]+k_6[HD])/(k_4[D_2]+k_5[HD])$ [Eq. (10)] which gives the variation of $[H]/[D]$ in the course of the reaction shows that $[H]/[D]$ becomes constant (K_{H_2}, K_{D_2} dissociation constants of H_2 and D_2; $K_1=k_3/k_5$; $K_2=k_4/k_6$). If the assumption $[H]/[D]=\text{const}$ is removed, and if no other assumption is made, then it becomes impossible to calculate the above ratio from experimental data alone. The same considerations apply to the k_3/k_4 values given by F and F and by VM. The only significant quantities which can be derived from this type of experiment are the over-all rate [proportional to $k_3k_4/(k_3+k_4)$] and the activation energy.

We can summarize our comments as follows:

(a) In the temperature interval 910 to 1010°K, where the heterogeneous production of HD molecules has become negligible, elimination of the perturbing effect of oxygen adsorbed at the walls of the reaction vessel leads to values of the over-all rate constant, for the exchange reaction, which are lower by a factor of 2 with respect to the values previously determined by F and F and by VM.

(b) The kinetics to which the reaction conforms is such as to make the determination of the ratio k_3/k_4 impossible, unless additional assumptions are introduced. From the theoretically determined values of the rate constants, a comparison can be made with the over-all rate of exchange $k_3/k_4/(k_3+k_4)$, which has been experimentally determined at various temperatures.

We wish to express our thanks to Professor J. O. Hirschfelder and to Dr. I. Shavitt for helpful discussions on this subject.

[1] I. Shavitt, J. Chem. Phys. **31**, 1359 (1959).
[2] G. Boato, G. Careri, A. Cimino, E. Molinari, and G. G. Volpi, J. Chem. Phys. **24**, 783 (1956).
[3] A. Cimino, E. Molinari, and G. G. Volpi, Gazz. chim. ital. **86** 609 (1956).
[4] A. and L. Farkas, Proc. Roy. Soc. (London) **A152**, 152 (1935).
[5] M. Van Meersche, Bull. soc. chim. Belg. **60**, 99 (1951).

Erratum: NMR Spectra of Some Simple Epoxides

[J. Chem. Phys. **32**, 1378 (1960)]

C. A. Reilly and J. D. Swalen
Shell Development Company, Emeryville, California

(Received June 15, 1960)

ON page 1383, the captions for Figs. 3 and 4 should be interchanged.

Erratum: Infrared and Raman Spectra of Fluorinated Ethanes XII. 1,1,2,2-Tetrafluoroethane

[J. Chem. Phys. **32**, 899 (1960)]

Peter Klaboe and J. Rud Nielsen
Department of Physics, University of Oklahoma, Norman, Oklahoma

(Received June 13, 1960)

THE last two sentences preceding the Discussion section on page 906 should read as follows:

Taking $a=2.6$ A, one finds

$$E_r \text{ (gauche)} = 1020 \text{ cal/mole}, \quad E_r \text{ (trans)} = 0.$$

These values agree quite well with those observed.

Erratum: Mechanics of Atomic Recombination Reactions

[J. Chem. Phys. **32**, 1001 (1960)]

Don L. Bunker
Los Alamos Scientific Laboratory, University of California, Los Alamos, New Mexico

(Received May 18, 1960)

EQUATIONS (5) and (6) should be corrected to read

$$\mu\ddot{r}-\mu r\dot{\theta}^2+dV/dr=0 \tag{5}$$

and

$$\tfrac{1}{2}\mu\dot{r}^2=E(1-b^2/r^2)-V. \tag{6}$$

Erratum: Reflected Shock Technique for Studying Fast Chemical Reactions

[J. Chem. Phys. 30, 257 (1959)]

ROGER A. STREHLOW AND ARTHUR COHEN

Ballistic Research Laboratories, Aberdeen Proving Ground, Maryland

(Received May 16, 1960)

ON p. 262, in our discussion of the appearance Mach number for bifurcation, we used the symbol M_s^* incorrectly in several places. To correct this usage, let us define M_s^+ as the experimental appearance Mach number and M_s^* as Mark's[1] theoretically calculated (and constant) Mach number.

The paper should then be corrected as follows:

Column 1, line 28: replace M_s^* by M_s

Column 2, lines 32, 33, and 53; replace M_s^* by M_s^+

[1] Herman Mark, *The Interaction of the Reflected Shock Wave with a Boundary Layer in a Shock Tube*, NACA TM 1418, March, 1958.

Erratum: f^2 Configuration in Crystalline Field

[J. Chem. Phys. 32, 573 (1960)]

ROBERT A. SATTEN AND JACK S. MARGOLIS

Department of Physics, University of California, Los Angeles, California

(Received June 9, 1960)

IN Table IIE: $(^3H_6 \| V_6 \| {}^3P_2) = (40/1287)(11)^{\frac{1}{2}}$ i.e., $(11)^{\frac{1}{2}}$ replaces $(3/11)^{\frac{1}{2}}$.

In Table III, p. 578, $^1\Gamma_1$, V_6: $(^1G_4\ ^1\Gamma_1 \mid V_6 \mid {}^1I_6\ ^1\Gamma_1) = -(4480/1573)(7)^{\frac{1}{2}}$, i.e., $(7)^{\frac{1}{2}}$ was omitted.

All the tables were checked again and no other misprints were found.

Erratum: Electrical Properties of Poly-Copper Phthalocyanine

[J. Chem. Phys. 32, 324 (1960)]

A. EPSTEIN AND B. S. WILDI

Research and Engineering Division, Monsanto Chemical Company, Dayton, Ohio

(Received June 6, 1960)

ON p. 327, fifth line from top, left-hand column, the expression R/δ should be replaced by R/ρ.

On p. 327, last line, right-hand column, the minus sign in $\rho=\rho_0 \exp(-\Delta E/2kT)$ should be replaced by a positive sign, and the expression should read $\rho=\rho_0 \exp(+\Delta E/2kT)$.

Notes

On the Structure of Dilute Solutions of Metals

E. CHARLES EVERS

John Harrison Laboratory of Chemistry, University of Pennsylvania, Philadelphia 4, Pennsylvania

(Received February 26, 1960)

RECENTLY, Symons[1] has proposed that the properties of dilute solutions of metals in a variety of solvents may be accounted for adequately in terms of two solute species, namely, ϵ^-, the "trapped" or "solvated" electron and M_2, a diamagnetic pair formed by the coupling of two electrons and two metal ions. He has termed this a hybrid model[2] which combines elements of the cavity model of Ogg and others[3] and the expanded metal or mass action model of Becker, Lindquist, and Alder.[4] This interpretation was based primarily upon a correlation of magnetic and optical data.[1,2,5]

The purpose of this note is to introduce evidence to the effect that the presence of monomers M, or "ion-pairs"[6] cannot be ignored except in special cases, e.g., at infinite dilution or perhaps in solutions in solvents such as the polyethers, which are diamagnetic. This conclusion is based upon analyses of the conductance data for solutions of sodium in ammonia[7] due to Kraus[8] and of lithium in methylamine,[9] which at present are the only quantitative data showing the concentration dependence of the phenomenon in question down to concentrations of the order of $1\times10^{-5}N$. Values of k_1 for the equilibrium $M^+ + \epsilon^- = M$, and k_2 for the equilibrium $M = \frac{1}{2}M_2$, derived from conductance data, employing methods described previously[7] are presented in Table I. Also tabulated are the calculated concentrations of the several species at two metal concentrations.[10] It is evident from the results of Table I that the presence of monomers in these solutions can hardly be neglected unless the method of analysis is completely invalid. It is also apparent that the relative concentrations of monomers are higher in solutions of methylamine than in ammonia, a result which is not

TABLE I. Mass action constants and the concentrations of various species derived from conductance data.

System	$N\times10^3$ $[M^+]=[\epsilon^-]$	$[M]$	$[M_2]$	[Metal]
Na in NH_3 (−34°)	1.02	0.07	0.004	1.1
$k_1=7.23\times10^{-4}$; $k_2=27.0$	8.47	1.32	1.28	12.4
Li in $MeNH_2$ (−78°)	0.30	0.72	0.015	1.1
$k_1=5.79\times10^{-4}$; $k_2=5.42$	1.32	6.23	1.14	9.8

unexpected; in fact, the monomer is the most prevalent species in methylamine in the concentration range recorded in Table I. Both systems are strongly paramagnetic,[3a,5] which is certainly in accord with the conductivity results.

Let us now examine the basis of the Symons proposal in more detail. It was pointed out that solutions which exhibited an absorption band maximum in the visible region only, at about 15 000 cm^{-1}, as those in the diamines,[5] were diamagnetic; those possessing a maximum in the infrared only, at about 6700 cm^{-1}, as dilute solutions in ammonia, were paramagnetic. If both bands were present, the solutions were also paramagnetic. Without discussing arguments for their choice the infrared band was identified with the species e^- and the visible band was attributed to the species M_2. There was no third band in any one system which might be identified with the species M.[11]

We feel that it is very probable that the presence of monomers cannot be detected optically in many cases. It seems likely, judging by the results discussed above, that the band maximum for the monomer lies close to that of the dimer and that band overlapping may often render the two indistinguishable. To illustrate the variability of the spectral data let us consider results cited for solutions of lithium. "Dilute" solutions in methylamine[11] at $-60°$ show practically a continuously increasing absorption with increasing wave length between 18 000 and 11 000 cm^{-1}, with a slight inflection at approximately 14 500 cm^{-1}. At higher metal concentrations,[11] the inflection disappears and at $-75°$ a maximum appears at about 8000 cm^{-1}; at $-55°$ this has shifted to 7350 cm^{-1}. Other authors[12] report band maxima at both 14 000 cm^{-1} and 7000 cm^{-1}. We have recently investigated the visible absorption spectrum at $-78°$ and have established the presence of a band maximum at 14 100 cm^{-1} for solutions ranging in concentration from 1×10^{-3} to $0.03N$.[13] Solutions in ammonia[11] show a band maximum at approximately 6700 cm^{-1}. The positions and relative intensities of the bands are temperature dependent. It is of interest to note that a solution approximately $1\times10^{-4}N$ in potassium in methylamine at $-78°$ is colored deep blue to the eye; at room temperature it is colorless.[14] It would be of considerable interest to have quantitative conductivity data on this system.

On the basis of the results cited above we feel there are not sufficient data available at present concerning the optical properties of metal solutions to warrant a decision regarding the relative importance of monomers in determining the state of these systems. The results of conductivity measurements would indicate their importance, expecially in solutions of lithium in methylamine. Paramagnetic resonance studies do not distinguish between the species M and e^-, but the results obtained are not in disagreement with those deduced from conductivity measurements on the systems cited before. Data are badly needed showing the concentration dependence of the various phenomena. In this way mass action constants may be calculated and compared. We have recently completed such a study on the optical density of lithium solutions in methylamine;[13] the results will be made available soon.

[1] M. C. R. Symons, J. Chem. Phys. **30**, 1628 (1959).
[2] M. C. R. Symons, Quart. Revs. (London) **13**, 99 (1959).
[3] (a) R. A. Ogg, J. Chem. Phys. **14**, 114 (1946); (b) T. L. Hill, *ibid.* **16**, 394 (1948); (c) W. N. Lipscomb, *ibid.* **21**, 52 (1953).
[4] E. Becker, R. H. Lindquist, and B. J. Alder, J. Chem. Phys. **25**, 971 (1956).
[5] (a) G. W. A. Fowles, W. R. McGreger, and M. C. R. Symons, J. Chem. Soc. (**1957**), 665; (b) H. C. Clark, A. Horsfield, and M. C. R. Symons, *ibid.* **1959**, 2478.
[6] C. A. Kraus, J. Chem. Ed. **30**, 83 (1953).
[7] E. C. Evers and P. W. Frank, Jr., J. Chem. Phys. **30**, 61 (1959).
[8] C. A. Kraus, J. Am. Chem. Soc. **43**, 749 (1921).
[9] D. M. Berns, E. C. Evers, and P. W. Frank, Jr., J. Am. Chem. Soc. (to be published).
[10] Total metal concentrations quoted by Clark *et al* (footnote reference 5b) for solutions of potassium in ammonia, who used different values of k_1 and k_2 in their calculations, are somewhat in error since they neglected to double the dimer concentration. Activity corrections were also neglected.
[11] Solutions of potassium in methylamine, however, possess a band maximum at 12 500 cm^{-1} as well as one at 15 100 cm^{-1} [H. Baldes and J. W. Hodgins, Can. J. Chem. **33**, 411 (1955)]; also, a band has been observed at 12 500 cm^{-1} when a large amount of sodium iodide was added to a dilute solution of sodium in ammonia (footnote reference 5b); it was suggested that this band may be due to the monomer.
[12] G. Hohlstein and U. Wannagat, Z. anorg. u. allgem. Chem. **288**, 193 (1956).
[13] M. H. Shatz, Ph.D. thesis, University of Pennsylvania, February, 1958.
[14] J. Varimbi (unpublished observations, this Laboratory).

Jahn-Teller Distortions in Cyclobutadiene, Cyclopentadienyl Radical, and Benzene Positive and Negative Ions

LAWRENCE C. SNYDER
Bell Telephone Laboratories, Inc., Murray Hill, New Jersey

(Received April 25, 1960)

JAHN and Teller[1] proved that orbital electronic degeneracy and stability of the nuclear configuration are incompatible except for linear molecules. New symptoms of such configurational instability have appeared as poor resolution in the ESR spectra of certain aromatic negative ions.[2,3] Quantitative molecular orbital descriptions of energies and bond lengths have been begun here and results are presented for the smaller cyclic polyenes which were earlier described by Liehr[4]: cyclobutadiene (C_4H_4), cyclopentadienyl radical (C_5H_5), and benzene positive ion ($C_6H_6^+$); and, in addition, benzene negative ion ($C_6H_6^-$).

Basic assumptions set forth by Lennard-Jones[5] and adopted by Liehr[4] are employed in this procedure: the total energy E is taken to be the sum of a π electronic part and a σ bond compression part; the resonance

TABLE I. Computed properties of symmetrical and distorted molecules. Units: energy[a] in kcal/mole, bond length in A.

Property	C_4H_4		C_6H_6		$C_6H_6^{+,-}$	
Distorted configuration of energy minimum						
Symmetry		D_{2h}		C_{2v}		D_{2h}
E_{min}		−108.800		−137.284		−163.103
Bond lengths	12, 34	1.540	12, 51	1.397	12, 34	
	23, 41	1.330	23, 45	1.356	45, 61	1.371
			34	1.442	23, 56	1.422
Spin density			1	0.428	1, 4	0.000
			2, 5	0.025	2, 3, 5, 6	0.250
			3, 4	0.261		
Distorted configuration of energy saddle point						
Symmetry				C_{2v}		D_{2h}
E_{sp}				−137.257		−162.869
Bond lengths			12, 51	1.372	12, 34	1.402
			23, 45	1.426	45, 61	
			34	1.349	23, 56	1.358
Spin density			1	0.000	1, 4	0.344
			2, 5	0.385	2, 3, 5, 6	0.078
			3, 4	0.115		
Symmetrical configuration						
Symmetry		D_{4h}		D_{6h}		D_{6h}
E_{sym}		−87.891		−135.204		−161.488
Bond length	all	1.401	all	1.385	all	1.386
$E_{min}-E_{sym}$	this study	−20.909		−2.080		−1.615
	Liehr[b]	−20.903		−1.602		−1.405
$E_{min}-E_{sp}$	this study			−0.027		−0.234
	Liehr[b]			−0.001		−0.139

[a] The energy is zero when all bond lengths are 1.54 A and each π electron is localized in a carbon π atomic orbital.
[b] Footnote reference 4.

integral β and the compression energy of a σ bond are assumed functions of bond distance; and a consistent relation of equilibrium bond distance to bond order is adopted. The absolute magnitude of β has been fixed so that $\beta(1.3903515\ \text{A}) = -29.913186$ kcal/mole.[6] The ground state π electronic wave function is built from Slater determinants of real molecular orbitals which are determined with a secular equation appropriate for the bond distances of the symmetrical or distorted instantaneous nuclear configuration. The properties of the molecule in a symmetric configuration are computed from a wave function, which is a linear combination of the degenerate lowest energy Slater determinants, having the given nuclear symmetry. An iterative procedure is employed to find the nuclear configuration which minimizes the total energy. The secular equation for a configuration slightly displaced from the symmetrical form is first solved and Coulson bond orders together with corresponding equilibrium bond distances are computed. The secular equation is then revised to correspond to these bond distances. These steps are repeated until no significant change in E or bond lengths occurs upon iteration. Any symmetry assumed for the initial distorted configuration is maintained through all iterations. The wave function for a distorted configuration in which the orbital degeneracy is removed is taken to be the lowest energy single determinant.

Liehr[4] determined the symmetry of displacements which remove the orbital degeneracy to be B_{1g} for C_4H_4, E_2' for C_6H_6, and E_{2g} for $C_6H_6^+$. In those cases in which a degenerate pair of displacements interact with the electronic structure, he found configurations which were minima and saddle points of the energy. In Table I are reported the newly computed properties of these configurations. Atoms are numbered consecutively around the ring of each molecule; bonds are denoted with pairs of integers.

There is qualitative agreement with the results of Liehr.[4] However, the energy difference between the symmetrical (sym) and minimal (min) energy configurations of C_6H_6 and $C_6H_6^+$ are somewhat larger, as are also the differences in energy between the minimal and saddle point (sp) configurations.

Under the assumptions of this study, all properties reported in Table I for $C_6H_6^+$ are computed to be identical with those for $C_6H_6^-$. The exact correspondence between computed electronic properties of aromatic positive and negative ions was shown to hold for all values of β.[3,7] The 234-cal energy difference between minimal and saddle point configurations of $C_6H_6^-$ is not enough to cause, at room temperature, the trapping of molecules in a statically deformed configuration of minimum energy. With such trapping, the spin density would be localized on four equivalent carbons and would lead to a five-line ESR spectrum. The observed spectrum[3] has seven lines and corresponds to equivalence of the six carbon atoms.

The present computational procedure is being applied to the study of Jahn-Teller distortions of larger aromatic systems and these results will be detailed later.

[1] H. A. Jahn and E. Teller, Proc. Roy. Soc. (London) **A161**, 220 (1937).
[2] M. G. Townsend and S. I. Weissman, J. Chem. Phys. **32**, 309 (1960).
[3] T. R. Tuttle, Jr., and S. I. Weissman, J. Am. Chem. Soc. **80**, 5342 (1958).
[4] A. D. Liehr, Z. physik Chem. (Frankfort) **9**, 338 (1956); also, to be published.
[5] J. E. Lennard-Jones, Proc. Roy. Soc. (London) **A158**, 280 (1937).
[6] C. A. Coulson and S. L. Altman, Trans. Faraday Soc. **48**, 293 (1952).
[7] A. D. McLachlan, Mol. Phys. **2**, 271 (1959).

Relations between Ultraviolet and Visible Absorption Peaks of Iodine Solutions*

JOHN WALKLEY, DAVID N. GLEW,† AND JOEL H. HILDEBRAND

Department of Chemistry, University of California, Berkeley, California

(Received February 22, 1960)

THE discovery by Benesi and Hildebrand[1] of strong ultraviolet absorption by nonviolet iodine solutions has led to extensive use of uv absorption for the study of electron-donor-acceptor complexes.

Especially noteworthy have been the papers by R. S. Mulliken[2] and co-workers. Infrared absorption also is now being widely used to throw additional light upon such complexes. But although the original observations were suggested by nonviolet colors of iodine in aromatic solvents, these colors were then considered, in the series benzene to mesitylene, to be mainly the effect of the invasion of the visible region by tails of the uv bands.

TABLE I. Wavelength of visible absorption peaks in mμ of iodine solutions and ionization potentials of the solvents, I_D

Solvent	I_D	λ_{vis}
C_7F_{16}	12.08	523
$CCl_2F\cdot CClF_2$	11.99	522
CCl_4	11.47	517
$CHCl_3$	11.42	512
CH_2Cl_2	11.35	506
CH_3CHCl_2	11.07	504
CH_3CH_2Cl	10.97	504
CH_2Br_2	10.48	500
CH_2ClCH_2Cl	11.08	497
CH_2BrCH_2Br	...	496
C_2H_5Br	10.29	490
C_2H_5I	9.33	478
c-C_6H_{12}	9.88	523
n-C_7H_{16}	10.06	522
i-C_8H_{18}	10.24*	522
C_6H_5Cl	9.07	508
C_6H_5Br	8.98	503
C_6H_6	9.24	502
c-$C_6H_{11}Cl$	...	498
$C_6H_5CH_3$	8.82	496
p-$C_6H_4(CH_3)_2$	8.55	495
s-$C_6H_3(CH_3)_3$	8.39	489
C_6H_5I	8.73	493

In 1956 Glew and Hildebrand[3] reported that the entropy of solution of iodine in the two dichloroethanes is slightly less than would be expected for a purely violet, "regular" solution, suggesting the presence of complexes. We noticed, also, that the colors of these solutions are not pure violet, and, upon determining wavelengths of the visible peaks in these and other solvents, obtained values shifting to shorter wavelength in the following order:

C_7F_{16}, CCl_4, $CHCl_3$, CH_2Cl_2, 1,1-$C_2H_4Cl_2$, 1,2-$C_2H_4Cl_2$, 1,2-$C_2H_4Br_2$, C_2H_5I.

This series is almost certainly in the order of decreasing ionization potential, like the blue shift reported by McConnell, Ham, and Platt.[4]

Solvents used were of "spectroscopic" grade wherever possible, all others C.P. grade reagents, further purified by appropriate procedures. Previous to spectra determinations, all solvents were run through a column of silica gel. The iodine used had been twice sublimed and dried over phosphorous pentoxide. Solutions were made up just prior to use. In no case was there any change in optical density with time. All solutions were of approximately the same molarity, 5×10^{-4}. The accurate molarity of all solutions was determined after optical measurements had been made by direct titration against thiosulfate. All absorption measurements were made on a Beckman D.U. spectrophotometer, the solutions under examination held at 25.00±0.1°C by efficient thermostating of the cell block. 10-mm "matched" silica cells were used, the comparison cell containing the pure solvent.

Table I gives the wavelength ($m\mu$) found for the positions of the visible peaks (λ_{vis}) for iodine solutions in a wide range of hydrocarbon and halogen-substituted hydrocarbon solvents, together with the value of the ionization potential (I_D) of the solvent (donor) molecule. The values of the ionization potentials are taken from the photoionization data of Watanabe[5] except for isooctane, where the value was obtained from electron-impact studies. The solvents are listed in two groups in accord with their different behavior as seen in Fig. 1, where the wavelength of the visible peaks are plotted against the corresponding ionization potentials. The two roughly parallel lines are separated by approximately 1.8 ev. It is seen that for iodine in the monohalogen substituted benzene solvents the position of λ_{vis} places them with the aromatics. No point for cyclochlorohexane is represented because no value of I_D could be found. The value of I_D for n-C_7F_{16} is, perhaps, questionable, but in the fluorocarbon solvents iodine, exhibits a visible absorption peak close to that for iodine in the vapor state.

The difference in the effects of the two groups of solvents is evidently correlated with the fact that the halogenated hydrocarbons are n-electron-donor and the aromatic compounds are π donors. It is noteworthy that the two hydrocarbons fall with the latter though it is doubtful if the correlation with ionization potential is meaningful for these solvents. Bromobenzene evidently acts as a π donor despite the possibility of I_2-halogen interaction.

It may be mentioned that the wavelengths of the uv peaks also divide the solvents into the same two groups.

The principal results are: (a) that the visible absorption peak of dissolved iodine shifts strongly to shorter wavelengths linearly with decreasing ionization potential of the solvent, and (b) π donors and n donors fall in this respect into two quite distinct groups.

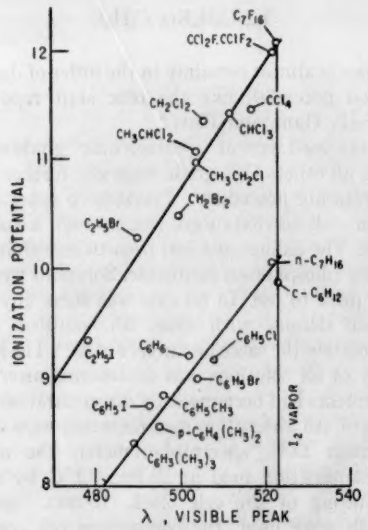

FIG. 1.

* This work has been supported by the National Science Foundation.

[1] H. A. Benesi and J. H. Hildebrand, J. Am. Chem. Soc. **70**, 2832 (1948); **71**, 2703 (1949).

[2] R. S. Mulliken, J. Am. Chem. Soc. **79**, 4839 (1957).

[3] D. N. Glew and J. H. Hildebrand, J. Phys. Chem. **60**, 618 (1956).

[4] H. McConnell, J. S. Ham, and J. R. Platt, J. Chem. Phys. **21**, 66 (1953).

[5] K. Watanabe, J. Chem. Phys. **26**, 542 (1957); also, K. Watanabe and T. Nakayama, Tech. Rept. 1-a, Ordnance Project.

Electron Spin Resonances in Irradiated Potassium Azide*

A. J. SHUSKUS, C. G. YOUNG, AND O. R. GILLIAM

Department of Physics, University of Connecticut, Storrs, Connecticut

AND

PAUL W. LEVY

Brookhaven National Laboratory, Upton, New York

(Received April 14, 1960)

PREVIOUS studies of radiation-induced color centers in potassium azide (KN_3) have been made using optical means.[1-4] Reported here is the observation by electron spin resonance (ESR) of a defect induced by ultraviolet or gamma-ray irradiation in a single crystal of potassium azide. The hyperfine structure and the orientation dependence of the spectra suggest that this defect is a linear N_4^- molecule-ion.

Measurements were made with a superheterodyne ESR spectrometer operating at 9400 Mc with 100-cps field modulation and phase detection. Single crystals of potassium azide (about 2×5×5 mm) were exposed at room temperature to unfiltered radiation from a Hanovia type SH low-pressure mercury lamp for four hours. No resonances were observed at room temperature. Subsequently, measurements at 77°K revealed hyperfine patterns of nine equally spaced lines due to two nonequivalent sites for the radiation-induced defect. The intensity ratios between lines in a nine-line pattern appear consistent with the ratios that are predicted for an electron interacting with four equivalent nuclei of spin one, namely, 1:4:10:16:22:16:10:4:1. Individual lines have a width of 1.5 gauss at inflection points and the overall width varies from about 23 to 75 gauss for different orientations. The g value is anisotropic, but it is close to that of the free electron. The observed paramagnetic defect anneals out at room temperature in approximately seven days. Similar results are obtained with 10^6-r CO^{60} gamma-ray irradiations at room temperature.

Potassium azide is a body-centered tetragonal crystal.[5] If the magnetic field is applied in the 001 direction, a

single nine-line spectrum is obtained as shown in Fig. 1(a). For this orientation the splitting between lines is minimum (2.9 gauss). Two nine-line spectra are observed with the field parallel to the 110 direction [Fig. 1(b)]. Also, the spectrum repeats every 90° when the field is rotated around the 001 direction. This signifies that the defect has two nonequivalent sites related by a 90° rotation about the c axis. Since maximum splitting occurs when the field is along the 110 direction, this is the major axis of quantization of this defect. Minimum splitting occurs for directions perpendicular to the 110 defect axis.

One would expect a single nine-line spectrum when the field is along the 100 direction [Fig. 1(c)], since the two sites would be equivalent for this orientation. Measured line intensities in the basic nine-line pattern actually indicate that the spectra of the nonequivalent sites overlap for this orientation. However, in addition, small lines appear between the lines of the larger pattern. The origin of these lines is undetermined. Their intensities, relative to the larger lines, vary by a factor of two for different crystals and different irradiation conditions. Thus, it seems plausible that these lines may be due to a defect similar to the one giving the major spectrum, but with an environment distorted by other types of crystal defects.

The magnitude of the hyperfine splitting in the spectra is consistent with values obtained in other nitrogen bearing compounds. Also, the relative intensities (obtained by integration) in the nine-line pattern shown in Fig. 1(c) agree nicely with those expected of an unpaired electron interacting with four equivalent nitrogen nuclei. For the orientations shown by Figs. 1(a) and 1(b) measured relative intensities in the nine-line patterns deviate somewhat, but not unreasonably, from the expected intensities.

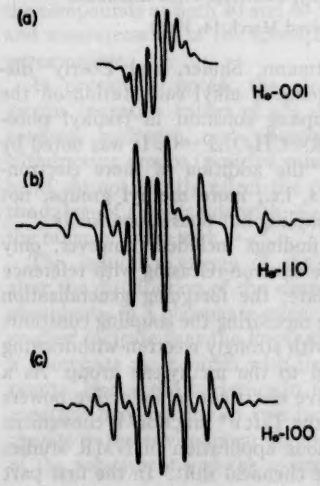

FIG. 1. First derivative of ESR spectra for selected orientations of magnetic field H_0. (All spectra are not to the same vertical scale.)

The model proposed to explain the ESR spectra is a linear N_4^- molecule-ion which lies in the 110 plane. The defect is thought to be located on a line joining two adjacent azide ion vacancies with its molecular axis directed in either the 110 or $1\bar{1}0$ direction, each site being equally populated. One can conceive of many ways of forming this N_4^- configuration in KN_3, especially when it is being irradiated with ultraviolet light or gamma rays. However, once the existence of this configuration is postulated, the properties and orientation expected for it are in agreement with those observed. Choosing the z axis, or the molecular axis, in the 110 direction, the x axis in the $1\bar{1}0$ direction, and the y axis in the 001 direction, the measured values of the g tensor are $g_z=2.005\pm0.001$, $g_y=1.997\pm0.001$, and $g_x=2.002\pm0.001$. The hyperfine interaction is found to be $A_x=A_y=2.9\pm0.2$ gauss and $A_z=9.4\pm0.2$ gauss.

The assistance of J. E. Mapes in the preparation and orientation of samples is gratefully acknowledged.

* Supported by the U. S. Atomic Energy Commission contracts with University of Connecticut and Brookhaven National Laboratory.

[1] P. W. M. Jacobs and F. C. Tompkins, Proc. Roy. Soc. (London) **A215**, 254 (1952).
[2] F. C. Tompkins and D. A. Young, Proc. Roy. Soc. (London) **A236**, 10 (1956).
[3] J. Cunningham and F. C. Tompkins, Proc. Roy. Soc. (London) **A251**, 27 (1959).
[4] J. E. Mapes, R. W. Dreyfus, and P. W. Levy, OMRO Rept. 13A, Watertown Arsenal Conference on Radiation Effects in Materials, October, 1957; Bull. Am. Phys. Soc. **3**, 116 (1958).
[5] R. W. G. Wyckoff, *Crystal Structures* (Intersience Publishers, Inc., New York, 1957).

Viscosity of Mixtures of Hydrogen and Water Vapor at 295°K

J. W. FOX AND A. C. H. SMITH*
Department of Physics, University College, London, England

(Received April 12, 1960)

IN the course of an investigation[1] of the viscosity of partially dissociated moist hydrogen by measuring the rate of damping of the oscillations of a small pendulum at pressures where the mean free path is not negligible compared with the diameter of the bob, we had to measure the viscosity of molecular hydrogen containing about 2½% of water vapor at about 20°C. The water vapor was added in order to obtain adequate concentrations of atomic hydrogen. Our results showed that the viscosity of the moist hydrogen was about 7% greater than that of the dry gas. Since we could find no experimental or computed values for comparison, we computed the first approximation to the viscosity of the mixture at 295°K over the complete range of water vapor content.

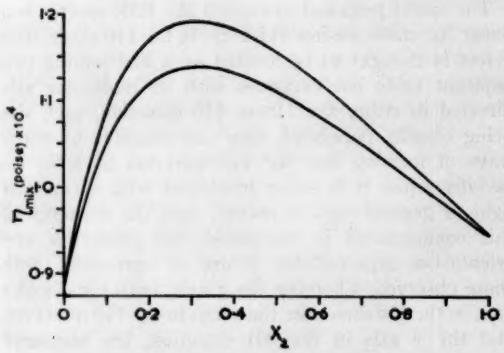

FIG. 1. Viscosity η_{mix} of mixtures of hydrogen and water vapor at 295°K plotted against molar fraction x_2 of water vapor; upper curve from diffusion data, lower from combining laws.

The method of computation and the notation are given by Hirschfelder, Curtiss, and Bird.[2] As accurate measurements have been made of the viscosities of the pure components, only the two quantities η_{12} and A_{12}^* are required, both of which depend upon the interaction of hydrogen (suffix 1) and water vapor (suffix 2) molecules. Two methods were applied for determining η_{12}, one involving empirical combining laws relating the force constants describing the molecular interactions and the other a value of the coefficient of diffusion D_{12} obtained from experimental data.

The constants used in the computation were as follows, viscosities being expressed in poises:

$T=295°K$

$\eta_1=0.8858\times10^{-4}$ calculated from the empirical formula given by Woolley, Scott, and Brickwedde[3]

$\eta_2=0.9440\times10^{-4}$ calculated from the measurements of Braune and Linke[4]

$\eta_{12}=0.9855\times10^{-4}$ calculated by applying combining laws[5]

$A_{12}^*=1.094$ from Table I—N[2]

$D_{12}=0.980$ cm^2 sec^{-1} at $T=295°K$, $p=1$ atm, extrapolated from the measurements of Schwertz and Brow[6]

$\eta_{12}=1.118\times10^{-4}$ calculated from D_{12}.[7]

The viscosity of the mixture is given by $\eta_{mix}=(1+Z)/(X+Y)$, where the first value of η_{12} gives

$$X=1.1289x_1^2+1.7889x_1x_2+1.0593x_2^2;$$
$$Y=0.6564(0.12633x_1^2+7.3859x_1x_2+9.4666x_2^2);$$
$$Z=0.6564(0.11190x_1^2+11.515x_1x_2+8.9365x_2^2),$$

and the second value changes the coefficients of x_1x_2 to 2.0294, 6.5106 and 9.9130 in X, Y, and Z, respectively. x_1 and x_2 are molar fractions of hydrogen and water vapor respectively.

Values of η_{mix} computed from these expressions are plotted in Fig. 1, the upper curve (η_{12} derived from diffusion data) being preferred. The rapid initial increase of viscosity with increasing water vapour content is seen to be due to the occurrence of a maximum of η_{mix} about 35% greater than η_1 at a value of x_2 of about 0.3 (upper curve). The main reason for this maximum is the similarity of the viscosities, combined with the large difference between the molecular weights of the pure gases. The fact that η_{12} is greater than either η_1 or η_2 is also a contributing factor. The maximum occurs nearer to $x_2=0$ than to $x_2=1$ because M_2 is much greater than M_1. The computed values of η_{mix} for a molar fraction of water vapour of 0.025 are 0.9541×10^{-4} and 0.9404×10^{-4} poise, respectively. These represent increases of 7.7% and 6.2% respectively over the viscosity of pure hydrogen and agree reasonably well with our experimental results.

* Now at Convair, A Division of General Dynamics Corporation, San Diego, California.

[1] J. W. Fox and A. C. H. Smith (to be published).

[2] J. O. Hirschfelder, C. F. Curtiss, and R. B. Bird, *Molecular Theory of Gases and Liquids* (John Wiley & Sons, Inc., New York, 1954).

[3] H. W. Woolley, R. B. Scott, and F. G. Brickwedde, J. Research Natl. Bur. Standards **41**, 379 (1948).

[4] H. Braune and R. Linke, Z. Phys. Chem. **A148**, 195 (1930).

[5] The Lennard-Jones potential is used for the interaction between the hydrogen and water vapor molecules. The combining laws are given[2] on p. 600 and the values of the constants used in applying them are also given on p. 214 and p. 947 of this book, except the force constants referring to the interaction of the hydrogen molecules. Here new values were calculated based on measurements[3] covering a temperature range centered about 295°K; these values were $\sigma_1=2.914$ A and $\epsilon_1/k=41.7°K$. The force constants calculated for the unlike molecules were $\sigma_{12}=2.747$ A and $\epsilon_{12}/k=147.1°K$.

[6] F. A. Schwertz and J. E. Brow, J. Chem. Phys. **19**, 640 (1951).

[7] In this derivation A_{12}^* was taken as 1.094. Since A_{12}^* is a slowly varying function of T^* this should produce no significant error.

H^1-P^{31} Spin Coupling in Phosphate Esters

GERALD O. DUDEK

Mallinckrodt Laboratory, Department of Chemistry, Harvard University, Cambridge 38, Massachusetts

(Received March 14, 1960)

RECENTLY Axtmann, Shuler, and Eberly[1] discussed the influence of alkyl substitution on the H^1-P^{31} spin-spin coupling constant in trialkyl phosphates of the type $(R—CH_2O)_3P=O$. It was noted by these authors that "the addition of more electron-releasing substituents, i.e., more methyl groups, not only decreases the coupling but does so markedly."

Their interesting findings included, however, only compounds which are electron-releasing with reference to trimethyl phosphate; the foregoing generalization was further tested by measuring the coupling constants in phosphate esters with strongly electron-withdrawing substituents attached to the methylene group. As a measure of the relative electronic or inductive powers of these compounds, the Taft σ^* function[2] is convenient and has found previous application in NMR studies involving the fluorine chemical shift.[3] In the first part

TABLE I. J_{CH_3-P} for trialkyl phosphates.

Compound	Formula	σ^*	J_{CH_3-P} cps
Trimethylphosphate	$(CH_3O)_3P{=}O$	0.00	11.19[b]
Triethylphosphate	$(C_2H_5O)_3P{=}O$	−0.100	8.38[b]
Tripropylphosphate	$(n{-}C_3H_7O)_3P{=}O$	−0.115	7.70[b]
Tributylphosphate	$(n{-}C_4H_9O)_3P{=}O$	−0.130	7.65[b]
Tri-isobutylphosphate	$[(CH_3)_2CHCH_2O]_3P{=}O$	−0.125	6.60[b]
Tri-neopentylphosphate	$[(CH_3)_3CCH_2O]_3P{=}O$	−0.165	5.24[b]
Tris-(2,2,2-trichloroethyl) phosphate	$(CCl_3CH_2O)_3P{=}O$	+1.0[a]	7.05±0.1
Tris-(2,2,2-trifluoroethyl) phosphate	$(CF_3CH_2O)_3P{=}O$	+0.92	8.34±0.1
Tri-(2,2-dichloroethyl) phosphate	$(CHCl_2CH_2O)_3P{=}O$	+0.7[a]	8.4±0.2
Tribenzylphosphate	$(C_6H_5CH_2O)_3P{=}O$	+0.215	9.07±0.1
Triallylphosphate	$(CH_2{=}CH{-}CH_2O)_3P{=}O$	+0.1[a]	8.3±0.2

[a] Estimated from the data in footnote reference 2.
[b] From footnote reference 1.

TABLE II. J_{CH_3-P} for unsymmetrical compounds.

Compound	Formula	Group	J_{CH_3-P}
Tetrabenzylpyrophosphate	$(C_6H_5CH_2O)_4P_2O_3$	Benzyl	8.62±0.2
Methyl tetramethylene phosphate	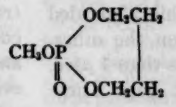	Methyl	11.2±0.1
Dibenzyl methylphosphate	$CH_3OP(OCH_2C_6H_5)_2$ ‖ O	Methyl	11.12±0.1
		Benzyl	8.68±0.1

of Table I, the results of the previous investigation are listed along with the Taft substituent constants (σ^*) for the alkyl component. With the exception of the isobutyl group, a correlation of the J_{CH_3-P} and σ^* exists.

The data for the compounds used in this study are presented in the second part of Table I. The separations were usually measured by the "wiggle-beat" method.[4] However triallyl phosphate and tri-(2,2-dichloroethyl) phosphate were measured by the "side-band" method[4] as the spectra of these two compounds are more complex than that predicted by first order theory. By studying the compounds at both 40 and 60 Mc, the identification and measurements of the spin-spin coupling constants were possible.

As previously noted, the electron-donating alkyl groups (negative values of σ^*) decrease the coupling between hydrogen and phosphorus. The electron-withdrawing groups (positive values of σ^*) on the other hand, do not greatly affect the coupling, even though the range of compounds with $+\sigma^*$ is about four times the range of those with $-\sigma^*$.

The inductive effects of the various substituents alter the distribution of the electronic cloud about the phosphorus in a phosphate ester. For example, infrared studies[5] indicate that the P=O stretching frequency of a phosphate ester varies with its alkyl or aryl substituents. Hence the variation in the spin-spin coupling constant may be due to two factors. The first is the change in the environment about the methylene group of the substituent and the second is the alterations in the electronic environment about the phosphorus induced by the substituents.

To separate these two effects, a few unsymmetrical compounds were studied, and the data are contained in Table II. The electronic environment about phosphorus is changed between tribenzyl phosphate and tetrabenzyl pyrophosphate, but the H^1–P^{31} coupling constant is only slightly different. In the other unsymmetrical phosphates, the methyl coupling constant is decreased very slightly by the substituents. Therefore the assumption can be made that the variations in the coupling constant are primarily due to the methylene group and not to the phosphorus. But the question of why there is a difference in the behavior of the electron-withdrawing and the electron-donating substituents is still unanswered.

[1] R. C. Axtmann, W. E. Shuler, and J. H. Eberly, J. Chem. Phys. 31, 851 (1959).
[2] R. W. Taft in *Steric Effects in Organic Chemistry*, M. S. Newman, Editor (John Wiley & Sons, Inc., New York, 1956), Chap. 13; see also P. Ballinger and F. A. Long [J. Am. Chem. Soc. 82, 795 (1960)] for values of σ^* not listed in the Taft article. In several cases the necessary value of σ^* was not available, but could be estimated by using Taft's value of 2.8 as a divisor per methylene group (i.e., $CHCl_2{-}{=}+1.940$), therefore $CHCl_2CH_2{-}{=}1.940/2.8$ or +0.7.
[3] J. A. Pople, W. G. Schneider, and H. J. Bernstein, *High-resolution Nuclear Magnetic Resonance* (McGraw-Hill Book Company, Inc., New York, 1959), Sec. 12.6a.
[4] J. A. Pople, W. G. Schneider, and H. J. Bernstein, footnote reference 3, Sec. 4.7a.
[5] J. A. A. Ketelaar and H. R. Gersmann, Rec. trav. chim. 78, 190 (1959).

Hole and Electron Drift Mobilities in Anthracene

OLIVER H. LEBLANC, JR.

General Electric Research Laboratory, Schenectady, New York

(Received April 22, 1960)

PHOTOCONDUCTION and semiconduction in organic solids have been studied extensively in recent years. A considerable part of the present difficulty in understanding these phenomena arises from our ignorance of the mobilities of the carriers involved. In the present experiment hole and electron mobilities in anthracene are determined with a technique used previously by a number of workers in investigating inorganic substances.[1]

A Harshaw scintillation grade single crystal in the form of a circular disk 4 cm in diameter and 0.625 cm thick (in the c crystal axis) was employed in a sandwich arrangement.[2] An evaporated Ag film of 50% transmission served as the electrode on one face, while a guarded electrode was prepared with Ag paint on the other. Light pulses, of duration considerably less than 1 μsec, were generated with a triggered spark gap. These impinged on the crystal through the transparent electrode, and the resulting photoconduction transients were displayed on a Tektronix model 545 oscilloscope.

A typical photocurrent transient is shown in Fig. 1. The current rises after the light pulse with time constant τ to a steady valve, and then at time t' abruptly decays with the same time constant τ. The time constant τ in Fig. 1, approximately 50 μsec, is determined entirely by external circuit parameters to the accuracy with which we can measure it. The time t' is observed to vary with the voltage V, applied to the crystal as $Vt'=0.39\pm0.01$ volt·sec with the illuminated electrode positive and as $Vt'=0.72\pm0.03$ volt·sec with the illuminated electrode negative, at 25°C.

We propose the following explanation. The extinction coefficient of the absorbed light is such that the light produces carriers only within a distance of approximately 10^{-3} cm of the illuminated electrode. Thus with the anode illuminated, for example, the current pulse arising from the drift of electrons to the anode will occur in 10^{-3} the time required for the holes to drift to the cathode, and will be too fast to observe with the present external circuit used. Hence the current transient we observe in Fig. 1 arises from the drift from anode to cathode of a hole pulse approximately 10^{-3} cm wide.

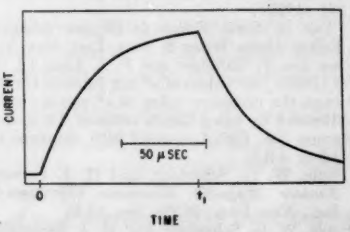

FIG. 1. Typical photocurrent transient. Submicrosecond light pulse occurs at zero time. Anode illuminated with 4200 v applied. Hole transit time 94 μsec.

The times t' are then identified as the transient times of the appropriate carrier, and we calculate the drift mobilities in the C axis for holes and electrons, respectively, to be 0.98 ± 0.04 and 0.54 ± 0.03 cm²/volt·sec at 25°C. Both mobilities vary with temperature approximately as T^{-1} between $+25°$ and $-100°$C.

The total charge transported per light pulse increases with applied voltage as V^n, where the exponent n is slightly larger than one. This indicates that either the quantum efficiency for carrier production is a function of the electric field strength or considerable carrier recombination occurs before the holes and electrons separated by their drift in the applied field.

It would be of considerable interest to observe the true rise and decay shapes of the drift pulse. Since the currents here are of the order of 10^{-8} amp or smaller and since the experimental arrangement almost inevitably involves 50–100 $\mu\mu$f capacitance from the collecting electrode to ground, we have as yet been unable to achieve the bandwidth ($\sim$1 Mc) and the signal/noise ratio required.

One would expect that the mobilities in anthracene would exhibit a strong anisotropy, and we are presently attempting to examine this. We also plan to study the effects of chemical impurities and crystal imperfections.

[1] F. C. Brown and F. E. Dart, Phys. Rev. **108**, 281 (1957).
[2] A. G. Chynoweth and W. G. Schneider, J. Chem. Phys. **22**, 1021 (1954).

EPR Studies of the Tetracyanoethylene Anion Radical*

W. D. PHILLIPS AND J. C. ROWELL

Central Research Department, Experimental Station, E. I. du Pont de Nemours and Company, Wilmington, Delaware

AND

S. I. WEISSMAN

Chemistry Department, Washington University, St. Louis, Missouri

(Received April 11, 1960)

STUDIES of the intense, visible absorption arising from complexes formed in solution between tetracyanoethylene (TCNE) and methylbenzenes or polynuclear hydrocarbons have shown that TCNE is among the strongest of the π acids.[1] A high π-acid strength for the molecule implies a large electron affinity[2] and indeed simple LCAO MO calculations[3] carried out on TCNE suggest that the lowest vacant π orbital of the molecule is slightly bonding.

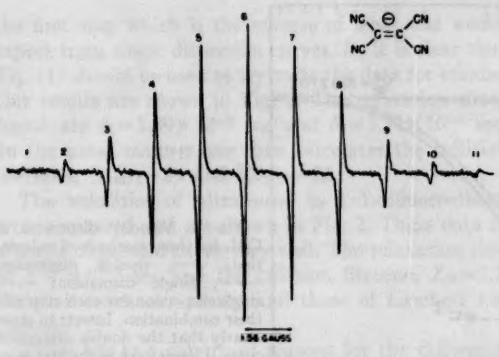

FIG. 1. EPR spectrum of 10^{-4} molar NaTCNE in tetrahydrofuran.

The ease of reduction of TCNE to its anion radical is consistent with the high electron affinity of the molecule. $TCNE\cdot^-$ is readily formed both in the vapor phase and in solution by reduction with sodium or potassium. We also have prepared $TCNE\cdot^-$ by reacting TCNE with both NaI and NaSCN in tetrahydrofuran and acetonitrile solutions.[4] When solutions of TCNE and NaI or NaSCN are mixed, a deep purple coloration develops instantaneously which changes to yellow in about five minutes. The purple color presumably arises from the charge-transfer band of the complexes formed between TCNE and the anions. The yellow solution exhibits an intense EPR spectrum (Fig. 1) characteristic of $TCNE\cdot^-$ ($\lambda_{max}=4320$ A). We have not as yet detected the I· and SCN· radicals presumably formed in these electron transfer reactions. However, lifetimes for these radical species in solution probably are short and EPR experiments employing a flow system are planned.

The EPR spectrum of $TCNE\cdot^-$ ($g=2.0026\pm 0.0002$) consists of 11 lines with a spacing of 1.56 ± 0.02 gauss. The nine lines designated 2–10 in Fig. 1 exhibit intensity ratios close to the 1:4:10:16:19:16:10:4:1 expected for four equivalent N^{14} ($I=1$) nuclei. Preliminary experiments with $TCNE\cdot^-$ tagged with C^{13} in the cyano groups indicates that the C^{13} splitting is an even multiple of the N^{14} splitting in this radical. Lines 1 and 11 in the spectrum of $TCNE\cdot^-$ are therefore attributed to C^{13} satellite splittings arising from the 4.4% of the radicals containing one $C^{13}N$ group. The intensities of lines 1 and 11 are consistent with $A_{C^{13}}=6A_{N^{14}}=9.4$ gauss. LCAO MO calculations carried out on $TCNE\cdot^-$ yield a value of 0.11 for the "odd" electron density at each nitrogen atom. This result would suggest that the isotropic hyperfine splitting for an electron on the nitrogen atom of a nitrile group is of the order of 15 gauss.

The rate of electron exchange between TCNE and $TCNE\cdot^-$ in solution has been studied by observing the effects of added TCNE on the widths of the $TCNE\cdot^-$ resonances.[5] A rate constant of 2.1×10^8 liter mol^{-1} sec^{-1} has been obtained at room temperature in tetrahydrofuran (THF) solutions for the assumed second order electron exchange process. Both the potassium and sodium salts of TCNE have given the same rate constant. The only other electron exchange process involving an organic molecule and its anion radical whose rate has been measured is that between naphthalene and its anion radical.[5] Second-order rate constants for this reaction in THF were found to be about 5.0×10^7 liter mol^{-1} sec^{-1} for the potassium and sodium salts and about 4.6×10^8 liter mol^{-1} sec^{-1} for the lithium salt. Experiments are in progress to determine the influences of solvent, temperature and associated cation on the rate of electron exchange between TCNE and $TCNE\cdot^-$.

* Contribution No. 615.

[1] R. E. Merrifield and W. D. Phillips, J. Am. Chem. Soc. **80**, 79 (1958).

[2] R. S. Mulliken, J. Am. Chem. Soc. **74**, 811 (1952).

[3] Values of the resonance and Coulomb integrals used in the LCAO MO calculation were taken from L. E. Orgel, T. L. Cottrell, W. Dick, and L. E. Sutton, Trans. Faraday Soc. **47**, 113 (1951).

[4] $Na^+TCNE\cdot^-$ and $K^+TCNE\cdot^-$ can be isolated from solution from the products of NaI and KI reduction of TCNE. For details of the chemical preparation and properties of the TCNE salts, see O. W. Webster, W. Mahler, and R. E. Benson, J. Org. Chem. (to be published).

[5] R. L. Ward and S. I. Weissman, J. Am. Chem. Soc. **79**, 2086 (1957).

Sound Dispersion in Ethane and 1·1-Difluoroethane

L. M. VALLEY AND SAM LEGVOLD*

Engineering Experiment Station, and Department of Physics, Iowa State University, Ames, Iowa

(Received March 24, 1960)

LAMBERT and Salter[1] have recently reported double dispersion of ultrasound in ethane and attribute the second step in the dispersion to hindered rotation. It appears that they analyzed their results in terms of single dispersion curves for each step. It is the purpose of this note to report a verification of double dispersion in ethane,[2] to suggest a more satisfactory method of treating data for double dispersion, and to compare our dispersion data on 1·1-difluoroethane with the work of Lambert and Salter[1] on this gas.

Richards[3] gives the basic equations for sound dispersion and it is possible to use these in a derivation to

TABLE I. The relaxation times in seconds for ethane and 1·1-difluoroethane.

Gas	Relaxation times: Lambert and Salter[1]	Relaxation times: This work
C_2H_6	1.79×10^{-8}, (2.8×10^{-9})[a]	1.39×10^{-8}, 1.24×10^{-9}
$C_2H_4F_2$	$<1.5\times10^{-9}$ (not observed)	3.37×10^{-9}

[a] An approximate (maximum) value.

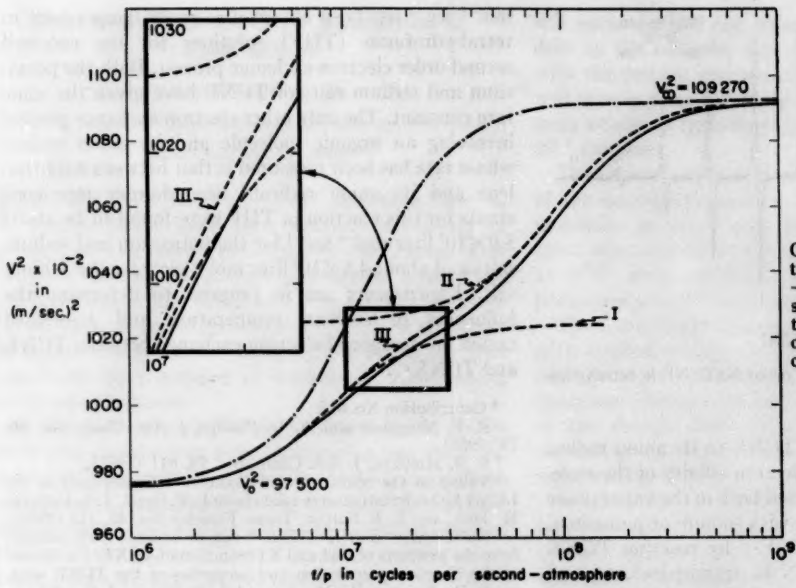

FIG. 1. Velocity dispersion in C_2H_6 by three methods of calculation: ——, double dispersion; —·—, single dispersion; ------, single dispersion for each step and their combination. Insert: to show clearly that the double dispersion curve is lower even in the first step.

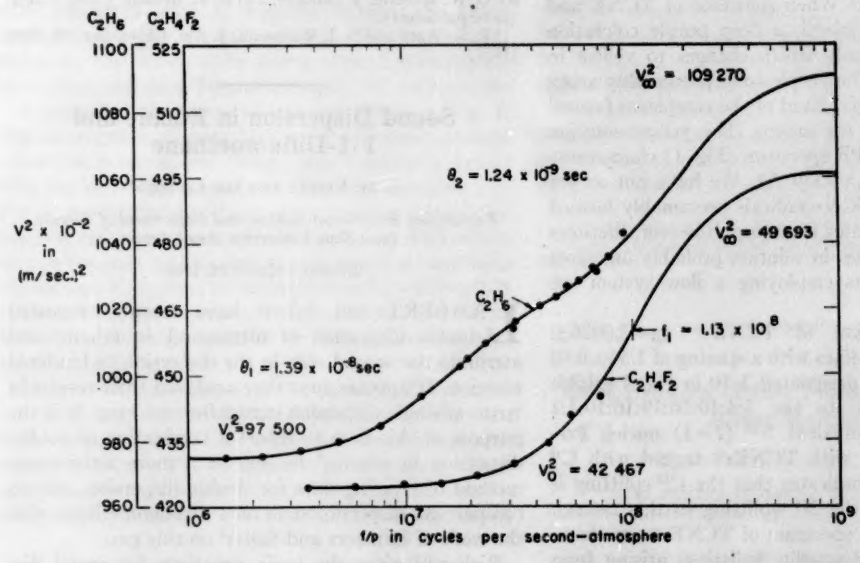

FIG. 2. Velocity dispersion in ethane at 296.4°K and in 1·1-difluoroethane at 296.1°K.

get, for double dispersion,

$$V_{\text{ideal}}^2 = (RT/M) \times [1 + R(C_0 + \omega^2 A + \omega^4 B)/(C_0^2 + \omega^2 D + \omega^4 E)], \quad (1)$$

where A, B, D, and E are constants for a particular gas or for a particular gas mixture, V is the velocity of sound, R the universal gas constant, T the absolute temperature, M the molecular weight, C_0 the specific heat at constant volume for low frequencies, and ω equals $2\pi f$ (f is the frequency). A, B, D, and E depend upon C_1 and C_2, the specific heats for each step in the dispersion, and upon θ_1 and θ_2, the relaxation times for each step.

Using the same relaxation times θ_1 and θ_2, and specific heats C_1 and C_2, as used in calculating the single dispersion curves (*I* and *II* of Fig. 1) for each step, Eq. (1) gives the curve shown in Fig. 1 (solid line). The curve of Eq. (1) is considerably lower and is in fact lower even through the first step than the single dispersion combination results (*III* of Fig. 1).

It is evident that the relaxation process of the second step has a very definite effect on the relaxation process of the first step. This interaction lowers the velocity in

the first step which is the reverse of what one would expect from single dispersion curves. So it is clear that Eq. (1) should be used to try to fit the data for ethane. Our results are shown in Fig. 2. The relaxation times found are $\theta_1=1.39\times10^{-8}$ sec and $\theta_2=1.24\times10^{-9}$ sec. In the usual manner one then calculates the collision lifetimes, $(Z_{10})_1=89$ and $(Z_{10})_2=13$.

The velocities of ultrasound in 1·1-difluoroethane were measured and are shown in Fig. 2. These data fit a single dispersion curve very well. The relaxation time is 3.37×10^{-9} sec and the collision lifetime, $Z_{10}=7.2$. Table I shows our results and those of Lambert and Salter.[1]

There are two important reasons for the difference. First, in this work, values of frequency, f/p, up to about 100 Mcs-atmosphere were reached. Dispersion was observed for the first time in 1·1-difluoroethane. Second, in the case of ethane, the use of Eq. (1) gives a better interpretation of the data.

* This research was supported by the U. S. Air Force through the Air Force Office of Scientific Research of the Air Research and Development Command. Reproduction in whole or in part is permitted for any purpose of the U. S. Government.

[1] J. D. Lambert and R. Salter, Proc. Roy. Soc. (London) **A253**, 277 (1959).

[2] L. M. Valley and Sam Legvold, Tech. Status Rept. No. 16, Air Force Office of Scientific Research (June, 1959).

[3] W. T. Richards, Revs. Modern Phys. **11**, 36 (1939).

Observation of the Overhauser Effect on Carbon-13 Nuclear Resonance Signals

D. J. PARKER,* G. A. MCLAREN, AND J. J. CONRADI

Shell Oil Company, Wood River, Illinois

(Received April 19, 1960)

NUCLEAR magnetic resonance signals from carbon-13 nuclei (1.1% natural abundance) have been observed by the technique of dynamic polarization.[1] They arise to a large extent from the solvent molecules of solutions of free radicals in hydrocarbons. This "Overhauser effect" technique may therefore provide a means of obtaining potentially very useful carbon-13 NMR spectral information—information which heretofore has been inaccessible because sufficiently sensitive spectrometers have not been available. We have made similar observations on the enhancement of proton signals and include them for the sake of completeness.

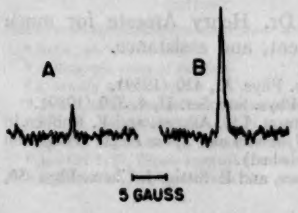

FIG. 1. A, Overhauser enhanced carbon-13 resonance from a solution of *I* in natural toluene; B, Overhauser enhanced carbon-13 resonance from a solution of *I* in toluene enriched to about 60% in toluene-α-C^{13}.

FIG. 2. Resolution of methyl quartet in Overhauser enhanced carbon-13 resonance from a solution of *I* in toluene enriched to about 60% in toluene-α-C^{13}.

The experimental appratus used for the Overhauser effect experiments consisted of a combination of most of the units of both a Varian V-4500 EPR spectrometer and a Varian V-4200B wide-line NMR spectrometer.[2] Relatively simple modifications were necessary to allow transformation of these instruments into an Overhauser effect spectrometer. The major modification required for these experiments was the substitution of a bridge circuit for the Varian probe to allow the use of a single radio-frequency coil for the detection of the nuclear resonance. This coil was designed to fit inside the microwave cavity and to produce the least disturbance on the microwave field. In addition, about a fourfold increase in the available microwave power was achieved by eliminating the hybrid tee of the microwave bridge and operating the klystron somewhat above its rated power. The sample size in this equipment is about 0.1 ml.

Figure 1 shows the Overhauser enhanced carbon-13 signals from solutions of 2,6,3′,5′-tetra-tert-butyl-4′-phenoxy-4-methylene-2,5-cyclohexadiene-1-one radical,[3] *I*, in natural toluene *A*, and in carbon-13-enriched toluene *B*, enriched to about 60% in toluene-α-C^{13}. The relative intensities of the signals indicate that the enhanced signals arise principally from the solvent molecules and that carbon nuclei not in the aromatic ring also are subject to dynamic polarization. The carbon-13 signals were too weak to be observed in our spectrometer in the absence of the Overhauser enhancement.

Proton resonance signals from solutions of *I* in natural benzene and in deuterated benzene of 99.5% isotopic purity have also been examined. The relative amplitudes of the unenhanced signal and the enhanced signal from *I* in natural benzene show an Overhauser enhancement of about 150-fold. The relative amplitude of the enhanced signal in deuterated benzene demonstrates that the enhanced signals arise principally from the protons on the solvent molecules.

By appropriate instrumental settings, the spectrum of the sample enriched in toluene-α-C^{13} shown in Fig. 1 can be resolved into the methyl quartet shown in Fig. 2. The coupling constant measured by the modulation sideband technique is 122 cps in good agreement with the value reported by Muller and Pritchard.[4]

We wish to thank Dr. S. I. Weissman and Dr. J. J. Townsend of Washington University for helpful discussions and the loan of carbon-13 tagged methyl iodide. We are also indebted to our associates Dr. J. D.

Swalen and Dr. C. H. Holm of Shell Development Company for their helpful discussions and suggestions and to E. R. Willerth of this Laboratory for his help in the construction of some of the electronic and mechanical devices required for this study.

* Present address, Minnesota Mining and Manufacturing Company, St. Paul, Minnesota.
[1] J. Combrisson, J. phys. radium **19**, 840 (1958).
[2] Varian Associates, Instrument Division, 611 Hansen Way, Palo Alto, California.
[3] G. M. Coppinger, J. Am. Chem. Soc. **79**, 501 (1957).
[4] Norbert Muller and Donald E. Pritchard, J. Chem. Phys. **31**, 1471 (1959).

Correlation of Experimental Results for the Vibrational Relaxation of Nitric Oxide

FRANK ROBBEN, PHILIP R. MONSON, AND JOHN J. ALLPORT

Research Laboratory, Lockheed Missiles and Space Division, Palo Alto, California

(Received May 9, 1960)

THE anomalous relaxation time of heated nitric oxide has been measured in the shock tube by two techniques. In the first method the density of vibrationally excited NO was followed by ultraviolet absorption due to the γ_{01} electronic transition.[1] A second method using infrared emission from excited vibrational states, principally the 1–0 and 2–0 transitions, indicated a somewhat longer but still anomalous relaxation time.[2,3] The purpose of this note is to show that agreement has now been obtained between the two methods with the previously reported ultraviolet results still considered valid. These results are further substantiated by the ultrasonic absorption experiment of Bauer, Kneser, and Sittig[4] (see Fig. 1).

New infrared observations in a 1-in. glass shock tube were made with an indium antimonide photoconductor detecting the radiation from the shock heated nitric oxide through a sapphire section. Since filters impose a severe intensity loss, they were sometimes avoided. In these cases a careful determination showed that practically all the radiation was from the fundamental band. A pair of metal slits limited the observed radiation to that from a thin cross section of gas in the shock tube. The slits were made narrow enough so that the shock transit time was smaller than the measured vibrational relaxation time. The results are plotted in Fig. 1 and give good agreement with the ultraviolet absorption results also shown. Similar earlier infrared experiments[3] with the 2–0 transition using a quartz test section and *black vinyl tape* slits were interpreted to give a P_{1-0} more than an order of magnitude smaller. Later investigation, however, showed that the use of vinyl tape causes an apparent broadening of the slit even though the tape was shown to be opaque by transmission measurements.

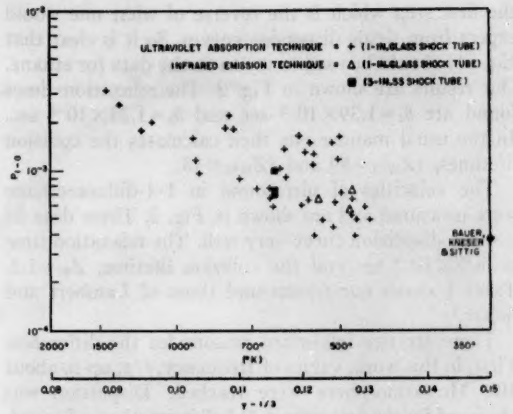

FIG. 1. Summary of vibrational deexcitation probabilities, P_{1-0}, as a function of $T^{-\frac{1}{3}}$.

New experiments were also performed on the 3-in. shock tube with an optical arrangement much the same as in the 1-in. tube described except that a sapphire *window* was used. Typical transition probabilities from these experiments are also plotted in Fig. 1. In earlier work internal reflections made it difficult to obtain unambiguous results in so large a tube but this problem was eliminated by starting with sufficiently low initial densities and using relatively weak shocks. The presumption is that, in previous experiments, radiation from gas behind the shock underwent many small angle reflections from the shock tube walls with the result that the pre-rise and post-rise in radiation masked the actual relaxation radiation.

The reflection hypothesis is corroborated by three items of evidence. First, with the glass shock tube the angular acceptance of the detector was varied for a series of otherwise identical runs. The preradiation and postradiation were found to decrease with smaller detector solid angles, as would occur with reflections. Second, two runs were made with the 3-in. stainless steel shock tube with initial densities differing by a factor of two and approximately equal shock velocities. The pre- and post-rises were the same for both densities and consequently are not connected with vibrational relaxation, which is density dependent. Third, with the steel shock tube it was found that when its interior was painted with a flat black enamel, the resulting reduction in reflectivity of the walls reduced the pre- and post-rises.

We wish to thank Dr. Henry Aroeste for much discussion, encouragement, and assistance.

[1] Frank Robben, J. Chem. Phys. **31**, 420 (1959).
[2] J. J. Allport, Bull. Am. Phys. Soc. Ser. II, **4**, 370 (1959).
[3] See article by P. R. Monson, J. J. Allport, and F. Robben in *Physical Chemistry in Aerodynamics and Space Flight* (Pergamon Press, New York, to be published).
[4] H. J. Bauer, H. O. Kneser, and E. Sittig, J. Chem. Phys. **30**, 1119 (1959).

Dipole Moment of Isotactic and Atactic Poly-Vinyl Iso-Butyl Ether

M. TAKEDA AND Y. IMAMURA

Department of Chemistry, Tokyo College of Science, Shinjuku-ku, Tokyo

AND

S. OKAMURA AND T. HIGASHIMURA

Department of Textile Chemistry, Faculty of Engineering, Kyoto University, Sakyo-ku, Kyoto

(Received March 7, 1960)

THERE has been considerable interest in the intrinsic physical properties of vinyl type polymer in solution which could be used as an index of stereoregularity[1] of vinyl type polymer. These polymers will have a different equilibrium distribution of conformation in the solution according to their different stereospecific molecular configuration.

Recently, the analysis of infrared absorption spectra has shown that the isotactic polystyrene has more helical conformation than the atactic polystyrene in CS_2 solution.[2] The dipole moment of a polymer in solution may be one of the appropriate intrinsic properties which is very sensitive to the different equilibrium distributions of conformation of vinyl type polymer.[3] Krigbaum and Roig[4] have presented the first experimental evidence of the difference in dipole moment between atactic and isotactic polystyrene in toluene solution. We have studied the same problem using the isotactic and atactic polymers of vinyl ether.

The siotactic polyvinyl isobutyl ether (PIBE-I) was polymerized by borontrifluoride-ether complex catalyst at −78°C using homogeneous 2.5 vol% solution of monomer in *n*-hexane. The precipitation temperature of the methyl ethyl keton solution of this isotactic polymer was around 0°C.[5] The atactic polyvinyl isobutyl ether (PIBE-A) was polymerized by the same catalyst at −20°C using homogeneous 20 vol % solution of monomer in *n*-hexane. The precipitation temperature of the methyl ethyl ketone solution of this atactic polymer was below −30°C.[5] Both samples have good solubility in benzene and are purified by repeated precipitation from benzene solution with methanol and the evaporation of solvent in vacuum at 50°C without fractionation. PIBE-I had $[\eta]$ in benzene of 0.197, and PIBE-A had $[\eta]=0.193$ in the same solvent at 30°C.

We have measured the dielectric constant of PIBE-I and PIBE-A in benzene solution at 25°C using the zero beat method with frequency of 1 Mc.

The results of experiment and the calculated dipole moment per monomer unit are tabulated in Table I, where the dipole moment obtained is in error within 0.03 debye unit.

It was established that the dipole moment of PIBE-I is about 10% larger than that of PIBE-A and this may be explained by the assumption that PIBE-I takes more helical conformation than PIBE-A in benzene solution.

The values $(\bar{\mu}^2/\mu_0^2)$ are 0.77∼0.98 and these can be compared with the values of other polymers, such as atactic polyvinyl chloride (0.70∼0.75),[6] polyvinyl acetate (0.75∼0.80) and polymethyl methacrylate (0.58∼0.65).

From theoretical calculation in the extreme case, where the polar side groups in the linear polymer are in

TABLE I. Dipole moment of P.I.B.E. in benzene.

Temp	Solute	100w[a]	ε[b]	d[c]	P_2 c.c.[d]	P_2^∞ c.c.[e]	$\bar{\mu}_{DU}$	$\bar{\mu}^2/\mu_0^{2[f-h]}$
	Benzene	0.0000	2.2725	0.87391				
	Isotactic	3.5621	2.3214	0.87640	56.79			
25°C	polymer	4.6630	2.3362	0.87701	56.70	57.1	1.16	0.90
	Atactic	3.8435	2.3115	0.87606	52.56			
	polymer	6.7576	2.3422	0.87731	52.19	53	1.07	0.77
	Benzene	0.0000	2.2232	0.84714				
	Isotactic	3.5621	2.2683	0.84941	56.43			
50°C	polymer	4.6630	2.2822	0.85025	56.20	57	1.21	0.98
	Atactic	3.8435	2.2625	0.84925	52.09			
	polymer	6.7576	2.2919	0.85107	51.62	52.6	1.11	0.83

[a] 100 w, wt % of solute.
[b] ε, dielectric const of solution.
[c] *d*, density of solution.
[d] P_2 c.c., total polarization per monomeric unit of solute.
[e] P_2^∞ c.c., extrapolated value of P_2 to zero concentration.
[f] $\bar{\mu}$, mean dipole moment per monomeric unit.
[g] $\mu_0=1.22$ D.U., Dipole moment of monomeric unit. See footnote reference 7.
[h] $R_D=29.4$ c.c., molecular refraction of solute.

fully free rotation, these values are to be expected to be near to unity.[8] However, in general, the agreement between the theoretical expected value of μ^2/μ_0^2 and the observed one is not yet obtained at the present stage of our investigation.

[1] G. Natta, Makromol. Chem. **16**, 213 (1955).
[2] M. Takeda, K. Iimura, A. Yamada, and Y. Imamura, Bull. Chem. Soc. Japan **32**, 1151 (1959).
[3] P. Debye and B. Bueche, J. Chem. Phys. **19**, 589 (1951).
[4] W. R. Krigbaum and A. Roig, J. Chem. Phys. **31**, 544 (1959).
[5] S. Okamura, T. Higashimura, and I. Sakurada, J. Polym. Sci. **39**, 507 (1959).
[6] Y. Imamura, J. Chem. Soc. Japan **76**, 217 (1955).
[7] "Table of electric dipole moment," Mass. Inst. Technol.
[8] Volkenstein, J. Polym. Sci. **29**, 441 (1958); T. M. Birstein and O. B. Ptitsyn, J. Tech. Phys. U.S.S.R. **24**, 1998 (1954).

Note on the Internal Rotation Problem*

WILLIAM L. CLINTON

Chemistry Department, Brookhaven National Laboratory, Upton, Long Island, New York

(Received February 15, 1960)

THE virial theorem for polyatomic molecules[1] can be written

$$\sum_{\alpha,i}^{3N} X_{\alpha i}(\partial W/\partial X_{\alpha i})+2W=\langle V\rangle, \qquad (1)$$

where $X_{\alpha i}$ is the ith Cartesian coordinate of the αth nucleus, W is the total molecular energy, and $\langle V\rangle$ is the average over the electronic space of the total electrostatic potential energy operator. In a molecular motion for which more than one internuclear configuration exists where all energy gradients are zero, the difference in energy, ΔW, between the configurations is

$$\Delta W=\tfrac{1}{2}\Delta\langle V\rangle=-\Delta\langle T\rangle, \qquad (2)$$

where T is the electronic kinetic energy operator.

It is clear by symmetry that the "staggered" and "eclipsed" configurations of the ethane molecule are such that no net forces exist. The barrier to internal rotation then is *exactly* given by Eq. (2).

Separating $\langle V\rangle$ into its various components, one may write

$$\Delta W=\tfrac{1}{2}\{\Delta\langle V_{ee}\rangle+\Delta\langle V_{en}\rangle+\Delta V_{nn}\},$$

where the terms refer respectively to electron-electron, electron-nucleus, and nucleus-nucleus interactions. In Table I a comparison is made of ΔW and $\frac{1}{2}\Delta V_{nn}$ for several molecules assuming that the staggered configuration is the more stable. It is clear that the barrier to internal rotation in these hydrides is one half the change in internuclear repulsion energy. That is, to a very good approximation $\Delta V_{ee}=-\Delta V_{en}$ and $\Delta W=\frac{1}{2}\Delta V_{nn}$.[2]

TABLE I. Comparison of barriers and nuclear repulsion energy.[a]

	ΔW (kcal)	$\frac{1}{2}\Delta V_{nn}$ (kcal)
CH_3—CH_3	2.7–3.0	2.6
CH_3—NH_2	1.9	2.1
CH_3—OH	1.1	0.9
CH_3—C≡C—CH_3	0.0	0.0

[a] The experimental barriers were taken from the review article by E. B. Wilson in *Advances in Chemical Physics* (Interscience Publishers, Inc., New York, 1959), Vol. II, p. 367. It should also be noted that ΔV_{nn} may vary as much as 0.2 kcal, depending upon the bond distances used.

Another significant conclusion that can be drawn from Eq. (2) is that any molecular model or calculation that does not allow for a change in electronic kinetic energy would predict a barrier of zero. Thus, unless the variation in the structure of the electron density as a function of the internal rotation coordinate is taken into account no potential barrier can exist. This of course does not imply that an approximate calculation that does not *strictly* satisfy the virial theorem is meaningless. Rather, such a calculation may be qualitatively correct and still differ quantitatively from Eq. (2).

In the absence of adequate information about the electron density we are forced to proceed semi-empirically. Assuming that the results in Table I are sufficient to establish a rule, we have: a C—H bond acts primarily as if it were a unit point charge of arbitrary sign located at the proton. One can now attempt to calculate the barrier in a substituted ethane, C_2H_5X, in the following way. Assuming that the other five C—H bonds are unaffected we have $\Delta W(C_2H_5X)=\frac{5}{6}\Delta W(C_2H_6)+\Delta U$, where U is the interaction between the C—X bond and the rest of the molecule. We know that C—H acts as a unit point charge of arbitrary sign, so that we need only guess something about the C—X bond. Let us suppose that C—X can be described as a unit charge at X having the same sign as C—H. Thus if the C—X bond distance is the same as that of C—H, $\Delta U=\frac{1}{6}\Delta W(C_2H_6)$ and $\Delta W(C_2H_5X)=\Delta W(C_2H_6)$. On the other hand if C—X is the opposite sign then $\Delta W(C_2H_5X)=\frac{1}{3}\Delta W(C_2H_6)$.

Now, one might argue as follows: Since many substituted ethanes exhibit barriers[3] close to that of C_2H_6 itself, the preceding analysis shows that both C—H and C—X appear as unit point charges of the same sign. However, any conclusion drawn concerning the true charge distribution would be rather precariously based since no mention has been made of the change in electronic kinetic energy which, as previously shown, is of paramount importance. One could require the various spherical charge distributions to expand and contract successively, although there is no obvious reason why they should if they are nonpenetrating. Thus we conclude that, although electrostatic models[4] involving nonoverlapping charge distributions may be successful

as methods for calculating barriers to internal rotation, they do not shed any light on the true physical situation unless they satisfactorily account for the change in the electron density.[5]

Finally, we summarize by noting that the present work has raised two theoretical questions. (1) Why, at least in C_2H_6, do ΔV_{ee} and ΔV_{en} cancel leaving only $\frac{1}{2}\Delta V_{nn}$ for the barrier? (2) What is the correct qualitative description of the change in electronic kinetic energy and the concomitant change in the electron density?

The author is indebted to Dr. Max Wolfsberg of this department for several important suggestions.

* Research performed under the auspices of the U. S. Atomic Energy Commission.

[1] A. C. Hurley, Proc. Roy. Soc. (London) **A235**, 224 (1956). For a more detailed treatment of the applicability of the virial theorem to molecules see W. L. Clinton, J. Chem. Phys. (to be published).

[2] Because of the lack of unambiguous evidence concerning the true equilibrium configurations of CH_3OH and CH_3NH_2 we should write $|\Delta W| = \frac{1}{2}|\Delta V_{nn}|$ and only in C_2H_6 is $\Delta V_{ee} = -\Delta V_{en}$ with certainty.

[3] See E. B. Wilson in *Advances in Chemical Physics* (Interscience Publishers, Inc., New York, 1959), Vol. II.

[4] Also included under this heading are, of course, the van der Waals force models—see, for example, R. A. Mason and M. M. Kreevoy, J. Am. Chem. Soc. **77**, 5808 (1955).

[5] There are many models to which these criteria will be applied in the future. See, for example, G. M. Harris and F. E. Harris, J. Chem. Phys. **31**, 1450 (1959), and references contained therein.

Excess Free Energy in Dehydrogenated Palladium†

SISTER JUDITH MARY SINGER,* O.P., AND GILBERT W. CASTELLAN

Department of Chemistry, The Catholic University of America, Washington 17, D. C.

(Received December 4, 1959)

WE have measured the potential of the palladium-palladous ion couple in hydrochloric acid solution using palladium which had been subjected to different treatments. The palladium pieces which were alloyed with hydrogen and then dehydrogenated using ceric sulfate solution were significantly less noble than those which were not alloyed with hydrogen. This indicates that the palladium lattice acquires an excess free energy, probably as distortion free energy, in the hydrogenation-dehydrogenation cycle. Some thermodynamic implications of this have been discussed by Ubbelohde.[1]

TABLE I.

Type	Average potential (vs S.H.E., European)	Probable error
"Untreated" Pd	0.726 v	0.003 v
Gas-charged Pd-H	0.707 v	0.005 v
Electrolytically charged Pd-H	0.707 v	0.003 v

Samples of palladium of three types were used. Type A: "untreated" Pd. The "untreated" Pd was pure (99.9%) metal from the supplier; it was flamed, dipped in conc HNO_3, rinsed with distilled H_2O, flamed again, and placed in the measuring cell. Type B: gas-charged Pd-H. The gas-charged alloy was prepared by heating a piece of 1-mil Pd foil and allowing it to cool slowly in an atmosphere of hydrogen. Type C: electrolytically charged Pd-H. This alloy was prepared by cathodizing a 1 mil foil at a current density of 0.02 amp/cm² for 20 min.

After the formation of the alloys, they were immersed in ceric sulfate solution. The removal of the hydrogen was followed by titrating samples of the ceric sulfate at intervals. In this same way the composition of the alloy was determined. After the hydrogen was completely removed the foils were rinsed with distilled water and placed in the measuring cell.

The measuring cell was thermostated at 28.5°C. It contained a solution which was 0.121 *M* in $PdCl_2$ and 1.113 *M* in HCl. The potential of the Pd foil was measured against a saturated calomel electrode using a Beckman H-2 *p*H meter which was calibrated against a slide wire potentiometer. Purified N_2 was passed through the cell during the potential measurements. The potential of each electrode was followed over a period of about five hours. The potential reaches a steady value in the latter part of that period; this value then drifts slowly apparently because of the evaporation of the solution by the N_2 stream.

The average atom ratio H/Pd in the electrolytically-charged alloys was about 0.9, while in the gas-charged alloys, the ratio ranged from 0.3 to 0.6; however, there seemed to be no correlation between variations of the potential and variations in the H/Pd ratio in the gas-charged alloys. The average values of the potential and the probable errors are tabulated in Table I. Ten determinations were done on each type.

It is interesting that the untreated metal is more noble than either of the others by 0.02 v. This difference is significant and shows that a distortion free energy of about 900 cal/mole remains in the metal after it has has been charged with hydrogen and then dehydrogenated. The magnitude of this distortion free energy is the same within the experimental error for the gas-charged and the electrolytically charged alloy.

This work had a quite interesting sidelight. The rate of removal of hydrogen from the gas-charged alloy by ceric sulfate may be more than five times slower than the rate of removal from the electrolytically charged alloy. This seems to depend on the details in the preparation of the gas-charged alloy.

This investigation was originally undertaken in the attempt to determine whether there was a measurable difference in the chemical potential of palladium be-

tween the gas-charged and the electrolytically-charged Pd-H alloys; such as was claimed by Castellan, Hoare, and Schuldiner.[2] The evidence finally obtained and presented here does not appear to bear directly on this question. In any case, the effects which first led to the postulate of a free energy difference between gas-charged and electrolytically charged β-Pd-H have been adequately explained on other grounds.[3,4]

* Present address: Rosary High School, Detroit, Michigan.
† This research was supported by the U. S. Air Force.
[1] A. R. Ubbelohde, Proc. Roy. Soc. (London) **A159**, 295 (1937).
[2] G. W. Castellan, J. P. Hoare, and S. Schuldiner, J. Chem. Phys. **28**, 16 (1958).
[3] T. B. Flanagan and F. A. Lewis, J. Chem. Phys. **29**, 1417 (1958).
[4] R. J. Fallon and G. W. Castellan, J. Phys. Chem. **64**, 4 (1960).

Bond Polarizability Components*

GEORGE W. CHANTRY AND ROBERT A. PLANE

Department of Chemistry, Cornell University, Ithaca, New York

(Received April 15, 1960)

IN two recent papers,[1] Smith and Mortensen have pointed out that it is impossible to deduce (from light depolarization data, Kerr constants, etc.) both the longitudinal and the transverse bond polarizability components for most polyatomic molecules. A tetrahedral XY_4 molecule is a case in point. Since the anisotropy is necessarily zero, only one combination of the two bond components can be measured, i.e., α_l+2_p where α_l is the polarizability along the bond axis and α_p that perpendicular to the bond axis. This difficulty can be overcome in two ways. The first, as used by Denbigh,[2] is to assume axial symmetry for the carbonyl bond in acetone. This assumption has been criticized, but shown in certain cases (C—H and C-halogen) to lead to approximately correct values. The second is to use the absolute Raman intensities to provide the needed additional information. This method was not considered by Smith and Mortensen, although it had been used earlier by Yoshino and Bernstein[3] for the case of methane. This method does, however, depend on the validity of the theory due to Wolkenstein,[4] and Yoshino and Bernstein assumed this validity without proof. Recently, Chantry and Woodward[5] have given strong evidence in support of Wolkenstein's theory, expecially for tetrahalides of Group IV. It seems permissible, therefore, to use available Raman intensity data to calculate the bond polarizability components for CCl_4 and to compare them with those for other molecules where this resolution has been made.

Allen and Bernstein[6] have given relative values for the squares of the four derived invariants for CCl_4($\bar{\alpha}_1'$, γ_2', γ_3' and γ_4'). Using the absolute value for $(\partial\alpha/\partial r)_{C-Cl}$ deduced by Chantry and Plane[7] it is possible to put these on an absolute scale. The values then are $\bar{\alpha}_1'=0.672$, $\gamma_2'=0.463$, $\gamma_3'=0.875$ and $\gamma_4'=0.547$. The units for these quantities are such that on substitution into the equation

$$\gamma_3'=8^{\frac{1}{2}}M_Y^{-\frac{1}{2}}(\alpha_l-\alpha_p)/r,$$

derived using the Wolkenstein theory, M_Y (the mass of atom Y) is in chemical atomic weight units, $(\alpha_l-\alpha_p)$ is in A^3, and r (the XY internuclear distance) is in A. It follows at once that $(\alpha_l-\alpha_p)$ is 1.73 A^3. (The positive sign is assumed to be the more reasonable from the arguments given by Bell.[8]) The mean polarizability[2] is 7.83 A^3 and, therefore, $\alpha_l=3.76$ A^3 and $\alpha_p=2.04$ A^3.

The two F_2 type invariants are given by equations of the form

$$\gamma_i'=2[l_{3i}(\alpha_l'-\alpha_p')+l_{4i}(\alpha_l-\alpha_p)/r]/3^{\frac{1}{2}}, \qquad i=3,4,$$

and $(\alpha_l'-\alpha_p')=(\partial\alpha_l/\partial r-\partial\alpha_p/\partial r)$. The l_{Ki} are entries in the F_2 block of the matrix $\mathfrak{L}$, which relates symmetry coordinates to normal coordinates, and the appropriate quantities for CCl_4 have been listed by Chantry and Woodward.[5] Therefore, from either γ_3' or γ_4', the derivative of the bond anisotropy can be calculated. The value found is $(\alpha_l'-\alpha_p')=3.73$ A^2. The mean derived polarizability is[7] 6.00 A^2; hence $\alpha_l'=4.49$ A^2 and $\alpha_p'=0.76$ A^2.

For methane, Yoshino and Bernstein[3] report, for the sign convention used above: $\alpha_l=0.858$ A^3, $\alpha_p=0.546$ A^3, $\alpha_l'=2.441$ A^2, and $\alpha_p'=0.34$ A^2. The nonderived components for both CH_4 and CCl_4 agree well with those obtained by Denbigh: for CCl_4, $\alpha_l=3.67$ A^3 and $\alpha_p=2.08$ A^3; for CH_4, $\alpha_l=0.79$ A^3 and $\alpha_p=0.58$ A^3.

It seems probable that the derived bond polarizabilities give more information concerning the bonding electrons than do the bond polarizabilities themselves, since the polarizability of the inner core electrons should vary only slightly with changing internuclear distance. An interesting aspect of the numbers quoted above is the small value of the ratio α_p'/α_l'. For cyanide ion, our measurements give these quantities as $\alpha_l'=2.61$ A^2 and $\alpha_p'=1.21$ A^2, and hence the ratio is much larger. A tentative hypothesis would be that this ratio is small for single bonds and larger for multiple bonds. However, even were this established, the rule would apply only to those cases where the bond has cylindrical symmetry (σ, $p_\pi-p_\pi$ triple bond and certain cases of $d_\pi-p_\pi$ double bond). Cases where the cylindrical symmetry is absent (e.g., p_π—p_π double bond) will have a large derived anisotropy even though multiple bonding is present.

* This research was supported by the United States Air Force through the Air Force Office of Scientific Research of the Air Research and Development Command. Reproduction in whole or in part is permitted for any purpose of the United States Government.
[1] R. P. Smith and E. M. Mortensen, J. Chem. Phys. **32**, 502, 508 (1960).
[2] K. G. Denbigh, Trans. Faraday Soc. **36**, 936 (1940).

[3] T. Yoshino and H. J. Bernstein, Molecular Spectroscopy **2**, 241 (1958).
[4] M. Wolkenstein, Compt. rend. acad. sci. U.R.S.S. **32**, 185 (1941).
[5] G. W. Chantry and L. A. Woodward, Trans. Faraday Soc. (to be published).
[6] G. Allen and H. J. Bernstein, Can. J. Chem. **32**, 1124 (1954).
[7] G. W. Chantry and R. A. Plane, J. Chem. Phys. **32**, 319 (1960).
[8] R. P. Bell, Trans. Faraday Soc. **38**, 422 (1942).

Dipole Moment and Conformation of 2-Chlorocyclohexanone

SAMUEL YAROSLAVSKY AND ERNST D. BERGMANN

Department of Organic Chemistry, Hebrew University, Jerusalem, Israel

(Received February 12, 1960)

KOZIMA and Yamanouchi[1] have recently shown for 2-chlorocyclohexanone that the intensity of the C–Cl vibration, in the *liquid* and *dissolved* (CS_2) state, of the axial conformation increases with rising temperature as compared with the intensity pertaining to the equatorial form They concluded, therefore, that the equatorial conformation is more stable in the liquid and dissolved state. Measurements of the dipole moment of 2-chlorocyclohexanone in benzene solution at varying temperatures support this conclusion.

The temperatures chosen were 27.4° and 52.0°C, while Kumler and Huitric[2] have carried out the determination in the same solvent at 30°C.

The measurements are reported in Tables I and II; the calculations have been carried out using the method of Halverstadt and Kumler.[3]

The angles between the carbonyl and the equatorial and axial bond on carbon atom 2 of cyclohexanone are 51°55′ and 110°32′(±2′), respectively.[4] Assuming the group moments of the carbonyl and chlorine to be 2.90 *D*[5] and 2.07*D*,[6] respectively, the theoretical moments of the equatorial and the axial conformations of 2-chlorocyclohexanone are 4.49*D* and 2.91*D*.

TABLE I.

N_2 (mole fraction of solute)	ϵ_{12}	ν_{12}
	52.0°C	
0.002281	2.257	1.18086
0.005757	2.315	1.17880
0.006878	2.327	1.17791
0.008642	2.359	1.17680
0.009931	2.382	1.17630
	27.4°C	
0.006766	2.400	1.14471
0.009109	2.451	1.14277

TABLE II.

ϵ_1	α	ν_1	β	$P_{2\infty}$	PE_2	$\mu(D)$
2.220	16.20	1.1823	−0.62	283.34	31.61	3.66
2.254	21.77	1.1495	−0.83	349.86	31.61	3.96

The percentage c_{eq} of the equatorial conformation at either of the two temperatures was computed using the equation[7]

$$\mu_{fd}^2 = c_{eq}\mu_{eq}^2 + c_{ax}\mu_{ax}^2.$$

The results summarized in Table III show that the relative quantity of the equatorial form decreases with rising temperature; in benzene solution it is, therefore, more stable than the axial form.[8]

TABLE III.

Temperature (°C)	Dipole moment (*D*)	Percentage (c_{eq}) of the equatorial conformation
27.4	3.96	61
30[a]	3.78	50
52.0	3.66	41

[a] See footnote reference 2.

In the infrared, 2-chlorocyclohexanone shows a doublet in the carbonyl region, both in the liquid and dissolved (CCl_4) state. The intensity of one band decreases somewhat with increasing temperature, as compared with the intensity of the other. The former band corresponds, therefore, to the equatorial conformation; the latter to the axial one. The assumption to the contrary, made by Josien,[9] appears thus to be untenable.

[1] K. Kozima and Y. Yamanouchi, J. Am Chem. Soc. **81**, 4159 (1959).
[2] W. D. Kumler and A. C. Huitric, J. Am. Chem. Soc. **78**, 3369 (1956). The paper does not indicate the temperature at which the authors carried out their measurements. The referee drew our attention to the fact that this temperature obviously was 30°C.
[3] I. F. Halverstadt and W. D. Kumler, J. Am. Chem. Soc. **64**, 2988 (1942).
[4] The calculation is based on the vector analysis method of E. J. Corey and R. A. Sneen, J. Am. Chem. Soc. **77**, 2505 (1955). J. Allinger and N. L. Allinger [Tetrahedron **2**, 64 (1958)] give the slightly different figures 51°, 54°, and 109° 51′; the above values are more accurate. See E. D. Bergmann and S. Yaroslavsky, J. Am. Chem. Soc. (to be published).
[5] R. J. W. Le Fèvre, *Dipole Moments* (Methuen & Company, Ltd., London, 1953), p. 63.
[6] O. Hassel and E. Naeshagen, Z. physik. Chem. **B15**, 373 (1932).
[7] C. P. Smyth, *Dielectric Behavior and Structure* (McGraw-Hill Book Company, New York, 1955), p. 294.
[8] For analogous computations regarding the various conformations of chloroacetone, see S. Mizushima *et al.*, J. Chem. Phys. **20**, 1720 (1952); **21**, 815 (1953); of acrolein, see R. Wagner, J. Fine, J. W. Simmons, and J. H. Goldstein, J. Chem. Phys. **26**, 634 (1957); of butadiene, see R. S. Rasmussen, D. D. Tunnicliff, and R. R. Brattain, J. Chem. Phys. **11**, 432 (1943).
[9] M. L. Josien and C. Castinel, Bull. soc. chim. France **1958**, 801.

F^{19} Spectra of Phosphorus(V) Fluorides

W. Mahler and E. L. Muetterties

Central Research Department, Experimental Station, E. I. du Pont de Nemours and Company, Wilmington, Delaware

(Received March 23, 1960)

THE NMR spectroscopic equivalence of fluorine atoms in PF_5[1] is unexpected because of the proven trigonal bipyramid structure.[2,3] Several explanations are possible: (1) small chemical shift between axial and equatorial fluorine atoms, (2) fast intermolecular exchange, (3) intramolecular exchange,[4] and (4) F_{axial}–$F_{equatorial}$ coupling≫chemical shift. At present, only one of these (2) can be eliminated. Since P^{31}–F^{19} coupling is observed, equivalence due to any intermolecular exchange process is not possible.

We have examined the F^{19} spectrum of the isologous CF_3PF_4 and infer that an exceedingly small chemical shift is the probable explanation for equivalence in PF_5.

The F^{19} spectrum at 56.4 Mc of CF_3PF_4 consists of a pair (P–F coupling, $J=1103$ cps) of two overlapping quadruplets (F_P–F_C couplings, $J=12$ cps), which, respectively, represent PF and PF_3 fluorine environments, and a pair ($J_{FC-P}=170$ cps) of two overlapping quadruplets which represent the CF_3 fluorine atoms.[5]

The CF_3PF_4 spectrum is consistent with a trigonal bipyramid structure in which the CF_3 group occupies an apical site. The fluorine atom at the other apex is chemically shifted from the three equatorial fluorines by just 0.07 ppm (Fig. 1). This temperature-independent ($-100°$ to $+25°$) shift is unaccompanied by second-order effects which limits J_{PF-PF_3} to 0.4 cps or less. In CF_3PF_4, therefore, there is a real but very small chemical shift between axial and equatorial fluorine atoms. The shift between fluorine atoms in analogous environments in the more symmetrical PF_5 is likely to be still smaller. We have reexamined PF_5 at 56.4 Mc with a resolution of 0.3 cps and observed "equivalence" of the fluorine atoms so that the chemical shift would be less than 0.05 ppm.[6]

The details of the CF_3PF_4 spectrum raise new questions. In particular, the very small chemical shift between axial and equatorial fluorine atoms is difficult to explain. An intramolecular exchange (e.g., as envisaged by Berry[4]) could account for the absence of a chemical shift in PF_5. However, this explanation seems unlikely in that an analogous process (e.g., positional exchange through a tetragonal pyramid intermediate), does not occur in CF_3PF_4 since there is a detectable and temperature-insensitive chemical shift. The small F_{axial}–$F_{equatorial}$ coupling, and the identical F–P couplings for apical and equatorial fluorine atoms, are also unexpected in view of the usual large shifts and coupling constants in fluorine compounds. For comparison, the base·PF_5 complexes[7] have internal fluorine shifts of about 7 ppm and F–F coupling constants of

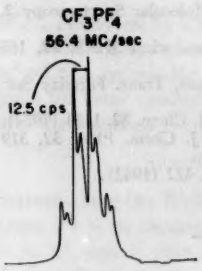

FIG. 1. One of the pairs of two overlapping quadruplets which represent the PF and PF_3 resonances in the F^{19} spectrum of CF_3PF_4.

45–70 cps; in SF_4 (structurally analogous to PF_5) the F–F shift is 47 ppm and the coupling constant is 78 cps.[8]

Because of the unusual spectral characteristics of the trigonal bipyramid structure,[9] we intend to explore this problem further with related MF_5 and substituted MF_5 molecules.

[1] H. S. Gutowsky, D. W. McCall, and C. P. Slichter, J. Chem. Phys. **21**, 279 (1953).
[2] H. Braune and P. Pinnow, Z. physik. Chem. **B35**, 239 (1937).
[3] L. O. Brockway and J. Y. Beach, J. Am. Chem. Soc. **60**, 1836 (1938).
[4] S. Berry [J. Chem. Phys. **32**, 936 (1960)] has proposed an intramolecular exchange in PF_5 based on pseudorotation.
[5] The chemical shifts are $PF_3=-10.00$ ppm, $PF=-9.93$ ppm and $CF_3=-3.37$ ppm (CF_3COOH reference).
[6] The chemical shift for liquid PF_5 is -0.68 ppm (CF_3COOH reference); owing to a calculation error, the value given by E. L. Muetterties and W. D. Phillips [J. Am. Chem. Soc. **81**, 1084 (1959)] is incorrect.
[7] E. L. Muetterties, T. A. Bither, M. W. Farlow, and D. D. Coffman, J. Inorg. & Nuclear Chem. (to be published).
[8] F. A. Cotton, J. W. George, and J. S. Waugh, J. Chem. Phys. **28**, 994 (1958); and E. L. Muetterties and W. D. Phillips, footnote reference 6.
[9] F. A. Cotton, A. Danti, J. S. Waugh, and R. W. Fessenden [J. Chem. Phys. **29**, 1427 (1958)] could detect only one C^{13} resonance in iron pentacarbonyl and one of their explanations for the spectroscopic equivalence of carbon atoms in this molecule is a small chemical shift (<40 cps).

Surface Catalyzed Excitation with N and O Atoms*

Gene G. Mannella, Robert R. Reeves, and Paul Harteck

Chemistry Department, Rensselaer Polytechnic Institute, Troy, New York

(Received April 18, 1960)

IN a previous publication[1] the formation of electronically excited species by atom recombination on a cool surface (about 300°K) and subsequent radiation or reaction of the excited species was reported. This surface catalyzed excitation (herein referred to as SCE) was, specifically, observed when N and O atoms were passed over Co, Ni, or prepared Ag at about 1 mm. pressure and room temperature. It had been postulated[1] that the luminosity observed was due to the formation of an electronically excited NO on the metal

surface which diffused into the gas phase and radiated or reacted with a ground state N atom to form an electronically excited N_2 molecule which then radiated.

The majority of the earlier work was done with Ni, which gave glows which were about 5 mm thick. The lifetime of the excited species calculated from the thickness of these glows was just long enough to fit with the upper limit of the lifetime of $NO(B\,^2\Pi)$ which is about 10^{-4} sec.[2] Under certain conditions the luminosity over Co grows much larger and the lifetime of the excited species is no longer compatible with the values suggested for $NO(B\,^2\Pi)$. The glow over Co is enhanced when a very low O atom concentration is used; spectroscopically, this glow consists almost entirely of the N_2 first positive system with the strongest bands from $v'=8$ and 6. Furthermore, when this glow is photographed through a red filter, the glow appears much larger than it does to the eye. When photographed through a blue filter, practically no blue NO radiation is seen. This seems to indicate that in the case of Co an excited N_2 is the primary product being formed.

It is possible to explain both the long lifetime of the species responsible for the glow and the intensity of the bands from $v'=8$ and 6 by assuming that the primary excited molecule is an $N_2(A\,^3\Sigma_u^+)$. The small amount of O atoms which are necessary to enhance the glow over Co are probably required to condition the surface of the metal and permit the absorbed N atoms which form the excited N_2 molecule to be attached with a binding energy of about 1 ev or less. The $N_2(A\,^3\Sigma_u^+)$ and $N_2(B\,^3\Pi_g)$ potential energy curves cross at about 8.5–9.0 ev or $v=6$–8. The meta-stable $N_2(A\,^3\Sigma_u^+)$, which is the upper level of the well-known Vegard-Kaplan system, forms on the metal surface, diffuses into the gas phase and, by collision, crosses into the $(B\,^3\Pi_g)$ state at $v=8$ and 6 and then radiates immediately from the $(B\,^3\Pi_g)$ back to the $(A\,^3\Sigma_u^+)$. The lifetime of the species responsible for the glow is estimated from both the diffusion distances and the linear velocity of the gas stream to be about 10^{-3} sec. This represents the time required for the $N_2(A\,^3\Sigma_u^+)$ to vibrationally relax into the crossing region and by collision cross into the $B\,^3\Pi_g$ state. The time interval of 10^{-3} sec is permissable since the radiative lifetime of the $N_2(A\,^3\Sigma_u^+)$ is reported to be at least 10^{-2} sec.[3]

When the glow over Ni is photographed through red and blue filters, it is apparent that two separate radiations are present. A large red glow similar to that observed over Co, but somewhat smaller in size is present. However, the blue filter shows a blue radiation extending out only several mm into the gas. Since spectrograms show the N_2 first positive system and NOβ system, it is logical to conclude that two separate mechanisms are involved here; i.e., the formation of $N_2(A\,^3\Sigma_u^+)$ as outlined before which gives the red glow and the formation of $NO(B\,^2\Pi)$ as detailed in (1) to give the β bands. The lifetime of the species responsible for the glow seen through the blue filter is estimated to be 10^{-6} sec, which fits in well with the reported values for $NO(B\,^2\Pi)$.

There is another interesting application of the $N_2(A\,^3\Sigma_u^+)$ crossing. The present accepted mechanism for the gas phase recombination of N atoms is the primary formation of an $N_2(^5\Sigma_g^+)$ which crosses the $(B\,^3\Pi_g)$ slightly above $v=12$.[4,5] The nitrogen afterglow consists of radiation from the $(B\,^3\Pi_g)$ to the $(A\,^3\Sigma_u^+)$, the most intense bands being from $v=12$, 11, and 10. However, an unusually intense band from $v=6$ has been discussed by several authors.[6,7] It may well be that the lower levels of the $(B\,^3\Pi_g)$ are populated by analogous mechanism via the formation of the $A\,^3\Sigma_u^+$ state.

A red glow similar to those produced over Ag, Ni, and Co can also be produced over Cu. But, if N atoms *alone* are passed over a Cu plate (maintained at a reasonably low temperature) the blue glow of the second positive system of nitrogen appears $(C\,^3\Pi_u \rightarrow B\,^3\Pi_g)$. This blue glow is less intense than the red glows reported earlier and extends only 1–2 mm into the gas phase.

Transitions from the $C\,^3\Pi_u$ level are indeed very striking, since the excitation of this level is about 11.2 ev, compared to D_{N_2} which is only 9.76 ev. Thus, SCE can give rise to the formation of species excited above the dissociation energy of the ground state. The mechanism for such a reaction must necessarily involve at least three atoms; possibly two excited molecules.

Thus it appears that what we believed to be a rather singular phenomenon now must include the formation of $NO(B\,^2\Pi)$, $N_2(A\,^3\Sigma_u^+)$, and even $N_2(C\,^3\Pi_u)$.

* The research reported in this document has been sponsored by the Geophysics Research Directorate of the Air Force Cambridge Research Center, Air Research and Development Command.

[1] R. R. Reeves, G. Mannella, and P. Harteck, J. Chem. Phys. 32, 946 (1960).
[2] J. C. Keck, J. C. Camm, B. Kivel, and T. Wentink, Ann. Phys. 7, 1 (1959).
[3] W. Lichten, J. Chem. Phys. 26, 306 (1957).
[4] J. Berkowitz, W. A. Chupka and G. B. Kistiakowsky, J. Chem. Phys. 25, 457 (1956).
[5] A. G. Gaydon, *Dissociation Energies* (Dover Publications, New York, 1950).
[6] O. Oldenberg, Phys. Rev. 90, 727 (1953).
[7] G. Gario and J. Kaplan, Z. Physik 58, 769 (1929).

Paramagnetic Resonance Absorption of Triphenylmethyl*

D. B. Chesnut and G. J. Sloan

Central Research Department, Experimental Station, E. I. du Pont de Nemours and Company, Wilmington, Delaware

(Received April 22, 1960)

THE resolved isotropic hyperfine structure of the electron paramagnetic resonance spectrum of the triphenylmethyl radical has been observed. Better than

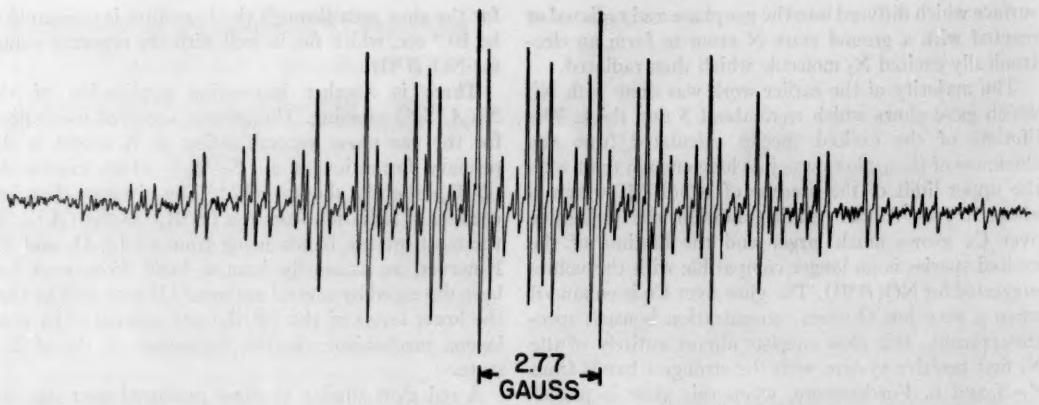

FIG. 1. The derivative of the resonance absorption of a 10^{-3} molar solution of triphenylmethyl in toluene. The spectrum was recorded at $-20°C$.

100 of the 196 theoretical lines have been resolved and analyzed in terms of the three ortho, meta, and para proton coupling constants.

The derivative of the resonance absorption of a 10^{-3} molar solution of triphenylmethyl in toluene is shown in Fig. 1. Spectra were recorded using a Varian X-band spectrometer employing 100-kc field modulation and a Varian 12-in. magnet. The measurements were carried out between $-20°$ and $-50°C$, since at higher temperatures line broadening begins to obscure some of the fine structure while at lower temperatures the decrease in the dissociation of the hexaphenylethane reduces the signal-to-noise ratio. A sweep field of approximately 5×10^{-3} gauss was used throughout the measurements; the observed line widths are close to 0.05 gauss.

The para proton coupling constant is 2.77 gauss[1] and can be assigned unambiguously since the separation of the two most intense lines of the spectrum is a direct measure of the para proton splitting. The other coupling constants of 2.53 and 1.11 gauss for the two six-proton sets cannot be so defined. However, theoretical calculations[2] indicate that the ortho set should have the larger splitting of the two so that we may tentatively assign the 2.53 gauss value to the ortho protons and the 1.11 gauss value to the meta protons.

Jarrett[3] has recently uncovered an error in the valence bond calculations by Brovetto and Ferroni[2] of the integrated spin densities for triphenylmethyl. Jarrett finds the integrated spin densities at the ortho, meta and para positions in the planar configuration to be $+0.159$, -0.105 and $+0.203$, respectively. These values yield the proper ordering of the magnitudes of the experimentally observed coupling constants but give Q values which are unequal and considerably lower than the currently accepted value of -22.5 gauss.[4]

* Contribution No. 621 from the Central Research Department, Experimental Station, E. I. du Pont de Nemours and Company.

[1] The errors in the absolute values of the three coupling constants are estimated to be ±0.02 gauss. The signs of the coupling constants are, of course, not determinable from the present experiment.

[2] P. Brovetto and S. Ferroni, Nuovo cimento **5**, 142 (1957); F. C. Adam and S. I. Weissman, J. Am. Chem. Soc. **80**, 2057 (1958).

[3] H. S. Jarrett (private communication).

[4] H. M. McConnell and D. B. Chesnut, J. Chem. Phys. **28**, 107 (1958); H. M. McConnell and H. H. Dearman, *ibid.* **28**, 51 (1958); S. I. Weissman, T. R. Tuttie, and E. de Boer, J. Phys. Chem. **61**, 28 (1957).